JOURNAL
OF
APPLIED PHYSICS

UNIVERSITY OF ILLINOIS
LIBRARY
SEP 25 1961
CHICAGO

ber

1

32

9

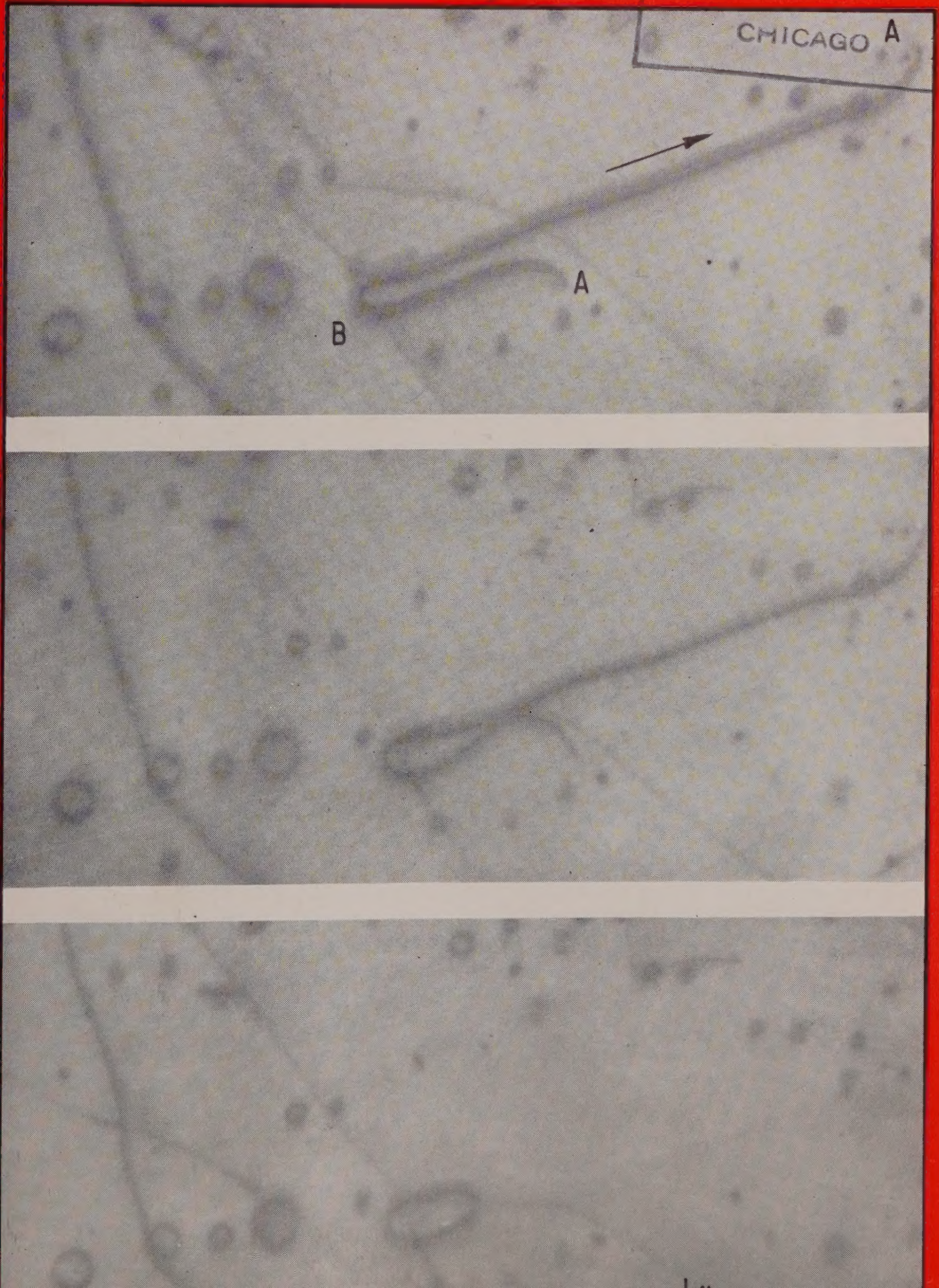

Formation
a Dislocatio
Loop in
Cadmium a
−100° C.

See Pages
1750 and 18

HARSHAW CRYSTALS are 1728
TIMES LARGER
than 25 years ago
with "Harshaw Quality" inherent in each crystal
1936
1″x 1″
1955
5″x 5″
1961
11½″x 11½″

This year Harshaw's Crystal Division celebrates its Silver Anniversary. In these 25 years the "art" of growing crystals has given way to scientific procedures. With expanded crystal research and development laboratories, and recently doubled production facilities, Harshaw stands ready to produce your crystals—regardless of technical nature or production magnitude. Our physics, chemistry, and engineering departments enjoy the challenge of increasingly stringent demands from scientists and instrument manufacturers for infrared and ultraviolet optical crystals, and scintillation phosphors.

OPTICAL CRYSTALS
For Infrared and Ultra Violet Transmitting Optics

- **Sodium Chloride**
- **Sodium Chloride Monochromator Plates**
- **Potassium Bromide**
- **Potassium Bromide Pellet Powder (through 200 on 325 mesh).**
- **Potassium Chloride**
- **Optical Silver Chloride**
- **Thallium Bromide Iodide**
- **Lithium Fluoride**
- **Lithium Fluoride Monochromator Plates**
- **Calcium Fluoride**
- **Barium Fluoride**
- **Cesium Bromide**
- **Cesium Iodide**

SCINTILLATION
Mounted NaI (Tl) Crystals

Crystal detectors designed for your most sophisticated counting problems. Our physics and engineering groups are available to assist you.

- **Other Phosphors—Rough Cut Thallium Activated Sodium Iodide Crystal Blanks**
- **Europium Activated Lithium Iodide (Normal)**
- **Europium Activated Lithium Iodide (96% Li⁶ Enriched)**
- **Thallium Activated Cesium Iodide**
- **Thallium Activated Potassium Iodide**
- **Anthracene**
- **Plastic Phosphors**

Write for our 36-page booklet "Synthetic Optical Crystals" or our 44-page booklet "Scintillation Phosphors"

The Harshaw Chemical Company HARSHAW **Crystal Division**
1945 East 97th Street • Cleveland 6, Ohio
Utrecht, Netherlands—Contact Harshaw-Van Der Hoorn N. V., Juffaseweg 186

JOURNAL OF APPLIED PHYSICS

Vol. 32, No. 9 SEPTEMBER, 1961

In This Issue

Mosaic Size in Lead from X-Ray Measurements . . . . Yosio Hiki and Ryukiti R. Hasiguti 1647
Electrical Conduction and Breakdown in High-Pressure (0.25–300 mm) Rare Gases . . . . . . R. Forman 1651
Role of Crystal Structure in Diffusion. I. Diffusion Paths in Closest-Paked Crystals . . . Leonid V. Azároff 1658
Role of Crystal Structure in Diffusion. II. Activation Energies for Diffusion in Closest-Paked Structures . . . . Leonid V. Azároff 1663
Properties of High-Resistivity Gallium Arsenide Compensated with Diffused Copper . . . . Joseph Blanc, Richard H. Bube, and Harold E. MacDonald 1666
Flash Method of Determining Thermal Diffusivity, Heat Capacity, and Thermal Conductivity . . . . . . W. J. Parker, R. J. Jenkins, C. P. Butler, and G. L. Abbott 1679
Surface Layer in $BaTiO_3$ Single Crystals . . . . Ennio Fatuzzo and Walter J. Merz 1685
Thermal Conductivity of Porous Media. I. Unconsolidated Sands . . . W. Woodside and J. H. Messmer 1688
Thermal Conductivity of Porous Media. II. Consolidated Rocks . . . W. Woodside and J. H. Messmer 1699
Cross-Section Ratios of Sensitizing Centers in Photoconductors . . . . Richard H. Bube 1707
Effect of Gaseous Ambients upon $1/f$ Noise in Germanium Filaments . V. E. Noble and J. E. Thomas, Jr. 1709
Fields in Cavity-Excited Accelerators . . . . E. G. Cristal and J. Van Bladel 1715
Application of the Three-Parameter Stress Function to Natural Rubbers of Widely Different Hardness . . . . A. J. Carmichael and H. W. Holdaway 1724
Effect of Temperature on the Exoemission of Electrons from Abraded Aluminum Surfaces . . . . W. T. Pimbley and E. E. Francis 1729
Effect of Pressure on the Energy Gap of Bi_2Te_3 . . . . . . Che-Yu Li, A. L. Ruoff, and C. W. Spencer 1733
Generalized Coupled Mode Theory . . . . M. C. Pease 1736
Thermorheological Simplicity in Extrusion Flow Curves of High Polymers . . . . Katsuhiko Ito 1743
Nonbasal Glide in Dislocation-Free Cadmium Crystals. I. The $(10\bar{1}1)$ $[1\bar{2}10]$ System . . . . P. B. Price 1746
Nonbasal Glide in Dislocation-Free Cadmium Crystals. II. The $(11\bar{2}2)$ $[\bar{1}\bar{1}23]$ System . . . . P. B. Price 1750
Electromagnetic Surface Waves on a Plane Interface . . . . B. A. Lengyel and K. M. Mitzner 1758
Precipitation Sites in Aluminum Alloys . . . . G. R. Frank, Jr., D. L. Robinson, and G. Thomas 1763
Transitions and Relaxations in Polytetrafluoroethylene . . . . R. K. Eby and K. M. Sinnott 1765
Characteristics of the Annealing Kinetics of Tin Films Deposited at 88°K . . . . J. Priest, C. Chiou, and H. L. Caswell 1772
Slip Patterns on Boron-Doped Silicon Surfaces . . . . H. J. Queisser 1776
Acoustical Study of Quench-Aging in α Cu-Al Alloys . . . . T. J. Koppenaal and M. E. Fine 1781

Letters to the Editor:

Resistance as Dissipation into Many Reactive Circuits: Landau Damping and Nyquist's Noise Theorem . . . . O. Buneman 1783
Thermionic Emission of UC-Nb . . . . R. H. Abrams, Jr., and F. E. Jamerson 1783
Forces in Dielectric Fluids . . . . James D. Horgan and David L. Edwards 1784
Formation of Liquid Jets in Nonuniform Electric Fields . . . . Herbert A. Pohl 1784
Phase Diagram for the Pseudobinary System $Ag_2Te-Sb_2Te_3$ . . . . J. P. McHugh, W. A. Tiller, S. E. Haszko, and J. H. Wernick 1785
Angular Dependence of Torque in Anisotropic Permally Films . . . W. D. Doyle, J. E. Rudisill, and S. Shtrikman 1785
Zero-Field Splitting of the Cr^{3+} Ground State in YGa and YAl Garnet . . . . . . J. W. Carson and R. L. White 1787
Preparation of Single-Crystal Boron . . . . Claude P. Talley 1787
Possibility of a Spin Wave Magnetic-Moment Detector . . . . T. B. Day and J. Sucher 1788
Photovoltaic Effects in Cs_3Sb Films . . . . Frederick Wooten 1789
Dislocation Density and Flow Stress of Sodium Chloride . . . . W. in der Schmitten and P. Hassen 1790
Quasi-Brillouin Electron Streams . . . . M. H. Miller 1791
Liquidlike Layers on Ice . . . . H. H. G. Jellinek 1793
Available Power from a Nonideal Thermal Source . . . . Paul Penfield, Jr. 1793
Equation of Motion of the Torsion Pendulum and the Complex Modulus . . . . N. W. Tschoegl 1794
Friction of Molybdenum Diselenide . . . . Melvin T. Lavik, T. Bruce Daniel, and A. Neal Abbott 1795
Similarity Function for Pattern Recognition . . . . Dan McLachlan, Jr. 1795
Reflection of Electromagnetic Waves at Electron Density Ramps . . . . Leonard S. Taylor 1796
Voids in Resolidified Drops of Molten Metal . . . . J. C. Kelly 1797
Thermal Conductivity in Two-Phase Alloys . . . . J. B. Schroeder 1798
Charged Dislocations in Ionic Crystals . . . . F. Rueda and W. Dekeyser 1799
Low-Temperature Internal Friction Peaks in Single Crystals of NaCl and LiF . . . . Anthony Taylor 1799
Angular Dependence of Magnetoresistance in HgSe . . . . Theodore C. Harman 1800
Thermoelastic Equations and Grueneisen's Relation . . . . A. M. Freudenthal 1801
Thermionic Emission from a Tantalum Crystal in Cesium or Rubidium Vapor . . . . H. F. Webster 1802
Errata: On Three-Dimensional Space Charge Flow . . . . J. Rosenblatt 1803
Erratum: Use of $PrCl_3$ in a Solid-State Infrared Quantum Counter . . . . John F. Porter, Jr. 1803

Books Reviewed 1803
Announcements 1806
Cover Photograph 1806
Index to Advertisers xxx

JOURNAL OF APPLIED PHYSICS

A journal of general physics and its applications to other sciences and to industry

Published by the

American Institute of Physics

GOVERNING BOARD

Members

Ralph A. Sawyer, *Chairman*
James G. Baker
R. H. Bolt
Wallace R. Brode
Harvey Brooks
Dirk Brouwer
J. H. Elliott
Herbert A. Erf
N. S. Gingrich
S. A. Goudsmit
W. W. Havens, Jr.
W. V. Houston
Winston E. Kock
R. Bruce Lindsay
David L. MacAdam
H. Victor Neher
Leonard O. Olsen
C. J. Overbeck
Ray Pepinsky
S. L. Quimby
Ralph A. Sawyer
Francis W. Sears
Frederick Seitz
C. Guy Suits
Mary E. Warga
William R. Willets

ADMINISTRATION

Elmer Hutchisson
Director

Wallace Waterfall
Secretary and Treasurer

Henry A. Barton
Administrative Consultant

W. C. Kelly
Director of Education

Eugene H. Kone
Director of Public Relations

Hugh C. Wolfe
Director of Publications

Kathryn Setze
Assistant Treasurer

James E. Mills
Supervisor, Editorial Department

Sistina Greco
Circulation Manager

Edward Tober
Manager, Production and Distribution

Theodore Vorburger
Advertising Manager

Emily Wolf
Manager, Special Services

Editor
J. H. Crawford, Jr.

Assistant Editor
Ethel McMillan

Editorial Board

J. E. Goldman
J. L. Tuck
C. A. Wert
Herman A. Haus
C. Lester Hogan
R. S. Rivlin
Henry Hurwitz
James A. Krumhansl
C. P. Slichter

THE JOURNAL OF APPLIED PHYSICS is devoted to general physics and its applications to other sciences, to engineering, and to industry. Previous to 1937, this journal was called PHYSICS.

The JOURNAL OF APPLIED PHYSICS welcomes articles of two distinct kinds: (1) Descriptions of new results in experimental or theoretical physics which are of general interest to physicists. The author should explain his contribution in such a way that a physicist or engineer in another field of specialization can appreciate its objectives and essential features. (2) Critical reviews of particular areas of physics or surveys of extensive investigations at a single laboratory. Authors contemplating writing such should correspond with the Editor before they begin writing.

The JOURNAL OF APPLIED PHYSICS welcomes Letters to the Editor which are short [approximately four (4) typewritten pages] communications without abstracts. Timeliness, briefness, and degree of current importance of the subject matter will be of primary concern in the publication of Letters. Letters should not be looked upon as partial publication or announcement of more comprehensive work, but rather self-contained presentations in themselves.

Manuscripts should be submitted to the Editor, J. H. Crawford, Jr., Solid State Division, Oak Ridge National Laboratory, Oak Ridge, Tennessee. Authors should read the "Information for Contributors," facing page 1 of the January issue, before writing articles or letters. The *Style Manual* of the American Institute of Physics is also helpful to writers preparing manuscripts for journals published by the American Institute of Physics. It can be obtained for $1.00 from the American Institute of Physics, 335 East 45 Street, New York 17, New York.

Corrected proofs and all correspondence concerning papers in the process of publication should be addressed to the Supervisor, Editorial Department, American Institute of Physics, 335 East 45 Street, New York 17, New York.

Subscriptions, renewals, and orders for back numbers should be addressed to the American Institute of Physics, 335 East 45 Street, New York 17, New York.

Subscription Price	**U.S. and Canada**	**Elsewhere**
To members of member organizations of the American Institute of Physics and Affiliated Societies ..	$12.00	$13.00
To all others	14.00	16.00

Back Number Prices

Yearly back number rate when complete year is available: $17.00.
Single copies: $1.75 each (exception: March, 1958—$3.00 each).

Changes of address should be sent to the American Institute of Physics.

Advertising rates supplied on request. Orders, advertising copy, and cuts should be sent to the American Institute of Physics.

The Journal of Applied Physics is published monthly at Prince and Lemon Streets, Lancaster, Pennsylvania.
Second-class postage paid at Lancaster, Pa.

FERRANTI ELECTRIC, INC.

Announces a New

RHEOLOGY CENTER

Ferranti Electric, Inc. announces the establishment of a new service believed to be unique in concept and scope as a commercial operation.

An expanded rheological laboratory has started operations at the Company's Plainview, Long Island facility under Dr. Duane Shuster, who has joined the organization to take charge, in the United States, of Ferranti operations related to the application of viscometers.

The laboratory will be fully equipped with Ferranti viscometers, together with the necessary ancillary equipment, to permit determinations to be made on a wide variety of materials and over an extended temperature range. Testing programs will be undertaken in the laboratory, or may be performed in the field where the nature of the materials makes this imperative.

Ferranti inaugurated this service because it was clearly needed to meet the requirements of many organizations, both large and small, who were increasingly aware of the importance of rheological determinations, but were having difficulty in getting assistance with them.

Dr. Shuster joins Ferranti from the Socony Mobil Oil Company. He is a graduate of RPI where he studied under Dr. Walter Bauer.

Rates for the service are available on application.

The existence of this service does not affect Ferranti's long established policy of testing, without charge, small quantities of samples for organizations interested in evaluating the Ferranti instruments for purchase. On the contrary, it was felt that much more substantial assistance would now be available for this purpose to the mutual benefit of all parties concerned.

Ferranti

FERRANTI ELECTRIC, INC.

INDUSTRIAL PARK NO. 1 • PLAINVIEW, LONG ISLAND, N. Y.
Tel. 516 WElls 8-7500 • TWX HKVL 2381 • WUX LBI Plainview, N. Y.

In this streak photograph of an exploding wire, the cylindrical conversion pattern at center of column verifies how reflected shock waves intersect as they move radially inward during 'restrike' phase. A 0.005 inch diameter silver wire was energized by a 0.25 micro-farad low inductance capacitor charged to 25 KV for this experiment. To the best of our knowledge the STL Image Converter Camera is first to photograph this phenomenon.

NEW STL IMAGE CONVERTER CAMERA
VERIFIES EXPLODING WIRE PHENOMENA

The STL Image Converter Camera is the only complete diagnostic tool for instrumentation of high speed luminous transient events encountered in plasma physics, chemical kinetics and hypervelocity experiments. Exposures can be made in less than 3 millimicroseconds—twice the speed of any previous technique. Electronic shuttering, image deflection and light amplification (50 X) enable both framing and streak photography over the entire millimicrosecond range. The image converter tube and STL's new concepts for generating fast-rising precision voltage pulses make possible time resolved photography that defines a new freedom for creative research.

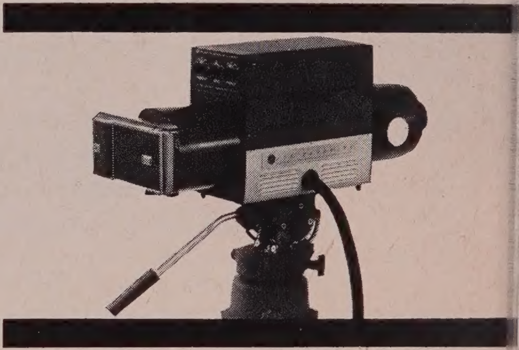

The STL Image Converter Camera is easil portable. It can be set up in the laboratory a readily as an oscilloscope. Four interchangeabl plug-in units allow low inductance connection and simplified switching. All voltages are prese so no adjustment by laboratory personnel i required. It is equipped with interchangeabl polaroid and cut film backs and regulated powe supply. Its standard price is $20,000.

Those interested in arranging a demonstrati of the STL Image Converter Camera at th facilities are invited to write David Fladlien STL Products, P.O. Box 95502, Los Angeles 4 California. A paper on the exploding wire expe iments is also available upon request.

STL PRODUCT

A DIVISION OF SPACE TECHNOLOGY LABORATORIES, I

*What's good for nuclides in New Haven is good for those in New Zealand**

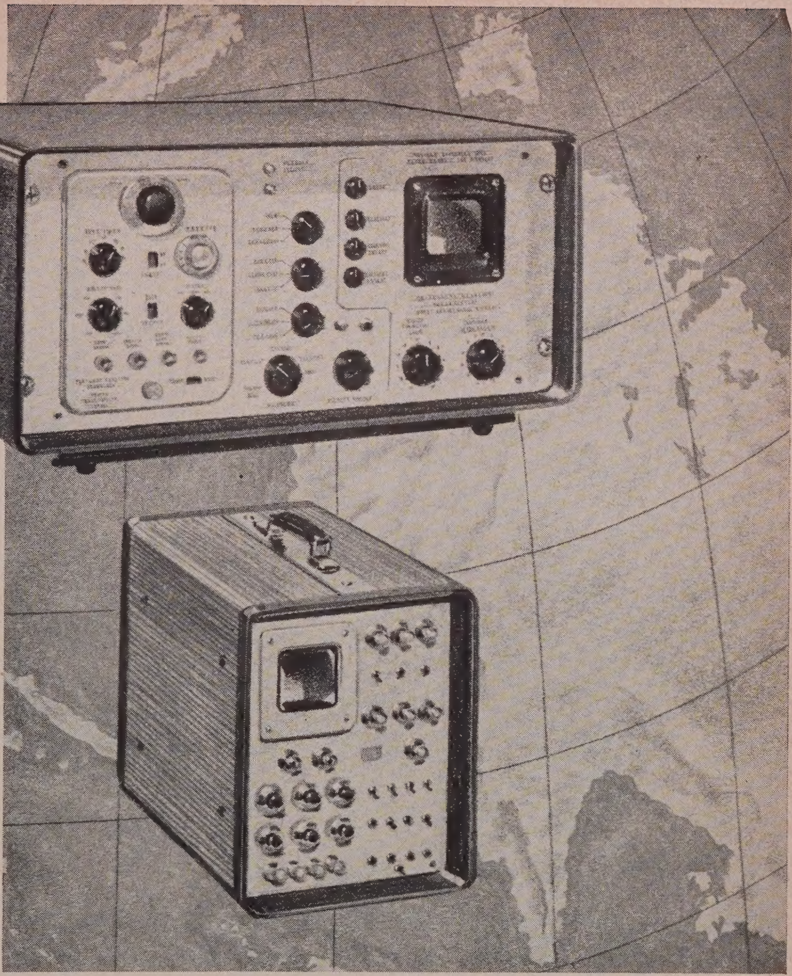

We think the reason people all over the world buy TMC pulse analyzers is pretty much the same reason they're widely purchased and used here: competently designed, bug-free circuits . . . straightforward operation with the same performance and stability today as yesterday . . . easy access to sub-assemblies and uncomplicated servicing if needed. Another way of putting it is the instruments give the user the information he wants in *his* work — with predictable behavior—regardless of where his site, lab or plant may be located. Here are two current examples:

The TMC CN-110 256 channel analyzer offers 7 interchangeable plug-in logics, including pulse height, time of flight, pulsed neutron, multiscaler, mass spectrometer, and coincidence pair. This widely used and thoroughly proven analyzer (over 100 units have been delivered) employs all-transistorized circuitry. Analog, binary, octal and decimal readout may be used. Data can be recorded on strip chart or X-Y recorders, printed paper tape, punched paper tape, or punched cards.

The Model 404 is a compact, 400-channel analyzer you can use anywhere there's a wall outlet and one square foot to put it down. It has a magnetic core memory that can be used in sub groups of two or four; four separate inputs and associated amplifiers; internal pulse routing circuity; pushbutton data transfer and display overlap; power requirement of *only 25 watts*, and many "system" advantages. While its versatility is a little less than the CN-110's, so are its size, price and purpose quite different from the 110's. Each does its *own* job well.

**Also wherever TMC Pulse Analyzers are used . . . in Canada, Brazil, Australia, Japan, Yugoslavia, France, Italy, Germany, Belgium, Sweden, Denmark, Switzerland, Israel, Formosa . . . as well as the United States.*

WRITE FOR LITERATURE.

TMC **TECHNICAL MEASUREMENT CORPORATION**
441 WASHINGTON AVE., NORTH HAVEN, CONN. • CE 9-2501

NEW . . . for high-level alpha-gamma hot cells—for handling pyrophoric, highly toxic gaseous or airborne particulate materials—wherever complete atmospheric control, prevention of dissemination by explosion or other accident is essential . . .

complete containment is provided by central research model A sealed manipulators

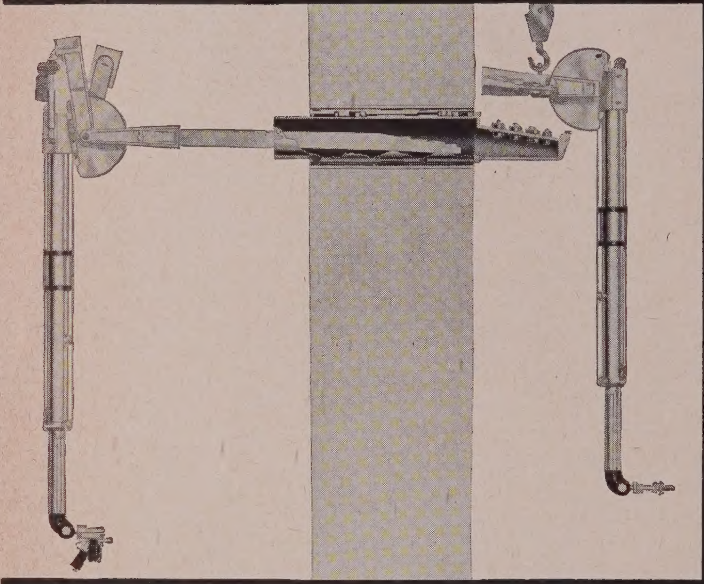

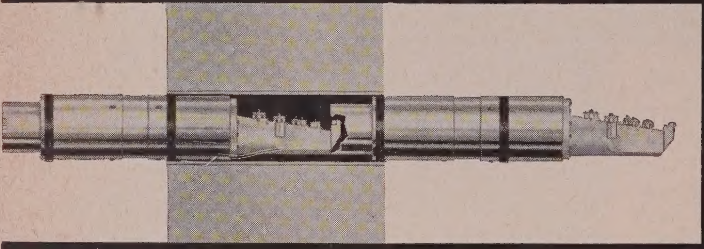

Sensitive and reliable, Model A manipulators are designed for dextrous, positive control and complete containment with shielded enclosures.

CONSIDER THESE IMPORTANT FEATURES:

SEALS—Double rotary mechanical seals between master and slave mechanisms insure reliability. Space between seals may be pressurized to monitor seal integrity. One seal is always operative even when changing seal tubes. "Push-thru" seal-tube replacement technique does not require complete wall port opening. Seal-tube features mean that all contaminated assemblies remain inside cell for disposal or decontamination and need never be brought out to the operating face.

OPERATION—Careful counterbalancing, reduction of mass, friction and lost motion make forces in the ounce range sufficient to initiate all motions. Easily handles 20-pound load per arm. Bilateral drive and force reflecting design characteristics give remarkable "sense of feel," reducing training time to a minimum.

MAINTENANCE—Three standard, interchangeable subassemblies: master arm, slave arm, and seal tube, simplify maintenance. A crane and simple fixture are sufficient for remote connection or removal of slave arm. Alignment pins assure positive slave arm positioning. All slave-end motions lock at disengagement for easy relocation.

**CENTRAL RESEARCH . . .
MANIPULATORS FOR EVERY NEED**

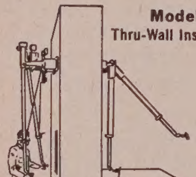

Model 8
Thru-Wall Installations

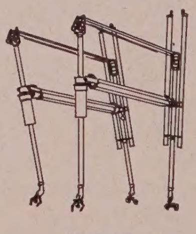

Model 7
Restricted Space Installations

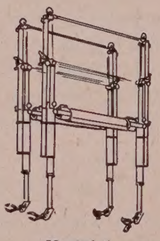

Model 4
Over-Wall Installations

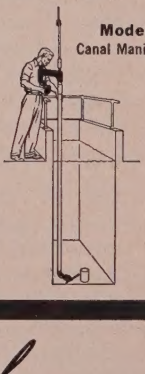

Model B
Canal Manipulator

For further information write:

Central Research
laboratories, inc.
Red Wing, Minnesota, Dept. 310

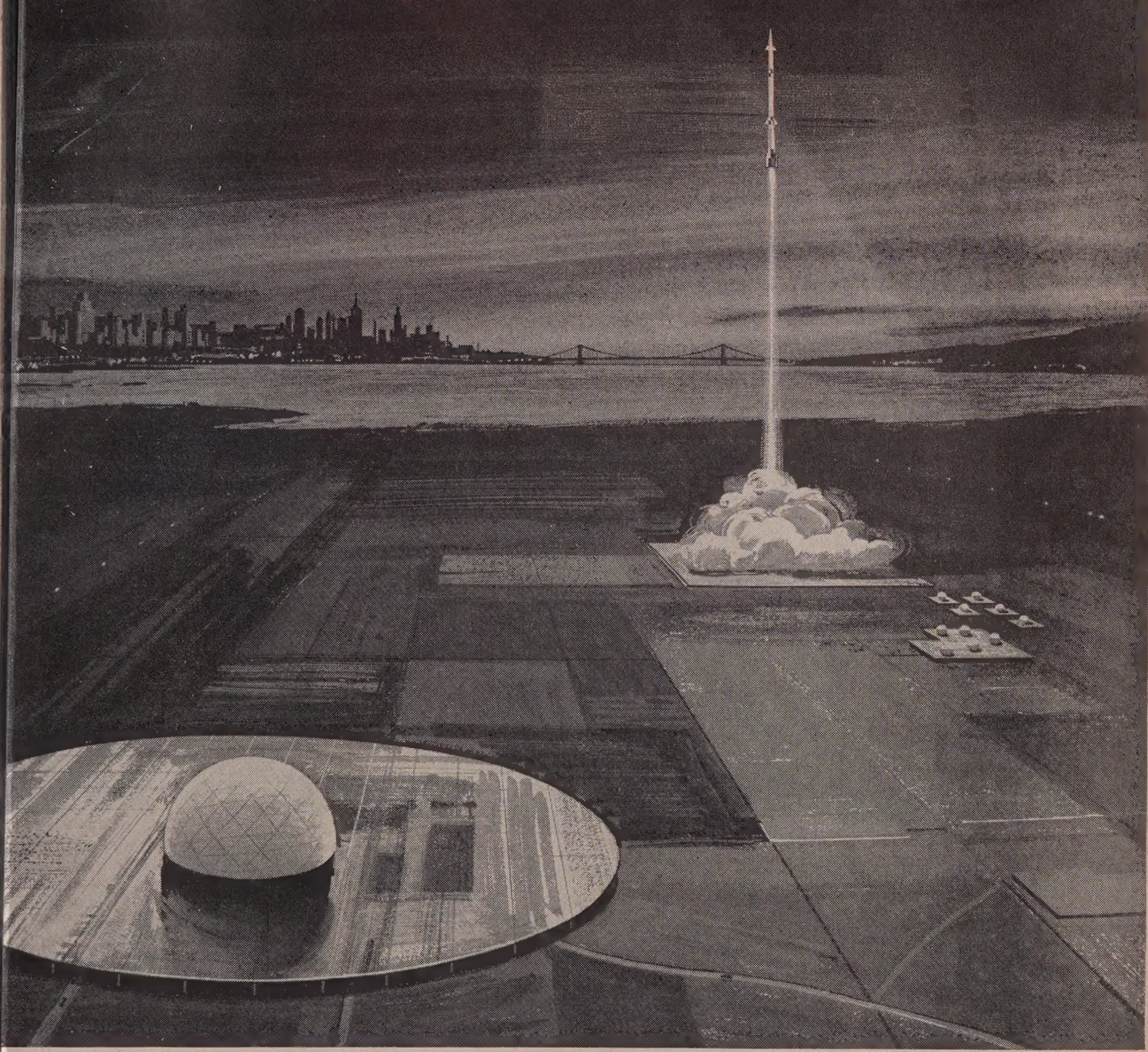

ore than 450,000 pounds of thrust lifts the U. S. Army's Nike Zeus missile skyward in a cloud of vapor. The Nike Zeus missile being developed for the project by the uglas Aircraft Company will be designed to intercept ballistic missiles traveling over 15,000 miles per hour, and destroy them at a safe distance from the defended area.

How do you stop an ICBM?

How do you detect, track, intercept—and destroy within inutes—an ICBM that is moving through outer space ten mes faster than a bullet?

Bell Telephone Laboratories may have designed the nswer: Nike Zeus, a fully automated system designed to tercept and destroy all types of ballistic missiles—not only CBM's but also IRBM's launched from land, sea or air. he system is now under development for the Army rdnance Missile Command.

Radically new radar techniques are being developed r Nike Zeus. There will be an acquisition radar designed detect the invading missile at great distances. And a iscrimination radar designed to distinguish actual warheads from harmless decoys that may be included to confuse our defenses.

The system tracks the ICBM or IRBM, then launches and tracks the Nike Zeus missile and automatically steers it all the way to intercept the target. The entire engagement, from detection to destruction, would take place within minutes and would span hundreds of miles.

Under a prime Army Ordnance contract with the Western Electric Company, Bell Laboratories is charged with the development of the entire Nike Zeus system, with assistance from many subcontractors. It is another example of the cooperation between Bell Laboratories and Western Electric for the defense of America.

BELL TELEPHONE LABORATORIES
World center of communications research and development

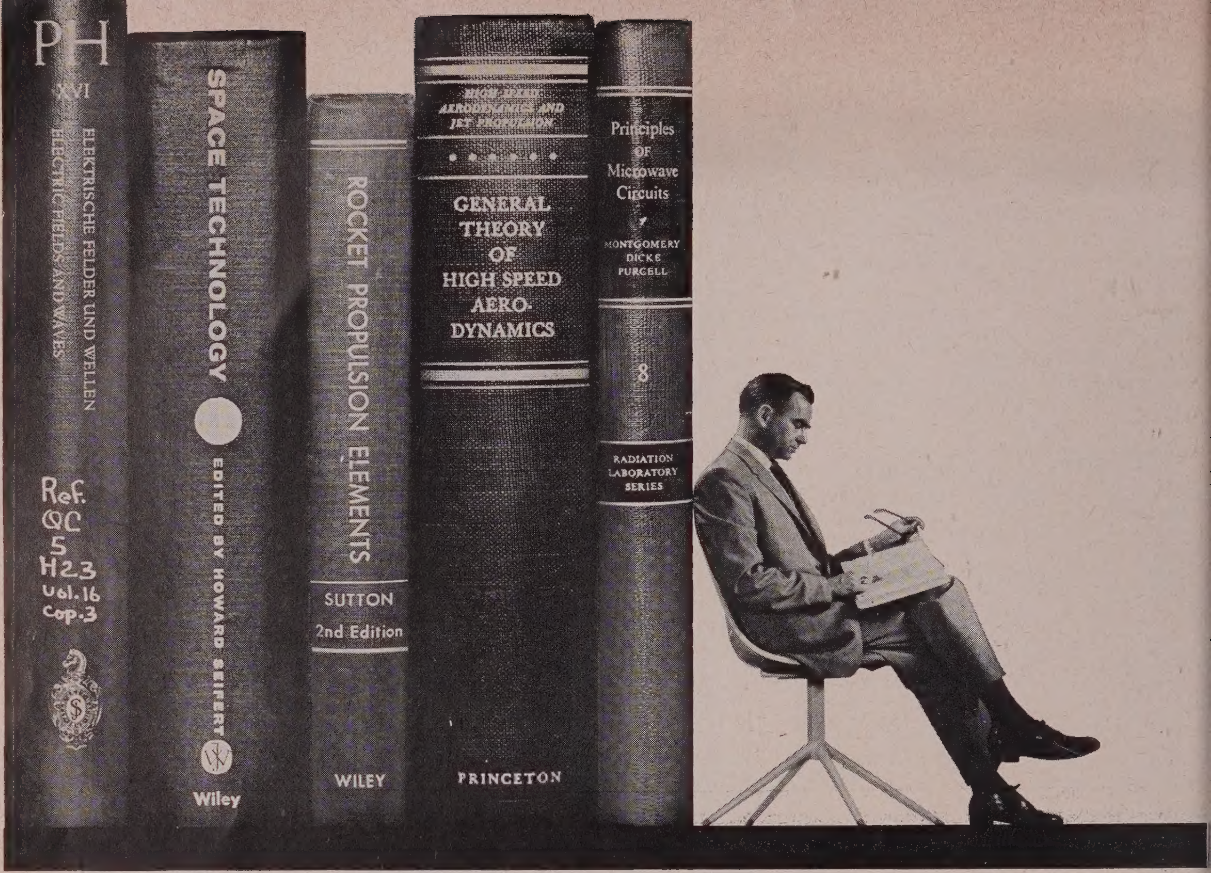
PH
XVI
ELEKTRISCHE FELDER UND WELLEN
ELECTRIC FIELDS AND WAVES
Ref. QC 5 H23 Vol.16 Cop.3
SPACE TECHNOLOGY
EDITED BY HOWARD SEIFERT
Wiley
ROCKET PROPULSION ELEMENTS
SUTTON
2nd Edition
WILEY
AERODYNAMICS AND JET PROPULSION
GENERAL THEORY OF HIGH SPEED AERO-DYNAMICS
PRINCETON
Principles of Microwave Circuits
MONTGOMERY DICKE PURCELL
8
RADIATION LABORATORY SERIES

scientists and engineers in a unique leadership role

The frontiers of space science and technology are being expanded at Aerospace Corporation. The scientists and engineers of this leadership organization are the critical civilian link uniting government and the scientific-industrial team developing space systems and advanced ballistic missiles. In providing broad scientific and technical leadership to every element of this team, they are engaged in a balanced program of activities spanning the spectrum from basic research and forward planning through general systems engineering. Included in the latter are technical supervision, integration and review of the engineering, development and test operations of industry to the extent necessary to assure achievement of system concept and objectives in an economical and timely manner. These people are privileged to view both the state-of-the-art and system development in their totality. Now more men of superior ability are needed: highly motivated scientists and engineers with demonstrated achievement, maturity, and judgment, beyond the norm. Such men are urged to contact Aerospace Corporation, Room 123, P. O. Box 95081, Los Angeles 45, California.

Organized in the public interest and dedicated to providing objective leadership in the advancement and application of space science and technology for the United States Government.

AEROSPACE CORPORATION

Kodak reports on:

Mr. Burnham's pitch on randomness...when to remember our name and when to forget it... the pencil that enrages the mind

rviving platemaker

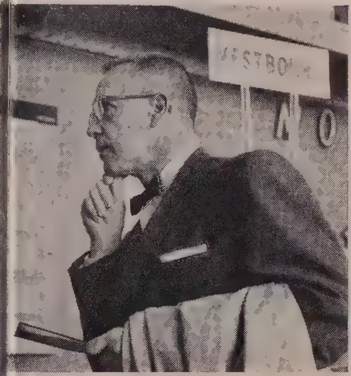

eet J. Mason Burnham, a brisk-look-
g Kodak man who has a problem.
r. Burnham sounds off like this:

"Characteristically, the random shift
position of an image on a Kodak
otographic plate is between 0.9 and
4 microns. Random, mind you.

"Positional error which is not ran-
om can be corrected. The correcting
uations can be cranked into the com-
tation program along with all the
her computations. A lot of computa-
on has to be done in any event when
ey measure the missile trail and the
r trails on the plates from a whole
ing of ballistic cameras along a range.

"Randomness is the only ultimate
itation on precision in such a situa-
on. The magnitude of the random
mponent of physical shift of an im-
e on a plate between exposure and
easurement is not great in compari-
n with the magnitude of the errors in
the other quantities that enter into
e computation. Small as the random
ift is, it is well that we now have a
etty good idea of its size.

"Among transparent materials which
n carry an image-bearing emulsion,
ass is the only one that has zero hu-
idity expansion coefficient. Of course,
thermal expansion coefficient is less
an that of any film base and even less
an that of hardened steel. This stabil-
can be handy when you don't have
computer available to remove non-
ndom errors.

"As for flatness, we have recently
rted accepting special orders for all Kodak plates on ¼-inch micro-flat glass, which means that the surface bearing the emulsion is planar to 0.2 micron per centimeter, for sizes from 4 in. x 4 in. to 12 in. x 12 in."

Mr. Burnham, as noted above, has a problem. The photographic plate was the product with which our founder started his one-man business. Mr. Burnham's problem is to keep this original rootstock of the business thriving despite all the competition for attention that the intervening 81 years have brought. He is going about it through contributions to modern instrumentation. If you would like to ask any questions about Kodak plates for instrumentation—for example, how to process a plate complete to dryness in 10 minutes without much spoiling the spatial stability of the image—write Eastman Kodak Company, Special Sensitized Products Division, Rochester 4, N. Y.

A little x-ray news

More precious than rubies is confidence in the importance of what one does for a living. One thing we do for a living is to manufacture x-ray film. Unkind words are rarely spoken about society's need for x-ray film. Now we have news about x-ray film and need to make it seem important. Easy.

The first piece of news has it that *Kodak Industrial X-ray Film, Type M* is now obtainable with emulsion on one side only instead of both sides, the way x-ray film usually comes in order to double the strength of the image. Simple, yes; trivial, no. Ties in to the very large subject of mankind's current push for great structural strength in small mass. Load-bearing members are now getting so thin that putative flaws on their radiographs have to be checked out with a microscope. Since a microscope can focus on only one side of the film at a time, it's better to have the other side blank. Enough of this is being done now so that x-ray dealers are stocking the single-coated film of high contrast and fine grain.

Eastman Kodak Company, X-ray Division, Rochester 4, N. Y., will be glad to guide you to such a dealer.

The second piece of news much exceeds the first in importance. The nuclear testing debate has gone on for years. As an intelligent citizen, you have been given estimates by various authorities of how much radiation you and your children can expect to soak up, barring disaster. You have been told how much to figure for medical and dental radiological examination over a lifetime. Meanwhile we have been quietly goofing up the statistics! We have been upping the response of the films. With the latest step, the same amount of examination requires half or a third as much radiation as had been estimated.

No action is required on your part. Just privately rejoice a little at how the deal has been sweetened a bit for you, statistically.

Forced drafting

The truly creative mind tends to shy away from the petty problems of the drafting room. Then the creative mind gets angry and upset when damnable antiquated drafting procedures impede the swift and smooth transformation of its output into physical reality. Perhaps the petty problems are worth a few moments of the creative mind's time. They have solutions like

- speeding revision of drawings by picking up photographically everything from the existing drawing that is to appear in the revision
- converting drawings into rigid, dimensionally stable, non-staining, non-glaring, long-wearing overlays for contour projector screens
- making working drawings out of photographs of existing equipment instead of drawing everything
- photographic templates for standard or repeating elements in a drawing
- photographic intermediates for protecting original drawings, restoring old and worn ones, or avoiding waits for extra prints.

The Kodak Compass *is an irregular publication that will be sent free to whoever in your organization ought to be concerned with such matters. The first issue deals very plainly with pencils, inks, and eradication techniques for the new Estar Base drawing-reproduction films. Submit names to Eastman Kodak Company, Graphic Reproduction Division, Rochester 4, N.Y.*
Same address for quick answers
to questions stirred up by
these remarks.

his is another advertisement where Eastman Kodak Company robes at random for mutual interests and occasionally a little evenue from those whose work has something to do with science

Kodak
TRADE MARK

Field Emission and Field Ionization

By Robert Gomer. This is the first study to offer a concise introduction to field emission and ionization including field-ion microscopy. Its emphasis is on the physical rather than theoretical aspects, employing simple mathematics. A practical tool for students and workers in field emission, the book offers a variety of applications and extensive references. Harvard Monographs in Applied Science, 9. Illustrated. $6.75

Tools of the Astronomer

By G. R. Miczaika and William M. Sinton. This book is a thorough discussion of modern astronomical instruments that will be useful not only to the student of astronomy but also to both the practicing professional and the serious amateur. Harvard Books on Astronomy. Illustrated. $7.75

HARVARD UNIVERSITY PRESS

TRAP A SUN IN A BOTTLE?

Sounds like an impossible job. Manage it, though, and you'll have the essential ingredients for controlled hydrogen fusion . . . and essentially unlimited power for centuries to come.

Scientists at the Oak Ridge National Laboratory*, Oak Ridge, Tennessee, are studying the possibility of the control of hydrogen fusion. They have a machine called the DCX (Direct Current Experiment) which in effect traps a tiny "sun" – a plasma of dissociated molecular deuterium ions – in a magnetic "bottle," under high vacuum.

VacIon 5000 Litre/second Pump

Varian's part in this? Varian's VacIon® pumps, up to 5,000 litres/second capacity, are used for the DCX experiment. Recently, a custom-designed VacIon pumping element with a much higher pumping speed was provided for installation inside the machine.

Perhaps Varian's broad experience in the electronic production of high vacuums can be of use to you. For fuller information, address Vacuum Division.

VARIAN associates

PALO ALTO 36, CALIFORNIA

BOMAC LABORATORIES, INC.
VARIAN ASSOCIATES OF CANADA, LTD.
S-F-D LABORATORIES, INC.
SEMICON ASSOCIATES, INC.
SEMICON OF CALIFORNIA, INC.
VARIAN A.G. (SWITZERLAND)

Oak Ridge National Laboratories, operated by the Union Carbide Corporation for the U. S. Atomic Energy Commission.

Mathemagical Machines?

Maybe they are not really magical, but modern computers are marvelous aids to solving the complex problems arising from research. With the addition of an IBM 7090 and the super-computer STRETCH, Los Alamos Scientific Laboratory has become one of the most advanced electronic computer centers in the world. Such machines are required to perform in a reasonable time the billions of computations involved, for example, in the design of nuclear weapons and nuclear reactors, and, in problems of molecular biology and magnetohydrodynamics.

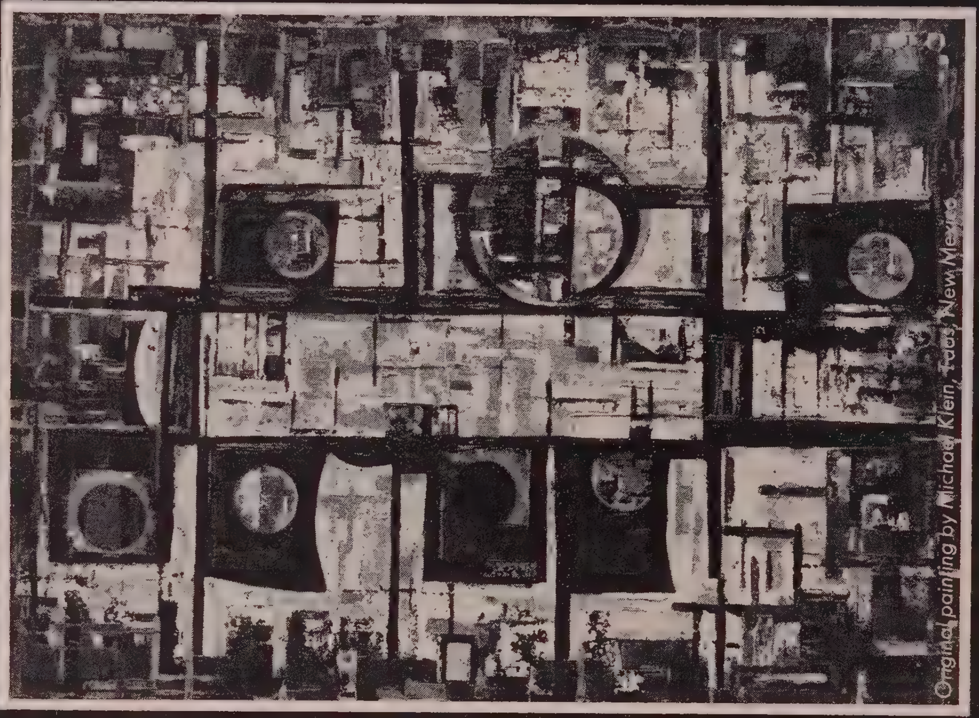

Original painting by Michael Klein, Taos, New Mexico

Qualified applicants are invited to send resumes to: Director of Personnel, Division 61-78

los alamos
scientific laboratory
OF THE UNIVERSITY OF CALIFORNIA
LOS ALAMOS, NEW MEXICO

All qualified applicants will receive consideration for employment without regard to race, creed, color, or national origin. U.S. citizenship required.

X-RAY DIFFRACTION AND SPECTROSCOPY

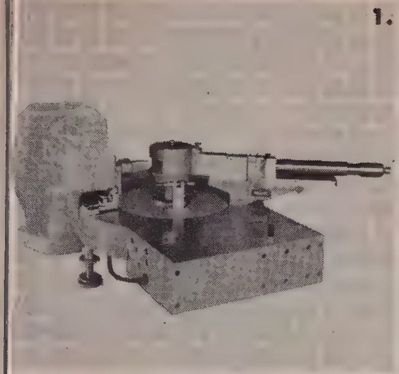

1.

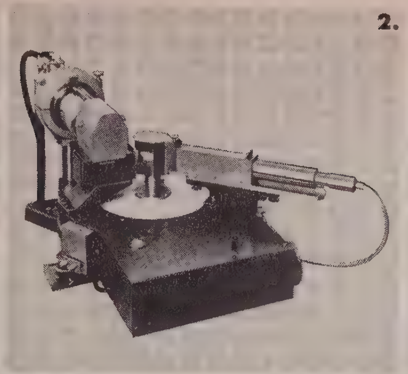

2.

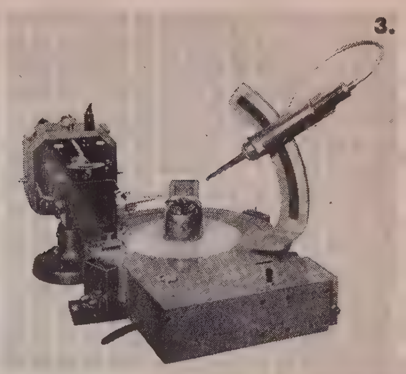

3.

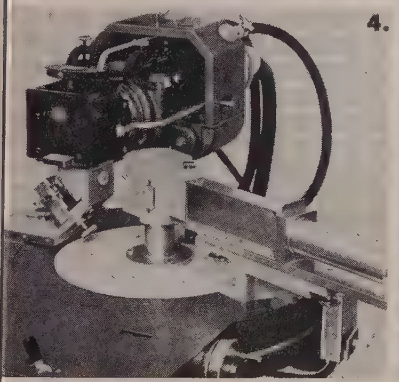

4.

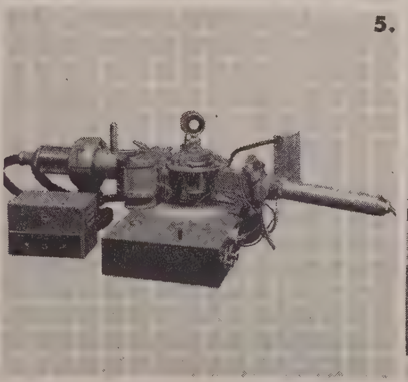

5.

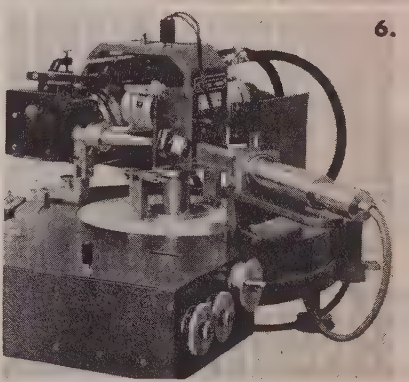

6.

1. Counter Tube Diffractometry. **2.** Spectroscopy. **3.** Single Crystal Studies. **4.** Spectroscopy of Small Areas. **5.** Vacuum Spectroscopy of Light and Heavy Elements. **6.** Studies of Orientation.

VERSATILITY!

RCA's horizontal goniometer performs 6 functions

Unusual versatility is an important distinguishing characteristic of RCA's X-Ray Diffraction and Spectroscopy Equipment. This versatility is graphically demonstrated by the horizontal goniometer which can perform six different functions merely by adding accessories, as illustrated above.

RCA X-Ray Diffraction and Spectroscopy Equipment offers many other outstanding features which make it one of today's most specified lines. For example, the DC regulated and filtered power supply; the option of mounting two tube stands on the Crystalloflex IV; a kit which permits conversion from diffraction to spectroscopy in minutes; and the new vacuum spectrometer for analysis of light and heavy elements. For those engaged in film studies of all kinds, the RCA Table Model Crystalloflex II can be bought, complete with cameras, for as little as $4000.

A NEW LEASING PLAN now makes it possible to obtain all RCA scientific instruments, including the Electron Microscope, with no down payment, low monthly terms, and a favorable option to buy.

For complete information write to RCA, Dept. Z-65, Bldg. 15-1, Camden, N.J.

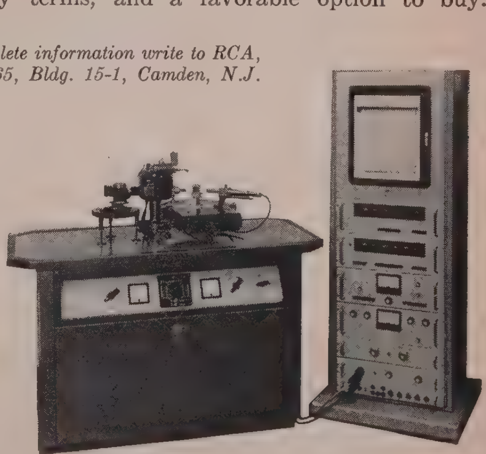

Crystalloflex IV and Electronic Circuit Panel with Diffractometer and Guinier Camera mounted on the generator.

RCA®

The Most Trusted Name in Electronics

RADIO CORPORATION OF AMERICA

Increased technical responsibilities in the field of range measurements have required the creation of new positions at the Lincoln Laboratory. We invite inquiries from senior members of the scientific community interested in participating with us in solving problems of the greatest urgency in the defense of the nation.

RADIO PHYSICS and ASTRONOMY

RE-ENTRY PHYSICS

PENETRATION AIDS DEVELOPMENT

TARGET IDENTIFICATION RESEARCH

SYSTEMS: Space Surveillance
Strategic Communications
Integrated Data Networks

NEW RADAR TECHNIQUES

SYSTEM ANALYSIS

COMMUNICATIONS: Techniques
Psychology
Theory

INFORMATION PROCESSING

SOLID STATE Physics, Chemistry,
and Metallurgy

A more complete description of the Laboratory's work will be sent to you upon request.

All qualified applicants will receive consideration for employment without regard to race, creed, color or national origin.

Research and Development
LINCOLN LABORATORY
Massachusetts Institute of Technology
BOX 33
LEXINGTON 73, MASSACHUSETTS

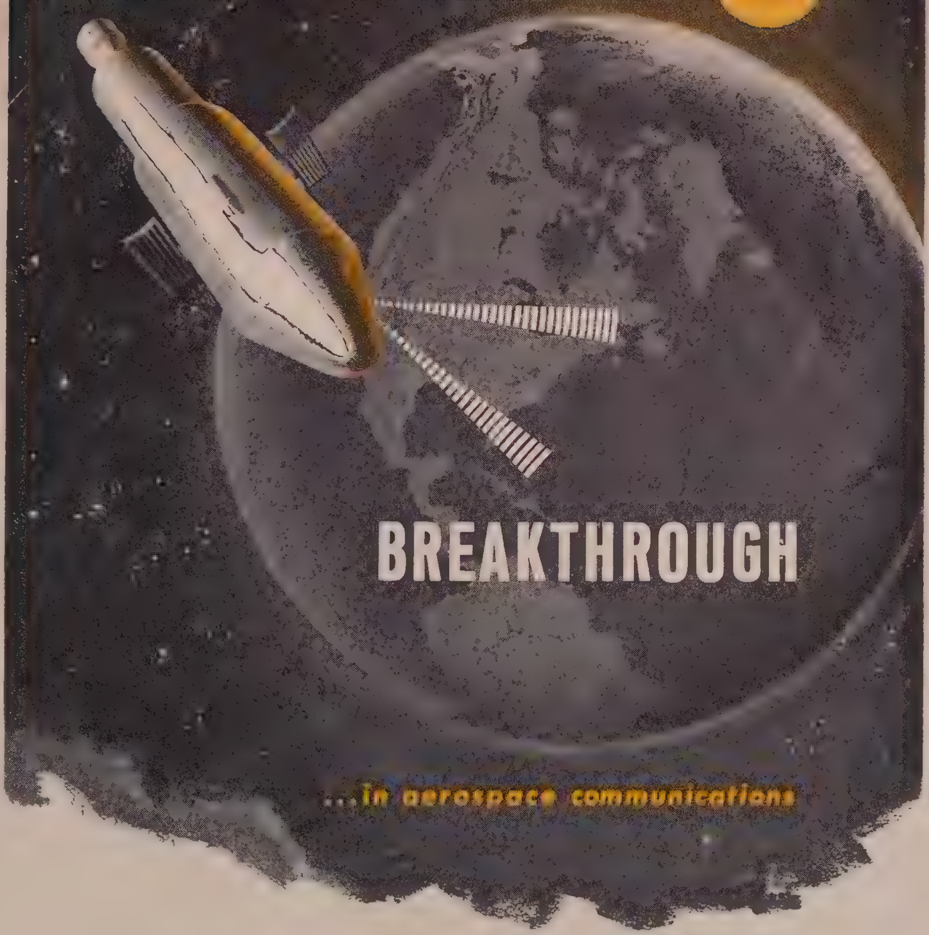

THE FIRST SUCCESSFUL MICROWAVE SOLID-STATE TRANSMITTER
WITH POWER CAPABILITY ADEQUATE FOR SATELLITE APPLICATION
A DEVELOPMENT BY THE SCIENTISTS AT AMHERST LABORATORIES

The objective assigned to the Amherst Laboratories' scientists was this: Advance the state-of-the-art of microwave space vehicle transmitters by increasing performance, reducing size, reducing weight and increasing reliability.

The time was June 1960. One year later, these objectives had been reached *and exceeded by a wide margin.*

The result: a solid-state transmitter applicable for satellite use, operating within the S-band, about half the size of a carton of cigarettes, and with a life expectancy of two years.

This significant achievement is representative of many challenges currently being met by the scientists at Amherst Laboratories.

PAPER ON REQUEST: The paper which explains the new techniques employed in development of the new microwave Solid-State Transmitter authored by W. J. Maciag is available to engineers and scientists on request. Write for the paper entitled "Solid State, S-band Single Side Band Suppressed Carrier Transmitter"

AMHERST LABORATORIES • 1184 WEHRLE DRIVE • WILLIAMSVILLE, NEW YORK

An equal opportunity employer

SYLVANIA **ELECTRONIC SYSTEMS**
Government Systems Management
for ***GENERAL TELEPHONE & ELECTRONICS***

Soviet Physics SOLID STATE

A translation, beginning with 1959 issues of "Fizika Tverdogo Tela" of the USSR Academy of Sciences. Offering results of theoretical and experimental investigations in the physics of semiconductors, dielectrics, and on applied physics associated with these problems. Also publishes papers on electronic processes taking place in the interior and on the surface of solids.

Soviet Physics TECHNICAL PHYSICS

A translation, beginning with 1956 issues of "Zhurnal Tekhnicheskoi Fiziki" of the USSR Academy of Sciences. Contains work on plasma physics and magnetohydrodynamics, aerodynamics, ion and electron optics, and radio physics. Also publishes articles in mathematical physics, the physics of accelerators and molecular physics.

Soviet Physics CRYSTALLOGRAPHY

A translation, beginning with 1957 issues of the journal "Kristallografiya" of USSR Academy of Sciences. Experimental and theoretical papers on crystal structure, lattice theory, diffraction studies, and other topics of interest to crystallographers, mineralogists, and metallurgists.

Orders and inquiries should be sent to:

American Institute of Physics
335 East 45 Street, New York 17, N.Y.

HIGH PURITY ELEMENTS

UTH PLAINFIELD, N. J., Sept. 1 -- ASARCO
NTRAL RESEARCH LABORATORIES, USING SPECIAL
FINING AND ANALYTICAL TECHNIQUES, HAVE
CCEEDED IN PURIFYING SELENIUM SO THAT NO
CKEL OR IRON CAN BE DETECTED AT 5 PARTS IN
0,000,000. LEVELS OF OTHER IMPURITIES IN
ARCO HIGH PURITY ELEMENTS CAN AT TIMES
MORE SPECIFICALLY LIMITED TO MEET
STOMERS' SPECIAL REQUIREMENTS.

ASARCO HIGH PURITY ELEMENTS as of SEPT. 1, 1961

Impurities sometimes found at maximum levels in parts per million
(< denotes less than ppm indicated)

lement and Grade		Bi	Cu	Fe	As	Pb	Ag	Tl	Sn	Te	Au	Na	Cl	Cd
NTIMONY	A-60	<1	<1	<1	<2	<1								
RSENIC	A-60		<1											
ISMUTH	A-58		2	1		1	2						<1	
ADMIUM	A-60		<1	<1		1								
OPPER	A-58	No Impurities Detectable by Spectrographic Analysis												
OLD	A-59		<1	<1		<1	1							
NDIUM	A-58		<1			1		<1	1					
EAD	A-59	<1	<1	<1										
ELENIUM	A-58		<1		<1					1			<1	
ILVER	A-59		<1	<1		<1								
ULFUR	A-58											1	1	
ELLURIUM	A-58		<1	<1										
HALLIUM	A-60		1	1		<1	<1					2	<1	
INC	A-59		<1	<1		<1								<1

enotes element improved since last published analyses.

ASARCO

The analyses above are among pertinent data compiled by Asarco's Central Research Laboratories in an up-to-date catalogue now available to users of high purity elements. For a copy, write on your company letterhead to American Smelting and Refining Company, 120 Broadway, New York 5, N. Y.

Sames

ELECTROSTATIC PARTICLE ACCELERATORS

These provide a wide range of particles and radiations: Electrons—Protons—Neutrons—Deuterons—X-Rays.

• Voltages to 600 KV, infinitely variable • Current to 4 ma • Stability to ±.01% • Ion current (Protons or Deuterons) to 0.6 ma continuous • Electron beam current to 3 ma continuous • X-Rays to 1000 Roentgens/sec • Beam diameters adjustable, 2 to 10 mm • Beam pulsing available, 10 to 200 μs

Maximum Safety: Low internal capacitance. Minimal short circuit currents. Remote adjustment and shut-down.

• *Write for literature* SAMES

Sames 30 Broad Street, Rm. 3702, New York 4, N.Y.

Physicists

The Hughes Research Laboratories offer an outstanding professional environment to Scientists and Engineers with an interest in basic and applied research. At these exceptional facilities you can realize maximum professional growth through programs including:

PLASMA PHYSICS

Thermionic energy conversion
Microwave plasma devices

SURFACE PHYSICS

Low work function surfaces
Thermionic electron emission
Thermionic ion emission

SOLID STATE PHYSICS RESEARCH

Microwave and millimeter wave magnetic resonance
Optical and infrared spectroscopy
Solid State masers
Semiconductor physics

ION PROPULSION

The facilities of the Hughes Research Laboratories are located in Malibu, California, overlooking the Pacific Ocean—immediately adjacent to major academic institutions—with programs of academic support and participation. These facilities were specifically designed for effective research efforts with private offices and complete research laboratories. In this uniquely creative atmosphere, Hughes scientists are continually adding to their record of accomplishments in electronics and physics research.

Your inquiry may be directed in strict confidence to: Mr. D. A. Bowdoin, Hughes Research Laboratories, Malibu, California.

All qualified applicants will receive consideration for employment without regard to race, creed, color or national origin.

creating a new world with electronics

HUGHES

HUGHES AIRCRAFT COMPANY
RESEARCH LABORATORIES

Welch Improved CATHETOMETER

Significant recent engineering improvements in this instrument insure better performance than ever and more years of satisfactory service.

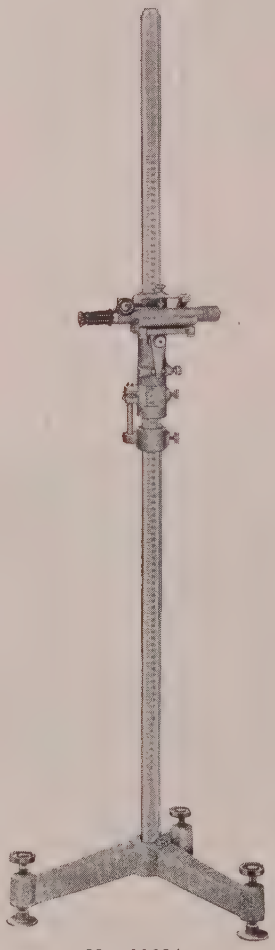

No. 0068A.

This cathetometer is designed for precise measurement of vertical distances through a range of 100 cm.

It is particularly useful where the object to be observed is not conveniently accessible, or may easily be disturbed by physical contact, or must be located in a position too hazardous to permit the observer to be in close proximity.

It is also commonly employed for qualitative telescopic viewing within the laboratory because of its versatile positioning adjustments and over-all stability.

Vertical Range	**100 cm**
Smallest Reading by Vernier	**0.05 mm**
Telescope	
Working Distance	**45 cm to Infinity**
Angular Magnification	**12× at 45 cm**
	8× at Infinity
Reticle	**90-degree crosshairs**
Level Sensitivity	**50 Seconds**

Cat. No. 0068A **Each $257.50**

Write for illustrated circular describing the many excellent features of this instrument.

THE WELCH SCIENTIFIC COMPANY

1515 Sedgwick Street, Dept. C-1 **Chicago 10, Illinois**

Manufacturers of Scientific Instruments and Laboratory Apparatus

Journal
of
Applied Physics

Volume 32, Number 9 September, 1961

Mosaic Size in Lead from X-Ray Measurements

Yosio Hiki
The Government Mechanical Laboratory, Suginami-ku, Tokyo, Japan

and

Ryukiti R. Hasiguti
Department of Metallurgy, University of Tokyo, Tokyo, Japan

(Received February 16, 1961)

The size of mosaic blocks in lead powder was determined on the basis of the primary extinction effect of x rays. Integrated intensities of nine reflection lines in the Debye-Scherrer spectrum with CuK_α radiation were measured with a Geiger counter spectrometer. The mosaic size was calculated by comparing these values with theoretical values of the intensities. Correction for absorption of x rays in the specimen powder was especially important because of the large absorption coefficient of lead. The order of magnitude of the mosaic size was found to be 10^{-4} cm. From this value, the dislocation density was calculated to be of the order of 10^8 cm^{-2}. The dislocation density decreased slightly when the specimen was annealed *in vacuo* at 150°C for a long time.

INTRODUCTION

THE "mosaic structure," which was introduced by Darwin as a mathematical model of an imperfect crystal,[1] has been found to actually exist in real crystals. Although abundant knowledge has been accumulated about the features of the mosaic structure, true understanding of it could be obtained after the development of the dislocation theory.[2] X-ray diffraction technique is one of the most powerful methods to determine the states of mosaics in crystal. Usually intensities, broadenings, and shapes of the diffraction lines are measured to estimate the mosaic sizes, and sometimes misorientations between mosaic blocks are directly determined. Some investigators have measured the intensities from polycrystalline or powdered specimens and calculated the dimension of the mosaic by comparing the observed intensities with theory on the basis of the extinction effect.[3–5] This method has become reliable, as the measurements of the integrated intensities in the Debye-Scherrer spectrum have become accurate, through the progress of Geiger counter spectrometers. The present investigation was intended to determine the size of mosaic blocks in filed and annealed powder specimens of lead.

EXPERIMENTAL METHODS

The measurements were carried out with a Geiger counter spectrometer of the usual type.[6] The CuK_α radiation was obtained from an x-ray tube operating at 35 kv and 15 ma with an Ni filter to eliminate the K_β radiation. The voltage and current were maintained constant within 0.5% by a two-step stabilizer. The slit system of the goniometer was as follows: divergence slit 1°, Soller slit 2.5°, scatter slit 1°, and receiving slit 0.2 mm. The x-ray beam diverged onto the flat specimen which was pressed into a shallow cavity on a copper disk, and the beam was reflected and focused on the Geiger counter. The integrated intensity of each line of the spectra was measured in the following way: The total number of pulses in the time interval between the goniometer scanning the diffraction peak were counted by an electronic scaling unit. The scanning speed was $\frac{1}{8}$°/min in twice the glancing angle. The starting and

---

[1] C. G. Darwin, Phil. Mag. **43**, 800 (1922).

[2] P. B. Hirsch, Progr. in Metal Phys. **6**, 236 (1956).

[3] B. L. Averbach and B. E. Warren, J. Appl. Phys. **20**, 1066 (1949).

[4] W. H. Hall and G. K. Williamson, Proc. Phys. Soc. (London) **B64**, 937 (1951).

[5] E. L. Gal'perin and Yu. S. Terminasov, Zhur. Tekh. Fiz. **27**, 1379 (1957).

[6] H. P. Klug and L. E. Alexander, *X-Ray Diffraction Procedures* (John Wiley & Sons, Inc., New York, 1954).

Copyright © 1961 by the American Institute of Physics.

stopping points of the scanning were determined appropriately after the diffraction pattern was charted. The background counts were the sum of the counts at the starting and stopping points in a time interval just half the time required to scan the peak. The integrated intensity was obtained by subtracting the background from the total counts.

The specimens were prepared from lead of 99.99% purity which was ground into powder with an iron file and an agate mortar; the iron powder which mingled with the lead powder was removed by a magnet. The powder was passed through sieves and divided into two sorts, 100–200 and 200–300 mesh/in. (250–130 and 130–85 μ). Measurements were made on these two specimens to determine the effect of the size of powder on the final results. It was difficult to prepare finer specimen powder because lead is apt to be oxidized. Each powder was moistened with 5% solution of Canada balsam in xylol and pressed into a circular cavity, 25 mm in diameter and 1 mm deep, engraved on a copper disk. The surface of the specimen was carefully finished to achieve flatness. The specimens were stored in an evacuated vessel to protect them from oxidation.

In the present investigation, it is necessary to compare the relative values of the integrated intensities of various reflection lines from one specimen. Errors which may occur in such a case will be enumerated as follows:

(a) The fluctuation of the incident x-ray intensity. This is caused by the change of the tube voltage and current. In the present case, this is smaller than 1% during the course of the measurement.

(b) Instrumental errors. These originate mainly from the geometrical aspects of the goniometer and have the effect of broadening the width of the reflection line.[6] It can be shown, however, that these errors do not affect the relative values of the integrated intensities.

(c) The effect of K_α doublet. No monochromator was used in the present experiment, and the doublets split distinctly at high-angle reflections. This effect contributes an error smaller than 2% to the integrated intensities.

(d) The counting loss of the counter. A Geiger counter cannot count two pulses in rapid succession and this produces a loss of efficiency which increases with increasing counting rate. The multiple-foil experiment[6] was carried out using Ni foils 0.01 mm thick to check the linearity of the counter. In consequence, the counting loss was found to be negligible in the present intensity measurements, because the reflection of x rays from lead was not strong, and the counting rate was at most 700 counts/sec.

(e) The statistical error. This originates from the statistical fluctuation of x-ray photons generated by the anode of the x-ray tube. The error increases with decreasing number of total counts and with decreasing ratio of the total counting rate to that of background. In the present experiment, the statistical error was in the range from 0.5% for the strongest reflection line to 4.5% for the weakest.

(f) Errors originating from the finite number of the specimen powder and the preferred orientation of the powder.[6] These errors decrease the reproducibility of the measured value of intensity. The following procedures were adopted to minimize the errors: The filed lead was ground in the mortar cooled with dry ice in order to make the shape of the powder as spherical as possible. The specimen disk was rotated in its own plane when the intensity was measured. The error was estimated experimentally by repeated measurements of the integrated intensity of a peak from a specimen. The fluctuation of the observed values was found to be smaller than 5%.

In conclusion, the errors of the relative values of the integrated intensities of reflections from a specimen may be smaller than 10%.

RESULTS AND DISCUSSION

Integrated intensities of nine reflections from specimens filed and then annealed *in vacuo* at 150°C for 5, 15, 40, and 80 hr were measured successively. As an example, relative values of the observed intensities I for the filed 100–200-mesh specimen are shown in column 3 of Table I, where the values are normalized so that I_{220} is unity. In columns 1 and 2, the indices of reflection (hkl) and the Bragg angle θ are shown. The intensities of (400), (440), and (600) reflections were weak and not applicable to accurate measurements. The line (420) was also omitted because it was close to (331) reflection.

To analyze the experimental results, we start from Darwin's formulas for extinction effects. When primary or secondary extinction exists, the ratio of the observed intensity I to the theoretical intensity I' is, respectively,

$$I/I' = \tanh pq/pq, \qquad (1)$$

$$I/I' = 1/(1+2gI'), \qquad (2)$$

where p is the number of given planes in a mosaic block, q the amplitude of reflection from an atomic plane,

TABLE I. Observed and calculated intensities of each reflection line for filed 100–200-mesh specimen.

1	2	3	4	5	6		7	8	9
					$A(\theta)$				
(hkl)	θ	I	K	f_T	100 mesh	200 mesh	$B(\theta)$	j	I/I'
111	15°39′	1.985	0.865	64.4	5.6	6.5	90.8	8	0.88
200	18°08′	1.074	0.825	60.9	7.2	8.2	57.7	6	0.88
220	26°12′	1.000	0.686	50.0	14.5	15.8	17.76	12	1.00
311	31°06′	1.279	0.609	44.3	20.5	21.7	10.32	24	1.01
222	32°39′	0.380	0.587	42.3	22.5	23.7	8.87	8	1.05
331	42°49′	0.554	0.503	32.4	37.0	38.2	4.37	24	1.08
422	49°41′	0.520	0.513	27.2	47.7	48.8	3.58	24	1.37
333 511	53°57′	0.521	0.547	24.7	54.8	55.8	3.52	8 24	1.11
531	67°09′	0.925	0.744	19.2	77.2	77.7	4.90	48	1.12

$g=[2(\pi)^{\frac{1}{2}}\eta]^{-1}$, and η is the mean angle of misorientation between the blocks. Some authors have proposed modified forms of these expressions.[7–9] Weiss' formulas[7] are applied to the present analysis; they can be obtained by expanding Eqs. (1) and (2), assuming that the mosaic block has spherical form. They are expressed as

$$I/I'=1-[7(e^2N\lambda/mc^2)^2D^2]K^2f_T^2, \qquad (3)$$

$$I/I'=1-[4\lambda(e^2N\lambda/mc^2)^2gD]Kf_T^2/\sin\theta, \qquad (4)$$

where N is the number of unit cells per unit volume, e and m are the electronic charge and mass, c is the velocity of light, λ the wavelength of the incident x ray, and D the diameter of the mosaic block in the specimen. The polarization factor is given by $K=(1+\cos^2 2\theta)/2$ when the monochromator is not used. f_T is the atomic scattering factor corrected for dispersion[10] and comprising also the temperature factor.[11] The following relation, which holds in the case of fcc crystals, was used: structure factor $F_T=4f_T$. The values of K and f_T are given in columns 4 and 5 of Table I. The Thomas-Fermi scattering factor[11] was adopted, and 88°K was chosen to be the characteristic temperature of lead.

The theoretical value of the integrated intensity I' can be calculated from the formula

$$I'=I_0N^2SKGLj|F_T|^2A(\theta)\equiv kA(\theta)B(\theta)jf_T^2, \qquad (5)$$

where I_0 is the intensity of the incident beam and S is the area of the surface of the specimen immersed in the beam which is inversely proportional to $\sin\theta$ in the present experimental condition. The geometrical factor $G=\frac{1}{2}\pi l\sin 2\theta$, where l means the distance between the specimen and the counter; the Lorentz factor $L=\frac{1}{4}\sin\theta$; j is the multiplicity factor, and $A(\theta)$ represents the absorption factor. The factor $B(\theta)$ becomes $(1+\cos^2 2\theta)/\sin^3\theta\cos\theta$, and k is a product of quantities not dependent upon the angle θ.

The incident and diffracted beams in passing through the specimen are partially absorbed, and the absorption factor $A(\theta)$ is necessary to correct this effect for calculating the diffracted intensity. When the specimen is made from fine powder with a small absorption coefficient, the x rays penetrate into the specimen deeply and the surface of the specimen may be considered to be a homogeneous flat plane. In such a case, it can be shown that the product $SA(\theta)$ is a quantity independent of the angle θ.[6] In the present case, however, the absorption coefficient of lead, μ, is very large, and the size of the specimen powder is not small. The effective depth of penetration $(1/\mu)$ of the CuK_α radiation is about 4×10^{-4} cm, and the incident beam can only penetrate into the powder situated at the top of the specimen. Accordingly, the correction for the absorption should be carried out considering that the x rays are diffracted by the particles which compose the surface of the specimen. In general, the problem of evaluating the absorption factor is so complex that it has been calculated for specimens with simple forms. Bradley calculated $A(\theta)$ for a cylindrical specimen assuming essentially parallel incident x rays which completely bathe the specimen.[12] Other authors extended these results to the case of a spherical particle.[13] In the present analysis, the calculated values of A(θ) for a spherical particle are adopted to be used in Eq. (5) on the assumption that each of the specimen powder particles of lead is a sphere with a smooth surface on the average. This proposition may be accepted even when the surface of the powder has smooth undulation or low unevenness, the height of which is sufficiently smaller than the effective depth of penetration of the x rays.[14]

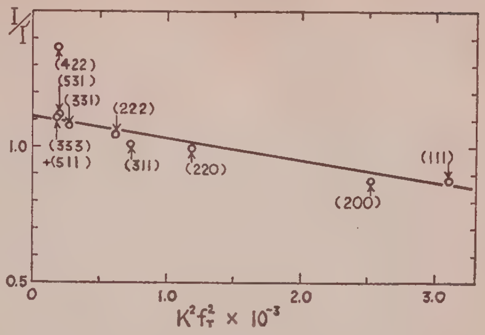

FIG. 1. Application of Eq. (3) to the results for filed 100–200-mesh specimen.

Relative values of $A(\theta)$ for 100- and 200-mesh particles of lead are shown in column 6 of Table I, where

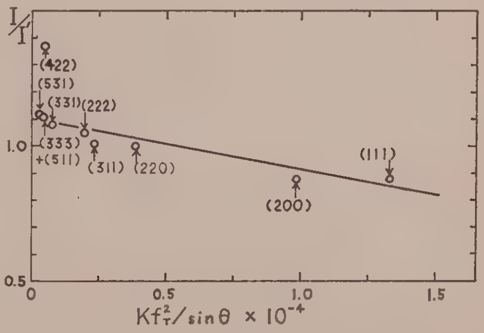

FIG. 2. Application of Eq. (4) to the results for filed 100–200-mesh specimen.

---

[7] R. J. Weiss, Proc. Phys. Soc. (London) **B65**, 553 (1952).

[8] A. R. Lang, Proc. Phys. Soc. (London) **B66**, 1003 (1953).

[9] G. K. Williamson and R. E. Smallman, Proc. Phys. Soc. (London) **B68**, 577 (1955).

[10] R. W. James, *The Optical Principles of the Diffraction of X-Rays* (G. Bell and Sons, Ltd., London, 1948).

[11] *Internationale Tabellen zur Bestimmung von Kristallstrukturen* (Gebrüder Borntraeger, Berlin, 1935), Vol. II.

[12] A. J. Bradley, Proc. Phys. Soc. (London) 47, 879 (1935).

[13] H. T. Evans, Jr. and M. G. Ekstein, Acta Cryst. 5, 540 (1952).

[14] Electron microscopic observation of the specimen powder showed that the surface of the powder was rather smooth; i.e., the proposition was considered to be adequate. The authors wish to thank Japan Electron Optics Laboratory for their kindness in elaborating the electron micrographs of the powder.

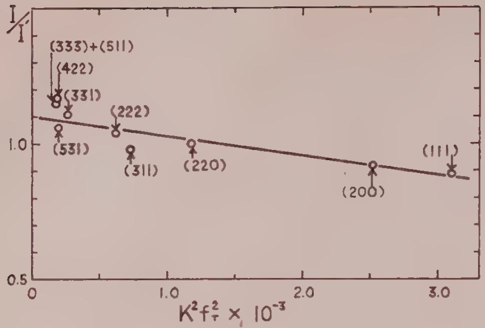

FIG. 3. Application of Eq. (3) to the results for 100–200-mesh specimen annealed at 150°C for 5 hr.

$A(90°)$ is chosen to be 100. $B(\theta)$ and j are tabulated in columns 7 and 8. The relative values of I/I' normalized at the (220) line can be seen in column 9; they are the averaged values for 100- and 200-mesh powder.

The values of I/I' are plotted against $K^2f_T{}^2$ and $Kf_T{}^2/\sin\theta$ in Figs. 1 and 2, respectively. Both of them seem to lie on straight lines, except for the (422) reflection. The lines are determined by the least-mean-square method, with eight experimental points exclusive of the (422) reflection. We cannot determine from these results whether the primary or secondary extinction occurs in practice. It may be anticipated, however, that the primary extinction effect is predominant in the present case. Since the effective depth of penetration of x rays in lead is in the same order of magnitude with the mosaic size usually accepted, there is little possibility of the occurrence of secondary extinction. When the primary extinction is assumed to occur, the diameter of the mosaic block D can be calculated with Eq. (3). The value of D for this specimen is 0.89×10^{-4} cm, which seems to be reasonable. The specimen was annealed at 150°C for various times successively, and the value of D was determined for each case. The results are summarized in Table II, where the results for the 200–300-mesh specimen are also shown. The values of D for two specimens are in the same order of magnitude, which shows the propriety of the absorption correction adopted above. The value of I/I' for the (422) line decreases when the specimen is annealed, as can be seen in Fig. 3. The origin of this phenomenon cannot be understood clearly. It may be possible that the diffraction line originating from some compounds of lead is superposed on the (422) line.

TABLE II. Mosaic size and dislocation density in two kinds of specimens filed and annealed.

	100–200 mesh		200–300 mesh	
	$D\times10^4$ cm	$\Lambda\times10^{-8}$ cm^{-2}	$D\times10^4$ cm	$\Lambda\times10^{-8}$ cm^{-}
Filed	0.89	3.8	0.76	5.2
Annealed at 150°C				
for 5 hr	0.85	4.2	0.85	4.2
15 hr	0.88	3.9	0.92	3.5
40 hr	...	...	0.93	3.5
80 hr	0.96	3.3	...	...

From the point of view of the dislocation theory, dislocation lines in metals are considered to form a three-dimensional network which divides the crystal into blocks. On the assumption that these blocks are equivalent to the mosaic blocks described above, the dislocation density Λ can be determined as[15]

$$\Lambda=3D^{-2}, \qquad (6$$

where it is further assumed that there is one dislocation line per one block face. The values of Λ thus obtained are shown in Table II in reasonable order of magnitude. The dislocation density seems to decrease only slightly after prolonged annealing. This may be explained as follows: Lead recrystallizes easily at room temperature, which suggests that unstable dislocations generated by cold working can move rapidly and become stable. Only a few unstable dislocations might exist in filed lead specimen powder.

One of the authors (Y. H.) has determined the dislocation density in a well-annealed single crystal of lead using an internal friction method.[16] The value obtained was about 1.0×10^8 cm^{-2}, in the same order of magnitude with the present results. Hiki also observed etch pits on a lead single crystal. The surface density of the pits was of the order of 10^7 cm^{-2} in the case of the annealed specimen.[17] There is probably no one-to-one correspondence between the etch pit and the emerging point of dislocation line on the crystal surface, because the impurity atmosphere on the dislocation line must be sufficiently dense to form the pit.

ACKNOWLEDGMENTS

The authors wish to express their sincere thanks to Dr. Hitosi Hagihara and Dr. Masao Kuriyama for their valuable discussions. They are grateful to A. Kawano, M. Minayoshi, I. Ueki, and M. Yoshida for their cooperation in the present investigation.

---

[15] G. K. Williamson and R. E. Smallman, Phil Mag. **1**, 34 (1956).
[16] Y. Hiki, J. Phys. Soc. Japan **13**, 1138 (1958); **14**, 590 (1959).
[17] Y. Hiki, J. Phys. Soc. Japan **13**, 970 (1958).

JOURNAL OF APPLIED PHYSICS VOLUME 32, NUMBER 9 SEPTEMBER, 1961

Electrical Conduction and Breakdown in High-Pressure (0.25–300 mm) Rare Gases

R. FORMAN
Parma Research Laboratory, Union Carbide Corporation, Parma, Ohio

(Received March 15, 1961)

The current-voltage characteristics of high-pressure (0.25—300 mm) rare-gas diodes have been measured. Data have been taken on diodes containing xenon, argon, and helium as the ambient gas, and tungsten, tantalum, rhenium, thoriated tungsten, and an oxide cathode as filamentary cathodes. Some unexpected phenomena have been observed and some of these general results can be summarized as: (1) The current vs voltage characteristics of argon- and xenon-filled diodes, at gas pressure above 1 mm, do not obey any space-charge law if the cathode temperature is above 2400°K. (2) The above violation of space-charge relations in argon- and xenon-filled diodes is found with tungsten, tantalum, or rhenium filaments, which can be operated above 2400°K. When thoriated tungsten or the oxide cathode, which operate below 2400°K, are used as filaments, the current-voltage characteristics of the diode follow a space-charge relation (current-voltage characteristics independent of temperature). (3) The current vs voltage characteristics of helium-filled diodes, however, do obey the space-charge relations at all filament temperatures available with the present cathode materials. (4) Some very unusual early breakdown phenomena (breakdown at potentials below ionization potential) were observed in these high-pressure rare-gas diodes employing a hot cathode. These data can be explained qualitatively by postulating the existence of thermally generated xenon or argon gas ions at temperatures in the range of 2400°K. An attempt will be made to justify this assumption by a semiquantitative theoretical treatment based on Saha's thermal ionization theory rather than the surface ionization theory of Langmuir and Kingdon.

INTRODUCTION

COLD-cathode high-pressure discharge literature is voluminous[1] and even though these studies go back many years, the field is still very active at the present time. However, no such enthusiasm seems to exist for the study of high-pressure gases using a hot emitting cathode. Most of the investigations of this nature go back 30 or 40 years,[2–4] with no apparent continuing interest. This lack of curiosity in the conduction mechanism probably arises from the general assumption that the conduction current from a hot cathode, through a high-pressure inert gas below breakdown voltages would be negligibly small.[5] Present interest in the mechanism of electron conduction in high-pressure gases was stimulated by some isolated experiments which seemed to indicate that argon and xenon were surprisingly good electrical conductors when placed in a diode structure which included a filament at sufficiently high temperatures. In order to verify the observations, a study was initiated which is the subject of this report.

VACUUM AND GAS FILLING PROCEDURE

Most of the measurements on the electrical conductivity and breakdown of the high-pressure gases were made on gas diodes whose construction is illustrated in Fig. 1. The tube illustrated as Fig. 1(a) has cylindrical symmetry; that in Fig. 1(b) has a planar anode.

After cleaning and assembly, the tubes, illustrated in Fig. 1, were mounted on an ultrahigh vacuum system, illustrated in Fig. 2(a).[6] The system shown in Fig. 2(a) was baked at 400°C for 8–10 hr. After the ion gauge, getter tube, filament, and anode of tube *F* were outgassed, the working pressure was in the range of 10^{-9} mm of mercury.

After all the above precautions were taken to eliminate contamination, vacuum measurements were made. Following these measurements, valve *A* was closed and one of the gas bottles, either *C* or *D*, was opened. The getter *B* was then flashed at this maximum gas pressure which was in the range of 300 mm. The tube characteristics were measured at this pressure. After these measurements were made, a glass connection was made between the system in Fig. 2(a) and Fig. 2(b), such as shown by the dashed line in Fig. 2. When break seal *E* was broken, the pressure in the system could be progressively lowered and measured over the range 0.25–300 mm by means of vacuum pump No. 2 and quartz manometer *J*.

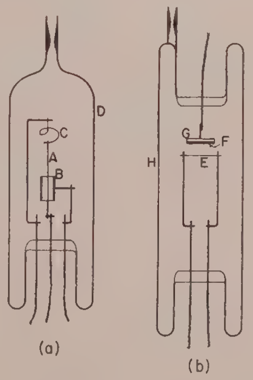

FIG. 1. Experimental tubes. (a) *A* is the filament (about 0.01 in. diameter and 3.5 cm long). *B* is a tungsten or tantalum cylindrical anode approximately 1 cm diameter and 1.25 cm long. *C* is a tantalum spring support and *D* is a Pyrex glass envelope. The supporting leads were either tungsten or tantalum. (b) *E* is a tungsten filament (0.01 in. diameter and 1.25 cm long). *F* is a tantalum anode disk 1.5 cm in diameter. *G* is a thin mica sheet over *F*. *H* is a Pyrex glass envelope. The supporting leads were either tungsten or tantalum.

---

[1] L. B. Loeb, *Handbuch der Physik* (Springer-Verlag, Berlin, Germany, 1956), Vol. 22; Revs. Modern Phys. **8**, 267 (1936).

[2] K. T. Compton and C. Eckart, Phys. Rev. **24**, 97 (1924).

[3] M. J. Druyvesteyn, Z. Physik **64**, 781 (1930).

[4] A. W. Hull, Gen. Elec. Rev. **12**, 622 (1932); Trans. Am. Inst. Elec. Engrs. **47**, 753 (1928).

[5] J. D. Cobine, *Gaseous Conductors* (Dover Publications, Inc., New York, 1958), p. 129.

[6] D. Alpert, J. Appl. Phys. **24**, 860 (1953).

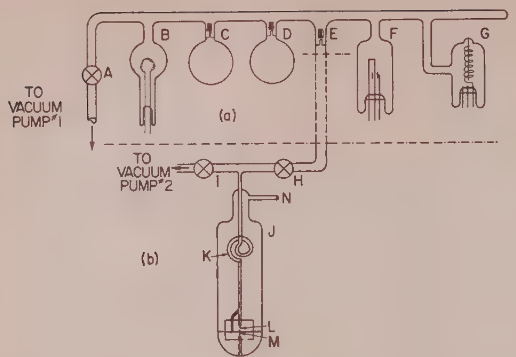

FIG. 2. Experimental vacuum system. *A* is an ultrahigh vacuum metal valve. *B* is a molybdenum getter tube. *C* and *D* are high-purity rare-gas break seal bottles. *E* is a break seal, *F* the tube under test, and *G* is an Alpert-type ionization gauge. *H* and *I* are two glass, high-vacuum stopcocks. *J* is a quartz spiral manometer, which consists of a quartz spiral *K*, whose internal and external pressures are equal when pointers *L* and *M* are lined up. The external pressure around *K* can be controlled and measured by a pump, air outlet, and mercury manometer connected to outlet *N*. Vacuum pumps Nos. 1 and 2 both have a three-stage oil diffusion pump system followed by a liquid nitrogen trap.

XENON AND ARGON EXPERIMENTS

Direct-current measurements were made on the tubes illustrated in Fig. 1, using the circuit in Fig. 3. The filament polarity illustrated in Fig. 3, where the anode power supply is connected to the negative end of the filament, was always used. This choice was made because the data showed breakdown occurred in the gas, under certain circumstances, at voltages considerably below the ionization potential, and this type of arrangement eliminated any possibility of having the filament voltage contribute to early breakdown.

The temperature of the tungsten filaments was determined from an application of the Jones-Langmuir tables[7] to the filament current under vacuum conditions. The temperature of the filament was then checked pyrometrically, through a small hole in the anode, by the use of a "Pyro" micropyrometer. After these measurements were made, the vacuum pyrometer settings for a given temperature were then used in the succeeding experiments with high-pressure gases to set filament temperatures.

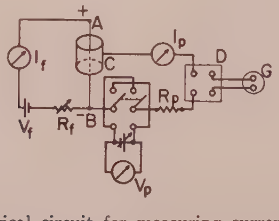

FIG. 3. Electrical circuit for measuring current-voltage characteristics of the experimental diodes. *AB* is the filament and *C* is the anode of the tube. The filament supply is V_f and the anode supply is measured by V_p. *D* is an Ayrton shunt and *G* a galvanometer. I_p is a milliammeter.

Figure 4 illustrates the anode current vs voltage data for a diode of the type illustrated by Fig. 1(a). This tube, labeled 7B, had a tungsten filament and anode. The points shown as dark squares are the vacuum data taken at a filament temperature of 2800°K. This curve is representative of space charge data and above +1 v is the same for all filament temperatures between 2400–3000°K.

However, if a high pressure of high-purity argon is the ambient, some very different anode current vs voltage curves are obtained. These are illustrated in Fig. 4 for tube 7B at an argon pressure of 107 mm of mercury. These curves are typical of the electrical characteristics of this tube at pressures above 2 mm. A few of the features which were observed should be pointed out. The ionization potential of argon is 15.68 v. Figure 4 shows that the gas is breaking down below this value when the filament temperature is 2400°K and above. It has been known for some time[2] that a discharge could be maintained at voltages below the ionization potential, but it was always considered necessary to initiate breakdown with voltages equal to or higher than the ionization potential. In this case the breakdown was initiated by a voltage which is about 3.5 v less than the ionization potential of the gas.

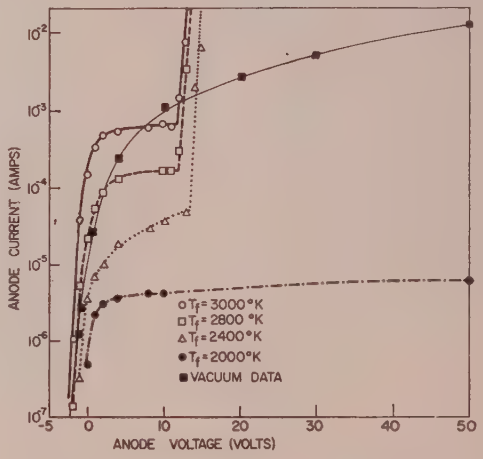

FIG. 4. Anode current-voltage characteristics of tube No. 7B at an argon pressure of 107 mm.

Another interesting property of the curves in Fig. 4 is that they are similar to the electron current curves one expects to find in a gas plasma with a Langmuir probe,[8] particularly the high-temperature curves. If the assumption about the existence of positive ions in the gas below breakdown is correct, then the curves of Fig. 4 can be analyzed using a similar reasoning to that used for the analysis of Langmuir probe data. As the negative potential on the anode decreases, the electron current rises exponentially and is given by the Langmuir probe theory as

---

[7] H. A. Jones and I. Langmuir, Gen. Elec. Rev. **30**, 310 (1927).

[8] I. Langmuir and H. Mott Smith, Gen. Elec. Rev. **27**, 449, 538, 616, 762, 810 (1924).

$$J = J_0 \exp\{-eV/kT_e\}, \qquad (1)$$

where J is the measured electron current, J_0 is the saturated current one would measure if all the electrons in the vicinity of the collecting electrode were collected as fast as they arrived, V is the magnitude of the retarding voltage, and T_e is the electron temperature associated with the Boltzmann distribution of electrons. As the negative voltage on the anode is further lowered, the exponential character of the curve changes and the electron current saturates at J_0 when the potential of the collector is at space potential. As the anode is made more positive than space potential, the electron current shows no radical change until some electrons are accelerated with a sufficiently high energy to form additional ions in the gas space. This leads to an avalanche effect and the gas breaks down at a sufficiently high voltage. Using this type of analysis of the 3000°K curve, one obtains a saturated electron current 6×10^{-4} amp and an electron temperature of about 3200°K.

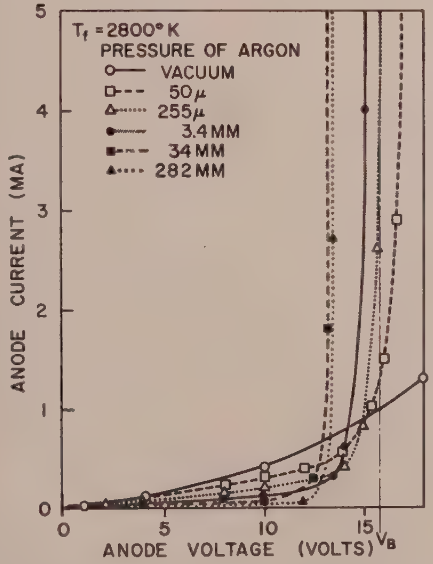

FIG. 5. Anode current-voltage characteristics of tube No. 8A with pressure of argon as the parameter.

The data in Fig. 5 show the breakdown characteristics of a tube as shown in Fig. 1(b) at a constant filament temperature, 2800°K, with the pressure of argon as the variable parameter. This tube, called 8A, had a 0.01-in. diameter tungsten filament and a tantalum disk anode. The abscissa and ordinate in this figure have the same interpretation as those of the previous figures. The vacuum curve follows the usual $V^{\frac{3}{2}}$ space-charge equation. One should note that at pressures above 1 mm, the gas breaks down before ionization potential (V_B) is reached. At lower pressures (250 μ and below), breakdown occurs at ionization potential or above.

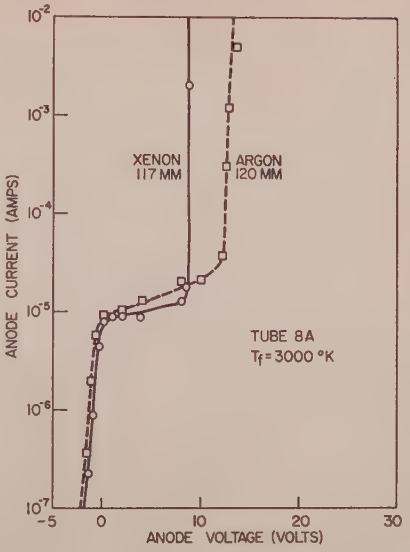

FIG. 6. Anode current-voltage characteristics of tube No. 8A in both xenon and argon.

Figure 6 is a comparison of the voltage-current data one obtains for xenon and argon at approximately the same pressure at a filament temperature of 3000°K. These data are typical of the comparative data at all pressures and temperatures for argon and xenon. It is interesting to note that the slope of the retarding voltage portions of the two curves is the same. In addition, the apparent saturated current value at positive voltages below breakdown for both curves is approximately the same at 10^{-5} amp. The big difference is that early breakdown occurs in both gases but at values

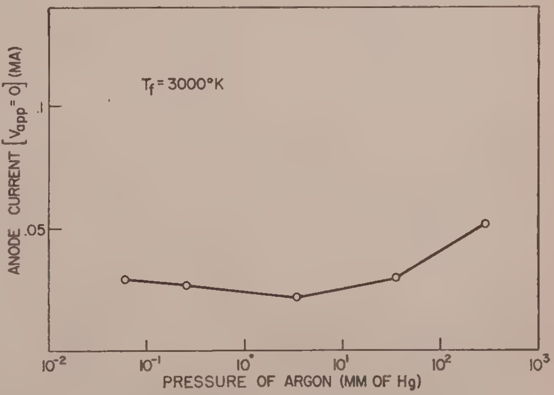

FIG. 7. Anode current with no applied voltage vs pressure for tube No. 8A.

whose difference is very close to the difference in ionization potentials of the two gases (3.6 ev).

Figure 7 is a plot of anode current for zero applied anode voltage to tube 8A, at a filament temperature of 3000°K, vs pressure of argon over five orders of magnitude in pressure. What is most surprising about these data is that the current is practically independent of pressure over such a wide range of pressure. The dip in the curve of Fig. 7 is probably not significant and is likely the result of experimental difficulty in setting the filament temperatures to better than ±25° at these high temperatures. A difference of 25–50°K in temperature setting, at these high temperatures, can easily lead to a 25–50% change in prebreakdown current as can be illustrated by the curves in Fig. 4. In Fig. 4 one can see that a 200°K spread in temperature leads to a saturated prebreakdown current change of a factor of five.

Attempts were made to determine how these above-mentioned anomalous characteristics were dependent on the filament materials. Tungsten, tantalum, and rhenium, refractory metals which are capable of being heated above 2400°K and are good thermionic emitters at these high temperatures, were tested. Argon diodes with either rhenium or tantalum filaments gave similar results to those shown in Fig. 4 for operating temperatures of 2400–3000°K.

DISCUSSION OF XENON AND ARGON RESULTS

The data on xenon and argon can be qualitatively explained by assuming thermal ionization of the gas in the vicinity of the hot filament. An attempt will be made to justify this assumption and present a physical model for this type of ionization phenomenon.

The original theoretical treatment of thermal ionization was developed by Saha.[9] He showed that at a sufficiently high temperature, collisions between neutral gas particles can lead to ionization. Mathematically, the Saha equation is expressed as[10]:

$$\frac{f^2}{1-f^2}p=\frac{g_e g_i}{g_0}\left(\frac{2\pi m}{h^2}\right)^{\frac{3}{2}}(kT)^{\frac{5}{2}}\exp\left\{-\frac{eV_i}{kT}\right\}, \qquad (2)$$

where f is the ratio of the ion concentration n_i to the total number of atoms and ions n. The neutral atom concentration is n_0 and the electron concentration is n_e, which is equal to the ion concentration n_i. g_e, g_i, and g_0 are the statistical weights for the electron, ion, and neutral atom, respectively, and V_i is the ionization potential of the gas. The other symbols have their usual meaning.

When Langmuir and Kingdon[11] tried to apply Eq. (2) to some of their early measurements on thermal ionization of cesium on tungsten, they found that it gave an incorrect result. To explain this inconsistency, Langmuir assumed that the electron concentration n_e was not equal to the ion concentration n_i, but was equal to the electron concentration, characteristic of a tungsten filament emitting at a given temperature. Under the assumption that n_i, n_e, and n_0 are in thermal equilibrium given by

$$(n_i n_e/n_0)=K(T), \qquad (3)$$

where K is a constant at a given temperature, the equation[12]

$$\frac{n_e n_i}{n_0}=\frac{g_e g_i}{g_0}\left(\frac{2\pi mkT}{h^2}\right)^{\frac{3}{2}}\exp\left\{-\frac{eV_i}{kT}\right\} \qquad (4)$$

was derived. When the electron density characteristic of an emitting filament,[13]

$$n_e=2\left(\frac{2\pi mkT}{h^2}\right)^{\frac{3}{2}}\exp\left\{-\frac{e\psi}{kT}\right\}, \qquad (5)$$

where ψ is the work function of the filament, was inserted into Eq. (4), the following expression was obtained by Langmuir and Kingdon:

$$\frac{n_i}{n_0}=\frac{g_e g_i}{2g_0}\exp\frac{e}{kT}\{\psi-V_i\}. \qquad (6)$$

In the present experiments, the pressure and temperature of the gases in question are much higher than those in the Langmuir-Kingdon experiment. Under their experimental conditions, the gas pressure was low and the mean free path of the gas atoms so high that they assumed the cesium atoms would collide mainly with the filament and tube walls and very rarely with one another. This made Eq. (2) inapplicable because the gas atoms were not in equilibrium with one another, and made Eq. (6) suitable because the ionization process was considered a filament surface reaction. This is not true in the present experiments on the rare gases. Here the gas pressure is so high that a gas atom hitting the filament will make many collisions with other atoms before it again hits the filament. Under these circumstances, the gas atoms near the filament (within a few mean free paths) are in equilibrium with other gas atoms at a temperature in the neighborhood of the filament temperature. Thus, it is possible to develop a bulk temperature of the gas in the vicinity of the filament, characteristic of the filament. It is to this gas that we propose to apply the original Saha equation [Eq. (2)] in order to account for the observed currents and supposed thermal ionization. Table I shows the results of applying this equation for a series of temperatures and two different pressures.

---

[9] M. N. Saha, Phil. Mag. **40**, 472 (1920).

[10] L. D. Landau and E. M. Lifshitz, *Statistical Physics* (Pergamon Press, Ltd., London, Paris, 1958), pp. 322–324.

[11] I. Langmuir and K. H. Kingdon, Proc. Roy. Soc. (London) **A107**, 61 (1925).

[12] R. H. Fowler, *Statistical Mechanics* (Cambridge University Press, New York, 1936), pp. 370–373.

[13] Reference 12, p. 345, Eq. (1023).

TABLE I. The fractional ionization of xenon and argon as given by the Saha equation [Eq. (2)].

Temperature °K	Gas	f (100 mm)	f (10 mm)	Ions/cm^3 at 100 mm $f\times3.54\times10^{18}$	Ions/cm^3 at 10 mm $f\times3.54\times10^{17}$
1000	Argon	1.0×10^{-38}	3.4×10^{-38}	...	...
2000	Argon	1.4×10^{-18}	4.2×10^{-18}	4.8	1.5
2400	Argon	3.3×10^{-15}	1.0×10^{-14}	1.2×10^{4}	3.7×10^{3}
2800	Argon	8.9×10^{-13}	2.8×10^{-12}	3.3×10^{6}	1.0×10^{6}
3000	Argon	8.5×10^{-12}	2.7×10^{-11}	3.0×10^{7}	9.5×10^{6}
1000	Xenon	1.2×10^{-29}	3.8×10^{-29}	...	...
2000	Xenon	4.7×10^{-14}	1.4×10^{-13}	1.7×10^{5}	5.2×10^{4}
2400	Xenon	2.0×10^{-11}	6.2×10^{-11}	6.9×10^{7}	2.3×10^{7}
2800	Xenon	1.6×10^{-9}	4.8×10^{-9}	5.5×10^{9}	1.7×10^{9}
3000	Xenon	8.9×10^{-9}	2.8×10^{-8}	3.1×10^{10}	1.0×10^{10}

TABLE II. The fractional ionization of xenon and argon as given by the Langmuir-Kingdon equation [Eq. (6)].

Temperature °K	Gas	(n_i/n_0) Eq. (6)
1000	Argon	10^{-57}
2000	Argon	7.7×10^{-28}
2400	Argon	3.4×10^{-23}
3000	Argon	1.5×10^{-18}
1000	Xenon	1.3×10^{-37}
2000	Xenon	8.9×10^{-19}
2400	Xenon	1.2×10^{-15}
3000	Xenon	1.7×10^{-12}

If instead of Eq. (2) we had applied the Langmuir-Kingdon expression [Eq. (6)], the results would have been as shown in Table II. The expression n_i/n_0 in Table II, which is independent of pressure in the Langmuir model, is to be compared with the values for f in Table I. Thus, it is clear that the original Saha equation is more consistent with a model for thermal ionization of the rare gases at high pressures than is the Langmuir-Kingdon expression.

In the early cesium experiments, ionization occurs during contact of the gas atoms with the hot filament which is surface ionization. This leads to a copious ion yield because of the low ionization potential of cesium. However, in the case of the high-pressure rare gases, this surface ionization effect is negligible because of the extremely high ionization potentials and a large yield of ions must be dependent on the relatively large number of available gas atoms and the bulk ionization given by the Saha equation. The existence of such a hot stationary gas layer close to the filament has been used by Langmuir[14] to explain the conductive heat loss from hot filaments in a gas near atmospheric pressure. In addition, it has been shown[15] that the presence of positive ions in the cathode-anode space can have a profound influence on electron current.

Although the presence of positive rare-gas ions is needed for a partial explanation of the data, it should be pointed out that an additional difficulty associated with getting a more quantitative understanding of these phenomena is the low electron mean free path associated with these high pressure measurements. On the basis of classical kinetic theory,[16] the electron mean free path through argon, at one-third of an atmosphere, is in the order of 5×10^{-5} cm. This is negligible compared to the anode cathode spacing which is 5 mm. However, it should be pointed out that the Ramsauer effect[17] is present in both argon and xenon, and in these gases the electron mean free path would be considerably higher than the classical value for low-energy electrons.[18] For argon at its minimum cross section (electron energy 0.6 v), the electron mean free path at 200 mm is about 4×10^{-3} cm. In xenon at the same pressure, the cross-section minimum (about 1.0 ev) gives an electron mean free path of about 10^{-3} cm. Although these numbers are still small compared to the electrode spacing, they are larger than the classical values and probably partly account for some of the unusually high prebreakdown conduction currents. Of course, at the lower pressures, say 10 mm, the Ramsauer effect in argon shows that the electron mean free path can be as high as 0.8 mm, which is approaching electrode spacing. Besides the presence of the Ramsauer effect in xenon and argon, it should be noted that, in general, the rare gases have a low collision cross section to low-energy electrons.[18]

On the premises inherent in the preceding sections, an attempt will now be made to explain the experimental data of Figs. 4–7. These premises are:

(1) Equation (2) predicts the existence of reasonable rare-gas ion densities at temperatures above 2400°K in both argon and xenon, as shown by Table I.

(2) The low-collision electron cross section and Ramsauer effect in xenon and argon permit one to sustain high electron currents in fairly high-pressure gases.

The fact that all of the pressure curves in Fig. 4 follow a different path below breakdown and do not obey a space charge law can be understood by the following argument. As one raises the filament temperature from T_0 to T_1, where $T_1>T_0$, two effects occur simultaneously. First, at the higher temperature the filament is a more copious electron emitter because its emissive capability is proportional to $\exp\{-e\psi/kT\}$. In addition, at the higher temperature more rare-gas ions are being formed. In vacuum the increased emission capability with temperature of the filament is effectively neutralized by the increased electronic charge built up in the vicinity of the filament. However, in the high-pressure rare-gas diode some of the increased space charge is neutralized by the additional ions formed and at the higher temperature more emission is observed, which can be attributed to the higher emissive capability of the filament.

---

[14] I. Langmuir, Phys. Rev. **34**, 401 (1912).

[15] I. Langmuir, Phys. Rev. **33**, 954 (1929).

[16] Reference 5, p. 22.

[17] C. Ramsauer, Ann. Physik **64**, 513 (1921).

[18] R. B. Brode, Revs. Modern Phys. **5**, 257 (1933).

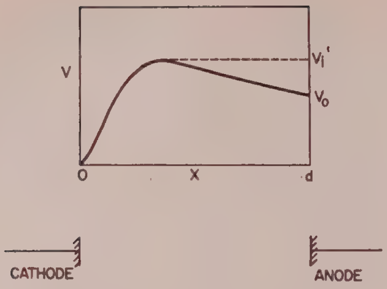

FIG. 8. Cathode-anode potential distribution in a diode displaying early breakdown effects.

The possible explanations for the high prebreakdown conduction currents in Fig. 4 have been discussed in the preceding paragraphs, but the early breakdown properties require some additional discussion. Early breakdown could be explained if one could show that the potential distribution in the space between cathode and anode could have the characteristics illustrated in Fig. 8. In the figure, cathode and anode are separated a distance d. The potential in the space, which is the ordinate V, is plotted as a function of distance x, in the space. If the applied voltage is V_0 and the ionization potential is V_i, then breakdown can occur with an applied potential V_0 if the maximum potential in the space $V_i' \geq V_i > V_0$. Such a potential might arise if a positive space charge close to the filament, resulting from the generation of positive ions, is assumed there. Von Engel[19] describes a simple diode model, which is not physically realizable, but has a potential distribution similar to that of Fig. 8.

It is easy to show that the proposed model predicts that the thermally generated ion density varies with pressure, p, as $\sqrt{p}$. Equation (2), when $f \ll 1$, shows that f is inversely proportional to $\sqrt{p}$ for a given gas and a given temperature. Since the density of ions is given by $f.n$, where n is the total density of ionized and unionized atoms, and n is proportional to p, then the density of ions is proportional to $\sqrt{p}$. On the prediction that the positive ion density increases with pressure as $\sqrt{p}$, and that an increased positive ion density leads to a potential distribution equivalent to that of Fig. 8, the proposed model predicts that higher pressures at equal filament temperatures would lead to lower breakdown voltage. This would explain the early breakdown effects shown in Fig. 5.

The early breakdown voltage difference between xenon and argon in Fig. 6 is easily explainable, but the equivalent saturated prebreakdown current for the two gases is not. Table I predicts a much higher ion density for xenon than argon. Although argon has a smaller collision cross section for electrons than xenon, it is felt that this is not large enough to explain the unexpected similarity between the two prebreakdown current curves. One possible explanation is that there are sufficient ions in both gases at this filament temperature to mitigate the space-charge effects. Under these circumstances, the current would be limited by the thermionic emission capability of the filament modified by the presence of the high-pressure gas.

Von Engel[20] has shown that the final drift velocity v_∞ for an electron in a weak electric field X can be expressed as

$$v_\infty = (e/m)^{\frac{1}{2}}(K/2)^{\frac{1}{4}}[X\lambda]^{\frac{1}{2}}, \tag{7}$$

where λ, the mean free path, is very small compared to electrode spacing. K in Eq. (7) is the average energy lost in an elastic collision between an electron and a gas molecule and e, m are electronic charge and mass, respectively. Since the mean free path is inversely proportional to the pressure, Eq. (7) can be expressed as

$$v_\infty = A(X/p)^{\frac{1}{2}}, \tag{8}$$

where A is a constant of proportionality.

In a high-pressure gas diode at a given filament temperature and electric field, one would expect the diode current to vary as $(\text{pressure})^{-\frac{1}{2}}$ if no positive ions are present, because the average electron charge density would be essentially independent of pressure, whereas the drift velocity would obey Eq. (8). Figure 7, however, shows that this current is independent of pressure in the xenon- and argon-filled high-filament temperature diodes. This would seem to indicate that the average electron charge density in the diode varies as $(\text{pressure})^{\frac{1}{2}}$ when positive rare-gas ions are present in these tubes. It is interesting to note that Eq. (2) predicts a $(\text{pressure})^{\frac{1}{2}}$ dependence for the positive ion density.

ADDITIONAL EXPERIMENTS

To check the validity of some of the basic assumptions of the proposed theory for thermal ionization, a number of experiments readily suggest themselves. For instance:

(1) The temperature-dependent current-voltage characteristics of Fig. 4 would not be expected to occur in argon or xenon containing an electron emitter, which operates efficiently at a lower temperature than 2400°K, if the proposed theory is correct.

(2) The temperature-dependent current-voltage characteristics of Fig. 4 would not be expected to occur in a diode containing helium because of its extremely high ionization potential.

(3) The prebreakdown current vs pressure curve at a constant field strength for the diodes described in (1) and (2) would follow a $(p)^{-\frac{1}{2}}$ relation given by Eq. (8).

The conclusions of statement (1) were verified by measuring the current-voltage characteristics of separate diodes containing (a) an oxide cathode and (b) a thoriated tungsten filament. These tubes were similar to those shown in Fig. 1(a). The oxide cathode was run in an atmosphere of xenon and the thoriated tungsten in an ambient of argon. The pressure in both cases was varied from 0.25–300 mm, and at all pressures the current-voltage curves followed a space-charge relation.

---

[19] A. von Engel, *Ionized Gases* (Oxford University Press, London, 1955), pp. 13–16.

[20] Reference 19, p. 104.

The verification of the statement that the current-voltage characteristics of a helium diode obey a space-charge relation is illustrated in Fig. 9. These data were obtained from diode 7B which is the same one used to obtain the data in Fig. 4. However, in this case the gas ambient is helium at 263-mm pressure. It is obvious that the curves are temperature independent and follow a space-charge law for all tungsten filament temperatures up to 3000°K.

The measurements in a helium diode using a high-temperature tungsten filament are also interesting from another point of view. Regardless of the refinements in technique to eliminate contaminants by using ultrahigh vacuum techniques and spectroscopically pure gas, there was always the possibility that infinitesimally small concentrations of contaminants could be responsible for some of the apparent thermal ionization phenomena which were observed. These could be coming from: (a) gas impurities below the spectroscopic limit; (b) the Pyrex glass walls of the tube; (c) foreign ions emitted by the hot filament; and (d) the existence of tungsten ions around the hot filament. On the basis of the helium diode experiments, to be described below, it is felt that the last three possible sources of minor contamination were absent.

After the high pressure measurements in the helium diode were made, shown by Fig. 9, we followed the usual procedure used in all these measurements by decreasing the pressure in progressive steps and making similar measurements down to, in this case, 0.7 mm. At all pressures in the range of 0.7–263 mm, space-charge characteristics were obtained on these helium diodes. No evidence for the thermal generation of ions in helium was found. After the helium in tube 7B was evacuated, a check was then run on the validity of the experiment by introducing argon at 96 mm and measuring the current-voltage characteristics. These measurements gave temperature-dependent curves identical to those of Fig. 4 and showed the presence of thermally generated ions. This seems to confirm the original hypothesis that the ions measured in these experiments are rare-gas ions.

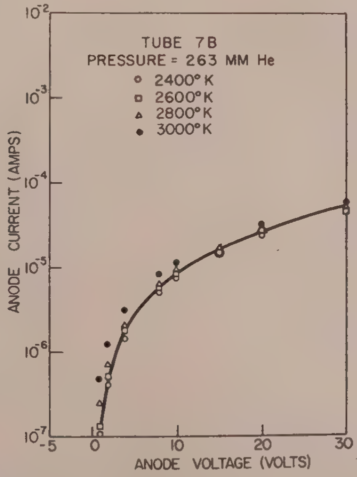

FIG. 9. Anode current-voltage characteristics of tube 7B in helium at 263 mm.

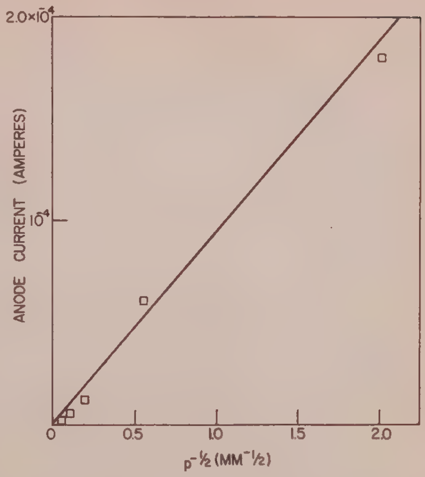

FIG. 10. Anode current vs (pressure)$^{-\frac{1}{2}}$ for tube 9A in xenon at a constant anode voltage of 8 v and a filament temperature of 870°C.

Figure 10 is confirmatory evidence for the validity of the statement that the prebreakdown current vs pressure at a constant field strength would follow a $p^{-\frac{1}{2}}$ relation if there is no thermal generation of ions in a high-pressure gas diode. Figure 10 is a plot of the prebreakdown current vs (pressure)$^{-\frac{1}{2}}$ for tube 9A (oxide cathode) in xenon at a constant anode potential of 8v and a filament temperature of 870°C. This curve should be compared with Fig. 7 and is evidence that without the thermal generation of ions Eq. (8) is obeyed.

It should be pointed out that current vs (pressure)$^{-\frac{1}{2}}$ curves similar to those of Fig. 10 were also obtained for thoriated tungsten in argon and tungsten in helium.

CONCLUSION

Current-voltage measurements on high-pressure xenon- and argon-filled diodes have provided some unexpected results. These data, taken at filament temperatures above 2400°K, have shown that the current-voltage characteristics of these diodes are temperature sensitive and do not follow a space-charge law. In addition, diodes containing these low ionization potential rare gases show breakdown characteristics at anode voltages considerably lower than the ionization potential for the particular gas. These unusual properties are not displayed by identical diodes containing a high ionization potential rare gas such as helium.

It is felt that these results can be explained by postulating the presence of positive ions in the low ionization potential rare-gas diodes. Using this concept as a fundamental premise, a theory based on a Saha type of thermal ionization is proposed to explain the above data. This theory, which is shown to be applicable at sufficiently high pressures, where the electron mean free path is much smaller than the tube dimensions, has been used to qualitatively explain these results. A more quantitative explanation will undoubtedly require a modification of the theory. This modification will have to consider other possible ionization mechanisms such as (a) multiple collision type processes involving electrons and photons from the hot filament and the resonant and metastable states of the rare-gas ions, and (b) impact ionization phenomena.[21,22]

ACKNOWLEDGMENTS

The author would like to express his appreciation to all those staff members of the Parma Research Center who helped in the formulation of some of the ideas expressed in this report by their discussion and critical comment. In particular, we are indebted to R. G. Lye, T. H. George, P. M. Stier, D. Redfield, and especially R. L. Cummerow. We would also like to acknowledge the contributions of J. A. Kallas and J. Muenter for their technical assistance during the course of this program.

---

[21] W. B. Nottingham, Mass. Inst. Technol. Research Lab. Electronics, Tech. Rept. No. 373, September 9, 1960.

[22] J. A. Michael and J. R. Reitz (private communication).

JOURNAL OF APPLIED PHYSICS VOLUME 32, NUMBER 9 SEPTEMBER, 1961

Role of Crystal Structure in Diffusion. I. Diffusion Paths in Closest-Packed Crystals*

Leonid V. Azároff†
Metallurigical Engineering Department, Illinois Institute of Technology, Chicago, Illinois

(Received March 13, 1961)

A consideration of the crystal structures of simple binary compounds shows that they can be represented by closest packings of the larger anions in which two kinds of interstices are available for occupation by the metal atoms. In hexagonal closest packings, the octahedral voids form continuous chains by sharing opposite faces while the tetrahedral voids form isolated pairs. In cubic closest packings, each kind of void shares faces only with unlike voids. The specific diffusion paths available in these compounds depend, therefore, on the manner in which the voids are occupied. Continuous diffusion paths comprised of normally unoccupied voids exist in ZnO and α-ZnS type structures so that voidal diffusion can take place without requiring defect formation. Similarly, voidal diffusion can occur in BiO_3, $CrCl_3$, and CdI_2 type structures. Conversely, all possible continuous diffusion paths are blocked by metal atoms in the NiAs, NaCl, and antifluorite-type structures so that vacancy or interstitialcy mechanisms are necessary to account for diffusion.

INTRODUCTION

EARLY theoretical investigations of diffusion in crystals concerned themselves with statistical considerations of the collective motion of the atoms and point defects involved. More recently, attention has focused on their individual movements so that the environment of the atoms, that is, the crystal structure, had to be considered in more detail. For a number of reasons, attention has focused primarily on simple metals and binary compounds crystallizing with the sodium chloride structure. Thus, it has been shown that the relatively small size of the interstitial sites in closest-packed metals precludes their utilization in self-diffusion and the atoms must move via vacancies or so-called ring mechanisms.[1] More sophisticated calculations taking various energy terms into account have also been performed supporting, for example, the conclusion that diffusion in alkali halides similarly takes place via vacancies.[2]

In the case of other binary compounds, the experimental evidence is meager and theoretical considerations of diffusion are virtually absent. The crystal structure of these compounds undoubtedly plays an important role although not necessarily a decisive one. It is of some interest, therefore, to see in what way the crystal structure can affect the diffusion process and how these considerations can be applied to explain presently available diffusion data. This analysis is presented in two separate parts. In Part I, the readily available diffusion paths in each structure type are established and the consequences of diffusion along such paths are considered. It turns out that the available diffusion paths in crystals already considered are consistent with diffusion mechanisms previously proposed.

---

[*] This investigation was supported by the U. S. Air Force Office of Scientific Research.

[†] This work was performed at Bookhaven National Laboratory.

[1] Harvey Brooks, *Impurities and Imperfections* (American Society for Metals, Cleveland, Ohio, 1955), pp. 1–27.

[2] N. F. Mott and M. J. Littleton, Trans. Faraday Soc. **34**, 485 (1938); E. S. Rittner, R. A. Hunter, and F. K. Du Pré, J. Chem. Phys. **17**, 198 (1949).

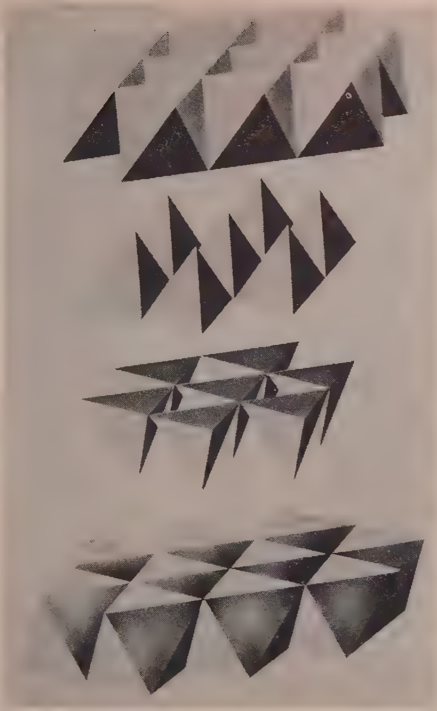

FIG. 1. Exploded view of the coordination polyhedra of voids in a hexagonal closest packing.

It is further shown that a hitherto undescribed diffusion process takes place in compounds crystallizing with more "open" structures such as the alpha and beta modifications of zinc sulfide. Finally, the way that available diffusion paths are related to the activation energy for diffusion is considered in Part II.[3]

CLOSEST PACKINGS

The crystal structures of most inorganic compounds can be described as a closest packing of the larger atoms (usually anions) with the smaller ones distributed amongst their interstices. The different kinds of closest packings found in nature have been described elsewhere[4] so that only a few principal features are noted here. Of the infinite possible closest packings, two are encountered most frequently. These are the cubic closest packing containing three closest-packed layers in the unit repeated along [111] and the hexagonal closest packing comprised of two layers repeated along the hexagonal c axis. All closest packings contain two kinds of interstices between the closest-packed atoms, namely, octahedral voids coordinated by six atoms and tetrahedral voids coordinated by four atoms. The total number of octahedral voids is equal to the number of atoms and to one-half the number of tetrahedral voids present in the closest packing. The ratio of the radius of a sphere that just fits into these voids to that of the closest-packed atoms decreases from 0.414 for an octahedral void to 0.225 for a tetrahedral void.

Owing to the relatively small size of these interstices, the closest-packed atoms cannot move from place to place unless some of them are missing inside the crystal. Thus, vacancies are necessary for self-diffusion in metal crystals and for the diffusion of closest-packed atoms in other crystals as well. Possible motions of atoms occupying interstitial positions in a closest packing, however, depend on how the two kinds of voids are disposed relative to each other and in what manner they are occupied. Since the array of these voids is of primary interest, it is instructive to represent them by their coordination polyhedra obtained by joining the midpoints of the closest-packed atoms coordinating each void. The two kinds of voids form interpenetrating arrays which can be seen in the exploded views of a hexagonal closest packing in Fig. 1 and of a cubic closest packing in Fig. 2. An examination of the hex-

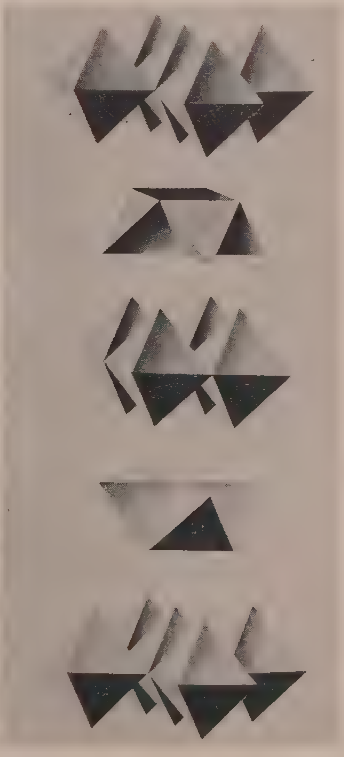

FIG. 2. Exploded view of the coordination polyhedra of voids in a cubic closest packing. The layers are shown separated parallel to (001), not the closest-packed (111) planes, in order to make the cubic symmetry more obvious.

---

[3] Leonid V. Azároff, J. Appl. Phys. **32**, 1663 (1961), following paper.

[4] N. V. Belov, *Struktura Ionnich Kristallov i Metallitcheskich Faz* (Akademiya Nauk S.S.S.R., Moscow, 1947); Leonid V. Azároff, *Introduction to Solids* (McGraw-Hill Book Company, Inc., New York, 1960), pp. 55–72.

agonal closest packing in Fig. 1 shows that the tetrahedral voids share one triangular face with each other in isolated pairs, and the other three faces with the octahedral voids within a closest-packed layer. The octahedral voids, on the other hand, share opposite faces with octahedral voids in the layer above and below, forming thereby continuous chains of octahedra normal to closest-packed layers, i.e., along the vertical c axis. By comparison, two like voids do not share a common face in the cubic closest packing shown in Fig. 2 so that tetrahedra share all their faces with octahedra and vice versa. Note also that atoms located at the centers of these voids can move from any void to an adjacent one most easily through the midpoints of the triangular faces shared by both voids.

CUBIC PACKINGS

As can be seen in Fig. 2, the tetrahedral voids in a cubic closest packing share only edges with each other as do the octahedral voids. Since the saddle-point configuration at the center of a shared face is more favorable than that at the center of a shared edge, the diffusion paths of least resistance in cubic closest packings must consist of alternating tetrahedral and octahedral voids. The specific diffusion paths available in various cubic packings, therefore, depend on which of the voids are normally occupied and which are normally empty.

In the sodium chloride structure, all the octahedral voids are occupied by the metal atoms. Since the octahedral voids form an integral part of any conceivable diffusion path, the metal atoms must be first removed from an octahedral void. This can happen in two ways. Either vacancies are formed in the crystal, as appears to be the case in most alkali halides,[5] or else the moving atom "displaces" the atom occupying an octahedral void in its path. This second process has been called the interstitialcy mechanism[6] and it has been shown that it can occur following the formation of Frenkel defects or directly as a result of atomic displacements during diffusion.[7] The interstitialcy mechanism appears to be responsible for the diffusion of silver atoms in AgCl and AgBr.[7,8] This is an example of diffusion in crystals where factors other than their structure determines the detailed atomic movements involved. It should be noted that the larger closest-packed halogen atoms in these crystals can diffuse only via vacancies.[9]

A number of binary compounds crystallize with structures that are closely related to sodium chloride except that the octahedral voids are only partially filled. These crystals, typified by the $CdCl_2$, $CrCl_3$, and Bi_2S_3 structures, are listed in Table I which also gives the fraction of occupied voids for each type. Since some of the octahedral voids are normally vacant in these crystals, diffusion can proceed via mechanisms differing from those described above. Thus, the presence of $33\frac{1}{3}\%$ "built-in" bismuth vacancies in Bi_2S_3 means that self-diffusion can proceed without requiring further defect formation. In the extreme case of the $CrCl_3$ structure, only one-third of the octahedral voids are occupied. This means that unoccupied octahedral voids link up with empty tetrahedral voids to form continuous diffusion paths comprised entirely of voids not normally occupied by metal atoms in this structure. In order to distinguish atomic movements along such paths from interstitial mechanisms previously described, the term *voidal diffusion* is suggested for this process. In cubic closest packings, such diffusion paths extend in several different directions. The decrease in crystal symmetry resulting from a partial occupation of the octahedral voids and the consequent distortion of the sodium chloride structure may, however, lower the activation energy for voidal diffusion along certain directions. Whether or not such small anisotropies can be detected must await future investigations of single crystals.

TABLE I. Diffusion paths in structures based on cubic closest packings.

Structure type	Occupied voids	Diffusion path	Diffusion mechanism
NaCl	All octahedral	oct-tet-oct	Vacancy or interstitialcy
Bi_2S_3	$\frac{2}{3}$ octahedral	oct-tet-oct	Vacancy
$CdCl_2$	$\frac{1}{2}$ octahedral	oct-tet-oct	Voidal(?)
$CrCl_3$	$\frac{1}{3}$ octahedral	oct-tet-oct	Voidal
α-ZnS	$\frac{1}{2}$ tetrahedral	tet-oct-tet	Voidal
Antifluorite	All tetrahedral	tet-oct-tet	Vacancy

An even better example of voidal diffusion is afforded by certain cubic crystals in which the octahedral voids are completely empty. As can be seen in Fig. 2, the tetrahedral voids form two crystallographically distinct sets. The tetrahedra of one set share only corners with each other and only edges with the tetrahedra of the second set. When all the tetrahedral voids belonging to one set are occupied, the zinc blende (α-ZnS) structure shown in Fig. 3 results. The unoccupied set of tetrahedral voids and the empty octahedral voids form veritable tunnels extending parallel to the [[110]] directions in the crystal. These tunnels obviously offer very easy diffusion paths which is the reason why naturally occurring ZnS crystals contain unusually large amounts of foreign atoms. Since each tetrahedral void is surrounded by such empty tunnels on all four sides, an atom in such a site can be considered to be already occupying a position along a permissible diffusion path comprised of alternating tetrahedral and octahedral voids. Once

---

[5] N. F. Mott and R. W. Gurney, *Electronic Processes in Ionic Crystals* (University Press, Cambridge, England, 1948), 2nd ed., pp. 44–45.

[6] C. W. McCombie and A. B. Lidiard, Phys. Rev. **101**, 1210 (1956).

[7] Robert J. Friauf, Phys. Rev. **105**, 843 (1957).

[8] Richard F. Reade and Don S. Martin, Jr., J. Appl. Phys. **31**, 1965 (1960).

[9] D. S. Tannhauser, J. Phys. Chem. Solids **5**, 224 (1958).

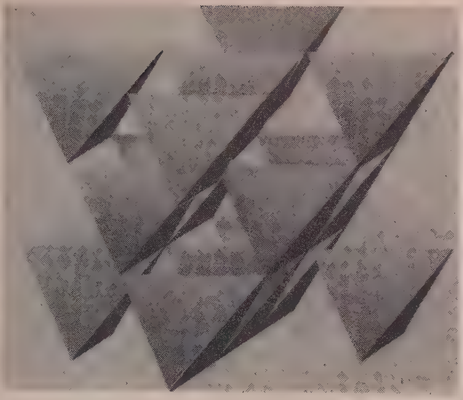

FIG. 3. Crystal structure of α-ZnS represented by a spatial distribution of ZnS_4 tetrahedra.

"launched," it is most likely to diffuse along the paths of least resistance parallel to the [[110]] directions. Since this means that diffusion takes place primarily through voids that are not normally occupied in the zinc blende structure, this is another example of voidal diffusion in crystals.

The fluorite (CaF_2) structure is somewhat unusual in that the smaller metal atoms are arrayed in a cubic closest packing while the anions occupy all the available tetrahedral voids. If the role of the cations and anions is reversed, for example in Na_2S, then the so-called antifluorite structure is obtained. Because the larger anions form the closest packing in the antifluorite structure, it is more directly comparable to the other structure types listed in Table I. The occupation of all the tetrahedral voids by metal atoms suggests that vacancies must be generated before diffusion can proceed in these structures. It should be borne in mind, however, that each occupied tetrahedral void is surrounded by four empty octahedral voids (Fig. 2). Thus it is equally likely that diffusion can take place in this structure by means of the interstitialcy mechanism. Although some preliminary calculations have suggested that the interstitialcy mechanism should be preferred by crystals having the antifluorite structure, final conclusions must await the obtainal of good diffusion data.

HEXAGONAL PACKINGS

As has been shown in Fig. 1, the octahedral voids in a hexagonal closest packing form continuous chains normal to the closest-packed layers. Within a layer, the two kinds of voids share faces with unlike voids only. Note that there are two sets of tetrahedral voids in each layer, one set with apices pointing up and the other with apices pointing down. The tetrahedra of one set share one of their faces with tetrahedra of the other set forming pairs of tetrahedra surrounded on six sides by octahedra. A hexagonal closest packing is somewhat unique, therefore, in that diffusion can take place via diffusion paths comprised of one kind of void (octahedral) only provided that the octahedral voids are not normally occupied by atoms. This is the case in the so-called zincite (ZnO) or wurtzite (β-ZnS) structure, in which the metal atoms occupy one-half of the available tetrahedral voids. After a Zn atom in ZnO has been displaced to an adjacent octahedral void, it can continue to move through the crystal without necessarily occupying another tetrahedral void. This does not mean that the actual path of a particular atom may not include some tetrahedral voids, but merely that a jump from an octahedral to an adjacent tetrahedral void is energetically favored only when both voids in the tetrahedral pair are unoccupied.[10] Diffusion in such crystals should proceed, therefore, primarily, through voids that are normally not occupied in the structure so that this is still another example of voidal diffusion. It is interesting to speculate at this point whether crystals having the zincite structure should show a pronounced anisotropy for diffusion parallel and normal to the *c* axis. At first glance it may appear that the existence of continuous chains of octahedral voids parallel to the *c* axis should greatly aid diffusion in that direction. It must be remembered, however, that a metal atom occupying an octahedral void has a larger energy than one in a correctly occupied tetrahedral void. Since voidal diffusion along a path comprised exclusively of octahedra does not provide a means for releasing this energy, the activation energy for this process actually may be greater than that for other kinds of interstitial diffusion. Further investigations are obviously required to clarify this matter.

TABLE II. Diffusion paths in structures based on hexagonal closest packings.

Structure type	Occupied voids	Diffusion path	Diffusion mechanism
ZnO	$\frac{1}{2}$ tetrahedral	tet-oct-oct	Voidal
NiAs	All octahedral	oct-tet-oct	Vacancy
Cr_2O_3	$\frac{2}{3}$ octahedral	oct-tet-oct	Vacancy
CdI_2	$\frac{1}{2}$ octahedral	oct-tet-oct	Voidal(?)
BiO_3	$\frac{1}{3}$ octahedral	oct-tet-oct	Voidal

Some of the other common structures in which the larger atoms form a hexagonal closest packing are listed in Table II. In the nickel arsenide structure, the nickel atoms form the closest packing and the arsenic atoms occupy all the octahedral voids. Because the only available diffusion paths in this structure include octahedral voids, diffusion can take place only if the atoms in octahedral voids are first displaced to tetrahedral sites or if there are vacancies already present. Like in the sodium chloride structure, the exact diffusion mechanism will depend on factors other than purely geometrical considerations.

---

[10] A simple analysis shows that each octahedral void in the ZnO structure is surrounded by three occupied and three empty tetrahedral voids as well as two empty octahedral voids. Although the statistical probability of a jump into a normally empty tetrahedral void is greater, the greater energy required to "stuff" a metal atom into a tetrahedron sharing a face with an occupied tetrahedron considerably decreases the actual probability for such a jump.

The octahedral voids are only partly occupied in the other structure types listed in Table II. In BiO_3, only one-third of the octahedral voids is occupied so that voidal diffusion is highly probable. On the other hand, with two-thirds of the octahedral voids occupied in the Cr_2O_3 structure, actual diffusion paths are likely to include octahedral sites normally occupied in this structure. The apparent presence of oxygen vacancies in the closely related $FeTiO_3$ structure[11] further complicates the elucidation of the exact diffusion mechanism. By comparison, the CdI_2 structure differs from the others in that the metal atoms occupy all the octahedral voids between alternate pairs of closest packed layers. (In Fig. 1, this means that alternate octahedral layers are all filled or all empty.) The resulting "layered" structure should show a marked anisotropy for diffusion parallel and normal to the c axis. Seith has observed such anisotropy in PbI_2 single crystals[12] in which the activation energy for diffusion normal to the closest-packed layers is about three times larger than that within the layers. He explains this by postulating that only lead atoms contribute to diffusion along c, but both lead and iodine atoms diffuse parallel to the layers. According to the data presented, this means that the larger iodine atoms move with a much lower activation energy than is required for lead atom diffusion! Since the experimental evidence presented is incapable of distinguishing between lead and iodine atom contributions to diffusion, an alternative process involving lead atoms only affords a more plausible explanation. Parallel to the c axis, the lead atoms can diffuse along octahedral chains only via an interstitialcy mechanism since alternate octahedra in the chain are normally occupied. On the other hand, voidal diffusion is possible in directions that are normal to the c axis since entire layers of unoccupied octahedral and tetrahedral voids are available in this structure. Since the atoms pass through similar triangular faces in going from one void to any other adjacent void, the saddle-point configurations for diffusion parallel and normal to c are similar and the activation energy for voidal diffusion parallel to the closest-packed planes should be considerably smaller, in agreement with the observed values.

CONCLUSIONS

It has been shown above how the crystal structures of binary compounds determine the available diffusion paths. The actual diffusion mechanism operative in a particular crystal depends on the occupation of these paths as well as on other factors, for example, the relative formation energies for vacancies and interstitials. Thus, two different kinds of mechanisms are possible in crystals having either the NaCl or the NiAs structure. Conversely, other crystals have diffusion paths comprised entirely from voids that are normally not occupied by atoms. Voidal diffusion is possible in such crystals, without the need for the formation of the point defects mentioned above. In the ZnO structure, for example, diffusion consists of the displacement of a Zn atom to an octahedral void and voidal diffusion along the chains of octahedra. Alternatively, a Zn atom entering the crystal from its surface can diffuse through the crystal without the need to displace any other zinc atoms. By comparison, the Zn atoms already "sit astride" a possible diffusion path in the zinc blende structure so that voidal diffusion can proceed without the need to first create a "voidal" atom. These different possible diffusion mechanisms obviously determine the relative activation energies for diffusion as discussed in the next part.[3]

Although only binary compounds have been considered above, similar analyses can be extended to more complex structures provided that they are based on closest packings. Fortunately, most inorganic compounds have such structures. Consider, for example, the spinel structure adopted by compounds having the general composition AB_2O_4. The A atoms normally occupy one-quarter of one set of tetrahedral voids, while the B atoms occupy one-half of the octehadral voids in a cubic closest packing of oxygen atoms. Thus, either interstitial or voidal diffusion is possible in such crystals. Recently Sun[13] has applied similar reasoning to the diffusion of cobalt and chromium atoms in $CoCr_2O_4$ but, as he correctly concluded, a great many more investigations of diffusion in different compounds crystallizing with the spinel structure are needed before the diffusion processes in these crystals can be clearly established.

ACKNOWLEDGMENTS

The author would like to express his gratitude to Dr. J. G. Dienes and Dr. A. Goland for reading and criticizing the original manuscript.

---

[11] J. J. Brophy, N. Rostoker, and L. V. Azároff, Phys. Rev. **98**, 228 (1955).

[12] W. Seith, Z. Elektrochem. **39**, 538 (1933).

[13] R. Sun, J. Chem. Phys. **28**, 290 (1958).

JOURNAL OF APPLIED PHYSICS VOLUME 32, NUMBER 9 SEPTEMBER, 1961

Role of Crystal Structure in Diffusion. II. Activation Energies for Diffusion in Closest-Packed Structures*†

LEONID V. AZÁROFF
Metallurgical Engineering Department, Illinois Institute of Technology, Chicago, Illinois

(Received March 13, 1961)

The effect of available diffusion paths on activation energies are considered for silver iodide, zinc oxide, and bismuth selenide. It is shown that the energy in β-AgI should be nearly twice that in γ-AgI because the Ag atoms in tetrahedral sites first must be displaced to octahedral voids before voidal diffusion can occur in the beta modification. The 2:1 ratio between the self-diffusion energies of Zn determined by radioactive tracer and electrical conductivity measurements in ZnO is similarly explained. It is also shown that the difference between the activation energies for diffusion in BiSe and Bi_2Se_3 can be used to determine the formation energy of vacancies in BiSe. The agreement between these predictions and experimentally determined values attests that qualitatively accurate explanations can be based on considerations of the crystal structure.

INTRODUCTION

THE paths available for diffusion in crystals whose structures are based on closest packings have been described in the previous paper.[1] Once the diffusion paths have been established, they can be used in calculations of the activation energy for diffusion. Partly because such calculations are difficult to make and partly because relatively little diffusion data is available for binary compounds not crystallizing with the NaCl structure, few calculations for such compounds have been reported. It is interesting to consider, therefore, whether a knowledge of the diffusion paths is sufficient to allow qualitative estimates of the required diffusion energies. To make such estimates meaningful, it is necessary to compare pairs of crystals that are similar in all respects except for the detailed paths, so that the effect of the existing difference can be evaluated. This has been done for three cases and is reported below. The apparent agreement between the predicted and observed relative values indicates that a careful analysis of the crystal structure is sufficient to yield qualitatively (although not quantitatively) accurate results.

A number of considerations must be met in such an analysis. Since the effect of the crystal's structure on diffusion is being evaluated, the comparison with experimental values is limited to the activation energies for diffusion in the intrinsic temperature range. Only those cases are considered in which there is evidence available that diffusion takes place primarily by metal atoms occupying voids in the packing. It is assumed that the metal atoms pass through the centers of the triangular faces separating two adjacent voids since they offer a more favorable saddle-point configuration than that at the centers of shared edges. The activation energy for such motion consists of the actual saddle-point energy plus the energy difference between the two voids. In hexagonal closest packings, the two voids are crystallographically equivalent, that is, they are related by the crystal symmetry so that the activation energy is exactly equal to the saddle-point energy provided defect formation is not required in the process. By comparison, the diffusion paths in cubic packings consist of alternating octahedral and tetrahedral voids so that their energy differences must be included. Their exact values depend, of course, on the way that the normally occupied voids are arranged in the structure. These assumptions are supported by the evidence that diffusion of similar atoms along identical paths requires similar activation energies. The activation energies for the diffusion of Cd and Zn through GaAs (zinc blende structure) are 2.43 and 2.49 ev, respectively.[2] As discussed below, the activation energies for In and Zn in ZnO are 3.1 and 3.16 ev, respectively. Similarly, the respective activation energies for Sn in the isostructural Bi_2S_3 and Bi_2Te_3 crystals are 0.41 and 0.50 ev.[3] The numerical difference between the last two values evidently reflects the effect of substituting Te for S in the structure.

SILVER IODIDE

As a simple test of the above hypothesis, consider the two polymorphous modifications of silver iodide. β-AgI has the zincite structure in which one-half of the tetrahedral voids in a hexagonal closest packing of iodine atoms is occupied by silver atoms. γ-AgI has the zinc blende structure in which one-half of the tetrahedral voids in a cubic closest packing is occupied. Although voidal diffusion takes place in both crystals, the diffusion path in β-AgI consists primarily of octahedral voids and in γ-AgI of alternating unlike voids. Furthermore, the silver atoms already occupy positions along a possible diffusion path in the cubic closest packing but must be first displaced from their tetrahedral sites in the hexagonal one. This means that the activation energy for diffusion in β-AgI consists of the energy required to displace the silver atom to an octahedral void plus the energy for motion along a path of octahedral voids

---

* This investigation was supported by the U. S. Air Force Office of Scientific Research.
† This work was performed at Brookhaven National Laboratory.

[1] Leonid V. Azároff, J. Appl. Phys. 32, 1658 (1961), preceding paper.

[2] B. Goldstein, Phys. Rev. 118, 1024 (1960).

[3] B. Boltaks, Zhur. Tekh. Fiz. 25, 767 (1955).

(saddle-point energy only). By comparison, the activation energy in γ-AgI equals the saddle-point energy directly. Ignoring any possible differences in the saddle-point energies of the two modifications, this means that the activation energy in β-AgI should exceed that of γ-AgI by the amount of energy required to displace the Ag atom in the former to an octahedral void. But the work done in such a displacement is essentially similar to the work done in going from a tetrahedral to an octahedral void in γ-AgI. Thus, the activation energy for diffusion in β-AgI should be very nearly twice as large as that in γ-AgI. The measured values are 0.61 and 0.38 ev for β-AgI and γ-AgI, respectively.[4] The fact that their ratio is not quite 2:1 is probably the result of differences in the energies for a transition between two octahedral voids as compared to that between two unlike voids. Also, differences between the interiodine distances in the two crystals undoubtedly alter these energy terms somewhat.

ZINC OXIDE

The results of a number of diffusion experiments carried out with zinc oxide crystals have recently been summarized in a review paper by Heiland *et al.*[5] It is interesting to note that two different values for the activation energy of zinc were reported depending on whether electrical conductivity or radioactive tracer methods were used in the experiments. A recent investigation of electron density distributions in different ZnO crystals[6] has clearly shown that these crystals contain an excess of zinc atoms in octahedral voids. Hence, electrical conductivity can be attributed primarily to ionized zinc atoms in interstitial sites acting as donors of excess electrons and not to oxygen vacancies. The interchange of an electrically active interstitial atom with one in a correctly occupied tetrahedral site does not affect the conductivity because the number of electrically active zinc atoms in octahedral voids is not altered by such an interchange. When the decrease in electrical conductivity resulting from diffusion of interstitial zinc atoms out of the crystal is measured, therefore, only atomic movements along continuous diffusion paths comprised of octahedral voids are involved. As shown above, the activation energy for such diffusion is equal to the saddle-point energy between two adjacent octahedral voids. The activation energy for diffusion of Zn measured in the intrinsic region, therefore, serves to establish the saddle-point energy.

The diffusion experiments carried out using radioactive Zn^{65} atoms consisted of first growing a "pure" ZnO crystal containing a number of radioactive zinc atoms in correct tetrahedral sites. These active crystals were next placed in an inert zinc atmosphere and the diffusion rate of the radioactive atoms out of the crystals was established by noting the resulting decrease in the crystal's activity.[5] Two distinct steps are involved in this diffusion process. First the radioactive atom is displaced to an octahedral void and then it proceeds to leave the crystal by voidal diffusion. As in the case of γ-AgI discussed above, the formation energy for the voidal should be of the same order as that of the saddle-point energy for voidal diffusion. It is expected, therefore, that the activation energy for diffusion of radioactive zinc atoms (saddle-point energy plus voidal formation energy) should be about twice that for the diffusion of ionized zinc atoms along octahedral voids (saddle-point energy only). The actual measured values are 3.0-3.2 ev for radioactive tracer diffusion and 1.7 ev for ionized zinc diffusion.[5]

A parallel case arises when Zn^{2+} atoms are replaced by In^{3+} during the growth of a ZnO crystal. Each indium atom contributes one electron to the conduction band so that its diffusion out of a crystal placed in a zinc-vapor atmosphere can be followed by noting the decrease in the crystal's conductivity. The diffusion of these vicarious In^{3+} ions also consists of two steps: displacement to an octahedral void and voidal diffusion along a wholly octahedral path. Assuming that the saddle-point and formation energies for In^{3+} are similar to those for Zn^{2+}(1.7 ev), the total activation energy for diffusion should be $1.7+1.7=3.4$ ev. The actual value determined by Thomas[7] is 3.16 ev. This apparent agreement is not surprising in view of the similarities of the electronic structure and ionic radii of the two ions ($r_{Zn}/r_{In}=0.914$).

Still another diffusion experiment should be considered in this discussion. In this case Zn^{65} was first deposited on the surface of a "pure" crystal which was next annealed for one hour in an oxygen atmosphere. In this experiment, the diffusion of radioactive zinc into the crystal takes place directly via empty octahedral voids. Because the formation of voidal atoms is not necessary in this case, the activation energy should be equal to the saddle-point energy only. The value obtained by Moore and Williams[8] is 1.63 ev, in excellent agreement with the other values reported above.

BISMUTH SELENIDE

As an example of similar reasoning applied to a different diffusion mechanism, consider the structures of BiSe and Bi_2Se_3. Both structures consist of cubic closest packings of selenium with the bismuth atoms occupying all of the octahedral voids in BiSe and two-thirds of the octahedral voids in Bi_2S_3.[9] By analogy to the isostructural sodium chloride, vacancies are responsible for diffusion in BiSe. Similarly, vacancy diffusion should be operative in Bi_2Se_3 also. Since $33\frac{1}{3}\%$ of the octahedral voids are vacant already, however, the activation energy for self-diffusion of Bi in Bi_2Se_3 consists primarily of the saddle-point energy. On the other hand, the vacancy formation energy must be added to the saddle-point energy in BiSe. Again, by analogy to alkali halides, the formation energy should be of the same order as the saddle-point energy so that the activation energy for diffusion in BiSe should be twice that in Bi_2Se_3. Using Zn^{65} which substitutes for Bi in both structures, Kuliev and Abdullaev[10] found the activation energies to be 1.46 and 0.765 ev, respectively, in BiSe and Bi_2Se_3. The difference between the two activation energies, 0.7 ev, is probably a fairly accurate measure of the energy required to form a bismuth vacancy in these crystals.

---

[4] P. Jordan and M. Pochon, Helv. Phys. Acta **30**, 33 (1957).

[5] G. Heiland, E. Mollwo, and F. Stöckmann, Advances in Solid State Phys. **8**, 191 (1959).

[6] G. P. Mohanty and L. V. Azároff, AFOSR Tech. Note TN60-1352.

[7] D. G. Thomas, J. Phys. Chem. Solids **9**, 31 (1959).

[8] W. J. Moore and E. L. Williams, Discussions Faraday Soc. **28**, 86 (1959).

[9] S. A. Semiletov and Z. G. Pinsker, Doklady Akad. Nauk S.S.S.R. **100**, 1079 (1955).

CONCLUSIONS

The foregoing examples clearly demonstrate the importance of considering diffusion paths in closest packings when interpreting the results of diffusion experiments in crystals having such structures. These results must be considered to be tentative, pending a quantitative evaluation of the different factors affecting the diffusion energies. It is quite clear, however, that it is not enough to assume that interstitial metal atoms diffuse in the same way in related yet different structures. As the results of diffusion experiments with ZnO crystals show, the nature of the experiment can modify the measured energy values even when the basic diffusion mechanism is the same.

Voidal diffusion takes place in all crystals in which one-half or less of one kind of voids is occupied. The contribution of the larger closest-packed anions is virtually absent in such crystals. This has been assumed to be the case by a number of authors even though diffusion experiments, unlike ionic conductivity experiments, do not usually permit such a distinction to be made. For example, Koch and Wagner[11] have reported that Cu is the principal contributor in copper halides which have the zinc blende structure. Similarly, Ketelaar[12] assumed that Cu and Hg both contribute to diffusion in Cu_2HgI_4. The structure of this compound is the same as that of zinc blende except that only $\frac{3}{4}$ of the voids of one tetrahedral set are occupied. Moreover, below 50°C, the Cu and Hg atoms arrange themselves in alternate layers (see Fig. 2 of part I) parallel to the c axis and form a tetragonal structure ($c/a=1.01$), whereas above 50°C, the crystal disorders and each tetrahedral void of one set is occupied by a statistically equivalent atom comprised of $\frac{1}{4}$ Hg$+\frac{2}{4}$ Cu$+\frac{1}{4}$ vacant.[13] Although Ketelaar assumed that diffusion takes place in these crystals via the 25% unoccupied tetrahedral voids of one set, it is clear from the above discussion that voidal diffusion through normally unoccupied tetrahedral and octahedral voids takes place in both the ordered and disordered modifications. This conclusion is borne out by his plot of diffusion coefficient as a function of temperature. Except in the immediate vicinity of the transition temperature, the natural logarithm of the diffusion coefficient exhibits the same linear dependence on reciprocal temperature for both modifications so that the activation energies in both structures must be the same also.

ACKNOWLEDGMENTS

The author would like to express his gratitude to Dr. G. J. Dienes and Dr. A. Goland for reading and criticizing the original manuscript.

---

[10] A. A. Kuliev and G. B. Abdullaev, Fiz. Tverdogo Tela **1**, 603 (1959).

[11] E. Koch and C. Wagner, Z. Physik Chem. **B38**, 295 (1937).

[12] J. A. A. Ketelaar, Z. physik Chem. **B26**, 327 (1934).

[13] J. A. A. Ketelaar, Z. Krist. **87**, 436 (1934).

JOURNAL OF APPLIED PHYSICS VOLUME 32, NUMBER 9 SEPTEMBER, 1961

Properties of High-Resistivity Gallium Arsenide Compensated with Diffused Copper*

Joseph Blanc, Richard H. Bube, and Harold E. MacDonald
RCA Laboratories, Radio Corporation of America, Princeton, New Jersey

(Received November 30, 1960)

Low-resistivity *n*-type GaAs crystals with silicon donors are compensated with diffused copper to produce high-resistivity crystals in a manner which is amenable to semiquantitative description in terms of a simple thermodynamic model. The high-resistivity GaAs:Cu crystals are subjected to photoelectronic analysis, including room temperature Hall and photo-Hall measurements, to obtain information about the effects of deep-lying imperfections on the properties of the initial *n*-type GaAs. In addition to three deep donors previously reported, five acceptors are revealed. A 0.42-ev acceptor level, when compensated, provides a long electron lifetime resulting in high *n*-type photosensitivity at low temperatures. Evidence for effects on the electron mobility is obtained for compensated deep donor levels, important mainly in high-resistivity *n*-type material, and for compensated acceptors lying 0.22 ev above the valence band, important mainly at low temperatures.

INTRODUCTION

GALLIUM arsenide is a heteropolar III-V semiconductor with a band gap of about 1.4 ev at 300°K. It thus occupies a position intermediate between the lower band gap group IV elemental semiconductors, e.g., Ge and Si, and the higher band gap II-VI photoconductors, e.g., CdS and other chalcogenides of Zn or Cd. When the resistivity of GaAs is low because of the incorporation of suitable imperfections, its electrical properties resemble, qualitatively at least, those of Ge and Si. When the resistivity is much higher (the intrinsic resistivity at 300°K is of the order of 10^8–10^9 ohm cm), behavior is found which is very similar to that encountered in II-VI compounds. A previous investigation[1] of high-resistivity crystals of *n*-type GaAs produced by normal growth processes has indicated the presence of donor levels lying about 0.5, 0.6, and 0.7 ev below the bottom of the conduction band. When these centers are compensated, they act as electron traps and can be so detected. Strong evidence was also found for a density of shallow trapping centers with an activation energy of about 0.2 ev.

The present investigation started with low-resistivity *n*-type GaAs (the donor impurity presumably being Si), and had for its aim the reproducible compensation of this material to resistivities greater than 10^3 ohm cm, so that experimental techniques suitable for the high-resistivity range might be usefully applied. In addition to revealing the properties of imperfections, both chemical and structural, in the compensated material, it was hoped that a comparison of properties before and after compensation would yield some insight into the effects of deep-lying imperfections on the properties of the initial low-resistivity *n*-type GaAs.

Copper was chosen as the compensating agent in this investigation because it is the most thoroughly studied acceptor in GaAs and offers several distinctive advantages. Fuller and Whelan[2] have studied the solubility of copper in GaAs as a function of temperature, and have shown that copper diffuses rapidly at relatively low temperatures. The acceptor ionization energy of 0.14 ev has been established by Meyerhofer[3] and by Whelan and Fuller,[4] who also showed that each copper atom acts as a singly ionized acceptor in *n*-type GaAs. Thus, a thermodynamic characterization of Cu in GaAs is possible, and diffusion experiments can be made on a reasonable time scale.

This paper describes both the phenomena involved in the compensation process as well as the results of photoelectronic analysis of the resultant high-resistivity GaAs:Cu crystals. To standard techniques[1] involving photoconductivity, spectral response, infrared quenching, and thermally stimulated current, have been added measurements of Hall effect and photo-Hall effect at room temperature. The location of five acceptor levels is determined, together with the behavior of these various centers relative to the photoconductivity process. The possible correlations between the existence of various levels and the mobility of the initial material are explored.

EXPERIMENTAL

Preparation of Crystals

All 14 samples of GaAs reported on in this investigation were monocrystalline slices cut from ingots grown by a conventional Bridgman technique.[5] The crystals are listed in Table I in order of increasing electron concentration at 300°K. This ranges from 1.0×10^{16} cm^{-3} to 5.0×10^{17} cm^{-3}; the electron mobility (also given in Table I) varies from 2700 to 5600 cm^2/v sec at 300°K,

---

* The research reported in this paper was sponsored by the Air Research and Development Command, United States Air Force, under contract. Some of these results were reported in preliminary form at the Prague Conference on Semiconductor Physics, 1960.

[1] R. H. Bube, J. Appl. Phys. **31**, 315 (1960).

[2] C. S. Fuller and J. M. Whelan, J. Phys. Chem. Solids **6**, 173 (1958).

[3] D. Meyerhofer, Prague Conference on Semiconductor Physics 1960; F. D. Rosi, D. Meyerhofer, and R. V. Jensen, J. Appl. Phys. **31**, 1105 (1960).

[4] J. M. Whelan and C. S. Fuller, J. Appl. Phys. **31**, 1507 (1960).

[5] L. R. Weisberg, F. D. Rosi, and P. G. Herkart, in *Properties of Elemental and Compound Semiconductors* (Interscience Publishers, Inc., New York, 1959), Vol. V of Metallurgical Society Conferences, pp. 25–65.

and from 2100 to 13 300 cm²/v sec at 78°K. In any given sample, the electron concentration did not decrease by more than 10% in going from 300° to 78°K; semiquantitative spectrochemical analysis, where available, is in accord with the assumption that the electron concentration is nearly equal to the Si impurity concentration. This supports the hypothesis[5] that Si is the principal shallow donor in these samples, and that it is not highly compensated.

The crystals listed in Table I fall into three categories. First, crystal 10G-32 was used as a reference exhibiting the "normal" Cu acceptor level with 0.14-ev ionization energy; after diffusion of Cu at 650°C, as described below, the crystal was *p* type with hole concentration of 9×10^{15} cm^{-3} and hole mobility of 270 cm²/v sec at 300°C, and had been previously measured by conventional Hall techniques by Meyerhofer. Second, there are the four crystals designated as the 631 series; these crystals had low initial electron concentrations within a factor of 10^{16} cm^{-3} and high ratios of electron mobility at 78°K to that at 300°K. Cu was diffused into the crystals of the 631 series at 500°C. Third, there are the other nine crystals listed in Table I, which were annealed at successively higher temperatures, as described below, until their resistivity exceeded 10^3 ohm cm.

Compensation by Cu was achieved through the following set of procedures. The low-resistivity *n*-type GaAs crystals, with dimensions of approximately $1\times2\times6$ mm³ (volume of about 0.01 cm³) were electroplated with 10^{17} atoms of Cu or greater. One or more samples were then placed in quartz vials, evacuated to a pressure of 10^{-5} mm Hg and sealed. The samples were annealed in a simple controlled furnace for a period of 16 hr, and then were quenched by manually plunging the vials into a water bath.

The nine specimens on which a detailed study of the compensation phenomenon was made as a function of increasing initial electron concentration are listed in Table II. These crystals were first annealed at 575°C; those samples which still had a resistivity below 10^3 ohm cm (*n* type) underwent the same treatment at 650°C. One sample was repeatedly annealed at 700° and 750°C before the resistivity increased to above 10^3 ohm cm. The details of the compensation process are summarized in Table II, and the final annealing temperatures before the beginning of photoelectronic analysis are given in Table I as well.[6] A separate set of control experiments showed that similar crystals annealed at the same temperatures, but in the absence of Cu did not become compensated. Spectrochemical analysis of two of the crystals for Cu content by Whitaker confirms that the density of Cu incorporated is within 25% of the initial electron concentration, and that therefore the high-resistivity behavior is indeed due to a close compensation of a shallow donor by the diffused Cu.

TABLE I. Initial properties of GaAs.

Crystal	*n* at 300°K, cm^{-3}	μ_n (300°K) cm²/v sec	μ_n (78°K) cm²/v sec	Diffusion temperature °C
631-14	1.0×10^{16}	5000	12 600	500
10G-32	1.1×10^{16}	4300	9300	650
631-9	1.2×10^{16}	5600	13 300	500
631-8	1.3×10^{16}	5200	12 400	500
631-1	1.9×10^{16}	3700	6900	500
GAJ-18-2a	3.8×10^{16}	4100	4800	575
ES 44	4.1×10^{16}	4900	7300	575
GAJ-18-2b	5.8×10^{16}	5000	6400	575
GAJ-18M	7.3×16^{16}	4600	5700	575
10G40-4	8.8×10^{16}	4200	4800	600
ES 36	1.2×10^{17}	4400	4900	650
ES 37	1.3×10^{17}	4300	4700	650
ES 41	3.4×10^{17}	3200	···	650
GAJ-18F	5.0×10^{17}	2700	2100	750

TABLE II. Electrical properties of GaAs after diffusion at various temperatures.

Crystal	Initial electron concentration, cm^{-3}	Electron concentration, cm^{-3}, after diffusion at: 575°C	650°C	750°C
GAJ 18-2a	3.8×10^{16}	$\rho>10^3$ ohm-cm	···	···
ES 44	4.1×10^{16}	$\rho>10^3$ ohm-cm	···	···
GAJ 18-2b	5.8×10^{16}	$\rho>10^3$ ohm-cm	···	···
GAJ 18M	7.3×10^{16}	$\rho>10^3$ ohm-cm	···	···
ES 36	1.2×10^{17}	1.1×10^{16}	$\rho>10^3$ ohm-cm	···
ES 37	1.3×10^{17}	5.0×10^{16}	$\rho>10^3$ ohm-cm	···
ES 27	2.2×10^{17}	1.9×10^{17}	$\rho>10^3$ ohm-cm	···
ES 41	3.4×10^{17}	3.4×10^{17}	$\rho>10^3$ ohm-cm	···
GAJ 18F	5.0×10^{17}	4.3×10^{17}	2.1×10^{17}	$\rho>10^3$ ohm-cm

Measurements

All measurements were made on crystals with ohmic indium contacts, melted onto the crystals in vacuum at about 350°C. Photoelectronic measurements as a function of temperature, light intensity, wavelength, etc., were made in an atmosphere of dry helium in a suitable cryostat. Measurements of Hall effect and photo-Hall effect were made using the apparatus described in a previous publication,[7] in which a Cary 31-31V vibrating-reed electrometer is used for measurement of both voltage drop in the crystal and of the Hall voltage. A conventional 6-contact arrangement was used, measurements being made with both directions of applied voltage and both directions of magnetic field.

Excitation by monochromatic radiation was obtained from a Bausch & Lomb grating monochromator, or with interference filters where indicated. Since the spectral response (see Fig. 8) of photoconductivity in these GaAs crystals is limited almost entirely to volume-absorbed light, i.e., to light with wavelength greater than the absorption edge, some measurements were made with a broad band of excitation derived from a No. 1497 microscope lamp operated at 6 v. The crystal

---

[6] Four more samples were diffused, which, after diffusion, were highly inhomogeneous as indicated by Hall measurements; longer annealing times did not remove the inhomogeneities. By the same criteria, the 14 samples reported on here were homogeneous, although not necessarily on a microscopic scale.

[7] R. H. Bube and H. E. MacDonald, Phys. Rev. **121**, 473 (1961).

TABLE III. Summary of photoelectronic data on GaAs:Cu crystals.

Crystal	Dark conductivity 300°K, mho/cm	Dark conductivity activation energy, ev		Majority carrier lifetime, μsec		Activation energy from Δi vs T, ev		Thermally stimulated current data	
		High T	Low T	300°K	90°K	High T[a]	Low T[a]	Trap depth, ev	Trap density cm^{-3}
631-1	10^{-8}	0.66	0.42	0.04	8	0.09	↑	0.26–0.43 0.59	10^{13} 2×10^{16}
631-8	10^{-8}	0.58	0.37	0.13	0.003	0.26		0.53, 0.69	10^{18}
631-9	10^{-7}	0.28	0.15	0.1	0.004	0.13		0.56	3×10^{16}
ES 41	10^{-6}	0.42	0.25	0.2	310	0.34			
ES 36A	10^{-6}	0.45		0.05	1600	0.30	b	0.23	2×10^{14}
10G 40-4	3×10^{-6}	0.45		0.14	1700	0.37		0.25	2×10^{14}
GAJ-18-2a	3×10^{-6}	0.40		0.2	200	0.21		0.26–0.32	4×10^{15}
GAJ-18-2b	3×10^{-6}	0.40		0.04	2	0.32		0.28–0.39	3×10^{14}
GAJ-18M	5×10^{-6}	0.43		0.3	43	0.34	↓	0.33	2×10^{12}
631-14	5×10^{-6}	0.43	0.12	0.2	0.002	0.28	0.03		
ES 37	10^{-5}	0.36	0.25	4	0.07	0.25	0.08, 0.04		
GAJ-18F	3×10^{-5}	0.35	0.22	3	0.007		0.10		
ES 36	3×10^{-4}	0.21		3	0.06		0.09, 0.03		
ES 44	8×10^{-4}	0.17		2	0.002		0.11, 0.05		
10G32	10^{-1}	0.12		46	0.04		0.09		

[a] Photocurrent increasing with increasing temperature.

[b] Photocurrent shows sudden temperature quenching with increasing temperature as described in the text. Equivalent activation energy for sensitizing centers is 0.41 ev. Confirmed also by infrared quenching data.

itself provided the effective short-wavelength cutoff of this band, and a water filter was normally used to give a long-wavelength cutoff at 1 μ to exclude optical quenching effects, as described in this paper. The use of this source had the advantage of providing a considerably higher exciting intensity; wherever corroborating checks were made with volume-absorbed monochromatic radiation, no differences, except that of intensity, were observed between the two types of excitation. In agreement with these findings, the nature of the effects observed and the magnitudes of the imperfection-level densities, calculated on the basis of the total volume of the crystal, were such as to confirm the contention that bulk properties were measured. The intensity of excitation was varied in a controlled manner by the use of calibrated wire-mesh neutral filters, accurate over 7 orders of magnitude.

RESULTS

Dark Conductivity

The GaAs:Cu crystals of this investigation are listed in order of increasing room temperature dark conductivity in Table III.[8] These conductivities cover the range from 10^{-8} to 10^{-1} mho/cm. With the exception of crystal 631-1, the room temperature conductivity of all crystals is p type, as will be discussed in more detail under the section of Hall measurements.

The dark conductivity of all these crystals was measured as a function of temperature within the range between 90° and 400°K, the lower limit actually used being set by the lower limit to current detectability which was 10^{-11} amp. About half the crystals showed only a single slope in a plot of log conductivity vs $1/T$, sometimes over as many as 7 orders of magnitude of conductivity. The rest of the crystals showed one slope at higher temperatures and a smaller slope at lower temperatures. In every case, a slope observed first only at lower temperatures in higher-resistivity crystals, was observed over the whole range or at higher temperatures in lower-resistivity crystals.

Since the crystals involved were partially compensated p type, with N_A acceptors partially compensated by N_D donors, in the range where $p \ll N_D$,[9]

$$E_f = E + kT \ln[N_D/(N_A - N_D)], \qquad (1)$$

where E_f is the height of the Fermi level above the top of the valence band and E is the activation energy of the uncompensated acceptor centers. Equation (1) holds over any range where conductivity is associated predominantly with only one type of acceptor. Since the slope of a plot of log conductivity vs $1/T$ is given by

$$\text{Slope} = (T/k)(dE_f/dT) - (E_f/k), \qquad (2)$$

the slope is equal to $-E/k$. This analysis assumes as a first approximation that the temperature dependence of the density of states cancels the temperature dependence of the mobility. Even if the temperature dependence of mobility departs appreciably from such an approximation, corrections of only a few hundredths of a volt in the given activation energies would be involved. If, for example, the mobility were independent of temperature, the true value of E would be about 10% less than the value given by the slope. It is possible that

---

[8] Crystal ES 36 underwent photoelectronic analysis and then had new contacts applied for Hall measurements. In the course of this heating procedure, the dark conductivity dropped from 3×10^{-4} mho/cm p type to 10^{-6} mho/cm p type, probably due to the precipitation of copper. The crystal with conductivity of 10^{-6} mho/cm has been called ES 36A and was subsequently subjected to both Hall and photoelectronic measurements.

[9] R. H. Bube, J. Chem. Phys. 23, 18 (1955).

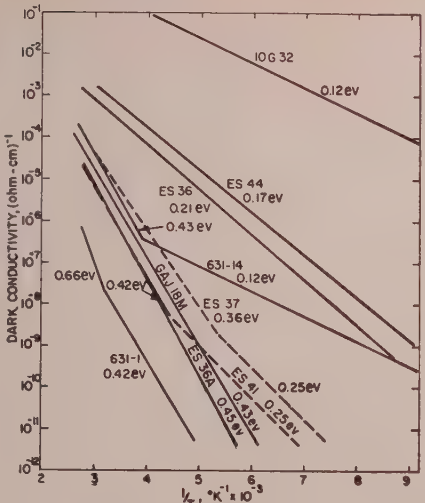

FIG. 1. Dark conductivity as a function of temperature for representative GaAs:Cu crystals. The data are taken from a continuous recording, and experimental points have been therefore omitted.

some of the observed variations in activation energy for a given imperfection level are traceable to variations in temperature dependence of mobility.

Typical curves of dark conductivity as a function of temperature for a number of the crystals are given in Fig. 1. The dark conductivity activation energies are summarized in the third column of Table III and are graphically represented as a function of room temperature dark conductivity in Fig. 2. The results can be interpreted in terms of four acceptor levels located at about 0.42, 0.34, 0.22, and 0.13 ev above the top of the valence band. In addition, evidence is obtained in the two highest-resistivity crystals of donor levels lying 0.6 and 0.7 ev below the bottom of the conduction band in agreement with past results[1]; the detailed reasons for this interpretation are given in the section on Hall measurements.

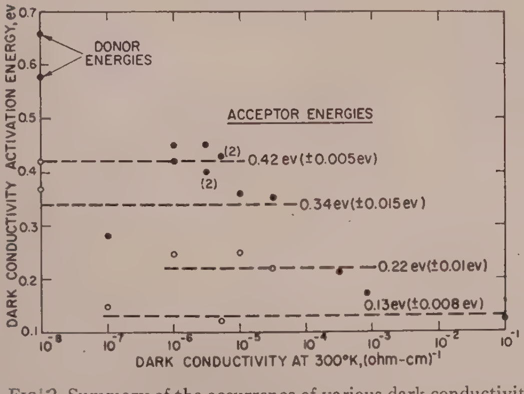

FIG. 2. Summary of the occurrence of various dark conductivity activation energies as a function of the dark conductivity of the GaAs:Cu crystals. Solid dots imply that the activation energy is found either over the whole temperature range or at higher temperature; open dots imply that the activation energy is found only at lower temperatures. The activation energies plotted are those given in Table III.

Photoconductivity vs Temperature

In general, the crystals listed in Table III can be divided into two oppositely behaving groups as far as the temperature dependence of photoconductivity is concerned. Crystals with room temperature dark conductivity less than 5×10^{-6} mho/cm show a rapid increase in photosensitivity upon cooling; crystals with room temperature dark conductivity greater than 5×10^{-6} mho/cm show a rapid decrease in photosensitivity upon cooling. This behavior is reflected in the values of the majority carrier lifetime given in the fourth column of Table III. The majority carrier lifetime is calculated from the equation

$$\tau_{\text{maj}}=(L^2G/\mu V), \tag{3}$$

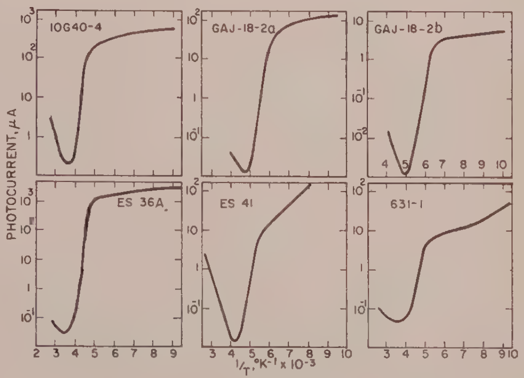

FIG. 3. Typical variation of photocurrent with temperature for GaAs:Cu crystals with a room temperature dark conductivity less than 5×10^{-6} mho/cm.

where L is the interelectrode spacing, G is the photoconductivity gain (i.e., the number of charge carriers between the electrodes for each photon absorbed), μ is the carrier mobility, and V is the applied voltage. The use of the concept of majority carrier lifetime implies simply that the photoconductivity is dominated by carriers of one type. Presumably the minority carriers will be captured first, and then recombination with majority carriers will take place at a later time. Naturally, the majority carrier lifetime under photoexcitation need not refer to the same carriers as are the majority carriers in the dark; only Hall effect measurements can identify the majority carriers under any particular condition of photoexcitation. The identity of the majority carriers is not specifically required for the calculation of a lifetime by Eq. (3), if one is willing to assume a reasonable value of mobility to obtain an order-of-magnitude figure for the lifetime. In those cases for which actual Hall measurements were not available, a mobility of 10^3 cm^2/v sec was assumed to give such order-of-magnitude lifetime values. An inspection of Table III shows that most of the crystals with conductivity less than 5×10^{-6} mho/cm are 10^2 to 10^4 times more sensitive at 90°K than at 300°K; crystals with conductivity greater than 5×10^{-6} mho/cm, however, although as much as 10^2 times more sensitive than the higher-resistivity crystals at 300°K, are 10^2 to 10^3 times less sensitive at 90°K than at 300°K.

Figure 3 gives a number of examples of those crystals for which photosensitivity increases with decreasing temperature. The increase occurs abruptly and over a narrow temperature range. Figure 4 shows the dependence of photocurrent on temperature for crystal GAJ-18M for two different intensities of excitation. Low-temperature Hall measurements by Whelan[10] on such materials have shown that the photoconductivity is *n* type. The behavior is therefore identical with that found in such materials as CdS and CdSe, where thermal quenching of photoconductivity is associated with the thermal freeing of holes from centers (called "sensitizing centers") with a much larger capture cross section for holes than for electrons. Such centers have an effective negative charge; photoexcited holes are readily captured, but the subsequent probability for capture of a photoexcited electron is small. Thus, the majority carrier lifetime is long and the photosensitivity is high. If this process is analyzed in terms of a rate equation analysis previously applied to such materials as CdS and CdSe,[11] it is possible to determine both the location of the energy level of these sensitizing centers and the ratio of the capture cross sections from the data of Fig. 4. If this is done, it is found that the sensitizing centers lie 0.41 ev above the top of the valence band, and the capture cross section of these centers for holes is 6×10^3 times larger than their subsequent cross section for electrons.

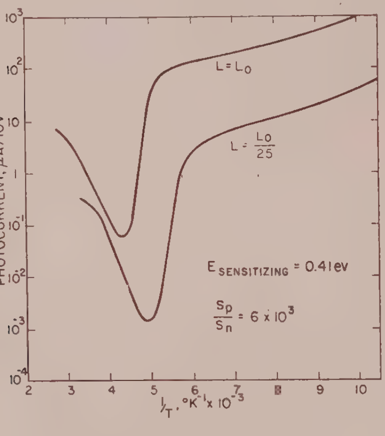

FIG. 4. Dependence of photocurrent on temperature for crystal GAJ-18M for two different light intensities. From the temperature breakpoint with increasing temperature, and its dependence on light intensity, the hole ionization energy for sensitizing centers is calculated to be 0.41 ev, and the ratio of hole capture cross section to electron capture cross section is calculated to be 6×10^3.

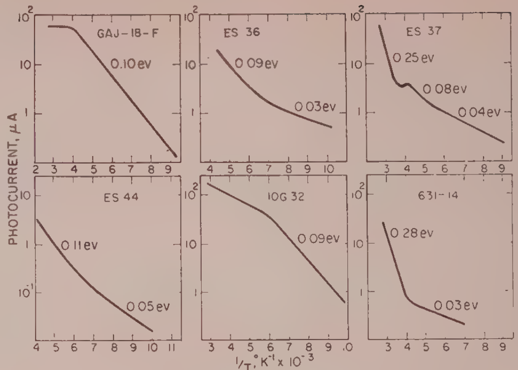

FIG. 5. Typical variation of photocurrent with temperature for GaAs:Cu crystals with a room temperature dark conductivity greater than 5×10^{-6} mho/cm.

As is indicated by the graphs of Figs. 3 and 4, the photocurrent in these crystals also rises exponentially with increasing temperature beyond a minimum following temperature quenching. The activation energies corresponding to this exponential rise in photocurrent are summarized in the left portion of the fifth column of Table III. These energies may be divided into three groups with the following average values: 0.33±0.01 ev (5 crystals), 0.25±0.01 ev (4 crystals), and 0.11±0.02 ev (2 crystals).

The temperature dependence of crystals with dark conductivity at room temperature in excess of 5×10^{-6} mho/cm is illustrated by the examples given in Fig. 5 and summarized in the right portion of the fifth column of Table III. The photosensitivity decreases exponentially with decreasing temperature, usually with one or both of two characteristic slopes: 0.09±0.004 ev (5 crystals), or 0.04±0.004 ev (4 crystals).

Obvious exceptions to the separation of the crystals into two groups depending on their room temperature

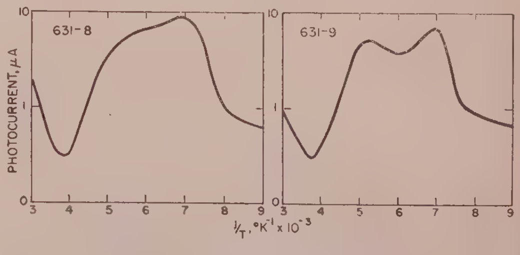

FIG. 6. Variation of photocurrent with temperature for GaAs:Cu crystals 631-8 and 631-9, indicating the rapid decrease of sensitivity observed with these crystals at low temperature.

---

[10] J. M. Whelan (private communication).

[11] R. H. Bube, J. Phys. Chem. Solids 1, 234 (1957).

dark conductivity are 631-8 and 631-9, which have a smaller majority carrier lifetime at 90° than at 300°K. The actual dependence of photocurrent on temperature for these crystals is shown in Fig. 6. It is seen that they are like other high-resistivity crystals in that the photosensitivity rises rapidly with decreasing temperature. They are unlike other high-resistivity crystals in that the photosensitivity falls off again sharply at low temperatures.[12] The curves of Fig. 6 are measured at high light intensity and indicate about equivalent photocurrent at 300° and 90°K. The majority carrier lifetimes, however, are calculated for low light intensities, and the difference between sensitivity at 300°K and 90°K for these crystals becomes much greater at low light intensities, as shown in Fig. 7. Thus, these two crystals do fit the general patterns of high-resistivity crystals except for an additional unidentified process which reduces sensitivity at low temperatures.

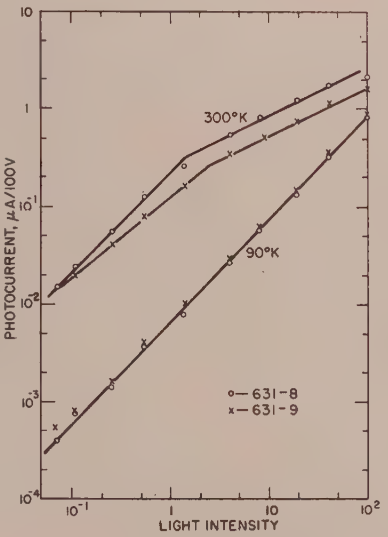

FIG. 7. Variation of photocurrent with light intensity for GaAs: Cu crystals 631-8 and 631-9 at 90° and 300°K. The difference in sensitivity is much greater between the two temperatures for low-intensity excitation than for high.

Spectral Response and Optical Quenching

The absorption edge of GaAs at 90°K is located at about 8400 A, corresponding to a band gap of about 1.47 ev. Spectral response curves are given in Fig. 8 for two crystals of GaAs: Cu; crystal ES 41 is one that has high sensitivity at low temperatures; crystal GAJ-18F is one that has low sensitivity at low temperatures. Both curves indicate that the photosensitivity for surface-absorbed light (in the spectral range where the absorption constant is very large) is very low. The surfaces of the measured crystals were subjected to abrasive blasting before attachment of electrodes, and the result of this treatment is apparently a high surface recombination velocity as is the case in Ge. The photosensitivity rises sharply as the exciting wavelength exceeds that of the absorption edge and volume excitation becomes predominant. Beyond the edge, the response stays high over quite a range during which excitation from imperfections dominates. The curve for insensitive crystal GAJ-18F is similar to those reported for high-resistivity

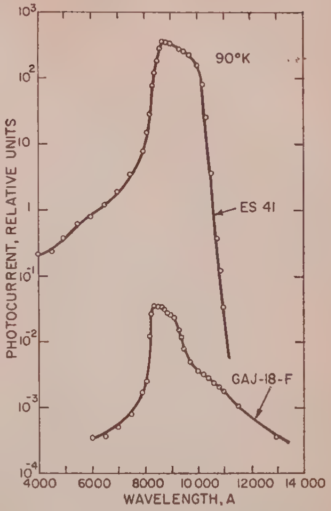

FIG. 8. Typical spectral response curves at 90°K for GaAs: Cu crystals with high sensitivity (ES 41) and with low sensitivity (GAJ-18F). The curves are corrected for equal photon incidence at each wavelength. The rapid decrease in sensitivity at wavelengths above 10 000 A for crystal ES 41 is the result of optical quenching.

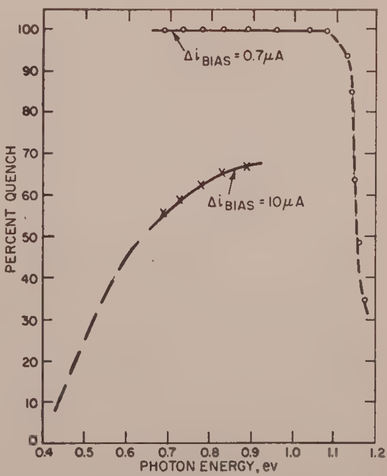

FIG. 9. Typical optical quenching spectra for GaAs: Cu crystal GAJ-18-2a, measured at 90°K, for two different values of the bias current generated by 8580 A.

---

[12] Over an appropriate range of light intensities and applied voltages at 90°K, an oscillating photocurrent was found in crystal 631-8, in the presence of steady illumination and a normal dc voltage. The phenomenon is essentially identical with that reported for CdS [S. H. Liebson, J. Electrochem. Soc. **102**, 529 (1955); R. H. Bube and L. A. Barton, RCA Rev. **20**, 564 (1959)] and for ZnSe [R. H. Bube and E. L. Lind, Phys. Rev. **110**, 1040 (1958)]. The oscillations are characterized by a slow buildup, often with accurately reproduced complex structure, followed by a sudden decrease. Buildup and relaxation of space-charge effects seems the most likely mechanism for such behavior.

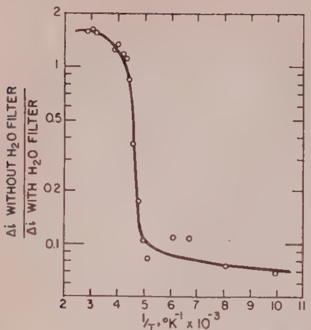

FIG. 10. Temperature dependence of optical quenching, measured in terms of the ratio of photocurrent without an H_2O filter to exclude the quenching radiation to the photocurrent with an H_2O filter; for crystal 631-1.

n-type crystals[1]: an appreciable fraction of the maximum response is still found when the exciting energy is as low as 0.9 ev.

The response for sensitive crystals, however, shows a sharp decrease as the exciting photon energy decreases below 1.2 ev, and is down by a factor of about 10^4 at 1.1 ev. This sharp decrease occurs as optical quenching by photons with energy less than about 1.2 ev exceeds the excitation by these same photons. Such optical quenching occurs when the light raises electrons from the valence band to the sensitizing centers, thus freeing holes which subsequently are captured at sites where recombination with free electrons is probable. The process of optical quenching was investigated by exciting a bias photocurrent by 1.45-ev light through an interference filter, and measuring the quenching effect as a function of wavelength of a secondary monochromatic radiation. The results are shown in Fig. 9 for two different intensities of the bias excitation. The quenching effect was extremely strong and only by going to high bias-excitation intensity was it possible to detect some shape in the curve apart from simply total quenching. The monochromator available for the quenching experiments did not permit coverage of the whole range, but a reasonable extrapolation of the spectrum indicates an optical quenching energy of about 0.4 ev. The decrease in percent quenching on the high-energy side is not the result of a decrease in actual quenching, but rather of an increase in excitation by these wavelengths which obliterates the quenching effect.

The temperature dependence of the optical quenching effect is pictured in Fig. 10 for crystal 631-1 to demonstrate that the optical quenching disappears as thermal quenching sets in, as is evident by comparison with the data for crystals 631-1 in Fig. 3. The data of Fig. 10 are given in terms of the photocurrent excited by a broad-band excitation spectrum from an incandescent lamp without interposing a water filter to that obtained when a water filter is interposed. The interposition of the water filter eliminates those wavelengths which cause optical quenching. Finally, at the high-temperature end, when optical quenching is no longer present, the current is higher without the water filter because of the reflection and scattering induced by the filter.

Thermally Stimulated Currents

The crystals of Table III fell into four categories as far as the possibility of measuring significant thermally stimulated currents was concerned. First, there were the crystals with room temperature dark conductivity greater than 5×10^{-6} mho/cm which had relatively high dark currents even at low temperatures and very short free carrier lifetimes at low temperatures; for these crystals no measurements of thermally stimulated currents were possible. Second, there were the crystals with room temperature dark conductivity less than 5×10^{-6} mho/cm which had high sensitivity at low temperatures, but still fairly high dark currents at higher temperatures; for these crystals only measurements of thermally stimulated current at low temperatures due to shallow traps were possible. Third, there were crystals 631-8 and 631-9, for which the low temperature sensitivity was too low to permit detection of shallow traps, but for which deep traps could be detected because of low dark conductivity at higher temperatures. Fourth, there was crystal 631-1 which combined the properties of high sensitivity at low temperatures with low dark conductivity at higher temperatures, for which both shallow and deep traps could be measured. These limitations on detection must be considered when interpreting the summary of thermally stimulated current data given in the sixth column of Table III. There is no evidence that the same basic pattern of a low density of shallow traps in the range 0.2 to 0.4 ev, and a higher density of deeper traps in the range 0.5 to 0.7 ev, is not characteristic of all the crystals of Table III.

Figure 11 shows the thermally stimulated current curves for three of the crystals for which only shallow traps were detectable. All of the curves are complex with indications of considerable structure; perhaps as many as four different trap depths are indicated by the three curves. On the reasonable assumption that the thermally stimulated current is contributed by majority carriers, i.e., those carriers for which the majority carrier lifetime has been determined, and that these majority carriers are electrons, as indicated by Hall effect on the photoconductivity in this temperature

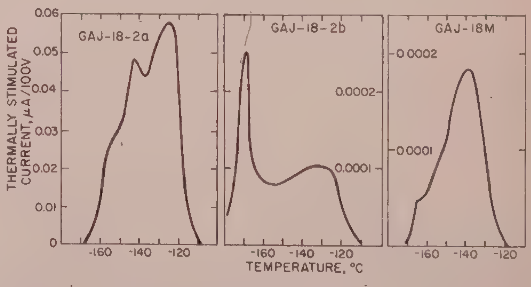

FIG. 11. Thermally stimulated current associated with a low density of shallow traps, typical of crystals with high photosensitivity at low temperature. Note structure in the curves.

range,[10] the trap depth may be calculated:

$$E_{\text{trap}}=E_{fn}=kT\ln(N_c/n), \qquad (4)$$

where E_{fn} is the distance of the steady-state electron Fermi level below the bottom of the conduction band, T is the temperature of the thermally stimulated current maximum, N_c is the effective density of states in the conduction band, and n is the density of free carriers at the thermally stimulated current maximum (calculated in this case from the measured conductivity assuming an electron mobility of 10^3 cm^2/v sec). The density of traps of a given depth can be determined from the area A under that portion of the curve

$$N_t=A/evG, \qquad (5)$$

where N_t is the trap density, e is the electronic charge, v is the volume of the crystal, and G is the gain calculated for steady-state excitation of a photocurrent with magnitude equal to that of the average thermally stimulated current.

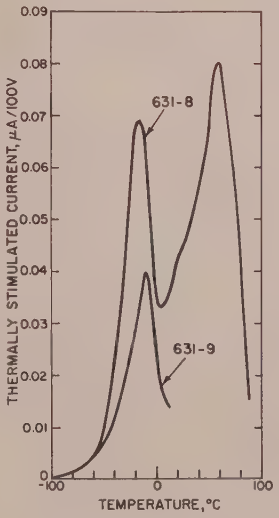

FIG. 12. Thermally stimulated current associated with a high density of deep traps, measurable only in the highest resistivity crystals. The traps found are the same as those previously reported for high-resistivity n-type crystals.

The thermally stimulated current associated with deep traps in crystals 631-8 and 631-9 is shown in Fig. 12. These curves are essentially identical with the curves associated with deep traps reported for high-resistivity n-type crystals previously.[1]

The happy combination of circumstances which permits both shallow and deep traps to be detected in crystal 631-1 gives rise to the curves of Fig. 13. The shallow traps again exhibit marked structure. In all the crystals, the density of shallow traps is relatively low; varying from about 10^{12} to 10^{15} cm^{-3}; the density of deep traps is considerably higher and of the same order as reported for high-resistivity n-type crystals[1]: about 10^{16} to 10^{18} cm^{-3}. No evidence is found for the high density of shallow traps with depth about 0.2 ev or less (probably hole traps lying above the valence band) and densities in the 10^{17} to 10^{18} cm^{-3} range, characterized by a single thermally stimulated current peak without structure, which was found so consistently in the previously described[1] high-resistivity n-type crystals (see reference 19).

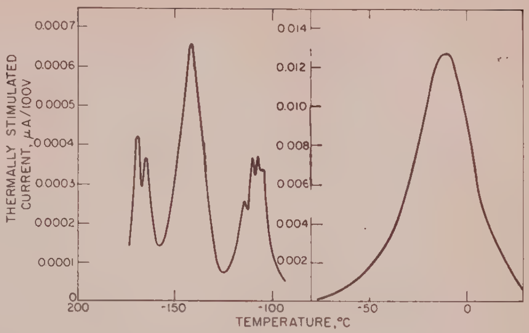

FIG. 13. Thermally stimulated current for GaAs:Cu crystal 631-1 showing both the small density of shallow traps and the higher density of deep traps.

The detailed structure of the low-temperature thermally stimulated current curve for crystal 631-1 stimulated an effort to measure this portion of the curve with increased resolution. The result of such an effort is given in Fig. 14. The fine structure is completely reproducible from run to run.

Hall and Photo-Hall Measurements

Hall-effect measurements were made in the dark and under high-intensity broad-band excitation (~6×10^3 ft-c) at room temperature on ten of the GaAs:Cu crystals, as listed in Table IV. Any differences between

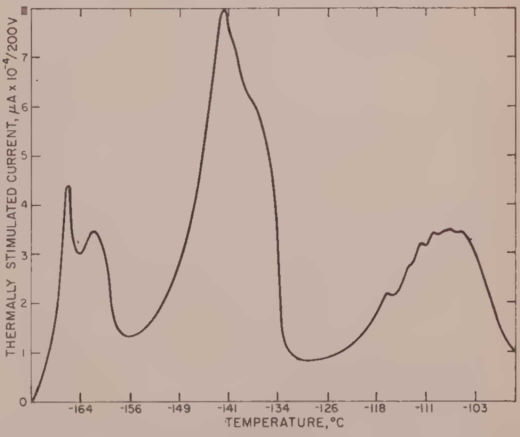

FIG. 14. The result of using higher resolution in the measurement of the shallow traps of Fig. 13. The data of Fig. 14 were measured at a heating rate of 0.29 deg/sec instead of 0.43 deg/sec used in Fig. 13; in addition, the data of Fig. 14 were recorded on an expanded temperature scale by a factor of about three. The detailed structure (11 peaks or indications of peaks are easily discernible) is completely reproducible.

TABLE IV. Summary of photo-Hall data on GaAs:Cu crystals.

Crystal	Conductivity mho/cm Dark	Conductivity mho/cm Light	Hall mobility, cm²/v sec Dark	Hall mobility, cm²/v sec Light	$\Delta p/\Delta n$
631-1	3×10^{-7}	6×10^{-6}	-65	-2220	...
631-8	9×10^{-7}	9×10^{-6}	$+90$	-39	60
ES 36A	10^{-6}	6×10^{-6}	$+173$	-232	26
631-9	2×10^{-6}	10^{-5}	$+3.7$	-312	14
10-G-40-4	5×10^{-6}	3×10^{-5}	$+106$	$+127$	...
GAJ-18M	6×10^{-6}	2×10^{-5}	$+103$	$+124$	...
GAJ-18-2b	6×10^{-6}	3×10^{-5}	$+146$	$+96$	230
631-14	10^{-5}	5×10^{-5}	$+183$	$+225$	...
ES 44	10^{-3}	2×10^{-3}	$+30$	$+36$	...
10-G-32	4×10^{-1}		$+267$		

the dark conductivities listed in Tables III and IV for the same crystal arose either as the result of heating to affix the Hall electrodes, or, in the case of the higher-resistivity crystals, as the result of not waiting a long time for the conductivity to drop to its equilibrium dark value after photoexcitation. For crystals with a dark conductivity greater than 5×10^{-6} mho/cm, the Hall mobility is positive in both dark and light and relatively independent of photoexcitation. For crystals with dark conductivity less than 5×10^{-6} mho/cm, the Hall mobility either changes from positive to negative under photoexcitation, or, in the case of crystal 631-1, increases rapidly with photoexcitation while remaining negative over the whole range. Figure 15 shows the dependence of Hall mobility on the crystal conductivity (as varied by photoexcitation) for crystals 631-8, ES 36A, and 631-9, all of which show conversion from p type to n type with photoexcitation, and for crystal 631-1, which shows a strong dependence of Hall mobility on intensity of photoexcitation.

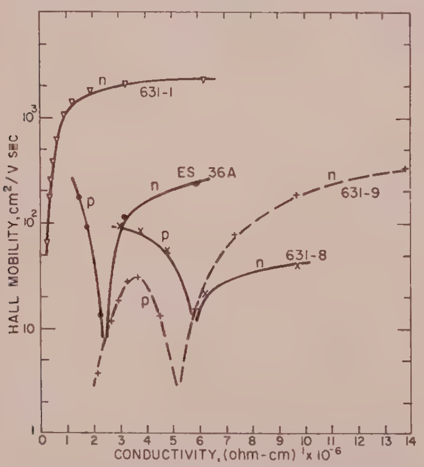

FIG. 15. Variation of Hall mobility with conductivity, as varied by increasing photoexcitation, for those crystals of high-resistivity GaAs:Cu showing a conversion from p type to n type under photoexcitation. See Table IV.

When both carriers are contributing to the conductivity, the Hall constant R is given by

$$R=\frac{p\mu_p^2-n\mu_n^2}{e(p\mu_p+n\mu_n)^2}=\frac{e(p\mu_p^2-n\mu_n^2)}{\sigma^2}, \tag{6}$$

where for the sake of simplicity we have assumed a correlation factor of unity between the Hall mobility μ_H and the microscopic mobility. If values for either μ_n or μ_p and the value of the mobility ratio $\mu_n/\mu_p=b$ are known, it is possible to solve the equations for R and σ simultaneously to obtain both n and p as a function of conductivity (or of light intensity) from such data as are given in Fig. 15. If $p_0=\sigma/e\mu_p$ and $n_0=\sigma/e\mu_n$, then the result may be expressed either as

$$n=\frac{p_0(1-\mu_H/\mu_p)}{b(1+b)} \tag{7a}$$

$$p=p_0-nb, \tag{7b}$$

or as

$$p=\frac{b^2n_0(1+\mu_H/\mu_n)}{(1+b)} \tag{7c}$$

$$n=n_0-p/b. \tag{7d}$$

Using Eqs. (7), assuming $b=10$, values of p and n as a function of light intensity were calculated for those crystals in which two-carrier conductivity effects under photoexcitation were indicated. If Δp and Δn are defined as the differences between the values of p and n, respectively, for high intensity excitation and no excitation, the effect of the photoexcitation on the conductivity can be evaluated as in the last column of Table IV. In those cases where the Hall coefficient is positive in the dark, such an analysis indicates that photoexcitation creates 10 to 10^2 free holes for each electron; the photoconductivity may therefore be said to be "p type" even though photoexcitation causes a change in the sign of the Hall coefficient.

The variation of mobility in n-type crystal 631-1 with photoexcitation intensity cannot be attributed to a two-carrier conductivity effect, i.e., the very low value of Hall mobility in the dark is a real electron mobility and not the result of the participation of both electrons and holes in the conductivity. A useful criterion that must be met by true two-carrier conductivity under thermal equilibrium is that the values of n and p calculated from Eqs. (7) must be consistent with the value of the np product given by

$$np=4[2\pi kT/h^2]^3(m_em_h)^{\frac{3}{2}}\exp(-E_G/kT), \tag{8}$$

where m_e is the effective electron mass, m_h is the effective hole mass, and E_G is the band gap. For GaAs at 300°K, using $m_e=0.07\ m_0$, $m_h=0.5\ m_0$, and $E_G=1.4$ ev, $np=2\times10^{12}$ cm^{-6}. This means that for the criterion of zero Hall mobility to be met, i.e., $p\mu_p^2=n\mu_n^2$, and the criterion of $np=2\times10^{12}$ cm^{-3} to be met with $\mu_n=2\times10^3$

cm²/v sec and $b=10$, then $n=10^5$ cm^{-3}, $p=10^7$ cm^{-3}, and $\sigma=3.5\times10^{-10}$ mho/cm. If an attempt is made to account for the low dark mobility of crystal 631-1 by a two-carrier conductivity model, the values of n and p resulting from Eqs. (7) have a product $np=7\times10^{17}$ cm^{-6}. It may therefore be concluded that the large increase in electron mobility with photoexcitation intensity in crystal 631-1 is the result of a change in the scattering, i.e., a change in the occupancy of charged scattering centers, as a result of the motion of the steady-state Fermi level with photoexcitation. Such a change in occupancy involves the deep compensated-donor trapping centers. Similar measurements of the variation of Hall mobility with photoexcitation have been made on a number of high-resistivity n-type GaAs crystals grown without any deliberately added impurity. All of these crystals show a marked increase in Hall mobility with increasing light intensity at fixed temperature. The effects are therefore quite comparable to those reported for similar experiments with CdS.[7] If the data are analyzed in terms of a model based on point scatterers, large scattering cross sections of the order of 10^{-11} to 10^{-10} cm² are calculated. An investigation of this problem by itself is to be reported later.

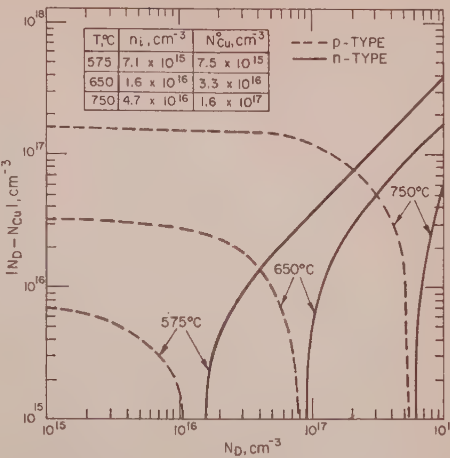

FIG. 16. Variation of carrier concentration with initial donor concentration after copper diffusion at three representative temperatures.

DISCUSSION

Analysis of the Compensation Process

An inspection of Tables I and II reveals considerable regularity in the compensation phenomena. Crystals with initial electron concentration of 10^{16} cm^{-3} became high resistivity after diffusion of Cu at 500°C; those with electron concentration in the range of 4 to 7×10^{16} after diffusion at 575°C; those in the range of 1 to 3×10^{17} after diffusion at 650°C. The one sample with initial electron concentration of 5×10^{17} cm^{-3} required a diffusion temperature of 750°C before becoming high resistivity. This regularity suggests an inherent correlation between the density of donors present and the solubility of Cu at any given temperature.[13]

By examination of a simple model in which only a shallow donor is present in the initial material, one can calculate both the enhancement of Cu solubility due to the presence of shallow donors and the carrier concentration at room temperature if none of the dissolved Cu precipitates in the quenching process. The results of an extension of this model by Reiss *et al.*[14] yield as a close approximation

$$N_{\mathrm{Cu}}=\frac{N_D}{1+[1+(2n_i/N_{\mathrm{Cu}}{}^0)^2]^{\frac{1}{2}}}+\left\{\left[\frac{N_D}{1+[1+(2n_i/N_{\mathrm{Cu}}{}^0)^2]^{\frac{1}{2}}}\right]^2+(N_{\mathrm{Cu}}{}^0)^2\right\}^{\frac{1}{2}},\quad(9)$$

where N_{Cu} is the solubility of Cu in the presence of N_D shallow donors, $N_{\mathrm{Cu}}{}^0$ is the solubility of Cu in the absence of other impurities, and n_i is the intrinsic electron concentration. Since both n_i and $N_{\mathrm{Cu}}{}^0$ are functions of temperature, N_{Cu} is also an implicit function of temperature. If n_i and $N_{\mathrm{Cu}}{}^0$ are known, it is possible to calculate N_{Cu} and the difference (N_D-N_{Cu}) which indicates the electrical type of the material and the carrier concentration after the quench to room temperature. The difference (N_D-N_{Cu}) as calculated using Eq. (9) may be either positive or negative, i.e., the resulting crystals may be n type or p type depending on conditions.

In order to carry out these calculations, the Cu solubility in the absence of impurities was determined by extrapolating the data of Fuller and Whelan[2] to the relevant temperatures, and the intrinsic carrier concentration was inferred from the high-temperature Hall data of Folberth and Weiss.[15] The results of these calculations for three temperatures are shown in Fig. 16, where the parameters entering the computation are also indicated. For crystals containing about 1 to 2×10^{16} shallow donors, diffusion at 575°C results in a difference $|N_D-N_{\mathrm{Cu}}|$ of 10^{15} cm^{-3} or less, which shows that in this range of initial electron concentrations, the material is expected to be fairly high resistivity after quenching. Similarly, for diffusions at 650°C, the initial donor concentration calculated for high-resistivity resultant crystals ranges from about 8 to 9×10^{16} cm^{-3}. For diffusions at 750°C, the computations yield 5 to 6×10^{17} cm^{-3} for this range. These calculations are in good semiquantitative agreement with the experimental results of Table II.

---

[13] There have been no experiments to date performed on these crystals to prove that diffusion at the respective temperatures for periods of 16 hr is sufficient to give compositional equilibrium. However, the data presented above indicate in two ways that equilibrium has in fact been reached. In crystal 631-8, a trap density of the order of 10^{18} cm^{-3} was calculated on the assumption that the whole volume of the sample was high resistivity; if the sample were not high resistivity throughout, it would be necessary to conclude the presence of a still higher trap density, which seems unreasonable. Also, the fact that the diffusions at 500°C with material of 10^{16} cm^{-3} yielded high-resistivity material is in accord with the equilibrium calculations outlined here. Since these remarks apply to diffusion at 500°C, *a fortiori* the diffusions at higher temperatures almost certainly yield equilibrium concentrations.

[14] H. Reiss, C. S. Fuller, and F. J. Morin, Bell System Tech. J. **35**, 535 (1956).

[15] O. G. Folberth and H. Weiss, Z. Naturforsch. **10a**, 618 (1955).

There are, however, certain objections which may be raised concerning the quantitative accuracy of Eq. (9) even for the simple case considered, quite apart from inaccuracies in the values of n_i and N_{Cu}^0 used. The first of such objections is that Si, which is the main shallow donor in these samples of GaAs, is known to act amphoterically.[16] A second difficulty is that Eq. (9) does not contain the acceptor ionization energy, which corresponds to the implicit assumption that all Cu atoms are ionized. It is difficult to calculate precisely what these effects will be, but both will tend to lessen the enhancement of Cu solubility. Order of magnitude estimates indicate that the amphoteric behavior of Si will not influence the results at concentrations less than 3×10^{17} cm^{-3}, and that the ionization energy of Cu will not become important unless $N_{\mathrm{Cu}}>2N_{\mathrm{Cu}}^0$.

Of more importance, for present purposes, are questions dealing with the behavior of deep donors and acceptors in the initial material, the presence of which may not be directly revealed by Hall measurements on the initial material. The enhancement of solubility in the presence of such impurities is a complicated function of concentration and ionization energy, but, once again qualitatively, the presence of deep donors will tend to enhance the solubility of Cu, and the presence of deep acceptors to repress it.[17]

It is noteworthy that the presence of deep donors or acceptors will be revealed when the difference (N_D-N_{Cu}) is less than the concentration of deep levels, since under that condition the Fermi level (in extrinsic material) is controlled by the deep levels. The variation of dark conductivity with temperature would then be controlled by ionization energies of the deeper levels and not by either Cu or Si. The main compensation effect is nevertheless the enhancement of Cu solubility by the shallow donor, although this effect by itself can clearly not account for a compensation, for example, of 10^{17} electrons before diffusion to 10^{11} cm^{-3} after diffusion, an implication that the Cu and donor concentrations are equal to one part per million.

That effects not ascribable to the shallow donors do indeed occur can be seen from a careful examination of Tables I and II. The most striking example is a comparison between crystals ES 36 and ES 37, which had initially identical electron concentrations and mobilities. The two samples, which were annealed at the same time and in the same vial, differed quantitatively after diffusion and quenching. After diffusion at 575°C, ES 36 had an electron concentration of 1.1×10^{16} cm^{-3}, while ES 37 had an electron concentration a factor of 5 higher. This difference in behavior persisted for diffusion at 650°C, after which ES 36 had a conductivity of 3×10^{-4} mho/cm, while ES 37 had a conductivity lower by a factor of 30. It is clear that these differences must be due to imperfections other than the shallow donor (if equilibrium was reached in each case), although it is not possible at this stage to decide which of the two crystals was "purer."

It may be concluded, therefore, that although the compensation phenomenon can be explained to first order by a simple compensation mechanism, the resulting high resistivities are the result of the presence of deep levels in the initial material.

Nature of Imperfections in GaAs:Cu Crystals

The presence of five levels located in the lower half of the forbidden gap of GaAs are indicated by the measurements of the present investigation. The height of these various levels above the valence band and the the various techniques used in their determination are summarized in Table V. Four of the levels are identified as acceptor levels by their effect on the *p*-type conductivity. The deepest of these levels, with hole ionization energy of about 0.42 ev, is also identified as the sensitizing center for *n*-type photoconductivity at low temperatures in crystals with room temperature dark conductivity less than 5×10^{-6} mho/cm. The data indicate that this center acts as a sensitizing center *only when it is compensated*; photoexcited holes are captured which then have a small probability of recombining with free electrons. It is only when the Fermi level lies high enough, i.e., when the conductivity is low enough, that a sufficient proportion of these centers are compensated (occupied by electrons in dark thermal equilibrium) to give rise to the low-temperature increase in sensi-

TABLE V. Summary of activation energies in GaAs:Cu crystals.

Phenomenon	Activation energy, ev				
p-type conductivity vs temperature	0.42	0.34	0.22	0.13	
Thermal quenching of photoconductivity	0.41				
Optical quenching of photoconductivity	0.4				
Photoconductivity vs temperature at higher temperatures		0.33	0.25	0.11	
Photoconductivity vs temperature at lower temperatures				0.09	0.04

---

[16] J. M. Whelan, J. D. Struthers, and J. A. Ditzenberger, Prague Conference on Semiconductor Physics, 1960.

[17] There is no particular difficulty in formally writing down equations relevant to the cases considered above. The expressions so obtained however are quite cumbersome, e.g., taking only Si amphotericism into account yields a biquadratic equation. Under the present circumstances, it hardly seems worthwhile to attempt numerical solutions to these equations.

TABLE VI. Estimates of imperfection center densities.[a]

Sample	Dark p, cm^{-3}	E_f, ev	E_A, ev	Occupancy by holes	N_D, cm^{-3}	Lower limit N_A, cm^{-3}	Upper limit N_A, cm^{-3}
10 G 32	9.1×10^{15}	0.18	0.12	0.15	1.1×10^{16}	10^{16}	2×10^{16}
ES 44	3.0×10^{14}	0.27	0.17	0.035	4×10^{16}	4×10^{14}	4×10^{16}
631-14	4.1×10^{11}	0.44	0.43	0.57	10^{16}	10^{12}	2×10^{16}
GAJ-18-2b	2.6×10^{11}	0.45	0.40	0.21	6×10^{16}	4×10^{11}	3×10^{17}
GAJ-18M	3.4×10^{11}	0.45	0.40	0.21	7×10^{16}	4×10^{11}	4×10^{17}
10 G 40-4	2.8×10^{11}	0.45	0.45	0.67	9×10^{16}	3×10^{11}	10^{17}
ES 36A	5.5×10^{10}	0.49	0.45	0.29	10^{17}	6×10^{10}	4×10^{17}

[a] Dark p, cm^{-3} from Hall effect at 300°K. E_f—height of Fermi level above the top of the valence band calculated from value of p. E_A—activation energy for dark conductivity; see Table I. N_D—density of donors in initial n-type GaAs before copper diffusion. Lower limit to N_A, the density of acceptors, calculated on the basis of a single acceptor level without any compensation being present; see text. Upper limit to N_A calculated on the basis of a single acceptor level with compensation present; see text.

tivity. It is significant in this connection that the dividing line between the photoconductivity characteristics of the crystals of Table III at 5×10^{-6} mho/cm corresponds to a location of the Fermi level about 0.47 ev above the top of the valence band; under these conditions, about $\frac{4}{5}$ of the 0.42-ev centers are compensated. As the Fermi level drops with increasing p-type conductivity, the sensitizing ability of these centers disappears. It is significant that the whole photoconductivity characteristics of crystal ES 36 were altered when its p-type conductivity was lowered to become crystal ES 36A as described in reference 8 of this paper. It is interesting to note that the hole ionization energy for sensitizing centers in Cu-compensated photoconducting CdS, CdSe, and GaAs is approximately the same fraction of the total forbidden gap: 1.0 ev out of 2.4 ev in CdS, 0.6 ev out of 1.7 ev in CdSe, and 0.42 ev out of 1.4 ev in GaAs.

The other four levels listed in Table V act as recombination centers for photoconductivity, i.e., photosensitivity decreases as the length of time a photoexcited hole stays captured by these centers. Hall-effect measurements show that for data on these centers obtained from the variation of photocurrent with temperature at higher temperatures, p-type photoconductivity is involved. For data obtained from the variation of photocurrent with temperature at lower temperatures in insensitive crystals, it is not currently known what type the photoconductivity is, but it may very well also be p type.

The level located at about 0.13 ev above the top of the valence band is the level normally associated with Cu as an acceptor in GaAs. It is clear that in all of the crystals of Table III, except reference crystal 10G32, these normal Cu levels are completely ionized at room temperature and the dark conductivity is supplied by deeper levels. Identification of the other levels listed in Table V is uncertain. Whelan[18] has mentioned a shallow acceptor level with ionization energy of 0.02 ev which might be related to the shallow level located at 0.04 ev in this investigation; Whelan and Fuller[4] suggested identification of this level with a Ga vacancy or a Ga vacancy-impurity complex.[19]

The two most resistive crystals, 631-1 and 631-8, show dark conductivity activation energies of 0.66 ev and 0.58 ev at higher temperatures. In view of the Hall and photo-Hall data of Table IV, it is believed that these crystals are p type in the dark at lower temperatures where the conductivity is characterized by activation energies of 0.42 and 0.37 ev, and that they become n type in the dark with increasing temperature, room temperature being about the transition point. Crystal 631-8 is still p type in the dark, whereas crystal 631-1 is n type in the dark. It therefore seems most reasonable to ascribe these dark conductivity activation energies of about 0.6 and 0.7 ev to deep donors; likewise to ascribe the deep traps of 0.5, 0.6, and 0.7 ev to compensated deep donors, as in the previous investigation.[1] It is evident that temperature measurements of Hall and photo-Hall effect on all of these crystals are required for a full and unambiguous interpretation; such an investigation is intended.

An effort has been made to obtain rough limits on the density of several of the levels summarized in Table V where sufficient data were abailable to permit it. A summary of such data is given in Table VI. The concentration of holes in the dark is obtained from Hall data. The lower limit to the density of acceptor levels N_A was obtained on the basis of a simple model of a single acceptor lying E_A ev above the top of the valence band, ignoring the effects of any other levels which might be present in the forbidden gap. In such a model, the density of free holes p is given by

---

[18] J. M. Whelan, paper in *Semiconductors*, edited by N. B. Hannay (Reinhold Publishing Corporation, New York, 1959), p. 154.

[19] By a combination of photoconductivity and photomagnetoelectric measurements, A. Amith (private communication) has found levels at 0.65 ev below the conduction band and 0.23 ev above the valence band in high-resistivity n-type GaAs without added impurity, and levels at 0.5 ev above the valence band in low-resistivity p-type GaAs prepared by Cu diffusion into high-resistivity n-type material. In our own work we have found conductivity activation energies of about 0.5 ev when Cu was diffused into high-resistivity n-type GaAs; high densities of the 0.2- and 0.5-ev trapping centers were also formed in such a diffusion process. In high-resistivity crystals grown without added impurities, but under excess As pressure, the photosensitivity increases with decreasing temperature according to an activation energy of 0.09±0.004 ev (5 crystals).

$$p=\frac{N_v}{2}\exp(-E_A/kT)\left\{\left[1+4\frac{N_A}{N_v}\exp(E_A/kT)\right]^{\frac{1}{2}}-1\right\}, \tag{10}$$

which generally simplifies to

$$p=(N_AN_v)^{\frac{1}{2}}\exp(-E_A/2kT), \tag{11}$$

where N_v is the effective density of states in the valence band. When $N_A \ll N_v$, $p=N_A$. The upper limit to the density of acceptor levels N_A' was calculated assuming a single acceptor level appreciably compensated so that occupancy by holes

$$=\frac{N_A-N_D-p}{N_A}=\frac{1}{\frac{1}{2}\exp[(E_f-E_A)/kT]+1}, \tag{12}$$

where N_D is the density of donors in the initial material, assumed given by the second column of Table I, and E_f is the height of the Fermi level above the top of the valence band, calculated from

$$p=N_v\exp(-E_f/kT). \tag{13}$$

It is probable that the true density is closer to that of the upper limit.

There remains finally consideration of the shallow trapping levels, present in densities between 10^{12} and 10^{15} cm^{-3}, which are probably electron traps lying between 0.2 and 0.4 ev below the conduction band. In order to be detected, these shallow traps require a crystal with high sensitivity at low temperatures. This may explain why they were not detected in the previous investigation of high-resistivity n-type GaAs.[1] These shallow traps are characterized by considerable structure which may be due to the presence of excited states or to a type of spin-orbit interaction; it is a detailed sharp structure not hitherto observed in thermally stimulated current data on any other materials to the best of our knowledge.

CONCLUSIONS

The compensation of n-type GaAs by diffused Cu can be semiquantitatively understood in terms of a simple thermodynamic model involving only the presence of shallow donors in the initial material. The direction which departures from this idealized model take is indicated.

The levels revealed by the present investigation are identical with the donor and electron trapping (compensated donor) levels located at 0.5, 0.6, and 0.7 ev below the bottom of the conduction band, as previously reported,[1] and in addition are comprised of acceptor levels lying 0.42, 0.34, 0.22, 0.13, and 0.04 ev above the valence band.

The 0.42-ev centers, when compensated, provide a long electron lifetime and hence give rise to high n-type photosensitivity. Such centers appear to be negatively charged centers under thermal equilibrium, with a cross section for capture of holes 6×10^3 times larger than the cross section for the subsequent capture of electrons. When the Fermi level lies above these levels, they capture photoexcited holes, reduce the hole lifetime, but increase the electron lifetime. When the Fermi level lies below these levels, the room temperature p-type photoconductivity increases as the lifetime of holes becomes longer. These levels must be predominantly associated with the copper compensation process of n-type GaAs because no evidence is found of high photosensitivity at low temperatures, associated with capture of photoexcited holes with an activation energy of 0.42 ev in high-resistivity n-type material grown without intentionally added impurities. A residual concentration of such centers in n-type material, however, can reduce the hole lifetime if the conductivity is high enough so that the hole demarcation level lies near the 0.42-ev levels (coincidence of the demarcation level and the 0.42-ev levels occurs for a room temperature conductivity of about 1.5 mho/cm).

Hall data reported here and found on other high-resistivity n-type GaAs crystals grown without intentionally added impurities, indicate that the Hall mobility is sensitive to photoexcitation in n-type materials. There is strong evidence, therefore, that deep donors can play a role in the scattering process. Their effect is most pronounced in high-resistivity n-type material, where they exist in the compensated charged state, which can be removed by raising the Fermi level by photoexcitation. In low-resistivity n-type material, they are present in the uncompensated, uncharged state and make only a much smaller contribution to the scattering.

Although the effect of photoexcitation on Hall mobility seems much less in p-type material than in n type, according to Table IV, this is only apparent and not real. Since the change in scattering is given by differences in $1/\mu$, the absolute changes in scattering for the smaller values of μ in p-type material are of the same order of magnitude as for the larger values of μ in n-type material.

The 631 series of GaAs:Cu crystals is characterized by a high ratio of electron mobility at 78°K to that at 300°K. The absence of the 0.22-ev acceptor from this series is outstanding. In crystal 631-14, for example, the conductivity activation energy does not shift from the 0.42-ev level at high temperatures to the 0.25-ev level at low temperatures, as in several other crystals, but shifts directly from the 0.42-ev level to the 0.13-ev level. Similarly, crystal 631-9 shows the 0.13-ev level at low temperatures under conductivity conditions much lower than would be expected in comparison with the other crystals (see Fig. 1). There is reason, therefore, to propose that the 0.22-ev center, when present as a compensated acceptor, is an efficient scatterer, particularly at low temperatures.

The marked absence of the high density of 0.2-ev trapping levels found so consistently in high-resistivity *n*-type GaAs grown without intentionally added impurity[1] (see also reference 19) suggests that these levels are associated with an imperfection which is not present in the final GaAs:Cu crystals.

ACKNOWLEDGMENTS

The authors are indebted to L. R. Weisberg for many stimulating and helpful discussions, and to E. J. Stofko for the preparation and mounting of the crystals for measurement.

JOURNAL OF APPLIED PHYSICS VOLUME 32, NUMBER 9 SEPTEMBER, 1961

Flash Method of Determining Thermal Diffusivity, Heat Capacity, and Thermal Conductivity*

W. J. Parker, R. J. Jenkins, C. P. Butler, and G. L. Abbott
U. S. Naval Radiological Defense Laboratory, San Francisco 24, California

(Received September 29, 1960)

A flash method of measuring the thermal diffusivity, heat capacity, and thermal conductivity is described for the first time. A high-intensity short-duration light pulse is absorbed in the front surface of a thermally insulated specimen a few millimeters thick coated with camphor black, and the resulting temperature history of the rear surface is measured by a thermocouple and recorded with an oscilloscope and camera. The thermal diffusivity is determined by the shape of the temperature versus time curve at the rear surface, the heat capacity by the maximum temperature indicated by the thermocouple, and the thermal conductivity by the product of the heat capacity, thermal diffusivity, and the density. These three thermal properties are determined for copper, silver, iron, nickel, aluminum, tin, zinc, and some alloys at 22°C and 135°C and compared with previously reported values.

INTRODUCTION

THERE has been a renewed interest in developing new methods of determining the thermal conductivity and the thermal diffusivity of materials in recent years. This is largely a result of the rapid advances of materials technology and the many new applications of materials at elevated temperatures. There are a number of presently existing steady-state and non-steady-state methods of measuring these parameters. However, there is some dissatisfaction with the length of time required to make reliable measurements, and in some cases, the large sample sizes required by these techniques impose intolerable limitations. The difficulty of extending these methods to high temperatures has proven to be a stumbling block in high-temperature technology.

The heat flow equation can be solved for a wide variety of boundary conditions, and these solutions can often generate values of the thermal properties. However, inability to satisfy the boundary conditions has led to difficulties in some of the classical techniques. Two of these difficulties are caused by surface heat losses and thermal contact resistance between the specimen and its associated heat sources and sinks. The problem of thermal contact resistance has been virtually eliminated in some recent thermal diffusivity determinations by thermally insulating the specimen and introducing the heat by an arc image furnace. A system of this type has been described by Butler and Inn[1] in which the thermal diffusivity is expressed in terms of the differences between the temperature versus time curves taken by thermocouples located at two points along a thermally insulated rod continuously irradiated at the front surface by a carbon arc. It has been suggested[2] that the Angstrom method, which utilizes a periodic front surface temperature variation for diffusivity measurements, can also be adapted to the arc image furnace. It is necessary to make these two types of determinations in a vacuum chamber in order to eliminate convective heat losses. However, above 1000°C the radiation losses create a problem of considerable magnitude.

The technique described in this report utilizes a flash tube to eliminate the problem of the thermal contact resistance, while the heat losses are minimized by making the measurements in a time short enough so that very little cooling can take place. Although this method has only been tested for metals in the vicinity of room temperature, there is no reason to believe that measure-

---

* This research was sponsored by the Wright Air Development Division of the Air Research and Development Command, U. S. Air Force, under contract.

[1] C. P. Butler and E. C. Y. Inn in *Thermodynamic and Transport Properties of Gases, Liquids and Solids* (American Society of Mechanical Engineers, 29 W. 39th St., New York, New York, 1959).

[2] A. Hirschman, W. L. Derksen, and T. I. Monahan, "A Proposed Method for Measuring Thermal Diffusivity at Elevated Temperatures," Armed Forces Special Weapons Project Report, AFSWP-1145, Material Laboratory, New York Naval Shipyard, April, 1959.

ments cannot be made for all types of solid materials in any temperature range simply by preheating or cooling the specimens.

THEORY OF THE METHOD

If the initial temperature distribution within a thermally insulated solid of uniform thickness L is $T(x,0)$, the temperature distribution at any later time t is given by Carslaw and Jaeger[3] as

$$T(x,t)=\frac{1}{L}\int_0^L T(x,0)dx+\frac{2}{L}\sum_{n=1}^{\infty}\exp\left(\frac{-n^2\pi^2\alpha t}{L^2}\right)\times\cos\frac{n\pi x}{L}\int_0^L T(x,0)\cos\frac{n\pi x}{L}dx, \quad (1)$$

where α is the thermal diffusivity in cm²/sec. If a pulse of radiant energy Q cal/cm² is instantaneously and uniformly absorbed in the small depth g at the front surface $x=0$ of a thermally insulated solid of uniform thickness L cm, the temperature distribution at that instant is given by

$$T(x,0)=Q/DCg \quad \text{for} \quad 0<x<g$$

and

$$T(x,0)=0 \quad \text{for} \quad g<x<L.$$

With this initial condition, Eq. (1) can be written as

$$T(x,t)=\frac{Q}{DCL}\left[1+2\sum_{n=1}^{\infty}\cos\frac{n\pi x}{L}\frac{\sin(n\pi g/L)}{(n\pi g/L)}\times\exp\left(\frac{-n^2\pi^2}{L^2}\alpha t\right)\right], \quad (2)$$

where D is the density in g/cm³ and C is the heat capacity in cal/g°C. In this application only a few terms will be needed, and since g is a very small number for opaque materials, it follows that $\sin n\pi g/L\approx n\pi g/L$. At the rear surface where $x=L$, the temperature history can be expressed by

$$T(L,t)=\frac{Q}{DCL}\left[1+2\sum_{n=1}^{\infty}(-1)^n\exp\left(\frac{-n^2\pi^2}{L^2}\alpha t\right)\right].$$

Two dimensionless parameters, V and ω can be defined

$$V(L,t)=T(L,t)/T_M \quad (4)$$

$$\omega=\pi^2\alpha t/L^2. \quad (5)$$

T_M represents the maximum temperature at the rear surface. The combination of 3, 4, and 5 yields

$$V=1+2\sum_{n=1}^{\infty}(-1)^n\exp(-n^2\omega). \quad (6)$$

Equation (6) is plotted in Fig. 1.

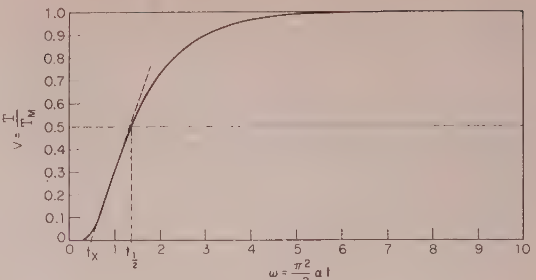

FIG. 1. Dimensionless plot of rear surface temperature history.

Two ways of determining α have been deduced from Eq. (6) and Fig. 1. When V is equal to 0.5, ω is equal to 1.38, and so

$$\alpha=(1.38L^2/\pi^2t_{\frac{1}{2}}), \quad (7)$$

where $t_{\frac{1}{2}}$ is the time required for the back surface to reach half of the maximum temperature rise.

The time axis intercept of the extrapolated straight line portion of the curve in Fig. 1 is at $\omega=0.48$, which yields another useful relationship,

$$\alpha=(0.48L^2/\pi^2t_x), \quad (8)$$

where t_x is the time axis intercept of the temperature versus time curve.

It is not necessary to know the amount of energy absorbed in the front surface in order to determine the thermal diffusivity. However, this quantity must be determined if measurements of specific heat or thermal conductivity are required. The product of the density and the heat capacity of the material is given by

$$DC=Q/LT_M, \quad (9)$$

and the thermal conductivity is found from the relationship

$$K=\alpha DC. \quad (10)$$

The foregoing treatment has neglected the variation of thermal diffusivity with temperature. Although the method produces an effective value of diffusivity for the sample, an effective value of the corresponding temperature is yet to be determined. This problem is common to all types of diffusivity measurements and is usually minimized by the fact that the range of temperatures in a single measurement is kept as small as possible. Clearly, the time of transit of the heat pulse will depend upon the range of temperature encountered en route. Without attempting a rigorous analysis, an effective temperature was simply picked as the time average of the mean of the front and back surface temperatures up to the time that the rear surface reaches one-half of its maximum value.

The dimensionless parameter $V(L,t)$ at the rear surface was given by Eq. (6). The dimensionless parameter $V(0,t)$ at the front surface obtained in a similar manner

---

[3] H. S. Carslaw and J. C. Jaeger, *Conduction of Heat in Solids* (Oxford University Press, New York, 1959), 2nd ed., p. 101.

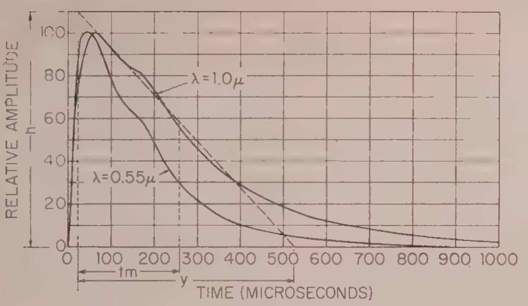

FIG. 2. Irradiance history of the flash lamp at two different wavelengths. Dashed lines represent the approximation used for the front surface temperature rise calculations.

is given by

$$V(0,t)=1+2\sum_{n=1}^{\infty}\exp(-n^2\omega), \tag{11}$$

and the mean value of $V(L,t)$ and $V(0,t)$ is

$$\frac{V(0,t)+V(L,t)}{2}=1+2\sum_{n=1}^{\infty}\exp(-4n^2\omega), \tag{12}$$

and the effective value of V is

$$V_e=1+\frac{2}{\omega_{\frac{1}{2}}}\int_0^{\omega_{\frac{1}{2}}}\sum_{n=1}^{\infty}\exp(-4n^2\omega)d\omega, \tag{13}$$

where $\omega_{\frac{1}{2}}=\pi^2\alpha t/L^2=1.38$,

$$V_e=1+\frac{2}{4(1.38)}\left[\sum_{n=1}^{\infty}\frac{1}{n^2}(1-\exp(-4n^2 1.38))\right]=1.6, \tag{14}$$

and finally, the effective temperature is given by

$$T_e=V_eT_M=1.6T_M. \tag{15}$$

MAXIMUM FRONT SURFACE TEMPERATURE

The front surface temperature may initially rise to a very high value because the energy is delivered in a very short time. It is important to know the upper limit of this temperature in order to avoid operating through temperature regions which may contain phase changes in the material being tested. An estimate of this temperature can be obtained from the following model. Consider the shape of the input power versus time curve to be a negative-going saw tooth given by $h(1-t/y)$ where the constants h and y are obtained by the construction shown in Fig. 2, and t is actually measured from the leading edge of the constructed triangle. Because the back surface temperature does not begin to rise within the duration of the input pulse, the specimen can be treated as a slab of infinite thickness. Carslaw and Jaeger[4] treat the case of an input power function $f(t)$ incident on the face, $x=0$, of a slab of infinite thickness and find that the temperature is given by

$$T(x,t)=\frac{1}{DC(\pi\alpha)^{\frac{1}{2}}}\int_0^t f(t-z)\exp(-x^2/4\alpha z)dz/z^{\frac{1}{2}}, \tag{16}$$

where z is simply a variable of integration, and so at the front surface of the specimen, irradiated by the flash lamp, this temperature is given by

$$T(t)=\frac{h}{DC(\pi\alpha)^{\frac{1}{2}}}\int_0^t\left[1-\frac{t-z}{y}\right]dz/z^{\frac{1}{2}}. \tag{17}$$

At t_m, the time of the maximum front surface temperature, $\partial T/\partial t=0$. Direct differentiation of Eq. (17) yields by Leibnitz' Rule

$$\frac{\partial T}{\partial t}=\frac{h}{DC(\pi\alpha)^{\frac{1}{2}}}\left[\frac{-1}{y}\int_0^{t_m}dz/z^{\frac{1}{2}}+t_m^{-\frac{1}{2}}\right]=0, \tag{18}$$

and so $t_m=y/2$. The maximum temperature T_f reached at the front surface is then given by combining Eqs. (17) and (18).

$$T_f=\frac{h}{DC(\pi\alpha)^{\frac{1}{2}}}\int_0^{y/2}\left[\frac{1}{2}+\frac{z}{y}\right]dz/z^{\frac{1}{2}}=\frac{4hy}{3DC(2\pi\alpha y)^{\frac{1}{2}}}. \tag{19}$$

If all of the energy of the pulse was represented by the area of the constructed triangle, Q would be equal to $\frac{1}{2}hy$. Since this is not the case, a correction factor β is introduced which is equal to the ratio of the area of the total pulse to that of the triangle.

$$Q=\tfrac{1}{2}\beta hy. \tag{20}$$

Taking Eq. (20) into account, Eq. (19) may be rewritten

$$T_f=\frac{8Q}{3\beta DC(2\pi\alpha y)^{\frac{1}{2}}}, \tag{21}$$

or since $Q=DCLT_M$,

$$T_f=\frac{8}{3\beta(2\pi y)^{\frac{1}{2}}}LT_M/\alpha^{\frac{1}{2}}. \tag{22}$$

The parameters β and y are characteristic of the flash lamp, and for the lamp used in this work they were estimated from the irradiance versus time curve at 1 μ to be 1.3 and 5×10^{-4}, respectively. A closer approximation would be obtained if the total radiant power curve could have been used instead of the power in a single wavelength band. The maximum temperature rise in any of the samples tested in this report can be estimated from Table I and Eq. (23).

$$T_f=38LT_M/\alpha^{\frac{1}{2}}, \tag{23}$$

where L is in centimeters, α is in centimeters squared

---

[4] H. S. Carslaw and J. C. Jaeger, *Conduction of Heat in Solids* (Oxford University Press, New York, 1959), 2nd ed., p. 76.

TABLE I. Thermal diffusivity.

Material	Alloy	Sample size cm	L Thickness cm	Thermal diffusivity[a] cm² sec⁻¹ at 22°C	Thermal diffusivity[b] cm² sec⁻¹ at 22°C	Thermal diffusivity[a] cm² sec⁻¹ at 135°C	α Other sources cm² sec⁻¹ at 20°C	T_M Final sample temperature rise °C
Aluminum	...	1.9 cm square	0.352	0.94	0.86	0.89	0.86[c]	2.4
Copper	OFHC	1.9 cm square	0.312	1.15	1.07	1.04	1.14[c]	1.8
Iron	Armco	1.9 cm square	0.100	0.19	0.18	0.15	0.17[c]	4.3
Nickel	...	1.26 cm round	0.100	0.16	0.15	0.14	0.16[c]	3.9
Silver	...	1.9 cm square	0.322	1.61	1.42	...	1.70[c]	2.5
Tin	...	1.9 cm square	0.306	0.39	0.35	0.33	0.38[c]	3.7
Zinc	...	1.9×1.16 cm rectangle	0.282	0.40	0.45	0.37	0.41[c]	2.7
Magnesium	HK31	1.9 cm square	0.352	0.54	0.48	0.57	0.56[d]	2.8
Steel	1020	1.9 cm square	0.100	0.14	0.13	0.13	0.15[d]	4.5
Steel	4340	1.9 cm square	0.107	0.096	0.10	0.090	0.091[d]	4.1
Titanium	6AL-4V	1.9 cm square	0.100	0.019	0.027	0.02	0.019[d]	6.0

[a] Obtained from Eq. (7).
[b] Obtained from Eq. (8).
[c] Taken from reference 5.
[d] Interpolated or extrapolated from reference 1.

per second, and T_M is the maximum back surface temperature.

EXPERIMENTAL PROCEDURE

The success of the method depends upon adequately meeting the boundary conditions of the theory. The front surface of the sample must be uniformly irradiated in a time short compared to the rise time of the back surface temperature, the thermocouple must measure the actual back surface temperature, and all losses must be as small as possible. Furthermore, the signal must be large enough to be well above the noise level present in the recording system, and the bandwidth of the amplifier and recorder must be wide enough to pass the signal without distortion.

The dimensions and shapes of the samples used are listed in Table I, along with the data obtained. The flash tube used was a commercially available unit (GE FT524) consisting of a four-turn quartz spiral with a Pyrex envelope, dissipating 400 joules of energy in each flash. The relative irradiance versus time curve for this lamp is shown in Fig. 2. The front surfaces of the samples were blackened with camphor black to increase the amount of energy absorbed, to ensure that all parts of the sample had equal absorption, and that the absorptivities of all specimens were identical. These samples were mounted in a ceramic holder approximately 1 cm from the envelope of the flash lamp with the plane of the front surface parallel to the axis of the quartz spiral and with 0.12-mm diam Chromel-Alumel thermocouple wires pressed against the back surface. The wires were separated by 1 to 2 mm where they contacted the surface so the electrical circuit was through the sample under test. This ensured that the temperature recorded was actually that at the back surface and not at some other wire junction. The output voltage from the thermocouple was presented on an oscilloscope and photographed with a Polaroid land camera.

The maximum signal voltages were from 40 to 400 μv, indicating a back surface temperature rise of 1° to 10°C, and were too low to record directly on the oscilloscope, which had a maximum gain of 1 mv/cm. A differential transistor preamplifier was therefore designed and built. This preamplifier had a gain of 36 and was very quiet, stable, and linear under the conditions of operation. The two transistors were mounted in a block of brass to ensure that they would both be at the same temperature, but no other attempt was made to stabilize the gain against temperature changes, as the unit was to be used only in the laboratory. The gain was measured so that the sample temperature rise could be determined, but it does not enter into any of the other calculations. The sample holders must be opaque to prevent any irradiation of the back surface of the sample, of low thermal conductivity to reduce edge losses, physically strong, and capable of standing the high irradiant thermal flux. The holder used was machined from lava and baked at 1100°C to give a hard ceramic material of considerable strength. The holder would accomodate samples 0.7 to 1.9 cm round or square and up to 0.5 cm thick, holding them in place with small spring wire retainers which obscured very little of the front surface. The thermocouple wires were clamped in a small pin vise and connected to a firmly mounted plug to simplify the connection to the external circuit. This plug formed the cold junction. The thermocouple support and the ceramic piece could be readily moved relative to each other, which considerably facilitated sample changing. The entire assembly of lamp and sample holder was mounted with conventional laboratory clamps on an inexpensive optical bench, which was used primarily because it provided a firm and solid support. The system is shown in a pictorial schematic in Fig. 3.

The 135°C measurements were obtained by heating the sample holder and sample with an infrared lamp. The output of the thermocouple was read on a millivolt meter during the heating process, which took 20–30 min to reach equilibrium. The cold junction and the flash lamp were air-cooled during this time.

The high voltage trigger pulse and the large current pulse which accompany the discharge of a flash lamp caused some electrical interference with the signal and required careful shielding of the wires and of the lamp, except for a small window through which the sample was exposed. It was not possible to completely eliminate the transient, but it was reduced to a point where it did not interfere with the amplifiers and to where it actually provided a convenient time zero point from which to measure. Because it proved to be convenient to have a length of baseline to assist in lining up the reading instrument, a time delay generator was designed and built which fired the lamp from 0.3 to 4700 msec after the oscilloscope had been triggered.

The minimum thickness of the sample is determined by the requirement that the flash duration must be short compared to the time the temperature begins to rise at the back surface. A sample that is too thin results in the recording of a low value of diffusivity. On the other hand, if the sample is too thick, the sensitivity is reduced and the time for losses to occur is increased. Using the flash lamp described previously, a satisfactory thickness is about 1 mm for samples of diffusivity less than 0.2 cm^2/sec and about 3 mm for samples of higher diffusivity.

To facilitate the reading of the Polaroid land prints, the device shown in Fig. 4 was constructed of $\frac{1}{16}$-in. Plexiglas. The vertical arms pivot about the points labeled A, maintaining the horizontal arms parallel to and equidistant from the engraved center line. In practice, the device is laid on top of the print, the lower horizontal arm is lined up on the base line, the upper arm at the top of the curve, and the fiducial on the zero point of the curve. The half-time is read from the center line in units of distance and can be converted to time by a simple multiplication involving the sweep speed of the oscilloscope. In Fig. 4 a temperature time curve is superimposed on the device to illustrate its use. The vertical scales are to assist in aligning the print accurately with the baseline.

Heat capacity measurements were made by comparing the temperature rise in the sample with that in a silver sample of similar shape and size. The values of heat capacity for silver and of the density for all the samples of the elements were taken from reference 5.

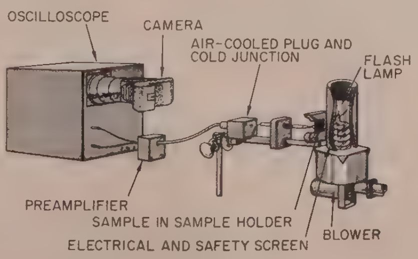

FIG. 3. Pictorial schematic of test setup.

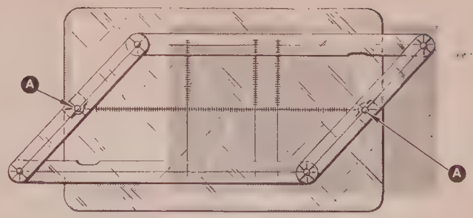

FIG. 4. Reading device.

The shape of the temperature versus time curve, if compared with Fig. 1, will reflect any appreciable deviations from the ideal boundary conditions of the experiment. If the final temperature is approached very slowly after an initially fast rise, or if the curve actually has a peak before seeking a lower temperature plateau, there was a nonuniform distribution of irradiance on the front surface. The latter effect will appear if the supporting structure masks an appreciable portion of the surface. The distortion in the curve is due to two dimensional heat flow which is slow because of the greater distances, and usually has a small effect on the early part of the curve.

A detailed analysis of the effect of cooling losses and the circumstances for which they can be neglected has not been accomplished in this report, but will be part of the basis for further work in connection with extending the flash technique to higher temperatures. The appearance of a flat region at the top of all of the data curves was an indication that cooling losses were not important in this case. Corrective measures to be taken if cooling is excessive would be to use thinner samples or to perform the experiment in a vacuum.

ERRORS AND ACCURACY

The largest errors in the system are probably the nonlinearity and distortion in the oscilloscope-camera recording system, and nonuniformity in the distribution of the radiant energy on the sample surface. The system layout was chosen to minimize the latter effect and careful calibration was used to minimize the former. The final precision of measurement was within ±5% and is about as well as can be done with the recording system that was used. (Tektronix 531 oscilloscope, Fairchild oscilloscope camera with a Polaroid land back.) The accuracy of the system is more difficult to estimate. Tables I and II and Fig. 5 compare the data obtained with some previously published.[3,5] The dotted lines in Fig. 5 represent a difference in the two figures of ±10%, and it can be seen that the agreement is within

---

[5] *Smithsonian Physical Tables*, compiled by W. E. Forsythe (The Smithsonian Institution, Washington, D. C., 1954), ninth revised ed.

TABLE II. Thermal conductivity and heat capacity (same samples as used for Table I).

Material	Alloy	*D* Density g cm^{-3} 20°C	*C* Heat capacity cal g^{-1} °K^{-1} 22°C	*K* Thermal conductivity cal cm^{-1} sec^{-1} °K^{-1} 22°C	*C* Other sources cal g^{-1} °K^{-1}	*K* Other sources cal cm^{-1} sec^{-1} °K^{-1}
Aluminum	...	2.70[a]	0.21	0.53	0.23[a]	0.50[a]
Copper	OFHC	8.96[a]	0.097	1.0	0.092[a]	0.92[a]
Iron	Armco	7.87[a]	0.11	0.16	0.11[a]	0.17[a]
Nickel	...	8.90[a]	0.12	0.16	0.11[a]	0.14[a]
Silver	...	10.49[a]	0.056[a]	0.95	0.056[a]	1.00[a]
Tin	...	7.30[a]	0.057	0.16	0.054[a]	0.15[a]
Zinc	...	7.14[a]	0.088	0.25	0.090[a]	0.27[a]
Magnesium	HK31		0.428[b]	0.23	...	...
Steel	1020		0.824[b]	0.12	...	...
Steel	4340		0.833[b]	0.08	...	...
Titanium	6AL-4V		0.614[b]	0.012	...	...

[a] Taken from reference 5.
[b] Density not available. Product of *D* and *C* calculated and listed.

these limits in practically all cases. Differences of this magnitude are found in data published by other investigators[3,5,6] and may represent differences in sample purity as well as methods since the parameters reported here are likewise affected by the physical treatment of the metals as well as by the composition.

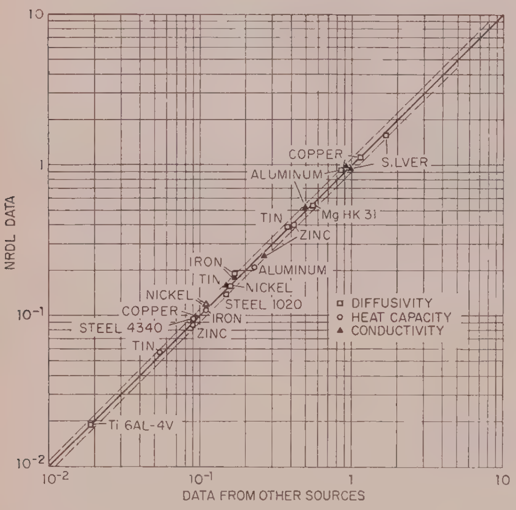

FIG. 5. Graphic comparison of NRDL data and data from other sources at ambient temperatures. The broken lines represent a ±10% variation from the mean.

The values of diffusivity determined by Eq. (7) are considerably less precise than those determined by Eq. (8). This method requires the finding, by eye, of the straight portion of a curve and the extrapolation of this line back to the baseline. This is a subjective method which is rather difficult and one in which a small error in the slope determination results in a relatively large error in the value of the diffusivity. Its advantage is that it is independent of the final height of the curve and does not require that the surface distribution of energy be as uniform as does the half-time method.

CONCLUSIONS

The results shown in Tables I and II indicate the very close agreement between the values measured here and those already published. It is a new system and the results presented are only a preliminary test of the basic method in the ambient and slightly above ambient temperature range and for materials for which values of the thermal properties can be found in the literature.

There are several advantages associated with this system. (1) A minimum of specialized equipment is required. (2) Data reduction is relatively easy. (3) The size of the specimen can be quite small. (4) The system can be used at high or low temperatures by preheating or cooling the specimen. (5) The amount of energy added to the sample to make a measurement is quite low. This should be an attractive feature for low-temperature measurements. (6) The three thermal properties, diffusivity, thermal conductivity, and heat capacity, can be deduced for the same sample with the same equipment.

---

[6] *ASME; Metal Properties*, edited by S. L. Hoyt (McGraw-Hill Book Company, Inc., New York, 1954).

JOURNAL OF APPLIED PHYSICS VOLUME 32, NUMBER 9 SEPTEMBER, 1961

Surface Layer in $BaTiO_3$ Single Crystals

ENNIO FATUZZO AND WALTER J. MERZ
Laboratories RCA Ltd., Zurich, Switzerland

(Received March 13, 1961)

The switching time and the coercive field in ferroelectric $BaTiO_3$ are known to depend on crystal thickness. A model along the following lines is proposed to explain the experimental results: on the crystal surface there is a thin layer of electrically biased and mechanically strained $BaTiO_3$ which has a much smaller dielectric constant than the bulk. It is proposed that the electrical bias and the mechanical strains in the surface are caused by a Schottky exhaustion layer. This model and the model proposed by Drougard and Landauer are discussed and their predictions are compared with experimental results.

I. INTRODUCTION

THE dependence of the switching time t_s on the applied field E in ferroelectrics has been investigated in a number of papers. For $BaTiO_3$ the following relation was found[1]

$$1/t_s=(1/t_\infty)\exp(-\alpha/E), \quad (1)$$

where t_∞ is the switching time for an infinitely large field and α is the "activation field."

Merz[2] showed that in Eq. (1), α has the following dependence on crystal thickness d:

$$\alpha=\alpha_\infty(1+d_0/d), \quad (2)$$

where α_∞ is the "activation field" for infinitely thick samples and d_0 is a constant with a value of about 10^{-2} cm.

In reference 2 this behavior is explained in the following way. On the surface of the crystal there is a layer of low dielectric constant material across which there is a voltage drop which makes the voltage across the bulk of the crystal smaller than the applied voltage. It was assumed that this layer can be treated as a simple condenser with a low dielectric constant of about five in series with the condenser formed by the bulk material. From this it follows that the layer thickness must be between 0.5×10^{-4} cm and 1.5×10^{-4} cm.

Drougard and Landauer[3] concluded that:

(a) When switched, a ferroelectric crystal acts not just as a single voltage divider but as a nonlinear conductance.[4,5]

(b) The displacement current between layer and bulk must be maintained during switching.

(c) A surface layer of foreign material might mask the domain pattern which is obtained by etching the crystal surface.

(d) Careful x-ray investigations[6] do not reveal the presence of any foreign layer as thick as 10^{-4} cm. If there is a surface layer it has to be thinner than about 80 A.

From condition (b) they concluded that the layer must have a reversible polarization, i.e., it must be ferroelectric like the bulk because in order to maintain continuity in the dielectric displacement, a normal low dielectric constant material would require electric fields as large as about 10^8 v/cm. On the other hand, they found it very difficult to assume a ferroelectric layer different from $BaTiO_3$ but with the same polarization as in $BaTiO_3$, and with a lower dielectric constant. They therefore proposed a model in which they assumed a very thin and lossy layer on the crystal surface across which there is a fixed voltage drop, which is independent of the applied voltage. Their model[3] gives the following equation for α:

$$\alpha=\alpha_\infty[E^2/(E-2P_s/dc_l)^2]=\alpha_\infty[1/(1-2P_s/dc_lE)^2], \quad (3)$$

where P_s is the spontaneous polarization, d the thickness of the sample, and c_l the capacitance per unit area of the layer. Drougard and Landauer approximated Eq. (3) as follows:

$$\alpha\cong\alpha_\infty(1+4P_s/Ec_ld), \quad (4)$$

and defined

$$d_0=4P_s/Ec_l, \quad (5)$$

so that Eq. (3) can be written as

$$\alpha=\alpha_\infty(1+d_0/d) \quad (6)$$

which is identical to the experimental Eq. (1).

II. NEW MODEL

In this section we discuss a model which meets the requirements (a) to (d) of the previous section. This model is similar to the one put forward by Merz[2] but with the additional condition that the surface of $BaTiO_3$ does not consist of a foreign nonferroelectric material but of $BaTiO_3$ with a low dielectric constant. This automatically fulfills the requirement of continuous dielectric displacement. It furthermore explains why Drougard[6] could not see a foreign layer on the crystal with x rays.

The principal question is, of course, why there should be a drop of the dielectric constant at the surface of the $BaTiO_3$ crystals. Since we are unable to give a detailed quantitative picture, we would like to mention the following experimental facts. The dielectric constant in a ferroelectric can be strongly reduced by mechanical clamping or by an electric bias. Roberts[7] has measured the dielectric constant as a function of bias field in $BaTiO_3$ ceramics and found a drop from 1150 to 675 with a field of about 43 kv/cm. Similar results were obtained by us on single crystals; a field of 10^5 v/cm gave a drop of 50% in ϵ. Furthermore, the dielectric constant of a mechanically clamped $BaTiO_3$ crystal is known to be much smaller than that of a free crystal.[8] In 1955, Kaenzig[9] proposed that in ionic conductors such as $BaTiO_3$ there exists a space charge layer at the surface, due to the fact that the surface is a source or a sink of vacancies. This is very similar to the electronic space charge on semiconductor surfaces. The electric potential between the surface and the bulk is of the order of a few volts. An impurity concentration of 10^{18} cm^{-3} in an extrinsic ionic conductor leads to an "ionic Schottky exhaustion layer" of a thickness of the order of 10^{-5} cm, similar to the electronic exhaustion layers in semiconductors. Hence, fields of the order of 10^5/cm may result, which are responsible for the reduction of the dielectric constant because they bias the crystal and also clamp the surface layer mechanically due to the high piezoelectric coupling.

---

[1] W. J. Merz, Phys. Rev. **95**, 690 (1954).

[2] W. J. Merz, J. Appl. Phys. **27**, 938 (1956).

[3] M. E. Drougard and R. Landauer, J. Appl. Phys. **30**, 1663 (1959).

[4] R. Landauer, D. R. Young, and M. E. Drougard, J. Appl. Phys. **27**, 752 (1956).

[5] M. E. Drougard, A. L. Funk, and D. R. Young, J. Appl. Phys. **25**, 1166 (1954).

[6] M. Drougard (private communication).

The question arises why the reduced field in the bulk is the only thing that matters for the domain wall motion and not the increased field in the surface layer. This can be explained if one assumes that the critical height of the nucleus is at least a few times larger than the layer thickness, which, however, is contrary to the model proposed by Miller and Weinreich.[10]

III. DISCUSSION OF THE TWO MODELS

There are a certain number of experimental facts which must be explained by any model, namely:

(1) The linear dependence of α on reciprocal thickness $1/d$,

(2) The linear dependence of the coercive field E_c on reciprocal thickness $1/d$,

(3) The increase of t_∞ with increasing thickness,

(4) The field-dependence of the switching time t_s, which is described by the law[1] $1/t_s=(1/t_\infty)\,(\exp-\alpha/E)$ over a range of as much as five decades, for *thin crystals* as well as thick ones,

(5) The domain wall velocity experiments performed by Miller,[11]

(6) The thickness independence of the small signal dielectric constant.

It will be shown that points (1) and (4) are explained by our model only, point (2) is fitted both by the DL (Drougard-Landauer[3]) and by our model, points (5) and (6) are explained by the DL model only, and point (3) is fitted by neither.

A. Thickness Dependence of α

The basic difference between the DL model and ours is the following. In our model there is a voltage drop across the surface layer which is always a certain fraction of the applied voltage, whereas in the DL model the voltage drop across the layer is constant. Thus, in our model there is always a voltage across the bulk of the material, no matter how thin the crystal may be. In the DL model there is a field-dependent critical thickness below which no more switching occurs, because the net voltage across the bulk becomes zero. This critical condition is reached when $E_L\cdot d_L$ is equal to the applied voltage, where E_L is the field in the layer and d_L the layer thickness.

Every model which assumes a thickness-independent voltage drop across the layer gives a threshold thickness for a given field. Referring to Drougard and Landauer's paper[3] it should be mentioned that the expansion of Eq. (3) yielding Eq. (4) is only permissible when

$$2P_s/EdC_1=d_0/2d\ll 1. \qquad (7)$$

Since d_0 was determined experimentally to be about 10^{-2} cm it follows that this approximation is valid only for crystals with a thickness of

$$d\gg 5\times 10^{-3}\text{ cm}. \qquad (8)$$

Equation (4) therefore can be used only for thick crystals. Since the experimental results[2] of the thickness dependence of α were obtained in the range of $d=3$ to 36×10^{-3} cm, it is not possible to explain them with Eq. (4). For thin crystals the nonapproximated Eq. (3) has to be applied.

The experimental points lie on a straight line in the whole range from 3 to 36×10^{-3} cm and therefore are well fitted by our model which yields a linear dependence of α on $1/d$. Equation (3) fits the experimental points just for very thick samples, but yields an infinite value for α at $d=d_0/2$.

B. Thickness Dependence of the Coercive Field

The thickness dependence of the coercive field E_c is given, for our model, as for Merz's model,[2] by the following relation:

$$E_c=E_\infty(1+d_0/d).$$

It can be easily shown that in the DL model, E_c is given by the expression

$$E_c=E_\infty+(2P_s/c_1d).$$

Both models therefore yield the right thickness-dependence for the coercive field.[3]

C. Thickness Dependence of t_∞

It is not straightforward to derive a thickness dependence of t_∞ from either model under investigation.

---

[7] S. Roberts, Phys. Rev. **71**, 890 (1947).

[8] For example: A. F. Devonshire, Phil. Mag. **42**, 1065 (1951).

[9] W. Kaenzig, Phys. Rev. **98**, 549 (1955).

[10] R. C. Miller and G. Weinreich, Phys. Rev. **117**, 1460 (1960).

[11] R. C. Miller (private communication).

From the field dependence of the switching time

$$1/t_s=(1/t_\infty)\exp(-\alpha/E), \tag{9}$$

it would appear that t_∞ is a constant, and does not depend on the thickness of the crystal. However, we know that this equation is not correct for high electric fields. A better fit can be obtained with the equation proposed by Pulvari and Kuebler[12]

$$1/t_s=kE\exp(-\alpha/E),$$

or with the equation proposed by Fatuzzo[13]

$$1/t_s=kE^{\frac{3}{2}}\exp(-\alpha/E).$$

Using Pulvari and Kuebler's expression, it follows from Eq. (9) that

$$1/t_\infty=kE.$$

For thin crystals the field E must be substituted by the effective field applied across the bulk, that is in our model by

$$E_{\text{eff}}=E/(1+d_0/d),$$

and in the DL model by

$$E_{\text{eff}}=E-(2P_s/c_ld).$$

Therefore, the expression for t_∞ becomes

$$t_\infty=k^{-1}E^{-1}\left(1+\frac{d_0}{d}\right),$$

and

$$t_\infty=k^{-1}\left(E-\frac{2P_s}{c_ld}\right)^{-1},$$

respectively.

Both equations give a decrease in t_∞ with increasing d, which is opposite from the experimental results.[2] Thus, neither model is able to explain the thickness dependence of t_∞.

D. Field Dependence of Switching Time

In our model the field dependence of the switching time for thin crystals can be represented by the following law:

$$1/t_s=(1/t_\infty)\exp[-\alpha_\infty/E_{\text{eff}}]$$
$$=(1/t_\infty)\exp\left[-\frac{\alpha_\infty(1+d_0/d)}{E}\right].$$

Thus, however thin the crystals are, our model gives a linear dependence of $\log(1/t_s)$ on $1/E$, in agreement with the experiments. In the DL model, the field dependence of t_s is represented by the law

$$1/t_s=(1/t_\infty)\exp[-\alpha_\infty/E_{\text{eff}}]$$
$$=(1/t_\infty)\exp\left[-\frac{\alpha_\infty}{E-(2P_s/dc_l)}\right].$$

For very thin crystals, the value of α can be as much as six times higher than the α_∞ value,[2] i.e., the value of the term $(2P_s/dc_l)$ can be as much as $\frac{5}{6}$ of E. Under these circumstances a plot of $\log(1/t_s)$ vs $1/E$ does not yield a straight line over several decades as observed experimentally.[1,2]

E. Domain Wall Velocity Experiments

Miller[10] found, with his experiments on sideways wall velocity of domains in crystals of different thickness, that in thin crystals the wall velocity is largest immediately after application of the electric field. With time the velocity decreases with a time constant of about 1 msec. This can be easily understood with the DL model,[1,13] because in 1 msec the wall moves the distance $2l$ (equal to twice the layer thickness[3]), after which the DL layer becomes effective in slowing down the motion. Our model cannot explain this experimental fact.

F. Thickness Dependence of Small Signal Dielectric Constants

Our model predicts that the dielectric constant should increase with crystal thickness whereas the DL model predicts a thickness independent behavior. Experimentally no thickness dependence has been observed by us.

IV. CONCLUSIONS

Both models can explain some of the experimental features in BaTiO$_3$ but neither model can explain all the facts.

It can be shown that the field dependence of the switching time and the thickness dependence of α could be explained by the DL model if the layer capacitance were proportional to the reciprocal effective field, which is not obvious.

It thus appears that a third model, combining some features of the two models discussed above, is required.

---

[12] C. F. Pulvari and W. Kuebler, J. Appl. Phys. **29**, 1315 (1958).

[13] E. Fatuzzo (to be published).

JOURNAL OF APPLIED PHYSICS VOLUME 32, NUMBER 9 SEPTEMBER, 1961

Thermal Conductivity of Porous Media. I. Unconsolidated Sands

W. Woodside and J. H. Messmer
Gulf Research and Development Company, Pittsburgh, Pennsylvania

(Received March 13, 1961)

The problem of determining the effective thermal conductivity of a two-phase system, given the conductivities and volume fractions of the components, is examined. Equations are described which have been proposed as solutions to this problem, including those of Maxwell, de Vries, and Kunii and Smith, the weighted geometric mean equation, and an equation based on a three-element resistor model found applicable to the analogous electrical conductivity problem. Experimental results are presented for five unconsolidated samples: three quartz sand packs, a glass bead pack, and a lead shot pack. The method of conductivity measurement using the transient line heat source (thermal conductivity probe) is described. Data are reported showing the variation of effective thermal conductivity with porosity, solid particle conductivity, saturating fluid conductivity, and the pressure of the saturating gas. From considerations based on the kinetic theory of gases, it is shown that the characteristic dimension of the pore space, with respect to heat conduction in the gas occupying this space, is smaller than the mean particle diameter by a factor of roughly 100. The thermal conductivity equations which best represent the observed data are those of de Vries, and Kunii and Smith, and a slightly modified version of the resistor model equation.

INTRODUCTION

THE effective thermal conductivities of several unconsolidated sand packs and porous rocks have been measured under a variety of test conditions. The reason for the need for such data is the current interest in thermal methods of petroleum production from underground oil-bearing sands and rocks. Knowledge of the thermal properties of such porous materials is important in many other fields also. Calculations of heat dissipation from underground nuclear explosions and of the rate of heat loss from the earth due to the geothermal gradient depend directly upon the thermal conductivity values of the rocks involved. Determinations of the current-carrying capacity of buried cables and of the heat losses from underground steam and hot water pipes require values for the conductivities of soils. The design of packed columns, thermal insulating, and refractory materials depends upon the heat transfer characteristics of porous media.

Few reliable thermal data on petroleum reservoir-type rocks are presently available in the literature. The properties of interest are the thermal conductivity k, the thermal diffusivity α, and specific heat c. Since these three quantities are interrelated, ($\alpha=k/\rho c$, where ρ is density) knowledge of any two determines the third. The heat capacity ρc of a rock or sand of porosity ϕ (ϕ=fractional void volume=1−rock volume fraction), containing oil and water at saturations S_o and S_w, respectively, may be closely approximated by

$$\rho c=(1-\phi)\rho_s c_s+\phi S_o\rho_o c_o+\phi S_w\rho_w c_w, \qquad (1)$$

where c_s, c_o, and c_w and ρ_s, ρ_o, and ρ_w are the specific heats and densities of the solid, oil, and water, respectively, all of which are known or easily measured. Thus if the effective thermal conductivity k can be measured, the thermal diffusivity may be calculated.

In connection with thermal oil recovery processes the variation of effective thermal conductivity with the following parameters is required: (a) porosity, (b) saturating fluid, (c) pressure of the saturating fluid, (d) over-burden pressure, and (e) temperature.

In addition to providing reliable thermal conductivity data, it is desirable to find a correlation, empirical or otherwise, between conductivity and other more easily measured parameters such as porosity, formation factor (formation factor=resistivity of a rock 100% saturated with fluid of resistivity $R_w\div R_w$), etc. Many of the equations proposed for the thermal conductivity of a heterogeneous system have therefore been examined in terms of the data presented herein.

This present paper describes the theoretical background, the method of conductivity measurement, and the results for unconsolidated media. A second paper will describe the results obtained for consolidated porous rocks.

THEORY

Consider any two-phase porous material, i.e., one consisting of a single solid component (subscript s) and a single saturating fluid in the pore space (subscript f). The effective thermal conductivity k of such a material depends on the following parameters: (a) the thermal conductivities of the two phases, k_s and k_f, (b) the volume concentrations of the two phases, $(1-\phi)$ and ϕ, where ϕ is the fractional porosity, and (c) the distribution of the two phases in the material. The effective conductivity will also depend upon the particle or pore size, at high temperatures when radiative heat transfer in a gaseous fluid is not negligible, or when the pore sizes are large enough that convection heat transfer may occur. Both of these mechanisms are neglected in this work, since the measurements to date have been performed at room temperature on samples none of which contained pores large enough to permit convection.

It is convenient to introduce the following dimensionless conductivity ratios:

$$x=k_s/k_f \quad y=k/k_f. \qquad (2)$$

The above statement is equivalent to

$$y=F(x,\phi,\text{ phase distribution}). \tag{3}$$

The problem of determining the functional relationship denoted by F, for a given phase distribution, is the same whether the k symbols represent thermal conductivities, electrical conductivities, diffusion coefficients, dielectric constants, or permeabilities.

For all cases considered here, $k_f<k_s$, and therefore $k_f<k<k_s$, or $1<y<x$. However, closer and much more useful limits may be placed on k, by considering two very simple phase distributions. These are the series and parallel distributions, which correspond to the minimum and maximum values of y, respectively, for given values of x and ϕ.

The series distribution, in which the two phases are thermally in series with respect to the direction of heat flow, results in the following:

$$k_{\min}=k_sk_f/[\phi k_s+(1-\phi)k_f]$$

or (4)

$$y_{\min}=x/[\phi(x-1)+1].$$

The parallel distribution, in which the two phases are thermally in parallel with respect to the direction of heat flow, results in the following:

$$k_{\max}=\phi k_f+(1-\phi)k_s$$

or (5)

$$y_{\max}=\phi+(1-\phi)x.$$

It should be noted that for both distributions

$$\left(\frac{dk}{dk_s}\right)_{k_s=k_f}=1-\phi$$

or (6)

$$\left(\frac{dy}{dx}\right)_{x=1}=1-\phi.$$

The fact that the equations for maximum and minimum conductivity both satisfy the relationship (6) means that the conductivity equation for any phase distribution must also satisfy it.

The parallel distribution (maximum k) corresponds to a weighted arithmetic mean of the conductivities of the two phases; the series distribution (minimum k) corresponds to the weighted harmonic mean of the solid and fluid conductivities. It is interesting to consider how the intermediate weighted geometric mean represents the conductivity of a natural porous medium. The weighted geometric mean corresponds to

$$k=k_f^{\phi}k_s^{1-\phi}$$

or (7)

$$y=x^{1-\phi}.$$

It is easily shown that this simple equation satisfies the required condition (6) as it must if it is to be a valid conductivity equation.

The properties of the three equations dealt with so far are summarized in the following table.

Minimum k	Intermediate k	Maximum k
$\phi/k_f+(1-\phi)/k_s$	$k=k_f^{\phi}k_s^{1-\phi}$	$k=\phi k_f+(1-\phi)k_s$
Series distribution Harmonic mean	Random distribution Geometric mean	Parallel distribution Arithmetic mean

The proposed geometric mean equation (7) corresponds to a weighted arithmetic mean of the logarithms of the individual conductivities.

$$\log k=\phi\log k_f+(1-\phi)\log k_s. \tag{8}$$

In other words, this equation predicts a linear relationship, on a log-log plot, between the effective conductivity of a porous medium and the conductivity of the fluid saturant.

Asaad[1] has proposed an empirical relationship which is very similar to the geometric mean equation.

Asaad's equation is

$$k/k_s=(k_f/k_s)^{\mathrm{m}}, \tag{9}$$

where $m=c\phi$ and $c\cong 1$. If $c=1$, this equation is identical to the geometric mean equation. Somerton[2] has attempted to correlate his conductivity data by means of Asaad's equation. Legg and Given[3] have also used an empirical relationship similar to the geometric mean equation for the analagous dielectric constant problem. The geometric mean is also a first term approximation to a solution of Brown's[4] for solid mixture permittivities. Recently Langton and Matthews[5] have applied the geometric mean equation in its logarithmic form, Eq. (8), to the calculation of the permittivity of mixtures of zinc oxide and rubber, the calculated values agreeing quite well with those measured. These authors attribute the equation to Lichteneker[6] who obtained it empirically in 1926.

Maxwell's[7] equation for the electrical conductivity of a random distribution of solid spheres (k_s) in a continuous medium (k_f) may be shown to be equivalent to

$$k=k_f\left[\frac{2\phi k_f+(3-2\phi)k_s}{(3-\phi)k_f+\phi k_s}\right]. \tag{10}$$

This equation is strictly applicable only when ϕ is large, since it was derived on the assumption that the solid spheres are far enough apart that they do not mutually interact. Eucken[8] generalized Maxwell's equation to the case of n dispersed phases and one continuous phase and applied the resulting equation to the thermal conductivity problem.

---

[1] Y. Asaad, Ph.D. thesis, University of California, June, 1955.

[2] W. H. Somerton, J. Petrol. Technol. **10**, 61 (1958).

[3] V. E. Legg, and F. J. Given, Bell System Tech. J. **19**, 385 (1940).

[4] W. F. Brown, Jr., J. Chem. Phys. **23**, 1514 (1955).

[5] N. H. Langton and D. Matthews, Brit. J. App. Phys. **10**, 306 (1959).

[6] K. Lichteneker, Z. Physik. **27**, 115 (1926).

[7] J. C. Maxwell, *A Treatise on Electricity and Magnetism* (Clarendon Press, Oxford, England, 1904), 3rd ed., Vol. 1, p. 440.

[8] A. Eucken, Forsch. Gebiete Ingenieurw, **B3**, VDI-Forschungsheft, 353 (1932).

de Vries[9] has applied Eucken's and Burger's extensions (to ellipsoidal particles) of Maxwell's equation to the calculation of unconsolidated soil thermal conductivities, the calculated values agreeing quite well with experimental data.[9–11] The equation for a two-phase medium with continuous fluid phase and dispersed solids is

$$k=\frac{\phi k_f+(1-\phi)F_1k_s}{\phi+(1-\phi)F_1},$$

where

$$F_1=\tfrac{1}{3}\sum_{i=1}^{3}\left[1+(k_s/k_f-1)g_i\right]^{-1} \tag{11}$$

and

$$\sum_{i=1}^{3} g_i=1.$$

The factor F_1 represents the ratio of the average temperature gradients in the continuous and dispersed phases. The factors g_i are particle shape factors. When $g_1=g_2=g_3$ (spherical particles) the equation reduces to Maxwell's original equation. de Vries chose $g_1=g_2=\frac{1}{8}$, and $g_3=\frac{3}{4}$. This corresponds to particles having the shape of ellipsoids of revolution with a major axis six times the minor axis.

Both Maxwell's and de Vries' equations satisfy the required condition (6), and furthermore all the preceding conductivity equations, except Asaad's, satisfy the requirements: (a) as $\phi\rightarrow 0$, $k\rightarrow k_s$ and (b) as $\phi\rightarrow 1$, $k\rightarrow k_f$. Asaad's equation satisfies these requirements only if $c=1$.

Kunii and Smith[12] have extended the work of Yagi and Kunii[13] on packed beds, and propose the following equation for the conductivity of an unconsolidated granular material, neglecting radiation and heat conduction through the grain contacts (which will be shown later to be a close approximation).

$$k/k_f=\phi+\left[(1-\phi)/(\epsilon+\tfrac{2}{3}k_f/k_s)\right],$$

where

$$\epsilon=\epsilon_2+(\phi-0.259)(\epsilon_1-\epsilon_2)/0.217. \tag{12}$$

The values of the parameters ϵ_1 and ϵ_2 are plotted as functions of k_s/k_f by Kunii and Smith. ϵ_1 corresponds to a cubic packing of uniform spheres ($\phi=0.476$) and ϵ_2 corresponds to a tetrahedral packing of uniform spheres ($\phi=0.259$). For intermediate porosities they calculate ϵ by linear interpolation between ϵ_1 and ϵ_2. For porosities less than 0.259 they recommend taking ϵ to be equal to ϵ_2, and for $\phi>0.476$, $\epsilon=\epsilon_1$. Wyllie and Southwick[14] suggested that the electrical conductivity of an aggregate of conductive particles saturated with a conducting electrolyte was compatible with an equivalent resistor model comprising three elements in parallel, as shown in Fig. 1. The three components of electrical conductivity suggested were (1) an element k_1, comprising particles and electrolyte in series with each other, (2) an element k_2, consisting of particles in sufficiently close contact with each other to form continuously conducting paths, and (3) an element k_3, consisting of the electrolyte filling the interstices between the particles. It was assumed that k_1, k_2, and k_3 were in parallel. The model is thus a combination of the series and parallel distributions considered earlier. It follows from Fig. 1 that k, the effective conductivity of the aggregate, is given by

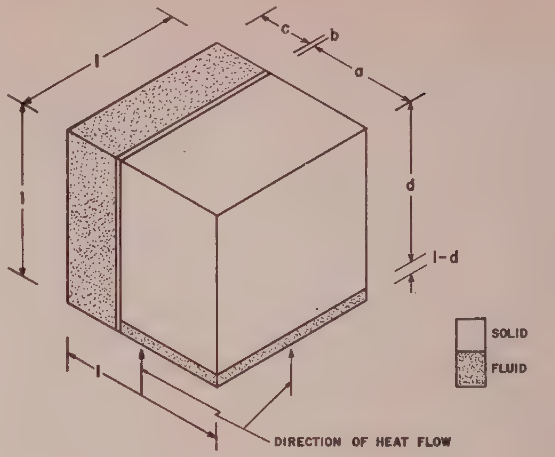

FIG. 1. Three-element resistor model of porous medium (Wyllie & Southwick).

$$k=\frac{ak_sk_f}{k_s(1-d)+dk_f}+bk_s+ck_f, \tag{13}$$

where $a+b+c=1$. If the solids are nonconductive ($k^s=0$), only element 3 contributes to the over-all conductivity, i.e., $k=ck_f$. Therefore

$$c=1/F, \tag{14}$$

where F is the electrical resistivity formation factor, defined as the ratio of the resistivity of a porous material fully saturated with an electrolyte to the resistivity of the electrolyte. This factor is used widely in the oil industry to characterize the pore structure of sedimentary rocks and sands. The relationship between F and the porosity ϕ is well established for both consolidated and unconsolidated media.[15]

---

[9] D. A. de Vries, Mededelingen van de Landbouwhogeschool te Wageningen (1952).

[10] W. Woodside and J. B. Cliffe, Soil Science **87**, 75 (1959).

[11] W. Woodside and C. M. A. de Bruyn, Soil Science **87**, 166 (1959).

[12] D. Kunii and J. M. Smith, A. I. Ch. E. Journal **6**, 71 (1960).

[13] S. Yagi and D. Kunii, A. I. Ch. E. Journal **3**, 373 (1957).

[14] M. R. J. Wyllie and P. F. Southwick, J. Petrol. Technol. **6**, 44 (1954).

[15] M. R. J. Wyllie and A. R. Gregory, Petrol. Trans. Am. Inst. Min., Met., Petrol. Engrs. **198**, TP 3541 (1953).

Sauer *et al.*[16] found the above resistor model to be consistent with their electrical conductivity data for aggregates of ion exchange resin particles saturated with several electrolytes.

The model may also be applied to the analogous thermal conductivity problem with which we are concerned here. From Fig. 1 it is apparent that

$$ad+b=1-\phi. \qquad (15)$$

This relationship also follows directly from Eq. (13) by application of the required condition (6). Similarly, the relation $a+b+c=1$ also follows from Eq. (13) by applying the condition that when $k_s=k_f$, k must also equal k_f. A fourth relationship is required in order to determine the four constants a, b, c, and d for a given material. From Eq. (13) it is evident that when $k_f=0$, $k=bk_s$; this is the second element of the model, representing the "straight-through" solid conduction. The condition, $k_f=0$ may be closely approximated by evacuating the medium. Thus the value of the parameter b should be given by

$$b=k_{\text{vac}}/k_s. \qquad (16)$$

It is hoped that an empirical relationship may be established between b and ϕ, corresponding to the already established formation factor-porosity relationship. In fact, the similarity between the two parameters b and c is rather striking.

$$b=k(k_f=0)/k_s; \quad c=k(k_s=0)/k_f. \qquad (17)$$

For consolidated rocks, $1/F=c\cong 4/3\phi^2$. It might perhaps be expected then, by analogy, that $b=b'(1-\phi)^2$, where b' is independent of porosity. For unconsolidated media, $1/F=c\cong\phi^{0.3}$ [17] or $1/F=c\cong\phi/(1.3219-0.3219\phi)^2$.[18]

Kimura[19] has applied the resistor model equation to the calculation of thermal conductivities of some unconsolidated packed beds. He assumed $b=0$ and $c=\phi^{1.3}$ but did not use the relationship (15); instead he calculated the value d must have to make the model consistent with experimental data, correlating $d/\phi^{1.5}$ with k_f/k_s.

Many other equations have been proposed for the thermal conductivity of a multiphase system, e.g., those of Gemant,[20] Russell,[21] Topper,[22] and Kersten.[23] However, these equations are not strictly applicable to the specific systems of interest here.

One difficulty in using the above equations for the calculation of thermal conductivities of such systems as rocks and sands is the assignment of the proper value to k_s, the conductivity of the solid component. Whereas the conductivities k_f of all the fluid saturants of interest are well known, there is some doubt as to the conductivity attributable to the solid component of rocks, expecially in the case of well-cemented rocks, where the cementing material, in the case of quartzitic sandstones, may have a conductivity quite different from that of the quartz particles. Furthermore, quartz is highly anisotropic, having a conductivity in the direction of the crystal axis twice that in the direction perpendicular to the crystal axis.[24] In a random distribution of crystal axis orientations, it is assumed that the average quartz conductivity is the arithmetic mean of these two values. For all quartzitic materials considered in this work, a value for k_s of 20×10^{-3} cal/cm sec°C at room temperature (i.e., 20 mcal/cm sec°C) has been assumed.

EXPERIMENTAL

Many experimental investigations have already been made of the thermal conductivities of rocks and sands. Niven,[25] Birch and Clark,[26] Zierfuss and van der Vliet,[27] Benfield,[28] Beck,[29,30] Asaad,[1] and Somerton[2] have presented data of interest from both the geophysical and oil production standpoints. Kannuluik and Martin,[31] Schuman and Voss,[32] Kling,[33] Waddams,[34] Kimura,[19] and van Rooyen and Winterkorn[35] have presented data for unconsolidated packed beds. In many cases, the results were not interpreted in terms of the properties and concentrations of the constituent materials; in others, the range of porosity studied was narrow. Niven, Birch and Clark, and Somerton have investigated the effect of temperature; however, there has been no detailed study of the effects of gas pressure or overburden pressure.

The conventional methods of thermal conductivity measurement are steady-state methods. These involve the simultaneous measurement of the steady-state heat flux and temperature gradient through test samples in the form of slabs, cylinders, or spheres, for which solutions to the differential equation of heat conduction are readily available. Since no perfect thermal insulation exists, complicated guarding systems are required to minimize edge or end effects. A further drawback common to all steady-state methods is the relatively long time required to attain thermal equilibrium. In the case of porous media, containing partial liquid saturations, many difficulties are encountered. The application of the temperature gradient for a long period of time results in a nonuniform liquid saturation distribution due to the effects of thermal osmosis.[10,11,36] The conductivity so measured may depend upon the sample size and the magnitude of the temperature difference applied.

---

[16] M. C. Sauer, P. F. Southwick, K. S. Spiegler, and M. R. J. Wyllie, Ind. Eng. Chem. **47**, 2187 (1955).

[17] G. E. Archie, Petrol. Trans. Am. Inst. Min., Met., Petrol. Engrs. **146**, 54 (1942).

[18] A. Slawinski, J. chim. phys. **23**, 710 (1926).

[19] M. Kimura, Kagaka Kikai **21**, 472 (1957).

[20] A. Gemant, J. Appl. Phys. **21**, 750 (1950).

[21] H. W. Russell, J. Am. Ceram. Soc. **18**, 1 (1935).

[22] L. Topper, Ind. Eng. Chem. **49**, 1936 (1957).

[23] M. C. Kersten, Univ. of Minnesota, Eng. Expt. Sta. Bull. 28 (1949).

[24] E. H. Ratcliffe, Brit. J. Appl. Phys. **10**, 22 (1959).

[25] C. D. Niven, Can. J. Research **A18**, 132 (1940).

[26] F. Birsh and H. Clark, Am. J. Sci. **238**, 529 and 613 (1940).

[27] H. Zierfuss and G. van der Vliet, Bull. Am. Assoc. Petrol. Geologists **40**, 2475 (1956).

[28] A. E. Benfield, Proc. Roy. Soc. (London) **A-173**, 428 (1939).

[29] A. E. Beck, J. C. Jaeger, and G. Newstead, Australian J. Phys. **9**, 296 (1956).

[30] A. E. Beck and J. M. Beck, Trans. Am. Geophys. Union **39**, 111 (1958).

[31] W. G. Kannuluik and L. H. Martin, Proc. Roy. Soc. (London) **A141**, 144 (1933).

[32] T. E. W. Schumann and V. Voss, Fuel **13**, 249 (1934).

[33] G. Kling, Forsch. Gebiete Ingenieurw. **9**, 28 (1938).

[34] A. L. Waddams, J. Soc. Chem. Ind. (London) **63**, 337 (1944).

[35] M. van Rooyen and H. F. Winterkorn, Proc. Highway Research Board **38**, 376 (1959).

In contrast with steady-state methods, transient methods are fast and therefore less likely to produce nonuniform saturation distributions in the case of partially saturated rocks. The method used in the present work is the transient line heat source ("probe" or "needle") method originated by Stalhane and Pyk[37] and van der Held and van Drunen[38] for the measurement of thermal conductivity of liquids. The method uses a line heat source, i.e., a straight wire through which is passed a constant electric current, and a temperature-sensitive device, e.g., a thermocouple, thermistor, or resistance thermometer. These two elements are embedded alongside each other in the sample under test. When the assembly is at a uniform and constant temperature, constant power is supplied to the heater element and the rise in temperature is recorded during a short heating interval. The rate of rise of temperature is determined by the ability of the test sample to conduct the heat generated away from the line source. The thermal conductivity of the sample may be calculated from the temperature-time record and the power input. The theory on which the method is based is developed by Carslaw and Jaeger.[39]

The temperature rise θ at a point in an infinite mass of material heated by a perfect line source is

$$\theta(r,t)=(Q/2\pi k)I[r/2(\alpha t)^{\frac{1}{2}}], \qquad (18)$$

where Q= power input per unit length of source, cal/cm sec, k= thermal conductivity of material, cal/cm sec°C, α= thermal diffusivity of material, cm^2/sec, r= radial distance of point from line source, cm, t= time from start of heating, sec, and

$$I(x)=C-\ln x+\frac{x^2}{2}-\frac{x^4}{8}+\cdots,$$

where C is Euler's constant (0.5772).

If $x=[r/2(\alpha t)^{\frac{1}{2}}]$ is small, i.e., large t and small r, the terms of order x^2 and above may be neglected and

$$\theta=(Q/2\pi k)\left[C-\ln\frac{r}{2(\alpha t)^{\frac{1}{2}}}\right]. \qquad (19)$$

Between times t_1 and t_2, the temperature rise $\Delta\theta$ is therefore given by

$$\Delta\theta=\theta_2-\theta_1=(Q/4\pi k)\ln(t_2/t_1)$$

or (20)

$$k=(Q/4\pi\Delta\theta)\ln(t_2/t_1).$$

The thermal conductivity may also be evaluated by measuring the slope $(Q/4\pi k)$ of the straight line obtained by plotting temperature rise θ versus $\ln t$.

There are several sources of error in the method: (a) The first is the error due to dropping the higher terms in the $I(x)$ series. This error is minimized by having the thermocouple close to the heater and by discounting the early part of the temperature-time record. (b) Secondly, the theory applies to a perfect line heat source, i.e., one with an infinitely large length to diameter ratio. Blackwell[40] has shown theoretically that probes with a length to diameter ratio of 30 or more will have negligible errors in this respect. (c) The theory also applies to a sample infinite in extent. However, if the testing interval is limited to the time before the heating effect is "felt" at the sample surface, then samples of practical dimensions behave as though they are infinite in size. (d) An error also arises due to the contact resistance between the probe and the surrounding sample. (e) Finally, there is an error due to variation in the resistance of the heater wire with temperature (nonconstant power input). This error can also be made negligible by using as the heater a wire with a low temperature coefficient of resistance.

For reasons of strength and ease of handling, the heater wire and thermocouple are usually encased in a protective metal sheath, and in this form the instrument has been called a thermal conductivity probe.[41] Probes have become quite popular in recent years for the measurement of thermal conductivity of thermal insulating materials and unconsolidated soils. The probe method does not appear to have been applied to rock conductivity measurements.

There are two conflicting requirements governing the size of a probe. To approximate an ideal line heat source the probe should have a large length to diameter ratio. On the other hand, thin probes produce large temperature gradients in the sample close to the probe, and may suffer from the same disadvantages as the steady-state methods, although to a lesser degree, with respect to thermal osmosis effects.[42]

DESCRIPTION OF PROBE

A schematic diagram of the probe design is shown in Fig. 2. The probe has a length of 6 in. and an outside diameter of 0.065 in. (16 gauge tubing), giving a length

---

[36] J. R. Philip and D. A. de Vries, Trans. Am. Geophys. Union **38**, 222 (1957).

[37] B. Stalhane and S. Pyk, Tek. Tidskl. **61**, 29, 389 (1931).

[38] E. F. M. van der Held and F. G. van Drunen, Physica **15**, 865 (1949).

[39] H. S. Carslaw and J. C. Jaeger, *Conduction of Heat in Solids* (Clarendon Press, Oxford, England, 1959), 2nd ed.

[40] J. H. Blackwell, Can. J. Phys. **34**, 412 (1956).

[41] F. C. Hooper and F. R. Lepper, Am. Soc. Heating Ventilating Engrs. Trans. **56**, 309 (1950).

[42] W. Woodside, Heating, Piping, Air Conditioning **30**, 163 (1958).

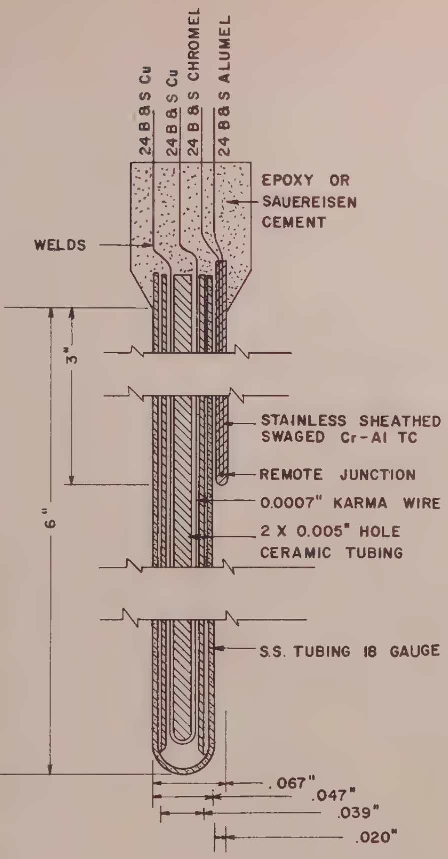

FIG. 2. Schematic diagram of thermal conductivity probe.

to diameter ratio of close to 100. The metal sheath is stainless steel hypodermic needle tubing (o.d. 0.065 in., i.d. 0.047 in.). The thermocouple is 0.003-in. copper-Constantan or Chromel-Alumel, with the thermojunction located at the mid-length of the probe. The heater wire is 0.0007-in. Karma (Driver-Harris Company) resistance wire, with a temperature coefficient of resistance of 0.00002/°C, and a resistance of 1633 ohms per foot of length. In the earlier probes the heater wire and thermocouple were enclosed in fine glass capillary tubes which were in turn enclosed in the metal tubing. The more recently built probes have had the four wires enclosed in a four-hole ceramic insulating tube with an o.d. of 0.045 in., which is inserted into the metal tubing. In all cases, one end of the metal tubing is sealed off and the four wires brought out to the other end and welded to heavier lead wires, the joint being strengthened by epoxy resin or Sauereisen cement. Some of the more recent tests have been conducted with a thermocouple attached to the outside surface of the metal tubing at its mid-length, resulting in a smoother temperature-time record (this design is shown in Fig. 2).

PROBE CIRCUITRY

The circuit used in association with the probe is shown in Fig. 3. The power source is a regulated dc power supply with output voltage continuously variable from 0 to 400 vdc and maximum current load of 200 ma. The heating current i is obtained by measuring the potential drop across a 1-ohm standard resistance in series with the probe heater (resistance approximately 1600 ohms) with a portable potentiometer of 160 mv range, readable to 1 μv. The reference junction of the probe thermocouple is sometimes attached to the outer surface of the sample and other times is located in a Dewar flask containing room temperature water. The emf corresponding to the probe temperature rise is amplified and then recorded on a single-point Speedomax recorder with a range of -0.1 to $+1.0$ mv, and a chart speed of approximately 3 in./min. The preamplifier has a maximum gain of 200, is zero-center, and has ranges of 50, 100, 200, 500, 1000, and 2000 μv.

The initial temperature rise (during the first 30 sec of heating for the probe design used here) cannot be used for calculating conductivity because of error (a) discussed above. Unfortunately a large fraction of the total temperature rise occurs during this time. It is therefore convenient to have a bias circuit built into the probe thermocouple circuit, permitting this first unusable part of the temperature time record to be biassed out, and the remaining useful part of the record to be further amplified and spread across the full width of the recorder chart, thus increasing the accuracy. This is permissible, since the calculation of k involves only the difference in temperature rises at two times, and not the absolute value of the rises [Eq. (20)].

EXPERIMENTAL PROCEDURE

In the case of unconsolidated samples, the material was packed into a cylindrical container of inside diameter 5 in. and inside height of 7 in., and the probe inserted in the center.

When the sample-probe system attained thermal equilibrium, as registered by a constant thermocouple reading, the current to the probe heater was switched on and the temperature rise recorded. The initial rise was biassed out and the amplifier gain increased after

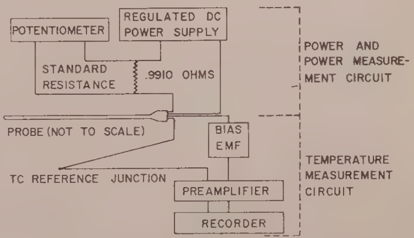

FIG. 3. Schematic circuit for probe thermal conductivity measurements.

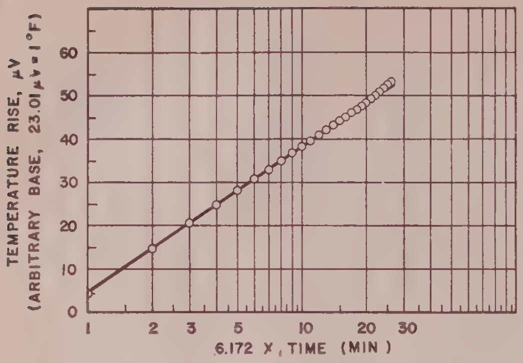

FIG. 4. Typical plot of probe temperature rise against logarithm of time from start of heating.

30 sec of heating as described above. Each measurement lasted approximately 3 min. During a test the current seldom changed by more than 0.1 percent. The final temperature rise at the probe was usually of the order of 5°C. All measurements were conducted near room temperature.

A sample plot of temperature rise versus the logarithm of the time from start of heating is shown in Fig. 4. The linearity of this plot is probably the best guarantee that the errors mentioned earlier are negligible, and that the probe in the vicinity of its mid-length is indeed behaving like a perfect line heat source.

The specific formula for the calculation of thermal conductivity from the probe data depends upon the calibration of the thermocouple used and also the resistance per unit length of the heater wire. For the probes used in this work, the formula is

$$k=\frac{0.1947i^2\log(t_2/t_1)}{V_2-V_1}\,\text{mcal/cm sec°C}, \tag{21}$$

where i=heating current (ma) and V_2, V_1=temperature rises (μv) at times t_2 and t_1.

The sample, probe, and sample container were placed inside a steel vessel with vacuum, gauge, and gas inlet connections. The probe leads were brought out through a Conax fitting in the top plate of the vessel.

In performing conductivity measurements as a function of air pressure, the sample was first evacuated and then air was allowed to leak in through a drying column to the desired pressure. To change from one gaseous saturant to another, the sample was evacuated, then filled with the desired gas to a pressure of one atmosphere, this process being repeated several times to ensure the purity of the gas in the sample.

Liquid saturations were achieved by vacuum saturation, the porosity of the sample being determined at the same time by weighing the sample before and after saturation.

ACCURACY AND REPRODUCIBILITY

To determine the reproducibility of the method, the conductivity of a foamed plastic insulation sample was measured several times, each time modifying some component of the equipment. The conductivity measured varied by only 2.5 percent, with two different probes, two different power sources, three different biassing circuits, with and without mercury surrounding the projecting probe head. Reproducibility of better than 2.5 percent was obtained in the sand and rock conductivity measurements.

Measurements were also made on several "standard" insulation samples, the results showing excellent agreement with values reported in the literature.

DESCRIPTION OF UNCONSOLIDATED SAMPLES

Measurements were made on three quartz sand packs, a glass bead pack, and a lead shot pack. The 59% porosity sand was a loose pack of 140/200 mesh (0.104–0.074 mm) Wassau quartz sand. The 36% porosity sand was a pack of 20/30 mesh (0.84–0.59 mm) Ottawa sand. The 19% porosity sand was a mixture of the 20/30 and 140/200 mesh sands packed in the following way. The 20/30 sand was packed alone into a Lucite container to a porosity of 31.5%; 140/200 mesh sand was then vibrated through an intermediate size mesh into the coarse sand pack until no more would enter. k_s for all three sand packs was assumed to be 20 mcal/cm sec°C.

The glass bead pack and the lead shot pack both had a porosity of 38%. The glass beads (Microbeads 405) are approximately 40/50 mesh (0.42–0.297 mm) and, according to the manufacturer, have a solid thermal conductivity of 2.5 mcal/cm sec°C, (k, mcal/cm sec°C ×0.242=k, Btu/hr ft°F). The mean particle diameter of the lead shot was 1.23 mm; the thermal conductivity of lead at 30°C is 82.0 mcal/cm sec°C.

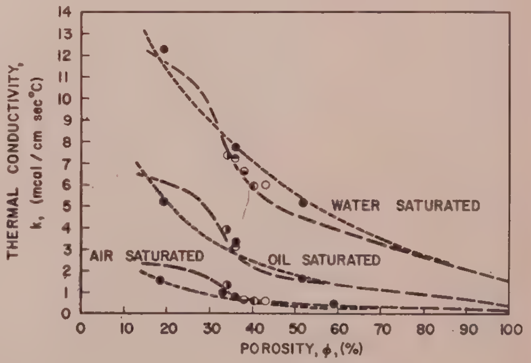

FIG. 5. Thermal conductivity of quartz sand packs as a function of porosity and saturating fluid. ● Probe data—Ottawa & Wassau sands; ○ DeVries—Wageningen sand[9]; ◑ Somerton—quartz sand[2]; ◐ Van Rooyen—white sand[35]; ◓ Wilson, *et al.* (private communication)—Ottawa sand; ◒ Woodside & Cliffe—Ottawa sand[10]; - - - - - - calculated—DeVries equation (11); – – – calculated—Kunii & Smith equation (12).

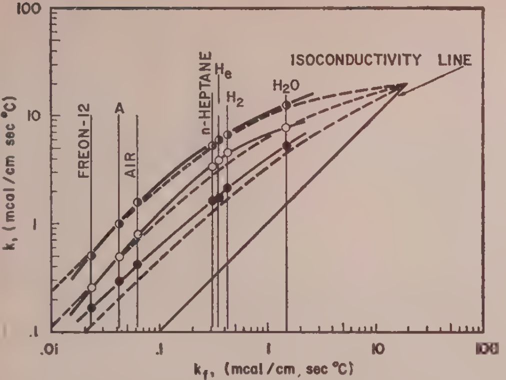

FIG. 6. Variation of effective thermal conductivity of unconsolidated quartz sands with the conductivity of the saturating fluid. ○ 20/30 mesh Ottawa sand, $\phi=0.361$; ◑ 20/30 Ottawa & 140/200 Wassau, $\phi=0.194$; ● 140/200 Wassau sand, $\phi=0.59$; --- calculated (DeVries' equation).

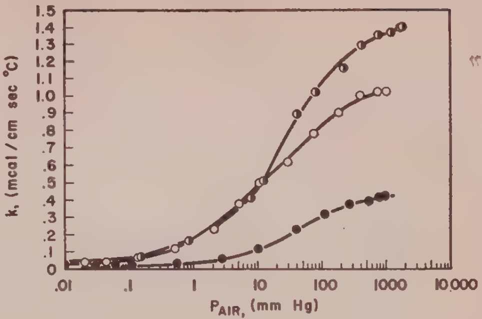

FIG. 8. Effective thermal conductivity of quartz sand packs as a function of the interstitial air pressure. ◑ 20/30 mesh Ottawa & 140/200 mesh Wassau sands, $\phi=0.18$; ○ 20/30 Ottawa sand, $\phi=0.33$; ● 140/200 Wassau sand, $\phi=0.59$.

EXPERIMENTAL RESULTS

Figure 5 shows some of the thermal conductivity data, obtained for the three quartz sand packs, plotted against porosity. The three groups of data correspond to air, oil (*n*-heptane), and water saturated conditions. In the case of the 59% porosity sand, the porosity decreased to 51.5% upon liquid saturation. The data of other investigators are also shown.

Figure 6 shows the effective thermal conductivities of the three sand packs plotted against the thermal conductivities of the saturating fluids on logarithmic scales. Also shown is the isoconductivity line, i.e., the line for which $k=k_f$. The conductivity of the solid particles of the pack k_s is determined by the intersection of the effective conductivity curve with the isoconductivity line. Unfortunately, the extrapolation of the curves from the water-saturated points to the isoconductivity line is doubtful. One measurement was therefore made on the 20/30 Ottawa sand pack, saturated with mercury (under a capillary pressure of approximately 120 cm Hg to ensure that the pore space was more than 99% filled with mercury). The thermal conductivity of mercury is 20.0 mcal/cm sec°C at 30°C.[43] The measured effective conductivity of the mercury-filled sand pack was 20.3 mcal/cm sec°C; however, too much reliance should not be placed on this result, since edge effects occurred relatively early in the measurement. The result does suggest that the assumption of 20 mcal/cm sec°C as the average solid conductivity of quartz grains is valid.

A similar plot of effective thermal conductivity versus saturant conductivity is shown in Fig. 7 for the lead shot and glass bead packs. All of the above measurements were conducted with the saturating fluid near atmospheric pressure.

The variation of the effective thermal conductivity with the pressure of the saturating air is shown in Fig. 8 for the three sand packs, and in Fig. 9 for the lead and glass bead packs, the air pressure being plotted on a logarithmic scale.

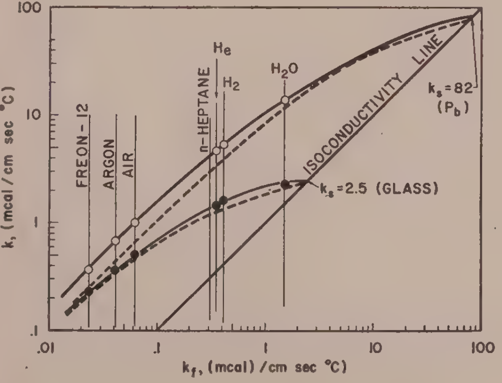

FIG. 7. Variation of effective thermal conductivity with the saturant conductivity for a lead shot and a glass bead pack. ○ Lead shot, $\phi=0.379$, $D_p=1.2$ mm; ● glass beads, $\phi=0.380$, $D_p=0.36$ mm; ---- calculated (DeVries' equation).

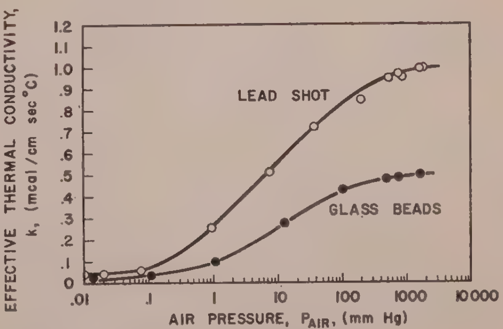

FIG. 9. Effective thermal conductivities of a lead shot and a glass bead pack as a function of the interstitial air pressure.

---

[43] W. H. McAdams, *Heat Transmission* (McGraw-Hill Book Company, Inc., New York, 1942), 2nd ed.

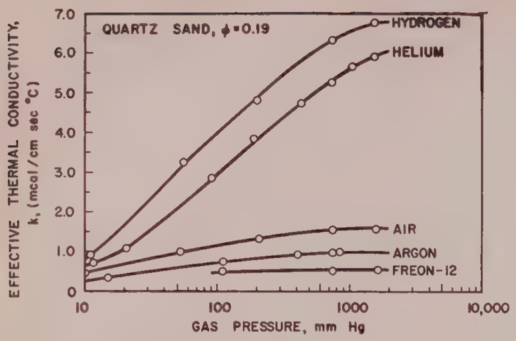

FIG. 10. Effective thermal conductivity of a low porosity quartz sand as a function of the interstitial gas pressure.

A similar plot is shown in Fig. 10 for one of the sand packs, over a more limited range of interstitial gas pressure, but with several different gases used as the saturating fluid.

DISCUSSION

Variation of k with Gas Pressure

One of the points of interest concerning the data presented in Figs. 8 and 9 is the low value of the effective thermal conductivity *in vacuo*. The highest value of the resistor-model parameter $b=k_{\text{vac}}/k_s$ is 0.0084 for the glass bead pack. The other four packs possess b values of 0.00155 or lower. Thus the neglect of the heat conduction through the grain contacts is warranted in the application of the resistor model equation and Kunii and Smith's equation to unconsolidated materials.

The kinetic theory expression for the thermal conductivity of a gas is[44]

$$k_f = A\rho c_v \bar{v}\lambda, \tag{22}$$

where A is a constant, ρ is the gas density, c_v is the specific heat at constant volume, $\bar{v}$ is the mean molecular velocity, and λ is the mean free path. Normally, thermal conductivities of gases are independent of the gas pressure P, since ρ is directly proportional to P, and λ is inversely proportional to P. As the pressure is lowered, the mean free path approaches the size of the gas enclosure, and the linear dimension of the gas enclosure becomes an upper limit to the mean free path. Thus at low pressures, the gas conductivity becomes proportional to the pressure, since the inverse relation between λ and P no longer holds. In the case of a gas contained in a porous medium, such as the unconsolidated packs considered here, the linear dimension of the gas enclosure is some characteristic dimension of the pore space, which will be denoted by d. The effective mean free path $\bar{\lambda}$ must depend upon d as well as the normal mean free path λ, since collisions between gas molecules and the solid surface must be taken into account. It can be shown that $\bar{\lambda}$ is given by the following expression:

$$\bar{\lambda} = \lambda d/(\lambda + d). \tag{23}$$

At high gas pressure, where $\lambda \ll d$, $\bar{\lambda} = \lambda$; at low gas pressures, where $\lambda \gg d$, $\bar{\lambda} = d$. Thus, for air contained in a porous medium

$$\begin{aligned} k_f &= A\rho C_v \bar{v}\bar{\lambda} = A\rho c_v \bar{v}\lambda[d/(\lambda+d)] \\ &= k_{\text{air}}[d/(\lambda+d)], \end{aligned}$$

where k_{air} is the normal thermal conductivity of air (i.e., when $\lambda \ll d$). Since $\lambda = B/P$ ($B=0.00486$ for air when λ is expressed in cm and P in mm Hg),

$$k_f = k_{\text{air}}[Pd/(Pd+B)]. \tag{24}$$

Thus as the pressure is lowered, k_f decreases and hence the effective conductivity k of the pack must decrease as observed in Figs. 8–10.

To determine whether or not the rate of decrease of k with decrease in pressure is consistent with kinetic theory, Fig. 11 must first be examined. This figure shows some of the data of Figs. 6 and 7 plotted on a linear scale. It is apparent that, for low values of k_f, the data may be approximately represented by an equation of the form

$$k = Wk_f + k_{\text{vac}}, \tag{25}$$

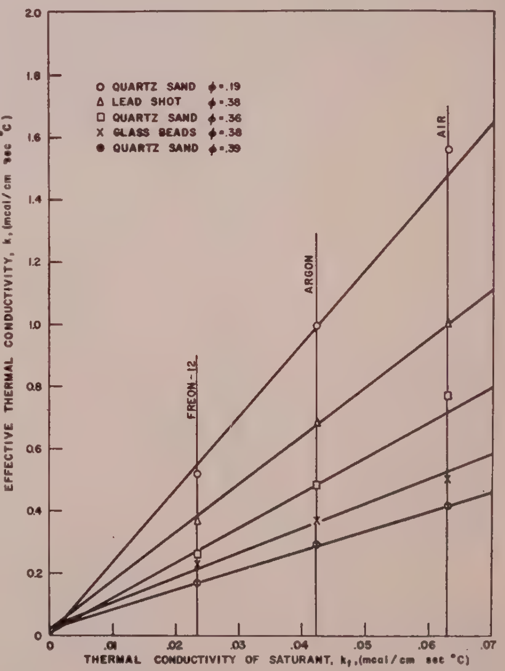

FIG. 11. Variation of effective thermal conductivity with the conductivity of saturating gas for low conductivity gases.

---

[44] E. H. Kennard, *Kinetic Theory of Gases* (McGraw-Hill Book Company, Inc., New York, 1938).

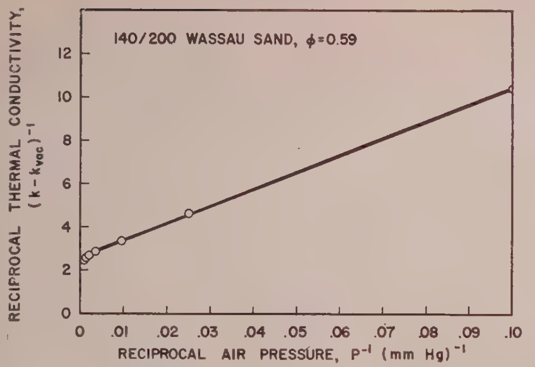

FIG. 12. Reciprocal thermal conductivity $1/(k-k_{\mathrm{vac}})$ plotted against reciprocal air pressure for a quartz sand pack.

where W represents the slope of the straight line drawn through each set of data.

Returning to Eq. (24), it follows that

$$k-k_{\mathrm{vac}}=Wk_f=Wk_{\mathrm{air}}[Pd/(Pd+B)]$$

or

$$1/(k-k_{\mathrm{vac}})=(1/Wk_{\mathrm{air}})\{1+[(1/P)(B/d)]\}. \quad (26)$$

Thus kinetic theory indicates that $1/(k-k_{\mathrm{vac}})$ should vary linearly with $1/P$. The experimental data do satisfy this relationship approximately as evidenced by Fig. 12, which is a plot of $1/(k-k_{\mathrm{vac}})$ against $1/P$ for one of the sand packs. Furthermore a value for d may be obtained from such a plot. The values of d obtained are considerably smaller than the mean particle diameter D_p. The values of D_p/d are 68.1 (20/30 mesh sand), 61.4 (140/200 mesh sand), 72.6 for the glass bead pack, and 170 for the lead shot. d represents a characteristic dimension of the pore space from the point of view of molecular conduction in the gas. If it is assumed that the solid particles are spherical, it is easily shown that the above D_p/d values indicate that the part of the gas phase, which is of prime importance in heat conduction, extends from the contact point between adjacent grains out to a distance of roughly one-sixth of the grain radius. This critical region is even smaller in the case of lead shot, possibly because of the higher solid conductivity, or possibly because the lead-air system possesses a nonunit accommodation coefficient. In the case of the low-porosity two-component sand mixture, two straight lines fit the data quite well, on a $1/(k-k_{\mathrm{vac}})$ versus $1/P$ plot. In this pack, the two most numerous types of particle contact are (a) small particle contacting small particle, and (b) large particle contacting small particle. Case (a) yields a value of 99 for D_p/d. For case (b), taking for D_p the harmonic mean of the two particle diameters, a value for D_p/d of 56 is obtained.

VALIDITY OF THERMAL CONDUCTIVITY EQUATIONS

Figure 13 shows a plot of the dimensionless conductivity ratios $y=k/k_f$ and $x=k_s/k_f$ for the glass bead and lead shot packs. For comparison, the values calculated from the several thermal conductivity equations are also plotted ($\phi=0.38$). It is apparent that Maxwell's equation[10] predicts values for k which are too low, whereas both de Vries' equation[11] and Kunii and Smith's equation[12] agree fairly well with the data. Kunii and Smith's equation appears to underestimate k when k_s/k_f is small; de Vries' equation underestimates k when k_s/k_f is very large. The geometric mean equation overestimates k when k_s/k_f exceeds 20. The resistor model equation (13) (not plotted) assuming $b=0$ and $c=\phi^{1.3}$, considerably underestimates k, predicting values slightly lower than those given by Maxwell's equation. Note how all the curves converge to the point $x=1$, $y=1$ with the same slope as required by Eq. (6). The plotting of both the lead shot and glass bead data on the same graph was possible since both packs possessed the same porosity.

The equations of de Vries, and Kunii and Smith are compared with the quartz sand data in Fig. 5. Again both equations are fairly consistent with the data. The rather abrupt change in slope of the Kunii and Smith curve at $\phi=0.26$ is caused by the use of ϵ_2 for ϵ for all values of ϕ less than 0.26. Comparisons are also made in Figs. 6 and 7.

As mentioned above, the resistor model equation, using for c the reciprocal electrical formation factor, predicts effective conductivities considerably lower than those measured. It was decided, therefore, to calculate the values c must have in order to make the resistor model equation match the observed data (while retaining the approximation $b=0$). The values of c thus calculated are remarkably constant for a given pack, varying only

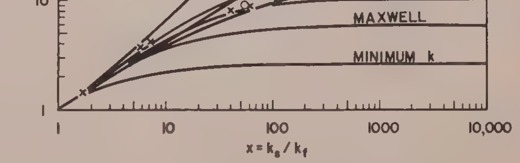

FIG. 13. Comparison of lead shot and glass bead conductivity data with the values calculated from the various conductivity equations. ○ lead shot, $\phi=0.38$, $K_s=82$ mcal/cm sec°C; × glass beads, $\phi=0.38$, $K_s=2.5$ mcal/cm sec°C.

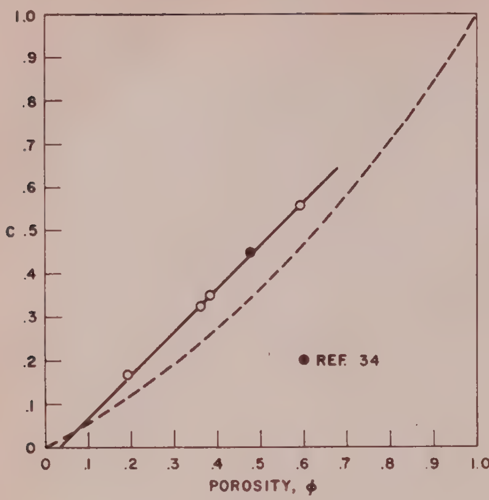

FIG. 14. Comparison of measured "thermal formation factor" with electrical formation factor for unconsolidated media. – – – $C=1/F=\phi/(1.3219-0.3219\phi)^2$, Slawinski electrical formation factor ($K_f/K_s\rightarrow\infty$).

$$\circ \quad C=\frac{\phi KK_s+(1-\phi)KK_f-K_sK_f}{\phi K_sK_f+KK_s-2K_sK_f+(1-\phi)K_f^2}$$

reciprocal thermal formation factor $K_f/K_s\sim 0.02$.

slightly with k_s/k_f until the latter approaches unity. For example, for the 19.4% porosity sand pack, the seven calculated values of c varied between 0.1631 and 0.1683 while k_s/k_f varied from 855 to 13.3. A value for c was also calculated from the experimental data of Stephenson and Woodside[45] for a model of a cubic pack of spheres at a porosity of 47.6%. The values of c obtained from the experimental data are plotted against porosity in Fig. 14. The points may be represented quite well by the linear relation

$$c=\phi-0.03. \qquad (27)$$

To show the comparison between this measured "thermal formation factor" and the electrical factor, Slawinski's[18] equation is also plotted. The disagreement between the thermal and electrical c values is not altogether surprising, when one considers that the electrical factor is associated with systems of electrically non-conducting particles contained in an electrolyte (i.e., $k_s=0$, $k_f\neq 0$), whereas in the thermal case the solid conductivity is never zero and in many practical cases much larger than k_f. In conclusion, the resistor model equation (13) if used with the auxiliary relations $b=0$, $c=\phi-0.03$, $a=1-c$, and $d=(1-\phi)/a$, predicts effective thermal conductivity values in fair agreement with those observed for unconsolidated media. This modified resistor model equation is plotted in Fig. 13.

CONCLUSIONS

(1) The line heat source (probe) method is satisfactory for the determination of effective thermal conductivities of unconsolidated sands under a variety of test conditions. The measurements are rapid and reproducible to within one or two percent. All measurements were performed at room temperature with a single saturating fluid occupying the pore space.

(2) Effective thermal conductivities were measured for three unconsolidated quartz sand packs, ranging in porosity from 0.19 to 0.59. With water as the saturating fluid, the conductivities ranged from 12.3 to 5.17; with air as saturant (near atmospheric pressure) the conductivities ranged from 1.57 to 0.416 mcal/cm sec°C. The variation with porosity is greater the higher the conductivity of the saturating fluid (Fig. 5).

(3) Effective thermal conductivities were measured for two unconsolidated packs having the same porosity, but with solid particle conductivities differing by a factor of 33. The effect of the higher solid conductivity increased as the conductivity of the saturating fluid increased. The ratio of the two effective conductivities was 2.0 for air as the saturant, but was 6.05 for water as the saturant (Fig. 7).

(4) The effective thermal conductivity of an unconsolidated pack increases with the conductivity of the saturating fluid, the increase being in almost direct proportion when the saturant conductivity is small relative to that of the solid (Fig. 11).

(5) The effective conductivities *in vacuo* of all five packs studied were less than one-hundredth of the conductivities of the respective solid particles. As the saturating gas pressure was increased from the evacuated condition the effective conductivity increased, continuing to increase, in some cases, at pressures higher than atmospheric (Figs. 8–10). The variation with gas pressure was shown to be consistent with the kinetic theory of gases.

(6) From considerations based on kinetic theory, it was determined that the characteristic dimension of the pore space, with respect to heat conduction in the gas occupying this space, is smaller than the mean particle diameter by a factor of roughly 100. It was concluded that the part of the gas phase, which is of prime importance in heat conduction, extends from the contact points between the solid particles out to a distance of roughly one-sixth of the particle radius.

(7) Equations which relate the effective conductivity of a two-phase medium to the conductivities and concentrations of the constituent phases were reviewed in the light of the observed data (Fig. 13). The geometric mean equation overestimates the effective conductivity when k_s/k_f exceeds about 20.

(8) Maxwell's equation underestimates the effective conductivity. However, de Vries' equation (based on an extension of Maxwell's equation by Burger and Eucken) and the equation of Kunii and Smith both

---

[45] D. G. Stephenson and W. Woodside, Trans. Am. Soc. Mech. Engrs. **80**, 1424 (1958).

show fair agreement with the observed values over the ranges of porosity, saturant conductivity and solid particle conductivity studied.

(9) The resistor model equation of Wyllie and Southwick, used in conjunction with a value of the parameter c determined electrically, leads to effective thermal conductivity values considerably lower than those measured. Good agreement with the observed data is achieved if c is calculated from the relationship $c=\phi-0.03$ obtained empirically.

JOURNAL OF APPLIED PHYSICS VOLUME 32, NUMBER 9 SEPTEMBER, 1961

Thermal Conductivity of Porous Media. II. Consolidated Rocks

W. Woodside and J. H. Messmer
Gulf Research and Development Company, Pittsburgh, Pennsylvania

(Received March 13, 1961)

Measurements have been made of the effective thermal conductivity of porous sandstones. The method is based on the transient heating effect resulting from use of a line heat source. Data are presented for six sandstones ranging in porosity from 3 to 59% and show the variation of thermal conductivity with porosity, the conductivity of the saturating fluid, the pressure of the gas filling the pore space, and overburden pressure. The results are compared with those previously obtained for unconsolidated sands. All samples, except one, exhibited a lower thermal conductivity when saturated with a gas at atmospheric pressure than when saturated with a liquid of the same conductivity as the gas. An explanation for this effect, in terms of the kinetic theory of gases, is advanced and substantiated by other data. Finally, the validity of certain equations for the thermal conductivity of two-phase systems is examined; the weighted geometric mean of the two constituent conductivities is found to agree well with the measured effective conductivities.

INTRODUCTION

PART I of "Thermal conductivity of porous media" described the theoretical background, the method used for thermal conductivity measurement, and the results obtained for several unconsolidated media. Part II presents the results obtained for consolidated rock samples.

EXPERIMENTAL PROCEDURE

The rock samples were cylinders $6\frac{1}{2}$ in. long and at least 3 in. in diameter. A hole 6 in. long and $\frac{3}{32}$ or $\frac{1}{8}$ in. in diameter along the central axis of the cylinder is necessary to accept the probe. All samples, except one, were successfully drilled. The exception, Berkeley sandstone, was very hard. This sample was finally cut in two longitudinally, and grooves of the appropriate dimensions were ground in the matching faces of the halves, which were then reassembled and held together by steel strips.

Wood's metal (mp=61°C) inserted between probe and specimen was found to eliminate contact resistance of probe to rock. The metal expands upon solidification, effecting a good bond between probe and rock. No evidence of metal penetration into the rock pores was found. The probe is easily removed, when necessary, by heating. All data presented here were obtained in this way. The probe length-to-diameter ratio is 64 or 48 for holes of diameter $\frac{3}{32}$ or $\frac{1}{8}$ in., respectively; however, this is still larger than the 30 theoretically required.[1]

For thermal conductivity measurements under a simulated overburden pressure, the sample, with probe in place, was encased in a half-inch thickness of an impervious rubber (Dow Corning Silastic RTV 501), placed in a pressure vessel, and subjected to hydraulic pressure. The apparatus is shown in Fig. 1. The electrical leads to the probe and high-pressure tubing, connected to the inside of the sample, were brought out through the rubber and pressure vessel, permitting the internal gas pressure to be varied. The tubing-pore space

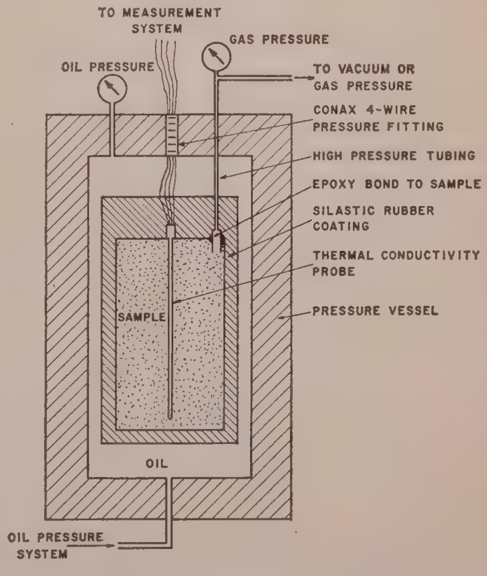

Fig. 1. Schematic diagram of apparatus for measurement of thermal conductivity as a function of overburden pressure.

---

[1] J. H. Blackwell, Can. J. Phys. 34, 412 (1956).

Table I. Properties of rock samples.

Sandstone	Porosity, %	Permeability md	Mineral composition Quartz	Kaolinite	Illite	Amorphous silica
Berkeley	3.0	<0.1	98–99	1–2		
St. Peters	11	3.4	98–99	1–2		
Tensleep	15.5	220	90–95			5–10
Berea	22	480	88–89	9–10	2	
Teapot	29	1960	88	7	5	
Tripolite	59	650	85–90			10–15

continuity was checked by observing the increase in pressure upon opening the tube connected to the sample into an evacuated system. The absence of penetration of the sample by the external pressuring fluid was checked by weighing the encased sample before and after the measurements.

DESCRIPTION OF TEST SAMPLES

In selecting rock samples for thermal conductivity study, two criteria were kept in mind. First it was desirable that as broad a porosity range as possible be covered at evenly spaced intervals. Secondly, it was desirable that the rocks be well-defined mineralogically, in order that the validity of the various thermal conductivity equations could be tested.

The porosity, permeability, and mineralogical analysis obtained by x-ray diffraction of the six sandstone samples finally selected are shown in Table I. A porosity range from 3 to 59% is covered; no "clean" sandstone sample with a porosity in the range 35 to 50% could be found. All samples contain at least 85% quartz; thus, from the standpoint of the conductivity equations, the assumption that the samples consist of a single solid component with a conductivity k_s of 20 mcal/cm sec°C is valid.

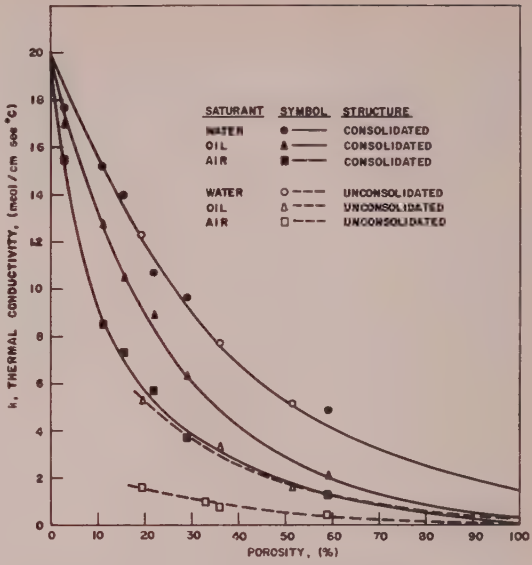

Fig. 3. Comparison of consolidated sandstone and unconsolidated sand thermal conductivity data.

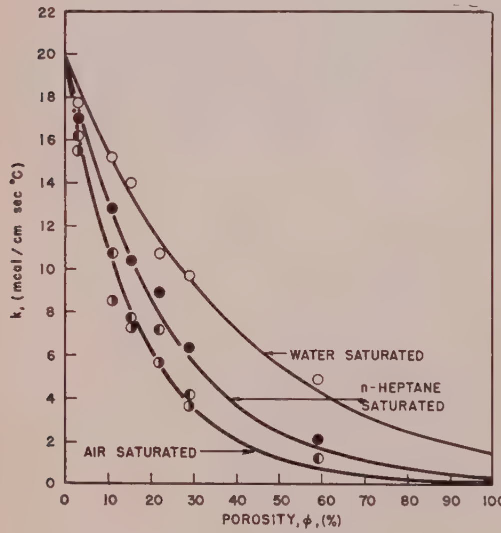

Fig. 2. Variation of effective thermal conductivity of consolidated sandstones with porosity, for air, oil (*n*-heptane) and water saturated conditions. — Calculated from geometric mean equation; ○ water saturated; ● *n*-heptane saturated; ◐ air saturated; ◑ air saturated, corrected for molecular effects.

RESULTS AND DISCUSSION

The effective thermal conductivities of the six sandstones with air, *n*-heptane, and water saturants are plotted against porosity in Fig. 2. The curves drawn on the figure represent the values calculated from the weighted geometric mean equation. As was the case for unconsolidated sands (Fig. 5, Part I), the effective conductivity decreases with increasing porosity (for $k_f<k_s$). It is of interest to compare the effective conductivities of consolidated sandstones with those of unconsolidated sands. Both sets of data are plotted in Fig. 3. Theoretically, the conductivities should be identical when the conductivity of the saturating fluid equals the conductivity of the solid matrix, i.e., when $k_f=k_s$, or at the porosity extremes $\phi=0$ and $\phi=1$. The data indicate that the conductivities differ by very little when water is the saturating fluid ($k_s/k_f=13.3$); a single curve represents both sets of data very well. With oil as saturant, the consolidated conductivities are appreciably higher than those for the unconsolidated sands, particularly at the lower porosities, e.g., at $\phi=0.2$ the sandstone conductivity is higher by a factor of 1.7. With air as saturant, the divergence between the conductivities of the two types of structure

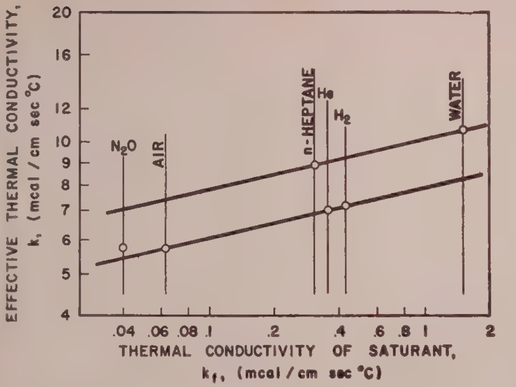

FIG. 4. Effective thermal conductivity of Berea sandstone saturated with various fluids at atmospheric pressure.

is even greater; at $\phi=0.2$, the sandstone conductivity is higher by a factor of 3.75.

The effective thermal conductivity k is plotted against the conductivity of the saturating fluid k_f on a logarithmic scale in Fig. 4 for Berea sandstone. These data were all obtained with the saturating fluid at a pressure of one atmosphere. Two parallel straight lines fit the data very well, the upper line corresponding to liquid saturants and the lower line to gaseous saturants. With nitrous oxide as saturant, a pressure decline was observed, indicating adsorption of the gas, which probably accounts for the slightly high conductivity value. It appears that a gaseous saturant at atmospheric pressure reduces the effective conductivity of Berea sandstone by a factor of about 1.3 below the value for a liquid saturant of the same conductivity as the gas. The gases behave as though they possess conductivities about one-seventh their values at atmospheric pressure. This thermal conductivity effect is, in some ways, analogous to the Klinkenberg[2] permeability effect. In low-permeability porous media, permeabilities to gases are higher than permeabilities to liquids. This effect is attributed to the phenomenon of gas slippage at the walls of capillaries whose radii are comparable to the mean free path of the gas. As the mean pressure of the gas is raised, gas permeability approaches the liquid value.

The data for Berea indicate that the sample contains pores which are smaller than the mean free paths of gases, even at atmospheric pressure. The mean free paths[3] at atmospheric pressure and 15°C of the gaseous saturants are: hydrogen, 0.118 μ (microns); helium, 0.186 μ; air, 0.063 μ; and nitrous oxide, 0.061 μ. To determine whether this sandstone does contain such small pores, the nitrogen desorption isotherm of the rock was measured, and the pore size distribution calculated by the method of Barrett, Joyner, and Halenda.[4] The results show the existence of pores as small as 0.004 μ in diameter, with 3.5% of the total pore volume in pores, less than 0.08 μ in diameter. The magnitude of the reduction in effective conductivity indicates that these "micropores" are situated at critical locations with respect to heat conduction, probably in the cementing material around the contacts between quartz grains. The effects of molecular mean free paths on heat conduction through porous rocks are discussed in greater detail in another paper.[5]

Similar effects were observed for the other rock samples, except Tripolite, as shown in Fig. 5. As with nitrous oxide, a pressure decline was observed with Freon-12 as gas saturant, again indicating adsorption and accounting for the higher conductivity. In general, the lines for gaseous and liquid saturants are not parallel. By extrapolating the liquid line toward lower k_f values, an estimate may be made of the effective conductivity which the rock would possess if the saturating air were operating at its normal conductivity. Values obtained in this manner are plotted in Fig. 2.

Figure 6 shows the effective thermal conductivity of Berkeley and Tensleep sandstones as a function of the internal air pressure. These data were obtained by first evacuating the sample and then performing thermal measurements at various air pressures, increasing stepwise to atmospheric pressure with dry air. Water vapor in the air, with the resultant condensation in the very small pores, increases the effective conductivity value, as evidenced by the several data for Berkeley sandstone obtained with room air as the saturant. In contrast with unconsolidated sands, consolidated sandstones possess a high thermal conductivity *in vacuo*, i.e., the resistor model parameter $b=k_{\mathrm{vac}}/k_s$, representing the "straight-through" solid conduction, is a major component of the over-all conductivity. The b values for the six sandstones range from 0.347 for Berkeley to 0.027 for Tripolite, whereas the highest b value observed for the unconsolidated sands was 0.00155. It would be expected, therefore, that thermal conductivity equations, such as Maxwell's, de Vries', and the geometric mean equation, which predict that $k=0$ when $k_f=0$ (i.e., *in vacuo*), will underestimate effective conductivities for consolidated sandstones. It should also be noted that the effective conductivity k is still increasing with air pressure P at pressures near atmospheric, i.e., $dk/dP>0$ at atmospheric pressure. This is consistent with the observed differences for gaseous and liquid saturants discussed earlier, and the explanation advanced for this behavior.

The variation of the effective thermal conductivity of Berea sandstone with saturating gas pressure over the pressure range from vacuum to 2000 psia is shown

---

[2] L. J. Klinkenberg, Am. Petrol. Inst. Drilling and Production Practice, p. 200 (1941).

[3] E. H. Kennard, *Kinetic Theory of Gases* (McGraw-Hill Book Company, Inc., 1938).

[4] E. P. Barrett, L. G. Joyner, and P. O. Halenda, J. Am. Chem. Soc. **73**, 373 (1951).

[5] W. Woodside and J. H. Messmer, J. Geophys. Research **65**, 3481 (1960).

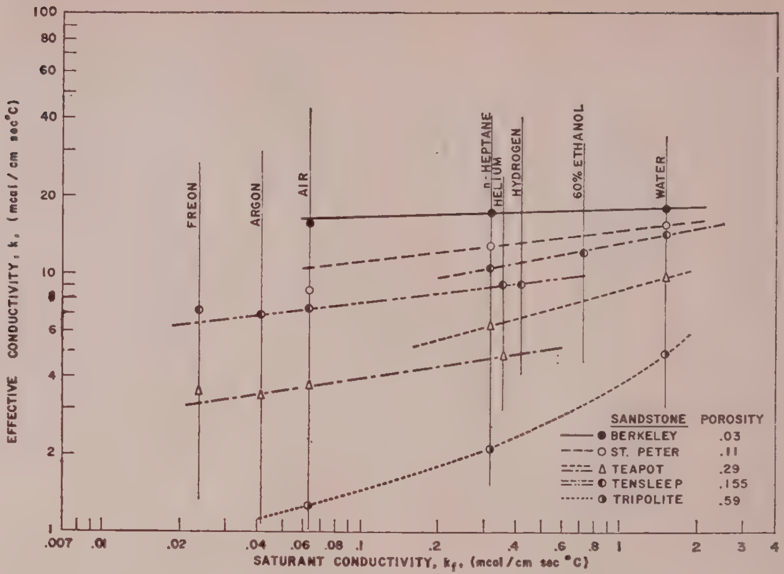

FIG. 5. Effective thermal conductivities of sandstones as a function of the conductivity of the saturating fluid.

in Fig. 7. The upper curve in this figure is discussed later. Also plotted on the pressure axis are the corresponding mean free paths. The pressure ranges over which the conductivity increases correspond to mean free path intervals and hence to pore sizes present in the rock; thus a qualitative estimate of the ranges of pore size (but not the number of pores in those ranges) present in the sample may be made from such data. However, the same effect that was observed for unconsolidated media, namely that the critical dimension d obtained from the conductivity variation with pressure is only a small fraction of the actual pore size, probably holds also for consolidated media. Thus Fig. 7 suggests the presence of pores as small as 5 A; the nitrogen desorption isotherm for Berea indicated the presence of pores as small as $0.004\,\mu = 40$ A.

Extrapolation of the liquid saturant line of Fig. 4 indicates that the effective conductivity of Berea sandstone, when saturated with a liquid having the same conductivity as nitrogen, would be 7.2 mcal/cm sec°C.

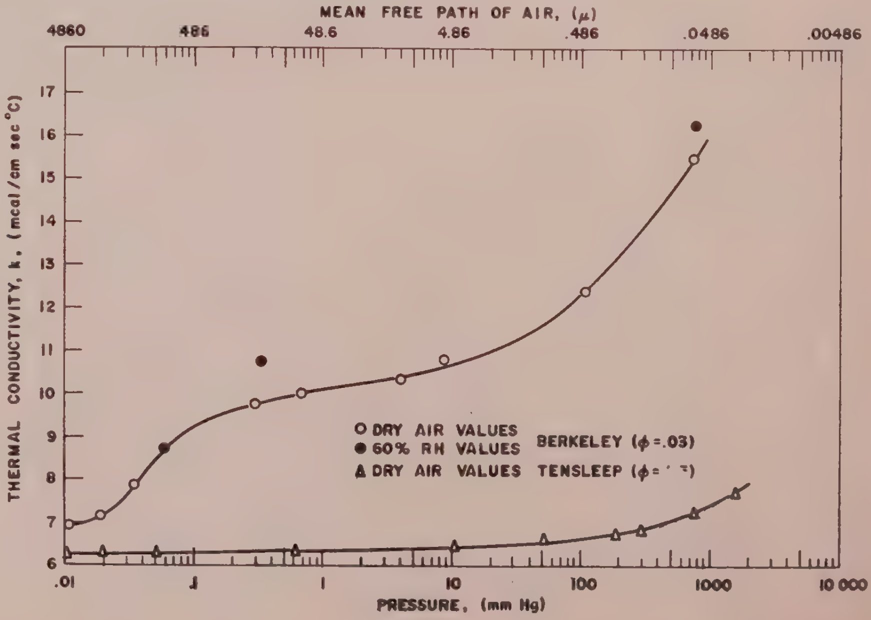

FIG. 6. Variation of effective thermal conductivity of Berkeley and Tensleep sandstones with air pressure.

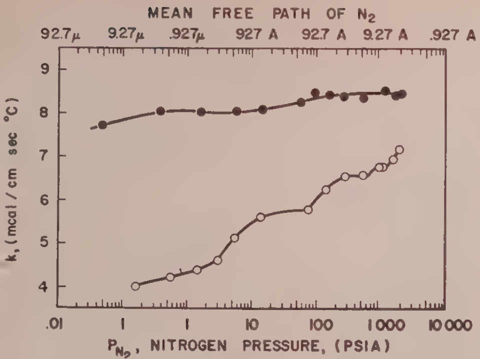

FIG. 7. The effect of internal gas pressure on the thermal conductivity of Berea sandstone with and without a large differential overburden pressure. ○ Zero net overburden pressure; ● 4000 psi net overburden pressure.

It is apparent that the nitrogen-saturated conductivity approaches this value as the gas pressure is raised to 2000 psia and the molecular mean free path reduced to 5 A. Thermal conductivities of gases increase with pressure at high pressures (when the proportionality between gas density and pressure breaks down); thus part of the above increase in effective conductivity is caused by the higher than normal conductivity of the nitrogen in the larger pores. This effect, however, is only secondary. The conductivity of nitrogen at 2000 psia and 25°C is 0.082; the value at atmospheric pressure is 0.063 mcal/cm sec°C.[6] This increase in the conductivity of the saturant corresponds at most to an increase of only 0.15 mcal/cm sec°C in the effective conductivity of Berea (Fig. 4), whereas an increase of 1.6 mcal/cm sec°C was actually observed. Thus the bulk of the increase in effective conductivity at high gas pressure is due to the reduction of molecular effects in the micropores.

Petroleum reservoir rocks sometimes occur at great depths, and are subjected to the pressure of the overlying strata. The net pressure [net pressure = geostatic pressure ($\rho_s=2.3$ gm/cc) − hydrostatic pressure] exerted on the rock increases by roughly 0.5 psi per foot of depth. The effect of a simulated overburden pressure on the thermal conductivity of air-saturated and evacuated Berea sandstone is shown in Fig. 8. The conductivity of the evacuated Berea is almost doubled by the application of 4000 psi overburden pressure; the increase is 37.5% for the air-saturated condition. In both cases, the conductivity appears to level off at a pressure between 3000 and 4000 psi, and returns to its initial value upon release of the pressure. The increase in effective conductivity with overburden pressure will be smaller the higher the conductivity of the saturant (as observed for the evacuated and air-saturated conditions above), since in the limit, when $k_f=k_s$, overburden pressure can have no influence on the effective conductivity. The application of overburden pressure to a rock increases the contact between adjacent grains and hence the over-all conductivity. This may be likened to an increase in the "degree of consolidation" of the rock. The similarity between thermal conductivities of consolidated and unconsolidated sands when water-saturated (Fig. 3) indicates that overburden pressure will have little or no effect upon the conductivities of water-saturated rocks. The effect will also be small even in partially water-saturated rocks, when water is the wetting phase and therefore occupies the smaller pores and the spaces around grain contacts. In oil-saturated rocks, and in partially oil-saturated rocks with oil as the wetting phase, the increase in effective conductivity with overburden pressure will probably be smaller than the 37.5% increase observed for the air-saturated Berea sample.

The data of the upper curve in Fig. 7 were obtained with the sample subjected to a differential overburden pressure of approximately 4000 psi. The differential overburden pressure (i.e., the net pressure on the solid matrix of the rock) is the difference between the external pressure applied hydraulically and the internal gas pressure (Fig. 1). Thus when the gas pressure inside the sample was 2000 psia, the external pressure was 6000 psia. The greater scatter in these data is probably due to the difficulty in maintaining the differential overburden pressure constant, although the value of

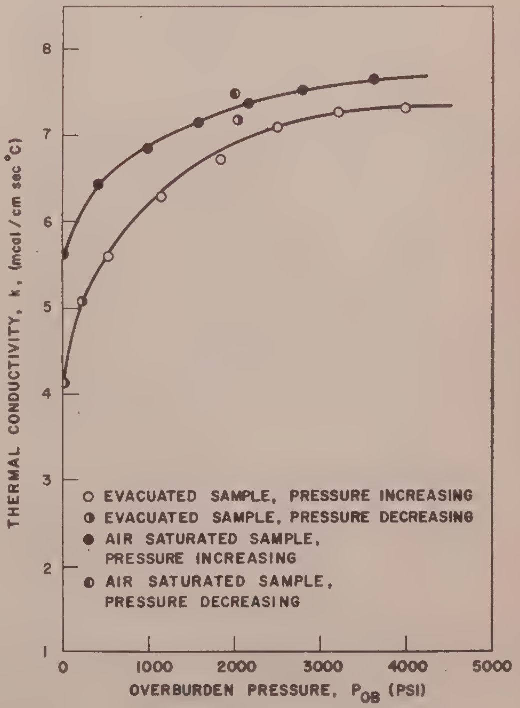

FIG. 8. Effect of overburden pressure on the thermal conductivity of air-saturated (1 atm) and evacuated Berea sandstone.

---

[6] C. A. Schaefer and G. Thodos, A. I. Ch. E. Journal 5, 367 (1959).

4000 psia was selected because of the relative insensitivity of the conductivity to small changes in overburden pressure at this level (Fig. 8). The effect of the differential overburden pressure is to increase the thermal conductivity at all gas pressures, but particularly at the lower gas pressures (i.e., lower k_f). Furthermore, the conductivity appears to be a less sensitive function of the gas pressure; the molecular effects are markedly reduced. This may mean that the micropores referred to earlier are actually very small gaps or cracks between or within quartz grains, which are partly closed upon the application of pressure on the rock; or, alternatively, heat conduction through these tiny spaces may be much less important because of the improved contact between the grains.

VALIDITY OF THE THERMAL CONDUCTIVITY EQUATIONS

Figure 9 is a plot of the conductivity ratios $y=k/k_f$ and $x=k_s/k_f$ for the Berea sandstone data. Values calculated from several of the thermal conductivity equations are also shown for comparison. Maxwell's equation underestimates the effective conductivity, except when x approaches unity. The geometric mean equation fits the data quite well over the range of x covered. The resistor model curve was calculated, using the measured value of the parameter $b=k_{\text{vac}}/k_s=0.20$, and using for c the value calculated from the electrical formation factor-porosity relationship: $c=1/F=4\phi^2/3$.

The weighted geometric mean equation is compared with the data for all six rock samples, with air, oil, and water saturants, in Fig. 2. The agreement is good in every case, except for the Tripolite sample.

Figure 10 is a plot of the product (thermal conductivity×formation factor) against porosity for water-saturated sandstones. The lower curve represents the empirical equation of Zierfuss and van der Vliet[7] derived from their data for 36 sandstones

$$\log_{10}kF=4.2524-15.29\phi+31.84\phi^2-27\phi^3.$$

The upper curve was calculated from the following equation:

$$kF=\tfrac{3}{4}\phi^{-2}k_s^{1-\phi}k_f^{\phi},$$

i.e., a combination of the geometric mean equation for thermal conductivity and a reasonable expression for the average electrical formation factor of consolidated rocks. The points plotted on the figure represent our experimental values multiplied by the corresponding formation factor calculated from $F=\frac{3}{4}\phi^{-2}$. The agreement is surprisingly good in view of the variability exhibited by natural sandstones.

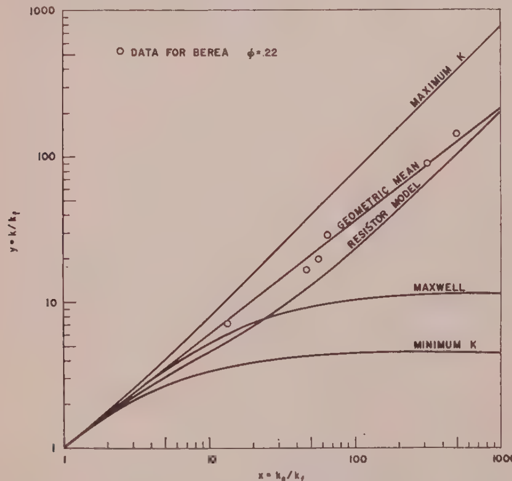

FIG. 9. Comparison of thermal conductivity data for Berea sandstone with values calculated from conductivity equations.

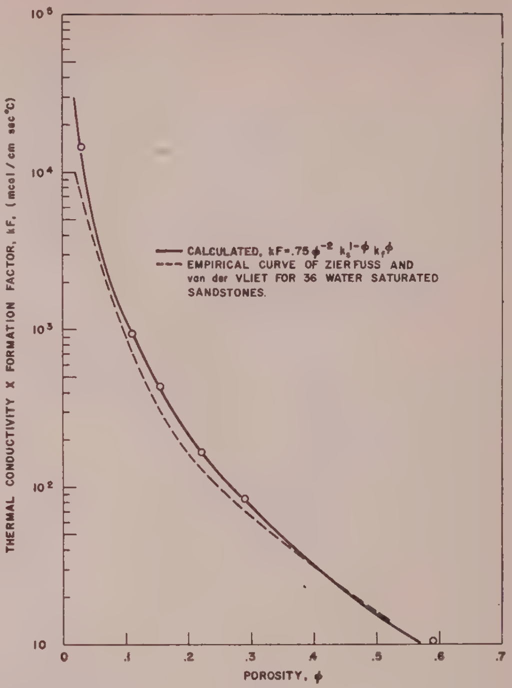

FIG. 10. Effective thermal conductivity×formation factor for water-saturated sandstones of varying porosity.

The resistor model equation,[8] using for the parameter b the value obtained from the measured *in vacuo* conductivity, and for c the value calculated from the electrical formation factor-porosity relationship, predicts effective conductivity values consistently lower than those measured. As was done for the unconsolidated media in Part I, the values c must have to match the resistor model with the observed data were calculated. The values of c thus obtained vary more for a given

---

[7] H. Zierfuss and G. van der Vliet, Bull. Am. Assoc. Petrol. Geologists **40**, 2475 (1956).

[8] M. R. J. Wyllie and P. F. Southwick, J. Petrol. Tech. **6**, TP3750 (1954).

TABLE II. Thermal conductivity results for consolidated sandstones.[a]

Sample	Fractional porosity, ϕ	Saturant	Saturant conductivity k_f, mcal/cm sec°C	Measured conductivity k, mcal/cm sec°C	b[b]	c[c]
Berkeley Sandstone	0.03	(*Vacuo*)	0.00	6.94	0.347	
		Air	0.063	15.5		0.029
		n-Heptane	0.307	17.0		0.028
		Water	1.50	17.7		0.021
St. Peters Sandstone	0.11	(*Vacuo*)	0.00	5.96	0.298	
		Air	0.063	8.50		0.103
		n-Heptane	0.307	12.77		0.103
		Water	1.50	15.2		0.093
Tensleep Sandstone	0.155	(*Vacuo*)	0.00	6.26	0.313	
		Freon-12	0.0234	7.17		0.149
		Argon	0.0422	6.87		0.137
		Air	0.063	7.26		0.140
		n-Heptane	0.307	10.45		0.144
		Helium	0.352	8.31		0.111
		Hydrogen	0.428	9.05		0.121
		Water	1.50	14.01		0.142
Berea Sandstone	0.22	(*Vacuo*)	0.00	4.02	0.201	
		Nitrous Oxide	0.040	5.76		0.213
		Air	0.063	5.71		0.209
		n-Heptane	0.307	8.93		0.206
		Helium	0.352	6.97		0.182
		Hydrogen	0.428	7.18		0.176
		Water	1.50	10.7		0.153
Teapot Sandstone	0.29	(*Vacuo*)	0.00	2.61	0.130	
		Freon-12	0.0234	3.50		0.282
		Argon	0.0422	3.40		0.272
		Air	0.063	3.69		0.272
		n-Heptane	0.307	6.34		0.269
		Helium	0.352	4.73		0.230
		Water	1.50	9.67		0.247
Tripolite	0.59	(*Vacuo*)	0.00	0.53	0.027	
		Air	0.063	1.26		0.577
		n-Heptane	0.307	2.10		0.558
		Water	1.50	4.86		0.538

[a] Results obtained at 30°C, with saturant at atmospheric pressure.

[b] $b = k_{\rm vac}/k_s \cdot k_s$ has been assumed to be 20 mcal/cm sec°C for all samples.

[c] Value of resistor model parameter c which, in conjunction with measured b, produces agreement between observed conductivity and that calculated from the resistor model equation.

sample than was the case for the unconsolidated samples (See Table II). For a given sample, c decreases as k_s/k_f decreases, with few exceptions. The average c value is plotted against the sample porosity in Fig. 11 together with the values obtained for the unconsolidated samples. Both sets of data may be represented very well by the same almost linear curve. Besides this single empirical curve of thermal formation factor are shown the electrical formation factor curves for consolidated and unconsolidated media. Thus the resistor model is not consistent with the observed thermal conductivity data when used with the electrical value for the parameter c. The value of c is not of major importance in itself, since the contribution of this component to the over-all conductivity is usually small. It derives its importance from its relationship to the value of a, the geometrical factor defining the solid-fluid series component, which does make a large contribution to the resultant conductivity.

CONCLUSIONS

(1) The line heat source (probe) method, when used with a metal insert to ensure good thermal contact, is satisfactory for the determination of effective thermal conductivities of consolidated rocks under a wide variety of test conditions.

(2) Measurements were made on six sandstone samples ranging in porosity from 3 to 59% and in permeability from 0.1 to 2000 millidarcys. All samples contained at least 85% quartz. The thermal conductivities ranged from 1.2 to 17.7 mcal/cm sec°C. For all saturating fluids used, thermal conductivity decreased as porosity increased.

(3) Thermal conductivities of consolidated sandstones and unconsolidated sands, having the same porosity, differ very little when water is the saturating fluid. With oil as saturant, the sandstones have appreciably higher conductivities, particularly at the lower porosities; with air as saturant, the difference is even greater.

(4) The effective rock conductivity increases with the conductivity of the saturating fluid, the effect being greater the higher the porosity. An approximately linear relationship between $\log k$ and $\log k_f$ is observed.

(5) All samples, except Tripolite, possessed a lower thermal conductivity when saturated with a gas at

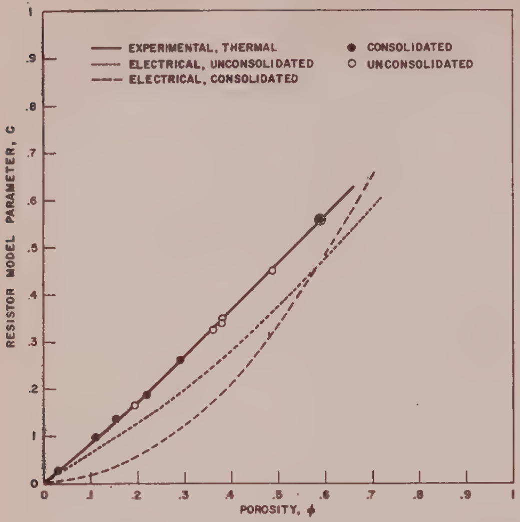

FIG. 11. Comparison of measured "thermal formation factor" with electrical formation factor for consolidated and unconsolidated samples.

atmospheric pressure than when saturated with a liquid of the same conductivity as the gas. This effect is attributed to the reduction in conductivity of the gas contained in pores of dimension comparable to the mean free path of the gas. The existence of such "micropores" is supported by pore size distribution data obtained by the nitrogen desorption method.

(6) In contrast with unconsolidated sands, sandstones possess a high thermal conductivity *in vacuo*. The conductivity increases with increase in saturating gas pressure, the increase continuing at pressures above atmospheric. In the case of Berea sandstone, the conductivity increased with gas pressure to 2000 psia (gas mean free path 5 A), when a value equal to the corresponding liquid-saturated value was attained.

(7) The Berea sandstone sample with air as saturant showed an increase of 37% in thermal conductivity when subjected to a simulated overburden pressure of 3500 psi; in the evacuated condition a greater increase was observed. In both cases, further increases in overburden pressure produced relatively little increase in conductivity. It is predicted that overburden pressure will have little or no effect on the conductivities of water-saturated rocks, or partially water-saturated rocks when water is the wetting phase.

(8) The effect of the application of a constant differential overburden pressure was (1) to increase the conductivity of Berea at all pressures of the saturating gas, but particularly at the lower gas pressures, and (2) to reduce the sensitivity of the conductivity to gas pressure.

(9) The resistor model equation, using for the parameter c values determined by electrical conductivity measurements, consistently underestimates the effective thermal conductivity of sandstones. Fair agreement with the observed data is achieved if c is calculated from the empirical relationship derived for unconsolidated media in Part I.

(10) The geometric mean equation predicts rock thermal conductivities which are in good agreement with those measured. This equation permits the estimation of sandstone conductivities from the porosity and conductivity of the saturating fluid.

(11) This work has dealt only with "clean" sandstones containing a single fluid in the pore space. Further work is required on other rock systems containing more than one fluid saturant.

ACKNOWLEDGMENTS

The authors gratefully acknowledge the stimulus afforded by discussions of this work with Dr. M. R. J. Wyllie and Dr. G. H. F. Gardner. Thanks are also due A. Gallagher of Instrument Service who constructed the probes.

JOURNAL OF APPLIED PHYSICS VOLUME 32, NUMBER 9 SEPTEMBER, 1961

Cross-Section Ratios of Sensitizing Centers in Photoconductors*

RICHARD H. BUBE
Radio Corporation of America, RCA Laboratories, Princeton, New Jersey

(Received February 27, 1961)

The ratio of the capture cross section of a sensitizing center for a photoexcited hole to the subsequent capture cross section for a free electron, in *n*-type photoconductors, can be determined from the measurement of the thermal quenching of photoconductivity as a function of excitation intensity. The magnitude of the ratio gives information about the charged state of the sensitizing center. A summary of many such measurements on seven different photoconductors of type II–VI or III–V supports the hypothesis that doubly charged sensitizing centers are present in some of these materials, but that singly charged sensitizing centers are present in the majority.

WHEN materials of group II–VI or III–V are prepared with particular care to purity, the resulting crystals are generally quite insensitive.[1] High photosensitivity in a number of such *n*-type photoconductors results from the incorporation of negatively charged sensitizing centers which have a larger cross section for the capture of photoexcited holes than for the subsequent capture of photoexcited electrons.[2] Comparative measurements of photoconductivity lifetime and photomagnetoelectric lifetime in CdS, for example, have shown that electron and hole lifetimes are approximately equal to 1 μsec and equal to each other in pure insensitive CdS, but that the electron lifetime increases to 10^{-2} sec while the hole lifetime decreases to 10^{-10} sec when the crystals are made photosensitive by suitable impurity incorporation.[3] The sensitizing centers which cause such an increase in photosensitivity may have either a singly negative charge or a doubly negative charge with respect to the rest of the crystal. Sensitizing centers which are singly negative in the absence of photoexcitation might be expected to have a cross section of 10^{-12} cm² for photoexcited holes, and a subsequent cross section of 10^{-16} cm² for photoexcited electrons; they would have a cross-section ratio S_p/S_n of about 10^4. Sensitizing centers which are doubly negative, on the other hand, might be expected to have a cross section of 4×10^{-12} cm² for holes, and a subsequent cross section of about 10^{-20} cm² for electrons because of the Coulomb repulsion existing[2]; they would have a cross-section ratio S_p/S_n of about 10^7 or 10^8. Knowledge of the cross-section ratios actually present in photoconducting materials therefore gives information as to the charged state of the sensitizing centers, something hitherto the subject of speculation but not of determination. Table I presents a brief summary of a typical series of data using representative numbers to illustrate the above remarks.

The cross-section ratio of sensitizing centers can be determined from the measurement of thermal quenching of photoconductivity.[4] The onset of thermal quenching corresponds to that condition for which the probability of thermal release of photoexcited holes captured at sensitizing centers equals the probability of recombination of these holes with free electrons, i.e., when the hole demarcation level[2] for these centers is located at the centers. The relationship can be expressed quantitatively by the equation

$$E_{dp}=E_{fn}+kT\ln(S_p/S_n), \tag{1}$$

where E_{dp} is the height of the hole demarcation level associated with the centers with cross sections S_p and S_n above the top of the valence band, and E_{fn} is the distance of the steady-state electron Fermi level below the bottom of the conduction band. When the value of E_{fn} at the onset of thermal quenching is plotted as a function of the temperature at which that onset occurs, therefore, a straight line is obtained with slope of $-k\ln(S_p/S_n)$ and intercept at $T=0$ equal to the height of the sensitizing center level above the top of the valence band. Various values of E_{fn} and T for the onset of thermal quenching can be obtained by making measurements at different intensities of excitation.

Thermal quenching data, obtained over the past six years,[5] on 23 different crystals of 7 different photoconductors have been analyzed in terms of Eq. (1), and values of S_p/S_n and the hole ionization energies of sensitizing centers have been obtained by the method of least squares. Results of this analysis are given in Table II, and typical plots of Eq. (1) are given in Fig. 1. The method is not particularly precise; small uncertainties in locating the onset of thermal quenching can produce relatively large effects in the values calculated. The use of least squares and the reproducibility of calculations on several crystals of the same type, however, give the assurance of reasonable reliability.

Nineteen of the crystals analyzed, listed in the top portion of Table II, give values of S_p/S_n which are

---

* This research was partially supported by the Air Research and Development Command, United States Air Force, under contract.

[1] R. H. Bube and L. A. Barton, RCA Rev. **20**, 564 (1959); R. H. Bube, J. Appl. Phys. **31**, 315 (1960).

[2] A. Rose, RCA Rev. **12**, 362 (1951); Phys. Rev. **97**, 322 (1955); Proc. Inst. Radio Engrs. **43**, 1850 (1955); R. H. Bube, *ibid.* **43**, 1836 (1955).

[3] H. S. Sommers, R. E. Berry, and I. Sochard, Phys. Rev. **101**, 987 (1956).

[4] R. H. Bube, J. Phys. Chem. Solids **1**, 234 (1957); Solid State Phys. **11**, 223 (1960).

[5] See reference 4, and also R. H. Bube and E. L. Lind, Phys. Rev. **105**, 1711 (1957); **110**, 1040 (1958); **115**, 1159 (1959); R. H. Bube and L. A. Barton, J. Chem. Phys. **29**, 128 (1958); J. Blanc, R. H. Bube, H. E. MacDonald, J. Appl. Phys. (to be published).

TABLE I. Illustrative relations between cross sections and lifetimes for a material containing N_s sensitizing centers, n_s of which are occupied by electrons, and N_r recombination centers, n_r of which are occupied by electrons.

$$(1)\quad 1/\tau_n = vS_{ns}(N_s-n_s)+vS_{nr}(N_r-n_r)$$
$$(2)\quad 1/\tau_p = vS_{ps}n_s+vS_{pr}n_r$$
$$(3)\quad [n_s(N_r-n_r)/n_r(N_s-n_s)]=(S_{ns}S_{pr}/S_{ps}S_{nr})\qquad \text{Let } N_s=N_r=10^{15}\text{ cm}^{-3}$$

Situation	S_{pr}, cm²	S_{nr}, cm²	S_{ps}, cm²	S_{ns}, cm²	τ_n, sec	τ_p, sec	n_s/N_s-n_s	n_r/N_r-n_r
No sensitizing centers[a]	10^{-16}	10^{-12}	...	...	10^{-6}	10^{-6}	...	10^{4}
Singly charged sensitizing centers	10^{-16}	10^{-12}	10^{-12}	10^{-16}	10^{-2}	10^{-10}	10^{4}	10^{12}
Doubly charged sensitizing centers	10^{-16}	10^{-12}	4×10^{-12}	10^{-20}	2×10^{-2}	5×10^{-11}	1	4×10^{12}

[a] These centers are assumed occupied by electrons in the dark, but neutral as far as charge is concerned.

either in the neighborhood of 10^4 or 10^8. The four crystals in the lower portion of Table II gave anomalously low values, the result principally of the fact that the calculated values of E_{fn} at the onset of thermal quenching were essentially independent of the onset temperature. Except to suggest that the onset of thermal quenching in these particular crystals might possibly be associated with the characteristics of levels in the upper half of the gap, not properly analyzed in terms of Eq. (1), we shall not comment further on these apparent exceptions.

Whenever impurities were intentionally added, such impurities are listed in Table II. The eight CdSe crystals without added impurities were prepared by heating insensitive CdSe crystals in vacuum at various annealing temperatures. CdSe 4, CdSe 11, and CdSe 10 were

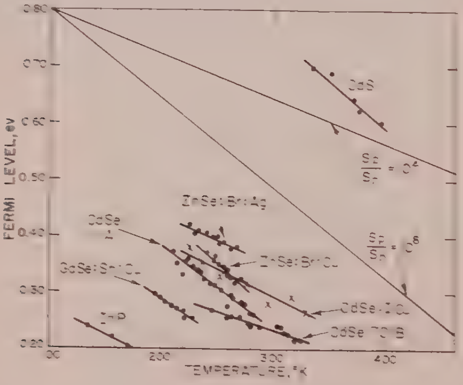

FIG. 1. The variation of the location of the electron Fermi level at the point of thermal quenching as a function of the temperature at this same point, for different intensities of photoexcitation. The slope of the lines gives the cross-section ratio; the intercept at $T=0$ gives the ionization energy of holes from the sensitizing centers. Guide lines corresponding to cross-section ratios of 10^4 and 10^8 are included for comparison.

TABLE II. Summary of data on sensitizing centers.

Crystal	Hole ionization energy, ev	Cross-section ratio	Number of different (E_{fn}, T) values used in analysis
CdS	1.28	5×10^{8}	5
CdS:Cl:Cu	1.06	2×10^{6}	2
CdSe:I:Cu	0.59	9×10^{4}	7
CdSe:I:Cu	0.52	4×10^{3}	7
CdSe:I:Cu	0.54	8×10^{3}	21
CdSe 4A	0.50	6×10^{2}	7
CdSe 4C	0.47	8×10	7
CdSe 11AC	0.73	10^{8}	8
CdSe 11A	0.67	2×10^{7}	18
CdSe 10AB	0.54	4×10^{4}	9
CdSe 10AC	0.51	3×10^{4}	7
CdSe 701A	0.48	10^{4}	14
CdSe 701B	0.43	2×10^{3}	14
ZnSe:Br:Cu	0.79	3×10^{7}	10
ZnSe:Br:Cu	0.79	6×10^{8}	10
ZnSe:Br:Ag	0.60	2×10^{4}	10
ZnSe:Br:As 92	0.51	5×10^{2}	9
GaAs:Si:Cu	0.45	4×10^{4}	6
InP:(X):Cu	0.37	7×10^{4}	3
GaSe:Sn:Cu	0.56	6×10^{6}	8
ZnSe:Br:Sb	0.36 0.43	2 5×10^{-3}	10 8
ZnSe:Br:As 93	0.29	8×10^{-2}	12
GaSe:Cl:Cu	0.34	10	10
ZnTe:In:Cu	0.34 0.60	2×10 8	2 2

heated at 200°, 300°, and 400°C, respectively, at about 10^{-2} mm Hg. CdSe 701 were heated at 300°C in a specially purified vial at about 10^{-5} mm Hg.

The values of S_p/S_n in Table II suggest the existence of doubly negative sensitizing centers in CdS, either with or without intentionally added impurities, in ZnSe:Br:Cu, in certain CdSe crystals sensitized under particular conditions, and possibly in GaSe:Sn:Cu. All other crystals can be interpreted as favoring the assumption of singly negative sensitizing centers.

An approximate systematic relationship seems to exist between the hole ionization energies of the sensitizing centers and the band gaps of the materials involved. A summary is given in Table III. In most of the materials, the hole ionization energy of the sensitizing centers is about $\frac{1}{3}$ the band gap.

TABLE III. Correlation between band gap and ionization energy of sensitizing centers.

Material	Band gap E_G ev	Ionization energy E_s ev	E_s/E_G
CdS	2.4	1.1 -1.3	0.46–0.54
CdSe	1.7	0.43–0.73	0.25–0.43
ZnSe	2.6	0.51–0.79	0.20–0.30
GaSe	2.0	0.56	0.28
GaAs	1.4	0.45	0.32
InP	1.3	0.37	0.28

JOURNAL OF APPLIED PHYSICS VOLUME 32, NUMBER 9 SEPTEMBER, 1961

Effect of Gaseous Ambients upon $1/f$ Noise in Germanium Filaments*

V. E. NOBLE† AND J. E. THOMAS, JR.‡
Wayne State University, Detroit, Michigan

(Received October 10, 1960)

The variation of $1/f$ noise in thin, single crystal germanium filaments was investigated by using gaseous ambients to change the surface potential of the sample. The noise samples, having a thickness of only 4 μ, were extremely sensitive to variations in the surface potential and exhibited large fractional changes of the total sample conductance as a result of the surface conductance fluctuations which were interpreted as the $1/f$ noise. These experimental results showed a definite noise minimum when the sample surface potential corresponded to the sample conductance minimum. The rms conductance fluctuation varied roughly linearly with ΔG, where ΔG is the increase of the sample conductance with respect to the minimum value. The slope of the curve for the condition of an accumulation layer on the sample surface was an order of magnitude less than that for the inversion layer. The amplitude of the accumulation noise agreed (within a factor of two) with the prediction of McWhorter's majority carrier trapping effect, but the inversion noise was an order of magnitude greater.

INTRODUCTION

In the present investigation, thin single crystal filaments have been used in the study of the dependence of $1/f$ noise upon the surface potential of germanium. This noise is a conductance fluctuation whose mean square value shows a $1/f$ frequency spectrum. The noise mechanism has been variously attributed to carrier trapping by the slow surface states, ionic diffusion, and inversion layer breakdown.[1–3] By using germanium filaments of the order of 4 μ thickness, greater sensitivity of the sample to the surface conditions was attained (because of the high surface-to-volume ratio) in this series of experiments than has been possible in previous work on semiconductor filaments.[4] In these experiments, the surface potential of the thin filaments was varied by using a modified Brattain-Bardeen ambient cycle.[5]

PREPARATION OF NOISE SAMPLES

Slabs were cut from single crystals of germanium, lapped to a thickness of 0.020 cm, and then etched to a thickness of 2 to 6 μ. The lateral dimensions of the slabs, before etching, were $\frac{5}{8}$ in. long by $\frac{1}{16}$ in. wide. After the cutting and lapping operations, copper leads were soldered to the ends of the slab and the assembly was mounted across the open ends of a glass horseshoe. In this case, the etching was done by flowing an etchant composed of H_2O_2, HF, and deionized water (1:1:4) over the slabs. The etching was slowed and finally stopped by continuous dilution of the etchant with deionized water. A second technique for the

---

* This work partially supported by the U. S. Air Force.

† Present address: Great Lakes Research Division, Michigan Institute of Science and Technology, Ann Arbor, Michigan.

‡ At present: Director, Research and Engineering, Sylvania Electric Products, Inc., Semiconductor Division, Woburn, Massachusetts.

[1] A. L. McWhorter, *Semiconductor Surface Physics*, edited by R. H. Kingston (University of Pennsylvania Press, Philadelphia, 1957), pp. 207–226.

[2] L. Bess, Phys. Rev. **103**, 72 (1956).

[3] R. L. Petritz, *Semiconductor Surface Physics*, edited by R. H. Kingston (University of Pennsylvania Press, Philadelphia, 1957), p. 226.

[4] A. U. MacRae and H. Levinstein, Phys. Rev. **119**, 62 (1960).

[5] W. H. Brattain and J. Bardeen, Bell System Tech. J. **32**, 1–41 (1953).

preparation of thin filaments is the photoelectrolytic method for etching thin films of n-type germanium described by Albers and Thomas.[6]

The thickness of the finished noise samples was measured by x-ray absorption. The output beam from a copper x-ray tube (excited by 11 kv) was collimated through a 2-mil pinhole and filtered with a vanadium window. The sample was placed in this collimated and filtered beam, and the x-ray absorption was measured with a geiger tube to determine the sample thickness. The system was calibrated by sectioning and microscopically measuring representative thin filaments. Under these conditions, the absorption coefficient was found to be equal to 251 cm^{-1}. ($I/I_0=e^{-\mu t}$, where $\mu=251$ cm^{-1}, and t is the sample thickness.)

Typical dimensions of the thin portion of the final sample are 0.3 cm ×0.1 cm ×4 μ. The samples finally selected for use in this series of measurements were required to be within 20% of the nominal thickness.

SURFACE POTENTIAL AND SAMPLE CONDUCTANCE

The carrier densities in the sample are given by the relations $n=n_i\exp(q\phi/kT)$, $p=n_i\exp(-q\phi/kT)$, where the electrostatic potential ϕ is defined by $\phi=(E_f-E_i)$. As usual, E_f is the fermi level, and E_i is approximately the mid-gap energy. The value of $\phi(x)$ is determined along a line from the center of the sample out to the surface by solving Poisson's equation

$$\frac{d^2\phi}{dx^2}=\frac{q\phi}{K\epsilon_0}(N_d-N_a+p-n), \tag{1}$$

where N_d and N_a are the number of ionized donors and acceptors in the bulk, respectively. The surface potential ϕ_s is the value of $\phi(x)$ evaluated at the sample surface ($x=x_s$). After $\phi(x)$ has been determined for different values of ϕ_s, the carrier concentration, and hence the sample conductance, may be calculated as a function of the surface potential. Figure 1 shows the sample conductance per unit surface area as a function of the sample surface potential, which has been calculated on the basis of bulk mobilities for 32-ohm cm n-type material, 6 μ thick. As shown, the conductance-surface potential relation may be approximated by a parabola given by

$$(g-g_m)=a(u_s-u_m)^2. \tag{2}$$

The numerical values assigned to the parabola were

$$g_m=15.7\times10^{-6}\text{ mho/cm}^2,\quad a=0.8\times10^{-6}\text{ mho/cm}^2,$$

and $u_m=-1.4$. In this relation, u_s is the surface potential in units of kT/q and u_m is the value of the surface potential corresponding to the sample conductance minimum.

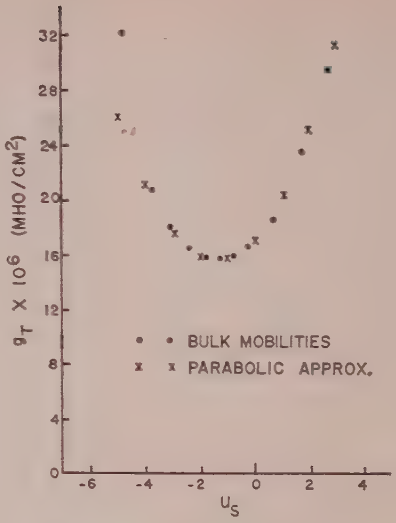

FIG. 1. Sample conductance as a function of surface potential, (32-ohm cm n-type, $t=6$ μ).

Schrieffer has considered the use of effective mobilities $(\mu_n)_{\text{eff}}$ and $(\mu_p)_{\text{eff}}$ to account for the scattering of the carriers in the potential well at the surface of the crystal, and has shown that, for large values of $|u_s-u_B|$, μ_{eff} is less than μ_B.[7] Since, however, for the region of greatest interest (near the condition of minimum conductance) the ratio μ_{eff}/μ_B is greater than 0.9, (corresponding to $|u_s-u_B|$ less than 6) the bulk mobilities have been assumed in the calculation of the conductance change. The parabolic approximation (shown in Fig. 1) gives lower values of sample conductance than those calculated from the bulk mobilities in the region where $|u_s-u_m|$ is large. Thus the parabolic approximation gives conductances which are closer to those that would be expected if the Schrieffer mobility corrections were used in the calculations.

Under the influence of the gaseous ambients, the measured sample conductance (G) was carried through the range $3.0\leq(G-G_m)/G_m\leq0$ for the accumulation layer, and $0\leq(G-G_m)/G_m<0.5$ for the inversion layer in the case of 32-ohm cm n-type material. G_m is the minimum sample conductance observed in the ambient cycle, and was approximately 7×10^{-6} mho for the samples used in this series of measurements. The ambient cycle was carried out over a period of six hours, during which time the ambient was slowly varied from wet nitrogen through ozone and back to wet nitrogen again.

The data which are presented in this paper are representative of 62 ambient cycles involving 10 germanium samples. Five of the samples were 32-ohm cm n-type material, three of the samples were 8.5-ohm cm n-type material, and two of the samples were 9-ohm

---

[6] W. A. Albers, Jr., and J. E. Thomas, Jr., Bull. Am. Phys. Soc. 3, 219 (1958).

[7] J. R. Schrieffer, Phys. Rev. 97, 641 (1955).

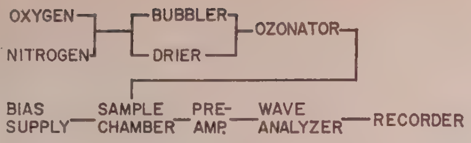

FIG. 2. Block diagram of complete noise measuring system.

cm p-type material. The results from the low-resistivity material were similar to those obtained from the near-intrinsic material, but the lack of sample sensitivity precluded the computation of quantitative relations for the low-resistivity material. In the following sections, only the results from the near-intrinsic material will be discussed.

Qualitative ac field-effect measurements (using copper field-effect electrodes separated from the sample by an air-gap) demonstrated conductance minimum as the samples were carried from an accumulation layer to an inversion layer under the effects of the ambient cycle. In the following experiments, the surface-trap density was due only to the effects of the gaseous ambient, with no possibility of interaction between the ambient and a dielectric field-effect spacer having any effect upon the trap distribution.

EXPERIMENTAL RESULTS

A block diagram of the complete noise-measuring system is shown in Fig. 2. The bias supply consisted of a 45-v battery in series with two, low-noise, 3.5-meg resistors. The effect of the changing sample conductance upon the sample bias current was considered for the computation of the absolute value of the rms conductance fluctuation. The sample chamber consisted of a light-tight box through which the ambient was passed at atmospheric pressure. The flow rate was the minimum possible value which would assure a positive flow through the sample chamber.

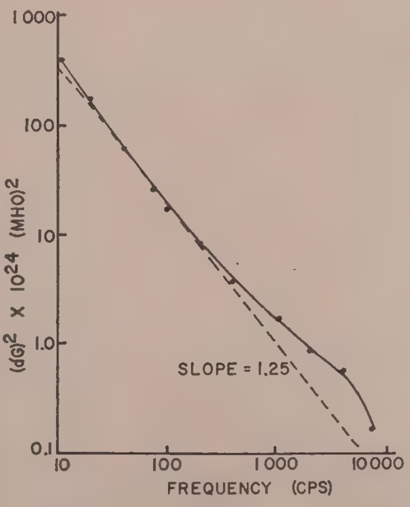

FIG. 3. Conductance noise spectrum of etched germanium filament, (32-ohm cm n-type material, wet nitrogen ambient $R_{\max}=140$ k).

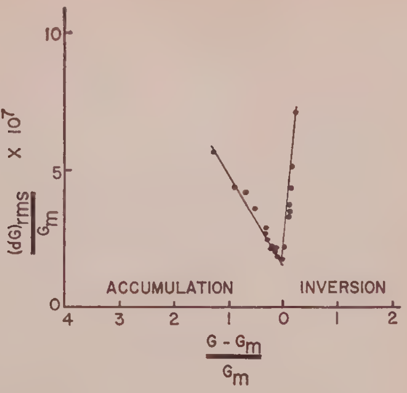

FIG. 4. Variation of $1/f$ noise as a function of sample conductance, (32-ohm cm n-type, 2 days aging, $R_{\max}=104$ k, $t=6\,\mu$, $f=20$ cps).

The frequency spectrum of the ratio of the measured mean square noise voltage to the thermal noise is given by

$$n=1+\frac{AI_d^2}{f^m}+\frac{BI_d^2}{1+(f/f_0)^2}, \tag{3}$$

where m is approximately equal to one, and I_d is the direct current through the sample. The first term is thermal noise, the second is $1/f$ noise, and the third term is shot noise. The mean square noise voltage is measured with no current flowing through the sample and subtracted from the mean square noise voltage measured with the bias supply turned on. The result is the mean square value of the current-dependent noise voltage. Since the mean square noise voltage is proportional to I_d^2, the noise mechanism is interpreted

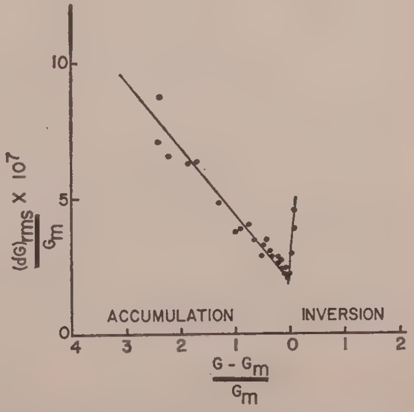

FIG. 5. Variation of $1/f$ noise as a function of sample conductance, (32-ohm cm n-type, 4 days aging, $R_{\max}=113$ k, $t=6\,\mu$, $f=20$ cps).

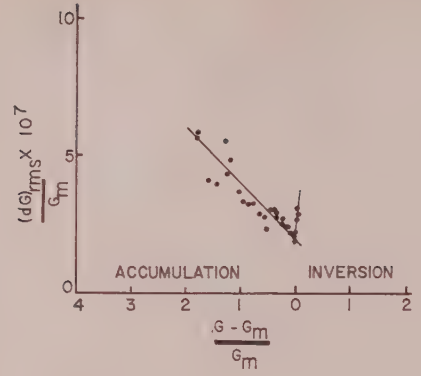

FIG. 6. Variation of $1/f$ noise as a function of sample conductance, (32-ohm cm n-type, 6 days aging, $R_{\max}=118$ k, $t=6\,\mu$, $f=20$ cps).

as a conductance fluctuation. The frequency spectrum of the noise (mean square value of the conductance fluctuation) is shown in Fig. 3. In this case, $m\simeq 1.25$. In order to be sure that the measured noise was dominated by the $1/f$ component, the subsequent measurements were carried out at 20 cps.

The sample surface potential was varied by the ambient, and the noise measurements were made as a function of the resulting conductance change. Figures 4–6 show the variation of the rms conductance fluctuation as a function of the conductance change of the sample. These figures also demonstrate a shift toward a surface accumulation layer on the sample as a result of aging of the freshly-etched surface in room atmosphere. Figure 7 gives the theoretical prediction of McWhorter's majority carrier trapping effect, calculated for 32-ohm cm n-type material, using bulk mobilities. (The details of the calculation are given in Appendix A.) It is seen that there is agreement to within a factor of 2 between the observed and calculated noise amplitudes in the accumulation layer condition. Further, the shape of the noise curves also agree, i.e., the measured noise is a minimum at the sample conductance minimum.

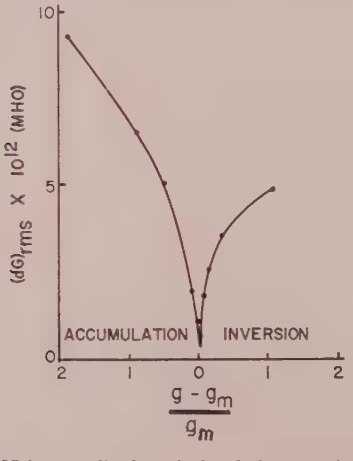

FIG. 7. Noise amplitude calculated from majority carrier trapping model, (bulk mobilities, 32-ohm cm n-type, $t=6\,\mu$, $f=20$ cps).

The observed noise data may be represented by the relation

$$\frac{(\delta G)_{\rm rms}}{G_m}=\alpha\frac{G-G_m}{G_m}+\beta, \qquad (4)$$

where G_m is the sample conductance minimum measured during the ambient cycle, G is the sample conductance, and $(\delta G)_{\rm rms}$ is the root mean square fluctuation in the conductance. The minimum noise value is represented by β, and the slope of the noise curve is given by α. The value of α for the inversion layer condition is an order of magnitude greater than for the accumulation layer condition.

The above results contrast with those of MacRae[4] who observed a constant value for the accumulation noise (i.e., $\alpha=0$ for the accumulation layer) while varying the surface potential in vacuum by means of the field effect. Inasmuch as MacRae's noise samples were an order of magnitude thicker than the ones used in this series of experiments, the lack of sufficient sample sensitivity may have prevented the observation of the accumulation noise.

The surface potential fluctuation associated with the conductance fluctuation is obtained from Eqs. (2) and (4). To a linear approximation, we may write

$$\frac{(\delta G)_{\rm rms}}{G_m}=\frac{d}{du_s}\left(\frac{g-g_m}{g_m}\right)\delta u_s, \qquad (5)$$

where G is the (measured) total conductance of the sample, and g is the (calculated) conductance per unit surface area of the sample. Finally, substituting Eqs. (2) and (5) into Eq. (4), we obtain the following relation for the dependence of the surface potential fluctuation upon the sample surface potential:

$$\delta u_s=\frac{\alpha}{2}|u_s-u_m|+\frac{\beta g_m}{2a|u_s-u_m|}. \qquad (6)$$

The first term in the above expression is a result of the linear relation between the noise and the sample conductance change. The second term arises from the fact that there is a nonzero minimum value for the noise at the sample conductance minimum.

The infinity arising from the second term (for $u_s=u_m$) is not inconsistent with a reasonable noise mechanism because the slope of the conductance-surface potential curve is zero at the conductance minimum. Hence a large potential fluctuation would be required to account for the observed minimum value.

Thus, interpreting the noise as conductance fluctuations caused by surface potential fluctuations and expecting only noninfinite (reasonably small) values of $(\delta u_s)_{\mathrm{rms}}$, the noise level would be zero at the sample conductance minimum (i.e., β would be zero) for a completely homogeneous surface. Furthermore, surface inhomogeneities would be expected to contribute to the noise at the conductance minimum and thus yield a nonzero value for β. (The conductance minimum is a condition of relatively low external charge, hence is expected to be quite sensitive to perturbations of the surface conditions.)

Therefore, if we let β approach zero, Eq. (6) becomes

$$(\delta u_s)_{\mathrm{rms}}=\frac{\alpha}{2}|u_s-u_m|, \qquad (7)$$

where α is greater for the inversion layer case than for the accumulation layer condition.

The surface potential fluctuation, which is predicted on the basis of the McWhorter theory, is shown as curve A in Fig. 8. (The computation of the surface potential fluctuation is described in Appendix B.) The result of this calculation predicts that $(\delta u_s)_{\mathrm{rms}}$ will be a maximum at $u_s=u_B$ (where u_B is the reduced bulk potential), whereas the experimental results [Eq. (7)] show a minimum at $u_s=u_m$.

The computation in Appendix C demonstrates that in order to have a noise minimum at $g=g_m$, it is not necessary for $(\delta u_s)_{\mathrm{rms}}$ to be a minimum at $u_s=u_m$, but only that $(\delta u_s)_{\mathrm{rms}}$ decrease less rapidly than $|u_s-u_m|^{-1}$. A surface potential fluctuation curve obeying the relation $(\delta u_s)_{\mathrm{rms}}=\gamma/|u_s-u_m|$ is compared with the prediction from the majority carrier trapping theory in Fig. 8. It is seen that the predicted curve does decrease less rapidly than $|u_s-u_m|^{-1}$ as required for a noise minimum. Furthermore, as shown elsewhere,[8] by substituting the values of $(\delta u_s)_{\mathrm{rms}}$ calculated from Eq. (22) into Eq. (23), the resultant noise curve shows a noise minimum at $g=g_m$, which agrees with the experimental observations.

When the effects of surface inhomogeneities are considered, it is expected that the noise minimum will be more shallow and broader than that predicted by the theoretical calculations. This effect might explain the difference between the experimental and theoretical potential variation curves.

The explanation of the high observed inversion noise level may lie either in the inversion layer breakdown predicted by Petritz or the injection-extraction effect which is a secondary result of the majority carrier trapping. The injection-extraction effect is the generation and absorption of hole-electron pairs caused by the local variation of the p-n product as a result of the sweeping of the minority carriers through the noise sample under the influence of the dc biasing potential. For the accumulation layer, McWhorter[1] has shown the injection-extraction noise to be of the same order of magnitude as the majority carrier trapping noise. The calculation of the injection-extraction noise for the inversion layer condition has not yet been carried out.

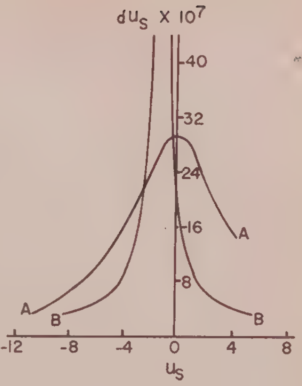

FIG. 8. δu_s as a function of surface potential. Curve A: surface potential variation calculated from majority carrier trapping effect [Eq. (22)]. Curve B: comparison curve obeying relation: $\delta u_s=\gamma|u_s-u_m|^{-1}$.

APPENDIX A

Calculation of Conductance Fluctuation from Majority Carrier Trapping Effect

The expression for the conductance fluctuation is taken to be (for $\omega\tau_1\ll 1\ll\omega\tau_2$) $\omega=2\pi f$

$$(\delta G)_{\mathrm{rms}}^2=\frac{LC}{\ln(\tau_2/\tau_1)}\left(\frac{q}{L^2}\right)^2\left[\frac{P_0\mu_p-N_0\mu_n}{N_0+P_0}\right]^2\frac{N_0+P_0}{f}, \qquad (8)$$

where L and C are the length and circumference of the noise sample, τ_2 and τ_1 are the upper and lower limits of the $1/\tau$ distribution of trapping times, ($\ln\tau_2/\tau_1=20$, after McWhorter), q is the electronic charge, f is the frequency, and N_0 and P_0 are given by

$$N_0=\frac{-kT}{qE_{s0}}(n_{s0}-n_0), \qquad (9)$$

$$P_0=\frac{kT}{qE_{s0}}(p_{s0}-p_0). \qquad (10)$$

In the above expressions, E_{s0} is the equilibrium field at the surface, n_0 and p_0 are the bulk concentrations of electrons and holes, and n_{s0} and p_{s0} are the equilibrium surface concentrations of the carriers. The values of n_{s0}, p_{s0}, E_{s0} and the total sample conductance are evaluated from the values of $\phi(x)$ given by the solution of Poisson's equation (1). In this case, $L=0.318$ cm, $C=0.266$ cm, μ_p and μ_n are the bulk mobilities for germanium, and f is 20 cps.

Equation (8) is derived from the assumption of localized surface patches of the order of a Debye length square having effective trapping times τ_i with a $1/\tau$ distribution of the τ's from τ_1 to τ_2.

---

[8] V. E. Noble, Ph.D. thesis, Physics Department, Wayne State University, 1960 (unpublished).

APPENDIX B

Calculation of Surface Potential Fluctuation from Majority Carrier Trapping Effect

As the first step in the calculation of the surface potential fluctuation from McWhorter's theory, we must first determine the change in surface potential due to a change of one trapped electron. (This is the change in the number of trapped majority carriers when considering the majority carrier effect in n-type material.) Integrating Poisson's equation over the surface of the sample, (considering only a change in potential normal to the sample surface), we may write

$$f(x)=\int_A \phi(x)dydz, \qquad (11)$$

where

$$\frac{d^2f}{dx^2}=-\frac{1}{K\epsilon_0}\int_A \rho dydz. \qquad (12)$$

Now the integrated field normal to the surface is given by

$$F=-\frac{df}{dx}=\int_A E_x dydz. \qquad (13)$$

A small variation of $f(x_s)$ from equilibrium at the surface is given by

$$\delta f_s=\frac{df}{dF}\delta F_s=-K\epsilon_0\frac{E_{s0}}{\rho_{s0}}\delta F_s. \qquad (14)$$

But for one negative charge trapped,

$$\delta F_s=q/K\epsilon_0. \qquad (15)$$

Therefore, for an increase of one trapped majority carrier in n-type material,

$$\delta f_s=A\delta\phi_s=-E_{s0}/\rho_{s0}q. \qquad (16)$$

Now ρ_{s0} is the equilibrium charge density at the surface of the sample and is given by

$$\frac{\rho_{s0}}{q}=p_{s0}-n_{s0}+N_d-N_a=(p_{s0}-p_0)-(n_{s0}-n_0), \qquad (17)$$

where n_0 and p_0 are the bulk concentrations of the electrons and holes. By using the substitutions

$$N_0=-\frac{kT}{qE_{s0}}(n_{s0}-n_0) \quad P_0=\frac{kT}{qE_{s0}}(p_{s0}-p_0), \qquad (18)$$

Eq. (17) becomes

$$\frac{\rho_{s0}}{q}=\frac{qE_{s0}}{kT}(N_0+P_0). \qquad (19)$$

Considering the reduced surface potential $u_s=q\phi_s/kT$, we may write the variation in u_s for the change of one trapped electron as given by Eq. (16)

$$(\delta u_s)_n=-[A(N_0+P_0)]^{-1}. \qquad (20$$

McWhorter calculates the power spectrum for the fluctuation in the number of trapped electrons to be,[1,9] (for $\omega\tau_1\ll 1\ll\omega\tau_2$),

$$G_n(f)=\frac{LC}{\ln(\tau_2/\tau_1)}(N_0+P_0)1/f, \qquad (21)$$

where L and C are the sample length and circumference, respectively. The power spectrum for the fluctuation in surface potential thus becomes

$$G_{u_s}(f)=[LC\ln(\tau_2/\tau_1)(N_0+P_0)f]^{-1}, \qquad (22)$$

where A, the surface area of the sample, is given by $A=LC$.

APPENDIX C

Dependence of Conductance Fluctuations upon Surface Potential Fluctuations

Recalling Eqs. (2) and (5) we may write

$$\frac{(\delta g)_{\mathrm{rms}}}{g_m}=2\frac{a}{g_m}|u_s-u_m|(\delta u_s)_{\mathrm{rms}}. \qquad (23)$$

Let us now consider the general case

$$(\delta u_s)_{\mathrm{rms}}=\frac{\alpha}{2}|u_s-u_m|^k. \qquad (24)$$

On substituting (24) into (23), and again using Eq. (2), we have

$$\frac{(\delta g)_{\mathrm{rms}}}{g_m}=\alpha_k\left(\frac{g-g_m}{g_m}\right)^{(k+1)/2}, \qquad (25)$$

where $\alpha_k=a(g_m/a)^{(k-1)/2}$.

Examination of Eqs. (24) and (25) shows that for $k>-1$, the noise will be a minimum for $g=g_m$. For $k=-1$, the noise will be constant (independent of the sample conductance). Therefore, in order to have a noise minimum at $g=g_m$, it is not necessary for $(\delta u_s)_{\mathrm{rms}}$ to be a minimum at $u_s=u_m$, but only that $(\delta u_s)_{\mathrm{rms}}$ decrease less rapidly than $|u_s-u_m|^{-1}$.

---

[9] A. L. McWhorter, Ph.D. thesis, Electrical Engineering Department, M.I.T., 1955.

OURNAL OF APPLIED PHYSICS VOLUME 32, NUMBER 9 SEPTEMBER, 1961

Fields in Cavity-Excited Accelerators

E. G. Cristal and J. Van Bladel
Midwestern Universities Research Association, and Department of Electrical Engineering*
University of Wisconsin, Madison, Wisconsin

(Received February 3, 1961)

Field configuration and resonant frequency are determined for the lowest azimuthally-independent mode of a coaxial cavity surrounding a circular tube, Several values of the width of the coupling gap are considered, and the central problem consists in determining the tangential electric field $\mathbf{E}_t$ in that gap. It was found that the fields near the axis of the accelerator are quite insensitive to the actual profile of $\mathbf{E}_t$, and that satisfactory results are obtained by assuming $\mathbf{E}_t$ to be constant. The problem is repeated for a parallel plane configuration, with the purpose of investigating the influence of the flattening of the cavity. Computations show that the two configurations yield fairly similar results.

I. INTRODUCTION

A CONFIGURATION in which a beam of charged particles, shot down a metallic tube, is accelerated by an electromagnetic field impressed across a gap, is of wide interest in klystron and accelerator technology. The voltage kick experienced by the particles, the penetration of the fields within the tube, the lateral momentum kick impressed on the particle, all these and other useful data can be determined, in principle at least, once the tangential electric field across the gap is known. But this is where the difficulty lies. The field depends on the outside sources (and even on the beam itself in high-current machines), and it is an extremely difficult task to find its precise structure in the gap. The customary procedure[1] consists of assuming a reasonable distribution, or one which makes calculations palatable, and to start from there. Thus, in a circular cylindrical tube of the type shown in Figs. 1 and 2, the field can be taken, in first approximation at least, to be constant throughout the gap. This is obviously wrong, for it is well known that the electric field will become infinite in the vicinity of the lips of the gap, but one can reasonably hope that if the gap is sufficiently narrow, the field along the axis of the tube will not be too sensitive to the details of the distribution. In the present paper we address ourselves to the task of accurately determining the gap field for a configuration where the tube is excited through a surrounding cavity. Cavity excitation has the obvious advantage of allowing very high fields to build up across the gap at the resonant frequency, a situation which in turn results in high voltage kicks for the particles. Our method of attack is not new.[2] It consists of expressing the magnetic field on both sides of the gap in terms of the tangential electric field there, and to obtain an integral equation for the latter by expressing continuity of the magnetic field. What is new, perhaps, is the use of a digital computer to carry the calculations to a reasonable degree of accuracy. To make the problem tractable, cavities and tubes of simple shapes have been chosen [see Fig. 1(a) and (b)]. It is felt that the results obtained for the circular and parallel planes geometries would allow, by simple interpolation, to predict the behavior of an intermediate configuration of the type shown in Fig. 1(c), and which is of interest to the MURA group. Notice also that the circular configuration is of great importance in itself, being basic, for instance, to the design of drift-tube loaded linacs.

Although the main interest of our work lies in an investigation of the fields at resonance, it was decided to obtain data for a whole range of frequencies, extending from zero to a value slightly above the first resonance. In order to simplify the problem, the particularly simple (but not necessarily practical) method of excitation shown in Fig. 2 was chosen. This choice, which conserves the mathematically desirable properties of symmetry, will still preserve the main features of the

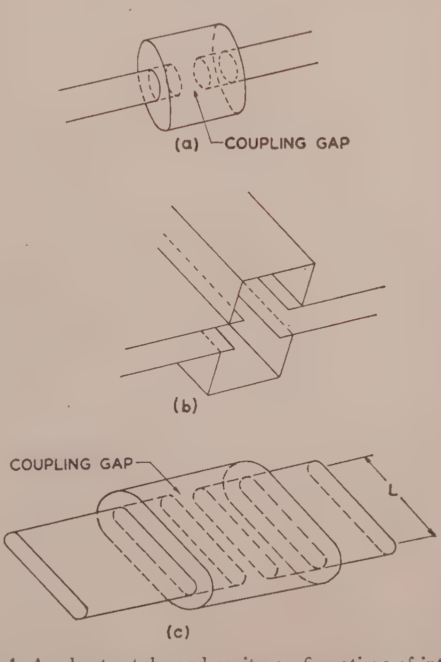

FIG. 1. Accelerator tube and cavity configurations of interest: (a) Circular geometry; (b) parallel planes geometry (seen in cross section); (c) intermediate "flattened" geometry.

---

* Supported by the U. S. Atomic Energy Commission.

[1] C. C. Wang, J. Appl. Phys. **16**, 351–366 (1945).

[2] See, for example, W. C. Hahn, J. Appl. Phys. **12**, 62–68 (1948), and L. S. Sheingold and J. E. Storer, *ibid.* **25**, 545–552 (1954).

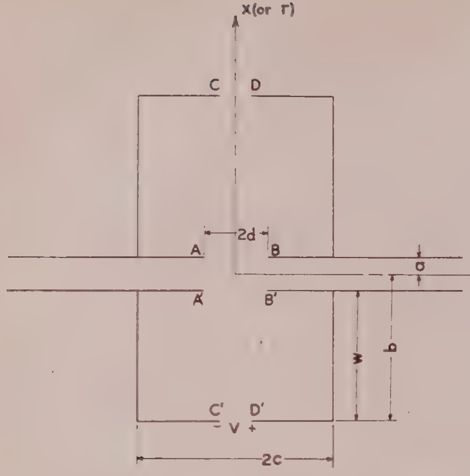

FIG. 2. Cross section of the cavity-accelerator configuration with relevant geometric parameters.

problem and, in particular, yield the correct frequency and fields of the first resonant mode.

II. MATHEMATICAL SOLUTION OF THE PROBLEM

(A) Consider first the parallel planes geometry of Figs. 1(b) and 2. The cavity is excited by a voltage $V \cos\omega t$, constant in magnitude and phase all along the very narrow gaps CD and $C'D'$. The resulting tangential electric field, written down in phasor form, is

$$\mathbf{E}_t = V\delta(z)\mathbf{u}_z, \tag{1}$$

where $\mathbf{u}_z$ is the unit vector in the z direction. Similarly, the tangential field in the broad gap AB will be

$$\mathbf{E}_t = Vs(z)\mathbf{u}_z, \tag{2}$$

where $s(z)$ is the function we seek to determine. It is immediately apparent that $s(z)$ is symmetric with respect to the $z=0$ plane, and that the field in gap $A'B'$ is the same as in AB.

The fields in any cavity can be expressed in terms of the volume currents (if any), and the tangential component of the electric field at the boundary. The methods are standard.[3] Applied to the cavity with rectangular cross section depicted in Fig. 2, they yield,[4] for unit voltage V:

$$E_z(z,x) = \frac{\sin k(a-x)}{2c \sin k(a-b)} + \frac{\sin k(x-b)}{c \sin k(a-b)} \int_0^d s(u)du + \frac{2}{c}\sum_{n=1}^{\infty} \frac{\sin \gamma_n(x-b)}{\sin \gamma_n(a-b)} \cdot \int_0^d s(u)\cdot \cos\frac{n\pi u}{c} du \cdot \cos\frac{n\pi z}{c}$$
$$+ \frac{1}{c}\sum_{n=1}^{\infty} \frac{\sin \gamma_n(a-x)}{\sin \gamma_n(a-b)} \cdot \cos\frac{n\pi z}{c}, \tag{3}$$

$$E_x(z,x) = \frac{2\pi}{c^2}\sum_{n=1}^{\infty} \frac{n \cos \gamma_n(x-b)}{\gamma_n \sin \gamma_n(a-b)} \cdot \sin\frac{n\pi z}{c} \int_0^d s(u)\cdot \cos\frac{n\pi u}{c} du - \frac{\pi}{c^2}\sum_{n=1}^{\infty} \frac{n \cos \gamma_n(a-x)}{\gamma_n \sin \gamma_n(a-b)} \cdot \sin\frac{n\pi z}{c}, \tag{4}$$

$$H_y(z,x) = j\omega\epsilon \Bigg\{ \frac{\cos k(a-x)}{2ck \sin k(a-b)} - \frac{\cos k(x-b)}{ck \sin k(a-b)} \cdot \int_0^d s(u)du + \frac{1}{c}\sum_{n=1}^{\infty} \frac{\cos \gamma_n(a-x)}{\gamma_n \sin \gamma_n(a-b)} \cdot \cos\frac{n\pi z}{c}$$
$$- \frac{2}{c}\sum_{n=1}^{\infty} \frac{\cos \gamma_n(x-b)}{\gamma_n \sin \gamma_n(a-b)} \cdot \left[\int_0^d s(u) \cos\frac{n\pi u}{c} du\right] \cos\frac{n\pi z}{c}, \tag{5}$$

where

$$k = 2\pi/\lambda, \quad \gamma_n = [k^2 - (n\pi/c)^2]^{\frac{1}{2}}.$$

Clearly, function $s(z)$ has to be determined before the fields can be computed. Similarly, in the accelerator "tube," i.e., between the planes AB and $A'B'$:

$$E_z(z,x) = \frac{2}{\pi}\int_0^{\infty} \frac{\cos(qz)\cos[\gamma(q)x]}{\cos[\gamma(q)a]} \cdot \left[\int_0^d s(u)\cos(qu)du\right] dq, \tag{6}$$

$$E_x(z,x) = -\frac{2}{\pi}\int_0^{\infty} \frac{q \sin(qz)\sin[\gamma(q)x]}{\gamma(q)\cos[\gamma(q)a]} \cdot \left[\int_0^d s(u)\cos(qu)du\right] dq, \tag{7}$$

$$H_y(z,x) = -\frac{2}{\pi}\int_0^{\infty} \frac{\cos[qz]\sin[\gamma(q)x]}{\gamma(q)\cos[\gamma(q)a]} \cdot \left[\int_0^d s(u)\cos(qu)du\right] dq, \tag{8}$$

---

[3] J. C. Slater, *Microwave Electronics* (D. Van Nostrand Company, Inc., Princeton, New Jersey, 1950), Chap. 4.

[4] For more details on this and other calculations, and for additional computer data, see E. G. Cristal's Ph.D. thesis, 1961, available from the Library of the University of Wisconsin.

where

$$\gamma(q)=[k^2-q^2]^{\frac{1}{2}}.$$

We now equate the tangential magnetic field on both sides of the gap, i.e., express the fact that (5) and (8) are equal for $x=a$. This gives us the fundamental integral equation for s:

$$\frac{1}{2ck\sin k(a-b)}+\frac{1}{c}\sum_{n=1}^{\infty}\frac{\cos(n\pi z/c)}{\gamma_n\sin\gamma_n(a-b)}=\frac{\cot k(a-b)}{ck}\int_0^d s(u)du+\frac{2}{c}\sum_{n=1}^{\infty}\int_0^d s(u)\cos\frac{n\pi u}{c}du\,\frac{\cot\gamma_n(a-b)\cos(n\pi z/c)}{\gamma_n}$$
$$+\frac{2}{\pi}\int_0^{\infty}\frac{\cos(qz)\tan[\gamma(q)a]}{\gamma(q)}\cdot\left[\int_0^d s(u)\cos(qu)du\right]dq. \quad (9)$$

(B) The same steps can be carried out, *mutatis mutandis*, for the circular cylindrical structure of Figs. 1(a) and 2. Within the cavity, then:

$$E_z(z,r)=\frac{1}{2c}\cdot\left[\frac{J_0(kr)N_0(ka)-J_0(ka)N_0(kr)}{J_0(kb)N_0(ka)-J_0(ka)N_0(kb)}\right]+\frac{1}{c}\int_0^d s(u)du\left[\frac{N_0(kr)J_0(kb)-J_0(kr)N_0(kb)}{J_0(kb)N_0(ka)-J_0(ka)N_0(kb)}\right]$$
$$+\frac{1}{c}\sum_{n=1}^{\infty}\frac{J_0(\gamma_n r)N_0(\gamma_n a)-J_0(\gamma_n a)N_0(\gamma_n r)}{J_0(\gamma_n b)N_0(\gamma_n a)-J_0(\gamma_n a)N_0(\gamma_n b)}\cdot\cos\frac{n\pi z}{c}$$
$$+\frac{2}{c}\sum_{n=1}^{\infty}\int_0^d s(u)\cos\frac{n\pi u}{c}du\cdot\frac{N_0(\gamma_n r)J_0(\gamma_n b)-J_0(\gamma_n r)N_0(\gamma_n b)}{J_0(\gamma_n b)N_0(\gamma_n a)-J_0(\gamma_n a)N_0(\gamma_n b)}\cos\frac{n\pi z}{c}, \quad (10)$$

$$E_r(z,r)=\frac{\pi}{c^2}\sum_{n=1}^{\infty}\frac{J_1(\gamma_n r)N_0(\gamma_n a)-N_1(\gamma_n r)J_0(\gamma_n a)}{J_0(\gamma_n b)N_0(\gamma_n a)-J_0(\gamma_n a)N_0(\gamma_n b)}\cdot\frac{n\sin(n\pi z/c)}{\gamma_n}$$
$$+\frac{2\pi}{c^2}\sum_{n=1}^{\infty}\int_0^d s(u).\cos\frac{n\pi u}{c}du\cdot\frac{J_0(\gamma_n b)N_1(\gamma_n r)-J_1(\gamma_n r)N_0(\gamma_n b)}{J_0(\gamma_n b)N_0(\gamma_n a)-J_0(\gamma_n a)N_0(\gamma_n b)}\cdot\frac{n\sin(n\pi z/c)}{\gamma_n}, \quad (11)$$

$$H_\theta(z,r)=j\omega\epsilon\left\{\frac{1}{2ck}\cdot\frac{J_1(kr)N_0(ka)-J_0(ka)N_1(kr)}{J_0(kb)N_0(ka)-J_0(ka)N_0(kb)}+\frac{1}{ck}\int_0^{\infty}s(u)du\cdot\frac{J_0(kb)N_1(kr)-N_0(kb)J_1(kr)}{J_0(kb)N_0(ka)-J_0(ka)N_0(kb)}\right.$$
$$+\frac{1}{c}\sum_{n=1}^{\infty}\frac{J_1(\gamma_n r)N_0(\gamma_n a)-N_1(\gamma_n r)J_0(\gamma_n a)}{J_0(\gamma_n b)N_0(\gamma_n a)-J_0(\gamma_n a)N_0(\gamma_n b)}\cdot\frac{\cos(n\pi z/c)}{\gamma_n}$$
$$\left.+\frac{2}{c}\sum_{n=1}^{\infty}\int_0^d s(u)\cos\frac{n\pi u}{c}du\cdot\frac{J_0(\gamma_n b)N_1(\gamma_n r)-J_1(\gamma_n r)N_0(\gamma_n b)}{J_0(\gamma_n b)N_0(\gamma_n a)-J_0(\gamma_n a)N_0(\gamma_n b)}\cdot\frac{\cos(n\pi z/c)}{\gamma_n}\right\}, \quad (12)$$

where J_0, J_1, and N_0, N_1 are Bessel and Neumann functions of order zero and one. In the cylindrical accelerator tube:

$$E_z(z,r)=\frac{2}{\pi}\int_0^{\infty}\frac{\cos(qz)J_0[\gamma(q)r]}{J_0[\gamma(q)a]}\left[\int_0^d s(u)\cos(qu)du\right]dq, \quad (13)$$

$$E_r(z,r)=\frac{2}{\pi}\int_0^{\infty}\frac{q\sin(qz)J_1[\gamma(q)r]}{\gamma(q)J_0[\gamma(q)a]}\cdot\left[\int_0^d s(u)\cos(qu)du\right]dq, \quad (14)$$

$$H_\theta(z,r)=j\omega\epsilon\frac{2}{\pi}\int_0^{\infty}\frac{\cos(qz)J_1[\gamma(q)r]}{\gamma(q)J_0[\gamma(q)a]}\cdot\left[\int_0^d s(u)\cos(qu)du\right]dq. \quad (15)$$

Equating the values of H_θ at $r=a$ yields the fundamental integral equation:

$$\frac{1}{\pi k^2 ac\cdot[J_0(kb)N_0(ka)-J_0(ka)N_0(kb)]}+\frac{2}{\pi ac}\sum_{n=1}^{\infty}\frac{\cos(n\pi z/c)}{\gamma_n^2[J_0(\gamma_n b)N_0(\gamma_n a)-J_0(\gamma_n a)N_0(\gamma_n b)]}$$
$$=\frac{1}{ck}\int_0^d s(u)du\cdot\frac{J_1(ka)N_0(kb)-J_0(kb)N_1(ka)}{J_0(kb)N_0(ka)-J_0(ka)N_0(kb)}+\frac{2}{c}\sum_{n=1}^{\infty}\left[\int_0^d s(u)\cos\frac{n\pi u}{c}du\right]\cdot\frac{J_1(\gamma_n a)N_0(\gamma_n b)-J_0(\gamma_n b)N_1(\gamma_n a)}{J_0(\gamma_n b)N_0(\gamma_n a)-J_0(\gamma_n a)N_0(\gamma_n b)}$$
$$\cdot\frac{\cos(n\pi z/c)}{\gamma_n}+\frac{2}{\pi}\int_0^\infty\frac{J_1[\gamma(q)a]\cos(qz)}{\gamma(q)J_0[\gamma(q)a]}\cdot\left[\int_0^d s(u)\cos(qu)du\right]dq. \quad (16)$$

(C) The main difficulty of the problem lies in the solution of integral Eqs. (9) and (16), which are of the general form

$$f(z)=\sum_n\int_0^d s(u)K_n(z,u)du$$
$$+\int_0^\infty K(z,q)dq\int_0^d s(u)G(q,u)du, \quad (17)$$

where f, K, G, K_n are given. We solved this equation by an approximate method consisting of dividing the $(0,d)$ interval into p equal parts (as shown in Fig. 3 for $p=6$), and of assuming $s(u)$ to be a linear function in each subinterval. Thus, in the first subinterval, $s(u)$ will be set equal to a constant a_1 (as justified by the horizontal tangent at $u=0$), in the second interval it will be set equal to $a_2[u-(d/p)]+a_1$, and the process will be repeated until the end of the interval is reached. Integral Eq. (17) now takes the form of a set of p linear equations

$$f(z)\approx\sum_{j=1}^{p}a_j h_j(z), \quad (18)$$

which can be solved either by equating both members of (18) at p points in the interval (say at $u=0$ and in the center of each subinterval), or by minimizing the mean square error:

$$\int_0^d[f(z)-\sum_{j=1}^{p}a_j h_j(z)]^2dz.$$

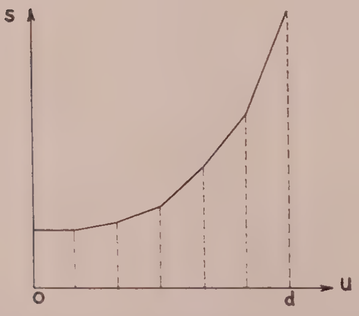

FIG. 3. Graph of the approximation to the gap field.

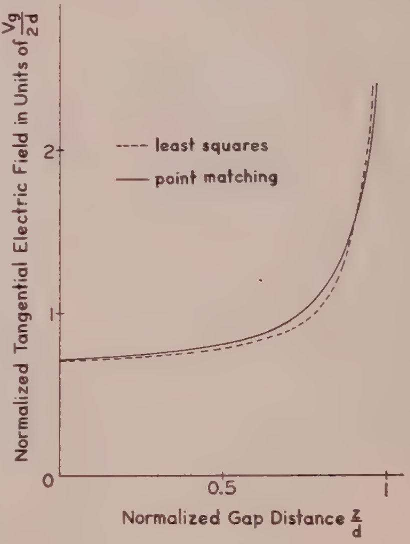

FIG. 4. A comparison of point matching and least-squares methods. The geometric parameters are $b/a=3.4$, $2c/w=1$ (the cavity has a square cross section), and $d/c=0.5$ (the gap is half open).

Both methods were tried, and gave satisfactory results. It turned out, in particular, (a) that the first method in most cases was not too sensitive to the choice of the matching points, (b) that computer time for this method was roughly 40% of the time required for the second method, (c) that both approaches gave comparable results, as evidenced by Fig. 4, established for $p=6$. Still better agreement would obviously be obtained for higher values of p. In our computer solution we consistently used method 1, and took $p=6$ to be our typical dividing ratio, a value which proved to give satisfactory convergence in most cases.

III. COMPUTER RESULTS

A. Tangential Field in the Gap

This fundamental quantity is plotted in Figs. 5 to 8 for several values of the relevant parameters. It was found, although the fact cannot be ascertained from the graphs, that the relative distribution of the field

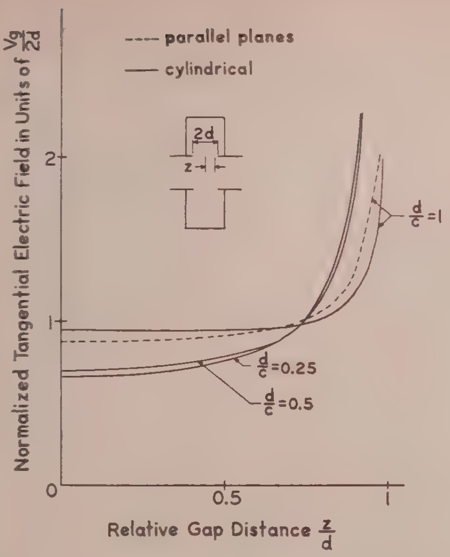

FIG. 5. Tangential electric field in the gap for $b/a=3.4$ and $2c/w=1$ (i.e., a cavity with square cross section). Cylindrical and parallel planes configurations yield undistinguishable curves for $d/c=0.25$ and 0.5.

throughout the gap was practically independent of frequency in the above-defined range. The only thing which varies is the total gap voltage

$$V_g=2\int_0^d E(z)dz,$$

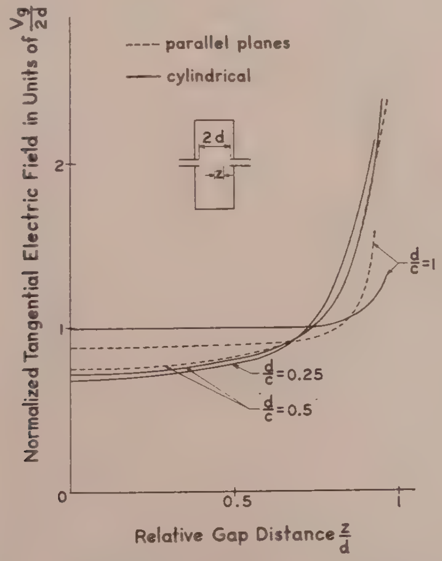

FIG. 6. Tangential electric field in the gap for $b/a=7$ and $2c/w=1$ (i.e., a cavity with square cross section). The curves for the cylindrical and parallel planes configurations are undistinguishable for $d/c=0.25$.

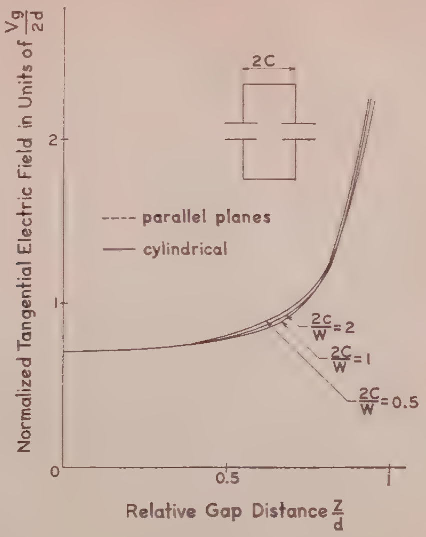

FIG. 7. Tangential electric field in the gap as a function of cavity length. Geometric parameters are $b/a=3.4$ and $d/c=0.5$ (i.e., half-gap opening). Curves for cylindrical and parallel planes configurations are undistinguishable.

which goes to infinity at the resonant frequency. We consequently choose to plot E_z in terms of its average value $V_g/2d$. The "universal" curves shown in the figures evidence a behavior which could be expected on intuitive grounds: the field is almost constant in the gap, but blows up like $(D)^{-\frac{1}{3}}$ (where D is the distance to the lips of the gap) as we approach the metallic boundary. When the gap occupies the full length of the

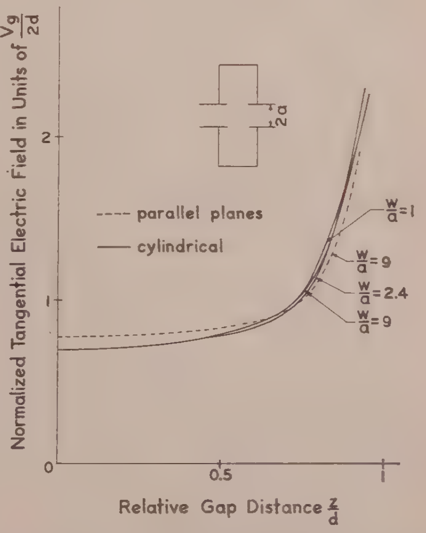

FIG. 8. Tangential electric field in the gap for several values of the inner radius of the cavity. The cavity has a square cross section (i.e., $2c/w=1$), and the gap is half open (i.e., $d/c=0.5$). Curves for cylindrical and parallel planes configurations are undistinguishable for $w/a=1$ and 2.4.

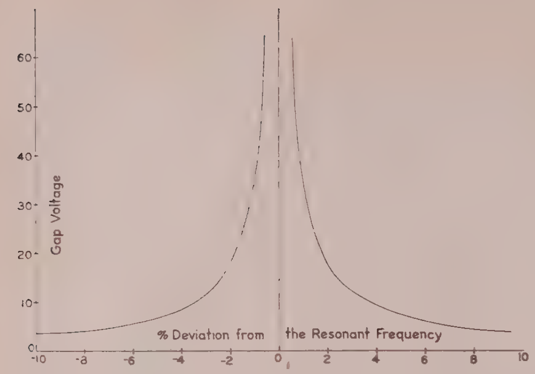

FIG. 9. Gap voltage vs frequency for unit excitation. The plot refers to the voltage magnitude, and does not evidence the fact that the gap voltage is in phase with the exciting voltage below resonance, and 180° out of phase above. The curve was obtained for $2c/w=1$, $w/a=2.4$, and $d/c=0.5$, but has a quasi-universal character.

cavity (i.e., for $d/c=1$), the metallic boundary shows a 90° corner, and the field blows up like $(D)^{-\frac{1}{3}}$.

To completely determine the tangential field, it now suffices to give the variation of the gap voltage in terms of the frequency. It turns out that, for unit voltage excitation, the variation is practically the same for all geometrical parameters considered, and follows a quasi-universal curve given in Fig. 9. At low frequencies, V_g obviously approaches one, i.e., the exciting voltage.

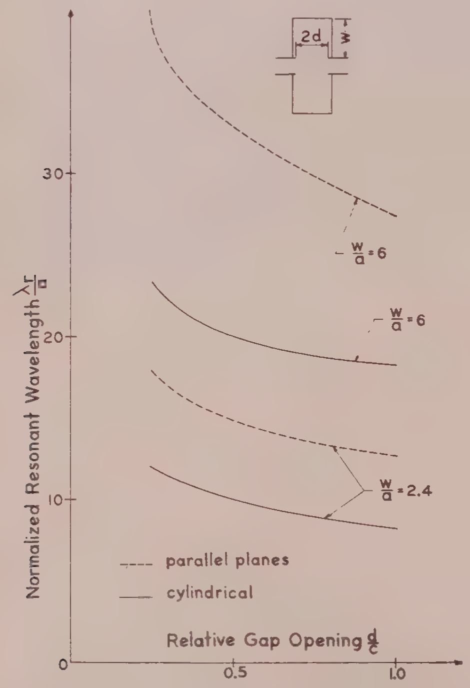

FIG. 10. Resonant wavelength for a cavity with square cross section, (i.e., $2c/w=1$). Several values of the outer radius are considered.

B. Resonant Frequency

The "gap voltage vs frequency" curve indicates quite accurately where the resonant frequency lies. A whole set of curves were obtained for various parameter values, and the results are presented in Figs. 10 to 12, where it was found convenient to plot the resonant wavelength in terms of a characteristic dimension of the structure, a in this case. It is interesting to notice that the resonant frequency decreases fast as the lips of the gap come close together. This is not a surprising phenomenon. The re-entrant klystron cavity shows the same characteristic behavior, as evidenced by the upper curve[5] of Fig. 13. In simple circuit terms, the resonant frequency decreases because the capacitance between the two re-entrant parts becomes very large as the latter come close together. The structure we are interested in has less capacitance, because of the penetration of the fields within the inner tube, and it is not surprising, on the basis of this simple qualitative picture, to find that its resonant frequency remains higher than that of a re-entrant structure of comparable dimensions. This point is evidenced in Fig. 13.

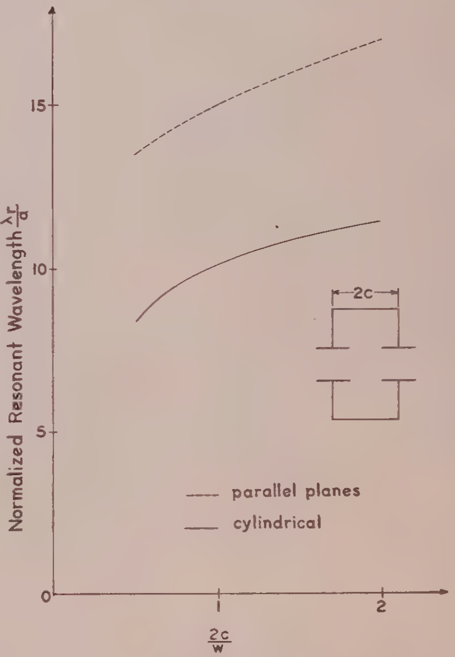

FIG. 11. Resonant wavelength as a function of cavity length (measured by $2c/w$). Constant gap opening ($d/c=0.5$) and constant radii ratio ($b/a=3.4$) are assumed.

---

[5] Taken from T. Moreno, *Microwave Transmission Design Data* (Dover Publications, New York, 1958).

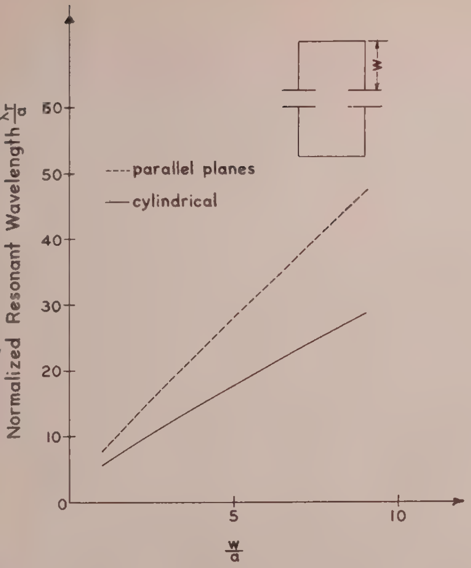

FIG. 12. Resonant wavelength as a function of outer radius (measured by w/a). The gap opening d/c is maintained constant at 0.5, and the cavity cross section is assumed to be square ($2c/w=1$).

C. Electric Field in the Accelerator Tube

Once $s(z)$ is found, it becomes a simple matter, in principle at least, to obtain the axial electric field E_z by simple substitution in (6) and (13). Typical curves

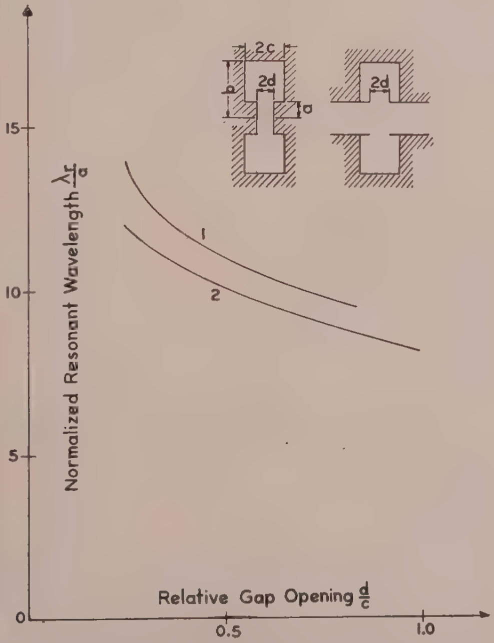

FIG. 13. Comparison between the resonant wavelengths of a re-entrant cavity ($b/a=3.5$, $c/a=1.2$, curve 1) and a comparable accelerator structure ($b/a=3.4$, $c/a=1.2$, curve 2).

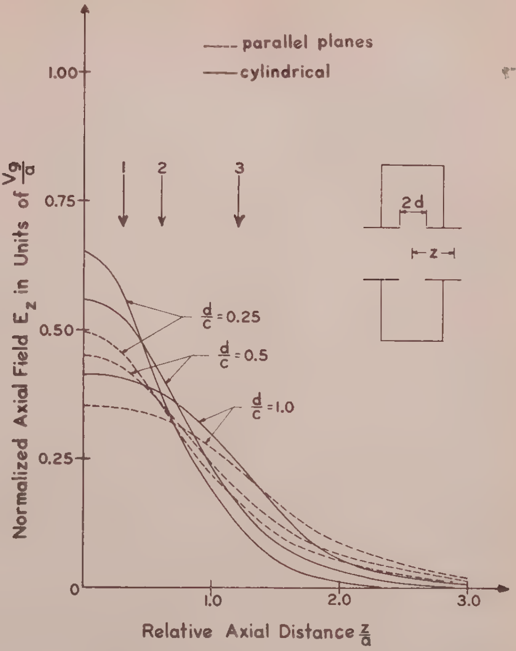

FIG. 14. Normalized axial field on axis of accelerator at resonant frequency. Geometric parameters are $2c/w=1$ (square cross section) and $b/a=3.4$. Arrows 1, 2, and 3 indicate positions right under the lips of the gap for d/c equal to 0.25, 0.50, and 1, respectively.

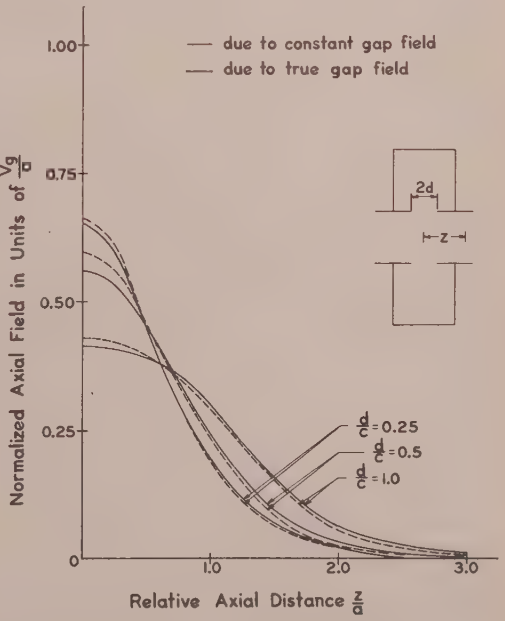

FIG. 15. Comparison between axial field of accelerator at resonant frequency for (a) actual gap field (b) constant gap field. Geometric parameters are $2c/w=1$ (square cross section) and $b/a=3.4$.

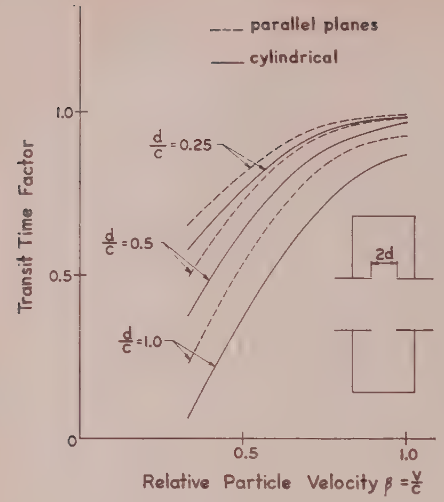

FIG. 16. Transit-time factor at resonant frequency. Geometric parameters are $2c/w=1$ (square cross section) and $b/a=3.4$.

are shown in Fig. 14 for points on the axis of symmetry of the structure. The field is obviously proportional to the gap voltage, and is expressed in terms of V_g/a, a unit which has the right dimensions volt m^{-1}. In each case the curve is drawn at the resonant frequency of the surrounding cavity. Curves for other values of the geometric parameters[6] show similar behavior, except that the fields are more spread out when the gap opening is larger, and show a tendency to peak right under the lips of the gap when the dimensions of the inner tube decrease. This effect is naturally more pronounced for points halfway between the axis and the gap. In the limit, the gap distribution itself is obtained as the tube boundary is approached. The relevant curves are not shown because of space limitations.

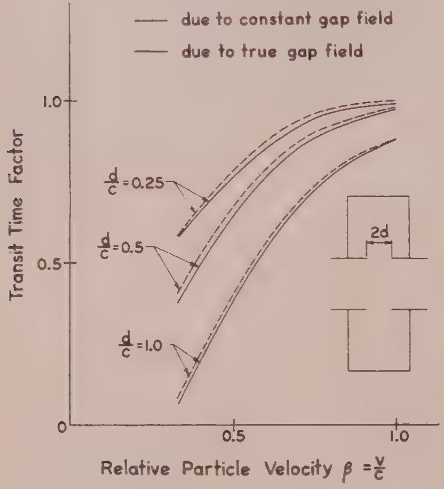

FIG. 17. Comparison between transit-time factor at resonant frequency for (a) actual gap field (b) constant gap field. The configuration is of the circular type, with geometric parameters $2c/w=1$ (square cross section) and $b/a=3.4$.

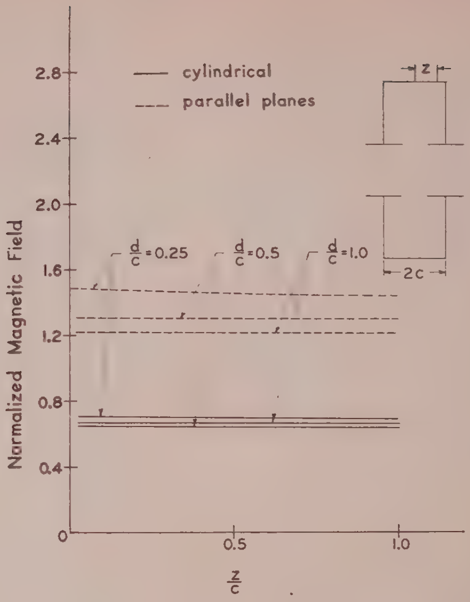

FIG. 18. Magnetic field at outer cavity wall. The structure is at resonance, and geometric parameters are $2c/w=1$ (square cross section) and $b/a=3.4$. The magnitude of the field, in ma/m, is obtained by multiplying the ordinate by V_g/a (expressed in volt/m).

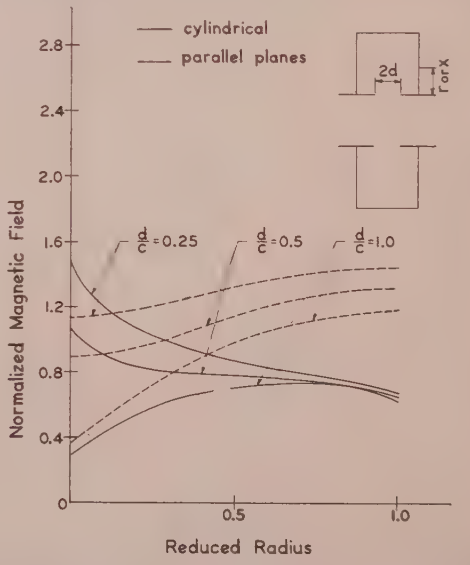

FIG. 19. Magnetic field at the face of the cavity, in the same conditions as in Fig. 18. The "reduced radius" is $r-a/w$ for the circular configuration, $x-a/w$ for the parallel planes case.

---

[6] (a) $w/a=6$, other parameters unchanged, (b) $2c/w=0.5$, 1.2; $d/c=0.5$; $w/a=2.4$, (c) $2c/w=1$; $d/c=0.5$; $w/a=1$, 2.4, 6.

To answer a question raised in the introduction, E_z along the axis was plotted (1) for the actual gap field, (2) for a constant gap field. Figure 15 shows that very little difference results, and that the field on the axis is quite insensitive to the actual structure of $\mathbf{E}_t$. The same conclusion holds for the other sets of parameters we considered[6]: the deviation was never more than 20%. More important differences will be found closer to the tube boundary.

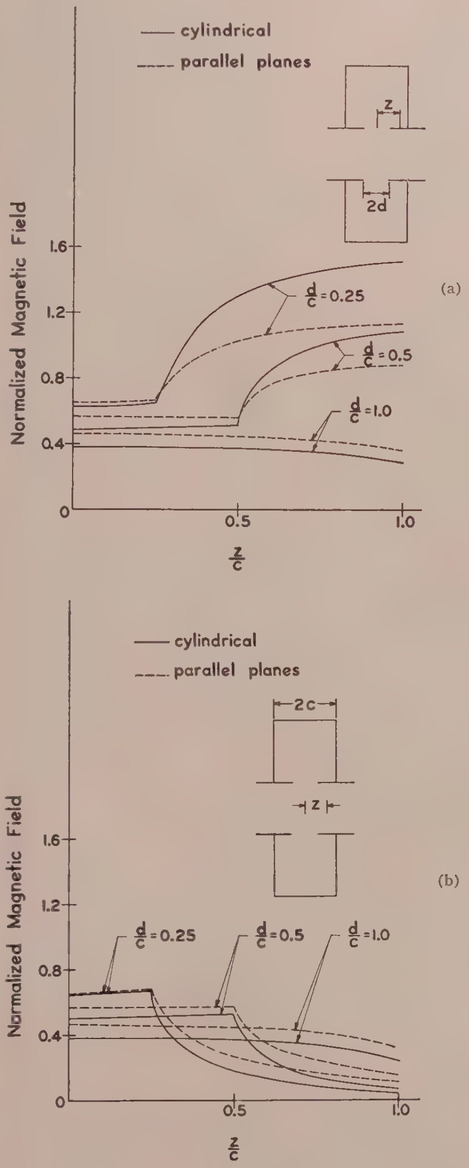

FIG. 20. Magnetic field at the boundary surface between tube and cavity: (a) on the cavity side (b) on the inner tube surface. Conditions are as in Fig. 18. The region to the left of the discontinuity corresponds to the gap opening, and is obviously common to both graphs. The region to the right corresponds to points at the metallic boundary, and is evidently absent for full gap opening ($d/c=1$).

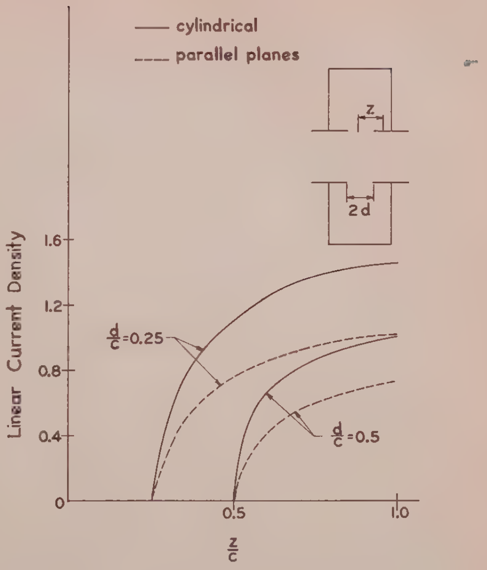

FIG. 21. Linear current density in the metallic boundary between tube and cavity. Conditions are the same as in Fig. 18.

One is often less interested in the details of the electric field than in the total energy kick which a particle experiences as it travels down the accelerator axis. With the usual assumption of a negligible velocity change across the gap region, the particle trajectory can be written as;

$$z=v(t-t_0)=\beta c(t-t_0)$$

and the energy kick becomes;

$$\begin{aligned}\Delta\mathcal{E}&=q\int_{-\infty}^{+\infty}E_z(z)\cdot\cos\omega t(z)\cdot dz\\&=qV_g\cos\omega t_0\left\{2\int_0^{\infty}\frac{E_z(z)}{V_g}\cdot\cos\frac{kz}{\beta}\cdot dz\right\}.\end{aligned}$$

The quantity between brackets, which represents the loss of voltage due to transit-time effects, is plotted in Fig. 16 for a representative set of geometric parameters. A comparison between the actual value of this transit-time factor, and the value which one would obtain on the basis of a constant gap field, is given in Fig. 17. There, again, very little difference is to be noticed.

D. Currents in the Walls

It is interesting, particularly for the calculation of losses in the walls, to know how strong the current density is at various points of the metallic boundary. Pertinent data for the magnetic field at the boundary (which, in mks units at least, is numerically equal to the linear current density) are given in Figs. 18 to 21.

The usual representative set of parameters has been used, but the results for other configurations[6] do not differ significantly from those presented. The fields are plotted at the resonant frequency, and their values correspond to the lowest resonant mode.

Before concluding this paragraph, we would like to give an approximate idea of the time it took to perform the various operations on the MURA IBM 704 computer:

(a) Calculate the electric field throughout a gap, with $p=6$: 3 to 4 min.
(b) Calculate the axial field E_z at a point on the axis: 12 sec.
(c) Calculate a transit time factor: less than 1 sec.
(d) Calculate a magnetic field at the boundary: less than 10 sec.

IV. EXPERIMENTAL CHECK

To get an idea of the accuracy of the computer results, we measured the resonant frequency of a model cylindrical cavity with dimensions $a=1.125$ in., $b/a=3.4$, $2c/w=1$, and $d/c=0.5$. The resonant frequency can be read off Fig. 10. The relevant point was determined to an accuracy of 0.05%, and yields a (computer) value of 1041 Mc. The measured value was 1034 Mc, satisfactory in view of the finite Q of the experimental device and the inevitable departure from ideal mechanical dimensions. The thickness of the inner tube, for example, was 0.01 in. instead of being vanishingly small. With the same geometrical proportions, a parallel plane configuration would yield a resonant frequency of 701 Mc. To check that the resonant frequency of a "flattened" cavity of the type shown in Figure 1(c) falls between these limits, a model with $L=4.59$ in. $=0.6\times$the outside diameter was constructed. The resonant frequency was found to be 811 Mc, showing that a rather modest "flattening ratio" brought us quite close to the figure calculated for the parallel plane configuration.

ACKNOWLEDGMENTS

The authors wish to acknowledge the support of the Midwestern Universities Research Association and of the National Science Foundation. The cavity models were ably made by R. Langdon and L. Marty.

JOURNAL OF APPLIED PHYSICS VOLUME 32, NUMBER 9 SEPTEMBER, 1961

Application of the Three-Parameter Stress Function to Natural Rubbers of Widely Different Hardness

A. J. CARMICHAEL
School of Civil Engineering, University of New South Wales, Sydney, Australia

AND

H. W. HOLDAWAY
Division Textile Physics, Commonwealth Scientific and Research Organization, Sydney, Australia

(Received March 20, 1961)

The previously reported three-parameter stress function has been applied to natural rubbers similar to those used for engineering purposes. These rubbers were selected to cover a harness range from 30 to 80 British Standard Degrees. A suitable choice of values for the parameters A, B, and β was found to give a good description of the stress-strain characteristics in pure shear, and positive and negative stretch squeeze. This agreement applied up to the maximum possible strains. Unique functional relationships were found to exist between the three parameters and rubber hardness. Theoretically, it would be possible to reduce the three-parameter stress function to a single-parameter stress function. As previously reported, this confirms and hence is indirectly confirmed by Blackwell's results [Trans. I. R. I. **28**, 75 (1952)].

IN a previous paper,[1] the three-parameter stress function shown below was developed.

$$\psi(x)=\tfrac{1}{2}\cdot A\exp\{\beta[x^{\frac{1}{2}}-(x^{-1})^{\frac{1}{2}}]\}-B(x+x^{-1}-2). \quad (1)$$

This stress function was found to yield stress vs strain relationships which were in good agreement with some experimental results due to Treloar.[2] It is the purpose of this paper to show that this three-parameter stess function gives a good representation of the measured stress-strain characteristics of a wide range of commercial natural rubbers. The hardness of these rubbers ranged from 30 to 80 British Standard Degrees. Details of the various compounds used are given in Appendix 1.

---

[1] A. J. Carmichael and H. W. Holdaway, J. Appl. Phys. **32**, 159 (1961).

[2] L. R. G. Treloar, Rubber Chem. and Tech. **17**, 813 (1944).

In this work, special specimens were prepared for esting in torsion, compression, and tension. Details of hese tests are given below.

LIST OF SYMBOLS

ymbol	Description	Dimensions
A	A material parameter	FL^{-2}
a	Radius of circular specimen	L
B	A material parameter	FL^{-2}
B.S.D.	Hardness, British Standard Degrees (Similar to Shore A scale)	
C_1	A material parameter	FL^{-2}
C_2	A material parameter	FL^{-2}
f_1	Force per unit of original area, or nominal stress	FL^{-2}
G	Modulus of Rigidity	FL^{-2}
k	A variable = tanσ	. . .
L	Torque	FL
γ	An arbitrary radial distance from the axis of a round specimen	L
t_{12}	Shear stress	FL^{-2}
x	A dummy variable	. . .
α	A specific principal extension ratio	. . .
β	A material parameter	. . .
ρ	Twist rate per unit length	L^{-1}
σ	Shear strain in simple shear	. . .
$\psi()$	Indicates some functional dependence	. . .

TORSION TESTS

Shear stress-strain data were obtained from torsion ests on right circular cylinders. These cylinders, which were 2 in. long, and with diameters of 1, 1½, and 2 in., were twisted at constant length. The torque was applied over the parallel ends of the cylinders. This was effected by cementing the end faces of the cylinders to steel torsion plates with a modified phenolic adhesive. The theoretical basis of a procedure for deducing shear stress-strain data from torque vs twist rate data is set out in Appendix 2.

In both Fig. 1, which covers moderate shear strains (up to 0.6), and Fig. 2 which covers large shear strains (up to 4.0), the theoretical relationship represents the observed data very well, with the appropriate choice of parameters A and β.

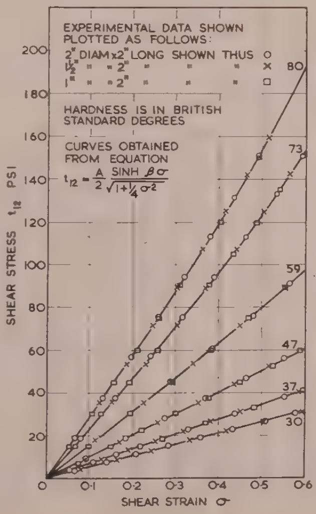

Fig. 1. Shear stress-strain curves for rubbers of different hardness. Moderate strains.

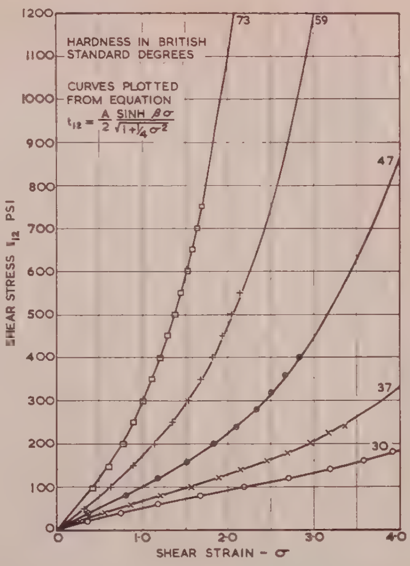

Fig. 2. Shear stress-strain curves for rubbers of different hardness. Large strains.

It is interesting to note from Figs. 1 and 2 the nonlinearity of the relationship between shear stress and shear strain, especially for large strains. The harder the rubber, the more pronounced is the departure from linearity. For soft rubbers experiencing moderate strains, the commonly used assumption of linearity between shear stress and shear strain seems reasonable. The same cannot be said, however, for the harder rubbers. This means that the parameter G of the statistical–kinetic theory, and the parameters C_1 and C_2 of the simple Mooney theory, do not adequately represent the characteristics of the harder engineering rubbers.

Values of the parameters A and β were obtained from the experimental data using Eqs. (26) and (27) of the previous paper. In Figs. 1 and 2, curves of the relation given by Eq. (2) were drawn through the appropriate sets of experimental points.

$$t_{12}=A/2\cdot\frac{\sinh\beta\cdot\sigma}{(1+\frac{1}{4}\sigma^2)^{\frac{1}{2}}}. \tag{2}$$

COMPRESSION TESTS

In order to evaluate the third parameter B, additional tests were required. These tests may be compression, extension, or two-dimensional extension. Simple compression tests were used again for this purpose.

The specimens used for these tests were right circular cylinders 2 in. in diameter and 1 in. long. Simple compression was obtained by compressing the specimens between steel plates with highly polished loading

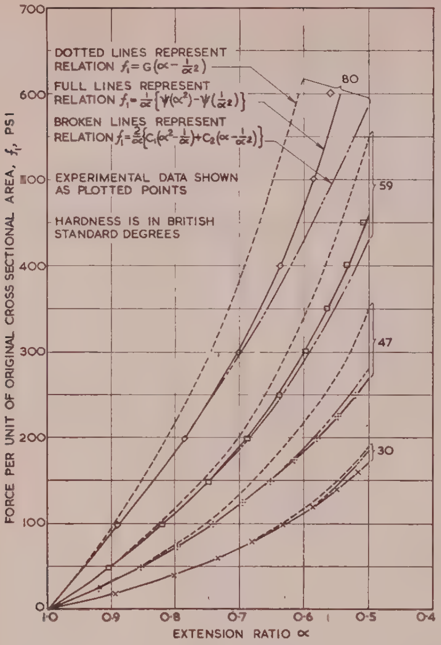

FIG. 3. Simple compression stress-extension curves for rubbers of different hardness. Comparison with various theories.

surfaces. These surfaces, and the parallel end faces of the specimens, were lubricated with a thin film of petrolatum immediately before the tests were made. The deformed shape of the specimens was taken as an indication of the effectiveness or otherwise of these "frictionless" compression tests.

The experimental data obtained for these specimens is shown in Fig. 3. Values for the parameter B were calculated to fit the data at $\alpha=0.7$. A summary of the values found for the parameters A, B, and β is given in Table I. Hardness values shown were the means of 20 readings.

Curves of the relation given in Eq. (3) are shown drawn through the corresponding sets of experimental points.

$$f_1=\tfrac{1}{2}\cdot\alpha^{-1}[A\{\exp\beta(\alpha-\alpha^{-1})-\exp-\beta(\alpha^{\frac{1}{2}}-\alpha^{-\frac{1}{2}})\}\\ -2B(\alpha^2+\alpha^{-2}-\alpha-\alpha^{-1})]. \quad (3)$$

TABLE I. Summary of values found for parameters A, B, and β.

Hardness British Standard Degrees	Hardness Shore A scale	β	A	B	$G=(A\beta/2)$	Source
...	...	0.528	215	1.56	56.7	Treloar
30	31	0.528	204	−9.5	63.8	Author
37	39	0.66	212	−18.0	70.0	Author
47	48	0.88	228	−25.0	100.4	Author
59	60	1.15	262	−32.5	150.8	Author
73	73	1.50	310	−67.1	233	Author
80	79	1.68	338	−108.0	284	Author

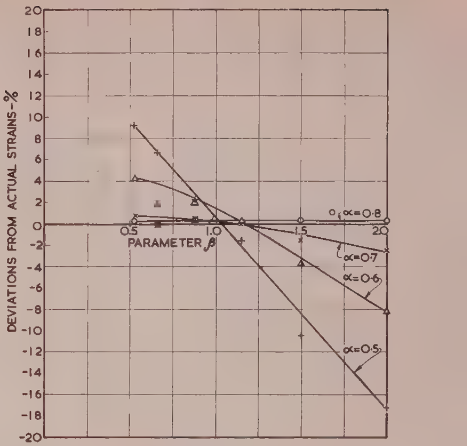

FIG. 4. Deviations between measured compressive strains and strains predicted by the simple Mooney theory.

In Fig. 3 a comparison is also shown between three theories using one-, two-, and three-material parameters. The three-parameter method is in good agreement with the experimental results as indicated previously. In all cases the statistical-kinetic theory predicted strains that were less than the actual strains. The simple Mooney theory with parameters C_1 and C_2 predicted strains that were less than actual strains up to a hardness of about 52. Above this hardness the predicted strains were greater than actual strains. In other words, at a hardness of about 52, the simple Mooney theory agrees reasonably well with the experimental results. At this value of hardness, $\beta=1$. This effect is shown diagrammatically in Fig. 4. For the condition where β

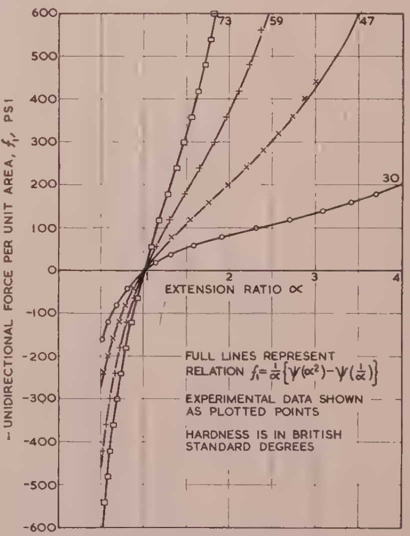

FIG. 5. Unidirectional stress-extension curves for rubbers of different hardness.

is unity, the modified relations given by Eqs. (4) and (5) apply for moderate strains.

$$C_2=\tfrac{1}{2}B, \tag{4}$$

$$C_1=\tfrac{1}{4}A-\tfrac{1}{2}B. \tag{5}$$

EXTENSION TESTS

Extension tests were also made on a series of rubber cylinders 1 in. in diameter and 12 in. long. Steel tags were cemented to the ends of the specimens so that they could be gripped and stretched in a testing machine. Extension measurements were made over the central 2 in. of specimen length. Some results of these tests are shown in Fig. 5. Here the experimental data are shown as plotted points, while the relation given in Eq. (3) is shown as continuous lines through the corresponding groups of points.

In order to present a complete picture for unidirectional stress, the compression data has been included. The agreement between measured strains and strains predicted by Eq. (3) is seen to be excellent.

VARIATION OF PARAMETERS *A*, *B*, AND β WITH RUBBER HARDNESS

Unique relationships were found to exist between the parameters *A*, *B*, β, and rubber hardness. These relationships are shown in Fig. 6. The simplest relationship is that between β and rubber hardness, and this is nearly linear.

The parameter *B* was found to be negative for all of the group of rubbers tested. The nature of the relationship between *B* and rubber hardness, together with the value of *B* calculated for Treloar's material, suggests the possibility of a zero value for *B* with a soft gum vulcanizate. This would explain the good agreement often obtained between simple theories and data from soft gum vulcanizates at moderate strains. However, it should be understood that it is difficult to determine accurately the hardness of soft rubbers in the vicinity of 30 British Standard Degrees.

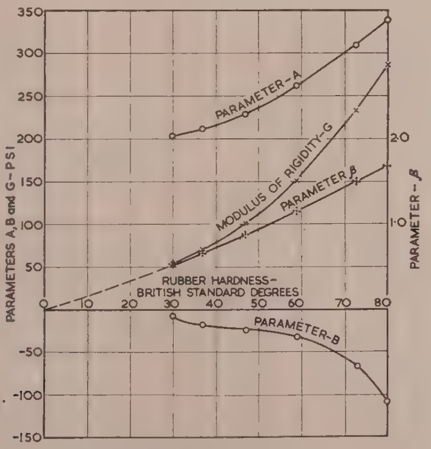

FIG. 6. Relationship between rubber hardness and the parameters *A*, *B*, β, and *G*.

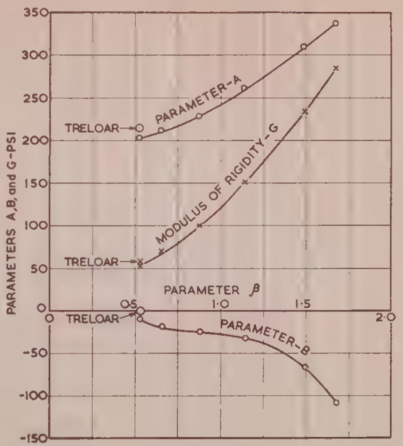

FIG. 7. Relationship between *A*, *B*, *G*, and β. Comparison with values of *A*, *B*, and *G* computed from Treloar's data.

COMPARISON WITH TRELOAR'S DATA

A direct comparison with the values of *A*, *B*, and β computed from Treloar's data may be made if Fig. 6 is replotted using β as the independent variable. This has been done in Fig. 7. The values of *A*, *B*, and *G* for Treloar's material are considered to be in reasonable agreement with the author's results. The difference between the values of *A* and *G* for Treloar's rubber and the author's rubber of 30 B.S.D. hardness was about 5%. This difference could be the result of differences in the rubbers used. It is possible that rubbers from different sources, and possibly with different composition, and prepared with different processing techniques, could have different sets of characteristic curves for *A*, *B*, and β.

MODULUS OF RIGIDITY

A unique relationship was found to exist between the modulus of rigidity and rubber hardness. This relationship was indicated previously in Fig. 6. Here it would appear to be reasonable to extrapolate the modulus of rigidity curve to give zero rigidity for zero hardness. If this is the case, then it would be necessary for either *A* or β to be zero for zero hardness, as $G=A\beta/2$. It is most likely that β tends to zero for zero hardness as shown in Fig. 6, whereas *A* appears to be approaching a finite value of approximately 180 psi.

CONCLUSIONS

It has been shown that the three-parameter stress function in Eq. (1) is excellent for describing the shear and unidirectional stress-strain characteristics of a group of natural rubbers of widely differing hardness. The three-parameter method was also shown to be superior to the single-parameter statistical-kinetic theory and the two-parameter simple Mooney theory. This superiority was shown to be the result of nonlinear shear in practical rubbers. The two simple theories mentioned above are based upon the postulate of linear shear.

It was also demonstrated that unique relationships existed between A, B, G, β, and rubber hardness. A fundamental near-linear relationship was shown to exist between rubber hardness and β. It was then shown that unique relationships existed between A, B, G, and β. In fact, this relationship, as shown in Fig. 7, indicates that it would be possible to reduce the three-parameter stress function of Eq. (1) to a relationship (admittedly inconvenient and complex) in which only one of the parameters A, B, β, or G need be used to typify the particular rubber.

APPENDIX 1

Composition of Natural Rubber Compounds Used for Thesis Investigations

The following compounds were prepared and supplied by the Hardie Rubber Company, Ltd. of Sydney, Australia.

Pure Gum Vulcanizate

B.S.D. *Hardness=30*

Rubber	100 parts
Sulphur	1 part
Zinc oxide	2 parts
Stearic acid	1 part
Accelerator	$\frac{1}{4}$ part

Reinforced Rubbers

B.S.D. *Hardness=37*

Rubber	100 parts
Sulphur	1 part
Zinc oxide	2 parts
Stearic acid	1 part
Accelerator	$\frac{1}{4}$ part
Carbon black	5 parts

B.S.D. *Hardness=47*

Rubber	100 parts
Sulphur	2 parts
Zinc oxide	15 parts
Stearic acid	1 part
Accelerator	1 part
Medium Thermal Black	30 parts

B.S.D. *Hardness=59*

Rubber	100 parts
Sulphur	2 parts
Zinc oxide	20 parts
Stearic acid	2 parts
Accelerator	1 part
M.T.B.	75 parts

B.S.D. *Hardness=73*

Rubber	100 parts
Sulphur	$2\frac{1}{2}$ parts
Zinc oxide	5 parts
Stearic acid	2 parts
Accelerator	1 part
M.T.B.	100 parts

B.S.D. *Hardness=80*

Rubber	100 parts
Sulphur	$3\frac{1}{2}$ parts
Accelerator	1.2 parts
Softener	5 parts
Rubber clay	100 parts
E.P.C. black	30 parts
S.R.F. black	30 parts

APPENDIX 2

At a radial distance r from the axis of a cylinder of radius "a" experiencing a twist rate of ρ radians per unit length, the shear strain σ satisfies the relation

$$\rho\times\gamma=\tan\sigma=k. \tag{A1}$$

If t_{12} is the shear stress at the radial distance r, then the torque L developed is given by Eq. (A2).

$$L=2\pi\int_0^a t_{12}\cdot\gamma^2\cdot dr. \tag{A2}$$

Substituting from Eq. (A1) into Eq. (A2) leads to the relationship

$$\rho^3\cdot L=2\pi\int_0^{a\rho} t_{12}\cdot k^2\cdot dk. \tag{A3}$$

In this integral, t_{12} is a function of $k=\tan\sigma$, and is in effect prescribed only by the rubber properties. The cylinder radius and twist rate appear through the substitution of the upper limit in the indefinite integral. On differentiating Eq. (A3) and rearranging,

$$t_{12(\sigma=\tan^{-1}a\rho)}=\frac{1}{2\pi a^3}[3L+\rho(dL/d\rho)]. \tag{A4}$$

Equation (A4) was used to determine shear stress vs shear strain data from torque–twist rate data.

OURNAL OF APPLIED PHYSICS VOLUME 32, NUMBER 9 SEPTEMBER, 1961

Effect of Temperature on the Exoemission of Electrons from Abraded Aluminum Surfaces

W. T. Pimbley and E. E. Francis
IBM General Products Division, Development Laboratory, Endicott, New York

(Received March 20, 1961)

A model and resulting theory for the exoemission of electrons from metal surfaces are presented. The model states that the exoemission is governed by the diffusion of vacancies in the metal, vacancies created by the abrasion. A vacancy, upon diffusing to the surface, may give up its energy to an electron. However, when in the same event, a photon also transfers its energy to the electron, the electron may be emitted. Experiments performed show the exoemission decay to be composed of two exponential decays. Both exponential decay constants vary with temperature according to the equation:

$$k=Fe^{-E/RT}.$$

Here, F is a constant and E is an activation energy which, measured, approximates 5.6 kcal/mole. A comparison between experiment and theory give the theory corroboration.

INTRODUCTION

When a metal undergoes a structural change such as is encountered in cold working, irradiation, or a phase change, the metal may emit electrons spontaneously for some time after such structural change has taken place. This phenomenon of exoemission was first reported by J. Kramer[1] in 1950. An excellent review article by L. Grunberg[2] was published in 1958.

W. Edlinger and H. Muller,[3] and L. Grunberg and K. H. R. Wright[4,5] have found that illuminating the surface with light greatly increases the exoemission. Indeed, in a great many cases, exoemission is impossible without such illumination. In those cases where illumination is necessary, it has been found that the exoemission effect is to shift the photoelectric threshold to much longer wavelengths than exist in the pure photoelectric emission. In the experiment described in this paper, illumination of the surface is necessary.

J. Lohff,[6] in his paper of 1956, mentioned that temperature affects the over-all intensity of the emission. However, his conclusions do not agree with the conclusions of this paper. He stated that a rise in temperature results in a drop in the over-all intensity of the emission.

A purpose of this paper is to present a mechanism for exoemission, a mechanism already introduced by T. C. Ku and W. T. Pimbley.[7] The paper also proposes to show the effect of temperature on exoemission. Furthermore, the experimental results will be compared with the theory emanating from the proposed model.

THEORY

The model proposed in this paper states that the exoemission of electrons from metal surfaces is associated with the diffusion of vacancies in the metal. The vacancies are created by some process such as abrasion, cold working, or irradiation. Many of these vacancies then diffuse to the surface. When a vacancy is in the region of the surface, it can be annihilated spontaneously after some time, statistical in nature, and transfer its energy to an electron. In general, this energy will not be sufficient to enable the electron to be emitted. If, however, a photon strikes the surface in the neighborhood of a vacancy, an induced annihilation can take place wherein an electron can receive the energy from both the vacancy and the photon. If this total energy is equal to or greater than the work function of the metal surface, then the electron can be emitted as an exoelectron.

The diffusion of vacancies in a metal crystal is a random walk process. The flux of vacancies across any plane is given by:

$$J=-D\,\mathrm{grad}\rho, \tag{1}$$

where ρ is the vacancy density. D, the diffusion constant, is temperature dependent according to the equation:

$$D=D_0e^{-E/RT}, \tag{2}$$

where E is the activation energy for the diffusion, R is the universal gas constant, and T is the absolute temperature. The temperature dependence of exoemission results from this dependence on temperature of the diffusion constant.

The continuity expression used in this derivation is:

$$\partial\rho/\partial t=-\mathrm{div}J, \tag{3}$$

where t is the time. The resulting second-order differential equation is:

$$\partial\rho/\partial t=D(\partial^2\rho/\partial x^2), \tag{4}$$

where x is the distance perpendicular from the surface. In obtaining Eq. (4), one considers plane symmetry to prevail.

Boundary conditions are imposed both at the surface and at a distance l below the surface. This distance l

---

[1] J. Kramer, *Der Metallische Zustand* (Vanderhoeck und Ruprecht, Göttingen, Germany, 1950).

[2] L. Grunberg, Brit. J. Appl. Phys. **9**, 85 (1958).

[3] W. Edlinger and H. Muller, Österr. Akad. Wiss. Math.-naturw. Kl., Anz. **91**, 89 (1954).

[4] L. Grunberg and K. H. R. Wright, Nature **171**, 890 (1953).

[5] L. Grunberg and K. H. R. Wright, Proc. Roy. Soc. (London) **A232**, 423 (1955).

[6] J. Lohff, Z. Physik **146**, 436 (1956).

[7] T. C. Ku and W. T. Pimbley, J. Appl. Phys. **32**, 124 (1961).

represents the depth of deformation caused by the abrasion. The boundary conditions are:

at $x=0$:

$$\partial\rho/\partial x=K\rho \tag{5}$$

at $x=1$:

$$\partial\rho/\partial x=-K\rho, \tag{6}$$

where K is a positive constant. A solution for the boundary value problem is:

$$\rho_n=\exp(-\lambda_n^2Dt)[\cos\lambda_nx+(K/\lambda_n)\sin\lambda_nx], \tag{7}$$

where the possible λ_n's are given by:

$$\tan\lambda_nl=2\lambda_nK/(\lambda_n^2-K^2). \tag{8}$$

A general solution of the problem can be written as a sum of the solutions shown in Eq. (7). The solution for $\lambda=0$ is a trivial solution. Also the solutions for negative λ's are the same as for positive λ's. Therefore, a general solution can be expressed as a sum from $n=1$ to infinity. So:

$$\rho=\sum_{n=1}^{\infty}C_n\exp(-\lambda_n^2Dt)\cdot\psi_n, \tag{9}$$

where the eigenfunction is:

$$\psi_n=\cos\lambda_nx+(K/\lambda_n)\sin\lambda_nx. \tag{10}$$

The initial conditions may be written:

$$\rho_{\text{initial}}=\sum_{n=1}^{\infty}C_n\psi_n. \tag{11}$$

Since it can be shown that the eigenfunctions form an orthogonal set, one can write:

$$C_n=\int_0^l\rho_{\text{initial}}\psi_ndx\bigg/\int_0^l\psi_n^2dx. \tag{12}$$

Or, one can prove:

$$C_n=\frac{2\lambda_n^2}{(\lambda_n^2+K^2)l+2K}\int_0^l\rho_{\text{initial}}\psi_ndx. \tag{13}$$

It is helpful at this point to break the problem into two cases. In case A, from Eq. (8):

$$\begin{gathered}\sin\lambda_nl=2\lambda_nK/(\lambda_n^2+K^2)\\ \cos\lambda_nl=(\lambda_n^2-K^2)/(\lambda_n^2+K^2).\end{gathered} \tag{14}$$

Case A is for the odd values of n. Case B, for the even values of n, is:

$$\begin{gathered}\sin\lambda_nl=-2\lambda_nK/(K^2+\lambda_n^2)\\ \cos\lambda_nl=(K^2-\lambda_n^2)/(K^2+\lambda_n^2).\end{gathered} \tag{15}$$

For case A, the equation used to find the λ_n's can be found from Eqs. (14):

$$(\lambda_nl/2)\tan(\lambda_nl/2)=lK/2. \tag{16}$$

In a like manner, the equation for case B from Eqs (15), is:

$$(\lambda_nl/2)\cot(\lambda_nl/2)+(Kl/2)=0. \qquad (17$$

Choose for the initial conditions:

$$\rho_{\text{initial}}=\rho_0(1-\delta x), \qquad (18$$

where δ is a constant such that:

$$0<\delta<1/l, \qquad (19$$

and ρ_0 is also a constant. Using Eq. (13), the values o C_n for case A are:

$$C_n=\frac{2\rho_0K(2-\delta l)}{(\lambda_n^2+K^2)l+2K} \qquad (20$$

and for case B:

$$C_n=\frac{2\delta\rho_0(2+Kl)}{(\lambda_n^2+K^2)l+2K}. \qquad (21$$

In the model presented here, the rate of electro emission is taken to be proportional to the flux o vacancies across the surface. From Eqs. (1) and (9), th flux across the surface is:

$$J=-\sum_{n=1}^{\infty}C_nK\exp(-\lambda_n^2Dt). \qquad (22$$

In the experiment reported in this paper, it is impossibl to observe all but the first two or three terms. This i due to the fact that the other terms decay to negligibl values by the time data can be taken. One can therefor write that the rate of electron emission I is:

$$I=\Gamma D\bigg\{\frac{K(2-\delta l)}{(\lambda_1^2+K^2)l+2K}\exp(-\lambda_1^2Dt)+\frac{\delta(2+Kl)}{(\lambda_2^2+K^2)l+2K}\exp(-\lambda_2^2Dt)+\frac{K(2-\delta l)}{(\lambda_3^2+K^2)l+2K}\exp(-\lambda_3^2Dt)\bigg\}. \qquad (23$$

In this expression, Γ is the proportionality constant tha depends on many factors such as light intensity an frequency, surface conditions and work functions.

EXPERIMENTAL

Apparatus

The experimental arrangement mentioned briefly i a previous paper,[7] was retained in this work and facilitie were added for controlling the specimen temperature For the latter, a circulating line from a constant tem perature bath was connected into a cell of special con struction which replaced the standard sample holde in a Nuclear Chicago model M-5 manual sample changer Details of the cell appear in Fig. 1. For the emissio

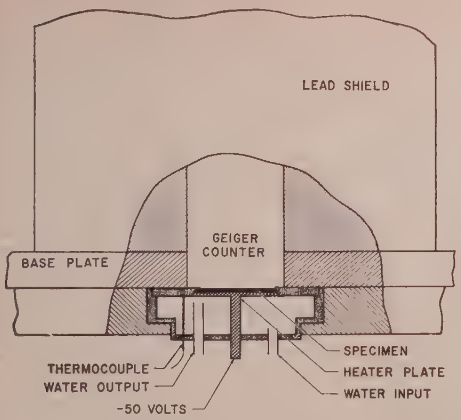

Fig. 1. The temperature control cell shown in position in the Nuclear Chicago model M-5 sample changer.

count the abraded sample mounted in this device was rotated into position under the windowless, open end of a Nuclear Chicago model D47 gas flow Geiger counter. The counting gas had the composition 98.7% helium, 1.3% butane. The signal was amplified in a model D47 preamplifier of the same make and passed to a Hewlett-Packard model 524B electronic counter. This digital scaler was set during operation at a 10-sec gate time giving counts then over a 10-sec interval and resting for the next 10-sec interval. The output was made to drive a H-P model 560A digital recorder. A schematic diagram of the equipment appears in Fig. 2.

Procedure

One-inch diameter specimens were cut from 26-gauge aluminum sheet of 99.999% purity. Standard cleaning techniques were observed but no effort was made to restrict oxide formation. Abrasion was performed using 400 or 600 grade silicon carbide paper from which a saturation level of deformation was reached after four or five passes over the paper. Tests were carried out to verify that no count above the background count could be obtained from the abraded paper itself nor from the freshly cleaned, unabraded aluminum specimen. The background from the Geiger counter amounted to less than 10 counts per 10-sec interval. While the sample was being readied for abrasion a carbon-14 (radioactive) source was maintained in the counting position. This standardizing count—12 000 counts per 10-sec gate time—served as a check on the over-all operation and reproducibility of the system. The high voltage was set for operation in the Geiger region. For each run the time interval between abrasion and start of the count was recorded. During the run the sample was held at a negative potential of 50 v. Illumination reached the sample, from below, through the Lucite temperature control cell. Without such light stimulation only the background count was obtained. A zirconium arc source was used in the first experiments but this was replaced by a "black light" ultraviolet source for higher excitation. This became necessary at the lower temperatures where appreciably lower emission intensities were experienced. The "black light" source contributed an additional 10 counts per 10-sec interval to the background, while there was no measurable rise in the noise level with the other source. For an acceptable run the temperature fluctuation as measured at the sample did not exceed 0.1°C.

Fig. 2. Block diagram of the equipment.

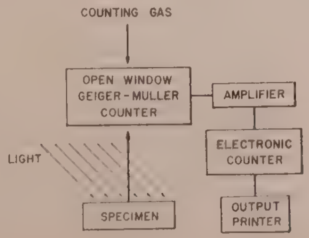

Table I. Values for the first and second decay constants for ten different temperatures.

Temperature °C	k_1 First decay constant $(\text{min})^{-1}$	k_2 Second decay constant $(\text{min})^{-1}$
44.4	0.0144	0.0820
39.6	0.0135	0.0608
36.8	0.0134	0.0805
36.0	0.0108	0.0516
33.7	0.0133	0.0535
32.2	0.00979	0.0487
27.9	0.0102	0.0449
25.4	0.00817	0.0430
15.8	0.00666	0.0325
9.9	0.00480	0.0221

RESULTS

Ten sets of data were taken for the exoemission decay from abraded aluminum. The constant temperature decay curves were taken for temperatures from 9.9° to 44.4°C. The time necessary for the emission to decay to about a sixth of its initial value varied from about 70 min for the high temperature to about 200 min for the low temperature. In one experimental run, taken at a temperature of about 0°C, the time required for decay was about 2200 min. Unfortunately, the temperature varied too much in this run for the decay data to be valid.

The decay curves were analyzed to see if they were composed of a sum of exponential decays. They were analyzed using the graphical method, employing a method reported by Gardner, Gardner, Laush, and Meinke,[8] and utilizing a least mean square fit method. The IBM 704 data processing system was used in the last two methods of analysis. The curves were found to be composed of two exponential decays according to the expression:

---

[8] D. G. Gardner, J. C. Gardner, G. Laush, and W. W. Meinke, J. Chem. Phys. 31, 978 (1959).

$$I=Ae^{-k_1t}+Be^{-k_2t}. \tag{24}$$

The k's that give the best fit are shown in Table I. Shown in Fig. 3 is one of the experimental decay curves and also the two exponential decays that, when added together, give the best fit to the data.

In Fig. 4, the logarithm of the decay constants are plotted versus the reciprocal of the absolute temperature. It can be seen that the decay constants are related to the temperature according to:

$$k=Fe^{-E/RT}, \tag{25}$$

where E is the activation energy, R is the universal gas constant, and T is the absolute temperature. Both the first and the second decay constants have the same activation energy, within experimental error. Furthermore, the ratio of the second to the first decay constant is 4.7.

The theoretical equation (23) compares favorably with the empirical equation (24) when one considers the third term of Eq. (23) to decay out before data can be taken. In Eq. (23), the temperature dependency enters only in D, the diffusion constant [see Eq. (2)]. It can be seen, therefore, that the decay constants should depend on temperature according to Eq. (25), and should have the same activation energy. The exoemission does behave this way.

In Eq. (23), the ratio of the second to the first decay constant is given by:

$$\mathrm{Ratio}=\lambda_2^2/\lambda_1^2. \tag{26}$$

A consideration of Eqs. (16) and (17) will reveal what this ratio should be. These equations are discussed in a text by Carslaw and Jaeger.[9] If K is set equal to infinity,

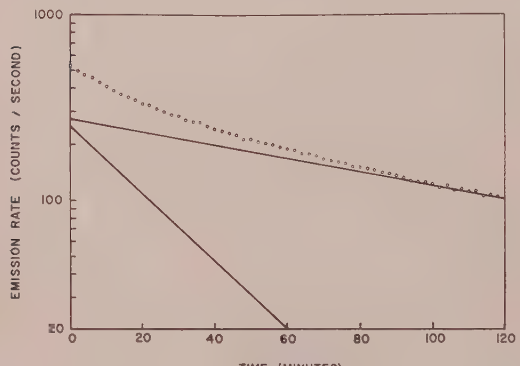

FIG. 3. The decay of exoelectrons from an abraded aluminum sample at a temperature of 25.4° C. The two lines are exponential decays that, when added together, fit the experimental curve.

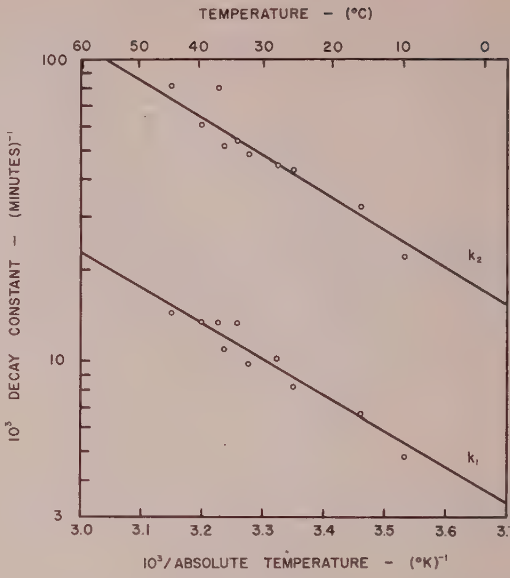

FIG. 4. A plot of the logarithm of the two decay constants vers the reciprocal of the absolute temperature. The activation ener for the first decay constant is 5.5 kcal/mole, and that for the seco constant, 5.7 kcal/mole.

the ratio is four to one. If, however,

$$K=8/l$$

$$\mathrm{Ratio}\approx 4.7. \qquad (2$$

The data is not accurate enough to find a good valı for K. However, this consideration does show that tl theory can and does yield the observed ratio betwe the decay constants.

The coefficients A and B of Eq. (24) are temperatu dependent. Good quantitative data for these coefficien were not taken; however, the tendency was pronounce The coefficients go up with increasing temperature aı down with decreasing temperature. This agrees wi the theoretical equation (23) in that the coefficients a directly proportional to D, the diffusion constant.

No comparison has been made between the activ tion energy found in this experiment, about 5.6 kca mole, and the activation energy for vacancy diffusio The activation energy for the diffusion of magnesiu in aluminum is about 30 kcal/mole.[10,11] However, tl self-diffusion activation energy in aluminum has n been found, nor has it been ascertained whether sel diffusion in aluminum proceeds by the vacancy mecha nism. Here, obviously, is a place where some furth work should be done.

According to the model, the energy necessary for tl emission of an electron is obtained both from a vacanc giving up its energy at the surface and from an impinging photon. Therefore, the condition for the emission of an electron is:

---

[9] H. S. Carslaw and J. C. Jaeger, *Conduction of Heat in Solids* (Clarendon Press, Oxford, England, 1947).

[10] F. Seitz, *The Physics of Metals* (McGraw-Hill Book Cor pany, Inc., New York, 1943).

[11] R. M. Barrer, *Diffusion in and Through Solids* (Cambrid University Press, New York, 1951).

$$E_v + h\nu \geqslant \phi, \tag{28}$$

where E_v is the energy released by a vacancy, h is Planck's constant, ν is the frequency of the light, and ϕ is the work function of the surface. It would be revealing if an experiment were to be performed wherein the shifting of the photoelectric threshold due to exoemission would be measured. From this, one could determine the energy released by a vacancy.

The mechanism and theory presented in this paper have received a great deal of corroboration from the experiments performed. The decay curves are composed of a sum of exponential decays. The behavior of exoemission with temperature agrees with the theory presented.

ACKNOWLEDGMENTS

The authors wish to thank Dr. T. C. Ku for his conception of the vacancy model and for his consultations throughout the experiment. Gratitude is also due W. B. Pennebaker and W. D. VonVoss for their contributions.

JOURNAL OF APPLIED PHYSICS VOLUME 32, NUMBER 9 SEPTEMBER, 1961

Effect of Pressure on the Energy Gap of Bi_2Te_3

CHE-YU LI, A. L. RUOFF, AND C. W. SPENCER
Cornell University, Ithaca, New York

(Received March 24, 1961)

The effect of hydrostatic pressure on the energy gap of Bi_2Te_3 has been investigated in the pressure range one to 30 000 atm. From resistivity measurements as a function of temperature and pressure, it has been determined that the energy gap decreases from 0.171 ev at one atmosphere to 0.104 ev at 30 000 atm, corresponding to $\partial E_g(0)/\partial p = -2\times10^{-6}$ ev/atm.

INTRODUCTION

THE pressure dependence of the energy gap has been reported for Ge,[1] Si,[1] Te,[2] P,[3] InSb,[4] InAs,[5] and GaSb.[6] Results of these investigations have been summarized by Keyes.[7] In these determinations either the intrinsic conductivity measurement method or the optical method was used.

The present investigation of bismuth telluride, Bi_2Te_3, is concerned with the resistivity of single crystals in the intrinsic temperature range at constant hydrostatic pressure. With increasing pressure a significant change in the slope of the intrinsic portion of the resistivity curve is observed, as is to be expected for materials which have a low energy gap. Therefore, the thermal method gives a direct measurement of the change in energy gap with pressure. The mobility variation with temperature of both electrons and holes of Bi_2Te_3 follows an approximate $T^{-\frac{3}{2}}$ law.[8] Uncertainties associated with the values of effective mass and mobility, which are required in the calculation of the energy gap from the intrinsic conductivity measurement, and difficulties associated with the interpretation of the shift in absorption coefficient curve, which is necessary in the optical method, are avoided.

Specimens approximately 0.16 cm wide, 0.018 cm thick, and 0.64 cm long, containing approximately 10^{17} extrinsic carriers per cm^3, were cut from the vicinity of a *p-n* junction of a large single crystal. The crystal was grown from a liquid of 50 weight percent Bi using the Bridgman method. Details of the phase diagram in this region and the procedures used for the crystal growth were given by Satterthwaite and Ure.[9] Bi and Te used were of 99.999+ purity and were obtained from the American Smelting and Refining Company. Specimens were mounted on a baked lava stone mount, which was fitted with spring loaded electrical connections as described in an earlier publication.[10]

The specimen-mount assembly was placed in the pressure chamber under silicon oil (Dow-Corning 200 Fluid). Pressure vessels of the Bridgman type were constructed by shrink-fitting sleeves into an annular cylinder. The pressure was calculated from the total pressure and the piston size. Friction correction was less than 5% of the total pressure. Resistivity lead wires and thermocouple wires were inserted through the lower piston. Details of the pressure vessel design are to be published at a later date.

---

[1] W. Paul, J. Phys. Chem. Solids **8**, 196 (1959).

[2] L.-J. Neuringer, Phys. Rev. **113**, 1495 (1959).

[3] R. W. Keyes, Phys. Rev. **92**, 580 (1953).

[4] R. W. Keyes, Phys. Rev. **99**, 490 (1955).

[5] J. Taylor, Phys. Rev. **100**, 1593 (1955).

[6] J. Taylor, Bull. Am. Phys. Soc. **3**, 121 (1958).

[7] R. W. Keyes, Solid State Phys. **11**, 149 (1960).

[8] N. B. Hannay, *Semiconductors* (Reinhold Publishing Corporation, New York, 1959), p. 421.

[9] C. B. Satterthwaite and R. W. Ure, Jr., Phys. Rev. **108**, 1164 (1957).

[10] M. J. Smith, E. S. Kirk, and C. W. Spencer, J. Appl. Phys. **31**, 1504 (1960).

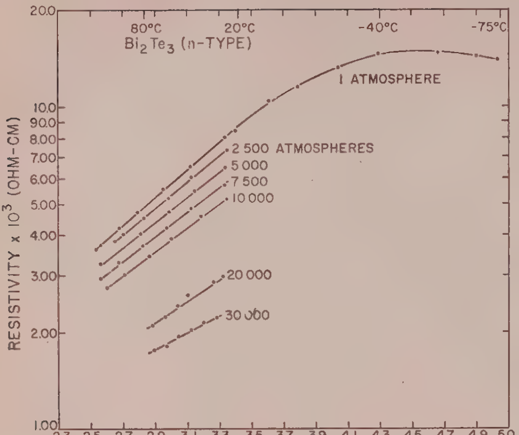

FIG. 1. Resistivity vs reciprocal absolute temperature plots for a Bi_2Te_3, single crystal at seven pressures.

EXPERIMENTAL RESULTS

Typical resistivity vs temperature curves at seven pressures, ranging from one atmosphere to 30 000 atm, are given in Fig. 1.[11] At 1 atm, data were taken from −74°C to 120°C, while at higher pressures, room temperature was the lower temperature limit. The slope of log resistivity vs reciprocal absolute temperature curve in the intrinsic range corresponds to $E_g(0)$ of 0.171 ev at one atmosphere, which is close to the value obtained by Black *et al.*,[12] Harman *et al.*,[13] and Satterthwaite and Ure.[9] It is possible that the present value is more accurate, since the specimen enters the intrinsic range at a lower temperature than has been reported for other specimens. All measurements have been duplicated with the exception of those at 20 000 atm. Data taken at 10 000 atmospheres pressure were obtained in two different types of pressure vessels and were in close agreement. No hysteresis was observed over complete temperature cycles at constant pressures. However, when the pressure was changed, it was necessary to allow several hours for equilibration in order to obtain reproducible data. A similar observation was made by Paul and Pearson[14] who suggested that this effect was due to the trapping in impurity levels.

A plot of values of $E_g(0)$, obtained from the slopes of the curves in Fig. 1, is shown in Fig. 2. There is no abrupt change in slope of this curve, and hence, no indication of phase transformation in the pressure range investigated.

DISCUSSION

Bismuth telluride is rhombohedral, although for convenience it can be represented as a hexagonal lattice.[15] The atomic arrangement has been described in terms o a "layer structure," in which layers or leaves of essentially stoichiometric composition lie perpendicular t the major axis of the unit rhombohedral cell. Each individual layer is composed of atoms in the sequence Te^I $BiTe^{II}$ $BiTe^I$.[16]

The band structure for Bi_2Te_3 is more complex than the band structures of Ge, Si, and intermetallic semiconductors with the zinc-blende structure. Optical and intrinsic conductivity measurements as a function of pressure for these cubic materials are interpreted in terms of three sets of conduction band minima, which shift relative to a valence band which is roughly spherical in shape.[1] In order to explain galvanomagnetic measurements on Bi_2Te_3, Drabble and co-workers[17] suggested a "six-tilted-ellipsoids" model for both the conduction and valence bands. Because of the more complicated band structure, in part a result of the more complex crystal symmetry, the same sets of minima used for the cubic crystals are not applicable to this structure. Within experimental error, Fig. 2, neglecting the value at 20 000 atmospheres, the pressure dependence of $E_g(0)$ shows a slight decrease in slope at higher pressures. This is not easily explained by the shift in band edges.

The energy gap of Se and Te also decreases with increasing pressure, although the decrease is at a faster rate than for Bi_2Te_3. In Se and Te, atoms are located in spiral chains oriented along the *c* axis of the hexagonal unit cell. The angle between adjacent bonds along the

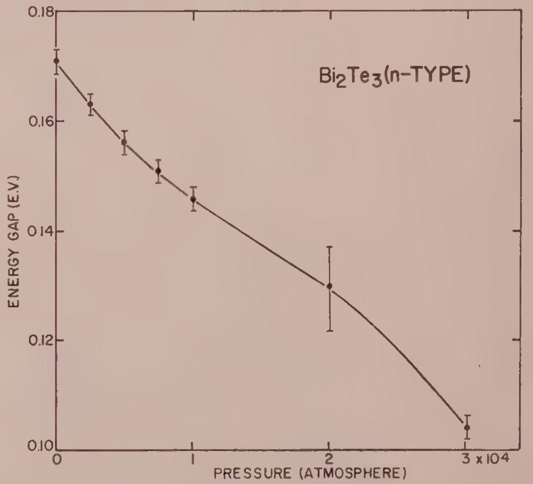

FIG. 2. Energy gas vs pressure for a Bi_2Te_3 single crystal.

---

[11] At the Very High Pressure Conference, Bolton Landing, New York, June, 1960, it was agreed to use the bar as the standard unit of pressure. 1 atmosphere = 1.013 bar.

[12] J. Black, E. M. Conwell, L. Seigle, and C. W. Spencer, J. Phys. Chem. Solids **2**, 240 (1957).

[13] T. C. Harman, S. E. Miller, and H. L. Goering, J. Phys. Chem. Solids **2**, 181 (1957).

[14] W. Paul and G. L. Pearson, Phys. Rev. **98**, 1755 (1955).

[15] M. H. Francombe, Brit. J. Appl. Phys. **9**, 415 (1958).

[16] J. R. Drabble and C. H. L. Goodman, J. Phys. Chem. Solids **5**, 142 (1958).

[17] J. R. Drabble, Proc. Phys. Soc. (London) **72**, 380 (1958).

chain is approximately 90°. Both materials show anisotropic thermal expansion and compressibility.[2] As the pressure is increased the unit cell expands along the c axis and contracts in the plane of the a axis, resulting in an increase in bond angle between atoms. An approximate band model for Te involving p band has been proposed by Reitz[18] in which an increase in bond angle corresponds to a decrease in energy gap.

Bonding in Bi_2Te_3 is more complicated than in Se and Te. Francombe[15] reports that upon heating the c axis of the hexagonal unit cell expands more rapidly than the a axis. Drabble and Goodman[16] propose that bonding between Te^{I} and Bi atoms originates from p orbitals and bonding between Te^{II} and Bi atoms originates from sp^3d^2 orbitals. It was suggested that the latter bonds determine the energy gap since these are the weaker of the two bond types. The effect of pressure on the band structure based on this model is not known. It is considered that the observed decrease in energy gap with pressure is associated with the anisotropic behavior of the material, i.e., with relative change in bond angle and length.

Using the optical method, the temperature dependence of energy gap of Bi_2Te_3 has been determined by both Black *et al.*[12] and Austin[19] as -9×10^{-5} ev/°K. The temperature coefficient of the energy gap can be separated into two terms by the thermodynamic relationship,[8]

$$\left(\frac{\partial E_g}{\partial T}\right)_P=\left(\frac{\partial E_g}{\partial T}\right)_V-\left(\frac{\alpha}{K}\right)\left(\frac{\partial E_g}{\partial P}\right)_T,$$

where α is the volume coefficient of thermal expansion and K is the isothermal compressibility. The first term on the right hand side of the equation represents the electron-lattice interaction effect, and the second term represents the thermal dilation effect. According to the present measurement $(\partial E_g/\partial P)_T$ is approximately -2×10^{-6} ev/atm. If α and K are of the same order of magnitude, as has been observed for Ge, Si, and Te,[2] the electron-lattice interaction effect dominates the temperature dependence of the energy gap and results in a negative temperature coefficient.

ACKNOWLEDGMENTS

The authors are very grateful to Mr. B. Vanderlinde for his help in building the equipment and data taking and, also, to Mr. Mac J. Smith for assistance in single-crystal preparation. This research was supported by the U. S. Air Force and by the Advanced Research Projects Agency. The portion of the program supported by the U. S. Air Force was under a contract monitored by the Air Force Office of Scientific Research at the Air Research and Development Command.

---

[18] J. R. Reitz, Phys. Rev. **105**, 1233 (1957).

[19] I. G. Austin, Proc. Phys. Soc. (London) **72**, 545 (1958).

Generalized Coupled Mode Theory

M. C. PEASE
Stanford Research Institute, Menlo Park, California

(Received March 7, 1961)

The pairwise coupling of modes in distributed systems such as the traveling-wave parametric electron-beam amplifier and many other types is shown to permit only two types of interaction. One type, called β coupling, results in the periodic interchange of the signal between the modes, as typified in the Kompfner-null coupler. The other, γ coupling, results in the exponential growth of the mode, as in the TWT and in the pump section of a parametric amplifier. The nature of the resultant interaction is a direct consequence of the underlying relations contained in the conservation law that applies throughout the system, i.e., in the separate parts of the system and that is independent of the various coupling coefficients. The "rank" and "signature" of th metric that expresses this conservation law is sufficient to determine the type of behavior. The direction of flow of energy in th coupled modes imposes a duality on these relations. Where mode of opposite directionality are coupled, β coupling causes syster amplification, while γ coupling causes system interchange. Thes relations are generalizations of effects that have been studied i detail for many specific systems. They are not, however, consequences of the details of the system but are, rather, the onl alternatives possible under assumptions that are broad in scop and generally applicable to devices of interest.

THE work reported here is concerned with the possible interactions between the modes of a distributed system. The properties of many such systems have been studied in considerable detail by many authors. Our purpose, here, is to study these systems by the use of an abstract formalism to show that their qualitative behavior is the consequence of certain rather deep relations that underlie the various specific devices.

The devices that are included in the scope of this analysis include not only conventional distributed passive networks, such as long slot directional couplers, but the distributed parametric circuits, such as that studied by Tien[1]; conventional electron beam tubes such as the TWT,[2] the BWO,[3] and the cyclotron-wave amplifier studied by Siegman[4]; the parametric electron-beam tubes of the traveling-wave variety as studied by Louisell and Quate[5] and Johnson.[6] The analysis is appropriate, in fact, to any system which is distributed in one dimension, which is representable at least approximately by linear equations, and for which a conservation law exists that holds throughout the device.

The analysis may be considered a generalization by formalistic methods of the coupled mode theory initiated by Pierce.[7,8] It differs from the usual development in that it takes as fundamental the conservation law of the system and derives the modal, or wave, representation from the properties of the applicable law.

The question of which is the more fundamental, the conservation law or the wave representation, is largely a question of convenience. In the general case, the analysis starts from the differential equations that describe the physics of the situation, linearized i necessary. If, by physical argument, intuition, o otherwise, it is possible to determine an appropriat wave representation, then it is generally simpler to d so, and to develop the analysis on that basis. Th existing analyses of the rectilinear electron beam b Haus[9,10] and of the cyclotron waves by Siegman[5] ofte provide the means of doing this.

If, however, it proves difficult to find an appropriat wave representation, then one may determine th conservation law directly and systematically from th differential equations.[11–13] The equations that ar applicable in one section of the device, e.g., the coupler or the pump section of a parametric TW beam-typ amplifier, will have a group of conservation laws. Th additional requirement that the chosen law must appl within the other sections as well, or that it must appl independently of the magnitude of a chosen couplin parameter, is a severe restriction. In many cases i determines completely, within a scalar factor, th conservation law.

The selected conservation law will be an expressio of the linearized Manley-Rowe[14] type combined wit Chu's kinetic power theorem.[10,15] That is, it is a quadrati form which gives an expression for a suitably reduce power that is conserved by the system.

A basis which will diagonalize the given conservatio law is a suitable wave basis for the system. Properl normalized, the squares of the magnitudes of th components on this basis are the reduced powers in th various waves.

---

[1] P. K. Tien, J. Appl. Phys. **29**, 1347 (1958).

[2] J. R. Pierce, *Traveling-Wave Tubes* (D. Van Nostrand Company, Inc., Princeton, New Jersey, 1950).

[3] H. R. Johnson, Proc. Inst. Radio Engrs. **43**, 684 (1957).

[4] A. E. Siegman, J. Appl. Phys. **31**, 17 (1960).

[5] W. H. Louisell and C. F. Quate, Proc. Inst. Radio Engrs. **46**, 707 (1958).

[6] C. C. Johnson, J. Appl. Phys. **31**, 338 (1960).

[7] J. R. Pierce, J. Appl. Phys. **25**, 179 (1954).

[8] W. H. Louisell, *Coupled Mode and Parametric Electronics* (John Wiley & Sons, Inc., New York, 1960).

[9] H. A. Haus, Mass. Inst. Technol. Rept. No. 316 (April 8 1958).

[10] L. D. Smullin and H. A. Haus, *Noise in Electron Device* (Technology Press, Cambridge, Massachusetts and John Wiley & Sons, Inc., New York, 1959), see particularly Chap. 3 by H. A Haus.

[11] M. C. Pease, Proc. Inst. Radio Engrs. **49**, 488 (1961).

[12] M. C. Pease, J. Appl. Phys. **31**, 1988 (1960).

[13] M. C. Pease, J. Appl. Phys. **31**, 2028 (1960).

[14] J. M. Manley and H. E. Rowe, Proc. Inst. Radio Engrs. 44 904 (1956).

[15] L. J. Chu, "A kinetic power theorem," paper presented at th IRE–PGED Electron Tube Research Conference, Durham, Nev Hampshire, June, 1951. See also reference 10.

This viewpoint, then, provides a systematic method for the development of a suitable wave representation of the system.

We will show here that this viewpoint allows us to develop the theory of forward and backward wave amplification and coupling. We will show that the principal effects that are exploited in various devices are the direct consequences of the structure of this conservation law and of the restriction of the coupling to that between pairs of modes.

For this purpose, we will start by considering the form of the equations that describes a system. We will assume that a common conservation law has been determined by the methods given elsewhere.[13] We will then show that, by the proper choice of basis, this can be put into what we shall designate as the "canonical form" which is, in effect, a generalization of Haus' parity matrix.[9,10] Based on the canonical form of the metric, we will show that there are only two types of pairwise modal coupling that is possible. These we shall call "β coupling" and "γ coupling," which Louisell[8] calls "passive" and "active" coupling. (We prefer the designation of β and γ coupling since the nature of the coupling is not determined simply by the presence or absence of active elements.) Finally, we shall show the consequence of the relative directions of flow in the modes concerned.

BASIC RELATIONS

We have assumed, in the first place, that there exists a conservation law of the system. This requirement is broad enough to be almost trivial. The combination of a lossless circuit and an electron beam under conditions that permit linearization of the beam equations will always have such a law. The circuit itself conserves power. The beam, at any one frequency, obeys Chu's kinetic power law.[15] If parametric coupling exists, then the small signal and idle form of the Manley-Rowe relations indicates the conservation of a reduced power flow. We can expect that any such system will conserve a quantity that can be considered to be a suitably reduced net power flow.

We also, however, require that this conservation law hold throughout the system. This is a far stronger requirement. It states the existence of a wave representation involving coupling between various waves, and such that the conservation law is unaffected by the presence or absence of this coupling.

Obviously, it is not true, in general, that a conservation law will exist which applies throughout the system. It appears, though, that one of the principle objectives of design effort is to obtain a system in which it is true. The failure of specific designs to meet this requirement appears, in many cases, to be a measure of their failure to perform as intended, leading to undesired results such as excess noise.

We assume, then, the existence of a conservation law throughout. The system itself we assume to be describable as a system of linear homogeneous differential equations. If $\mathbf{x}$ is a column vector (the state vector), describing the state of the system as a function of the single space variable z, then this system of equations can be written

$$d\mathbf{x}/dz = -j\mathbf{R}\mathbf{x}, \tag{1}$$

where $\mathbf{R}$ is an $n\times n$ square matrix. $\mathbf{R}$ is constant within any region, although it will change from section to section as different coupling effects occur.

The existence of a conservation law that applies over a region described by Eq. (1) has been shown[11,13] to depend on the existence of an $n\times n$ matrix $\mathbf{K}$, a "metric," which is independent of z, and such that

$$\mathbf{K}\mathbf{R} = \mathbf{R}^{\dagger}\mathbf{K}, \tag{2}$$

where (†) means the Hermitian conjugate, i.e., the conjugate transposed matrix.

The condition in Eq. (2) is necessary and sufficient to assure that

$$s = \mathbf{x}^{\dagger}\mathbf{K}\mathbf{x}, \tag{3}$$

does not change with z. The scalar s determined by Eq. (3) is a quadratic form in the amplitude variables that describe the system. A law such as the conservation of a reduced energy can be written, for example, as the sum of terms each of which is the product of a constant (e.g., $1/\omega_n$ in the Manley-Rowe case) times a voltage times a current, which is a "quadratic form."

That s should be conserved throughout requires that $\mathbf{K}$ be a metric of the system as $\mathbf{R}$ assumes the forms appropriate to the different parts of the system. Equation (2) then, should be written

$$\mathbf{K}\mathbf{R}_i = \mathbf{R}_i^{\dagger}\mathbf{K},$$

where $\mathbf{R}_i$ changes as we pass, for example, from coupler to pump section to coupler.

The problem then is to determine the implications contained in the statement that a given $\mathbf{K}$ is a metric throughout the system.

REDUCTION OF K

To simplify the problem, we can consider a change of the basis of the representation, i.e., what happens if we describe the system in terms of variables that are different from those originally chosen, but which are related to them in a linear homogeneous manner.

If the original representation of the state vector at a given value of z was $\mathbf{x}(z)$, and if we change to a new representation in which it is $\mathbf{y}(z)$, these are related as follows:

$$\mathbf{y} = \mathbf{S}\mathbf{x}, \tag{4}$$

where $\mathbf{S}$ is a nonsingular square matrix that is independent of z. If we substitute this into Eq. (1), we see that the form of Eq. (1) is maintained if we replace

$\mathbf{R}$ by

$$\mathbf{R}'=\mathbf{SRS}^{-1}. \tag{5}$$

As might be expected, this is a "similarity transformation."

If we substitute Eq. (5) into Eq. (2), we obtain

$$\mathbf{KS}^{-1}\mathbf{RS}=\mathbf{S}^{\dagger}\mathbf{RS}^{-1}\mathbf{K} \tag{6}$$

since the Hermitian conjugate of a product is the product of the Hermitian conjugates in reverse order.

To reduce Eq. (6) to the same form as Eq. (2) requires that $\mathbf{K}$ be replaced by $\mathbf{K}'$ where

$$\mathbf{K}'=(\mathbf{S}^{-1})^{\dagger}\mathbf{K}(\mathbf{S}^{-1}). \tag{7}$$

This type of transformation is different from a similarity one. Whereas the latter preserves the eigenvalues, a transformation of this type does not. We need a few preliminary remarks, however, before considering what it can do.

In the first place, we can restrict our attention to Hermitian $\mathbf{K}$'s ($\mathbf{K}^{\dagger}=\mathbf{K}$). For, if $\mathbf{K}$ is not Hermitian, and not a scalar times a Hermitian metric, then it implies two independent Hermitian $\mathbf{K}$'s. The assumption that two independent metrics exist which are simultaneously valid throughout the system is much too strong for our purposes here. Therefore, we assume the given $\mathbf{K}$ to be itself Hermitian.

Secondly, a Hermitian matrix has all of its eigenvalues real, and its eigenvectors are complete.

Now it is well known that a Hermitian matrix can be put into diagonal form, with its eigenvalues on the diagonal, by a unitary transformation. That is, we can find a unitary matrix, $\mathbf{U}(\mathbf{U}^{\dagger}=\mathbf{U}^{-1})$ such that

$$\mathbf{K}'=\mathbf{U}^{-1}\mathbf{KU}=\mathbf{U}^{\dagger}\mathbf{KU} \tag{8}$$

is diagonal in the eigenvalues of $\mathbf{K}$ and hence real.

We can now pre- and postmultiply this diagonalized $\mathbf{K}$ by a diagonal matrix with terms equal to the reciprocals of the square root of the nonzero eigenvalues of $\mathbf{R}$. This reduces it to a diagonal matrix with ± 1, or 0, on the diagonal.

Finally, we can apply a symmetrical permutation matrix in Eq. (7) to rearrange the order in which the terms appear.

We cannot, however, find an $(\mathbf{S}^{-1})$ which, in the transformation of Eq. (7), changes one of these signs or eliminates a zero eigenvalue.

To summarize, the general transformation of Eq. (7) preserves the "rank" of $\mathbf{K}$, i.e., the number of nonzero eigenvalues, counting multiplicities, and its "signature," the difference between the number of positive and negative eigenvalues. (The "Law of Inertia" of linear operations.)

We can assume that there are no zero eigenvalues since these indicate terms that are not propagated, and that are, therefore, of no significance.

There is, then, a basis in terms of which the metric $\mathbf{K}$ is either the identity matrix, or else of the form

$$\mathbf{K}=\begin{pmatrix}\mathbf{I}_r & 0\\ 0 & -\mathbf{I}_s\end{pmatrix}, \tag{9}$$

where $\mathbf{I}_r$ and $\mathbf{I}_s$ are the identity matrices of dimensionality r and s, with $r+s=n$.

This basis is not unique, but an appropriate one can be obtained by the usual methods.

Such a basis is a "wave basis" for the system. If, on this basis, the state vector is

$$\mathbf{y}=\begin{bmatrix}a_1\\ a_2\\ \cdot\\ \cdot\\ \cdot\\ \cdot\end{bmatrix} \tag{10}$$

then the conservation law is

$$s=\sum_{1}^{r} a_i a_i^{*}-\sum_{r+1}^{n} a_i a_i^{*}.$$

Hence the a_i's are wave amplitudes. The squares of their magnitudes have the form of reduced power terms, taken either positive or negative as the "parity" is plus or minus.

It is therefore only necessary to consider systems with the specified $\mathbf{K}$ in its "canonical" form, i.e., either $\mathbf{I}_n$ or of the form Eq. (9), since any system can be reduced to this form by representing on an appropriate wave basis.

$K=I$

The simplest case is when the canonical $\mathbf{K}$ is the identity matrix. In this case Eq. (2) states that $\mathbf{R}=\mathbf{R}^{\dagger}$. Hence, on this basis, all the $\mathbf{R}_i$ in the system must be Hermitian. If the $\mathbf{R}_i$ are Hermitian, their eigenvalues are real.

Now there is a simple relation between the eigenvalues of $\mathbf{R}$ and those of the system operator, $\mathbf{M}$. If the solution of (1) is written

$$\mathbf{x}(z)=\mathbf{M}(z)\mathbf{x}(0), \tag{11}$$

and if $\mathbf{x}_n$ is an eigenvector of $\mathbf{M}$ not containing the z dependency, so that

$$\mathbf{x}(z)=\mathbf{M}(z)\mathbf{x}_n=\lambda_n(z)\mathbf{x}_n, \tag{12}$$

then we can substitute this into Eq. (1)

$$(d\lambda_n/dz)\mathbf{x}_n=-j\mathbf{R}\lambda_n\mathbf{x}_n, \tag{13}$$

or

$$[\mathbf{R}-j(1/\lambda_n)(d\lambda_n/dz)\mathbf{I}]\mathbf{x}_n=\mathbf{0}. \tag{14}$$

Hence $\mathbf{x}_n$ is also an eigenvector of $\mathbf{R}$. Since $\mathbf{R}$ is independent of z, so are its eigenvalues β_n, and we obtain the relation:

$$\lambda_n=\exp(-j\beta_n z). \tag{15}$$

Since, in this case, the eigenvalues of **R** are all real, the real parts of the eigenvalues of the system operator **M** vary sinusoidally with distance.

Coupling between waves that preserve such a metric can only result in a periodic transfer of signal back and forth between the coupled waves as typified by the theory of Kompfner-null couplers.[16,17]

This does not preclude the possibility of effective amplification or even oscillation, as has been pointed out by Muller[18] and others. If the real power flow on the circuit is in the opposite direction to the beam, the input boundary conditions require that the signal on the beam at the gun end be zero, and that the circuit at the opposite end be small or, in the oscillatory case, zero. These conditions can be met by combining properly the system eigenvectors. As a consequence of interference effects resulting from their differing propagation constants, the system as a whole may amplify, even though no eigenvector of the system is amplified. We shall have more to say of this in the section on "Contraflow."

Let us consider, further, the effect of such coupling. Let us suppose that the **R**'s of the system can be written

$$\mathbf{R}=\begin{pmatrix}\mathbf{A} & \mathbf{B}\\ \mathbf{B}^{\dagger} & \mathbf{D}\end{pmatrix}, \tag{16}$$

where $\mathbf{A}=\mathbf{A}^{\dagger}$, $\mathbf{D}=\mathbf{D}^{\dagger}$. We may suppose that **A** and **D** are the terms of the uncoupled system, and **B** represents the coupling factor. It is in general possible to so choose the basis, i.e., so define our wave variables, that **A** and **D** are diagonal and, therefore, real, with the various propagation constants along the diagonal. It is not, however, necessary to assume this, and we shall not do so.

Now the eigenvectors of the system are those of **R**. The eigenvalues of **M** and **R** are related as in Eq. (15), with those of **R** being the propagation constants. It is therefore sufficient to see what can be said about the eigenvectors and eigenvalues of **R**.

About the general **R** of the form of Eq. (16) very little additional can be said. There are, however, some interesting results that apply to particular situations of interest.

In the first place, suppose we couple between eigenvectors of the subsets of variables. That is, we wish to couple between **u** and **v** where **u** and **v** are vectors of suitable dimensionalities such that

$$\begin{aligned}\mathbf{A}\mathbf{u}&=\mu\mathbf{u}\\ \mathbf{D}\mathbf{v}&=\nu\mathbf{v}.\end{aligned} \tag{17}$$

A vector **x** of the form

$$\mathbf{x}=\begin{pmatrix}\mathbf{u}\\ \mathbf{v}\end{pmatrix} \tag{18}$$

will be an eigenvector of **R**, and hence of **M**, when

$$\mathbf{R}\mathbf{x}=\beta\mathbf{x}. \tag{19}$$

We may note that this is not as restrictive an assumption as it perhaps sounds. In many cases, we wish to couple one beam mode to one circuit mode. Then (17) is necessarily true. In other cases, we wish to couple mode to mode by pairs. Again (17) is necessarily true. In still other cases, e.g., a parametric amplifier with thin hollow beam, the modes are highly degenerate. In this case, we can so define the modes that the coupling occurs by pairs. Again, therefore, Eq. (17) applies.

Equation (17) then, describes a situation of considerable importance even though it does not exhaust the possibilities. We shall restrict our attention to those cases in which it is true.

Proceeding, then, on this assumption, we substitute Eq. (16) in Eq. (19) and use Eq. (17) to obtain

$$(\mu-\beta)\mathbf{u}+\mathbf{B}\mathbf{v}=\mathbf{0} \tag{20}$$

$$\mathbf{B}^{\dagger}\mathbf{u}+(\nu-\beta)\mathbf{v}=\mathbf{0}. \tag{21}$$

In the first place we note that, as we might expect, an eigenvector of a subgroup that is not coupled into the other subgroup generates an eigenvector of the system with the same eigenvalue. That is,

$$\begin{pmatrix}\mathbf{0}\\ \mathbf{v}\end{pmatrix}$$

is an eigenvector if $\mathbf{B}\mathbf{v}=\mathbf{0}$, and its eigenvalue is $\beta=\nu$. Likewise,

$$\begin{pmatrix}\mathbf{u}\\ \mathbf{0}\end{pmatrix}$$

is an eigenvector if $\mathbf{B}^{\dagger}\mathbf{u}=\mathbf{0}$, and its eigenvalue is $\beta=\mu$. This simply says that waves that are not coupled by **R** remain unaffected.

Now suppose that they are coupled in such a way as to retain the form of Eq. (18) with Eq. (17). This is not the most general form coupling, but it is probably the most interesting.

Then, clearly, we must have $\beta\neq\mu$ and $\beta\neq\nu$. Otherwise, either Eq. (20) or Eq. (21) degenerates. If this is so, then we can solve Eq. (20) for **u** and Eq. (21) for **v**:

$$\mathbf{u}=-\mathbf{B}\mathbf{v}/(\mu-\beta), \tag{22}$$

$$\mathbf{v}=-\mathbf{B}^{\dagger}\mathbf{u}/(\nu-\beta), \tag{23}$$

so that the relation between **u** and **v** is determined.

If we substitute Eq. (22) in Eq. (21) we obtain

$$\mathbf{B}^{\dagger}\mathbf{B}\mathbf{v}=\kappa\mathbf{v}, \tag{24}$$

where

$$\kappa=(\beta-\mu)(\beta-\nu). \tag{25}$$

Likewise, if we substitute Eq. (23) in Eq. (20), we obtain

$$\mathbf{B}\mathbf{B}^{\dagger}\mathbf{u}=\kappa\mathbf{u}. \tag{26}$$

---

[16] R. Kompfner, J. Brit. Inst. Radio Engrs. **10**, 283 (1950).
[17] M. C. Pease, J. Appl. Phys. **32**, 1145 (1961).
[18] M. Muller, Proc. Inst. Radio Engrs. **42**, 1651 (1954).

Equations (24) and (26) are eigenvector relations. The vector **v** must be an eigenvector of $\mathbf{B}^\dagger\mathbf{B}$, and **u** of $\mathbf{BB}^\dagger$. Both have the same eigenvalue κ given by Eq. (25).

If we are given a relation of the form Eq. (24), and premultiply it by **B**, we obtain directly the form Eq. (26) if we define **u** as proportional to **Bv**. Hence, the similarity of form of Eqs. (24) and (26) is a direct consequence of the structure of $\mathbf{BB}^\dagger$ or $\mathbf{B}^\dagger\mathbf{B}$. Furthermore, any eigenvector of $\mathbf{BB}^\dagger$ that has a nonzero eigenvalue generates an eigenvector of $\mathbf{B}^\dagger\mathbf{B}$ with the same eigenvalue and vice versa. However, if **B** is an $n\times m$ $(n\neq m)$ matrix, the dimensionality of $\mathbf{BB}^\dagger$ is different from that of $\mathbf{B}^\dagger\mathbf{B}$. Since both are Hermitian, each has a complete set of orthogonal eigenvectors. It follows, then, that the number of eigenvectors with nonzero eigenvalues of either matrix is, at most, the dimensionality of the smallest. The remaining eigenvectors of either must have zero eigenvalue. These are the eigenvectors which have either $\mathbf{u}=\mathbf{0}$ or $\mathbf{v}=\mathbf{0}$, whichever is of lowest dimensionality.

Consider, now, Eq. (26) for $\kappa\neq 0$. On premultiplying by $\mathbf{u}^\dagger$ and using Eq. (23) and its conjugate transpose,

$$\mathbf{v}^\dagger\mathbf{v}(\nu-\beta)(\nu-\beta)^*=\kappa\mathbf{u}^\dagger\mathbf{u}. \qquad (27)$$

Since $\mathbf{u}^\dagger\mathbf{u}$ and $\mathbf{v}^\dagger\mathbf{v}$ are necessarily nonnegative, it follows that κ must be zero or positive. The forms $\mathbf{BB}^\dagger$ and $\mathbf{B}^\dagger\mathbf{B}$ are nonnegative definite (or positive semidefinite).

Since κ is positive, we may write it as k^2 and solve Eq. (25) for β:

$$\beta=\tfrac{1}{2}[\mu+\nu\pm\{(\mu-\nu)^2+4k^2\}^{\frac{1}{2}}].$$

On writing β_+ and β_- for these two solutions, the corresponding eigenvectors are, from Eq. (23),

$$\begin{pmatrix}(\beta_+-\nu)\mathbf{u}\\ \mathbf{B}^\dagger\mathbf{u}\end{pmatrix}_{\beta_+} \quad\text{and}\quad \begin{pmatrix}(\beta_--\nu)\mathbf{u}\\ \mathbf{B}^\dagger\mathbf{u}\end{pmatrix}_{\beta_-}.$$

At the input, we may require that the signal be only on the circuit modes, say the upper subset. This condition is met by the difference of these eigenvectors. Since the variation with z is sinusoidal, maximum interchange occurs at that value of z where the relative phase is reversed, i.e., where the resultant is the sum of these eigenvectors. At this position the total vector is

$$\begin{pmatrix}(\beta_++\beta_-+2\nu)\mathbf{u}\\ 2\mathbf{B}^\dagger\mathbf{u}\end{pmatrix}=\begin{pmatrix}(\mu-\nu)\mathbf{u}\\ 2\mathbf{B}^\dagger\mathbf{u}\end{pmatrix}.$$

The entire signal is not transferred to the beam at any value of z unless $\mu=\nu$, i.e., synchronism. In fact, the ratio of the residual amplitude at its minimum to the initial amplitude is

$$(\mu-\nu)/\{(\mu-\nu)^2+4k^2\}. \qquad (28)$$

Under nonsynchronous conditions, the stronger the coupling the better the transfer, but it is never perfect.

These conclusions agree with the established analyses of many simple situations. What is of interest here i that they can be obtained under such general condition

$K\neq I$

If the canonical **K** is not the identity matrix bu has the form

$$\mathbf{K}=\begin{pmatrix}\mathbf{I} & 0\\ 0 & -\mathbf{I}\end{pmatrix}, \qquad (29$$

where the two **I**'s have the appropriate dimensionality then the situation can be analyzed by similar methods but with different results.

In this case, instead of Eq. (16), we find that th most general **R** has the form

$$\mathbf{R}=\begin{pmatrix}\mathbf{A} & \mathbf{B}\\ -\mathbf{B}^\dagger & \mathbf{D}\end{pmatrix}, \qquad (30$$

where $\mathbf{A}=\mathbf{A}^\dagger$, $\mathbf{D}=\mathbf{D}^\dagger$ as before. Within the subsets c variables, the **R** operator is Hermitian. Between th subsets, it is skew Hermitian. (A matrix **P** is skew Hermitian if $\mathbf{P}^\dagger=-\mathbf{P}$.) More precisely, the Hermitia component of **R** contains **A** and **D** with no crossterm The skew Hermitian component contains only the cros term **B** and $-\mathbf{B}^\dagger$.

As an immediate consequence of this apparentl minor change, we can no longer state that its eigenvalues are real, or, in fact, that they obey any genera theorem.

If, as before, we confine our attention to those case in which the eigenvectors of **R** are of the form Eq. (18 with **u** an eigenvector of **A**, and **v** an eigenvector of **D** then we must have

$$(\beta-\mu)\mathbf{u}=\mathbf{B}\mathbf{v} \qquad (31$$

$$(\beta-\nu)\mathbf{v}=-\mathbf{B}^\dagger\mathbf{u}, \qquad (32$$

where β is the eigenvalue of **R**.

If now, $\mathbf{u}=\mathbf{0}$, then we must have $\mathbf{Bv}=\mathbf{0}$ and $\beta=\nu$ The vector **v** must be orthogonal to **B** so that no signa is coupled between the subsets.

Or, if $\mathbf{v}=\mathbf{0}$, then $\beta=\mu$ and $\mathbf{B}^\dagger\mathbf{u}=\mathbf{0}$, so that **u** i orthogonal to $\mathbf{B}^\dagger$. These relations are precisely the sam as the first case.

If, instead, $\beta\neq\mu$ or ν, then, in the same way a before, we obtain

$$[\mathbf{B}^\dagger\mathbf{B}+(\beta-\nu)(\beta-\mu)]\mathbf{v}=\mathbf{0}, \qquad (33$$

so that **v** must be an eigenvector of $\mathbf{B}^\dagger\mathbf{B}$ with eigenvalu

$$\kappa=-(\beta-\nu)(\beta-\mu). \qquad (34$$

Likewise,

$$[\mathbf{BB}^\dagger+(\beta-\nu)(\beta-\mu)]\mathbf{u}=\mathbf{0}, \qquad (35$$

so that **u** must be an eigenvector of $\mathbf{BB}^\dagger$ with the sam eigenvalue κ.

These equations are the same as Eqs. (22) and (23 except for the sign of the relation between κ and λ.

As before, if we premultiply Eq. (33) by $\mathbf{v}^\dagger$,

$$(\mathbf{v}^\dagger\mathbf{B}^\dagger)(\mathbf{B}\mathbf{v})=(\mathbf{B}\mathbf{v})^\dagger\mathbf{B}\mathbf{v}=\kappa\mathbf{v}^\dagger\mathbf{v}, \tag{36}$$

and substitute Eq. (31), we obtain

$$[(\beta-\mu)(\beta-\mu)^*\mathbf{u}^\dagger\mathbf{u}/\mathbf{v}^\dagger\mathbf{v}]=\kappa. \tag{37}$$

Since the left-hand side is positive, so is the right. Therefore, κ can be written as k^2, where k is real. Then Eq. (34) can be solved to give

$$\beta=\tfrac{1}{2}[\mu+\nu\pm\{(\mu-\nu)^2-4k^2\}^{\frac{1}{2}}]. \tag{38}$$

β is real if

$$k<|\tfrac{1}{2}(\mu-\nu)|. \tag{39}$$

If

$$k>|\tfrac{1}{2}(\mu-\nu)|, \tag{40}$$

then β is complex. The eigenvalues of the system operator $\mathbf{M}$ grow and decay exponentially with distance. There is, in addition, a real part of β which leads to the usual propagation term of the eigenvalue. It is, however, the same for both values of β and therefore does not lead to an interference effect. It is simply a common phase factor on the two eigenvectors.

When the eigenvalue has a complex part, so that amplification of the mode exists, we call it "γ coupling."

As before, we can regard k as a measure of the strength of coupling. If synchronous conditions exist between the uncoupled modes $\mathbf{u}$ and $\mathbf{v}$, then $\mu=\nu$, and γ coupling exists, for all nonzero values of k.

In the nonsynchronous condition, however, when $\mu\neq\nu$, then the coupling strength must exceed a minimum value, given by Eq. (40), for γ coupling. At less than this coupling strength, there is β coupling, i.e., sinusoidal variation with distance of the combined result of the two eigenvectors.

CONTRAFLOW

The preceding is based on "coflow" conditions in which energy flows toward increasing (or decreasing) z in all modes. It is now necessary to consider the "contraflow" situation in which the direction of energy flow are different on the different modes.

The significance of this lies in the way in which the boundary conditions are imposed. In the coflow case, all the inputs occur at one value of z, and our problem is to calculate the results at some other value. In the contraflow case, the input conditions are imposed on certain of the modes at z_1, the remaining modes at z_2. We wish to calculate the consequence on the first set at z_2, and the second at z_1.

As has been previously shown, and as we have mentioned above, this situation has important effects. Under conditions of pure β coupling, in which the usual system eigenvectors do not amplify, the system as a whole can amplify. We may, if we wish, view this as the consequence of interference between nonamplifying modes. Insofar as the whole system or subsystem (e.g., the coupler) is concerned, however, the effect is simply that, with β coupling, we now obtain effects that, in the coflow case, are possible only with γ coupling.

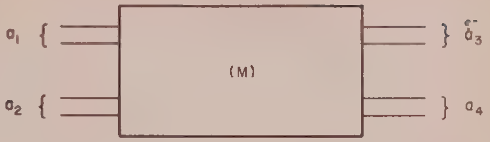

FIG. 1. Generalized two-port network.

This suggests that the effect of reversing the flow in a subset of the modes reverses, in some sense, the significance of β and γ.

We shall here show the precise formulation of this statement under rather general conditions. Specifically, we assume that the mode structure and coupling are such that a conservation law exists with K of the form

$$\mathbf{K}=\begin{pmatrix}\mathbf{K}_{11} & 0\\ 0 & \mathbf{K}_{22}\end{pmatrix}, \tag{41}$$

where $\mathbf{K}_{11}$ and $\mathbf{K}_{22}$ may or may not be diagonal (i.e., we do not require that the problem be stated on a wave amplitude basis, but only that the basis is such that the conservation law shall not include cross terms between the two subsets). The matrix $\mathbf{K}$ is appropriate to the coflow situation. We can, however, establish a matrix $\mathbf{H}$, which plays a similar role for the contraflow situation, i.e., where the flow of power is oppositely directed in the two subsets. $\mathbf{H}$ is related to $\mathbf{K}$ by

$$\mathbf{H}=\begin{pmatrix}\mathbf{K}_{11} & 0\\ 0 & -\mathbf{K}_{22}\end{pmatrix}. \tag{42}$$

Thus, the signs of these terms of the metric for which the flow is backward are reversed. In the canonical form this reverses the signs of those elements that describe the contribution on the contraflowing waves. If, for example, the canonical form of $\mathbf{K}$ is the identity matrix, so that the coupling is always pure β coupling, and coflow amplification is not possible, then in the contraflow case, $\mathbf{H}$ is of the form of Eq. (9) and the effective coupling may be of the γ type so that amplification is possible.

Specifically, we use the equivalence developed by Redheffer[19] for a different purpose which is essentially a generalization of the relation between the transmission and scattering matrices.

If we have the system shown in Fig. 1, then its description as a transmission system is given by

$$\begin{pmatrix}\mathbf{a}_1\\ \mathbf{a}_2\end{pmatrix}=\mathbf{M}\begin{pmatrix}\mathbf{a}_3\\ \mathbf{a}_4\end{pmatrix}=\begin{pmatrix}\mathbf{A} & \mathbf{B}\\ \mathbf{C} & \mathbf{D}\end{pmatrix}\begin{pmatrix}\mathbf{a}_3\\ \mathbf{a}_4\end{pmatrix}. \tag{43}$$

Note that $\mathbf{a}_1\cdots\mathbf{a}_4$ may be themselves column vectors and $\mathbf{A}$, $\mathbf{B}$, $\mathbf{C}$, $\mathbf{D}$ square or rectangular matrices. Hence, we are not specifying the dimensionality of the system.

---

[19] R. Redheffer, J. Math and Mech. 8, 349 (1959).

We assume that $\mathbf{a}_1$ and $\mathbf{a}_2$ are measured at one value of z, and $\mathbf{a}_3$ and $\mathbf{a}_4$ at another. In the coflow situation, then, the input conditions are imposed on $\mathbf{a}_1$ and $\mathbf{a}_2$, and the response determined as $\mathbf{a}_3$ and $\mathbf{a}_4$ (or vice versa).

In the contraflow case, the input conditions are imposed on $\mathbf{a}_2$ and $\mathbf{a}_3$, and the response on $\mathbf{a}_1$ and $\mathbf{a}_4$ desired. Hence, we require the scattering matrix $\mathfrak{M}$ such that

$$\begin{pmatrix}\mathbf{a}_3\\ \mathbf{a}_2\end{pmatrix}=\mathfrak{M}\begin{pmatrix}\mathbf{a}_1\\ \mathbf{a}_4\end{pmatrix}. \tag{44}$$

It may be readily found that the relation between $\mathbf{M}$ and $\mathfrak{M}$ is

$$\mathfrak{M}=\begin{pmatrix}\mathfrak{A} & \mathfrak{B}\\ \mathfrak{C} & \mathfrak{D}\end{pmatrix}=\begin{pmatrix}\mathbf{A}^{-1} & -\mathbf{A}^{-1}\mathbf{B}\\ \mathbf{C}\mathbf{A}^{-1} & \mathbf{D}-\mathbf{C}\mathbf{A}^{-1}\mathbf{B}\end{pmatrix}, \tag{45}$$

and that the inverse relation has the same form

$$\mathbf{M}=\begin{pmatrix}\mathfrak{A}^{-1} & -\mathfrak{A}^{-1}\mathfrak{B}\\ \mathfrak{C}\mathfrak{A}^{-1} & \mathfrak{D}-\mathfrak{C}\mathfrak{A}^{-1}\mathfrak{B}\end{pmatrix}. \tag{46}$$

The multiplication of $\mathbf{M}$ matrices, which represents the connection in cascade of such systems, goes into the "star product" defined by Redheffer.[19]

$$\begin{pmatrix}\mathfrak{A}_1 & \mathfrak{B}_1\\ \mathfrak{C}_1 & \mathfrak{D}_1\end{pmatrix}*\begin{pmatrix}\mathfrak{A}_2 & \mathfrak{B}_2\\ \mathfrak{C}_2 & \mathfrak{D}_2\end{pmatrix}=\begin{pmatrix}\mathfrak{A}_2(\mathbf{I}-\mathfrak{B}_1\mathfrak{C}_2)^{-1}\mathfrak{A}_1 & \mathfrak{B}_2+\mathfrak{A}_2(\mathbf{I}-\mathfrak{B}_1\mathfrak{C}_2)^{-1}\mathfrak{B}_1\mathfrak{D}_2\\ \mathfrak{C}_1+\mathfrak{D}_1\mathfrak{C}_2(\mathbf{I}-\mathfrak{B}_1\mathfrak{C}_2)^{-1}\mathfrak{A}_1 & \mathfrak{D}_1(\mathbf{I}-\mathfrak{C}_2\mathfrak{B}_1)^{-1}\mathfrak{D}_2\end{pmatrix}, \tag{47}$$

providing, of course, the various inverses exist.

The relation between these two methods of analysis is an isomorphism. That is, if $\mathbf{M}_1\mathbf{M}_2=\mathbf{M}_3$, then $\mathfrak{M}_1*\mathfrak{M}_2=\mathfrak{M}_3$. This may be seen from the derivation of the star product from the cascade connection of two systems. Or, it may be proved directly by some rather tedious calculations.

We cannot translate directly either the differential equation, Eq. (1), or the $\mathbf{R}$ matrix itself into these terms. If we consider $\mathbf{M}$ as a function of z, then Eq. (43) describes the variation along the system under constant input conditions. $\mathfrak{M}$, on the other hand, describes the variations of the outputs under varying total length since a part of the input conditions is at the position described by z. Hence, $\mathfrak{M}(z)$ does not describe the internal state of the system (except indirectly) and we cannot expect an equation of the form of Eq. (1).

However, we can still expect an invariant of the form of (3). Now $\mathbf{K}$ is defined, in terms of Eq. (43), such that

$$(\mathbf{a}_1{}^\dagger\mathbf{a}_2{}^\dagger)\mathbf{K}\begin{pmatrix}\mathbf{a}_1\\ \mathbf{a}_2\end{pmatrix}=(\mathbf{a}_3{}^\dagger\mathbf{a}_4{}^\dagger)\mathbf{K}\begin{pmatrix}\mathbf{a}_3\\ \mathbf{a}_4\end{pmatrix}, \tag{48}$$

which requires, as we have shown elsewhere, that

$$\mathbf{M}^\dagger\mathbf{K}\mathbf{M}=\mathbf{K}. \tag{49}$$

The comparable form $\mathbf{H}$ for the situation of Eq. (44) is

$$(\mathbf{a}_3{}^\dagger\mathbf{a}_2{}^\dagger)\mathbf{H}\begin{pmatrix}\mathbf{a}_3\\ \mathbf{a}_2\end{pmatrix}=(\mathbf{a}_1{}^\dagger\mathbf{a}_4{}^\dagger)\mathbf{H}\begin{pmatrix}\mathbf{a}_1\\ \mathbf{a}_4\end{pmatrix}. \tag{50}$$

Substituting Eq. (44) and requiring that this be true for any $\mathbf{a}_1$ and $\mathbf{a}_4$ shows that we must have

$$\mathfrak{M}^\dagger\mathbf{H}\mathfrak{M}=\mathbf{H}, \tag{51}$$

the same form as Eq. (49). Since Eq. (51) uses normal matrix multiplication rather than the star product, $\mathbf{H}$ is not simply the equivalent of $\mathbf{K}$. Equation (51), in other words, is not simply the result of applying the equivalence Eq. (47) to Eq. (49). $\mathbf{H}$ must be separately determined.

In the case where $\mathbf{K}$ does not couple the subsets of modes so that $\mathbf{K}$ has the form of Eq. (41), the relation of $\mathbf{K}$ to $\mathbf{H}$ can be found immediately from Eq. (48). On substituting Eq. (41) in Eq. (48):

$$\mathbf{a}_1{}^\dagger\mathbf{K}_{11}\mathbf{a}_1+\mathbf{a}_2{}^\dagger\mathbf{K}_{22}\mathbf{a}_2=\mathbf{a}_3{}^\dagger\mathbf{K}_{11}\mathbf{a}_3+\mathbf{a}_4{}^\dagger\mathbf{K}_{22}\mathbf{a}_4$$

or

$$\mathbf{a}_3{}^\dagger\mathbf{K}_{11}\mathbf{a}_3-\mathbf{a}_2{}^\dagger\mathbf{K}_{22}\mathbf{a}_2=\mathbf{a}_1{}^\dagger\mathbf{K}_{11}\mathbf{a}_1-\mathbf{a}_4{}^\dagger\mathbf{K}_{22}\mathbf{a}_4.$$

Hence,

$$\mathbf{H}=\begin{pmatrix}\mathbf{K}_{11} & 0\\ 0 & -\mathbf{K}_{22}\end{pmatrix}. \tag{52}$$

This relation can also be found from Eq. (45) by, again, a rather tedious calculation. We write down the relations between the components of $\mathbf{M}$ from Eq. (49). On assuming that $\mathbf{H}$ is diagonal in the submatrices $\mathbf{H}_{11}$ and $\mathbf{H}_{22}$, we write the relation given by Eq. (51) between the components of $\mathbf{M}$ as given by Eq. (45). Comparison of these relations shows that $\mathbf{H}$ must have the form of Eq. (42).

The significance of Eq. (12), as discussed above, is that a change from coflow to contraflow conditions reverses the sign of the appropriate elements of the canonical $\mathbf{K}$ and thereby allows an interchange of the significance of β- and γ-type coupling.

CONCLUSIONS

The phenomena that we have studied here are not new. They have been analyzed by a number of workers for many different types of systems.

What is of interest here is that the results are of such generality. We have shown that, under the assumed conditions, there exists a canonical form of the $\mathbf{K}$ matrix. This is a generalization of Haus' parity matrix.

But whereas Haus assumed a wave amplitude representation and showed by example that these waves could have either parity (± sign), we have here shown that this is a direct consequence of the existence of a conservation law. From this, then, it is possible to derive a suitable wave amplitude representation.

Given, then, the canonical **K** matrix, we have shown that, for the types of modal interaction that are of interest, we obtain two types of effect. If the coupled modes are of the same parity, then we can obtain only β coupling, leading to an oscillating transfer of signal between the two modes. If the modes are of opposite parity, we may also obtain this kind of effect (in the nonsynchronous case), but may also obtain γ coupling in which the signal behaves exponentially in the two modes.

In the contraflow case, in which the boundary conditions are applied to some of the modes at opposite ends of the device, the above conclusions still apply but need reinterpretation. The appropriate metric that generates a conservation law that relates the boundary state to the resultant state reverses the signs of the terms of the **K** matrix that correspond to the contraflowing modes. Hence, in this situation where the boundary conditions are split between different values of z, β coupling allows amplification by the system, while γ coupling does not.

These results, because of their generality, allow the description and classification of a wide class of devices in a graphic and significant way.

ACKNOWLEDGMENTS

The author is indebted to Dr. Casper W. Barnes, Jr., Stanford Research Institute, and to Dr. A. E. Siegman, of Stanford University, for many valuable discussions and suggestions.

The work reported in this paper was supported, in part, by the Wright Air Development Division of the United States Air Force, Wright-Patterson Air Force Base, Dayton, Ohio, under contract.

JOURNAL OF APLLIED PHYSICS VOLUME 32, NUMBER 9 SEPTEMBER, 1961

Thermorheological Simplicity in Extrusion Flow Curves of High Polymers

KATSUHIKO ITO
The Institute of Physical and Chemical Research, Komagome, Bunkyo-ku, Tokyo, Japan

(Received September 27, 1960)

Thermorheological simplicity is available for the extrusion flow curves of polymers in a way similar to the case of creep or stress relaxation. The true consistency curves for acrylic resin which were obtained from the extrusion flow curves at various extrusion temperatures by the help of the end-correction factor ξ are superimposed by shifting along the log D_w' (where D_w' is apparent maximum shear rate at the die wall). Thus the consistency curves by extrusion which are useful for evaluating the viscoelastic behavior of amorphous linear polymers can easily be determined over a sufficiently wide range of shear rates by the change of extrusion temperature.

I. INTRODUCTION

THE rheological behavior of high polymers should be analyzed on the basis of experimental data obtained over a sufficiently wide range of shear rates. For this, the use of an extrusion[1,2] rheometer is useful for large[3] shear rates, while the parallel-plate compression[4] rheometer is best for small shear rates. Data obtained at high shear rates with an extrusion rheometer are highly informative for the evaluation of practical high-speed molding of plastics which has been developed recently, since the extrusion rheometer follows the same principle as that of practical molding machines. It must be mentioned however, that generally it is not an easy matter to determine the viscoelastic behavior of plastics over a sufficiently wide range of shear rates by means of an extrusion rheometer alone.

Viscoelastic behavior can also be studied by means of a creep or stress relaxation method, but this method requires taking a large amount of data and so is quite time-consuming. However, the method of reduced variables[5] or the temperature-time superposition principle[6] works well for thermorheologically simple[7] materials. The present paper shows that a similar procedure is applicable to the consistency curves obtained from the extrusion flow curves of thermorheologically simple materials.

II. EXTRUSION RHEOMETER AND CONSISTENCY CURVE

For the sake of thermorheological simplicity, acrylic resin (Lucite), one of the most typical amorphous linear polymers, was employed as a test material in the ex-

---

[1] J. P. Tordella, Trans. Soc. Rheol. **1**, 203 (1957).

[2] A. B. Metzner, E. L. Carley, and I. K. Park, Modern Plastics **37**, 133 (1960).

[3] K. Ito, Kagaku Kenkyusho Hôhoku **28**, 353 (1952).

[4] K. Ito, J. Polymer Sci. **40**, 133 (1959).

[5] J. D. Ferry, J. Am. Chem. Soc. **72**, 3746 (1950).

[6] A. V. Tobolsky and R. D. Andrews, J. Chem. Phys. **1**, 1251 (1943).

[7] F. Schwarzl and A. J. Starverman, J. Appl. Phys. **23**, 838 (1952).

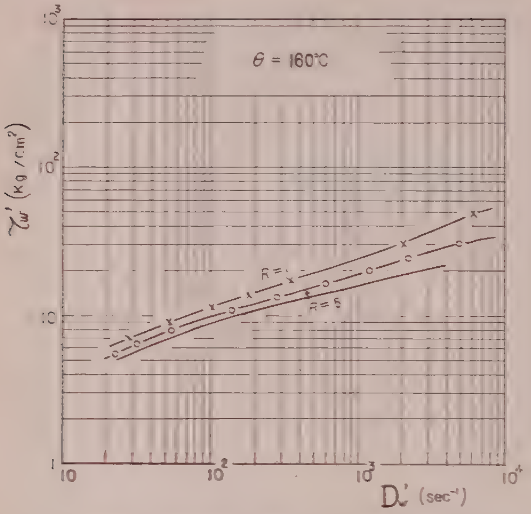

FIG. 1. Extrusion consistency curves for acrylic resin at 160°C.

trusion study. The extrusion rheometer is theoretically valid for the establishment of the simplest one-dimensional flow. However, it is almost impossible to extrude such plastics as are used in practical molding through a die having a large ratio of $R=l/d$, where l is the length of hole of die and d is the diameter of hole of die. Therefore, dies having comparable dimensions of l and d were installed in the extrusion rheometer and the flow of linear polymers was tested at a very high shear rate. In this study, test materials were placed in the cylinder (height: 10 mm, diameter: 10 mm) and were extruded through flat circular dies of $R=5\sim1$. Extrusion temperature was kept constant within an accuracy of ±0.5°C by means of a thermoregulator.

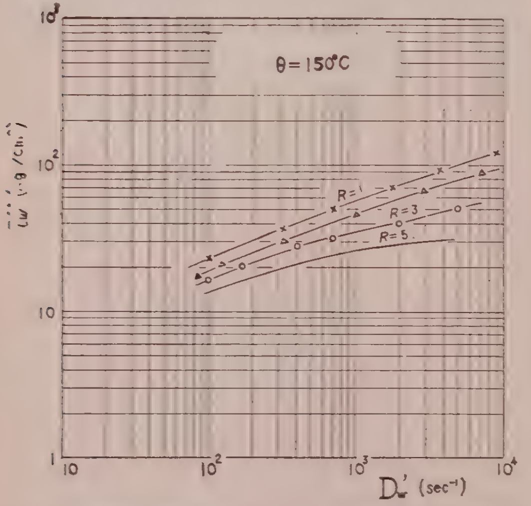

FIG. 2. Extrusion consistency curves for acrylic resin at 150°C.

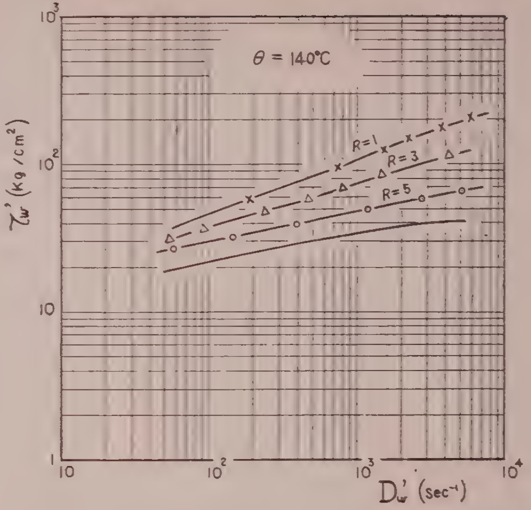

FIG. 3. Extrusion consistency curves for acrylic resin at 140°C.

Thus extrusion flow curves were obtained both at temperatures θ and at various pressures p of extrusion. For the sake of convenience the results obtained are plotted in the apparent consistency curves using the following notations,

$$\tau_w' = (pd/4l)\cdots, \tag{1}$$

$$D_w' = (32Q/\pi d^3)\cdots, \tag{2}$$

where τ_w' is the apparent maximum shear stress at the die wall, D_w' is the apparent maximum shear rate at the die wall, and Q is the output rate in extrusion.

The results obtained are shown in Figs. 1–4, expressed in terms of the parameter R.

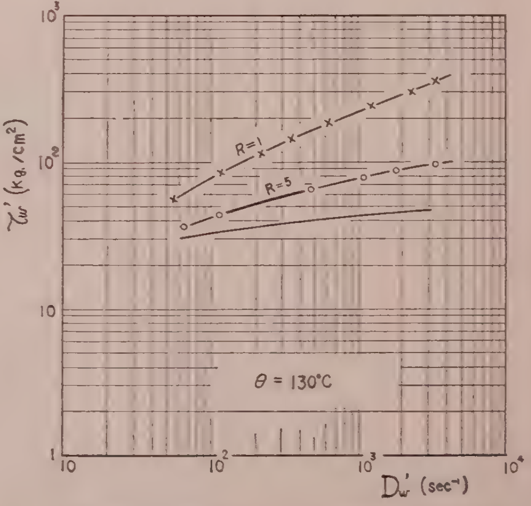

FIG. 4. Extrusion consistency curves for acrylic resin at 130°C.

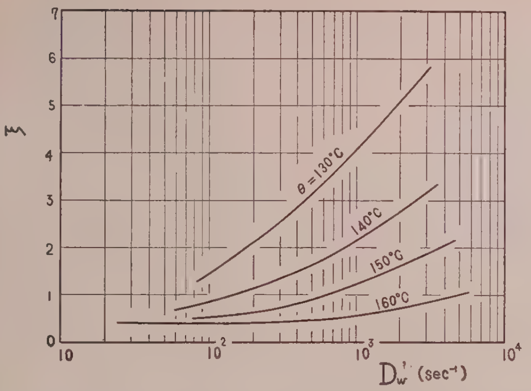

FIG. 5. End-correction factor ξ versus logarithm of the apparent maximum shear rate of the die wall for acrylic resin at various extrusion temperatures.

These apparent consistency curves are influenced by R. Therefore the true consistency curves, which should be obtained in the extrusion rheometer installed with a die having very large value of R, are derived by the introduction of the end-correction factor[8] ξ of the extrusion die. Hence the corrected length $\bar{l}$ of extrusion die is used for computation, where $\bar{l}$ is,

$$\bar{l}=l+\xi d\cdots. \tag{3}$$

The most probable value of ξ is determined by the apparent consistency curves obtained from the experimental results at various values of R, assuming that ξ is dependent upon D_w'. The relation between ξ and D_w' is shown in Fig. 5, and we see that the non-Newtonian effect of acrylic resin on the extrusion flow through a flat circular die increases with decreasing temperature. The true consistency curve computed by the above procedure is shown by the smooth curves in Figs. 1–4. The true consistency curves for acrylic resin extrusion at various temperatures are shown is Fig. 6.

III. THERMORHEOLOGICAL SIMPLICITY IN CONSISTENCY CURVES

A justification for the horizontal shift along the log t axis may be made for viscoelastic behavior of thermorheologically simple materials. For stress relaxation or creep, the time and temperature influences occur only in the combination $\varphi=t/\eta=t/f(T)$, where T is the absolute temperature, because the temperature sensitivity of shear modulus G is negligible and that of viscosity η is given by the general relation $\eta=f(T)$, where one possible form of $f(T)$ is exp $(\Delta h^*/kT)$, where k is Boltzmann's constant and Δh^* is the free energy of the barrier. Taking the logarithm of his expression, we obtain,

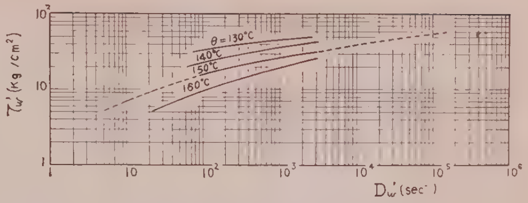

FIG. 6. True consistency curves for acrylic resin at various extrusion temperatures and a composite consistency curve for acrylic resin at 150°C (standard temperature).

$$\log\varphi=\log t-\log f(T)\cdots. \tag{4}$$

The relationship between τ_w' and D_w' is given by the apparent viscosity η'.

$$\tau_w'=\eta' D_w'\cdots. \tag{5}$$

While η' is tentatively named "apparent" because of the above specification, it seems that the temperature sensitivity of η' is quite similar to that of η. Therefore, taking the logarithm of (5), the following is obtained,

$$\log\tau_w'=\log\eta'+\log D_w'=\log f(T)+\log D_w'\cdots. \tag{6}$$

Thus the horizontal shift along the $\log D_w'$ axis instead of $\log t$ axis would be justified in determining the consistency curves over the wide range of shear rates.

In accordance with this principle as modified above, one continuous line could be composed by shifting the consistency curves of acrylic resin obtained at different temperatures along the $\log D_w'$ axis, without need for any corrections. The smooth master consistency curve was obtained at 150°C as a standard temperature. This is shown by the dotted line in Fig. 6. Irregularities which are often observed in master consistency curves due to the molecular and segmental motions associated with the flow phenomenon, especially melt fracture,[9] were not observed in this study.

It may be expected that thermorheological simplicity is vague for extrusion, since the possible molecular orientation in an extrusion die is much higher than that in creep or stress relaxation. As proved in this study, however, the temperature-time superposition principle can be converted into the temperature-shear rate superposition principle which can be used successfully for superimposing consistency curves in extrusion. Thus the consistency curves in extrusion, which are useful for evaluating the viscoelastic behavior of amorphous linear polymers, can be easily determined over a sufficiently wide range of shear rates if one changes the extrusion temperature.

---

[8] E. B. Bagley, J. Appl. Phys. **28**, 624 (1957).

[9] J. P. Tordella, J. Appl. Phys. **27**, 454 (1956).

JOURNAL OF APPLIED PHYSICS VOLUME 32, NUMBER 9 SEPTEMBER, 1961

Nonbasal Glide in Dislocation-Free Cadmium Crystals. I. The $(10\bar{1}1)$ $[1\bar{2}10]$ System

P. B. Price
General Electric Research Laboratory, Schenectady, New York

(Received April 20, 1961)

Electron-transparent dislocation-free platelets of cadmium were deformed in tension parallel to the basal plane, inside an electron microscope, in the temperature range from +25° to −150°C. At high strain rates the crystals twinned. At low strain rates ($\lesssim 10^{-2}$ sec^{-1}) the glide system depended on α, the angle between the tensile axis and a close-packing direction. For $0 \leq \alpha \lesssim 20°$ pyramidal glide on the $(11\bar{2}2)$ $[\bar{1}\bar{1}23]$ system occurred. For $20° \lesssim \alpha \lesssim 30°$ a new glide system, $(10\bar{1}1)$ $[1\bar{2}10]$, was identified which has not yet been observed in large cadmium crystals. Edge dislocations with a $\frac{1}{3}[1\bar{2}10]$ Burgers vector moved across the entire crystal on $(10\bar{1}1)$ planes without multiplying or forming obstacles to further glide. Occasionally, at high strain, fracture occurred on a $(10\bar{1}1)$ plane. The observations suggested that, in the temperature range studied, the flow stress for $(10\bar{1}1)$ $[1\bar{2}10]$ glide was considerably lower than that for prismatic glide on the $(10\bar{1}0)$ $[1\bar{2}10]$ system, slightly higher than that for $(11\bar{2}2)$ $[\bar{1}\bar{1}23]$ glide, and independent of strain for a given temperature.

INTRODUCTION

It was recently reported[1] that single crystals of zinc could be grown from the vapor in the form of platelets which were only a few hundred to a few thousand angstroms thick. These crystals were transparent to 100-kv electrons, so that the transmission electron microscope technique[2] could be used to study the formation and movement of dislocations, without the necessity for any mechanical or electrothinning.

While under observation in the electron microscope, these platelets were deformed in tension in a special straining stage, at room temperature and also at lower temperatures. Provided they were not mishandled during removal from the growth chamber to the straining stage, they were found to be completely free of dislocations before being strained. The deformation proceeded either by the nucleation and growth of a twin[3] or by pyramidal glide on the $(11\bar{2}2)$ $[\bar{1}\bar{1}23]$ system.[3] During pyramidal glide large numbers of sessile dislocation loops were formed, and the behavior of these loops at room temperature[3] and at lower temperatures was studied,[3] as well as the interaction of glide dislocations with the loops.[4]

In view of the large amount of interesting information obtained from the experiments on zinc platelets, it was decided to extend the electron transmission studies to the deformation of thin crystals of other metals. Electron-transparent crystals of cadmium have now been produced from the vapor under conditions similar to those necessary for the growth of thin zinc platelets, and some of the results of a study of their modes of deformation are presented in this and the following paper.

EXPERIMENTAL TECHNIQUES

Large quantities of cadmium crystals of the proper dimensions for the study were grown, using the technique of Coleman and Sears,[5] in sealed-off Pyrex tubes containing high-purity helium. The vapor source was high-purity (99.9999%) cadmium held at 350°C, the temperature gradient was about 40°/in., and the growth time was about five hours.

The straining stage, shown in Fig. 1, was developed in collaboration with J. A. Venables at the Cavendish Laboratory and is described in detail elsewhere.[3] A specimen, which was mounted between two bimetal strips, was both cooled and strained in tension when the temperature of the strips was lowered by means of an external cold finger. With this device one could observe the formation and movement of dislocations in a temperature range from +25° to −150°C and at strain rates up to about 3×10^{-4} sec^{-1}.

For deformation at room temperature and at higher strain rates, the straining device developed by Fisher[6] was employed.

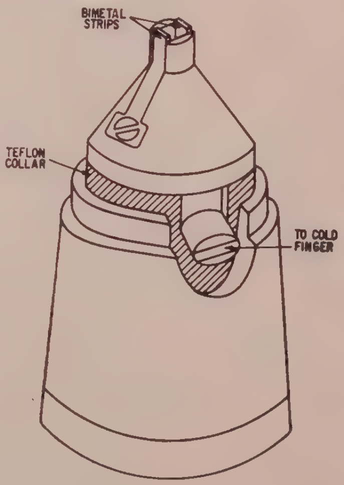

Fig. 1. Low-temperature straining stage for Siemens electron microscope.

---

[1] P. B. Price, Phil. Mag. **5**, 417 (1960).

[2] P. B. Hirsch, R. W. Horne, and M. J. Whelan, Phil. Mag. **1**, 677 (1956).

[3] P. B. Price, Proc. Roy. Soc. (London) **A260**, 251 (1961); P. B. Price, Phil. Mag. **5**, 873 (1960); **6**, 449 (1961).

[4] F. Kroupa and P. B. Price, Phil. Mag. **6**, 243 (1961).

[5] R. V. Coleman and G. W. Sears, Acta Met, **5**, 131 (1957).

[6] R. M. Fisher, Rev. Sci. Instr. **30**, 925 (1959).

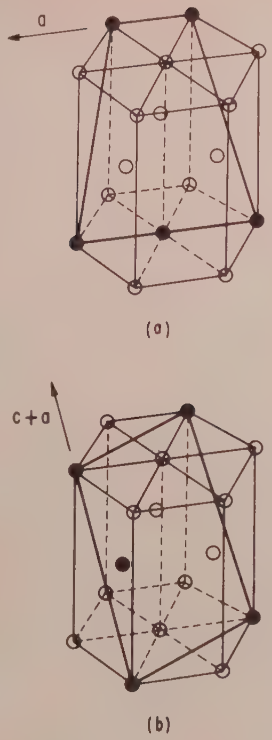

Fig. 2. Nonbasal glide systems in cadmium crystals. (a) First-order pyramidal glide occurs when dislocations with a $\frac{1}{3}[1\bar{2}10]$ Burgers vector move on $(10\bar{1}1)$ planes. (b) Second-order pyramidal glide occurs when dislocations with a Burgers vector $\frac{1}{3}[\bar{1}\bar{1}23]$ $=\mathbf{c}+\mathbf{a}$ move on $(11\bar{2}2)$ planes.

All of the experiments were performed in a Siemens Elmiskop I, operating at 100 kv.

MODES OF DEFORMATION OF CADMIUM PLATELETS

The crystals had prominent basal plane faces, usually bounded by $\{10\bar{1}0\}$ type planes, and were parallelogram-shaped, with widths ranging from a few microns to several mm. With this type of crystal habit the tension axis was always parallel to the basal plane, so the only orientation angle which could be varied was α, the angle between the tension axis and a close-packing $\langle 11\bar{2}0\rangle$ direction. In the temperature range studied, the mode of deformation was found to be dependent both on α and on the strain rate, but not on the temperature.

At high strain rate deformation started with the nucleation of a very narrow twin at one side of the crystal. In the twin orientation there was usually a finite shear stress resolved onto the basal planes, and the subsequent deformation consisted of a combination of twin growth and basal glide in the twin. Differences in the twinning behavior of zinc and cadmium will be discussed in a future paper.

At low or moderate strain rates, 10^{-5} to $\sim 10^{-2}$ sec^{-1}, glide on either first or second order pyramidal planes was observed, depending on the value of α. The two glide systems are shown in Fig. 2. In this paper we consider only first order pyramidal glide, which usually occurred when α was between $\sim 20°$ and $30°$. The dislocations had Burgers vectors of the type $\frac{1}{3}\langle 1\bar{2}10\rangle = \mathbf{a}$, were of edge orientation, and extended from the top surface to the bottom surface of the platelet on $\{10\bar{1}1\}$ (first-order pyramidal) planes. In the following paper we consider second-order pyramidal glide, which occurred for $0° \leq \alpha \lesssim 20°$. The dislocations responsible for this type of glide had Burgers vectors of the type $\frac{1}{3}\langle\bar{1}\bar{1}23\rangle = \mathbf{c}+\mathbf{a}$, were of screw orientation, and moved predominantly on $\{11\bar{2}2\}$ (second-order pyramidal) planes, although cross-glide onto other planes was frequently observed.

IDENTIFICATION OF THE GLIDE SYSTEMS

The glide plane on which a dislocation moved was determined from the projected length of the dislocation on the basal plane, the direction of motion and the thickness of the crystal. The direction of motion was obtained from a diffraction pattern. The thickness of the crystal was determined to an accuracy of better than 10% by increasing the strain rate so that a twin was nucleated and then measuring the projected width of a coherent twin boundary, which is known to lie on a $\{10\bar{1}2\}$ plane. The $\{11\bar{2}2\}$ glide plane in zinc platelets was identified in this way,[4] and in the present study of cadmium platelets the $\{11\bar{2}2\}$ and $\{10\bar{1}1\}$ planes were also identified.

The glide directions were deduced from the behavior of dislocations moving under an applied stress. When a screw dislocation changes its glide plane, its Burgers

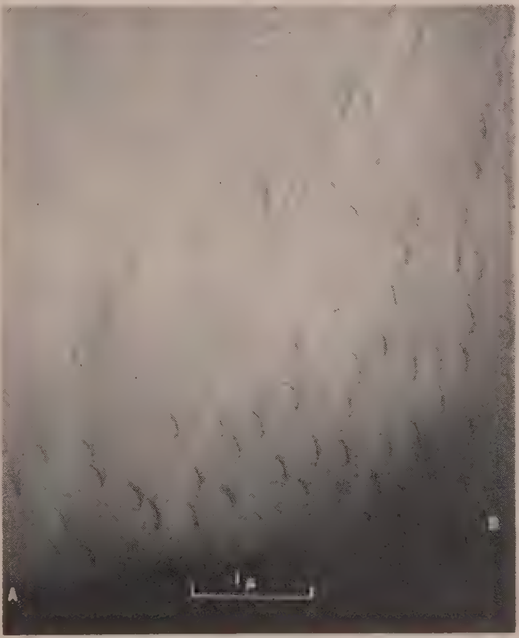

Fig. 3. Edge dislocations with a $\frac{1}{3}\langle 1\bar{2}10\rangle$ Burgers vector being produced in a cadmium platelet at the line of attachment to the grip AB. The temperature was $\sim -30°$C and the strain $\sim 3\%$.

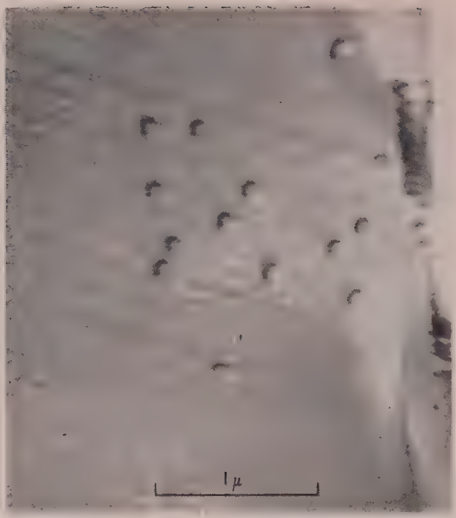

FIG. 4. Production of $\frac{1}{3}\langle 1\bar{2}10\rangle$ edge dislocations at the edges of another platelet at −24°C and ~2% strain.

vector is simply the zone axis of the set of planes on which it moves. The $\langle\bar{1}\bar{1}23\rangle$ glide direction was thus determined from the observation that screw dislocations on $\{11\bar{2}2\}$ planes frequently cross-glided onto $\{10\bar{1}1\}$ and other planes which were parallel to a common $\langle\bar{1}\bar{1}23\rangle$ direction, namely the Burgers vector of the dislocations. During first-order pyramidal glide, dislocations on $\{10\bar{1}1\}$ planes always moved in straight lines precisely parallel to a $\langle 1\bar{2}10\rangle$ direction. When these dislocations moved completely across the crystal they left offsets in the $\langle 1\bar{2}10\rangle$ direction at the edge of the crystal. The offsets were particularly noticeable when a large number of dislocations moved on the same plane. It was concluded that these dislocations were of edge orientation with a $\frac{1}{3}\langle 1\bar{2}10\rangle$ Burgers vector.

FORMATION AND MOVEMENT OF $\frac{1}{3}\langle 1\bar{2}10\rangle$ DISLOCATIONS ON $\{10\bar{1}1\}$ PLANES

All of the cadmium platelets examined were initially free of dislocations. After the elastic limit was exceeded, dislocations were produced along the line where the specimen was glued to the straining device, as shown in Fig. 3, and at the edges of the crystal, as shown in Fig. 4. Once glide had started on a few planes, it usually continued on these same planes even up to high strains. Often many thousands of dislocations were produced and moved across the entire crystal on a single $(10\bar{1}1)$ plane, resulting in an offset of several microns, which was easily observable in an optical microscope.

The motion of dislocations on $(10\bar{1}1)$ planes was rarely uniform. They often encountered obstacles which were not observable in the microscope and were held up temporarily until the external stress level rose or until a pile-up occurred. Then they continued to glide on the same planes. No observable debris, such as dislocation loops, was left behind in the path of these dislocations, and rarely were any dislocations formed on intersecting planes during straining. Never were new dislocations generated by existing dislocations, nor did the regions in which glide was occurring propagate sideways like a Lüders band.

At the strain rate normally applied, $\sim 10^{-4}$ sec^{-1}, the dislocations usually moved with velocities between 10^{-5} and 10^{-4} cm/sec and the average dislocation density, taken over the entire crystal, was $\sim 10^{8}$ cm^{-2}. In Fig. 3, for example, the local density was $\sim 3\times 10^{8}$ cm^{-2}. At a higher strain rate, $\sim 10^{-3}$ sec^{-1}, the dislocations moved at velocities up to $\sim 10^{-3}$ cm/sec but the average density remained about the same. These quantities fit the usual strain rate relation, $\dot{\gamma}=bN\bar{v}$, quite well.

Although stress-strain curves have not yet been obtained for first-order pyramidal glide, it is felt that the flow stress was probably fairly constant, since most of the dislocations traversed the entire crystal and since no sources of internal stress were created during the deformation.

The observations of first-order pyramidal glide were qualitatively the same over the temperature range from +25° to −150°C, except that at the higher temperatures, $\gtrsim 0$°C, dislocations moved so readily, due to the stresses set up by even a low-intensity beam, that it was very difficult to take photographs. On the other hand, it was found in the earlier study[3] that dislocations in zinc platelets remained stationary and were easily photographed at room temperature.

FRACTURE

Most of the crystals were still deforming plastically, in the way described, at the highest strain obtainable with either of the straining devices used, ~20%. Occasionally, however, failure occurred at a somewhat lower strain by the formation of a crack on a $(10\bar{1}1)$ plane. The crack was formed when a large number of dislocations of one sign, moving on the same glide plane, interacted with a large number of dislocations of the opposite sign, moving in the opposite direction on a nearby glide plane. The situation is depicted in Fig. 5. In a typical case the two glide planes were separated by ~5000 A and the spacing of dislocations was of the order of 100 A near the origin of the crack and increasing

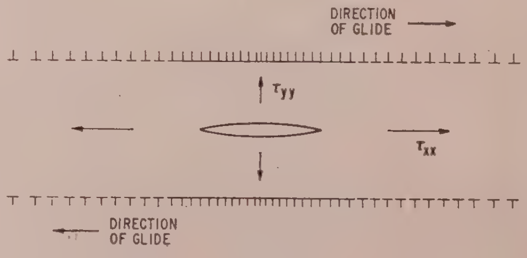

FIG. 5. Dislocation configuration resulting in the nucleation of a crack on a $(10\bar{1}1)$ plane.

with distance from the origin. For this configuration the stress τ_{yy} at the origin, perpendicular to the glide plane, was tensile and very large, of the order of 10^2 kg/mm^2. The tensile stress τ_{xx} at the origin was even larger, and yet no cracks perpendicular to the glide plane were developed, perhaps indicating that a $\{10\bar{1}1\}$ plane is much preferred over a $\{1\bar{2}10\}$ plane as a fracture plane.

DISCUSSION

The orientation dependence of the mode of deformation of cadmium platelets at low strain rate appears to be related to the variation of the resolved shear stress $\tau = \sigma \sin\chi \cos\lambda$ with orientation, where σ is the applied tensile stress and χ, λ are the angles which the tensile axis makes with the glide plane and the glide direction. This is illustrated in Fig. 6, in which $\sin\chi \cos\lambda$ is plotted as a function of α for first- and second-order pyramidal glide and for prismatic glide on the $(10\bar{1}0)$ $[1\bar{2}10]$ system. For a given tensile stress, the resolved shear stress for second-order pyramidal glide is a maximum for $\alpha = 0$ and a minimum for $\alpha = 30°$. When $\alpha \simeq 20°$, the orientation for which both first- and second-order pyramidal glide were observed, the resolved shear stress on the first-order system is about 20% higher than on the second-order system. For $20° \lesssim \alpha \lesssim 30°$, τ is more than 20% higher on first order than on second order, whereas for $0 \leq \alpha \lesssim 20°$ τ is less than 20% higher. This suggests that in the temperature range studied the critical τ for first-order pyramidal glide is about 20% greater than that for second-order pyramidal glide.

It is clear from Fig. 6 that the resolved shear stress for a given tensile stress and for any orientation is greater for prismatic glide than for either first-order or second-order pyramidal glide, and yet prismatic glide was never observed in platelets. Observations of nonbasal glide in large cadmium crystals are almost nonexistent. Gilman recently made a few tensile tests parallel to the basal plane[7]; because of the prevalence of twinning at the lower temperatures he was only able to observe nonbasal glide above ~150°C. He identified the glide direction as $\langle 1\bar{2}10 \rangle$ but, because of the lack of surface markings at the high temperature, he could only assume a glide plane. This he took to be $\{10\bar{1}0\}$, but in view of the present results on platelets he has agreed (private conversation) that the glide plane may have been $\{10\bar{1}1\}$.

Neither first-order pyramidal nor prismatic glide was observed in zinc platelets deformed at or below room temperature,[3] whereas prismatic glide has been found to occur in large zinc crystals at temperatures above ~250°C.[8]

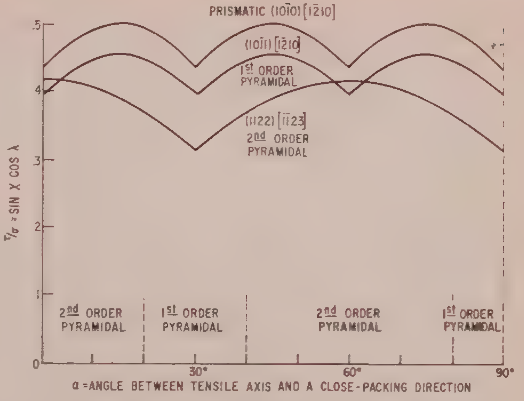

FIG. 6. Orientation factor, $\sin\chi \cos\lambda$, as a function of α, the angle between the tensile axis and a close-packing direction, for first- and second-order pyramidal glide and prismatic glide. The types of glide which were observed in the various ranges of α are indicated at the bottom of the graph.

Two factors which are important in determining whether a $\frac{1}{3}\langle 1\bar{2}10 \rangle$ dislocation in a large crystal can move on a nonbasal plane are the stress necessary for cross-glide from the basal plane onto the nonbasal plane[9] and the frictional or Peierls stress on the nonbasal plane,[10] both of which are temperature dependent. In a platelet cross-glide is not involved, since the dislocations are nucleated on the nonbasal plane at the beginning. We should, therefore, be able to explain the observed glide systems in cadmium and zinc platelets entirely in terms of the Peierls stress. We conclude that in cadmium in the temperature range +25° to −150°C the Peierls stress is lowest for second-order pyramidal glide, ~20% higher for first-order pyramidal glide, and much higher for prismatic glide. In zinc in the same temperature range the Peierls stress is much lower for second-order pyramidal glide than for either first-order pyramidal or prismatic glide. Gilman's observations on large crystals of zinc and cadmium suggest that at high temperature the Peierls stress for first-order pyramidal and/or prismatic glide is low enough so that second-order pyramidal glide does not occur.

We further conclude that, in view of its rather frequent occurrence in cadmium platelets, first-order pyramidal glide should also take place at low temperature in suitably oriented large cadmium crystals, provided the strain rate is low enough to inhibit twinning.

Finally, a remark should be made about the absence of strain-hardening. The dislocations responsible for first-order pyramidal glide in cadmium were of pure edge orientation. It is therefore not surprising that in nearly perfect platelets they moved great distances along the same glide planes without multiplying or leaving behind obstacles to further glide, since jogs on edge dislocations can move conservatively along the glide direction. In fact, these jogs were simply short *a* dislocations moving on basal planes. On the other hand, jogs on screw dislocations cannot move conservatively along with the dislocations. This restriction for screws completely changes the nature of the deformation and of the dislocation configurations, as will be seen in the following paper, which deals with the movement of screw dislocations and with the concomitant strain-hardening which occurs during second-order pyramidal glide.

---

[7] J. J. Gilman (to be published).

[8] J. J. Gilman, Trans. Am. Inst. Mining Met. Petrol. Engrs. **206**, 1326 (1956).

[9] J. Friedel, *Internal Stresses and Fatigue in Metals*, edited by G. M. Rassweiler and W. L. Grube (Elsevier Publishing Company, Inc., New York, 1959), p. 220.

[10] D. Kuhlmann-Wilsdorf, Phys. Rev. **120**, 773 (1960).

CONCLUSIONS

(1) At low strain rates the mode of deformation of cadmium platelets extended parallel to the basal plane is determined by the resolved shear stress and the Peierls stress. At room temperature or lower, the Peierls stress is lowest for $(11\bar{2}2)$ $[\bar{1}\bar{1}23]$ or second-order pyramidal glide, somewhat higher for $(10\bar{1}1)$ $[1\bar{2}10]$ or first-order pyramidal glide, and very much higher for prismatic glide; at high temperature it is lower for first-order pyramidal glide than for second-order pyramidal glide.

(2) In the temperature range from +25° to −150°C, some first-order pyramidal glide should take place in large cadmium crystals of suitable orientation deformed at low strain rate.

(3) Since all the dislocations in first-order pyramidal glide are of pure edge orientation and completely traverse the platelet without multiplying or leaving debris, there is no strain-hardening.

(4) Under suitable stress concentrations fracture can take place on a $(10\bar{1}1)$ plane in cadmium.

JOURNAL OF APPLIED PHYSICS VOLUME 32, NUMBER 9 SEPTEMBER, 1961

Nonbasal Glide in Dislocation-Free Cadmium Crystals. II. The $(11\bar{2}2)$ $[\bar{1}\bar{1}23]$ System

P. B. PRICE
General Electric Research Laboratory, Schenectady, New York

(Received April 20, 1961)

The $(11\bar{2}2)$ $[\bar{1}\bar{1}23]$ glide system was studied in thin, dislocation-free cadmium platelets by transmission electron microscopy and compared with observations on zinc platelets. Screw dislocations with a $\frac{1}{3}\langle\bar{1}\bar{1}23\rangle$ Burgers vector were formed at the edges of the crystal and moved primarily on $\{11\bar{2}2\}$ planes. Elongated, sessile dislocation loops were formed on basal planes when screws developed large jogs during cross-glide. Smaller numbers of secondary $\frac{1}{3}\langle\bar{1}\bar{1}20\rangle$ dislocations were also formed and moved on basal planes. Observations in the temperature range −150° to +25°C showed that the behavior of the long loops and of the other dislocations in cadmium and zinc varied with temperature as follows: (1) At temperatures lower than ∼−120° in Cd and ∼−80° in Zn, the long loops were stable and practically no recovery took place. High densities of loops and networks of secondary dislocations were built up and hardened the crystal. (2) In the intermediate temperature range −120° to −40° for Cd and −80° to +10° for Zn, the long loops split up into rows of circular loops, which were then stable. The process involved the pipe-diffusion of material around the long loops and required a lower activation energy than that for climb. Some of the circular loops were found to contain stacking faults. (3) At high temperature, above ∼−40° for Cd and ∼+10° for Zn, circular loops annealed out by climb with an activation energy ∼0.8 ev for Cd and ∼0.95 ev for Zn; secondary dislocation networks dispersed by climb; and the dislocation density, and therefore the work-hardening, was small.

At high beam intensities dislocation loops often grew by climb, probably as a result of the formation of point defects by ion bombardment, the ions being formed by the interaction between electrons and residual gas molecules.

INTRODUCTION

In the preceding paper it was reported that the mode of deformation of dislocation-free platelets of cadmium with (0001) faces depended primarily on the strain rate and on α, the angle between the tensile axis and a close-packing direction. At high strain rates the crystals deformed by twinning and at low strain rates by one of two types of nonbasal glide:

First-order pyramidal glide. For $20°\lesssim\alpha\lesssim 30°$, edge dislocations with $\frac{1}{3}\langle 1\bar{2}10\rangle$ Burgers vector were produced and moved on $\{10\bar{1}1\}$ planes. This $\{10\bar{1}1\}$ $\langle 1\bar{2}10\rangle$ glide system has not been reported in large single crystals of cadmium or zinc.

Second-order pyramidal glide. For $0°\leq\alpha\lesssim 20°$, screw dislocations with a Burgers vector $\frac{1}{3}\langle\bar{1}\bar{1}23\rangle=\mathbf{c}+\mathbf{a}$ moved on $\{11\bar{2}2\}$ planes and on cross-glide planes such as $\{10\bar{1}1\}$. The $\{11\bar{2}2\}$ $\langle\bar{1}\bar{1}23\rangle$ glide system was first identified by Bell and Cahn in large zinc crystals[1] and has recently been studied by the author in electron-transparent zinc platelets.[2,3] There is also evidence that it can occur in large cadmium crystals.[4]

In this paper transmission electron microscope observations of second-order pyramidal glide in thin cadmium platelets will be reported for the temperature range from −150° to +25°C and will be compared with similar observations on zinc platelets. The techniques of platelet crystal growth and low-temperature deformation in the electron microscope were described in the preceding paper.

---

[1] R. L. Bell and R. W. Cahn, Proc. Roy. Soc. (London) **A239**, 494 (1957).

[2] P. B. Price, Phil. Mag. **5**, 873 (1960).

[3] P. B. Price, Phil. Mag. **6**, 449 (1961).

[4] J. H. Wernick and E. E. Thomas, Trans. Am. Inst. Mining Met. Petrol. Engrs. **218**, 763 (1960).

RESULTS

Low-Temperature Second-Order Pyramidal Glide

Because of its low melting point (~321°C) and its low activation energy for self-diffusion (~0.79 ev for diffusion parallel to the *c* axis[5]), some recovery takes place in cadmium after and even during deformation unless the temperature is very low. In this section observations are presented of dislocation behavior in the temperature range −150° to −120°C, in which very little recovery was detected. The next two sections deal with dislocation behavior at higher temperatures, at which various modes of recovery became active.

At low temperature, after the elastic limit was exceeded, dislocations with a $\frac{1}{3}\langle\overline{11}23\rangle=\mathbf{c}+\mathbf{a}$ Burgers vector were produced in a localized region, either at the edge of the crystal or at one of the ends which was glued to the straining device, depending on where the stress was highest. These dislocations were initially of screw character and extended from the top surface to the bottom surface of the platelet on a $\{11\bar{2}2\}$ plane. During glide many of them deviated from their original direction of motion by various amounts of cross-glide to avoid internal stresses. Frequently different portions of a screw cross-glided by different amounts, with the result that a large jog of edge character was formed, allowing the two portions above and below the jog to glide past the obstacle.

Figure 1 is a sequence of electron micrographs taken at ~−100°C, showing the behavior of a **c**+**a** dislocation after it encountered some obstacle of an unknown nature. In (a) the screw segments are labeled A and the jog B. The segments A were prevented from gliding very far by two lengths of dislocation, called a dislocation dipole, connecting B to A. After both screw segments had moved past the stress center, they were able to free themselves from the dipole by cross-gliding back onto the original glide plane, as shown in (b). This process resulted in the formation of an elongated dislocation loop, seen in (c). Sometimes a loop formed in this way was very long and narrow, the exact shape depending on the nature of the internal stress center and the velocity of the **c**+**a** dislocation. The other loops in Fig. 1 were formed earlier, at a temperature of ~−90°C, during the passage of other screws.

All of the loops were oriented parallel to the basal plane and initially had a **c**+**a** Burgers vector, the same as that of the dislocations from which they were formed. Some of the loops underwent a decrease in Burgers vector from **c**+**a** to **c** (as determined by their diffraction contrast[2]). This decrease in Burgers vector, and hence in line energy, was always observed after a **c**+**a** dislocation had intersected or passed very close to a loop. The **c**+**a** dislocation probably catalyzed the reaction $\frac{1}{3}\langle\overline{11}23\rangle\rightarrow\frac{1}{3}\langle\overline{11}20\rangle+\langle0001\rangle$, by means of which a **c**+**a** loop dissociated into two concentric loops, the outer having a **c** Burgers vector and the inner having an **a** Burgers vector. The inner loop then collapsed by glide, leaving only a **c** loop.

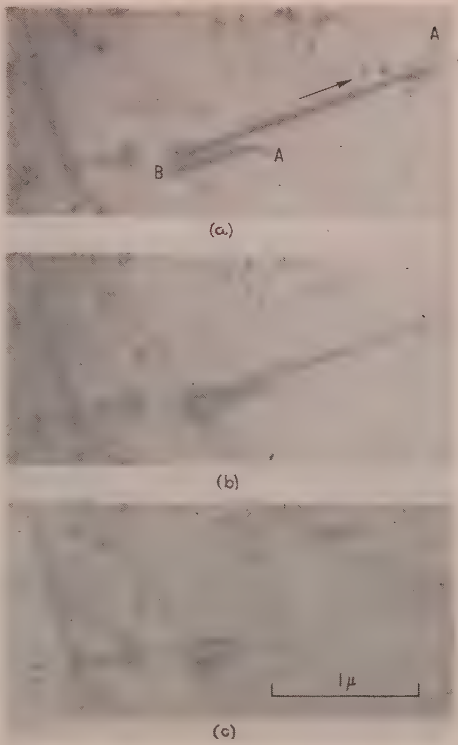

FIG. 1. Formation of a sessile dislocation loop on a basal plane in a cadmium platelet at −110°C. A screw dislocation, moving in the direction of the arrow, became jogged at B and left behind an elongated loop. See text and Fig. 5 for explanation.

Since both **c**+**a** loops and **c** loops had Burgers vectors out of the basal plane, they could only move in this plane by a diffusional process, and this was not observed at temperatures below ~−120°C. (Note, however, that the loops in Fig. 1, which were formed at −90° to −100°C, have become rounded by a diffusional process to be described in the next section.) Prismatic glide along the direction of the Burgers vector was never observed at any temperature. At low temperature, therefore, the density of loops increased with the strain and the number and shape of loops remained the same during a low-temperature anneal of up to two hours' duration.

During second-order pyramidal glide, secondary dislocations with Burgers vectors $\frac{1}{3}\langle\overline{11}20\rangle=\mathbf{a}$ were produced at the edges of the platelet and moved on basal planes, being subjected to a stress only on segments which jogged from one basal plane to another. The stress fields of the loops were such that they strongly resisted the movement of **a** dislocations on nearby basal planes. As a result of this interaction, which has recently been

---

[5] E. S. Wajda, G. A. Shirn, and H. B. Huntington, Acta Met. **3**, 39 (1955).

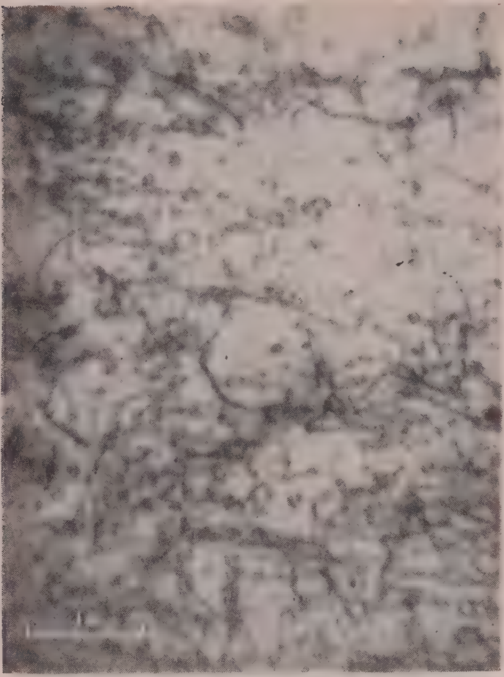

FIG. 2. Typical arrangement of **a** dislocations and loops, at −120°C and 6% strain, through which **c**+**a** dislocations had to move during second-order pyramidal glide.

analyzed by Kroupa and Price,[6] **a** dislocations could not move far through the crystal without becoming pinned at loops. Examples of pinned **a** dislocations can be seen in Figs. 1 and 3. In addition, groups of **a** dislocations with Burgers vectors at 120° to each other reacted to form networks which, together with the loops and pinned **a** dislocations, acted as strong obstacles to the movement of **c**+**a** dislocations on {$11\bar{2}2$} planes. Figure 2 shows a typical tangle of dislocations and loops through which the **c**+**a** dislocations had to move.

This pinning effect was observed to influence second-order pyramidal glide in several ways:

(1) The dislocation density increased rapidly with strain.

(2) Instead of moving with constant velocity, the **c**+**a** dislocations were forced to move by jerks, being temporarily held up until they could cut through **a** dislocations and cross-glide around loops.

(3) The region in which glide was taking place did not remain localized but propagated as a Lüders band until, after several percent strain, the entire platelet was filled with loops, individual dislocation lines, and networks.

At the highest strain obtainable with the low-temperature tensile device, ∼20%, most of the cadmium platelets were still deforming by second-order pyramidal glide. Occasionally a platelet twinned at high strain, particularly if, as a result of improper mounting it was not being loaded uniformly across its width.

Intermediate Temperature Second-Order Pyramidal Glide

At temperatures higher than ∼−120°C, the lon loops which were formed during the cross-glide of scre dislocations were able to lower their line energy b splitting up into rows of circular loops. This clearly in volved climb, since the movement occurred in the basa

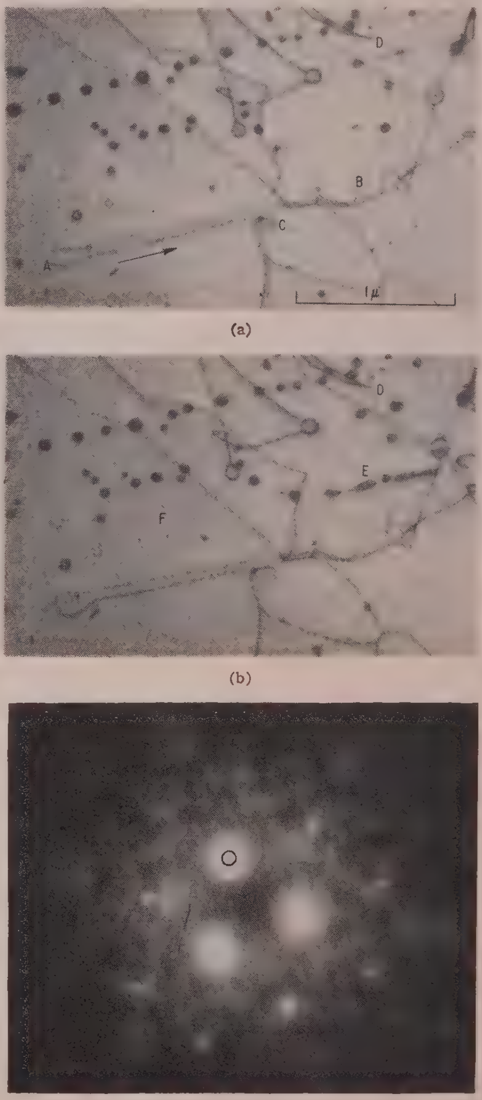

(a)

(b)

(c)

FIG. 3. (a), (b). Sequence taken at a 30-sec interval at ∼−95° showing the splitting up of long, sessile dislocation loops at A, I and E. (c) Selected area diffraction pattern from (a), showir strong $10\bar{1}0$ and $1\bar{1}00$ reflections. The central spot is encircled.

---

[6] F. Kroupa and P. B. Price, Phil. Mag. 6, 243 (1960).

plane and not along the glide cylinders of the loops. The same process was recently observed in zinc platelets[3] at higher temperatures and was called conservative climb,[6] since the total area enclosed by dislocation was found to be conserved during splitting. It was suggested[3] that the material inside the loops was redistributed by pipe-diffusion around the periphery of the loops. This type of diffusion requires a lower activation energy than that for volume self-diffusion and therefore occurs at temperatures considerably lower than those at which ordinary climb can take place.

The splitting of long loops in cadmium by conservative climb is illustrated by the sequence of micrographs in Fig. 3. In (a) a screw dislocation became jogged at A and moved ahead as two segments, B and C, which were connected to A by a long dipole. Soon after (b) was taken, the segment C rejoined B by cross-glide, pinching off a long loop. During the 30-sec interval between exposures the looplike configuration started rearranging near A to reduce its energy. The end became fatter and the part near the end became narrower, gradually forming a circular loop in a manner similar to that of water droplet formation at the end of a vertical pipe. Comparison of the two micrographs showed that the area inside the configuration indeed remained the same, so that volume diffusion was not involved.

At D in Fig. 3 a long loop split up into two circular loops during the interval between exposures. Also between exposures a **c**+**a** dislocation moved across the field of view, leaving behind a long loop at E which, when (b) was taken, was in the process of breaking up into several loops. The glide trace F left by the **c**+**a** dislocation is clearly visible in (b).

It will be noticed that many of the loops in Fig. 3 exhibited a dark contrast which is associated with the presence of a stacking fault. The selected area diffraction pattern, shown in (c), indicated that the contrast in (a) and (b) arose mainly from the $10\bar{1}0$ and $1\bar{1}00$ reflections, both of which would give dark contrast inside a loop containing a stacking fault. Loops with dark contrast have also been observed in zinc platelets when the reflecting planes responsible for the image were of $\{10\bar{1}0\}$ type. This point will be considered further in the discussion.

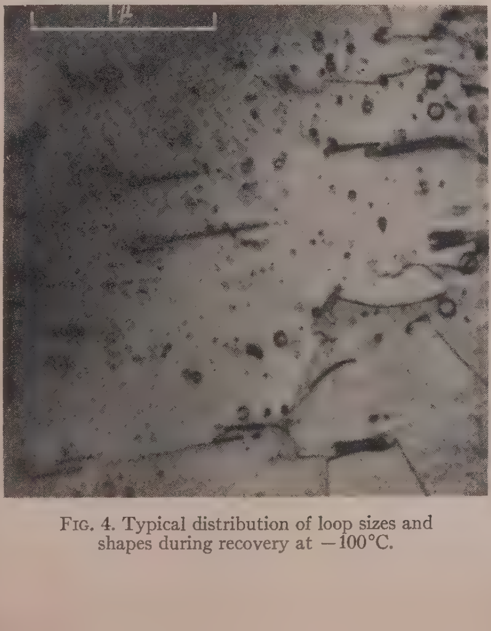

FIG. 4. Typical distribution of loop sizes and shapes during recovery at −100°C.

Figure 4, taken at −100°C, shows a typical arrangement of loops, some of which have split up into circular loops and some of which are still present as long loops. The rate of breakup of long loops was found to depend both on their size and on the temperature. At −120°C only the smallest ones, $\lesssim 200$ A in width, were observed to split up within a reasonable time, whereas at ~ -40°C even the largest ones, ~ 1000 A wide, split up within a few seconds. In the intermediate temperature range from −120° to ~ -40°C, the circular loops, once formed, were quite stable and remained the same diameter over a long period of time.

High-Temperature Second-Order Pyramidal Glide

At temperatures higher than ~ -40°C volume diffusion, and therefore also dislocation climb, took place at rates which increased rapidly with temperature. The most important recovery process was the annealing out of circular loops, the driving force being the line tension of the curved dislocations. For vacancy-type loops the climb presumably occurred by the formation and movement of vacancies from the loops to the surface of the platelet.

At −30°C only the smallest loops shrank at a noticeable rate, whereas at room temperature the rate was so fast that only large loops, $\gtrsim 500$ A in diameter, remained in the crystal long enough to be observed, and these all disappeared within a few seconds.

In the recent study of zinc platelets[2] it was found that loops disappeared in a time $\tau \propto r_0^2 \exp(E_D/kT)$, which was in agreement with the rate equation derived by Silcox and Whelan.[7] From measured values of τ, initial loop radius r_0, and temperature T, the activation energy E_D for self-diffusion parallel to the c axis in zinc was calculated and found to agree with the generally accepted value, ~ 0.95 ev.

In the present investigation measurements of loop decay in cadmium were complicated by a phenomenon to be described in the next section. Fairly consistent results could be obtained, provided the proper precautions were taken. Values for E_D obtained using the rate equation of Silcox and Whelan[7] ranged from ~ 0.75 to ~ 0.88 ev, whereas Wajda *et al.*,[5] using the radioactive tracer technique, obtained the value $E_D = 0.79$ ev for diffusion along the c axis.

In addition to the shrinking of loops, the climb of individual dislocation lines and of networks was also

---

[7] J. Silcox and M. J. Whelan, Phil. Mag. **5**, 1 (1960).

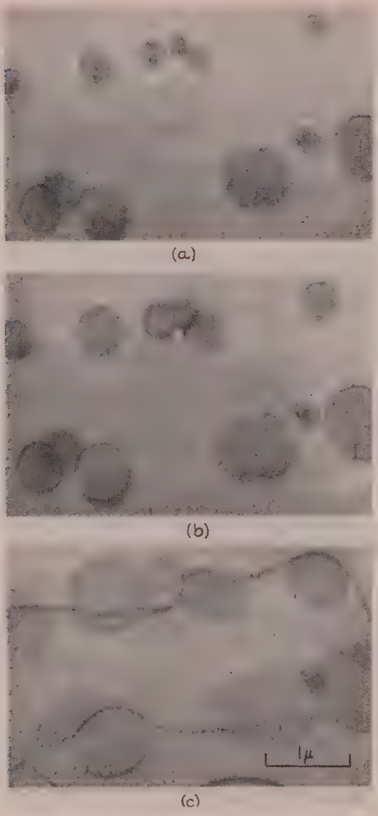

FIG. 5. Sessile dislocation loops which increased in size during observation in the electron microscope. The loops had already begun to grow before (a) was taken and continued to grow and interact with other loops after (c) was taken.

observed at increasing rates at temperatures above ~-40°C. Networks moved through the crystal by climb and sometimes completely disappeared at the surface. It became easy at the higher temperatures for $\mathbf{c}+\mathbf{a}$ dislocations either to cut through **a** dislocations or to drag them along, by a combination of glide and climb, until the obstructing portions were removed from the crystal.

At room temperature recovery by climb took place so rapidly during straining that very few dislocations stayed in the crystal. As a result there was little tendency, at low strain rate, for a Lüders band to form. Furthermore, as was mentioned in the preceding paper, the dislocations in a region under observation moved so readily as a result of stresses produced by even a low-intensity beam that it was difficult to take photographs at temperatures above about 0°C.

An additional temperature-dependent effect was observed which will only be briefly mentioned here, since it will be discussed in detail in another paper. All of the platelets were covered with a thin, epitaxial oxide layer; this was readily detected in the transmission diffraction patterns of the thinner platelets. At low temperatures $\mathbf{c}+\mathbf{a}$ dislocations had difficulty in moving through platelets which had been exposed to air for some time and which, presumably, had a fairly thick surface film. Frequently long edge components were left behind, probably near the metal-oxide interface, and were only able to penetrate the film and escape from the platelet if the temperature was raised. The temperature at which dislocations became stuck appeared to be higher for thicker oxide layers. In the remainder of this paper we will be concerned only with crystals whose oxide films were too thin to have a significant effect on the movement of dislocations.

Growth of Loops

During the study of the kinetics of loop decay, the very interesting and at first disturbing observation was made that loops sometimes grew instead of shrank. This growth was observed at low temperature as well as at room temperature. Figure 5 is a sequence, taken at -40°C, showing an array of loops which expanded until they began to coalesce. Once growth started it continued at a fairly rapid rate, with the composite loops sometimes reaching diameters as great as 10 μ before suddenly disappearing from the platelet. The elastic interactions and dislocation reactions between loops of various Burgers vectors expanding on different basal planes frequently gave rise to beautiful geometrical patterns. These interactions will be analyzed in another paper.

It was eventually discovered that loop growth was associated with electron bombardment at high beam intensities, which were frequently necessary because of the relatively low transmissivity of cadmium to electrons. Loops in zinc could also be made to expand by temporarily operating at high beam intensity, either by increasing the beam current or by removing the condenser aperture. In order to reduce spurious effects in measuring loop decay rates in cadmium, it was therefore necessary to operate at low intensity and to use long exposures in taking micrographs.

Second-Order Pyramidal Glide in Zinc

Detailed studies of second-order pyramidal glide in zinc platelets in the temperature range from $-150°$ to $+25$°C, made during the present investigation for purposes of comparison, showed that the behavior of $\mathbf{c}+\mathbf{a}$ dislocations and the formation of loops and networks were qualitatively the same as in cadmium, the

TABLE I. Temperature dependence of recovery.

Observations	Zinc	Cadmium
Very little recovery	$T\lesssim-80°\mathrm{C}$	$T\lesssim-120°\mathrm{C}$
Recovery only by splitting of long loops	$-80°\lesssim T\lesssim+10°$	$-120°\lesssim T\lesssim-40°$
Recovery by loop annealing and climb	$T\gtrsim+10°$	$T\gtrsim-40°$

main difference being that all of the recovery processes occurred at higher temperatures in zinc than in cadmium. The results are summarized in Table I.

In addition, it should be pointed out again that first-order pyramidal glide was not observed in zinc at all, whereas it was often observed in suitably oriented cadmium platelets.

DISCUSSION

Formation of Long Loops

In order to visualize better the mechanism of loop formation illustrated in the micrographs in Fig. 1, several stages in the process were drawn in perspective in Fig. 6. The drawing shows an obstacle (of unknown nature) which blocked the screw and caused it to cross-glide. The first stages, (a) to (c), always occurred so fast that it is not certain precisely how the configuration in (d) was reached, but it is certain that the dipole connecting the jog to the screw components was formed by pure glide, because it appeared too fast, even at temperatures as low as −120° in both zinc and cadmium, for much movement of point defects to have taken place.

Fourie and Wilsdorf[8] have recently proposed several mechanisms, not involving cross-glide, to explain the formation of long loops, each of them requiring that a supply of point defects be present to allow the components of a narrow dipole to move apart by climb. The above observations of rapid dipole formation are conclusive evidence that long loops are formed in zinc and cadmium platelets by a cross-glide mechanism and not by the climb mechanism suggested by Fourie and Wilsdorf. There is also less direct evidence that long loops are formed in bulk specimens by glide rather than by climb. For example, Segall *et al.*[9] have found long loops in nickel specimens which were cyclically strained at 25°C, a temperature at which vacancies are certainly not mobile.

Splitting of Long Loops

In order for a long loop with initially straight sides to split by conservative climb, jogs must be formed and moved along the dislocation, the activation energy being that for pipe-diffusion. Whether a long loop will split into smaller loops at a relatively low temperature or simply anneal out as a narrow loop at a higher temperature (at which climb can occur) will depend on the relative difficulty of jog formation and movement. If the dislocation is separated into partials, they will have to be forced together at the point where the jog is formed. Long loops should thus break up only in materials which have a high stacking fault energy associated with the separation into partials. It follows that these materials will have a low activation energy for pipe-diffusion.

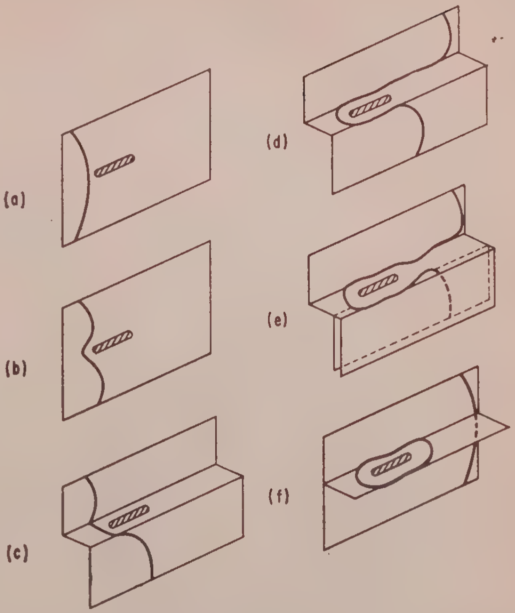

FIG. 6. Formation of a long dislocation loop. Stages (a) to (d) happened very rapidly, presumably when a **c**+**a** screw dislocation attempted to cross-glide around an obstacle. Stages (d), (e), and (f) were actually observed many times, e.g., in Fig. 1.

Segall *et al.*[9] have indeed found that long loops in low stacking fault energy metals such as copper tend to shrink without pinching off and that those in high stacking fault energy metals such as nickel decompose into smaller loops. Small loops which probably pinched off from longer loops have recently been observed in other materials with a high stacking fault energy—magnesium oxide,[10] niobium,[11] and molybdenum.[12] Mechanisms similar to the above were proposed for their formation and splitting.

From the observed breakup of long **c**+**a** loops in cadmium and zinc, together with the observed ease of cross-glide of **c**+**a** dislocations at very low temperatures, it is concluded that **c**+**a** dislocations probably do not separate into partials and that the stacking fault energy associated with such an extended dislocation would be very high. Since the Burgers vector of a loop in cadmium and zinc is very large, ∼6 A, it is not surprising that pipe-diffusion and loop splitting occur at temperatures too low for climb to take place.

Stacking Fault Loops

There appear to be at least two ways in which a loop consisting of a partial dislocation enclosing a stacking fault on the basal plane might develop:

---

[8] J. T. Fourie and H. G. F. Wilsdorf, J. Appl. Phys. **31**, 2219 (1960).

[9] R. L. Segall, P. G. Partridge, and P. B. Hirsch, Phil. Mag. (to be published).

[10] J. Washburn, G. W. Groves, A. Kelly, and G. K. Williamson Phil. Mag. **5**, 991 (1960).

[11] R. L. Segall (private communication).

[12] G. Thomas (private communication).

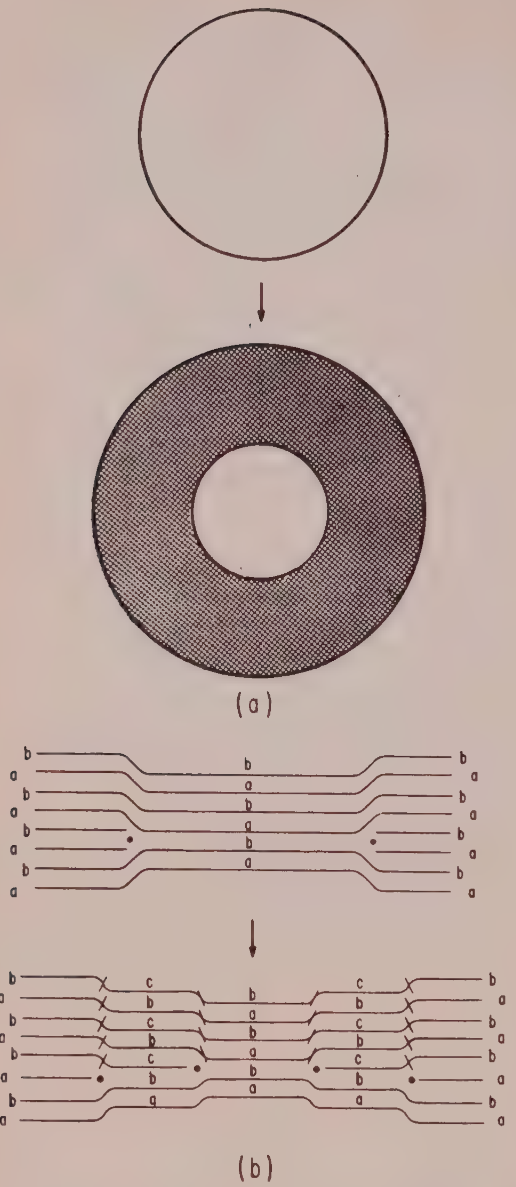

FIG. 7. Decomposition of a **c**+**a** loop into two partial dislocation loops through the reaction $\frac{1}{3}[\bar{1}\bar{1}23] \rightarrow \frac{1}{6}[\bar{2}023]+\frac{1}{6}[0\bar{2}23]$. One loop grows at the expense of the other, leaving finally a single $\frac{1}{6}[\bar{2}023]$ loop containing a stacking fault.

(1) Some of the tiny loops in Fig. 3 might have been formed by the collapse of vacancy disks, the vacancies having been emitted at single jogs and then having clustered into disks.

(2) Most of the loops in Fig. 3, in particular the long loops at D and E and the circular loops arranged in rows, were formed by the process illustrated in Fig. 6, so that they were initially perfect dislocation loops. A possible way in which these loops could have developed a stacking fault is shown in Fig. 7, where the notation of Frank and Nicholas[13] has been used to indicate the stacking of close-packed planes about the dislocations. It involves the reaction $\frac{1}{3}[\bar{1}\bar{1}23] \longrightarrow \frac{1}{6}[\bar{2}023]+\frac{1}{6}[0\bar{2}23]$, which can take place on the basal plane only by climb.[13] One can envisage a **c**+**a** loop, with two layers of atoms missing, as made up of two loops with a $\frac{1}{6}\langle\bar{2}023\rangle$ type Burgers vector, one directly above the other and each having a missing layer of atoms. (These loops are the same type as those formed by vacancy condensation.) At a suitable temperature, one loop would then grow at the expense of the other by means of radial diffusion along the stacking fault bounded by the two loops. Assuming that no volume diffusion took place, the final area of the one remaining loop containing the stacking fault would be twice that of the original **c**+**a** loop. This process should lead to a reduction of energy, provided the initial area of the loop is not too large.

On the original plates from which Fig. 3 was made, small light loops were actually observed in the centers of some of the dark loops, suggesting that such a process was going on when the exposures were made.

Clearly more observations must be made before a detailed calculation of the kinetics of this process can be justified.

Work-Hardening

The electron microscope observations of loops, and of the resulting tangle of dislocations which acted as strong obstacles to second order pyramidal glide, have emphasized the importance of jogs on screw dislocations as a cause of work-hardening. From the wide distribution of observed loop sizes (~5000 A down to the limit of resolution of the transmission technique, ~50 A) it is clear that, during deformation, jogs are formed in a wide range of sizes, probably down to atomic size. Atomic jogs will, of course, produce rows of point defects rather than loops. At temperatures which are not too low these point defects will influence the deformation by clustering into disks, which collapse to form loops, and by interacting with other dislocations, causing climb and kinking.

Hirsch[14] has recently developed a theory which explains qualitatively many of the features of work-hardening of face-centered cubic metals by considering the behavior of jogs. Although he has not extended the theory to hexagonal metals, the electron microscope observations are taken as evidence that jogs on screw dislocations, and the pinning effect of loops produced at jogs, are the major causes of work-hardening during nonbasal glide in zinc and cadmium. In the preceding paper it was seen that no buildup of dislocation density, and therefore no work-hardening, occurred in cadmium when the dislocations were of pure edge orientation and were not intersected by dislocations on another glide system.

---

[13] F. C. Frank and J. F. Nicholas, Phil. Mag. **44**, 1213 (1953).

[14] A summary of Hirsch's theory is given by N. F. Mott in Trans. Am. Inst. Mining Met. Petrol. Engrs. **218**, 962 (1960).

It is quite likely that work-hardening during the basal glide of suitably oriented crystals occurs in a similar way, the jogs on **a** dislocations with a screw component being responsible for loop formation. In fact, Seeger and Träuble[15] have recently proposed such a mechanism to explain their observations of the temperature dependence of work-hardening during basal glide in zinc.

Loop Growth

The growth of sessile dislocation loops during observation in the electron microscope was first observed by Fourdeux *et al.*[16] in an electrothinned zinc foil. They concluded that some oxidation occurred during irradiation in a moderate vacuum and that the transfer of zinc atoms from the zinc lattice to the zinc oxide lattice resulted in the formation at the metal-oxide interface of points defects which condensed on the loops.

In view of the present observation that loop growth occurred in both zinc and cadmium at very low temperatures, it is not likely that point defects would be formed at the metal-oxide interface. Oxidation at low temperature should take place primarily by the removal of metal atoms from steps at the metal surface and by the diffusion of the metal atoms through the oxide layer to the oxide surface.[17] Thus no point defects would be formed during the movement of steps across the metal surface.

There is growing evidence that point defects are produced during electron bombardment as a result of ionization of residual gas molecules, which are then accelerated and damage the crystal. Pashley[18] has shown conclusively that the appearance of the black spotlike structure in gold films during observation in the microscope is due to radiation damage by ions which are almost certainly produced in the gun. Brandon and Bowden[19] have recently found that ion bombardment at energies as low as 80 ev results in extensive radiation damage near the surface. It is therefore felt that the point defects which cause the growth of dislocation loops arise during radiation damage by ions rather than during oxidation.

CONCLUSIONS

(1) Pyramidal glide on the $\{11\bar{2}2\}$ $\langle\bar{1}\bar{1}23\rangle$ system took place in initially dislocation-free cadmium platelets by the movement of $\frac{1}{3}\langle\bar{1}\bar{1}23\rangle$ screw dislocations, primarily on $\{11\bar{2}2\}$ planes. Much smaller numbers of secondary dislocations with $\frac{1}{3}\langle\bar{1}\bar{1}20\rangle$ Burgers vectors were formed on basal planes.

(2) Elongated sessile dislocation loops were formed on basal planes when screws became jogged during cross-glide. The possibility that loop formation was assisted by point defect movement was ruled out because of the observation that it occurred rapidly even at very low temperatures.

(3) Observations in the temperature range from −150° to +25°C showed that the behavior of dislocations in cadmium at a given temperature was qualitatively the same as in zinc at a somewhat higher temperature. Three temperature regions were found in which the recovery processes were distinctly different:

(a) At temperatures lower than $\sim -120°$ in Cd and $-80°$ in Zn the long loops were stable and practically no recovery took place. High densities of loops and tangled $\frac{1}{3}\langle\bar{1}\bar{1}20\rangle$ dislocations were built up which resisted the motion of $\frac{1}{3}\langle\bar{1}\bar{1}23\rangle$ dislocations and which, therefore, probably hardened the crystal.

(b) In the intermediate temperature range, $-120°$ to $-40°$ for Cd and $-80°$ to $+10°$ for Zn, long loops broke up into circular loops but the total area enclosed by loops remained the same. The process, called conservative climb, involved the pipe-diffusion of material around the long loops; this took place by the formation and movement of jogs, which required a lower activation energy than that for ordinary climb.

(c) At high temperature, above $\sim -40°$C in Cd and $\sim +10°$C in Zn, climb occurred more or less rapidly during deformation. Circular loops annealed out by volume diffusion with an activation energy of ~0.8 ev in Cd and ~0.95 ev in Zn. Secondary dislocation networks dispersed by climb. The density of dislocations in the crystal, and therefore the work-hardening, was small and very dependent on temperature and strain rate.

(4) Some of the loops produced during the deformation of both cadmium and zinc were made up of partial dislocations containing stacking faults.

(5) The growth of loops which was sometimes observed in both cadmium and zinc at high beam intensities probably resulted from the condensation of point defects produced near the surface by ion bombardment, the ions being formed by the interaction between electrons and residual gas molecules.

---

[15] A. Seeger and H. Träuble, Z. Metallk. **51**, 435 (1960).

[16] A. Fourdeux, A. Berghezan, and W. W. Webb, J. Appl. Phys. **31**, 918 (1960).

[17] D. A. Vermilyea (private communication).

[18] D. W. Pashley (private communication).

[19] D. G. Brandon and P. B. Bowden, Phil. Mag. (to be published).

JOURNAL OF APPLIED PHYSICS VOLUME 32, NUMBER 9 SEPTEMBER, 1961

Electromagnetic Surface Waves on a Plane Interface

B. A. LENGYEL AND K. M. MITZNER
Hughes Research Laboratories, A Division of Hughes Aircraft Company, Malibu, California

(Received February 13, 1961)

Surface waves are defined as waves exponentially decreasing on both sides of a plane interface. It is shown how all such waves can be generated from a single Hertz vector perpendicular to the interface. The relations between the propagation parameters of the waves and the material constants are derived in a general case which includes media with different magnetic permeabilities. The condition for the existence of surface waves is derived.

I. INTRODUCTION

A GREAT deal already has been written on the existence and the excitation of surface waves. Yet it is desirable to make a few historical remarks to define the scope of the work reported here and to put it in proper perspective.

In 1907, Zenneck[1] discussed the propagation of electromagnetic radiation near the plane interface of water and air and deduced the existence of special solutions of Maxwell's equations which represent electric and magnetic fields decaying exponentially on both sides of the interface. Two years later Sommerfeld[2] showed that such exponentially decaying waves arise in the analysis of the radiation of a dipole placed at or near the plane interface of air and a lossy dielectric medium. The physical significance of these waves has been discussed at length with prime emphasis on the excitation of these waves by specific sources and on the detectability of such waves. Among the numerous review papers in this field, those of Barlow and Cullen[3] and of Goubau[4] are particularly instructive. The latter includes the review of a broader group of phenomena, some associated with curved surfaces, others with boundaries more complicated than a single dielectric interface.

In this paper we shall examine the conditions for the existence at a plane interface of surface waves which are not tied to waves of other kinds. In other words, we will study the conditions for the existence (in appropriate regions) of solutions of Maxwell's equations which decay exponentially in both directions normal to a plane interface and which satisfy the usual boundary conditions in the absence of other waves. We will permit these waves to be excited by an entirely general system of currents outside of the region of interest; we leave aside the question of other waves also excited by these sources.

Our main concern will be with the general nature of the surface waves and the conditions which the material constants of the two media must satisfy in order that surface waves may exist at the plane interface separating such media. We will show that these conditions are independent of the particular form or mode of the surface wave, and we will also show that only transverse magnetic surface waves may exist, where transverse means parallel to the interface. Many of the results to be derived here have already been published as pertaining to surface waves of special types, but here their validity will be demonstrated as being independent of the particular mode or waveform assumed. In addition, calculations which have heretofore been confined to nonmagnetic materials will be extended to cover the case of paramagnetic and diamagnetic materials. Finally, problems pertaining to the energy flow in surface waves will be considered.

II. FORMULATION OF THE PROBLEM

Let the plane $z=0$ separate two isotropic, homogeneous media M_1 and M_2 of infinite extent. Each medium is characterized by a dielectric constant ϵ, permeability μ, and conductivity σ. These are positive quantities, with the conductivity permitted to be arbitrarily small. It is assumed that sources of electromagnetic radiation are present outside of the region of interest. We make no restriction on these sources other than that they be harmonic in time, i.e., they vary with t in the manner $\exp(-i\omega t)$.

We adopt rationalized mks units and introduce the complex wave numbers by means of the equation

$$k^2=\epsilon\mu\omega^2+i\mu\sigma\omega. \tag{2.1}$$

For a fixed frequency each medium may be characterized by the complex number k^2 and the positive number μ. Clearly k^2 must lie in the first quadrant. The parameters of the material, k^2 and μ, will be provided with the suffixes 1 and 2 when they pertain to media M_1 and M_2, respectively. Without restricting generality, the indices will be so chosen that

$$\arg k_1^2 \leqq \arg k_2^2, \tag{2.2}$$

and the coordinate system will be so oriented that M_1 occupies the upper half-space $z>0$.

We will define surface waves in regions limited as follows: the region contains an area of the $z=0$ plane in its interior; moreover no electromagnetic sources are contained in the region or in the least cylinder whose elements are parallel to the z axis and which contains the region. In the case of a single dipole source, e.g., the region may consist of the entire space with the exclusion of a cylinder surrounding the dipole. *A surface wave as here defined is then a solution of Maxwell's equations which has no singularities within the region, satisfies the usual boundary conditions at the interface $z=0$, and which decreases exponentially with $|z|$ on both sides of the interface.* This definition of a surface wave emphasizes the separate nature of surface waves. The evanescent waves occurring on one side of the interface in total reflection are not to be regarded as surface waves according to this definition, since their presence is bound to the presence of an incident and a reflected wave on the other side of the interface, and at least one of these waves is not exponentially decreasing with $|z|$.

---

[1] J. Zenneck, Ann. Physik **23**, 846 (1907).

[2] A. Sommerfeld, Ann. Physik **28**, 665 (1909); see also A. Sommerfeld, *Partial Differential Equations* (Academic Press, Inc., New York, 1949), Chap. VI.

[3] H. M. Barlow and A. L. Cullen, Proc. Inst. Elec. Engrs., (London) **100, Pt. III,** 329 (1953).

[4] G. Goubau, I.R.E. Trans. on Antennas and Propagation **AP-7,** S 140 (1959).

The construction of surface waves is greatly facilitated by the use of the Hertz vectors. It is known that the same field can be generated in a variety of ways by means of the electric and magnetic potentials. The choice of the form of representation is accomplished by means of the following theorem of Whittaker, as restated by Nisbet[5]:

"*In vacuo*, at points away from sources, a general electromagnetic field can be expressed in terms of two scalar functions F and G, each satisfying the homogeneous wave equation. The fields are derived from the Hertz vectors

$$\mathbf{\Pi}_e=F\mathbf{u},\quad \mathbf{\Pi}_m=G\mathbf{u},\tag{2.3}$$

where $\mathbf{u}$ is a unit vector in a fixed direction."

This theorem is immediately applicable to steady-state fields in any uniform, homogeneous, and isotropic medium, since the field equations in this medium are obtained from those valid in vacuo by replacing ϵ_0 by $\epsilon+i\sigma/\omega$ and μ_0 by μ.

In the case under consideration, the analytic form of the Hertz vectors, and thus the scalar functions F and G, will be different in the two media M_1 and M_2, since in M_1 the Hertz vectors satisfy the differential equation

$$\nabla^2\mathbf{\Pi}_1+k_1^2\mathbf{\Pi}_1=0,\tag{2.4}$$

while in M_2

$$\nabla^2\mathbf{\Pi}_2+k_2^2\mathbf{\Pi}_2=0.\tag{2.5}$$

Each of the last two equations is applicable to the electric and the magnetic Hertz vectors separately.

The electric and magnetic fields are given by

$$\mathbf{E}=\nabla\times\nabla\times\mathbf{\Pi}_e+i\omega\mu\nabla\times\mathbf{\Pi}_m,\tag{2.6}$$

$$\mathbf{H}=\frac{k^2}{i\omega\mu}\nabla\times\mathbf{H}_e+\nabla\times\nabla\times\mathbf{\Pi}_m.\tag{2.7}$$

Clearly all quantities in (2.6) and (2.7) except ω carry a subscript 1 in the upper half-space and 2 in the lower half-space.

We will choose $\mathbf{u}$ as the unit vector pointing in the positive z direction. The surface wave may be derived from Hertz vectors of the form

$$\mathbf{\Pi}=\frac{1}{\lambda}P\exp\lambda z\mathbf{u}.\tag{2.8}$$

In this last equation the subscripts e, m, 1, and 2 have been suppressed; actually one has four equations each involving one of the constants λ_{e1}, λ_{m1}, λ_{e2}, λ_{m2} and the corresponding scalar function P of two variables, e.g., x and y. The λ in the denominator is simply for convenience, as will become apparent later.

Exponential decay is assured when the real parts of λ_{e1} and λ_{m1} are negative and those of λ_{e2} and λ_{m2} are positive. Thus we will demand

$$\mathrm{Re}\lambda_{e1}<0,\ \mathrm{Re}\lambda_{m1}<0,\ \mathrm{Re}\lambda_{e2}>0,\ \mathrm{Re}\lambda_{m2}>0.\tag{2.9}$$

On substituting (2.8) into (2.4) and (2.5) we obtain

$$\nabla^2P_{ei}+(k_i^2+\lambda_{ei}^2)P_{ei}=0,\quad i=1,2;\tag{2.10}$$

$$\nabla^2P_{mi}+(k_i^2+\lambda_{mi}^2)P_{mi}=0,\quad i=1,2.\tag{2.11}$$

Thus we have four differential equations in two variables (x,y) of the form

$$\nabla^2P+p^2P=0,\tag{2.12}$$

and (apparently) four constants:

$$p_{e1}^2=k_1^2+\lambda_{e1}^2,\quad p_{m1}^2=k_1^2+\lambda_{m1}^2,$$
$$p_{e2}^2=k_2^2+\lambda_{e2}^2,\quad p_{m2}^2=k_2^2+\lambda_{m2}^2.$$

The special case $p=0$ does not correspond to a surface wave. In fact, when one of the p's is 0, the corresponding P satisfies Laplace's equation, and the vector potential $Pe^{\pm ikz}$ represents an inhomogeneous plane wave propagating perpendicular to the interface, decaying exponentially at a rate characteristic of the medium. It is rather obvious that the boundary conditions at $z=0$ cannot be satisfied by a pair of such waves traveling *away* from the interface in both media. On the other hand, a wave traveling *toward* the interface would not decrease as $|z|$ increases. For these reasons the case $p=0$ will be excluded.

Substitution of (2.8) into (2.6) and (2.7) gives the following expressions for the tangential and normal components of the fields:

$$E_{\tan}=e^{\lambda_e z}\nabla P_e+e^{\lambda_m z}\frac{i\omega\mu}{\lambda_m}\nabla P_m\times\mathbf{u},\tag{2.13}$$

$$H_{\tan}=e^{\lambda_e z}\frac{k^2}{i\omega\mu\lambda_e}\nabla P_e\times\mathbf{u}+e^{\lambda_m z}\nabla P_m,\tag{2.14}$$

$$E_z=\frac{1}{\lambda_e}e^{\lambda_e z}p_e^2P_e,\tag{2.15}$$

$$H_z=\frac{1}{\lambda_m}e^{\lambda_m z}p_m^2P_m.\tag{2.16}$$

---

[5] E. T. Whittaker, Proc. London Math. Soc., Ser. 2 **1**, 367 (1903); A. Nisbet, Proc. Roy. Soc. (London) **A231**, 250 (1955).

In the last four equations the subscripts 1 and 2 have been omitted, since the equations are formally identical in both media. The continuity of the tangential components at the interface $z=0$ requires that

$$\nabla(P_{e1}-P_{e2})+i\omega\nabla\left(\frac{\mu_1}{\lambda_{m1}}P_{m1}-\frac{\mu_2}{\lambda_{m2}}P_{m2}\right)\times\mathbf{u}=0, \tag{2.17}$$

$$\frac{1}{i\omega}\nabla\left(\frac{k_1^2}{\mu_1\lambda_{e1}}P_{e1}-\frac{k_2^2}{\mu_2\lambda_{e2}}P_{e2}\right)\times\mathbf{u}+\nabla(P_{m1}-P_{m2})=0. \tag{2.18}$$

These equations enable us to calculate the p's and P's. To reduce the number of constants and (apparently) different functions, we take the divergence of Eqs. (2.17) and (2.18) and note that for any scalar P and fixed vector $\mathbf{u}$:

$$\nabla\cdot(\nabla P\times\mathbf{u})=\mathbf{u}\cdot(\nabla\times\nabla P)-\nabla P\cdot(\nabla\times\mathbf{u})=0;$$

therefore

$$\nabla^2(P_1-P_2)=p_2^2P_2-p_1^2P_1=0 \tag{2.19}$$

holds for both the electric and the magnetic quantities. In terms of the normal components this means that

$$\lambda_{e1}E_{z1}-\lambda_{e2}E_{z2}=0, \tag{2.20}$$

$$\lambda_{m1}H_{z1}-\lambda_{m2}H_{z2}=0, \tag{2.21}$$

as may be verified by comparing (2.15), (2.16), and (2.19).

Now we shall show that $p_{e1}^2=p_{e2}^2$ and $p_{m1}^2=p_{m2}^2$. The proof is equally applicable to the electric and to the magnetic case; therefore, the subscripts e and m will be omitted. Since the case $p=0$ may be left out of consideration, Eq. (2.19) asserts that the ratio of the functions $P_1(x,y)$ and $P_2(x,y)$ is a constant. Therefore

$$P_1\nabla P_2-P_2\nabla P_1\equiv 0. \tag{2.22}$$

Using this in Green's theorem, it follows that for any region in the (x,y) plane where P_1 and P_2 are not singular

$$\int(P_1\nabla^2P_2-P_2\nabla^2P_1)dxdy \equiv\int(P_1\nabla P_2-P_2\nabla P_1)\cdot\mathbf{n}ds=0. \tag{2.23}$$

Hence, with the aid of (2.12),

$$P_1\nabla^2P_2-P_2\nabla^2P_1\equiv P_1P_2(p_1^2-p_2^2)\equiv 0. \tag{2.24}$$

Thus, leaving aside the case of an identically vanishing field, we have

$$p_1^2=p_2^2. \tag{2.25}$$

Further, from (2.19) and $p^2\neq 0$ we conclude that

$$P_{e1}\equiv P_{e2},\quad P_{m1}\equiv P_{m2}. \tag{2.26}$$

[This simple result motivated the use of λ's in the denominator of Eq. (2.8).] Now the boundary conditions (2.17) and (2.18) simplify to

$$\left(\frac{\mu_1}{\lambda_{m1}}-\frac{\mu_2}{\lambda_{m2}}\right)\nabla P_m=0, \tag{2.27}$$

$$\left(\frac{k_1^2}{\mu_1\lambda_{e1}}-\frac{k_2^2}{\mu_2\lambda_{e2}}\right)\nabla P_e=0. \tag{2.28}$$

The coefficient of ∇P_m in (2.27) can never vanish because the μ's are both positive and the λ's belong to different quadrants of the complex plane. Therefore $\nabla P_m=0$, P_m is a constant which may be set equal to zero, and the $\mathbf{\Pi}_m$ vector does not generate surface waves.[6]

The coefficient of ∇P_e in Eq. (2.28) will vanish when

$$k_1^2/\mu_1\lambda_1=k_2^2/\mu_2\lambda_2. \tag{2.29}$$

This equation expresses the equality of wave impedance in the two media. It is the general form of the Sommerfeld relation, which for the case $\mu_1=\mu_2$ is customarily written in the form

$$k_1^2(p^2-k_2^2)^{\frac{1}{2}}+k_2^2(p^2-k_1^2)^{\frac{1}{2}}=0; \tag{2.30}$$

the apparent difference in sign arises from the freedom of choice in selecting the square root of a complex number. Under certain circumstances Eq. (2.29) may be satisfied and in this case *every solution of Eq. (2.12) generates a surface wave.*

III. CONDITIONS FOR THE EXISTENCE OF SURFACE WAVES

We shall now examine the conditions which the materials must satisfy in order that surface waves may exist at the interface of two materials and determine the constants λ_1 and λ_2 from the material parameters. It is thus required to determine what the limitations are on the parameters k_1^2, k_2^2, μ_1 and μ_2 which ensure that the equations

$$p^2=k_1^2+\lambda_1^2=k_2^2+\lambda_2^2 \tag{3.1}$$

and

$$k_1^2/\mu_1\lambda_1=k_2^2/\mu_2\lambda_2 \tag{3.2}$$

have solutions with $\mathrm{Re}\lambda_1<0$ and $\mathrm{Re}\lambda_2>0$.

The important case $\mu_1=\mu_2$ permits a very elegant solution. Let us introduce the quantities $p^2=k^2+\lambda^2$, $iq=k^2/\lambda$. These must be independent of the index, in view of (3.1) and (3.2); therefore, they are symmetric functions of k_1^2 and k_2^2. In fact, by eliminating the λ's we obtain

$$q^2=k_1^2+k_2^2, \tag{3.3}$$

$$p^2q^2=k_1^2k_2^2. \tag{3.4}$$

Hence

$$1/p^2=(1/k_1^2)+(1/k_2^2). \tag{3.5}$$

---

[6] Sommerfeld noted that a magnetic dipole perpendicular to the interface generates no surface waves. [Ann. Physik **81**, 1139 (1926).]

Naturally, p^2 and q are symmetric functions of the λ's as well:

$$p^2=-\lambda_1\lambda_2, \quad q=i(\lambda_1+\lambda_2). \tag{3.6}$$

Now, p^2 and q^2 both lie in the first quadrant because k_1^2 and k_2^2 are both in that quadrant. Thus q is either in the first or in the third quadrant. Moreover, from

$$\lambda_2/\lambda_1=k_2^2/k_1^2 \tag{3.7}$$

and the assumptions concerning the k's, it follows that

$$0<\arg\lambda_2-\arg\lambda_1<\pi/2. \tag{3.8}$$

Then from $\mathrm{Re}\lambda_1<0$ and $\mathrm{Re}\lambda_2>0$ it follows that λ_1 must lie in the third quadrant and λ_2 in the fourth. The situation is shown in Fig. 1 which also shows that the angle included between the λ's is equal to that included between the k^2's. Then $q=i(\lambda_1+\lambda_2)$ *must lie in the first quadrant*. It follows then immediately that

$$\lambda_1=k_1^2/i(k_1^2+k_2^2)^{\frac{1}{2}}, \quad \lambda_2=k_2^2/i(k_1^2+k_2^2)^{\frac{1}{2}}, \tag{3.9}$$

where $(k_1^2+k_2^2)^{\frac{1}{2}}$ is in the first quadrant. We have thus determined the algebraic form of p, λ_1, and λ_2, provided that the problem admits a solution which corresponds to surface waves. This will be the case when the λ's determined formally by means of (3.9) lie in the proper parts of the complex plane. There is clearly no problem about λ_2; it will always lie in the fourth quadrant because

$$0<\arg k_2^2-\tfrac{1}{2}\arg(k_1^2+k_2^2)<\pi/2; \tag{3.10}$$

hence

$$-\pi/2<\arg[k_2^2/i(k_1^2+k_2^2)^{\frac{1}{2}}]<0. \tag{3.11}$$

But λ_1 will lie in the third quadrant only if

$$2\arg k_1^2<\arg(k_1^2+k_2^2). \tag{3.12}$$

This is the condition for the existence of a surface wave.

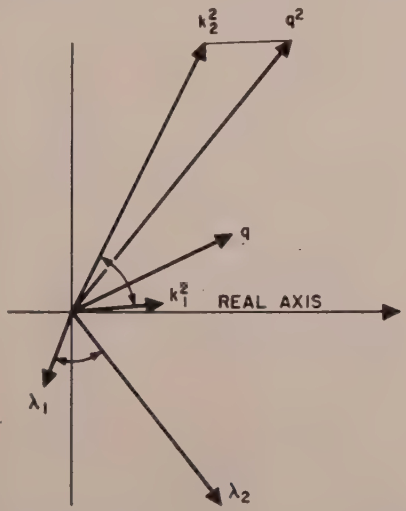

FIG. 1. Disposition of the wave numbers and related quantities.

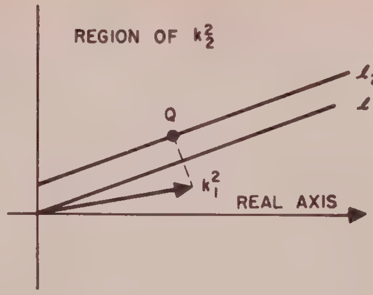

FIG. 2. Representation of the existence condition for surface waves.

The last inequality means that the arithmetic mean of k_1^2 and k_2^2 must lie above the line $\arg z=2\arg k_1^2$ shown as line l_1 in Fig. 2. Consequently k_2^2 must lie in a region of the first quadrant bounded from below by the line l_2 which is parallel to l_1 and which passes through the mirror image Q of k_1^2 with respect to l_1. This condition is clearly satisfied when the first medium is nearly lossless and the second is highly lossy, as is the case for the air-water interface. It is not satisfied, however, when the loss angles of the two media are not radically different.

The calculation in the general case $\mu_1\neq\mu_2$ is quite similar, although the expressions are more involved. We set $p^2=k^2+\lambda^2$ and $iq=k^2/\lambda\mu$. Then we obtain

$$q^2=[(k_2^4/\mu_2^2)-(k_1^4/\mu_1^2)]/(k_2^2-k_1^2), \tag{3.13}$$

which reduces to $k_1^2+k_2^2$ for $\mu_1=\mu_2$. In passing from q^2 to q, the ambiguity in the argument is resolved by the requirements that q is in the first quadrant when $\mu_1=\mu_2$ and that q^2 is a continuous function of μ_1 and μ_2 for positive values of these variables. We may write (for $\mu_1>0$)

$$\begin{aligned}\arg q=&\tfrac{1}{2}\arg[k_2^2-(\mu_2/\mu_1)k_1^2]\\&+\tfrac{1}{2}\arg[k_2^2+(\mu_2/\mu_1)k_1^2]-\tfrac{1}{2}\arg(k_2^2-k_1^2).\end{aligned} \tag{3.14}$$

When t is real, the points representing the complex numbers $k_2^2-tk_1^2$ lie on a straight line which does not intersect the positive real axis; therefore none of the arguments in (3.14) pass through zero as μ_1 and μ_2 are varied. Consequently, the argument of q is determined uniquely by (3.14) if all arguments are reckoned from 0 to 2π.

Having determined q, the λ's are calculated from $\lambda=k^2/iq\mu$; therefore the condition for λ_1 to be in the third quadrant is

$$-\pi<\arg k_1^2-\arg q-\pi/2<-\pi/2, \tag{3.15}$$

and that for λ_2 to be in the fourth quadrant is

$$-\pi/2<\arg k_2^2-\arg q-\pi/2<0. \tag{3.16}$$

The final condition for the existence of surface waves is a combination of these conditions, namely

$$\arg k_1^2 < \arg q < \arg k_2^2, \tag{3.17}$$

where the central term is defined by Eq. (3.14). In the special case $\mu_1 = \mu_2$, the second half of the inequality is automatically fulfilled and the first half becomes identical to (3.12).

Propagation along the interface is characterized by the parameters $\pm p$, which are the roots of

$$p^2 = \frac{k_1^2 k_2^2}{(k_1^4/\mu_1^2) - (k_2^4/\mu_2^2)} \left[\frac{k_1^2}{\mu_1^2} - \frac{k_2^2}{\mu_2^2} \right]. \tag{3.18}$$

This equation is equivalent to the expression found by Sommerfeld[2]; it reduces to (3.5) for $\mu_1 = \mu_2$. The parameters $\pm p$ are thus independent of the wave configuration, the latter being characterized by the function $P(x,y)$.

It is obvious from (2.8) that the penetration of the field into the media is characterized by the two "skin depths":

$$\delta_1 = -1/\mathrm{Re}(\lambda_1); \quad \delta_2 = 1/\mathrm{Re}(\lambda_2); \tag{3.19}$$

but $\lambda = k^2/iq\mu$, so this becomes

$$\delta_1 = -\mu_1/\mathrm{Im}(k_1^2/q), \quad \delta_2 = \mu_2/\mathrm{Im}(k_2^2/q). \tag{3.20}$$

This leads to an interesting characterization of the cutoff phenomenon of (3.17): the lower cutoff occurs when $\delta_1 = \infty$, the upper when $\delta_2 = \infty$. As we recede from cutoff into the surface-wave region, the skin depth decreases from infinity on one side of the interface and increases on the other side. The regions where no surface waves exist are regions where formal solution of (3.20) leads to a negative δ.

IV. ENERGY FLOW

The average rate of energy flow in a harmonic electromagnetic field is expressible in terms of the complex Poynting vector

$$\mathbf{S} = \tfrac{1}{2} \mathbf{E} \times \mathbf{H}^*, \tag{4.1}$$

where the star designates complex conjugate. The energy dW transferred per unit time through a surface element da, whose normal is $\mathbf{n}$ is given by[7]

$$dW = \mathrm{Re}(\mathbf{S} \cdot \mathbf{n} da). \tag{4.2}$$

Let us find the energy transfer due to a surface-wave field, assuming for the moment that no other fields are present. We have shown that a surface wave is derivable from an "electric" Hertz vector of the form

$$\mathbf{\Pi}_i = \frac{1}{\lambda_i} P(x,y) e^{\lambda_i z} \mathbf{u}, \tag{4.3}$$

where the subscript i is 1 in medium M_1 and 2 in M_2, and where $\mathbf{u}$ is the unit vector $\mathbf{e}_z$. Then the field vectors have the form:

$$\mathbf{E}_i = e^{\lambda_i z} \left[\nabla P + \frac{p^2}{\lambda_i} P \mathbf{u} \right], \tag{4.4}$$

$$\mathbf{H}_i = e^{\lambda_i z} \frac{k_i^2}{i\omega\lambda_i\mu_i} \nabla P \times \mathbf{u}. \tag{4.5}$$

The last equation may be given another form by the introduction of the symmetric function $q = k^2/i\mu\lambda$ which was already used in the preceding section. Thus

$$\mathbf{H}_i = e^{\lambda_i z} \omega^{-1} q \nabla P \times \mathbf{u}. \tag{4.6}$$

Consequently,

$$\mathbf{S} = \frac{q^*}{2\omega} \exp(\lambda_i + \lambda_i^*) z \left[\nabla P + \frac{p^2}{\lambda_i} P \mathbf{u} \right] \times [\nabla P^* \times \mathbf{u}]$$

$$= \frac{q^*}{2\omega} e^{2\mathrm{Re}(\lambda_i z)} \left[\frac{p^2}{\lambda_i} P \nabla P^* - |\nabla P|^2 \mathbf{u} \right]. \tag{4.7}$$

Thus the rate of energy flow in the positive z direction—perpendicular to the interface—is

$$-|\nabla P|^2 e^{2\mathrm{Re}(\lambda_i z)} \,\mathrm{Re}(q)/2\omega.$$

Since q is in the first quadrant, as is apparent from (3.17), the z component of the energy flow is negative in both media. Energy is transferred from the less lossy medium to the more lossy one at the rate of $|\nabla P|^2 \,\mathrm{Re}(q)/2\omega$ per unit area of the interface. In a special case this transfer of energy into the more lossy medium has been noted by Barlow and Cullen.[3]

In any actual situation the surface-wave field will not stand alone, but will exist in conjunction with other waves which are known as radiation modes. Furthermore, the power in the surface wave and the power in the radiation modes will not be additive; cross terms will appear. Thus, the quantity which we have calculated should be considered the "self-power" of the surface wave only.

V. DISCUSSION AND SUMMARY

We have shown that surface waves may exist at the plane interface of the media M_1 and M_2 if and only if certain inequalities are satisfied between the material constants characterizing these media. When one of the media is essentially lossless and the other highly lossy, these inequalities are satisfied. This is the case when M_1 is air and M_2 water or soil. However, the conditions expressed in (3.17) represent real limitations when both media are lossy.

When the existence of surface waves is permitted, all surface waves have the same propagation constants $\pm p$ along the interface and the same pair of penetration constants λ_1 and λ_2 perpendicular to the interface. We have calculated these constants not only in the well known and most useful special case $\mu_1=\mu_2$, but generally. The attenuation of a surface wave in the plane of the interface progresses at the rate of Imp. From Eq. (3.5) it appears that this rate is intermediate between the loss rates of plane waves propagating in the two media.

---

[7] J. A. Stratton, *Electromagnetic Theory* (McGraw-Hill Book Company, Inc., New York, 1941), p. 137.

The general formalism evolved in the paper contains as special cases the quasi-plane surface waves of Zenneck, $P=e^{ipx}$, and the radial cylindrical wave, $P=H_1^{(1)}(pr)$.

In this paper, surface waves appeared as solutions of Maxwell's equations which by themselves satisfy the proper boundary conditions at the interface. Therefore, in this formulation their existence is not tied to the presence of waves of other types. Once they are excited by a source they propagate along the interface unaffected by other waves. The questions raised pertaining to their existence in various regions in specific problems, such as the radiation of a dipole, are really questions concerning first the fact of their excitation by the assumed source, and second, the relative magnitude of the fields associated with surface waves when compared to fields of other types present in the region.

JOURNAL OF APPLIED PHYSICS VOLUME 32, NUMBER 9 SEPTEMBER, 1961

Precipitation Sites in Aluminum Alloys

G. R. Frank, Jr., and D. L. Robinson
Alcoa Research Laboratories, Aluminum Company of America, New Kensington, Pennsylvania

and

G. Thomas
Department of Mineral Technology, University of California, Berkeley, California

(Received February 27, 1961; in final form, May 29, 1961)

Frank sessile dislocations surrounding a region of stacking fault are shown to be nucleation sites for γ' phase precipitation in aluminum-silver alloys. The segregation of silver to these regions is explained in terms of extinction fringe contrast. Direct evidence for "pipe" diffusion along dislocations to a grain boundary is also presented.

INTRODUCTION

EVIDENCE has been obtained for the preferential precipitation on dislocations and at special sites along grain boundaries in an aluminum-20 weight percent silver alloy. The results of this investigation were obtained by the use of transmission electron microscopy of thin foils prepared from bulk material.[1]

PRECIPITATION ON DISLOCATIONS

When the alloy is quenched rapidly into cold water from 520°C, the microstructure reveals a high concentration of defects in the form of dislocation loops and helices (e.g., at L and H, Fig. 1). As expected for aluminum alloys,[2,3] these form by the precipitation of excess vacancies retained by quenching. Unlike pure aluminum[4] and other aluminum alloys,[2] however, where the loops are always prismatic $\frac{1}{2}$ a $\langle 110\rangle$ dislocations, the helices and loops in the Al-Ag alloy become converted into Frank sessile dislocations of Burgers vector $\frac{1}{3}$ a $\langle 111\rangle$ surrounding a region of stacking fault. This is characterized by the familiar striped contrast[5] seen in Fig. 1. This occurs after a few minutes of aging and is similar to the results reported by Nicholson.[6] The formation of stacking faults must be due to a local lowering of the stacking fault energy at the defects. This probably occurs by the diffusion of silver to the defects, e.g., by association with mobile vacancies retained in solution by the quench. Some confirmation of this can be obtained by considering the extinction fringes observed in Fig. 1. The normal to the foil is [110] and the reflection operating to produce the contrast is (111), hence the extinction distance, by measurement, is 210 A- to be compared with the calculated value of 250 A for a (111) reflection in silver.[5] Since the extinction distance for aluminum is 646 A for the same reflection, we deduce that the presence of stacking faults is due to the segregation of silver to the dislocation loops and helices. It should be pointed out, however, that accurate determinations of extinction distances can only be made when the stacking faults intersect both surfaces of the foil (this is not the case in Fig. 1), and when the crystal is very close to a Bragg reflection.

These defects are thus expected to be preferential sites for precipitation. This has been found to be the case as shown in Fig. 2 (obtained after aging for 4 hr at 180°C), where at A and B, precipitation of γ' Ag-Al has occurred on the loops and helices. The contrast

---

[1] R. B. Nicholson, G. Thomas, and J. Nutting, Brit. J. Appl. Phys. **9**, 25 (1958).

[2] G. Thomas, Phil. Mag. **4**, 1123 (1959).

[3] G. Thomas and M. J. Whelan, Phil. Mag. **4**, 511 (1959).

[4] P. B. Hirsch, J. Silcox, R. E. Smallman, and K. H. Westmacott, Phil. Mag. **3**, 897 (1958).

[5] P. B. Hirsch, A. Howie, and M. J. Whelan, Phil. Trans. Roy. Soc. (London) **A252**, 499 (1960).

[6] R. B. Nicholson, *Structure and Properties of Thin Films* (John Wiley & Sons, Inc., New York, 1959), p. 193.

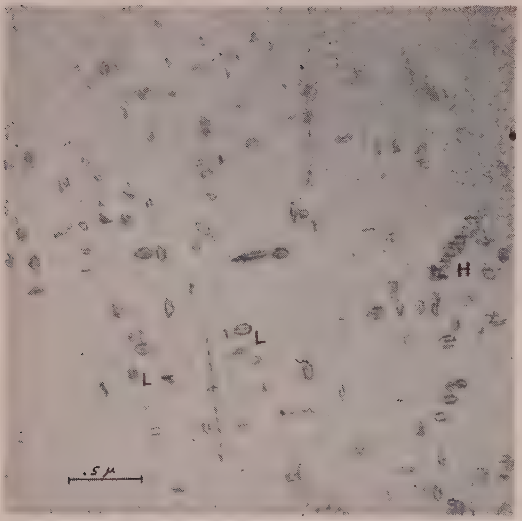

Fig. 1. Al-20% Ag. Cold-water quenched, aged 8 hr at 148°C. 22 500×.

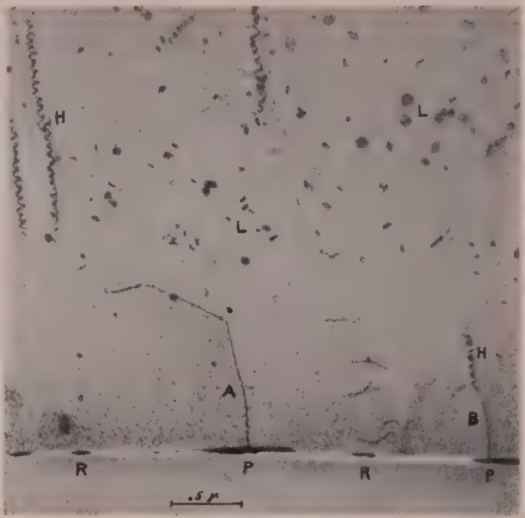

Fig. 3. Aged 1 hr at 148°C. 22 500×.

effects at A and B are now due to the hexagonal nature of the precipitate, i.e., thin plates of a hexagonal phase in a face-centered cubic matrix are analogous to a stacking fault. This explains the fringe contrast. The effects at A are analogous to those observed for the tetrahedra of stacking faults in quenched gold,[7] and the precipitates must be bounded by partial dislocations. Similar results have been obtained by Nicholson *et al.*,[8,9] Robinson *et al.*,[10] and Fukano and Ogawa[11,12] although the latter workers carried out their experiments on thin evaporated foils.

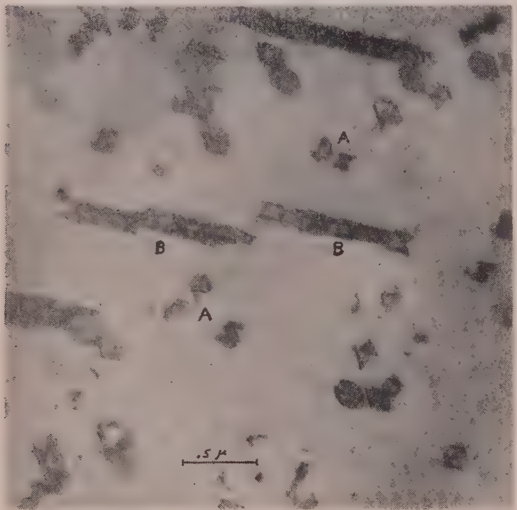

Fig. 2. Aged 4 hr at 180°C. 22 500×.

PRECIPITATION AT GRAIN BOUNDARIES

Interesting effects have also been observed at grain boundaries. Figure 3 shows the formation of elongated precipitates P at the termination of helical dislocations A and B at the boundary. The absence of loops L near the grain boundary shows that the latter acts as a sink for vacancies. Thus the helices A and B lose vacancies to the boundary by the reverse process of climb which formed them. For this reason, they become straight near the boundary.

Since it is expected that silver is also segregated to the helices, we then expect that both silver atoms and vacancies will be lost to the boundary as the helix climbs. Thus the ends of the dislocation at the boundary now become preferential sites for precipitation. We believe that this is direct evidence for diffusion along a dislocation. Since the regions adjacent to the boundaries are also depleted of silver, the precipitates at P can only continue to grow along the boundary by (a) loss of silver atoms and vacancies from the helices until eventually they become completely straight (e.g., at B) and (b) diffusion of silver atoms along the grain boundary. This explains the mode of precipitation at P and the fact that the precipitates at R unconnected to dislocations are very much smaller than those at P.

---

[7] J. Silcox and P. B. Hirsch, Phil. Mag. 4, 72 (1959).

[8] R. B. Nicholson and J. Nutting, Acta Met. 9, 332 (1961).

[9] R. B. Nicholson, G. Thomas, and J. Nutting, J. Inst. Metals 87, 429 (1959).

[10] D. L. Robinson and E. G. Haney (to be published).

[11] Y. Fukano and S. Ogawa, Acta. Cryst. 9, 971 (1956).

[12] Y. Fukano and S. Ogawa, J. Phys. Soc. Japan 14, 1671 (1959).

JOURNAL OF APPLIED PHYSICS VOLUME 32, NUMBER 9 SEPTEMBER, 1961

Transitions and Relaxations in Polytetrafluoroethylene

R. K. EBY AND K. M. SINNOTT
Polychemicals Department, E. I. du Pont de Nemours and Company, Du Pont Experimental Station, Wilmington, Delaware

(Received February 9, 1961)

The modulus and internal friction of polytetrafluoroethylene were measured with longitudinal waves at a frequency of 12 Mc between 248° and 548°K and the fluorine magnetic resonance was studied between 77° and 375°K. The samples covered a wide range of crystallinities and included a specimen which had not been sintered (as polymerized material which had not been heated above the melting temperature). The results resolve discrepancies which existed in the literature and introduce new information about the relaxations and first-order transitions in polytetrafluoroethylene. In the ultrasonic work it is shown that the "19°C" and "30°C" diffuse first-order crystalline transitions can be studied independently of the crystalline relaxation which occurs at 418°K at 12 Mc. The "19°C" transition is not observed but the "30°C" transition causes an appreciable decrease in the modulus. X-ray data show that this accompanies a decrease in the rotational order of the lattice. This transition is found to occur over a wider temperature range in unsintered polymer (possibly because of a distribution of the lengths of the molecular segments in the ordered regions). An NMR absorption line from the crystalline regions is resolved and its narrowing above 280°K is attributed to rotational motions associated with the first-order transitions. Comparison with published data shows that the narrowing occurs over a wider temperature range in unsintered polymer. Consideration of a distribution of relaxation times suggests that the narrowing above 190°K of an NMR absorption line from the amorphous regions results from the molecular motion which gives rise to a relaxation observed at 263°K in the ultrasonic measurements. Another amorphous relaxation is observed at 470°K in the ultrasonic measurements and the activation parameters are obtained. Examination of these parameters for the two relaxations suggests that the higher-temperature relaxation should be assigned to the larger molecular segments. For all the relaxations, the parameters follow a relation which obtains for activated processes in inorganic solids.

INTRODUCTION

DISCREPANCIES exist in certain publications dealing with relaxations or transitions in polytetrafluorethylene. There is no satisfactory correlation of the narrowing of the fluorine nuclear magnetic resonance absorption from the amorphous regions with the amorphous relaxation observed in dynamic mechanical measurements.[1] Mechanical measurements at low frequencies[2–5] show one amorphous and two crystalline relaxations above room temperature, but measurements at a frequency only a few decades higher[6] show no relaxations from 300° to above 575°K. The diffuse first-order crystalline transitions which occur near 19° and 30°C[7–10] appear more diffuse in some nuclear magnetic resonance measurements[1,11,12] than in other types of experiments.[7–9] However, another magnetic resonance measurement[13] reports this transition to be abrupt. In mechanical measurements, the crystalline transitions have not been studied in detail independently of their effect on the crystalline relaxations.[4]

This paper reports the results of ultrasonic and nuclear magnetic resonance measurements on a variety of polytetrafluoroethylene samples, and attempts to resolve the discrepancies noted above. In addition, new information about the transitions and relaxations in polytetrafluoroethylene is presented.

TABLE I. Properties of the polytetrafluoroethylene samples.[a]

Sample No.	Crystallinity	Density at 296°K
1	60%	2.168
2	73%	2.197
3	88%	2.238
4	95%	2.279
5	98%	2.27
6	48%	
7	71%	
8	83%	

[a] Sample 5 was formed by compressing particles of the unsintered polymer at 2×10^4 psi; the other samples were cut from sintered sheets. The samples for the ultrasonic experiment were surface ground to between 1.305 and 1.458 mm thick.

EXPERIMENTAL

Details of the samples of polytetrafluoroethylene are given in Table I. The variation in the crystallinity of the molded samples was obtained by cooling at different rates from the molding temperature, 650°K. The crystallinites were measured by infrared[14] and x-ray[15] methods. The densities, which are required in the ultrasonic analysis, were measured by water displacement at 296°K. The small correction for the densities at other temperatures was determined by using the coefficient of linear expansion.

The ultrasonic measurements were carried out with 10–15 Mc longitudinal waves using a technique devised by McSkimin.[16] Results are presented in terms of the internal friction (attenuation per wavelength) and the modulus at 12 Mc. This modulus is the combination

---

[1] J. G. Powles and J. A. E. Kail, J. Polymer Sci. **31**, 183 (1958).
[2] K. Schmieder and K. Wolf, Ricerca sci. **25**, (1955).
[3] A. K. Schultz, J. chim. phys. **53**, 933 (1956).
[4] K. H. Illers and E. Jenckel, Kolloid-Z. **160**, 97 (1958).
[5] N. G. McCrum, J. Polymer Sci. **34**, 355 (1959).
[6] M. Baccaredda and E. Butta, J. Polymer Sci. **31**, 189 (1958).
[7] C. W. Bunn and E. R. Howells, Nature **174**, 549 (1954).
[8] F. A. Quinn, D. E. Roberts, and R. N. Work, J. Appl. Phys. **22**, 1085 (1951).
[9] R. H. H. Pierce, Jr., E. S. Clark, J. F. Whitney, and W. M. D. Bryant, presented at the 130th Meeting of the American Chemical Society, Atlantic City, New Jersey, September, 1956.
[10] G. Furakawa, R. McCoskey, and G. King, J. Research Natl. Bur. Standards **49**, 273 (1952).
[11] W. P. Slichter, J. Polymer Sci. **24**, 173 (1957).
[12] J. A. S. Smith, Discussions Faraday Soc. **19**, 207 (1955).
[13] C. W. Wilson, III, and G. E. Pake, J. Chem. Phys. **27**, 115 (1957).
[14] R. E. Moynihan, J. Am Chem. Soc. **81**, 1045 (1959).
[15] A. L. Ryland, J. Chem. Educ. **35**, 80 (1958).
[16] H. J. McSkimin, J. Acoust. Soc. Am. **23**, 429 (1951).

$\lambda+2\mu$ of the Lamé constants and was determined from the measured sonic velocity and the density of the samples. The estimated limits of error in the acoustical results are ±7% and in the temperature ±0.5°K, although the precision is usually better in both cases.

The nuclear magnetic resonance measurements were made using a Varian spectrometer model V-4200 with a model V-4012 A magnet. The technique for controlling the sample temperature has been described elsewhere.[17] Temperatures were measured to within 0.2°K and the estimated error in the linewidths is ±3%.

RESULTS

The temperature variation of the internal friction and modulus at 12 Mc for samples 1, 2, and 4 is shown in Fig. 1. All samples have an internal friction maximum near 263°K and another maximum or marked increase near 470°K. In sample 4, there appear to be two further increases in internal friction at about 298° and 413°K. In every case, decreases in the moduli correspond to the maxima in internal friction.

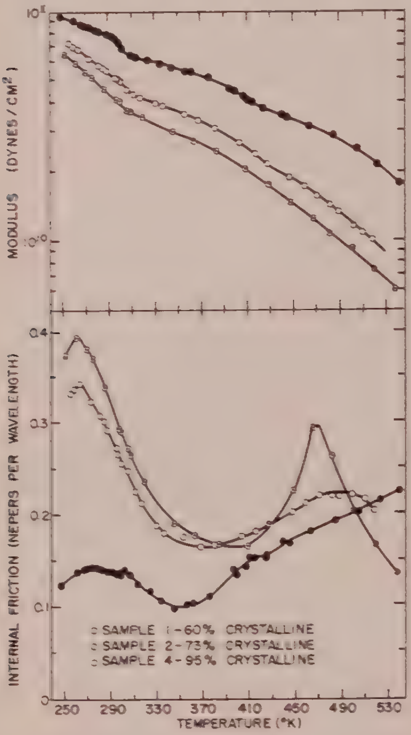

FIG. 1. Variation of internal friction and modulus ($\lambda+2\mu$) with temperature for samples 1, 2, and 4 (12 Mc).

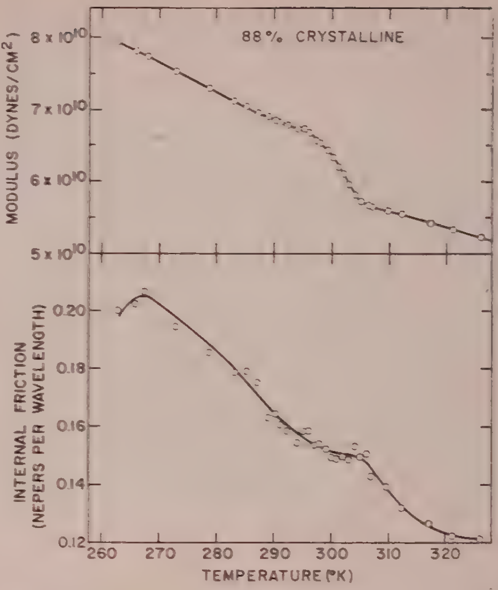

FIG. 2. Variation of internal friction and modulus ($\lambda+2\mu$) with temperature for sample 3 (12 Mc).

Figure 2 shows the results of more detailed measurements on sample 3 between 262° and 326°K. The modulus exhibits a single large decrease which begins at 295 and continues to 307°K. The less precise internal friction curve exhibits, in addition to the peak near 263°K, only one significant rise and this also occurs between 295° and 307°K. The detailed variation of modulus with temperature for the unsintered polymer, sample 5, is shown in Fig. 3. There is a gradual decrease in the modulus between 272° and 308°K.

Figure 4 shows the variation in the width of the fluorine magnetic resonance absorption line with temperature for samples 6, 7, and 8. The linewidth was taken as the separation in gauss between the corresponding maxima and minima of the first derivative of the absorption with respect to the applied magnetic field. At low temperatures, a single line was observed in all three samples. In sample 6 this line decreased rapidly in width above 190°K, and although another broad compo-

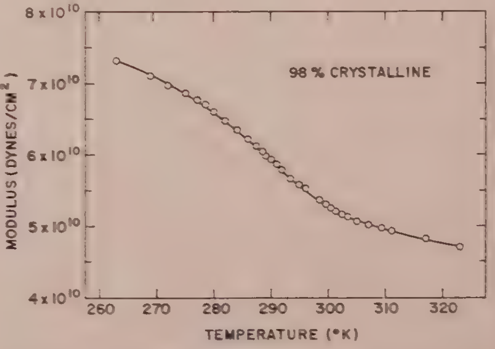

FIG. 3. Variation of the modulus ($\lambda+2\mu$) with temperature for the unsintered sample 5 (12 Mc).

---

[17] K. M. Sinnott, J. Polymer Sci. 42, 3 (1960).

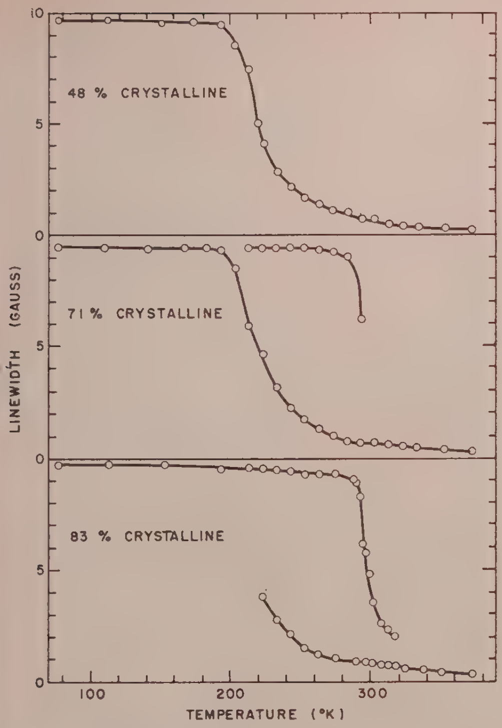

Fig. 4. Variation of the nuclear magnetic resonance linewidth with temperature for samples 6, 7, and 8.

nent was observed between 248 and 298°K, it could not be resolved well enough to determine its width. In sample 7, this broad component was sufficiently intense that it could be resolved above 213°K. The width remained constant at 9.5 gauss until 280°K when it decreased rapidly until the line could no longer be resolved. The other component observed in this sample decreased in width in a similar manner to the single line of sample 6. In sample 8, the most crystalline, the broad component could be resolved at all temperatures up to 323°K. Above 280°K the width of this component decreased sharply. The other component of the absorption was less intense in this sample than in those of lower crystallinity and could first be resolved at 323°K when its width had decreased to 3.8 gauss.

DISCUSSION

A. Glass II[18] Relaxation

The internal friction peak at about 263°K and the associated decrease in modulus can be attributed to the amorphous regions of the polymer.[19] This is demonstrated by the decrease in the magnitude of the peak and in the slope of the modulus-temperature curve when the crystallinity is increased. In previous work, an amorphous relaxation has been identified with measurements of the internal friction at 1 cps,[3–5] the acoustic attenuation coefficient at 10^6 cps[20] and the dielectric loss tangent at 10^3 to 10^6 cps.[21,22]

Figure 5 shows a log frequency vs reciprocal temperature plot for the previous observations[2–5,9–18,20–25] together with the present ultrasonic results. With few exceptions, there is a good approximation to a straight line over a temperature range of 80°K and a frequency range of eight decades. Some of the exceptions may arise not from experimental error but from physical differences in the coupling to the relaxing mechanism in the

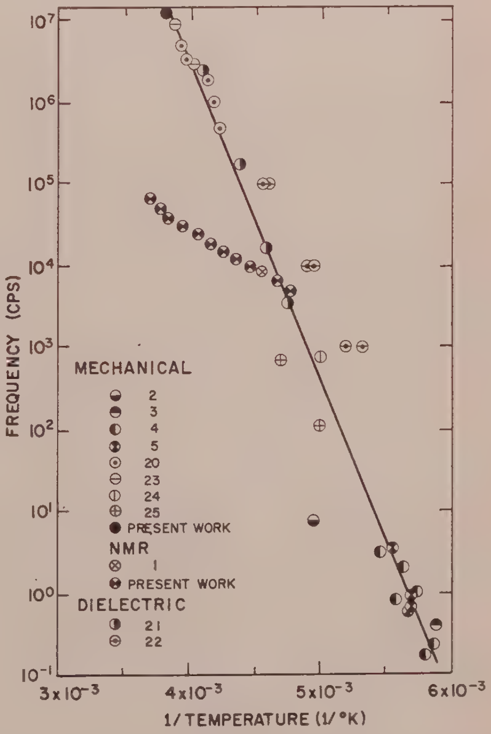

Fig. 5. Frequency of maximum internal friction and dielectric loss tangent, and NMR correlation frequency versus reciprocal temperature for the glass II relaxation. Data of other workers taken from their publications.

---

[18] This terminology has been suggested by N. G. McCrum, Makromol. Chem. **34**, 50 (1959).

[19] The terminology used in this discussion implies the presence of distinct amorphous and crystalline regions. Recent advances in polymer morphology indicate that this is not correct, but rather that there are poorly separated regions of relative order and disorder. Thus, for example, a relaxation loss peak which increases with decreasing "crystallinity" could be characteristic of small imperfections in the ordered regions rather than of large disordered regions. This interpretation has not yet been fully developed, and therefore the more elementary terminology is used here. See A. Kellar, Makromol. Chem. **34**, 1 (1959).

[20] S. P. Kabin, Soviet Phys.—Tech. Phys. **1**, 2542 (1956).

[21] G. P. Mikhailov, S. P. Kabin, and A. L. Smolianskii, J. Tech. Phys. (U. S. S. R.) **25**, 2179 (1955).

[22] F. Krum and F. Müller, Kolloid-Z. **164**, 81 (1959).

[23] Yō Maeda, Chem. High Polymers (Tokyo) **14**, 442 (1957).

[24] J. A. Sauer and D. E. Kline, J. Polymer Sci. **18**, 491 (1955).

[25] Measurements by D. Robinson, quoted in reference 12.

TABLE II. Activation parameters for the relaxations in polytetrafluoroethylene.[a]

Relaxation	$\Delta H_1^{\ddagger}$ kcal/mole	$\Delta H^{\ddagger}$ kcal/mole	$\Delta S^{\ddagger}$ cal/°C/mole	4α °C^{-1}	$\Delta S^{\ddagger}/\Delta H^{\ddagger}$ °C^{-1}	β cm^2/dyne	$\Delta V_{av}^{\ddagger}$ cm^3/mole	$\Delta V_{av}^{\ddagger}$ molar volume of CF$_2$ groups
Glass II	5.7	18	46	0.97×10^{-3}	2.6×10^{-3}	19×10^{-12}	102	5
Glass I	24.5	88	162	2×10^{-3}	1.8×10^{-3}	35×10^{-12}	499	22
Crystalline	...	34	59	1.6×10^{-3}	1.7×10^{-3}	31×10^{-12}	159	8

[a] $\Delta H^{\ddagger}$ and $\Delta S^{\ddagger}$ are the activation energy and entropy, respectively, obtained from log frequency vs reciprocal temperature data. $\Delta H_1^{\ddagger}$ is the activation energy obtained from the half-width of the loss peak. α and β are the isobaric coefficient of volume thermal expansion and the isothermal compressibility, respectively. $\Delta V_{av}^{\ddagger}$ is the average value of the activation volumes calculated from Eqs. (1) and (2) in the text.

various experiments or from unspecified differences in the polymer "state." In agreement with reference 4, the present data appear to indicate an increase in the temperature of the loss peak with increasing crystallinity (Figs. 1 and 2). It appears certain that all observations refer to the same molecular rate process, which takes place in the amorphous regions with an activation enthalpy of about 18 kcal/mole and an activation entropy of 46 cal/°C/mole.[4,18,20]

In the present nuclear magnetic resonance work, it is clear that the line which decreases in width above 190°K must arise from the fluorine nuclei in the amorphous or disordered regions of the polymer since it increases in intensity with decreasing crystallinity. The correlation frequencies calculated[26] from the width of this line between 210° and 270°K for sample 7 are shown in Fig. 5. Outside this range the slope changes. However, these frequencies are uncertain below 210°K because of the influence of the broad line and above 270°K because of the uncertainty of the final value of the linewidth. Similar results were obtained for the samples 6 and 8. The correlation frequency near the midpoint of the line narrowing (linewidth of 5 gauss) agrees well with the frequency data for the amorphous relaxation obtained from the mechanical and dielectric measurements, but the agreement is not good at other linewidths. Rather, the correlation frequencies indicate a lower activation energy (4.5 kcal/mole). This probably results from the presence of a distribution of relaxation times not considered in the analysis. The assumption of a single relaxation time, moreover, leads to a low value when the activation energy is determined from the half-width of the internal friction peaks.[5] The present discrepancy is reduced if the data are analyzed assuming the presence of two relaxation times, as has been done for polyisobutylene,[27] or a continuous distribution of relaxation times.[28] This suggests that the narrowing of the line from the amorphous regions may be assigned to the molecular motion which gives rise to the mechanical and dielectric relaxations. It should, however, be noted that the analysis based on a continuous distribution cannot be quantitative because a sufficiently detailed knowledge of this distribution is not yet available.

Figure 5 also shows the correlation frequency computed for the center of the line narrowing observed by Powles and Kail[1] at about 223°K in 55% crystalline polytetrafluoroethylene. The close agreement of this point with the other data confirms their tentative assignment of this line narrowing to the amorphous regions.

B. Glass I[15] Relaxation

The width of the line from the fluorine nuclei in the amorphous[19] regions decreased to less than one gauss at 296°K. As a result, the effect of the amorphous relaxation, which occurs near 400°K at a frequency of 1 cps in mechanical measurements,[2–5] was not observed. However, a second amorphous relaxation was observed in the ultrasonic measurements at 470°K (Fig. 1). The assignment to the amorphous regions is confirmed by the smaller internal friction peak and the less rapid change of modulus with temperature in the more crystalline samples. Baccaredda and Butta[6] did not observe this relaxation probably because of high sample crystallinity.

Ultrasonic measurements on copolymers of hexafluoropropylene and tetrafluoroethylene[29] confirm that this relaxation corresponds to that observed at low frequencies.[2–5] The relaxation temperature is depressed with increasing hexafluoropropylene content in the same manner as in the low-frequency measurements.[15]

The frequency dependence of the temperature of the internal friction peak yields an activation enthalpy ($\Delta H^{\ddagger}$) of 88 kcal/mole and an activation entropy ($\Delta S^{\ddagger}$) of 162 cal/°C/mole. The half-width of the peak in the 60% crystalline sample yields an activation enthalpy ($\Delta H_1^{\ddagger}$) of 24.5 kcal/mole. The ratio ($\Delta H^{\ddagger}/\Delta H_1^{\ddagger}$) is a measure of the distribution of relaxation times.[15] In the present case this ratio is 3.6:1, indicating a relatively wide distribution. The activation enthalpies determined by both methods and the activation entropies are given in Table II for both the glass I and II relaxations. Also included are the activation parameters for a crystalline relaxation which will be discussed in Sec. D.

It has been shown that the following relations obtain for activated processes in inorganic solids[30,31]

$$\Delta S^{\ddagger}=\alpha/\beta\Delta V^{\ddagger}, \tag{1}$$

and

$$\Delta V^{\ddagger}=4\beta\Delta H^{\ddagger}. \tag{2}$$

---

[26] H. S. Gutowsky and G. E. Pake, J. Chem. Phys. 18, 163 (1950).

[27] J. G. Powles and K. Luszczynski, Physica 25, 455 (1959).

[28] J. G. Powles, presented at Symposium on Macromolecules, Wiesbaden, October, 1959.

[29] R. K. Eby (to be published).

[30] A. W. Lawson, J. Phys. Chem. Solids 3, 250 (1957).

[31] R. W. Keyes, J. Chem. Phys. 29, 467 (1958).

In these equations, α is the isobaric coefficient of volume thermal expansion; β is the isothermal compressibility; and $\Delta V^\ddagger$ is the activation volume. Eliminating $\Delta V^\ddagger$ yields the equation

$$\Delta S^\ddagger/\Delta H^\ddagger = 4\alpha, \qquad (3)$$

which Lawson[32] has shown to be approximately true for the diffusion of impurities in amorphous polymers. Since $\Delta H^\ddagger$ and $\Delta S^\ddagger$ might vary with temperature and since the available data permit the determination of average values only, values of α were taken at temperatures between the 1 cps and 12 Mc relaxation temperatures.[33] In Table II, the agreement between 4α and $\Delta S^\ddagger/\Delta H^\ddagger$ is good considering the uncertainty in the measured quantities and the approximations in Eq. (3). This is especially true for the glass I and the crystalline relaxations. The gross values of α have been given because they yielded better over-all agreement than the "crystalline" or "amorphous" values.[19] These gross values would change with changing degree of crystallinity. Thus, increasing the crystallinity would decrease α at low temperatures. The results in reference 22 do indicate that under these circumstances, the value of $\Delta S^\ddagger/\Delta H^\ddagger$ does decrease for the glass II relaxation. It is not certain, however, that $\Delta S^\ddagger/\Delta H^\ddagger$ would follow the changes in α with temperature near the melting point of a partially crystalline polymer. These questions cannot be answered without more work.[34]

The good agreement between the two sides of Eq. (3) suggests that Eqs. (1) and (2) might apply individually to polymer relaxations. In this case, the activation volumes can be calculated. In Table II are shown the values of β calculated from published data[35,36] for temperatures between the 1 cps and 12 Mc relaxation temperatures. The averages of the activation volumes from Eqs. (1) and (2) are also shown. The relation of the activation volume to the volume of the relaxing segment is not clear. For unassociated, small molecules[37] and for inorganic solids,[31] the quantities are of the same order of magnitude. If this is also true for the present case, dividing the activation volume by the volume of one mole of CF_2 groups will yield an estimate of the number of carbon atoms involved in the relaxation. The numbers calculated in this way are given in Table II. They suggest that the glass I relaxation involves a larger segment than does the glass II.

C. "19°C" and "30°C" Crystalline Transitions

At low frequencies, crystalline relaxation processes which are thought to be associated with hindered rotation about the chain axis are observed between 273° and 313°K.[3–5] The two diffuse first-order transitions which occur in this range are detected by their effect on the relaxation times and hence on the relaxation loss.[4] In the present acoustical measurements these crystalline relaxations occur at much higher temperatures and the diffuse first-order transitions can be observed independently of them. The relaxations are discussed in the next section.

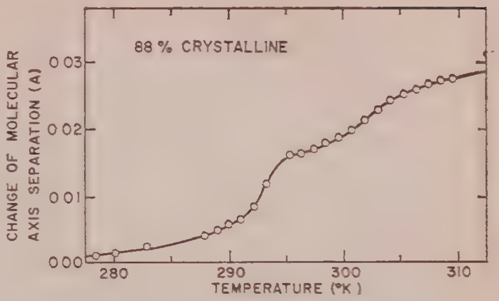

Fig. 6. Variation of the molecular axis separation with temperature for sample 3.

As the crystalline order changes with increasing temperature, there is a sharp decrease in the modulus near 300°K and the internal friction rises to a higher level (Fig. 1). The effects are small, even in the most crystalline samples, and are apparently too small to be detected definitely in the 60% crystalline material. Maeda[23] did not observe this transition, probably because of low sample crystallinity.

Figure 1 suggests that only one transition is observed and, therefore, sample 3 was examined at small temperature intervals between 262° and 326°K. The sample was first held at 262°K for two hours and then heated at a maximum rate of one degree per hour to minimize any nonequilibrium or hysteresis effects.[8] The results, shown in Fig. 2, confirm that only one transition is observed. Comparison of these results with precision x-ray data obtained on the same material with approximately the same temperature variation makes possible the assignment of the transition. The variation of molecular chain axis separation with temperature is shown in Fig. 6. The rapid increase in the separation at 293°K is associated with a change from triclinic to disordered hexagonal packing and an uncoiling of the helical molecule from 13 to 15 carbon atoms per 180° twist.[9] The smaller increase near 303°K is associated with the further disordering of the hexagonal lattice to a form with an irregular repeat unit. Throughout the whole range there is oscillation of molecular segments about the chain axis.[38] Temperature derivatives of the modulus and molecular axis spacing are shown as a function of temperature in Fig. 7. It is clear that the "30°C" transition and not the "19°C" transition is observed in the ultra-

---

[32] A. W. Lawson, J. Chem. Phys. **32**, 131 (1960).

[33] L. E. Peterson (unpublished data).

[34] Equation (3) is apparently satisfied for a large number of relaxations in both partially crystalline and amorphous polymers. R. K. Eby, Bull. Am. Phys. Soc. **6**, 143 (1961).

[35] R. I. Beecroft and C. A. Swenson, J. Appl. Phys. **30**, 1793 (1959).

[36] C. E. Weir, J. Research Natl. Bur. Standards **50**, 95 (1953).

[37] G. Gee, Proc. Chem. Soc. **1957**, 111 (1957).

[38] E. S. Clark and L. T. Muus, presented at the 132nd Meeting of the American Chemical Society, New York, September, 1957.

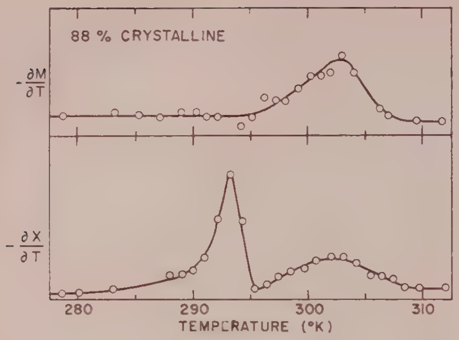

FIG. 7. Temperature derivative of the modulus $\partial M/\partial T$ and molecular axis spacing $\partial X/\partial T$ as a function of temperature for sample 3. The derivative units are arbitrary.

sonic data. The 11% decrease in modulus suggests that there is appreciable change in the forces of the crystalline lattice. A similar conclusion can be drawn from the x-ray diffraction results which indicate a loss of "rotational order" but a continuation of the "linear order" between and along the chain axis. The decrease in modulus accompanies a decrease in the rotational order of the lattice.

In view of this interpretation, the modulus of a highly crystalline "as polymerized" (unsintered) polymer was measured (Fig. 3). Although the results may be in error as a result of the higher void content, this error should be nearly constant over the temperature range of interest and the temperature derivative of the modulus will be significant. Figure 8 shows this derivative together with that of sample 3 (sintered) for comparison. The transition in the unsintered polymer is more diffuse extending from 272 to 308°K. This is also apparent from heat capacity measurements.[10] A linear fluorocarbon ($C_{16}F_{34}$), which is shorter than the ordered molecular segments in polytetrafluoroethylene,[39] undergoes a similar transition at 103°K.[7] This suggests that the diffuse nature of the transition in unsintered polymer may result from a distribution in the lengths of the segments in the ordered regions. If this is correct, sintering the polymer increases the average segment length and narrows the distribution. The former would be an effect similar to the increase in the long period of polyethylene crystals with increasing temperature.[40]

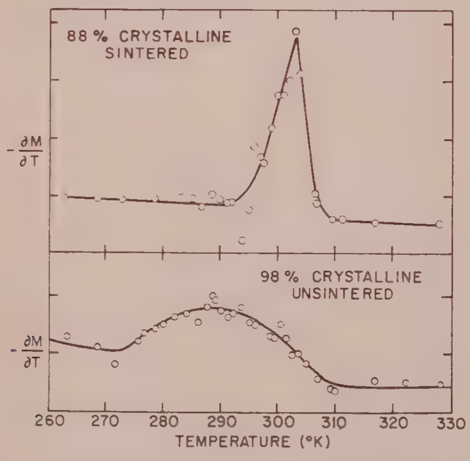

FIG. 8. Temperature derivative of the modulus $\partial M/\partial T$ for samples 3 and 5 as a function of temperature. The arbitrary derivative units are the same for both curves but different from those in Fig. 7.

The narrowing of the crystalline line observed in the present NMR work begins as a small effect at 250°K followed by a rapid decrease between 285° and 305°K (Fig. 4). This narrowing may be attributed mainly to rotational motion associated with the crystalline transition since this motion will lead to line narrowing, whereas changes in the crystal lattice will not have as large an effect on the linewidth. It is possible, however, that detailed measurements of the linewidth at small temperature intervals between 285° and 305°K may also detect the effect of these configuration changes.

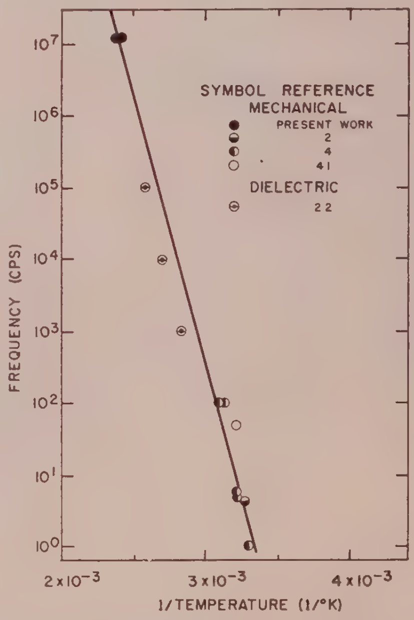

FIG. 9. Frequency of maximum internal friction and dielectric loss tangent versus reciprocal temperature for the crystalline relaxation. Data of other workers taken from their publications.

In the NMR work of Powles and Kail,[1] the narrowing of the crystalline line occurred over a much wider temperature range than in the present measurements. This probably resulted because Powles and Kail observed the crystalline line in an unsintered sample, whereas the present samples had been sintered. The ultrasonic measurements discussed above show that one of the crystalline transitions is more diffuse in the unmelted polymer. This would also explain the diffuseness of this crystalline transition in the NMR data of Slichter,[11] who studied unsintered polymer.

---

[39] C. W. Bunn, A. J. Cobbold, and R. P. Palmer, J. Polymer Sci. 28, 365 (1958).

[40] A. Keller and A. O'Connor, Discussions Faraday Soc. 25, 114 (1958).

D. Crystalline Relaxation

An internal friction peak and an associated decrease in modulus were also observed near 413°K (Fig. 1). From the variation in the magnitude of the loss peak and of the decrease in modulus with crystallinity, it is clear that this relaxation occurs in the crystalline regions. Figure 9 shows a log frequency vs reciprocal temperature plot of previous observations of an analogous relaxation in mechanical,[2,4] dielectric,[22] and creep measurements,[41] together with the present data. The linearity of this plot suggests that the same relaxation was observed in all measurements. It is the relaxation which occurs at about 1 cps at a temperature just above the 30°C transition and is probably related to the increasing crystalline disorder above that temperature.[38] The activation enthalpy as determined from Fig. 9 is 34 kcal/mole, and the activation entropy is 59 cal/°C/mole. These quantities have been discussed in Sec. B.

The dielectric data of Krum and Müller[22] show several relaxations which do not occur in the data of Mikhailov *et al.*[21] It can be seen from Fig. 9 that one of the additional relaxations observed by Krum and Müller is probably identical with one observed in mechanical measurements. Thus, the discrepancy may have resulted from the introduction into the sample of reference 22 of polar groups which would make additional relaxations detectable dielectrically. A similar effect has been observed in polyethylene.[42]

The apparent shift of the glass I relaxation to higher temperatures with increasing crystallinity and the rise in internal friction above 513°K in the 95% crystalline sample may be the result of other unresolved crystalline relaxations.

CONCLUSIONS

The present ultrasonic and nuclear magnetic resonance measurements, which were made using samples of polytetrafluoroethylene having a wide range of crystallinities, resolve some of the discrepancies among previous work and introduce new information.

The decrease above 190°K in the width of the fluorine resonance from the amorphous regions results from the same molecular motion responsible for the glass II relaxation observed in mechanical measurements. The glass I relaxation can be observed in high-frequency mechanical measurements. The activation parameters for this relaxation have been determined. These values and those for the glass II relaxation are consistent with the assignment of the glass I relaxation to larger molecular segments than those of the glass II relaxation. For both the amorphous and crystalline relaxations, these parameters appear to follow a relation which obtains for activated processes in inorganic solids.

The effects of the crystalline transitions have been observed in both the NMR and ultrasonic measurements. In the ultrasonic work, the first-order transitions could be studied independently of the crystalline relaxations which occur at much higher temperatures. The "19°C" transition has no observable effect on the ultrasonic modulus, whereas the "30°C" transition causes an appreciable decrease. This accompanies a decrease in the rotational order of the lattice. This transition occurs over a wider temperature range in "as polymerized" unsintered resin. The rapid narrowing of the NMR absorption line from the crystalline regions is attributed to the rotational motion associated with these first-order transitions. Comparison with previous NMR work shows that this line narrowing occurs over a wider temperature range in unsintered polymer, an effect analogous to that observed in the ultrasonic measurements. This effect probably results from a distribution of the lengths of the ordered molecular segments.

ACKNOWLEDGMENTS

The x-ray measurements were made by Dr. E. S. Clark, to whom we wish to express our appreciation. We also thank R. Roberts, Dr. C. W. Fairbanks, and Dr. H. W. Starkweather for preparation of the samples. Most of the ultrasonic measurements were made by Mrs. M. G. Talley.

---

[41] K. Nagamatsu, T. Yoshitomi, and T. Takemoto, J. Colloid Sci. 13, 257 (1957). Data converted to internal friction in reference 4.

[42] W. G. Oakes and D. W. Robinson, J. Polymer Sci. 14, 505 (1954).

JOURNAL OF APPLIED PHYSICS VOLUME 32, NUMBER 9 SEPTEMBER, 1961

Characteristics of the Annealing Kinetics of Tin Films Deposited at 88°K

J. Priest, C. Chiou, and H. L. Caswell
Thomas J. Watson Research Center, International Business Machines Corporation, Yorktown, New York

(Received August 30, 1960)

The electrical resistance of evaporated, high purity tin films deposited at 88°K decreases rapidly in two temperature regions as determined by isothermal annealing studies. One pronounced annealing peak occurs at 110°K and has an activation energy of 0.34 ± 0.06 ev. The second much less pronounced peak at 180°K has an activation energy of 0.74 ± 0.10 ev.

The annealing characteristics of five pure films varying in thickness from 960 A to 4100 A and a film deposited in a high partial pressure of N_2 are quite reproducible. The presence of O_2 during evaporation, however, drastically altered the annealing kinetics and increased the activation energy at any given temperature. The defect resistivity at the time of evaporation was the same for all five pure films and a film deposited in a high partial pressure of N_2, but is about 75% higher for the film deposited in the presence of O_2.

I. INTRODUCTION

Metal films formed from the condensation of metallic vapor on cold substrates are highly imperfect as shown by the large amount of annealable resistance in the films.[1–7] Of these experiments, the work of Buckel and Hilsch[1,2] on tin films and Rasor[3] on copper films is particularly related to the studies to be reported here. The annealable resistance may be attributed to the migration and subsequent annihilation of defects in the lattice structure of the metal. However, the annealing kinetics of these films often is not simple since many types of defects may be present. The situation is further complicated by the presence of impurities in the film which may impede the motion of these defects.

An important source of impurities in evaporated films is the residual gas present during the film deposition. Oxygen is known to have a decided effect on the structure and superconducting properties of a tin film.[8] However, the presence of nitrogen at a comparable pressure (10^{-5} mm Hg) has no detectable effect. To determine how these gases alter the annealing characteristics, tin films were deposited onto liquid nitrogen cooled substrates in high partial pressures of these two gases. These partial pressures were two to three orders of magnitude higher than their normal background partial pressure. Comparisons between the pure and doped films were made by considering: (a) the defect resistivity at the time of deposition; (b) the rate and temperature at which the defect resistivity anneals; (c) the activation energy for migration of the defects; (d) the number of lattice jumps required by the defect prior to annihilation; and (e) the room temperature resistivity of the annealed films.

II. EXPERIMENTAL TECHNIQUES

The special, high vacuum evaporator employed in this investigation has been described previously.[9] A 280 liters $\sec^{-1}$ Vac Ion pump was used in place of the more conventional oil diffusion pump to minimize contamination from pump oils and their decomposition products. Pressures in the 10^{-8} mm Hg range were easily attained. The maximum pressure during evaporations was less than 3×10^{-7} mm Hg. The residual gases in the system were analyzed using a Diatron 20 mass spectrometer.[10] A typical spectrum of the positive ion currents due to the major residual gases is shown in Fig. 1. Evaporation rates varied from 50 to 300 A/sec. Thus the partial pressure requirements previously established for obtaining high quality tin films on room temperature substrates were satisfied, as shown in Table I. Any alteration in these requirements necessitated by the use of liquid nitrogen cooled substrates in this experi-

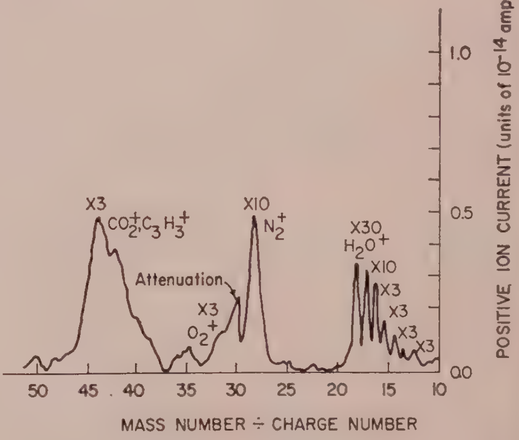

FIG. 1. Mass spectrometer analysis of vacuum system before an evaporation. The principal constituents are seen to be nitrogen and water vapor.

---

[1] W. Buckel and R. Hilsch, Z. Physik. **131**, 420 (1952).

[2] W. Buckel and R. Hilsch, Z. Physik. **138**, 109 (1954).

[3] N. S. Rasor, Phys. Rev. **98**, 1555(A) (1955); Tech. Rept. No. 14, Case Institute of Technology, Cleveland, Ohio (1955).

[4] R. Suhrmann and H. Schnackenberg, Z. Physik. **119**, 287 (1942).

[5] C. C. Evans and J. W. Mitchell, *Structure and Properties of Thin Films* (John Wiley & Sons, Inc., New York, 1959), p. 263.

[6] V. Vand, Proc. Phys. Soc. (London) **55**, 222 (1943).

[7] P. G. Wilkinson, J. Appl. Phys. **22**, 419 (1951).

[8] H. L. Caswell, J. Appl. Phys. **32**, 105 (1961).

[9] H. L. Caswell, IBM J. Research Develop. **4**, 130 (1960).

[10] Manufactured by Consolidated Electrodynamics Corporation, Pasadena, California.

TABLE 1. Partial pressure requirements for producing evaporated tin films with sharp magnetic transitions.

Partial pressure requirements necessary for producing tin films with sharp magnetic transitions	Partial pressures of various gases in the evaporator used for this work
$P_{O_2} < 5\times10^{-8}$ mm Hg	$P_{O_2} = 3\times10^{-9}$ mm Hg
$P_{H_2O} < 4\times10^{-7}$ mm Hg	$P_{H_2O} = 1\times10^{-7}$ mm Hg
$P_{CO_2} < 8\times10^{-7}$ mm Hg	$P_{CO_2} = 7\times10^{-9}$ mm Hg
P_{H_2}, P_{N_2}, P_{CO}, P_{Ar}, and $P_{CH_4} < 10^{-5}$ mm Hg	$P_{N_2} = 3\times10^{-8}$ mm Hg $P_{\text{gauge}} = 9\times10^{-8}$ mm Hg

ment is not known, but the high degree of reproducibility in the results indicates the vacuum was adequate.

The substrate holder (Fig. 2) consists of a copper block in which four 1500-w tungsten heaters and a set of liquid nitrogen cooling coils are imbedded. With this arrangement and an electronic regulator, the substrate temperature could be maintained to within ±¼°K in the temperature range 85° to 700°K. In addition, temperature changes of 10°K could be made in less than 2½ min. The resistance vs temperature characteristics of a copper film deposited onto a single-crystal quartz substrate and placed in thermal contact with the substrate holder was employed as a thermometer. It had been calibrated previously against a copper-Constantan thermocouple.

Each film was deposited onto a single crystal quartz substrate which was held at a temperature of 88°K. The film was in the form of a four-terminal network as indicated in Fig. 2. A constant current was supplied to the film and the voltage was measured with a Leeds and Northrup type K-3 potentiometer. To convert resistance to resistivity, the thickness of each film was measured to ±100 A by interferometer methods at the ends and the center of the film. Because of the nonuniformity of the film thickness and the error in the width measurement, the error in the resistivities quoted is of the order of 15%.

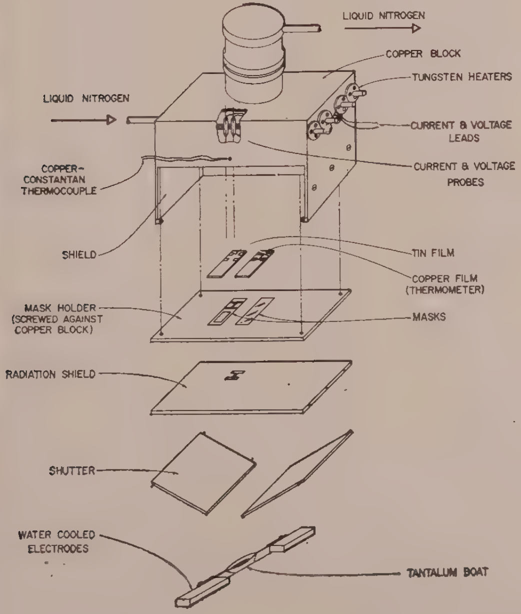

FIG. 2. Exploded view of the substrate holder and temperature controlling devices. All parts which are clamped to the main copper block are separated by a gold foil for better thermal contact.

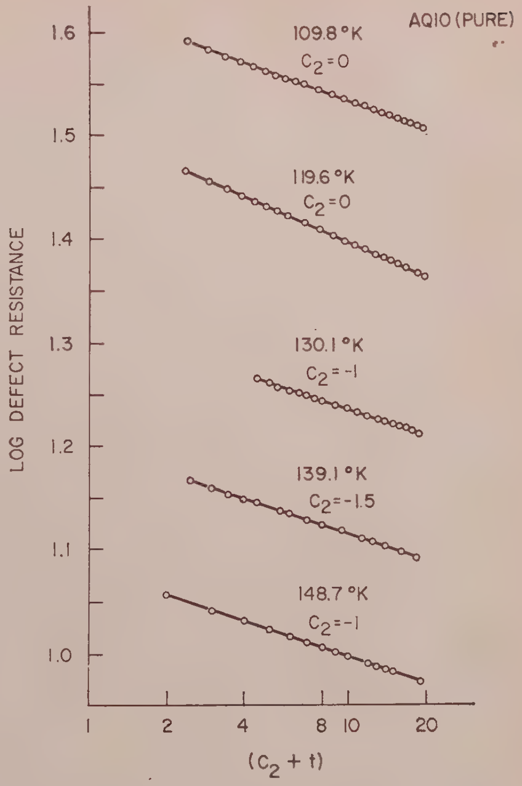

FIG. 3. Illustrations of the linear relationship observed when the log of the defect resistance is plotted versus log time plus a constant.

Immediately after deposition the resistance of the film was measured at the deposition temperature every half-minute or minute up to 20 min, at which time the temperature was abruptly increased by approximately 10°K. As soon as the film came to the equilibrium temperature another isothermal anneal was begun and was concluded 20 min after the end of the previous anneal. The procedure was followed until no appreciable change was observed in the film resistance during the isothermal anneal. The film was then cooled to liquid nitrogen temperature a second time and allowed to warm up slowly while its electrical resistance was recorded as a function of temperature. The resistance of the annealed film was subtracted from that recorded on the initial run to give the net resistance due to defects.

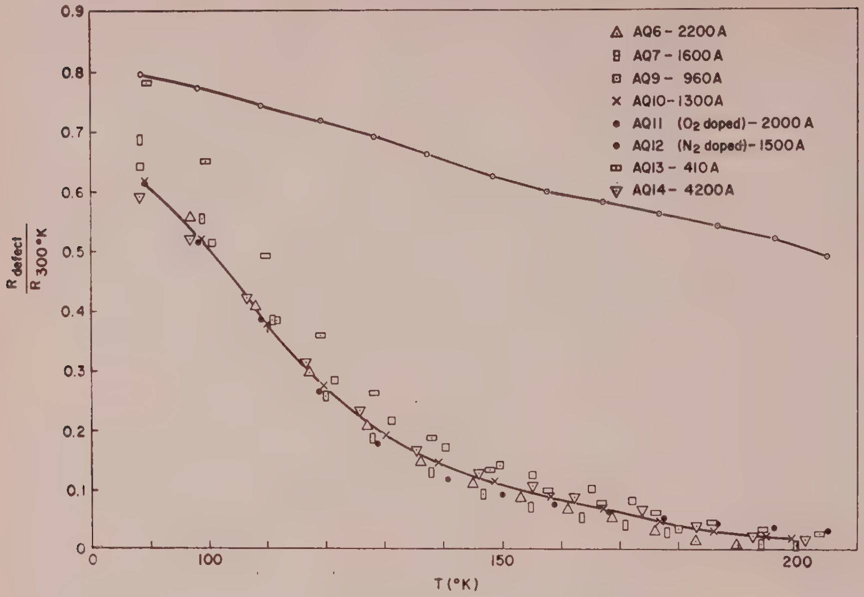

FIG. 4. Defect resistance remaining at the end of each 20-min isothermal anneal divided by the resistance at 300°K plotted as a function of the annealing temperature.

III. ANALYSIS OF THE DATA

The isothermal annealing data in all cases were fitted by an empirical relation of the form

$$R_d = R_{d0}(Kt + C_2)^{C_1}, \tag{1}$$

where R_d is the defect resistance, t is the time, K is the rate constant, and C_1 and C_2 are constants.

An equation of this form was chosen initially because it is a solution of the generalized rate equation

$$dR/dt = AR^N, \tag{2}$$

where A is a constant and N is the reaction order. Reaction orders of 12 to 14 were required to fit the experimental data to Eq. (1), whereas it is difficult to attach any physical significance to reaction orders greater than three. However, use of the empirical equations facilitates extrapolation of the defect resistivity to times longer and shorter than measured experimentally, and calculation of dR_d/dt, so that the method of Rasor[3] may be used to calculate the activation energy for migration of defects. The activation energy E_m is given by:

$$\frac{[dR_d(T_1)/dt]R_{d_1}=R}{[dR_d(T_2)/dt]R_{d_2}=R} = \exp\left\{\frac{E_m}{K}\left(\frac{1}{T_2} - \frac{1}{T_1}\right)\right\}. \tag{3}$$

The activation energies were also calculated by a second method which required extrapolation of the defect resistance at the lower temperature to very long times at which point it was comparable to that at the higher temperatures. The activation energies calculated by the two methods agreed within ±10%.

Knowing the activation energy E_m, the number of jumps n required to annihilate the defect may be calculated from[11,12]

$$n = \tau\nu \exp -(E_m/kT), \tag{4}$$

where τ is the time required to anneal the defects and ν is the defect vibrational frequency. The significance of n as calculated from Eq. (4) has been discussed by Lomer and Cottrell.[11] In particular, they show that if defects are trapped by impurities with a binding energy B, then Eq. (4) is modified to

$$n = \tau\nu C^{-1} \exp -\{(E_m + B)/kT\}, \tag{5}$$

where C is the concentration of impurities.

IV. EXPERIMENTAL DATA

Pure tin films deposited at 88°K have a defect resistivity of 8.5±1.0 μohm cm (the error lies principally in measurements of the film dimensions). However, this resistivity is appreciably lower than the value of 35 μohm cm one would expect from an extrapolation of the data of Scala and Robertson[13] for "molten" tin at this temperature.

In Fig. 3 the logarithm of the defect resistance is plotted as a function of the logarithm of the annealing time plus a constant for a series of isothermal anneals. The linear relationship illustrates the excellent fit of Eq. (1) to the experimental data. For this reason extrapolation and differentiation of the analytic expression is felt to be quite valid.

In Fig. 4 the ratio of defect resistance remaining after each isothermal anneal divided by the annealed resistance at 300°K is plotted as a function of the annealing temperature. This ratio was plotted rather than the defect resistivity so that errors which arise from uncertainties in the film dimensions are eliminated. With the exception of the 410 A film, which is the thinnest of the films studied, the data for five pure films ranging in thickness from 960 to 4100 A agree within the experimental error, indicating that the defect concentration is not strongly dependent on thickness in this thickness range. The shape of the curve for the 410 A film is similar to the other data but it is displaced by approximately 25%. Figure 4 also illustrates the effect on the annealing when nitrogen or oxygen is present during evaporation. A high partial pressure of nitrogen had no detectable effect, whereas one of oxygen produced a significant shift in the annealing to higher temperatures. The annealed room temperature resistivity of the film heavily doped with oxygen was 17.9 μohm cm as opposed to 11.9–13.1 μohm cm for the pure films and nitrogen-doped film, indicating that the oxygen is trapped in the film.

---

[11] W. M. Lomer and A. H. Cottrell, Phil. Mag. 46, 711 (1955).
[12] C. A. Wert, Phys. Rev. 79, 601 (1950).
[13] E. Scala and W. D. Robertson, J. Metals 5, 1144 (1953).

Because of the importance of determining temperature regions of rapid anneal, the change in defect resistivity during each isothermal anneal is plotted as a function of the annealing temperature in Fig. 5. One pronounced region is peaked at 110°K and a second much less pronounced region is peaked at 180°K for all films with the exception of the heavily oxygen-doped film AQ 11.

The activation energies calculated from Eq. (3) are plotted in Fig. 6 as a function of the average temperature of the two anneals used for each calculation. To within the accuracy of the measurements, the activation energies for the N_2 doped film agree with those for the pure films. However, the activation energies for the O_2 doped film is consistently higher than for the pure and N_2 doped films.

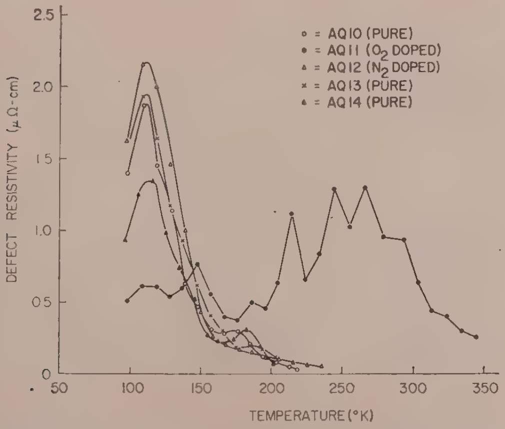

FIG. 5. Change in defect resistivity during each isothermal datum. These data have not been normalized as in Fig. 6. The principal discrepancy in the conversion to resistivity lies in the errors in the film dimensions.

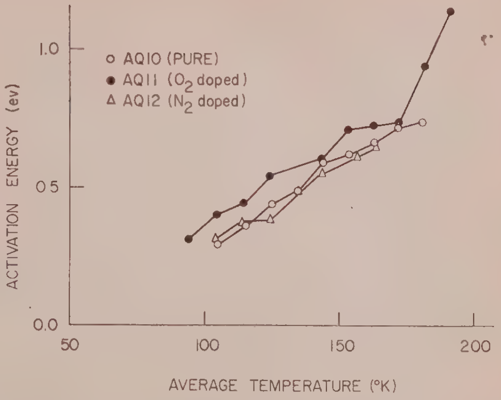

FIG. 6. Activation energies calculated from Eq. (3) plotted as a function of the average temperature of the two anneals and for the calculation.

V. DISCUSSION OF EXPERIMENTAL RESULTS

Consider first the large annealing peak observed at 110°K. The number of jumps required to annihilate these defects as calculated from Eq. (4) is 40. The value is reasonable for an evaporated film and implies that that the measured activation energy of 0.34 ev may be associated with the mobility of the defect. However, it is difficult to specify what type of defect is involved. With the exception of the work of De Sorbo[14] who obtained an activation energy of 0.68 ev for the migration of vacancies in tin, the majority of defect studies have been made on fcc metals and the applicability of these results to tetragonal tin ($c/a=0.5456$) is questionable. Theoretical work[15–17] on copper indicates that the activation energy for migration of divacancies is approximately one-half that required for vacancies. Even though the activation energy at 110°K is one-half of De Sorbo's value for vacancies, it appears unreasonable that the annealing is due to divacancies since a comparable peak associated with vacancy annealing is absent.

The decrease in the rate of decay of the defect resistance and increase in activation energy at a given temperature for the oxygen doped film may be interpreted in the manner suggested by Lomer and Cottrell.[11] In this model, the defects during migration can not only be annihilated, but can be trapped by impurity atoms. Before a trapped defect can migrate to an annihilation center, it must first be freed from the trap. The specimen must then be raised in temperature until the defect-impurity atom combination receives enough thermal energy to overcome its binding energy. The measured activation energy is thus larger, as indicated by Eq. (5).

The small annealing peak at 180°K has an activation energy of 0.75 ev in good agreement with De Sorbo's value for vacancy migration. However, a value of 10^{-4} is obtained from Eq. (4) for the number of jumps required to annihilate the defect. This is unreasonably low and suggests this peak may not be due to single vacancies but to defects which were initially trapped in the film.

---

[14] W. De Sorbo, J. Phys. Chem. Solids **15**, 7 (1960).
[15] H. B. Huntington and F. Seitz, Phys. Rev. **61**, 315 (1942).
[16] J. H. Bartlett and G. J. Dienes, Phys. Rev. **89**, 848 (1953).
[17] H. B. Huntington, Phys. Rev. **91**, 1092 (1953).

Buckel and Hilsch[1,2] who measured the resistance of tin films deposited on substrates below 10°K as a function of temperature report a minimum in the curve at 150°K and an inflection point at 110°K. In the present work utilizing isothermal annealing techniques, the resistance minimum was also observed and the large annealing peak (Fig. 5) is near their inflection point.

VI. CONCLUSIONS

Tin films deposited on liquid nitrogen cooled substrates undergo a rapid annealing process near 110°K. Due to insufficient data on defects in bulk tin, it is difficult to ascribe this annealing to a specific type of defect. The presence of oxygen during the film deposition was found to alter drastically a film's annealing characteristics, whereas the presence of nitrogen did not. Because of the important role residual gases may play in determining the annealing kinetics of evaporated films, extreme caution should be used in interpreting data obtained on films deposited in poor vacua.

ACKNOWLEDGMENTS

The authors are indebted to Dr. A. S. Nowick who critically reviewed the manuscript and gave many helpful suggestions for its improvement. The help of Dr. D. P. Seraphim during the course of the experiments was also greatly appreciated.

JOURNAL OF APPLIED PHYSICS VOLUME 32, NUMBER 9 SEPTEMBER, 1961

Slip Patterns on Boron-Doped Silicon Surfaces*

H. J. QUEISSER
Shockley Transistor, Unit of Clevite Transistor, Palo Alto, California

(Received December 5, 1960)

Diffusion of a high concentration of boron impurities into a shallow surface layer of silicon and subsequent etching reveals regular arrays of etched lines with crystalline symmetries. These patterns are interpreted as slip lines introduced by the stress from the nonuniformly distributed, undersized substitutional boron impurities in the silicon lattice.

I. INTRODUCTION

DISLOCATIONS may be introduced into crystals in a variety of ways.[1] Generation of dislocations occurs during crystal growth due to propagation from the seed, nucleation and collapse of vacancy disks, and thermal stresses. Varying impurity concentrations may be built into the crystals because of fluctuations of the freezing rate. Such variations in concentration cause strain in the lattice and may also result in dislocations, as was shown by Goss *et al.*,[2] for germanium-silicon alloys and by other authors for metals.[3,4]

After the crystal has been grown, dislocations may be introduced by plastic deformation, such as bending, twisting, or indentation.[5,6] If the deformation is performed at elevated temperatures or if the crystal is annealed, the dislocations may become sufficiently mobile to form regular arrays ('polygonization'). Patterns of dislocation arrays and slip lines may be observed after suitable etching.

This article reports another method of introducing dislocations.[7] Diffusion of impurities into silicon is shown to give dislocations which can be detected by their slip patterns. The undersized substitutional impurity atoms cause a strain in the lattice which is relieved by the formation of dislocations. Prussin[8] has detected individual diffusion-induced dislocations in silicon by etching cleavage planes perpendicular to the plane of impurity deposit. This paper discusses the slip patterns of dislocations which appear after etching a heavily boron-doped silicon surface.

Experimental conditions which lead to the observation of these slip patterns are discussed first. Typical patterns are shown for different crystallographic surfaces. In the discussion it is shown that the observed patterns are in accordance with the known slip properties of silicon. Using energy considerations suggested by Shockley,[9] the minimum impurity content necessary

---

* Work supported by the Air Force Cambridge Research Laboratory.

[1] For a recent review of the literature on introduction of dislocations into semiconductor crystals, see W. Bardsley in *Progress in Semiconductors* (John Wiley & Sons, Inc., New York, 1960), Vol. 4, p. 160ff.

[2] A. J. Goss, K. E. Benson, and W. G. Pfann, Acta Met. 4, 332 (1956).

[3] W. A. Tiller, J. Appl. Phys. 29, 611 (1958).

[4] V. V. Damiano and G. S. Tint, Acta Met. 9, 177 (1961).

[5] Reviews of these experiments may be found in reference 1, also in P. Haasen and A. Seeger, *Halbleiterprobleme* (Friedrich Vieweg und Sohn, Braunschweig, 1958), Vol. IV, p. 68.

[6] A. Seeger, *Handbuch der Physik*, edited by S. Flügge (Springer-Verlag, Berlin, 1958), Vol. VII, Part 2, p. 1ff.

[7] H. J. Queisser, Bull. Am. Phys. Soc. 6, 106 (1961).

[8] S. Prussin, J. Appl. Phys. (to be published). The information was graciously made available to us before publication.

[9] W. Shockley (to be published).

to generate dislocations is estimated and found to be consistent with the observations. Finally, the importance of diffusion-introduced dislocations for solid-state devices is pointed out.

II. EXPERIMENTAL

This section describes first the experimental conditions which give rise to typical patterns. Structure and depth of the patterns are discussed. The second part describes variations in the experimental conditions and their influence upon the formation of the patterns as well as control experiments to establish the hypothesis that the patterns are caused by the boron diffusion.

Many of the samples investigated contained a small angle grain boundary. The slip patterns were first observed during studies of diffusion down grain boundaries. Subsequently, the patterns were used as a convenient method to study the relative orientation of the grain boundary.

A. Procedure Yielding Surface Patterns

The silicon slices used in the experiments were cut in a defined crystallographic plane from single crystals or bicrystals. The thickness of the slices varied between 0.1 and 1 mm. The slices were lapped, then polished with Linde A to a mirror finish. After cleaning and degreasing with organic solvents, the samples were rinsed in hydrofluoric acid for about 1 minute. They were then chemically polished with an "iodine etch" [125 cc glacial acetic acid, 100 cc HNO_3 (70%), 25 cc HF (49%), 2 gm I_2] to remove the surface portions that were damaged by mechanical polishing.

The diffusions were carried out in a platinum box[10] with a boron trioxide source at 1150°C for 25 min in a nitrogen ambient. Under these conditions, the total impurity content Q was about 5×10^{16} boron atoms/cm^2 silicon surface. The surface concentration was approximately 5×10^{20} atoms/cm^3. These values were determined through measurements of the sheet resistance and junction depth, using the Backenstoss[11] data for the mobilities.

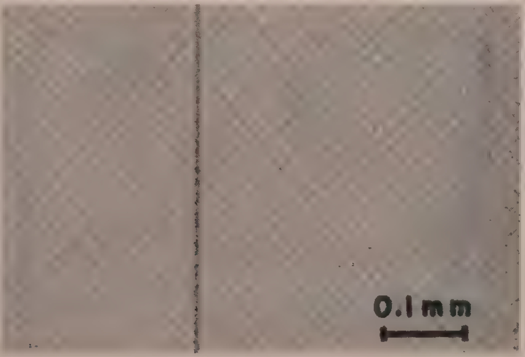

FIG. 1. Etch pattern on (100) surface of a silicon bicrystal after boron diffusion. Grain boundary with 11° misfit angle in (010) plane.

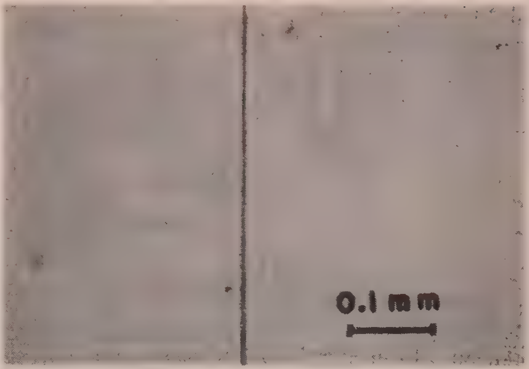

FIG. 2. Etch pattern on (100) surface. Nonsymmetrical grain boundary with 6° misfit angle in (011) plane.

After diffusion, the slices were rinsed for 2 min in hydrofluoric acid. They were then etched for 30 sec to a few minutes in the "iodine etch". The "Dash etch[12]" may also be used with the same effect, but it requires much longer etching time.

Slices so treated show regular patterns of etched lines on the surface. In all cases the lines are parallel to the intersections of (111) planes with the surface, as is further discussed in Sec. III.

A typical pattern is reproduced in Fig 1. The sample was cut to (100) faces from a silicon bicrystal with a [100] growth axis. For this crystal two seeds were used, rotated around their parallel [100] axes, to give a grain boundary in a (010) plane. The misfit between the two grains is 11°. The grain boundary appears in the center of the photograph as a deeply etched dark line. The two grains exhibit rectangular networks of etched lines, which run along [110] directions. The relative misfit of the two grains and the orientation of the grain boundary can be measured with reasonable accuracy from the pattern. These results were confirmed by x-ray orientation measurements.

Figure 2 shows a (100) surface of a bicrystal with [100] growth axis and a grain boundary in a (011) plane. Again the etched lines follow the [110] direction. It is seen in this picture that the boundary is not a plane of symmetry for the two grains.

A typical pattern for a (111) surface is given in Fig. 3. A hexagonal network of lines is observed. Figure 4 shows the etch pattern obtained on a $(1\bar{1}0)$ surface. Only one set of parallel lines is observed. The direction of the lines is [110].

Surfaces other than the low-indexed planes do not yield such regular patterns. This is demonstrated by Fig. 5 which shows a surface cut at about 7° off the

---

[10] L. A. D'Asaro, Solid State Electronics **1**, 1 (1960).

[11] G. Backenstoss, Bell System Tech. J. **37**, 699 (1958).

[12] W. C. Dash, J. Appl. Phys. **27**, 1193 (1956).

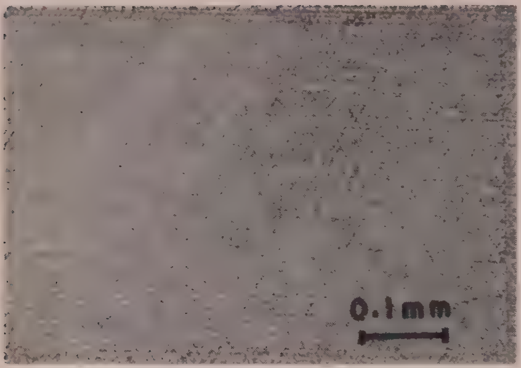

FIG. 3. Etch pattern after boron diffusion on a (111) surface.

(100) plane. The appearance is that of two or more sets of lines, irregularly superimposed on each other.

The depth to which the patterns extend was roughly determined in the following experiment. A sample was protected on one side against the boron diffusion by a SiO_2 layer. After diffusion, the protected side was slowly etched with a diluted iodine etch until the pattern became visible. The 40-μ slice which was used for this experiment was reduced to a thickness of approximately 15 μ before traces of the pattern became visible. The disturbance which produces the surface pattern therefore must propagate in some way to a depth of about 15 μ. This depth is considerably greater than the diffusion length of the boron impurities. The diffusion length $L=(Dt)^{\frac{1}{2}}=0.4\ \mu$ with $t=0.5$ hr diffusion time and $\sqrt{D}=0.6\ \mu/\mathrm{hr}^{\frac{1}{2}}$ for 1150°C.[13] It therefore seems unlikely that the patterns are caused by precipitation as are Widmanstätten patterns,[14] or as was assumed in the recently published report on "Mondrian patterns".[15]

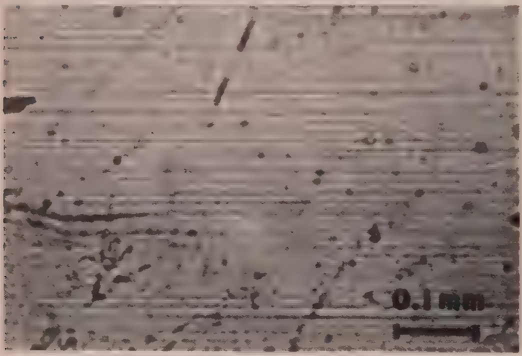

FIG. 4. Etch pattern after boron diffusion on $(1\bar{1}0)$ surface. Direction of the slip lines is [110].

B. Critical Parameters

A number of experiments were performed to determine which parameters were essential for the formation of the patterns.

Starting Material

Different types of single crystals were tried. Crucible-pulled, float-zone refined, and crystals grown by the Dash "pedestal method[16]" showed no variation in behavior. This indicates that initial oxygen and dislocation content are not critical. Both *p*- and *n*-type materials were used, with resistivities ranging from a few hundredths to a few hundred ohm-cm, but the same type of patterns were obtained. A dependence upon the initial dopant concentration should not be expected since the concentrations in this resistivity range are orders of magnitude smaller than those of the diffusing boron impurities.

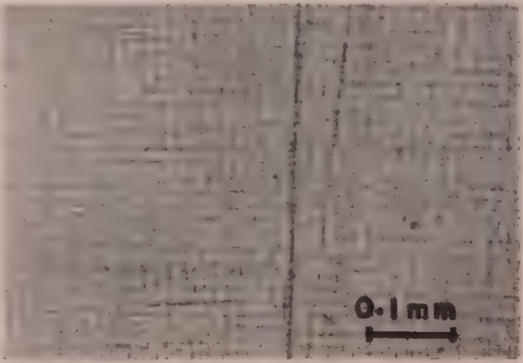

FIG. 5. Etch pattern near grain boundary, surface disoriented approximately 7° from (100) plane. Grain boundary in (011) plane.

Surface Treatments

Samples which were lapped and chemically polished showed the same patterns as did slices which were lapped, mechanically polished, and then chemically polished. Slices that were not etched after the mechanical polishing showed no different effect. Polishing damage, therefore, does not influence the patterns.

Diffusion

Heat treatment alone yielded no patterns. Obviously, the patterns are not caused by thermal effects.

The "platinum box diffusion" is not a necessary procedure, as the same results were produced by open-tube diffusion. Boron trioxide is not essential. Doping with BCl_3, with a nitrogen flow, produced the patterns. This experiment rules out oxygen as the cause of the patterns.

Phosphorus was diffused into silicon in an attempt to produce the patterns. Only for very high concentrations of phosphorus were similar patterns observed.

---

[13] C. S. Fuller and J. A. Ditzenberger, J. Appl. Phys. **27**, 544 (1956).

[14] For instance, see, B. Chalmers, *Physical Metallurgy* (John Wiley & Sons, Inc., New York, 1959), p. 391.

[15] W. S. Williams, J. Appl. Phys. **32**, 552 (1961).

[16] W. C. Dash, J. Appl. Phys. **31**, 736 (1960).

The spacing between the lines appears considerably larger than in the boron patterns. As discussed below, this result is consistent with the difference in ion size.

For a constant diffusion time of 0.5 hr, the influence of the diffusion temperature was studied. No patterns appeared after diffusions below 1000°C. At temperatures higher than 1150°C and up to 1200°C, the surface is increasingly damaged by corrosion, but the effect is still present.

The total amount of boron diffusing into the sample depends upon the diffusion time, and strongly upon diffusion temperature. One might therefore suspect that it is the total impurity content which determines whether or not slip patterns will result after a certain diffusion. Such a "critical impurity content" is to be expected from theory, and will be discussed below in more detail.

III. DISCUSSION

Experimental evidence indicates that the boron impurities are responsible for the observed patterns. The heavy deposit of the smaller boron atoms leads to a reduction of the lattice parameter within a shallow surface layer, which introduces strain. If this strain becomes sufficiently large, the formation of dislocations will be favored energetically. If these dislocations are lined up on common slip planes, it is the traces of these slip planes that are revealed by etching the surface.

Note added in proof. Recent x-ray measurements by G. H. Schwuttke, performed on boron-diffused Si samples as described here, gave evidence of dislocations in [110] directions. This is in accordance with the interpretation given here.

The geometry of all observed patterns is in accordance with this interpretation. The lines of all patterns can be explained as traces of (111)-type planes. It has been established that these planes are the slip planes of silicon.[17,18]

In each case all possible slip planes are observed. This also holds true for the experiment on the $(1\bar{1}0)$ surface, illustrated in Fig. 4. Here only two sets of possible slip planes are present $(\bar{1}11)$ and $(\bar{1}1\bar{1})$. Both exhibit the same trace on the $(1\bar{1}0)$ plane, therefore only one set of lines is observed.

Evidence for the stress introduced by the boron can be seen when a thin ($\sim 50\,\mu$) silicon slice is subjected to a boron deposit on one side only. A warping occurs, with the diffused side being concave. Quantitatively, the stress may be calculated[8] from the known values of the lattice parameters of silicon-boron mixed crystals.[19] However, these calculations have not been carried out in this investigation.

A different method may be used to calculate the distribution of dislocations under the conditions of impurity diffusion. This method was developed by Shockley.[9] Only one of his results is included here. This is an energy consideration which shows that a minimum amount of impurities is necessary to favor formation of dislocations over a strained lattice.

Shockley's analysis,[9] which is based on a simplified image treatment, shows that the energy released by slipping one dislocation with Burgers vector b down the slip plane to a depth r is:

$$E_s=[2^{\frac{1}{2}}G(1+\nu)/(1-\nu)]br\epsilon_0, \tag{1}$$

where G is the shear modulus, ν is Poisson's ratio, and ϵ_0 is the strain in the diffused layer.

The energy required to create the dislocation may be taken as[20]:

$$E_d=[G/4\pi(1-\nu)]b^2\ln(2^{\frac{3}{2}}r/r_0), \tag{2}$$

where r_0 is the effective core radius. Thus energy considerations favor the formation of the dislocation if E_s is greater than E_d. This can be re-expressed as:

$$r\epsilon_0/b>[1/4\pi(1+\nu)\sqrt{2}]\ln(2^{\frac{3}{2}}r/r_0). \tag{3}$$

For a layer not having a uniform ϵ_0, $r\epsilon_0$ may be well approximated by an average value which depends only upon Q, the total number of solute atoms per unit surface area.

$$Q\equiv\int N_{\mathrm{Si}}f(x)dx, \tag{4}$$

where the integral extends from the surface through the diffused layer, N_{Si} is the density of silicon atoms, and $f(x)$ is the atomic fraction of the solute. In terms of a new constant α defined by the relationship

$$\epsilon_0=\alpha f, \tag{5}$$

which assumes linearity between lattice constant and impurity concentration, the appropriate average for $r\epsilon_0$ is

$$\langle r\epsilon_0\rangle=\int\alpha f(x)dx=\alpha Q/N_{\mathrm{Si}}. \tag{6}$$

This leads to a condition for slip in terms of a minimal Q as follows:

$$Q_{\mathrm{min}}=(N_{\mathrm{Si}}b/\alpha)[4\pi\sqrt{2}(1+\nu)]^{-1}\ln(2\sqrt{2}r/r_0). \tag{7}$$

Taking the following values:

$N_{\mathrm{Si}}\equiv$ density of silicon atoms in crystal $=5\times10^{22}\ \mathrm{cm}^{-3}$
$b\equiv$ Burgers vector $\cong 4$ A
$\alpha\equiv$ fractional reduction in lattice constant per atomic fraction of boron[19,21] $=0.3$
$\nu\equiv$ Poisson's ratio $\cong\frac{1}{3}$
$r_0\equiv$ effective dislocation core radius $\cong b/2$,

---

[17] See reference 5.

[18] U. F. Kocks, Trans. Am. Inst. Mining, Met., Petrol. Engrs. **212**, 251 (1958); F. L. Vogel, Acta. Met. **6**, 532 (1958); J. R. Patel, J. Appl. Phys. **29**, 170 (1958).

[19] F. H. Horn, Phys. Rev. **97**, 1521 (1954).

[20] A. H. Cottrell, *Dislocations and Plastic Flow in Crystals* (Clarendon Press, Oxford, England, 1953), p. 55.

[21] The effect of over- or undersized substitutional impurities on the lattice parameter can also be estimated by using Pauling's tetrahedral standard radii with allowance for ionization of donor or acceptor. L. Pauling, *Nature of the Chemical Bond* (Cornell University Press, Ithaca-London, 1948), 2nd ed., p. 169.

we find for an r value of 0.5 μ (approximately $(Dt)^{\frac{1}{2}}$ for the boron diffusions used) that the minimum Q is approximately

$$Q_{\min}=3\times10^{15}\text{ boron atom/cm}^2. \tag{8}$$

The total impurity content Q may be measured experimentally from junction depth and sheet resistance measurements. For the "typical treatment" mentioned before, Q was measured to 5×10^{16} boron atoms/cm^2 which is about one order of magnitude above the critical value of Eq. (8). The diffusion at 1000°C, which did not yield a pattern, gave a Q value of 3×10^{15} cm^{-2} which is just the critical value. This agreement with the predictions further substantiates the hypothesis that the boron diffusion is the reason for the patterns.

The fact that only very high concentrations of diffusing phosphorus yield patterns is understandable. The misfit of phosphorus in silicon is considerably smaller than for boron. The ionic radii[21] are: Si—1.17 A; P^+—1.07 A; B^-—0.98 A.

The optimum configuration for joining two regions of different lattice parameters would be a wall of parallel dislocations at the interface.[9] This was not observed here, and apparently not observed by Prussin.[8] Shockley[9] proposes rate effects as an explanation. Increase in strain forms new dislocations at an existing slip plane. The repulsion between two dislocations of equal sign apparently forces the earlier generated dislocations on the plane to glide deeper into the material. Shockley's preliminary estimates give a depth of penetration which is considerably greater than one diffusion length of the impurity.

IV. CONCLUSIONS

High-temperature diffusion of large concentrations of substitutional impurities into shallow surface layers of silicon produces dislocations which are arranged in regular patterns along common slip planes. This method of producing uniform strain has been found useful for crystallographic orientation studies. It should also be of interest for investigations of plastic properties and dislocations.

On the other hand, p-n junctions produced by diffusion with high impurity concentrations will be affected by the high dislocation densities. To mention only a few of the effects of dislocations on electrical properties[1]: minority carrier lifetimes will be reduced, the reverse currents are increased, and lower reverse breakdown will result. Preferential microplasma formation has been observed by Chynoweth and Pearson[22] and recently also by Goetzberger.[23] The regular patterns of light emission from reverse biased, shallow junctions which have been observed by these authors may have the same origin as the patterns described. Goetzberger[24] reports that he observes such patterns only when very high impurity concentrations are diffused into the silicon, which is in accordance with the model.

The high dislocation density for the case of a shallow boron diffusion with high concentrations must be taken seriously from a device standpoint. "Emitter-diffusions" on transistors will in many cases involve high enough impurity concentrations to give dislocations which in turn produce the unwanted electrical effects mentioned above. Commercial solar cells normally consist of a shallow, very heavily boron-doped layer diffused into n-type base material. The dislocations which are introduced probably act as recombination centers and thus lower the efficiency of the cell.[25] Dopants with smaller misfits in silicon, e.g., arsenic, phosphorus, gallium, or aluminum, should give more perfect junctions than boron.

ACKNOWLEDGMENTS

The author wishes to express his thanks to Dr. W. Shockley for his aid in many discussions, and for permission to include some of his unpublished work in this paper. The assistance of colleagues in this Laboratory is gratefully acknowledged, especially that of G. Fraser who carried out much of the experimental work. Dr. V. Macres did the x-ray measurements for this study. The author especially appreciates receiving results from Dr. S. Prussin prior to their publication, so that a discussion of his results could be included in the final version of this article.

---

[22] A. G. Chynoweth and G. L. Pearson, J. Appl. Phys. **29**, 1103 (1958).

[23] Adolf Goetzberger, Paper Q4, International Conference on Semiconductor Physics, Prague (1960).

[24] Adolf Goetzberger (private communication, 1961).

[25] W. Shockley and H. J. Queisser, J. Appl. Phys. **32**, 510 (1961).

JOURNAL OF APPLIED PHYSICS VOLUME 32, NUMBER 9 SEPTEMBER, 1961

Acoustical Study of Quench-Aging in α Cu-Al Alloys*

T. J. Koppenaal† and M. E. Fine
Department of Materials Science, The Technological Institute, Northwestern University, Evanston, Illinois

(Received April 3, 1961)

Young's modulus at 21°C in quenched α Cu-Al alloys increases with time. This correlates with a decrease in resistivity which has been attributed to vacancy-enhanced diffusion and short-range ordering [M. S. Wechsler and R. H. Kernohan, Acta Met. **7**, 599 (1959); R. H. Kernohan and M. S. Wechsler, J. Phys. Chem. Solids **18**, 175 (1961)]. The total change in modulus during aging increases with Al content and quenching speed and is also a function of the quenching temperature. An effective activation energy of 0.69 ev was determined 38 min after quenching. This is an effective energy of motion for the point defects involved in the diffusion process at this point in the reaction.

INTRODUCTION

THE resistivity of Cu-15 at.% Al single crystals quenched in water from 450°C decreases with time in the temperature range 45–100°C.[1] The decrease in resistivity appears as the result of an increase in the degree of local order[1,2]; the presence of quenched-in vacancies enhances diffusion allowing local ordering to take place rapidly at these low temperatures.[1,2]

A similar investigation of Young's modulus was undertaken just prior to Wechsler and Kernohan's first publication[1] and similar results were obtained. Young's modulus, after quenching from 450°C, increases with time during isothermal aging at room temperature and this, too, appears as the result of an increase of local order. Actually, modulus changes in many ordering alloys occur during isothermal aging at room temperature after quenching from relatively high temperatures. Such effects have been observed in $AuCu_3$, Au_3Cu, and α brass.[3]

The existence of local order in α Cu-Al alloys has been established in at least three sets of diffuse x-ray scattering investigations.[4–6]

EXPERIMENTAL PROCEDURE AND RESULTS

Polycrystalline Cu (99.999%) alloy specimens of 5, 10, 14, and 16.5 at.% Al (99.996%) were melted, fabricated, and homogenized as described in a previous investigation.[7] In addition, one 14 at.% Al single-crystal specimen was grown from the melt using the technique previously described.[7] The specimens were about 0.13 cm×0.5 cm×3.5 cm. The fundamental resonant frequency f for longitudinal vibrations was measured using electrostatic excitation and detection.[8] Young's modulus M is proportional to f^2 and relative changes in Young's modulus $\Delta M/M$ equal $2\Delta f/f$, neglecting any length changes which might occur in the specimen.

Each of the polycrystalline specimens was sealed off in a Pyrex tube under a vacuum of 1×10^{-6} mm of Hg, annealed $1\frac{1}{2}$ hr at 450°C, and quenched into cold water (shattering the Pyrex tubing); resonant frequencies were then measured as a function of time at room temperature, 21±1°C. The initial reading was obtained 6–8 min after quenching, and the frequency immediately after quenching was obtained by extrapolating the readings back to zero time.

$\Delta f/f_i$ (f_i is the value obtained on extrapolating to zero time) is shown versus time in Fig. 1 for the four polycrystalline specimens. In the 5 and 10 at.% Al alloys, $\Delta f/f_i$ reaches the final value in about 270 and 1700 min, respectively, while the resonant frequency was still changing after 3000 min in the 14 and 16.5 at.% specimens.

$\Delta f/f_i$ of the polycrystalline 14 at.% Al specimen was also measured as a function of time at room temperature following cooling in still air from 325[9] and 400°C

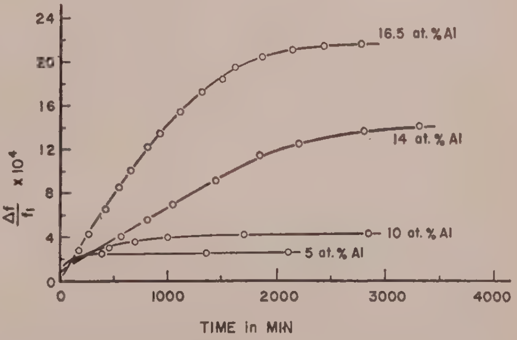

FIG. 1. Relative change in resonant frequency $\Delta f/f_i$ vs annealing time at room temperature for polycrystalline specimens, water quenched from 450°C. The initial value of Young's modulus was 13.40, 12.82, 12.29, and 12.09×10^{11} d/cm² for the 5, 10, 14, and 16.5 at.% Al alloys, respectively.

---

[*] This research, based on the Ph.D. research of T. J. Koppenaal, was supported by the Office of Naval Research of the United States government.

[†] Present address: Armour Research Foundation, Technology Center, Chicago 16, Illinois.

[1] M. S. Wechsler and R. H. Kernohan, Acta Met. **7**, 599 (1959).

[2] R. H. Kernohan and M. S. Wechsler, J. Phys. Chem. Solids **18**, 175 (1961).

[3] M. E. Fine (unpublished research).

[4] C. R. Houska and B. L. Averbach, J. Appl. Phys. **30**, 1525 (1959).

[5] R. G. Davies and R. W. Cahn, Phil. Mag. **5**, 1119 (1961).

[6] B. Borie, Oak Ridge Natl. Lab. Rept. **2632**, 38 (October 10, 1958).

[7] T. J. Koppenaal and M. E. Fine (to be published).

[8] M. E. Fine and C. Chiou, Trans. Am. Inst. Mining, Met., Petrol. Engrs. **212**, 553 (1958).

[9] Initial cooling rate was 6.0°C/sec and this decreased steadily as the temperature decreased.

(Fig. 2). The initial resonant frequency f_i decreased from 54 264 to 54 114 cps as the annealing temperature was lowered from 400 to 325°C. Further, the water quench from 450°C gave a much lower f_i, 53 770 cps. As may be seen in Fig. 2, the rate of change of f and the total change in f decrease as f_i increases.

To determine an effective activation energy for the annealing process, the 14 at.% Al single crystal was water quenched from 450°C and f was measured at 49.7±0.3°C. After holding here long enough to accurately determine the rate of change, the annealing temperature was rapidly lowered to 28.7±0.2°C and further readings of f were taken. Figure 3 shows f as a function to time at both temperatures. df/dt values of 1.27 and 0.25 cps/min at 49.7 and 28.7°C, respectively, were observed. An effective activation energy for this stage in the annealing process (38 min after the quench) was calculated to be 0.69 ev.

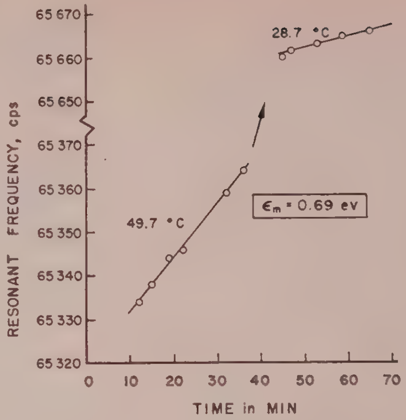

FIG. 3. Resonant frequency vs annealing time in a Cu-14 at.% Al single crystal, water quenched from 450°C.

DISCUSSION

The structural change producing the decrease in resistivity observed by Wechsler and Kernohan[1] during isothermal annealing of quenched specimens also produces an increase in the resonant frequency or Young's modulus, Fig. 1. Similar resonant frequency effects have been observed in quenched α brass, $AuCu_3$, and Au_3Cu.[3] The values of $\Delta f/f_i$ shown in Fig. 1 increase rapidly with aluminum content. This behavior is compatible with the ordering mechanism discussed by Wechsler and Kernohan[1,2] since the amount of ordering which can take place increases with Al content.

As previously noted, local order has been found in these alloys by three independent investigators.[4-6] Further, a yield-point effect[7] has been observed in these alloys and an investigation of this phenomenon clearly seems to point to short-range ordering as the source.

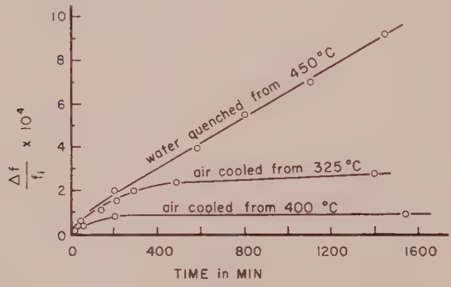

FIG. 2. Relative change in resonant frequency $\Delta f/f_i$ vs annealing time at room temperature for Cu-14 at.% Al polycrystalline alloy after various cooling procedures. Initial values of f given in text.

The effect of annealing temperature and quenching rate (Fig. 2) can be understood in terms of the concentration of point defects and the amount of ordering during the quench indicated by f_i. f_i increases with the amount of local order. Thus, on water quenching from 450°C, large quantities of vacancies are quenched in, little ordering occurs during the quench, f_i is small, and the changes in f are large. On air cooling, f_i is larger and the changes in f are smaller. More ordering occurs during cooling in air from 400°C than from 350°C since f_i is larger for the former.

From the data given in Fig. 3, an effective activation energy of 0.69 ev was computed. This corresponds to the effective activation energy of motion of the point defects involved in the ordering reaction. Wechsler and Kernohan[1] observed that the effective ϵ_m increases as this aging progresses. Their initial value is about 0.65 ev and their final value about 1.2 ev. Several different kinds of point defects are apparently involved in the diffusion process and thus there is a spectrum of ϵ_m's. The defect with the greatest mobility (lowest ϵ_m) would anneal out faster and the effective ϵ_m would then increase with time.[1]

Our value of effective ϵ_m corresponds to aging 38 min at 49.7°C after water quenching from 450°C. According to the data of Wechsler and Kernohan,[1] about 20% of the aging process has occurred to this point. Their value corresponding to this amount of aging is 0.75 ev which agrees reasonably well with our value.

In summary, the modulus data give further evidence that ordering of alloys can occur at low temperatures provided point defects are supplied to aid the diffusion process.

Letters to the Editor

Resistance as Dissipation into Many Reactive Circuits: Landau Damping and Nyquist's Noise Theorem

O. Buneman
Stanford Electronics Laboratories, Stanford, California*

(Received March 2, 1961)

NONRADIATIVE dissipation, such as friction and ohmic resistance, is not a loss of energy but its dispersal into a large number of degrees of freedom. Irreversibility is the improbability of reconcentration of energy into its initial ordered form.

One would therefore expect a network of very many undamped resonating circuits to exhibit resistive properties in its transient response. Indeed, it should be possible to simulate resistances by such purely reactive elements, in close analogy with the physical process of ohmic heating, i.e., conversion of electrical energy into molecular and lattice vibrations. (In a closed, nonradiating system these are undamped.)

Let

$$Y=\sum_\nu \frac{1}{2jL_\nu(\omega-\Omega_\nu)}$$

be the admittance of a network with resonance frequencies Ω_ν and associated inductances L_ν. Let the frequencies Ω_ν be ordered in ascending magnitude. Both Ω_ν and $-\Omega_\nu$ should occur in the summation, with the same inductance.

If there are many terms and the values L_ν are related to Ω_ν in a nonerratic fashion, a convenient method of evaluating the sum is to consider small ranges $d\Omega$ of the resonant frequencies, to define the amount of inverse inductance L^{-1} in such a range as $Bd\Omega$ and to convert[1] the sum into an integral:

$$Y=\frac{1}{2}\int_{-\infty}^{+\infty}\frac{Bd\Omega}{j(\omega-\Omega)}=\frac{1}{2}\int_{-\infty}^{+\infty}\frac{Bd\Omega}{s-j\Omega}.$$

We are concerned with a problem of transience; hence, the introduction of the "s" used in Laplace transform theory, in place of $j\omega$.

In general, B depends on Ω. The case of constant B leads to divergence of the integral but this simple and interesting case can be approximated arbitrarily closely, without loss of convergence, by taking

$$B=B_0/(1+\Omega^2/\Omega_0^2)$$

with sufficiently large Ω_0. The integration is effected by completing the path around a large semicircle in the upper half-plane and contracting around the only pole at $\Omega=+j\Omega_0$. The pole at $\Omega=-js$ is in the lower half-plane, by the rules of Laplace transform theory (Re $s>0$).

The result,

$$Y=\pi B_0/[2(1+s/\Omega_0)],$$

shows that the effective impedance of our network consists of a resistance $2/\pi B_0$ and an inductance $2/\pi B_0\Omega_0$. The latter vanishes in the limit $\Omega_0\to\infty$. The simulation of resistance by reactive elements is thus established. The conductance with $\Omega_0\neq\infty$ is $\frac{1}{2}\pi B/(1+\omega^2/\Omega_0^2)=\frac{1}{2}\pi B(\omega)$, and this formula for the conductance is obtained also with more general forms of $B(\Omega)$ than that assumed here.

Our picture of dissipation assists the understanding of Landau[2] damping of disturbances with wave number k in a collision-free plasma. The electron streams passing through the plasma with their continuously distributed velocities v provide a continuous range of resonance frequencies $\Omega=kv$.

Moreover, Nyquist's[3] noise theorem is readily obtained from this resonant-circuit model of resistance. If the network is shorted at the port of measurement after having been in thermal contact with the surroundings, each circuit will be left oscillating with energy

$$\tfrac{1}{2}L_\nu|I_\nu|^2+\tfrac{1}{2}C_\nu|V_\nu|^2=L_\nu|I_\nu|^2=C_\nu|V_\nu|^2=KT,$$

from which we deduce

$$|I|^2=KT/L_\nu=KTBd\Omega=2KTGd\Omega/\pi,$$

where G is the "conductance" identified above. This is Nyquist's formula.

---

* The work reported here was supported by the Air Force.

[1] The spacing $\delta\Omega$ in any actual discrete frequency spectrum sets a limit to the validity of this conversion, consequently, our deductions are restricted to time intervals less than about $1/\delta\Omega$.

[2] L. Landau, J. Phys. (U.S.S.R.) **10**, 25 (1946).

[3] H. Nyquist, Phys. Rev. **32**, 110 (1928).

Thermionic Emission of UC-Nb*

R. H. Abrams, Jr., and F. E. Jamerson
General Motors Research Laboratories, Warren, Michigan

(Received March 29, 1961)

RECENT experiments on thermionic conversion of heat to electricity utilizing reactor heat sources[1] have stimulated interest in uranium-bearing cathodes.[2,3] The thermionic constants and spectral emissivity have been measured on a uranium carbide-niobium disk, UC (80 volume %)-Nb (20 volume %), of 2.34 cm in diameter and 0.51 cm in thickness.

The sample was prepared[4] by green pressing a powder mix containing 80 volume % UC of 6 w/o carbon and 20 volume % Nb into a 2.54-cm disk. The green press was then loaded into a carbon-coated niobium container and was pressure bonded for 3 hr at 1700°K under a helium gas pressure of 680 atm. After pressure bonding, the niobium cladding was machined. The UC-Nb was metallographically polished, examined, and vacuum heated to 1970°K without evidence of melting. The sample was then repolished, and vacuum heated to 1970°K.

Spectral emissivity was found by comparing optical pyrometer readings of the surface and a hohlraum, assuming the surface and the interior of the disk to be at the same temperature. The emissivity at 0.65 μ varies from 0.7 at 1100°K to 0.6 at 1700°K.

For the emission experiment, the UC-Nb served as an electron bombarded cathode of a plane parallel diode in a vacuum of $\sim 10^{-5}$ mm Hg. To minimize anode heating, voltage was swept rapidly by hand. Data were recorded with an oscillograph over the temperature range 1380° to 1960°K for electric field strengths up to 23 000 v/cm. Corrected current densities of 6×10^{-4} to 1.4 amp/cm² were obtained. Schottky temperatures were lower than the observed temperatures (pyrometer readings corrected for emissivity) indicated field-strength limitations. Values of saturated current were obtained by passing a line with an observed-temperature slope through the highest data points. This is deemed reasonable since Schottky temperatures agree with

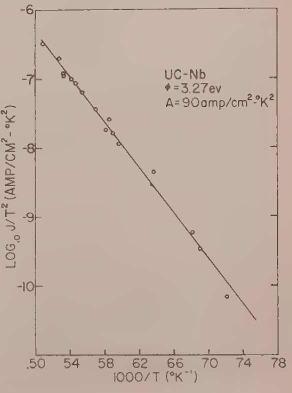

FIG. 1. Richardson plot for UC-Nb obtained from corrected Schottky curves.

observed temperatures at considerably higher fields for uranium carbide.[3] This analysis yields saturated current values that may be conservative. The resulting Richardson plot of Fig. 1 was analyzed by a method of least squares to obtain the Richardson constants $\phi=3.27$ ev, and $A=90$ amp/cm^2 °K^2. Expressed in terms of a temperature dependent work function,

$$\phi(T)=3.27+2.5\times10^{-5}T \text{ ev.}$$

The contributions of R. F. Hill, C. B. Leffert, W. J. Le Gray, and R. Silver to this experiment are gratefully acknowledged. The continued support of Dr. D. H. Loughridge and Dr. L. R. Hafstad of this work is greatly appreciated.

* This work is supported in part by the Office of Naval Research.

[1] G. Grover, Nucleonics **17**, 54 (1959); F. E. Jamerson, IRE Natl. Conv. Record **8**, 66 (1960).

[2] R. W. Pidd, G. M. Grover, D. J. Roehling, E. W. Salmi, J. D. Farr, N. H. Kinkorian, and W. G. Witteman, J. Appl. Phys. **30**, 1575 (1959).

[3] G. A. Hass and J. T. Jensen, Jr., J. Appl. Phys. **31**, 1231 (1960).

[4] Fabricated by Battelle Memorial Institute.

Forces in Dielectric Fluids*

James D. Horgan and David L. Edwards
Department of Electrical Engineering, Marquette University, Milwaukee, Wisconsin

(Received April 17, 1961)

THE purpose of this letter is to point out that certain electrihydrodynamic phenomena observed in dielectric liquids are most likely due to the ionization of the fluid, rather than to the polarization of the dielectric as previously supposed. Consider the arrangement shown in Fig. 1. The ring is of copper, with 2.54 cm i.d. and 0.635 cm axial length. The shield is brass foil, 12.7 cm in diameter and 15.24 cm in length. The fluid is a commercial transformer insulating oil. A similar arrangement, without the shield and disk was described by Pohl.[1]

When the shield and disk are removed and 9000–14 000 v dc applied to the electrodes, fluid is pumped vertically upwards as a fountain originating at the point of the needle. Because very similar results are obtained with the needle at either polarity it may seem that the principal action is due to the dielectrophoretic process described by Pohl, i.e., due to the forces experienced by molecular dipoles in a nonuniform field. The direction of such forces is not directly dependent on the direction of the field. If the principal effect was due to ionization produced by contamination, cosmic rays, and terrestrial radioactivity as suggested by Pierce[2] then, since ions of one sign would be dominant, the effect of changing polarity should be quite noticeable. Ionization can also be caused by a corona discharge at the needle point as stated by Stuetzer.[3] In such phenomena, the polarity of the charged particles in the body of the fluid is the same as that of the needle, and very similar results should be observed with the needle at either polarity.

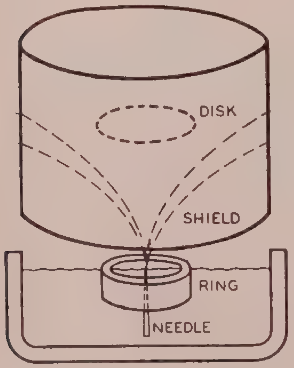

FIG. 1. Schematic of ring, needle, shield, and disk.

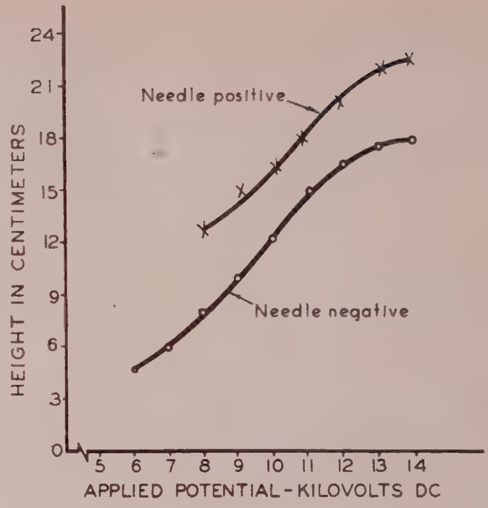

FIG. 2. Fountain height vs applied voltage.

To demonstrate that this is indeed a phenomenon dependent on the presence of charged particles rather than the dielectrophoresis process, the shield shown in Fig. 1 was added to the basic configuration. If the dielectrophoresis process is dominant, then changes in the potential and polarity of the shield should have little effect on the height of the fountain observed, since this is dependent primarily on the electric field intensity at the needle. In fact, however, reversal of the polarity of the shield potential relative to the needle potential results in very marked effects on the fountain height.

With ring and shield grounded and the needle positive, relatively large fountains are generated as shown in Fig. 2. Similarly, with ring and shield positive and the needle grounded, large fountain effects are observed. However, if the shield and needle are positive and the ring grounded, a relatively small (1–2 cm) fountain effect was observed for voltages in the range 8000–14 000 v. Similar small effects were observed with shield and needle grounded and ring positive. Such observations indicate that ions of the same polarity as the needle are dominant in the fluid, are therefore repelled from the needle and attracted to or repelled from the shield, depending on the polarity of the latter. To further demonstrate this, a conducting disk was lowered into the field region, as indicated in Fig. 1. When the disk is at the same potential as the ring, the fountain height can be increased 5–8 cm. When the disk is at the same potential as the needle, the fountain height is decreased, and can in fact be reduced to zero by properly lowering the disk.

* This work was supported by the National Science Foundation.

[1] H. A. Pohl, J. Appl. Phys. **29**, 1182 (1958).

[2] E. T. Pierce, J. Appl. Phys. **30**, 445 (1959).

[3] O. M. Stuetzer, J. Appl. Phys. **30**, 984 (1959).

Formation of Liquid Jets in Nonuniform Electric Fields

Herbert A. Pohl
Plastics Laboratory, Princeton University, Princeton, New Jersey

(Received May 8, 1961)

THE present note by Horgan and Edwards demonstrates that the energy required for sustaining pumping action on liquids in nonuniform electric fields is supplied by current flow, and therefore involves electrophoresis.

This same conclusion is reached by thermodynamic arguments, for dielectrophoretic motion, which arises in a sense by induced capacitance changes between electrodes, cannot produce continuous work in a static field. Electrophoresis, which involves charge transfer to and from, say, an external battery or other current source, on the other hand, can produce continuous work on the liquid.

As noted by Pohl,[1] the droplets of the liquid jet produced in a nonuniform field are "charged, hence the effect is a combination of dielectro- and electrophoresis." Dielectrophoresis acts in producing an attraction of the material toward the greater field intensity, near the point. However, the high intensity of the field produces "incipient corona"[2,3] and appreciable local charging of the fluid. Electrophoresis then results. The sharp, positive electrode, for example, may be considered to have stripped the locally present fluid of some electrons, leaving the fluid positively charged. The latter is then repelled, ejected as the upward jet in the pumps shown by Pohl,[1] Steutzer,[4] and others, including M. Faraday. The local incipient corona may conveniently be considered to arise as a result of the "second Wien effect," where in weak electrolytes,[5,6] high field strength increases the effective dissociation.

The experiment cited by Horgan and Edwards again demonstrates the correct nature of the pumping phenomenon.

[1] H. A. Pohl, J. Appl. Phys. **29**, 1187 (1958).
[2] H. A. Pohl and J. P. Schwar, J. Appl. Phys. **30**, 72 (1959).
[3] H. A. Pohl and J. P. Schwar, J. Electrochem. Soc. **107**, 384 (1960).
[4] O. M. Steutzer, J. Appl. Phys. **31**, 137 (1960).
[5] M. Wien, Ann. Physik [4] **83**, 327 (1927).
[6] M. Wien, Ann. Physik [4] **85**, 795 (1928).

Phase Diagram for the Pseudobinary System Ag_2Te-Sb_2Te_3

J. P. McHugh,* W. A. Tiller,* S. E. Haszko,† and J. H. Wernick†
Westinghouse Research Laboratories, Beulah Road, Churchill Borough, Pittsburgh 35, Pennsylvania

(Received April 20, 1961)

Armstrong, Faust, and Tiller[1] have recently shown that $AgSbTe_2$ is not a congruently melting compound as has been previously assumed[2] and that material of this composition is two-phase for most temperatures below the melting point. They also proposed a form for the phase diagram of the Ag_2Te-Sb_2Te_3 pseudobinary system. This letter gives the results of two independent determinations of the liquidus and solidus for the Ag_2Te-Sb_2Te_3 pseudobinary system.

Both investigations were carried out by thermal methods and the results substantiated by metallographic and by x-ray powder techniques. Haszko and Wernick obtained their thermal data by a differential thermal analysis technique. McHugh and Tiller used conventional cooling and heating curves. McHugh and Tiller also obtained some useful data by the normal freeze technique.[3]

The results of these investigations are shown in Fig. 1 where it can be seen that the agreement between the two sets of data is quite good. The δ phase is the low-temperature form of Ag_2Te, the γ phase is the high-temperature form, and the β phase has the disordered NaCl structure.[2,4] From the phase diagram, we see that the $\beta+L$ region exists in a temperature range of about 4°C or less for compositions consisting of more than about 55 mole % Sb_2Te_3. The boundaries of the β phase in this region are closely spaced and nearly horizontal, making it difficult to determine the exact composition of the β phase formed by the peritectic reaction. We estimate this composition to be in the range 70 to 72 mole % Sb_2Te_3.

The location of the β-field boundaries below about 500°C are difficult to determine by (a) thermal techniques since the thermal effects are small or (b) homogenization techniques since the diffusion rate at these temperatures appears to be small. However, it was felt that diffusion might be enhanced by heavy deformation and that phase equilibration would be reached in reasonable times even at temperatures below 500°C. Accordingly, samples of the 50:50 composition were quenched, extruded at 300°C to a 10:1 reduction in area and annealed at 400°C for 48 and 200 hr to see if the material was single phase. Photomicrographs revealed the existence of a second phase in the vicinity of grain boundaries after extrusion, after the 48-hr anneal and after the 200-hr anneal. Since x-ray photographs of the as-extruded material indicated the presence of some δ phase, it is likely that this was the phase seen in the photomicrographs. The volume fraction of this phase was smaller after the 48-hr anneal than before but was relatively unchanged after the 200-hr anneal compared to the 48-hr anneal (the remaining volume of second phase was a few percent of the total volume). It was thus felt that the 200-hr anneal produced phase equilibration at 400°C and that at this temperature the 50:50 composition lies in the two phase $\beta+\gamma$ field as indicated in Fig. 1.

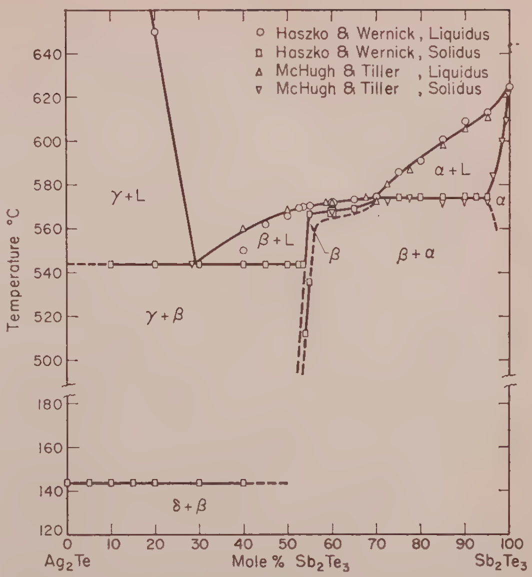

FIG. 1. The equilibrium phase diagram for the pseudobinary cut, Ag_2Te-Sb_2Te_3, in the Ag-Sb-Te system.

* Dr. McHugh and Dr. Tiller are associated with the Westinghouse Research Laboratories.
† Dr. Haszko and Dr. Wernick are associated with the Bell Telephone Laboratories.
[1] R. W. Armstrong, J. W. Faust, Jr., and W. A. Tiller, J. Appl. Phys. **31**, 1954 (1960).
[2] J. H. Wernick, S. Geller, and K. E. Benson, J. Phys. Chem. Solids **23**, 240, (1958).
[3] J. P. McHugh and W. A. Tiller, Trans. AIME **215**, 651 (1959).
[4] S. Geller and J. H. Wernick, Acta Cryst. **12**, 46 (1959).

Angular Dependence of Torque in Anisotropic Permalloy Films*

W. D. Doyle, J. E. Rudisill, and S. Shtrikman†
The Franklin Institute Laboratories, Philadelphia, Pennsylvania

Torque curves in thin permalloy films have been studied using a high-sensitivity (10^{-3} d-cm) continuous recording torque magnetometer.[1] The results reported here are for a 1500 A, 77% Ni film, prepared by vacuum deposition in a magnetic field.[2] The hysteresis loop taken at 1000 cycles was rectangular in the easy direction with a coercive force $H_c=1.0$ oe. In the hard direction, it was reversible with an anisotropy field $H_k=5.8$ oe.

The experimental results are summarized in Figs. 1–3. Examples of the recorded torque curves,[3] all of which had a period of 180°, are shown in Fig. 1. For applied fields $H<H_c$, or in the more convenient reduced field notation, $h<h_c$, where $h=H/H_k$ and

$h_c = H_c/H_k$, the torque was essentially zero. For $h_c < h < 1$, the curves were irreversible, i.e., showed rotational hysteresis and were of the type shown in Fig. 1(a). For $h > 1$, the hysteresis vanished and curves similar to Fig. 1(b) were observed. This last result is in disagreement with the earlier work of Mayfield[4] who, using a different technique, reported a nonzero value of rotational hysteresis even for fields as large as $h = 15$.

The anisotropy constant K was 2.5×10^3 ergs/cc. It was determined from the magnitude of the high-field torque curves which became field independent for $h > 0.9$. For $h > 6$, the curves assumed a nearly pure size dependence.

The rotational hysteresis loss per unit volume[5] was computed from the torque curves and is plotted versus the reduced field in Fig. 2. Figure 3 shows the field dependence of θ_c, the critical angle between the easy axis and the applied field at which the torque reverses.

The experimental results were compared with various theoretical pictures of magnetization processes in ferromagnets as shown in Figs. 1–3. Three models were considered: (a) coherent rotations as described by Stoner and Wohlfarth[6]; (b) 180° wall motion in a uniaxial single crystal as discussed by Kondorsky[7]; and (c) an adaptation of the results of the calculations by Shtrikman and Treves[8] on noncoherent reversal in an infinite circular cylinder.

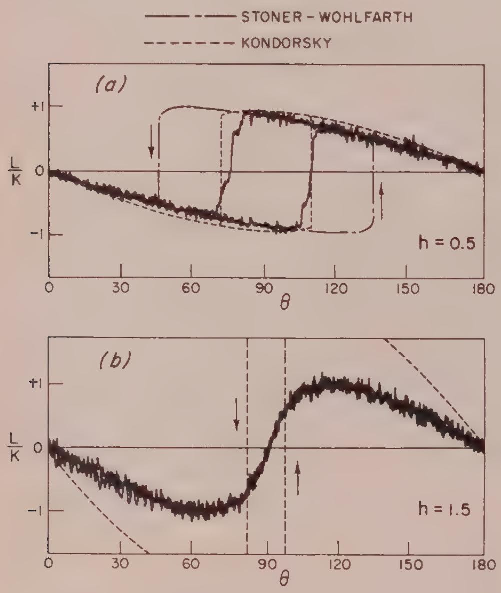

FIG. 1. Angular dependence of the torque L, plotted in reduced units, for two values of the reduced applied field; (a) $h = 0.5$, (b) $h = 1.5$. The broken curves are those calculated from the Stoner-Wohlfarth and Kondorsky models. Reversible portions of the Stoner-Wohlfarth curves are not shown in both (a) and (b), since they fall on the experimental curves. Arrows indicate the direction of rotation of h.

(a) Coherent rotation: Here the film is considered to be a single domain particle with uniaxial anisotropy. The saturation magnetization I_s is given by $I_s = 2K/H_k$. Using the experimental value of H_k and K, I_s was calculated to be 860 emu/cc which is in close agreement with the bulk value.[9] As shown in Fig. 1, the reversible parts of the experimental torque curves are in very good agreement with the calculated ones. The onset of irreversible torque reversal as well as the magnitude of the rotational hysteresis are, however, in wide disagreement with this model except in fields approaching $h = 1$.

(b) 180° wall motion: Here it is assumed that the hysteresis loop is rectangular and that only the component of the field parallel to the applied field is effective. This should be a good approximation as long as the magnetization is parallel to the easy axis, i.e., for $h \ll 1$. It follows accordingly that the rotational hysteresis W_r is field independent, with a value

$$W_r = 4H_cI_s. \tag{1}$$

The critical angle θ_c is given by $\cos\theta = -h_c/h$. (2)

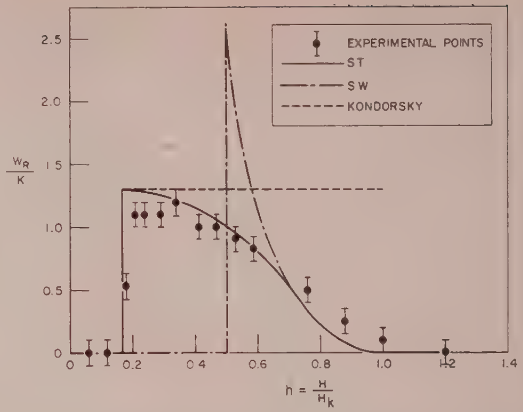

FIG. 2. Rotational hysteresis W_r, plotted in reduced units, vs reduced applied field. The theoretical curves are those derived from the treatments by Shtrikman and Treves (S-T), Stoner and Wohlfarth (S-W), and Kondorsky.

Since the magnetization is parallel to the easy axis, the torque L is simply

$$\begin{aligned} L &= -HI_s \sin\theta \quad \theta < \theta_c \\ L &= HI_s \sin\theta \quad \theta > \theta_c. \end{aligned} \tag{3}$$

Examination of Figs. 1–3 shows that for $h \ll 1$, the predictions based on this model are in good agreement with experiment. However, as h approaches 1, discrepancies appear which grow as h increases.

(c) Noncoherent rotation: Here the torque curves are identical to those calculated from the Stoner-Wohlfarth model except when

$$h^2 < 1 - 3h_c + 3h_c^2. \tag{4}$$

When Eq. (4) is satisfied, the critical angle is given by

$$\cos\theta_c = \frac{-h_c}{(1-2h_c)^{\frac{1}{2}}} \left\{ \left[\left(\frac{1-h_c}{h} \right)^2 \right]^{-1} \right\}^{\frac{1}{2}}, \tag{5}$$

although in the regions where the curves are reversible, they are

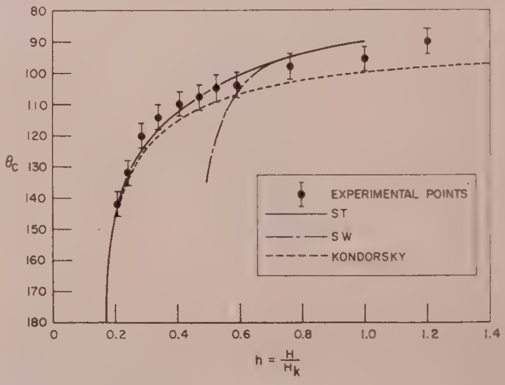

FIG. 3. The critical angle θ_c vs reduced applied field. The theoretical curves are those derived from the treatments by Shtrikman and Treves (S-T), Stoner and Wohlfarth (S-W), and Kondorsky.

the same as the Stoner-Wohlfarth curves, calculated for corresponding regions.

The hysteresis losses are computed as described by Shtrikman and Treves. Comparison with experiment, Figs. 2–3, shows that the above formulas fit the experimental results reasonably well over the entire field range. Moreover, the value of the rotational hysteresis integral[10] for this film is 2.6, in agreement with the Shtrikman-Treves model, whereas the Stoner-Wohlfarth and Kondorsky models yield values of 0.4 and 4.0, respectively.

These favorable results are in fact no surprise. For cases where $h_c<1$, as for this film ($h_c=0.17$), the model is equivalent to the Stoner-Wohlfarth one in the region $h\sim 1$ and to the Kondorsky one for $h\ll 1$. As it is hard to attach physical meaning to the picture assumed in the derivation of Eq. (5), i.e., an infinite circular cylinder describing a thin film, it is perhaps best to regard it as an interpolation scheme between the limits of the Stoner-Wohlfarth and the Kondorsky models.

---

[*] This research was supported by the United States Air Force, monitored by the Wright Air Development Division.

[†] On leave from the Weizmann Institute of Science, Rohovot, Israel.

[1] Franklin Institute Laboratories Quarterly Progress Report Q-A2277–4.

[2] M. S. Blois, Jr., J. Appl. Phys. **26**, 975 (1955).

[3] To define its magnetic history prior to measurement, the film was demagnetized in a slowly decreasing 1000-cycle field. In addition, before recording each curve, the applied field was cycled 180°.

[4] J. R. Mayfield, J. Appl. Phys. **30**, 256S (1959).

[5] R. M. Bozorth, *Ferromagnetism* (D. Van Nostrand Company, Inc., Princeton, New Jersey, 1951), p. 514.

[6] E. C. Stoner and E. P. Wohlfarth, Phil. Trans. Roy. Soc. (London) **240A**, 599 (1948).

[7] E. Kondorsky, J. Phys. (U.S.S.R.) **2**, 161 (1940).

[8] S. Shtrikman and D. Treves, J. phys. radium **20**, 286 (1959).

[9] See reference 5, p. 109.

[10] I. S. Jacobs and F. E. Luborsky, J. Appl. Phys. **28**, 467 (1957).

Zero-Field Splitting of the Cr^{3+} Ground State in YGa and YAl Garnet

J. W. Carson and R. L. White
Hughes Research Laboratories, Malibu, California

(Received January 9, 1961)

THE Cr^{3+} ion has been the subject of considerable investigation in recent years, occasioned largely by its potential as a maser material. We report here on the paramagnetic resonance spectra of Cr^{3+} in the diamagnetic gallium and aluminum garnets, $Y_3Ga_5O_{12}$ and $Y_3Al_5O_{12}$. The measurements were made at 35 kMc, at 300° and 77°K, on oriented single crystals having about 3% of the Ga (or Al) sites occupied by Cr^{3+} ions. The Cr^{3+} enters predominantly a site of sixfold cubic coordination with a slight trigonal distortion along the crystal (and local) [111] direction. It is the trigonal distortion which gives rise to the zero-field splitting ($2D$) of the ground state spin quartet into two doublets. Davis and Strandberg[1] have worked out thoroughly the theory of the Cr^{3+} ion in such a site, and our data were fully compatible with their theory both as to absorption positions and relative intensity. The parameters resulting from our measurements are summarized in Table I.

TABLE I. Summary of zero-field splitting $2D$ and $g_{\|}$ for Cr^{3+} in $Y_3Ga_5O_{12}$ and $Y_3Al_5O_{12}$.

Garnet	300°K $g_{\|}$	300°K $2D$	77°K $g_{\|}$	77°K $2D$
YGa	1.98	21.0 kMc	1.98	20.9 kMc
YAl	1.98	15.3 kMc	1.98	15.7 kMc

For the YGa garnet, the room temperature results agree with those reported by Geschwind and Nielsen.[2] The sign of the temperature dependence of the zero-field splitting differs for the two kinds of garnets. The explanation of this is not obvious. X-ray diffraction pictures of the YAl garnets indicated a considerable degree of strain. At room temperature the $g_{\|}$ and $2D$ were the same for all the aluminum garnets (within experimental error), but $2D$ at 77°K varied from 15.5 to 15.7 kMc among the samples examined. Annealing at 1200°C for 24 hr produced no detectable change in $2D$ at 300° or 77°K for any of these samples.

The difference in zero-field splitting of the Cr^{3+} ion in the two types of garnets is strongly dependent on the exact positions of the oxygen neighbors, and accurate crystal parameter information is not available on these two garnets. However, the work of Abrahams and Geller[3] indicates that the oxygen octahedron in grossalurate (an aluminum garnet) is appreciably more regular than that of yttrium iron garnet. Since the Ga^{3+} ion is very similar in size to the Fe^{3+} ion, one is tempted to extrapolate these results to predict that the oxygen octahedron is more regular in $Y_3Al_5O_{12}$ than in $Y_3Ga_5O_{12}$. This conclusion is in agreement with the reduced zero-field splitting in $Y_3Al_5O_{12}$ observed in these experiments.

[1] C. F. Davis, Jr. and M. W. P. Strandberg, Phys. Rev. **105**, 447 (1957).

[2] S. Geschwind and J. W. Nielsen, Bull Am. Phys. Soc. **5**, 252 (1960).

[3] S. C. Abrahams and S. Geller, Acta. Cryst. **11**, 437 (1958).

Preparation of Single-Crystal Boron

Claude P. Talley
Exploratory Research Laboratory, Texaco Experiment Incorporated, Richmond 2, Virginia

(Received April 3, 1961)

SEVERAL attempts to produce single crystals of elemental boron by floating-zone melting have been reported, but to the author's knowledge no one heretofore has been successful.[1–4] Small single-crystal boron specimens of fractional millimeter size have been prepared by chemical vapor plating,[5,6] but thus far it has not been possible to grow larger ones.

A single crystal of β-rhombohedral boron approximately 1.5 mm in diameter and about 1 cm in length has been recently prepared in this laboratory by floating-zone melting with electron bombardment heating under vacuum.[7] X-ray diffraction transmission photographs revealed both the extent of single-crystal growth and its form. The density of a similarly prepared sample was found to be 2.345 ± 0.005 g/cm³ by a flotation technique, and this also corresponds to β-rhombohedral boron within experimental uncertainty.[8] The zone-melted boron rod was much stronger than the original polycrystalline rod.

To provide an exceptionally "clean" vacuum for floating-zone melting, an ion pump manufactured by the Ultek Corporation was used. Before starting the ion pump, the system was roughed to about 10 μ Hg pressure by sorption onto a molecular sieve cooled to liquid nitrogen temperatures. The zoning process was carried out at about 10^{-5} mm Hg at a travel rate on the order of 1 mm/min. The bombarding electrons were supplied by a concentric loop of 20-mil tungsten heated electrically to a temperature near 2300°K. The accelerating potential was about 7 kv, and a power of approximately 150 w was required to melt the boron. Nickel deflection plates, mounted above and below the emission filament and maintained at a 200-v negative potential with respect to it, served to focus the bombarding electrons into a thin sheet.

The starting boron rods were prepared by chemical vapor plating onto 25-μ-diam tungsten filaments at incandescent temperatures with boron tribromide and hydrogen. The calculated amount of tungsten impurity in a 1.5-mm-diam boron rod is about 0.2% by weight. Wet chemical analysis for total boron in these preparations was typically in excess of 99% by weight. Emission spectrographic analysis for detectable impurities indicated 40 ppm Fe, 20 ppm Si, 3 ppm Cu, and 1 ppm Mg.

An x-ray shadowgraph (Fig. 1) of a partially zone-melted boron rod revealed that the original tungsten core had dissolved in the boron and apparently concentrated with other impurities in the advancing molten zone. Because boron itself is relatively transparent to x rays, quantitative x-ray absorption measurements are expected to be quite useful in following the progress of purification by floating-zone refining.

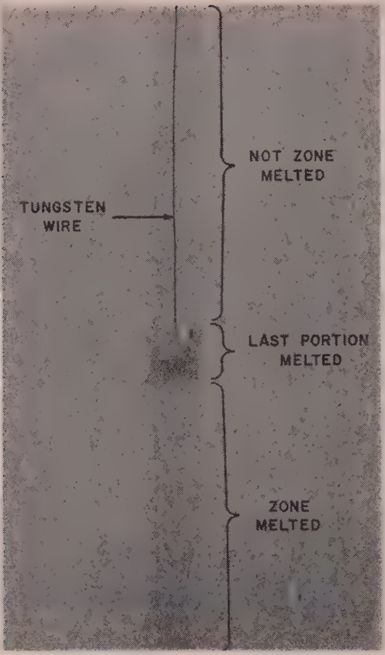

FIG. 1. X-ray shadowgraph of a partially zone-melted boron rod.

The author would like to acknowledge the assistance of Gerald R. Taylor, Jr., and Quinton D. Overman, Jr., of Texaco Experiment Incorporated for their participation in this work and Professor Ben Post of the Polytechnic Institute of Brooklyn for making and analyzing the x-ray diffraction transmission photographs. Appreciation is also due Dr. C. D. Richardson, Jr., who kindly let the author use his dental x-ray equipment for making the x-ray shadowgraphs. The author also wishes to thank Dr. Lloyd E. Line, Jr., of Texaco Experiment Incorporated for his sustained encouragement and the Wright Air Development Division, Air Research and Development Command, United States Air Force, for support of this work.

[1] E. S. Greiner, J. Appl. Phys. **30**, 598 (1959).
[2] A. Calverley, Nature **184**, 690 (1959).
[3] R. J. Starks and W. E. Medcalf in *Boron Synthesis, Structure and Properties* (Plenum Press, Inc., New York, 1960), p. 59.
[4] A. J. Hagenlocher in *Boron Synthesis, Structure and Properties* (Plenum Press, Inc., New York, 1960), p. 128.
[5] A. W. Laubengayer, D. T. Hurd, A. E. Newkirk, and J. L. Hoard, J. Am. Chem. Soc. **65**, 1924 (1943).
[6] A. G. Shinn, "Growth of boron single crystals," thesis, Iowa State College, 1950.
[7] M. Davis, A. Calverley, and R. F. Lever, J. Appl. Phys. **27**, 195 (1956).
[8] E. Sands and J. L. Hoard, J. Am. Chem. Soc. **79**, 5582 (1957).

Possibility of a Spin Wave Magnetic-Moment Detector*

T. B. DAY AND J. SUCHER
Physics Department, University of Maryland, College Park, Maryland
(Received February 2, 1961)

WE would like to report here briefly[1] on some results of an investigation which was started with the question: Is it possible, at least in principle, to think of a device which could electromagnetically signal the presence of a neutral particle? Wording the question in this form, of course, restricts consideration to those neutral particles with a magnetic moment. But since magnetic moment interactions are so weak,[2] one is then led to a search for any possible cooperative phenomena which could somehow enhance this interaction.

Now consider the lecture-demonstration apparatus of a two-dimensional array of compass needles suspended on pins, over which you pass a little bar magnet. The waves so generated are a very nice signal of the passage of the bar magnet, but they damp out rapidly,[3] and are a short-range phenomenon. Another type of cooperative effect (at least in a broad sense), namely the Čerenkov effect, is of long range and actually would give radiation from a point magnetic dipole moving through a medium, although the intensity would be very low.[2] It was conjectured that if one could use the magnetic fields of the Čerenkov effect to generate spin waves (the microscopic analog of the lecture-demonstration above), which would in turn enhance the magnetic field, etc., then it might be possible to "ring" the system at some resonant frequency and thus, perhaps, to see the changing magnetic fields of the whole cooperative system.

In order to study the possibility of the above behavior, one needs the solutions of the combined Maxwell and spin-wave[4] equations giving the changes in magnetic field and magnetization due to the presence of external currents. These may be written separately (when Fourier analyzed).

Maxwell's equations[5] $(c=1)$

$$(-k^2+n^2\omega^2)\mathbf{H}(\mathbf{k},\omega)=\mathbf{J}(\mathbf{k},\omega)-n^2\omega^2\mathbf{M}(\mathbf{k},\omega)+\mathbf{k}(\mathbf{k}\cdot\mathbf{M}) \qquad (1)$$

and the approximate spin-wave equations[6]

$$M_\pm=(\omega_s/D_\pm)H_\pm, \qquad (2)$$

with

$$D_\pm=k^2\mathfrak{D}+\omega_0\pm\omega. \qquad (3)$$

In Eq. (2), $M_\pm$ and $H_\pm$ are particular combinations of the components of the changes in the magnetization and magnetic field vectors, e.g.,

$$\begin{aligned} M_\pm&=M_z\pm iM_y\\ H_\pm&=H_z\pm iM_y. \end{aligned} \qquad (4)$$

In the above equations,

$$\begin{aligned} \omega_0&=\omega_0{}^1+i\alpha\omega\\ \omega_0{}^1&=\gamma H_0\\ \omega_s&=\gamma M_0\\ n^2&=\epsilon\mu_0(1+i\sigma/\omega\epsilon), \end{aligned} \qquad (5)$$

where α is the damping constant and $\mathfrak{D}$ the exchange constant[6] of the magnetic medium for spin waves, γ the gyromagnetic moment, ϵ and σ the dielectric constant and conductivity, H_0 the constant (uniform) external magnetic field applied to the sample, and M_0 the (uniform) magnetization which results (when there are no other sources), both chosen to point in the x direction (M_0 may point in the negative x direction). $\mathbf{J}(\mathbf{k},\omega)$ is the Fourier transform of $\mathbf{J}(\mathbf{r},t)$, which for a point particle of charge e and magnetic moment $\boldsymbol{\mu}$, is

$$\mathbf{J}(\mathbf{r},t)=-\nabla\times[e\mathbf{v}\delta(\mathbf{r}-\mathbf{v}t)] \\ +\left[\epsilon\mu_0\left(\frac{\partial}{\partial t}+\sigma/\epsilon\right)\frac{\partial}{\partial t}-\nabla(\nabla^0)\right]\boldsymbol{\mu}\delta(\mathbf{r}-\mathbf{v}t). \qquad (6)$$

One sees that the conjecture outlined above corresponds to solving the combined Eqs. (1) and (2) by iteration. The zeroeth-order solution for H is

$$\mathbf{H}^{(0)}(\mathbf{k},\omega)=\mathbf{J}(\mathbf{k},\omega)/(-k^2+n^2\omega^2) \qquad (7)$$

which will give the usual Čerenkov effect (in $\mathbf{r}$ space). If this $\mathbf{H}^{(0)}$ is used in Eq. (2), and the resulting $\mathbf{M}^{(0)}$ put back in Eq. (1), then the expected "ringing" of the system would occur at the "radiative pole" $k^2=n^2\omega^2$ for an ω such that

$$n^2\omega^2\mathfrak{D}+\omega_0\pm\omega=0; \qquad (8)$$

since $n^2\omega^2\mathfrak{D}$ is small ($\sim 10^{-3}$ in the kMc region), the resulting resonance is almost at ω_0. The usual Čerenkov cone is guaranteed by the δ function in $\mathbf{J}$.

While the above iterative treatment of Eqs. (1) and (2) is intuitively appealing, and makes more plausible the original conjecture, it is really misleading and should not be taken too seriously. For when the complete solution of Eqs. (1) and (2) is obtained we get (dropping all indices and sums over indices),

$$H(\mathbf{k},\omega)=\tilde{G}[k^2;(\mathbf{k}\cdot\hat{x})^2;\omega]J(\mathbf{k},\omega), \tag{9}$$

where $\hat{x}$ is a unit vector in the direction of the field H_0, and G is a rational function of its arguments. The Fourier transform then gives

$$H(\mathbf{r},\omega)=\int d^3r^1G(\mathbf{r}-\mathbf{r}^1;\omega)J(\mathbf{r}^1,\omega), \tag{10}$$

where $(\boldsymbol{\varrho}=\mathbf{r}-\mathbf{r}^1)$

$$\begin{aligned} G(\boldsymbol{\varrho};\omega)&=\int d^3k\exp(-i\mathbf{k}\cdot\boldsymbol{\varrho})\tilde{G}\\ &=\int d^3k\frac{\sin k\rho}{k\rho}\tilde{G}[k^2;(\boldsymbol{\varrho}\cdot\hat{x})^2;\omega]+\Delta G. \end{aligned} \tag{11}$$

The integral in the last form of Eq. (11) is obtained by one integration by parts with respect to the polar angle of **k** measured from $\boldsymbol{\varrho}$; the integrand, then, does not depend on the angles of **k** any longer, so the integral can now be performed by contour integration. ΔG is proportional to $(1/\rho)^2$ and is given in the appendix of reference (1). We assume that the neglect of ΔG does not change the qualitative results of this note. Now, several interesting new points are found.

Firstly, the usual electromagnetic "radiative pole" $k^2=n^2\omega^2$, which might be expected from inspection or iteration of Eqs. (1) and (2) to be present in the complete answer, is found, instead, to be a pole in the integrand of the Green's function only at a direction of observation perpendicular to the applied field H_0. Moreover, at that angle of observation (90°) and in that mode $(k^2=n^2\omega^2)$ it is found that for point charges or magnetic moments, the radiation field vanishes due to the vanishing numerator of the integrand of the Green's function. Thus, the expected mode $k^2=n^2\omega^2$, which is the only mode in the Čerenkov effect in nonmagnetic insulators (i.e., in the above when $\omega_s=0$), does not appear at all in the case of magnetic materials $(\omega_s\neq 0)$.

Secondly, at the other angle of especial interest, viz. 0° (along H_0),[7] there do exist modes which are almost "radiative," for example (to lowest order in $\mathfrak{D}$)

$$k^2\simeq n^2\omega^2[(\omega_0+\omega_s\pm\omega)/(\omega_0\pm\omega)], \tag{12}$$

and for which the Green's function resonates at a particular frequency. However, this frequency is in the region around ω_0 only for the H_- combination of components of field intensity [corresponding to the minus sign in Eq. (8)], and only when $\omega_s<0$ (i.e., M_0 in negative x direction, H_0 in positive x direction). For that case, the resonant frequency is given by ω, where

$$(\omega_0-\omega)^2\simeq 4n^2\omega_0^2\mathfrak{D}|\omega_s|. \tag{13}$$

Actually, what we call here resonant frequencies really correspond, in Soohoo's language, to double zeros of the fourth-order secular determinant for k^2. Or, speaking in the terms of reference 1, they are double poles of the integrand of the Green's function at particular frequencies ω for a given angle.

Thirdly, the characteristic modes, and hence the frequencies at which the system "rings" depend on the polar angle of the direction of observation as measured from the direction of H_0. Thus, unless the point charge or point dipole moment is moving in the x direction, so that the Čerenkov cone coincides with a cone of constant polar angle of observation, the "ringing" frequency is expected to be different at different azimuthal angles about the direction of motion of the particle. In this case, the expected change in the peaked frequency distribution of the Čerenkov radiation, as a function of azimuthal angle about the direction of motion, will depend on the properties of the magnetic material. Finally, while the dependence of the opening angle of the Čerenkov cone on the particle velocity is the same as usual, it is also expected that the resonant radiation will be polarized, that is [see discussion after Eq. (12)] that the resonant condition will be met in one of the circular polarization H_+ or H_-, but not in both.

In all of the above discussion, we have assumed a perfect insulating magnetic material, [i.e., see Eq. (5)], $\alpha=\sigma=0$, so that the resonant frequencies were real, and that the corresponding poles in the integrand of the Green's function were also real (no decaying exponentials). In the actual case of finite relaxation times $(\alpha\neq 0)$, the resonant frequencies are complex, and so, although the system comes near resonance, the appropriate denominators never actually vanish for real frequencies. However, even for the materials now available, the enhancement can be by many orders of magnitude.

This enhancement is independent of the nature of the source, and is expected to occur for charges as well as magnetic moments. Thus, if the effect discussed here is shown to actually exist, the question of background from charged particles in a neutral particle detector will have to be explored further, as well as the possibilities of using charged particles themselves as probes in the study of the properties of magnetic materials.

We would like to thank Professor J. Weber and Professor R. D. Myers for several useful discussions.

---

* Supported in part by a National Science Foundation grant, and in part by the U. S. Air Force Office of Scientific Research of the Air Research and Development Command.

[1] A fuller account of this work will be published in *The Physical Review*.

[2] See W. K. H. Panofsky and M. Phillips, *Classical Electricity and Magnetism* (Addison-Wesley Publishing Company, Reading, Massachusetts, 1955), Chap. 19, particularly problem 8 on p. 313.

[3] Playing further with this toy shows the marked dependence of the amplitude of the waves on the velocity and orientation of the little magnet.

[4] A very extensive literature on spin waves exists and we refer here only to the recent review of J. Van Kranenkonk and J. H. Van Vleck, Revs. Modern Phys. **30**, 1 (1958).

[5] See reference 2.

[6] See, for example, C. Kittel, Phys. Rev. **110**, 1295 (1958); H. Suhl, Proc. I.R.E. **44**, 1270 (1956).

[7] See R. F. Soohoo, Phys. Rev. (to be published); Massachusetts Institute of Technology, Lincoln Laboratory Report 53G-0041. We would like to thank Dr. Soohoo for sending us the preprint of his work, which we received after this calculation was essentially completed. He considers the special case of Eqs. (1) and (2) when the current J is zero, but the characteristic modes for that case are, to the approximation considered here, the poles of the integrand of our Green's function. (See reference 1.)

Photovoltaic Effects in Cs_3Sb Films*

FREDERICK WOOTEN
Lawrence Radiation Laboratory, University of California,
Livermore, California

(Received March 20, 1961)

THIS letter reports some photovoltaic effects observed in Cs_3Sb films, their implications with regard to band bending, and the influence of band bending on photoemission.

Thin films of Cs_3Sb were prepared by standard techniques[1] on the flat end windows of Corning 7740 glass envelopes. These films were rectangular (2×16 mm) and 200–500 A thick. The thicknesses of the antimony layers first deposited were estimated from transmission measurements. An expansion factor of 6.3, calculated from the crystal structure of Cs_3Sb,[2] was used to obtain Cs_3Sb film thickness. Previously deposited aluminum strips provided electrical contacts at the ends of the Cs_3Sb films. The measured dark resistance was typically about 10^8 ohms. A rough measurement of thermoelectric power indicated p-type conductivity with Seebeck coefficient of 0.6 mv/°K at 320°K, which is in agreement with all previous determinations of conductivity type.[3] Average luminous sensitivity was 40 μa/lu, on the basis of a

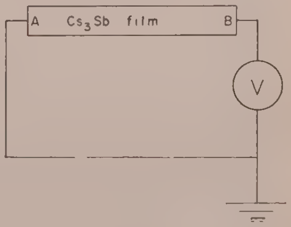

FIG. 1. Schematic of arrangement for measuring photovoltage.

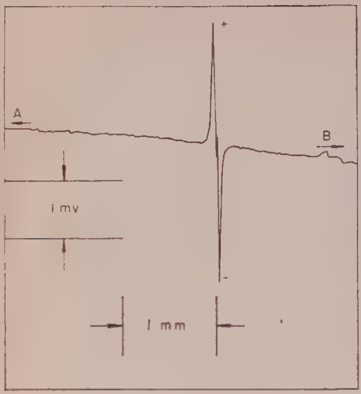

FIG. 2. Photovoltaic effect observed at imperfection in glass substrate of Cs_3Sb film. The reversal of polarity in this case was such as to indicate a trap for holes.

tungsten filament light source operated at a color temperature of 2870°K.

When the Cs_3Sb films were scanned with a small light spot ($20\ \mu$ in diameter) from one electrode to the other, photovoltaic effects were frequently observed. These effects could nearly always be correlated with the presence of either scratches ($<5\ \mu$ wide) in the glass substrate or of small specks of CeO_2 ($\approx 5\ \mu$ in diameter) used as a glass polishing agent. Figure 1 presents a schematic of the arrangement for measuring photovoltage. A typical result is shown in Fig. 2. Note that Fig. 2 is referenced to Fig. 1 by means of the markers A and B. The sign of the effect corresponded nearly always to a barrier which acts as a trap for holes. Such a barrier is illustrated in Fig. 3. Photovoltaic effects of opposite sign accounted for $\approx 10\%$ of the effects observed and were always of smaller magnitude. No correlation of the latter effects with imperfections in the glass substrate was noted.

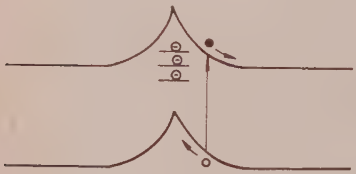

FIG. 3. Band bending in vicinity of a barrier which acts as a trap for holes.

Because the imperfections are small, band bending in the vicinity of these imperfections is a three-dimensional effect. It thus has a component parallel to the film (which results in the photovoltaic effects reported here) and also a normal component. It is this latter component which has been suggested as a cause of enhanced photoemission in *p*-type photoemitters.[4] That is, the accelerating field, provided by the presence of bands which bend down in the direction of the vacuum, should result in enhanced photoemission. Studies of photoemission in the vicinity of imperfections produced some evidence of enhanced photoemission which could be attributed to the presence of these imperfections. One example of enhancement is presented in Fig. 4, in which the direction of scanning was from right to left. In most cases, however, the results were not conclusive with regard to enhanced photoemission.

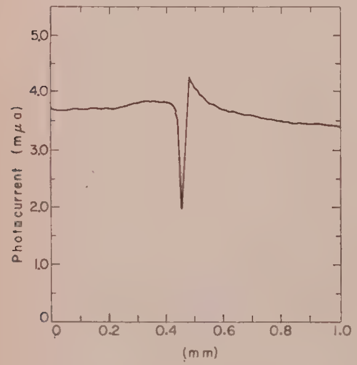

FIG. 4. Photoemission in vicinity of CeO_2 speck.

---

* Work done under the auspices of the U. S. Atomic Energy Commission.

[1] A. H. Sommer and W. E. Spicer, in *Methods of Experimental Physics*, edited by L. Marton (Academic Press, Inc., New York, 1959), Vol. 6, Part B, p. 385.

[2] K. H. Jack and M. M. Wachtel, Proc. Roy. Soc. (London) **A239**, 46 (1957).

[3] T. Sakata, J. Phys. Soc. Japan **9**, 1030, 1031 (1954).

[4] W. E. Spicer, RCA Rev. **19**, 555 (1958).

Dislocation Density and Flow Stress of Sodium Chloride

W. IN DER SCHMITTEN AND P. HAASEN
Institut fuer Metallphysik, Universitaet Göttingen, Germany

(Received April 20, 1961)

IN recent years etching techniques have been developed which make it possible to locate dislocations intersecting a crystal surface. The etch pits are particularly clear in ionic crystals.[1] These have the additional advantage of being available in a state of reasonably good perfection. Gilman and Johnston,[2] in a series of ingenious experiments, have studied the plastic deformation of LiF by this method and have thus checked and guided dislocation theory. While several aspects of the theory could be confirmed, one of its fundamental predictions about the relation between the flow stress τ after strain hardening and the dislocation density N, the Taylor law $\tau\sim(N)^{\frac{1}{2}}$, was not confirmed at all in the dislocation counts on deformed LiF. Instead, Gilman and Johnston found a linear dependence of over-all dislocation density on stress with a hardening coefficient of 4 d per dislocation. This note reports on a similar investigation on NaCl crystals which does, however, result in a Taylor-type relation.

Large NaCl crystals from Leitz, Wetzlar,[3] were cleaved into rectangular compression specimens measuring about $4\times4\times25$ mm³. The specimens were annealed for 22 hr at 760°C and furnace cooled. The surfaces were carefully polished on wet silk to the exact dimensions of $3\times3\times20$ mm³ and rinsed in alcohol and ether. The specimens were then deformed in compression using an Instron machine. To improve axiality during compression[4] a hemispherical steel ball was put with its flat side on the upper end of the crystal. After plastic deformation to a preset flow stress at a certain strain rate, the specimen was polished down to the transverse cross section in half its height by the method described above. It was then immersed in a 1:2 methanol-ethanol mixture for 5 min and afterwards into a 1% HgCl in ethanol solution to develop etch pits.[5] According to deformation geometry the etch pits on the transverse cross section belong to screw dislocations on the four $\{110\}\langle110\rangle$ slip systems operating in $\langle100\rangle$ compression. (Edge dislocation counts on planes parallel to the compression direction would include an unknown proportion of double trails or dislocation *dipoles* dragged behind by screw dislocations[2] which would contribute little to the mean internal stress.) A representative area of the transverse cross section was photographed and etch pits were counted on photos magnified 360×. The pits were not arranged in slip bands but showed a more or less statistical distribution, perhaps due to frequent cros slip. All the deformation was carried out at room temperature bsecause of difficulties in avoiding thermal stresses that would introduce extra dislocations. Two strain rates, 4.2×10^{-5} and 8.4×10^{-4} sec^{-1}, were used.

The initial dislocation density was around $2\text{–}5\cdot10^4$ cm^{-2}. The stress-strain curves showed a smooth transition from the elastic to a linear plastic stage (with rarely any yield instability). The interpolated critical shear stress measured $\sim$41 g/mm², the work-hardening coefficient about 1 kg/mm^2 at the lower strain rate. Figure 1 shows how the over-all screw dislocation density N increased with shear stress in $\{110\}\langle 110\rangle$ at a strain rate of 4.2×10^{-5} sec^{-1}. The crossed bars indicate the maximum deviations in the measured values of N and τ from the average of five equally treated specimens. At higher values of N than about $2\cdot 10^6$ cm^{-2} the etch pits could no longer clearly be resolved. Figure 2(a) shows that the measurements are best to be represented within the experimental error by the relation

$$\tau=A(N)^{\frac{1}{2}},\quad A=7.2\cdot 10^{-3}\text{ kg/cm}. \tag{1}$$

For each of the four operating slip systems the same law should hold with a coefficient $2A$ instead of A. It is interesting to see that Eq. (1) extrapolates right to the origin so that no additional friction mechanism seems to work at this strain rate besides dislocation interaction (for $\dot{\epsilon}=8.4\cdot 10^{-4}$ sec^{-1}, curve (b), the corresponding curve did, however, extrapolate to a finite friction stress of 22 g/mm^2). If one interprets τ in terms of *Taylor's theory* as mean elastic stress of a statistical array of parallel screw dislocations, Eq. (1) is obtained with

$$2A_T=[(C_{11}-C_{12})/4\pi](a/\sqrt{2})\cdot\alpha.$$

The C_{ik} are the elastic constants,[6] and a is the lattice parameter of NaCl at room temperature. Comparison with experiment yields $\alpha=13$. The factor α could arise from the additional influence of edge dislocations not considered in Eq. (1) and/or from the action of groups of (less than) α dislocations. The screw dislocation etch pits rarely showed piled-up arrays. Each pit, measuring several microns in diameter, might correspond to more than one dislocation though. A *forest hardening* mechanism would also result in a relation of the type of Eq. (1) with another meaning of A. It differs from the Taylor mechanism especially in that it should depend stronger on temperature and strain rate. Experimentally, Eq. (1) was found to hold also at the higher strain rate ($8.4\cdot 10^{-4}$ sec^{-1}) with almost the same value of A ($7.1\cdot 10^{-3}$ kg/cm) [Fig. 2(b)]. It is therefore unlikely that forest hardening accounts for a major part of our observations. Also, the critical shear stress of NaCl at 300°K is about the same as that at 1000°K[7] where the forest ought to be transparent already.

That there is a small thermally activated contribution to plastic flow of NaCl at room temperature can be seen in another type of experiment. If the strain rate is suddenly changed from $\dot{\epsilon}_1$ to $\dot{\epsilon}_2$ thermal activation should give a reversible change in flow stress of $\Delta\tau=-[kT/(dU/d\tau_r)]\cdot\ln(\dot{\epsilon}_2/\dot{\epsilon}_1)$ if $U(\tau_r)$ is the activation energy of the process and $\tau_r=\tau-A_T\cdot(N)^{\frac{1}{2}}$. In a linear approximation $-dU/d\tau_r$ equals W, the activation volume. Experimentally we found that, contrary to the observation on metals, the flow stress did not change quite *reversibly* with NaCl. The stress increment for an increase of strain rate was always somewhat larger than the decrease in flow stress on the reverse change. Generally the strain rate can alter by changes in the number of dislocations contributing to flow and in their average velocity V:

$$\Delta\dot{\epsilon}/\dot{\epsilon}=\Delta N/N+\Delta V/V.$$

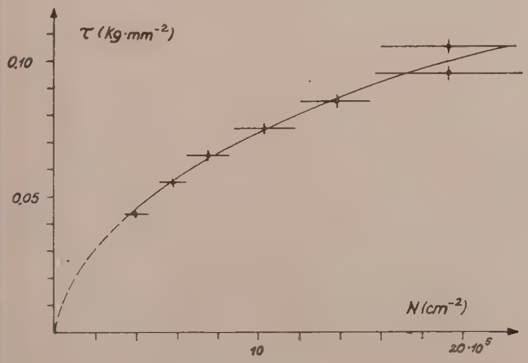

FIG. 1. Flow stress of NaCl vs etch pit density for $\epsilon=4.2\times 10^{-5}$ sec^{-1}.

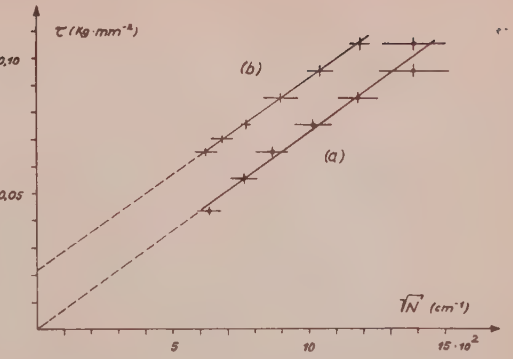

FIG. 2. Illustrating Taylor's law between shear stress and square root of dislocation density. (a) $\dot{\epsilon}=4.2\times 10^{-5}$ sec^{-1}; (b) $\dot{\epsilon}=8.4\times 10^{-4}$ sec^{-1}.

We assume the (smaller) *decrease* in flow stress $\Delta\tau$ on lowering the strain rate to be due to a change in dislocation velocity only and this to be controlled by the thermally activated process. From the measured $\Delta\tau\approx 10^{-2}$ kg/mm^2 for an order of magnitude decrease in strain rate we get $W=b^2l=10^{-19}$ cm^3 which corresponds to an obstacle spacing l of about 10^{-4} cm.

In conclusion, the flow stress of NaCl seems to depend on the screw dislocation content as expected by theoretical arguments about long range elastic dislocation interaction. This result is similar to conclusions drawn by Seeger and others from experiments on fcc metals and quite unlike the observations on LiF.[2] The reasons for this difference can only be speculated about at present.

We wish to thank Professor J. Gilman for advice during his visit to Göttingen and candidate physicists, Joachim Hesse, Miss H. Siebert, Mrs. B. Rannenberg, and Miss M. Reitz, for assistance in the polishing and counting procedures. The Deutsche Forschungsgemeinschaft has supported this work.

[1] S. Amelinckx, Acta Met. **2**, 848 (1954).

[2] W. G. Johnston and J. J. Gilman, J. Appl. Phys. **30**, 129 (1959), and numerous other papers by the same authors.

[3] We thank Dr. Nitschmann for the selection of specimens.

[4] W. in der Schmitten, Trans. AIME (to be published).

[5] P. R. Moran, J. Appl. Phys. **29**, 1768 (1958).

[6] H. B. Huntington, Progr. Solid State Phys. **7**, 213 (1958).

[7] J. D. Eshelby, C. W. A. Newey, P. L. Pratt, and A. B. Lidiard, Phil. Mag. **3**, 75 (1958).

[8] A. Seeger, *Handbuch der Physik*, edited by S. Flügge [Springer-Verlag, Berlin, Germany, 1955), Vol. VII/2, p. 1.

Quasi-Brillouin Electron Streams

M. H. MILLER
Electron Physics Laboratory, Department of Electrical Engineering, University of Michigan, Ann Arbor, Michigan

(Received April 12, 1961)

THE analysis of rectilinear M-type electron tubes is usually based on a laminar Brillouin flow electron stream model. Because of the peculiarities associated with launching a crossed-field stream, the assumption of laminar flow is somewhat optimistic. One measure of this optimism is the discrepancy between experimental and theoretical stream current densities; in practice, current densities as low as ten percent of the theoretical value are found.

In the stream model derived below the assumption of laminar flow is discarded. The discrepancy noted above is easily explained in terms of nonlaminarity, and other significant results are noted.

The hydrodynamic description of a dc particle flow is given in terms of the following three conservation equations[1]:

$$\nabla\cdot\rho\bar{v}=0, \tag{1}$$

$$-\eta[\bar{E}+\bar{v}\times\bar{B}]=(\bar{v}\cdot\nabla)\bar{v}+\frac{1}{\rho}\nabla\cdot\rho\tilde{P}, \tag{2}$$

$$2\eta\Phi=\bar{v}\cdot\bar{v}+\langle\bar{u}\cdot\bar{u}\rangle. \tag{3}$$

The average electric field, magnetic field, velocity, and space-charge density associated with the electron velocity distribution in a given volume element are represented by $\bar{E}$, $\bar{B}$, $\bar{v}$, and ρ, respectively. The magnitude of the electron charge-to-mass ratio is η, and Φ is the electrostatic potential corresponding to $\bar{E}$. The excess-over-average velocity $\bar{u}$ is the difference between the velocity of a particular electron and the local average velocity $\bar{v}$. The enclosures $\langle\ \rangle$ denote the average over the velocity distribution of the enclosed quantity. The symmetrical tensor $\tilde{P}$ is defined by its elements $\langle u_\alpha u_\beta\rangle$, where α and β form all combinations in pairs of the rectangular coordinates x, y, z.

As written, Eq. (3) is predicated on the assumption that the electron velocity distribution is a distribution in direction only, i.e., all electrons in a given volume element have the same magnitude of velocity. This assumption is justified provided it is acceptable to consider the electrons to leave a unipotential cathode with negligible initial velocities. In the case of an M-type flow this assumption is equivalent to assuming that the predominant cause of turbulence in the dc flow stems from the asymmetry in the gun structure.

Equations (1) through (3) are no full substitute for the Boltzmann transport equation from which they are derived. It is necessary to supplement these equations by one means or another with further information about the electron velocity distribution. The most common additional specification made is that of laminar flow; in this case $\bar{u}$ is identically zero by definition, and the equations reduce to their familiar laminar form. [Equation (3) becomes the result of taking the gradient of Eq. (2).]

For the nonlaminar flow model being derived, additional information about the velocity distribution function is provided indirectly by specifying some of the average properties of the flow. The specifications are made by analogy to laminar Brillouin flow. In essence, what is done is to assume a model, and then to determine the conditions under which the model is consistent with physical laws.

In particular, the stream is assumed to be confined by appropriately oriented electric and magnetic fields so as to flow between planar boundaries $y=a$, b, with $a\leq b$. The average stream velocity is assumed to be

$$\bar{v}=\Omega y\bar{x}, \tag{4}$$

where Ω is an as yet undetermined constant, and $\bar{x}$ is a x-directed unit vector. The space-charge density is assumed to be constant.

It will be noted that the model is very much like laminar Brillouin flow, except that no constraints have been placed on the magnitudes of $\bar{v}$ and ρ as yet.

Under the specified conditions, the solution of Eqs. (1) through (3) is straightforward. It is found (with the help of Poisson's equation) that,

$$\langle u_x^2\rangle=\langle u_y^2\rangle=(\omega_p^2-\omega_c^2)(y-a)(y-b)/2, \tag{5}$$

$$\langle u_xu_y\rangle=\langle u_yu_x\rangle=0, \tag{6}$$

$$2\eta\Phi=\omega_c^2y^2+(\omega_p^2-\omega_c^2)(y-a)(y-b), \tag{7}$$

$$\Omega=\omega_c, \tag{8}$$

$$\omega_p^2\leq\omega_c^2. \tag{9}$$

The plasma frequency ω_p and the cyclotron frequency ω_c are defined as usual.

These results are based on the boundary condition that $\bar{u}$, and hence all its averages, is identically zero on the stream boundaries. This requirement follows from the condition that all electrons in a given volume element have the same magnitude of velocity, and because there is no normal (y-directed) velocity component of any electron on the stream boundaries. Since all electrons have the same magnitude and direction of velocity on the stream boundaries, the excess-over-average velocity of any electron is zero.

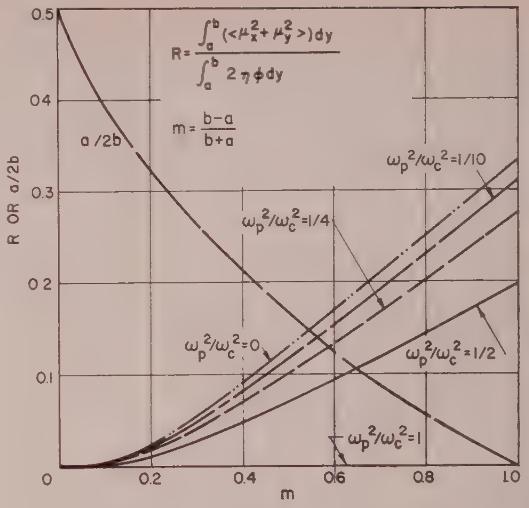

FIG. 1. Comparison between quasi-Brillouin and laminar Brillouin flows.

It might be noted that this model can be derived by requiring the pressure tensor $\tilde{P}$ to be diagonal, with equal diagonal elements, i.e., "hydrostatic."

It is interesting to note that there is no choice as to the value of the velocity slip Ω; it must be equal to ω_c. At the same time, the plasma frequency can be less than the cyclotron frequency. This situation is quite different from the laminar Brillouin model where $\omega_p^2=\omega_c^2$, or from the partially neutralized model where the effective plasma frequency can be less than the cyclotron frequency, but the velocity slip is ω_p^2/ω_c.

The requirement of Eq. (9) follows, in the present model, from considering Eq. (5) in the light of the fact that $\langle u_x^2\rangle$ and $\langle u_y^2\rangle$ are inherently positive quantities. When the equality applies, the nonlaminar model reduces to laminar Brillouin flow. For this reason the nonlaminar model is referred to as "quasi-Brillouin" flow.

As an index of comparison between a quasi-Brillouin stream and a laminar flow of the same geometry, use can be made of the fraction, denoted by R, of the total stream energy involved in the excess-over-average motion;

$$\frac{1}{R}=\frac{\int_a^b 2\eta\Phi dy}{\int_a^b(\langle u_x^2\rangle+\langle u_y^2\rangle)dy}=1+\frac{2}{1-(\omega_p^2/\omega_c^2)}\,\frac{m^2+3}{4m^2}, \tag{10}$$

where m is a convenient geometric parameter,

$$m=(b-a)/(b+a). \tag{11}$$

Figure 1 is a graph of R as a function of m, for various values of ω_p^2/ω_c^2. Also drawn for convenience is a conversion curve relating m and a/b.

For a nominal value of $m=1/3(b=2a)$, a value of R equal to only 0.04 corresponds to a space-charge density (and current density) which is 0.4 that of a laminar flow of the same geometry. Increasing R to 0.06 reduces the space-charge density to 0.1 of the laminar Brillouin value.

It is, of course, questionable whether the quasi-Brillouin flow model is any more realistic than the laminar flow model. However, the nonlaminar flow model has the advantage of recognizing the existence of nonlaminar motion. It thus stands some chance to profit from the philosophy that the general characteristics of an electron stream are not critically dependent on the exact details of the flow. One particular case where this might bear fruit is the analysis of the rf properties of a crossed-field flow.

[1] S. Chapman and T. G. Cowling, *Mathematical Theory of Nonuniform Gases* (Cambridge University Press, New York, 1952).

Liquidlike Layers on Ice

H. H. G. Jellinek
Department of Chemistry, Essex College, Assumption University of Windsor, Windsor, Ontario, Canada

(Received December 7, 1960)

RECENTLY Kingery[1] described experiments on the growing together of ice spheres. The experiments seem to indicate that the growth process is due to surface diffusion. However, a very high value was found for the effective surface diffusion coefficient, "several orders of magnitude larger than is to be expected." Also the energy of activation for this diffusion process was found to be rather large.

Faraday[2] explained his experiments "on regelation" by the assumption of a liquidlike layer on ice below its melting point. This view was opposed by Thomson[3] and Thomson[4] who maintained that regelation is due to pressure melting. However, more recently, the liquidlike layer theory was revived by Weyl[5] on theoretical grounds and by Nakaya and Matsumoto[6] and Jensen,[7] who showed that ice spheres, once having touched one another, behaved on separation as if a liquidlike layer were present on the ice surfaces. Jensen was able to show that, in water vapor saturated atmospheres, indication of a liquidlike layer persisted down to −25°C, whereas in a dry atmosphere the liquidlike layer seemed to be absent at temperatures lower than −3°C.

Kingery attempts to explain the growth of a neck between two ice spheres by assuming high surface mobility of molecules and tends to the view that a liquidlike layer is not necessary to account for his results. The following quotation from his paper is noteworthy: "Nakaya and Weyl have interpreted observations of the adhesion between ice particles and regelation phenomena in terms of a mobile "liquid like" surface structure. If this is considered as a layer of several atomic dimensions having appreciable atomic mobility, the experimental results would be as expected here; this would provide a mechanism for rapid surface diffusion. At the same time, there is nothing in the present experimental results that is not adequately explained on the basis of a surface layer one or a few molecules in any case." He then goes on to discard the liquidlike layer concept on the grounds that "it is difficult to accept the fact that we have a liquid layer at a temperature some 25° below the melting point."

It should be pointed out, however, that his view and the liquidlike layer theory are very close and differ only by degree, i.e., thickness of the mobile layer. Further, the experiments by Jensen with spheres in a saturated atmosphere show that a liquidlike layer seems to exist down to −25°C. There might also well be a break in the curve of temperature dependence (Fig. 5, Kingery[1]) at a temperature in the neighborhood of −9°C. The present writer has made an extensive investigation of the adhesive properties of ice.[8] Tensile and shear experiments with ice sandwiched between disks of stainless steel, various polymers, and quartz optical flats were carried out. The shear experiments with highly polished metal and optically flat quartz surfaces showed distinct characteristics of sliding similar to those which one should except from a liquidlike layer between ice and the respective surface, whereas the tensile experiments led only to cohesive breaks in the ice. These results seem only to be comprehensible on the basis of the assumption of a liquidlike layer not only for the ice/air interface but also for the ice/metal, ice/polymer, and ice/quartz interfaces. The tensile experiments lead to cohesive breaks because of the action of surface tension forces inherent in the liquidlike layer sandwiched between the ice and the respective metal, polymer, or quartz surfaces. The ice "adheres" to the respective surfaces due to the pressure difference across the curved liquidlike layer/air interface, governed by the equation $\Delta p=\gamma(1/r_1+1/r_2)$, where Δp is the pressure difference, γ the interfacial tension (liquidlike layer/air), and r_1 and r_2 the principal radii; for a liquidlike layer of thickness 2×10^{-6} cm or 70 water molecules and $\gamma=76.4$ d/cm (r_2 being large), one obtains for $\Delta p=70$ kg/cm^2, appreciably above the tensile strength of bulk ice (12 to 15 kg/cm^2), although it should be noted that the tensile strength of ice increases with decreasing volume.[9] In contrast, shear experiments show that only very small stresses are needed to produce sliding eventually leading to an adhesive break. Reasonable estimates of the viscosity and thickness of the liquidlike layer could be made from the experiments, assuming the liquid to be Newtonian as a first approximation. It must be realized that such layers will probably show a continuous transition from the crystalline solid to a fairly viscous liquid and will also be dependent on the nature of the interface (metal, polymer, quartz). Estimates of the thickness and viscosity of the layers deduced from experiments at −4.5°C ranged from about 10^{-5} to 10^{-6} cm and viscosities from 70 to 700 poises for ice/stainless steel and 15 to 150 poises for ice/quartz. Shear experiments with thin water films (0.2 to 1 μ) between optically flat glass plates[10] showed very similar characteristics to those obtained from the experiments with ice. Thus it appears that Kingery's results, considered in conjunction with the experiments on adhesion of ice, rather support the liquidlike layer theory.

It may also be remarked that work by Hori[11] on the properties of thin water films sandwiched between glass and quartz plates revealed abnormal vapor pressures and freezing points at low temperatures even after taking into consideration interfacial free energies and curvatures of surfaces. Thus, for instance, films 1.3×10^{-4} cm thick placed between glass plates did not freeze even at −96°C.

The investigations on ice adhesion,[8] tensile strength of ice,[9] and frictional properties of thin water films[10] were carried out at the U. S. Army Snow Ice and Permafrost Research Establishment, Corps of Engineers, Wilmette, Illinois.

[1] W. D. Kingery, J. Appl. Phys. **31**, 833 (1960).

[2] M. Faraday, Phil. Mag., 4th Ser. **17**, 162 (1859); Proc. Roy. Soc. (London) **10**, **440** (1860); see also J. Tyndall, *ibid.* **9**, 141 (1858).

[3] J. Thomson, Proc. Roy. Soc. (London), **A10**, 152 (1859); **11**, 198, 473, (1861).

[4] W. Thomson, Proc. Roy. Soc. (London) **A9**, 761 (1858).

[5] W. A. Weyl, J. Colloid Sci. **6**, 389 (1951).

[6] U. Nakaya and A. Matsumoto, J. Colloid Sci. **9**, 41 (1954), also U. S. Army Snow Ice and Permafrost Research Establishment, Corps of Engineers, Research Paper 4 (1953).

[7] D. C. Jensen, M. S. thesis, Pennsylvania State University (1956).

[8] H. H. G. Jellinek, Adhesive Properties of Ice, U. S. Army Snow Ice and Permafrost Research Establishment, Corps of Engineers, Research Report 38 (1957), and Research Report 62 (1960). See also J. Colloid Sci. **14**, 268 (1959).

[9] H. H. G. Jellinek, Proc. Phys. Soc. (London) **71**, 797 (1958), also U. S. Army Snow Ice and Permafrost Research Establishment, Corps of Engineers, Research Report 23 (1957).

[10] H. H. G. Jellinek, U. S. Army Snow Ice and Permafrost Research Establishment, Corps of Engineers, Special Report 37 (1960).

[11] T. Hori, U. S. Army Snow Ice and Permafrost Research Establishment, Corps of Engineers, Translation 62, also Teion Kagaku Butsuri Hen **A15**, 34 (1956).

Available Power from a Nonideal Thermal Source*

Paul Penfield, Jr.
Department of Electrical Engineering and Research Laboratory of Electronics, Massachusetts Institute of Technology, Cambridge 39, Massachusetts

(Received April 28, 1961)

MANY analyses of heat engines, including thermoelectric generators, are based on the availability of heat reservoirs with which heat may be exhanged reversibly. An exception is the analysis of Gray,[1] who discusses thermoelectric generators and their efficiency optimization, when they are connected to a nonideal heat source consisting of two heat reservoirs, with finite thermal resistances separating the reservoirs from the thermocouple. Gray's device is a special case of the device pictured in

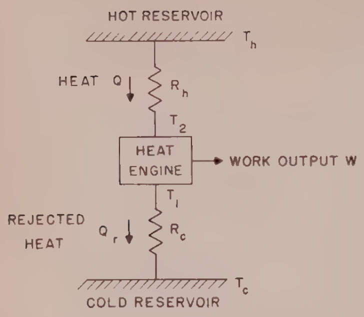

FIG. 1. Heat engine run from a nonideal thermal source.

Fig. 1, in which the heat engine shown is assumed to be a thermoelectric generator.

An electrical analogy of the nonideal heat reservoir is a voltage source e with a finite series resistance r. The fact that this source has a maximum amount of power that can be drawn from it (the "available power" $e^2/4r$), suggests that the nonideal thermal source may have a similar maximum. We have calculated this "available power," which cannot be achieved with practical thermoelectric generators, because of associated irreversible effects (joule heating and heat conduction).

Observe from Fig. 1 that the heat engine is limited by the Carnot efficiency, so the useful work output W is given by

$$W \leq [(T_2 - T_1)/T_2]Q, \tag{1}$$

where the equality sign holds only for reversible (Carnot) engines. When Q is small, the work output is small. On the other hand, suppose Q is large. Then there is an appreciable temperature drop across the thermal resistances and $(T_2 - T_1)$ is small, so that, again, the useful work output is small. A maximum value of W is obtained for reversible heat engines, and for an intermediate value of Q.

To find this maximum value for W, we use the equations that relate T_2 and T_1, which are the temperatures of the heat engine, to T_h and T_c, the reservoir temperatures:

$$\begin{aligned} T_1 &= T_c + Q_r R_c \\ &= T_c + QR_c - WR_c \end{aligned} \tag{2}$$

$$T_2 = T_h - QR_h. \tag{3}$$

Substituting Eqs. (2) and (3) in the efficiency expression of Eq. (1), we solve for W. We find that R_h and R_c appear only together as a sum; if this total thermal resistance is

$$R = R_h + R_c, \tag{4}$$

then

$$W \leq [(T_h - T_c - QR)/(T_h - QR)]Q. \tag{5}$$

Observe that in Eq. (5), the equality sign holds if the heat engine is reversible; otherwise the inequality sign holds. The right-hand side has a maximum that occurs when Q is

$$Q_{\mathrm{opt}} = [T_h - (T_h T_c)^{\frac{1}{2}}]/R. \tag{6}$$

The useful work output, the heat input, and the heat rejected under optimum conditions, with a Carnot engine, are:

$$W_{\mathrm{opt}} = \frac{T_h - T_c}{R} \frac{(T_h)^{\frac{1}{2}} - (T_c)^{\frac{1}{2}}}{(T_h)^{\frac{1}{2}} + (T_c)^{\frac{1}{2}}} \tag{7}$$

$$Q_{\mathrm{opt}} = \frac{T_h - T_c}{R} \frac{(T_h)^{\frac{1}{2}}}{(T_h)^{\frac{1}{2}} + (T_c)^{\frac{1}{2}}} \tag{8}$$

and

$$(Q_r)_{\mathrm{opt}} = Q_{\mathrm{opt}} - W_{\mathrm{opt}} = \frac{T_h - T_c}{R} \frac{(T_c)^{\frac{1}{2}}}{(T_h)^{\frac{1}{2}} + (T_c)^{\frac{1}{2}}}. \tag{9}$$

Furthermore, under these optimized conditions, the efficiency is

$$\eta_{\mathrm{opt}} = \frac{W_{\mathrm{opt}}}{Q_{\mathrm{opt}}} = \frac{(T_h)^{\frac{1}{2}} - (T_c)^{\frac{1}{2}}}{(T_h)^{\frac{1}{2}}}. \tag{10}$$

Equations (1) and (10) show that under optimized conditions,

$$(T_2/T_1)_{\mathrm{opt}}{}^2 = T_h/T_c. \tag{11}$$

Note that the first factor in the expressions for W_{opt}, Q_{opt}, and $(Q_r)_{\mathrm{opt}}$ is the heat that would flow between the reservoirs if the heat engine were replaced by an infinitely conducting path; that is, it is the "short-circuit heat flow."

These expressions are interesting in that only the total resistance between the reservoirs appears; thus, as far as these fundamental limits are concerned, it does not matter whether all of the resistance is at one reservoir, or is split between them. Also, note that the efficiency under optimum power-output conditions is independent of R. Since all physical sources may be expected to have some finite thermal resistance, it appears that if a Carnot engine is operated between practical heat reservoirs in such a way as to have a maximum power output, then the efficiency must be reduced, in accordance with Eq. (10), from the Carnot efficiency calculated from the reservoir temperatures, regardless of the size of the thermal resistances.

I wish to thank Professor P. E. Gray, who made valuable comments on this work.

---

* This work was supported in part by a Ford Foundation Fellowship; and in part by the U. S. Army Signal Corps, the Air Force Office of Scientific Research, and the Office of Naval Research.

[1] P. E. Gray, Trans. Am. Inst. Elec. Engrs. Part I, **79**, No. 47, 15 (1960)

Equation of Motion of the Torsion Pendulum and the Complex Modulus

N. W. TSCHOEGL
Bread Research Institute of Australia, North Ryde,
New South Wales, Australia

(Received March 9, 1961)

IN a paper published several years ago, Nielsen[1] made an erroneous attempt to express the differential equation describing the motion of the simple torsion pendulum, operating in free oscillation, in terms of the complex shear modulus. This treatment has since been adopted in a number of other publications[2–4] the last mentioned having appeared quite recently in this journal. Nielsen wrote

$$I(d^2\theta/dt^2) + kG^*\theta = 0, \tag{1}$$

where I is the moment of inertia, G^* the complex modulus, k a shape constant, and θ is the angle of twist.

Substituting the equation for the angle of twist of the freely oscillating torsion pendulum,

$$\theta = \theta_0 \exp(j\omega - \alpha)t, \tag{2}$$

where ω is the radian frequency of the oscillation and α is the attenuation factor into Eq. (1), he arrived at the expression

$$G' = I(\omega^2 - \alpha^2)/k \tag{3}$$

for the real part of the complex modulus G^*. However, the correct relation is known to be

$$G' = I(\omega^2 + \alpha^2)/k. \tag{4}$$

This can be derived readily by substituting Eq. (2) into the usual form of the differential equation for the freely oscillating torsion pendulum

$$I(d^2\theta/dt^2) + k\eta'(d\theta/dt) + kG'\theta = 0, \tag{5}$$

where η' is the real part of the complex viscosity.

It is then seen that Eq. (1) incorrectly assumes that one may substitute $j\omega k\eta'$, or jkG'', for the middle term of Eq. (5) while the correct substitution is $(j\omega - \alpha)k\eta'$, or $(j - \alpha/\omega)kG''$. If, therefore, Eq. (5) is to be written in terms of the complex modulus, it must take the form

$$I(d^2\theta/dt^2) + k(G^* - \alpha\eta')\theta = 0 \tag{6a}$$

or

$$I(d^2\theta/dt^2) + k(G^* - \alpha G''/\omega)\theta = 0. \tag{6b}$$

It should be noted that, in case of forced oscillation, the equation

$$I(d^2\theta/dt^2)+kG^*\theta=\Theta \exp j\omega' t, \qquad (7)$$

where ω' is the impressed radian frequency and Θ is the torque, will lead to the correct particular integral as may be seen by substituting the steady-state solution

$$\theta=\theta' \exp j(\omega' t-\phi), \qquad (8)$$

into Eq. (7). This is so since the substitution of $j\omega' k\eta'$, or jkG'', for the term containing the first derivative, is valid for the steady-state solution. However, the complete integral containing the transient solution cannot be obtained from Eq. (7).

[1] L. E. Nielsen, Rev. Sci. Instr. **22**, 690 (1951).
[2] R. Buchdahl, in *Rheology*, edited by F. Eirich (Academic Press, Inc., New York, 1958), Vol. 2, pp. 148–150.
[3] L. E. Nielsen, R. Wall, and G. Adams, J. Colloid Sci. **13**, 441 (1958).
[4] D. G. Flom, J. Appl. Phys. **31**, 310 (1960).

Friction of Molybdenum Diselenide*

Melvin T. Lavik, T. Bruce Daniel, and A. Neal Abbott
Midwest Research Institute, Kansas City 10, Missouri
(Received May 4, 1961)

The friction of lamellar solids is markedly influenced by adsorbed vapors. For example, the slickness normally associated with graphite depends on moisture adsorbed from the air. MoS_2 and WS_2 friction, on the other hand, is least in vacuum and increases in the presence of air, water vapor, nitrogen, argon, and helium. Furthermore, in vacuum MoS_2 and WS_2 exhibit transient frictional characteristics that are not observed in the presence of an atmosphere or with graphite either in vacuum or with an atmosphere present.[1,2] As pellets of compressed MoS_2 or WS_2 powder are rubbed against a circular metal plate, a continuous track of pellet material builds up on the plate until the coefficient of friction μ reaches an equilibrium value μ_e corresponding to pellet material sliding against itself. If a pellet which has been sliding in vacuum is allowed to stand in vacuum, then, upon resumption of sliding, the initial coefficient of friction μ_i will be higher than μ_e. Continued sliding reduces μ to μ_e. $(\mu_i-\mu_e)$ increases with stop time T but reaches a plateau for T greater than about 4 hr. This behavior has been explained by the assumption that sulfur is liberated during sliding and forms an adsorbed layer on the surfaces.[1,3] The adsorbed sulfur layer is presumed to play the same role in MoS_2 and WS_2 friction that water vapor plays in graphite friction. Evaporation of the sulfur during the stop time would account for the difference between μ_i and μ_e.

Compounds similar to MoS_2 can be employed to test the adsorbed sulfur theory. $MoSe_2$ has the same crystal form as MoS_2 and in air at room temperature both have essentially the same friction coefficient. However, the vapor pressure of bulk selenium is much less than the vapor pressure of bulk sulfur. Our initial supposition was that an adsorbed selenium film would evaporate more slowly from $MoSe_2$ than would an adsorbed sulfur film evaporate from MoS_2. Extension of the adsorbed sulfur theory to $MoSe_2$ suggested that $(\mu_i-\mu_e)$ should increase more slowly with T than it does for MoS_2 friction.

We have measured the friction of $MoSe_2$ in vacuum (10^{-9} atm) using apparatus which has been described in detail elsewhere.[4] Since pump oil vapor is known to increase MoS_2 friction, we only need point out here that a large dry ice-acetone cold trap was placed between pump and chamber. Data were taken for 11 stop time values ranging from 5 min to 695 hr. In all of the experiments, the pellet load was 132 g and the sliding speed 310 cm/sec. The nominal pressure at the sliding interface, computed from the apparent area of contact, was 10^4 d/cm^2. Figure 1 shows the essential features of $MoSe_2$ friction. To avoid crowding, only 4 curves are included.

In vacuum the mean value of μ_e is 0.108 with a standard deviation of 0.004. (Cf. $\mu_e=0.065$ for MoS_2 under identical conditions.) In air or helium μ_e is about twice the vacuum value as is the case for MoS_2 friction. Contrary to our initial expectation, the dependence of $(\mu_i-\mu_e)$ on T is very nearly the same as for MoS_2, at least for $T<2$ hr. For $T>2$ hr there is a qualitative change in frictional behavior. μ does not decrease smoothly from μ_i to μ_e but pauses at an intermediate value $\mu_m\approx 0.3$. It remains at this value for a short time, then decreases to μ_e. The duration of the pause at μ_m increases almost linearly with stop time. This behavior suggests the presence of a contaminant film which is removed by sliding. Such an effect could result from leakage of pump oil past the cold trap although in the same apparatus MoS_2 does not show similar behavior even after a 192-hr stop time.

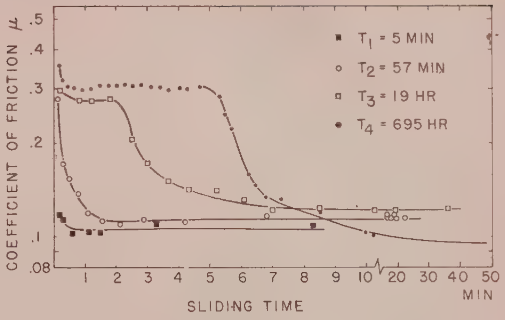

Fig. 1. Coefficient of friction of $MoSe_2$ sliding in vacuum against $MoSe_2$ after standing in vacuum for stop times T. The curve for $T=695$ hr reaches $\mu=0.09$ after 80 min sliding (point not shown).

In addition to the experiments just described, we investigated the friction of single crystals of MoS_2 (natural molybdenite). The question had arisen whether the behavior reported for MoS_2 and WS_2 could be accounted for, at least to some extent, by a property of compressed powders. The single-crystal experiments, however, gave the same results as experiments previously done with compressed MoS_2 powder at room temperature in vacuum and in atmospheres of air, nitrogen, and helium. The one discrepancy was that the single crystals would not deposit a track in vacuum, their shear strength being so small that they wore away almost immediately. On the other hand, if the initial sliding was done in air, a satisfactory track built up and subsequent sliding in vacuum caused very little wear. All of the data were taken with the crystals oriented so that the basal planes made an angle of about 10° with the plane of sliding.

Further experiments that would help interpret the frictional behavior of MoS_2-type solids include measurement of adsorption energies for sulfur on MoS_2 and selenium on $MoSe_2$ and an investigation of $MoTe_2$ friction. More to the point, however, would be observation of the rubbing surfaces for direct evidence of adsorbed films.

* This work was supported by Materials Central, Wright Air Development Division, United States Air Force.
[1] V. R. Johnson and G. W. Vaughn, J. Appl. Phys. **27**, 1173 (1956).
[2] V. R. Johnson, M. T. Lavik, and G. W. Vaughn, J. Appl. Phys. **28**, 821 (1957).
[3] M. T. Lavik, G. E. Gross, and G. W. Vaughn, Lubrication Engr. **15**, 246 (1959).
[4] V. R. Johnson, G. W. Vaughn, and M. T. Lavik, Rev. Sci. Instr. **27**, 611 (1959).

Similarity Function for Pattern Recognition

Dan McLachlan, Jr.
Stanford Research Institute, Menlo Park, California
(Received April 10, 1961)

Since many of the aspects of mechanical, optical, and electrical machines for information retrieval, translation of languages, and data processing are dependent upon sensing devices which are capable of recognizing patterns, much could be gained from having on hand a mathematical function which expresses the identity of, or the similarity between, two patterns on a plane.

This similarity function, as we call it, should recognize any given motif in a planar sea of other motifs, regardless of (a) the position on the plane, (b) the orientation, and (c) the size (or magnification). The similarity function herein described fulfills only the first two of the requirements and fails on the third.

The proposed method of pattern recognition leans heavily upon Wiener's correlation function, which when applied to crystallography is known as the Patterson[1] function. By imagining a pattern on a page to be repeated periodically in two dimensions indefinitely (as structures occur in crystals) edge effects are taken care of. Letting a pattern on a page be represented by some repeating property ρ (such as density, blackness, reflectivity, etc.) as a function of position x and y, then the autocorrelation $A(uv)$ is defined as

$$A(uv)=\frac{1}{ab}\int_0^a\int_0^b \rho(xy)\rho(x+u,\,y+v)dxdy, \tag{1}$$

where a and b are the outside dimensions of the single pattern.

In order to use the autocorrelation in pattern recognition, we must convert it to a *radial* autocorrelation function because the first principle upon which the present reasoning is based is that a radial autocorrelation $A(r)$ of any pattern $\rho(xy)$ is an invariant, independent of the position and orientation of the initial pattern $\rho(xy)$. Equation (1) can be transformed to polar coordinates r and θ through the relations $x=r\cos\theta$ and $y=r\sin\theta$ so that $A(uv)=B(r\theta)$. By a radial autocorrelation $C(r)$, we mean the "projection" of $B(r\theta)$ on r:

$$C(r)=\frac{1}{2\pi}\int_0^{2\pi} B(r\theta)d\theta. \tag{2}$$

This function $C(r)$ is a one-dimensional function and is independent of the position or orientation of the design or motif comprising the original pattern $\rho(xy)$.

Next we wish to introduce the idea of cross-correlating two radial autocorrelation functions. Suppose we have two patterns $\rho(xy)$ and $\rho'(xy)$ and that we have used the procedure outlined above to get their respective radial autocorrelations, $C(r)$ and $C'(r)$. The cross-correlation of these two one-dimensional functions is

$$D(s)=\frac{1}{R}\int_0^R C(r)C'(r+s)dr, \tag{3}$$

where R is the maximum radius of the pattern.

The second principle[2] of use to our reasoning is that the integral over the area of the squared cross-correlation between two radial autocorrelations derived from two patterns $\rho(xy)$ and $\rho'(xy)$ varies with the similarity between the original patterns $\rho(xy)$ and $\rho'(xy)$. Finally, the similarity function is

$$S_{\rho\rho'}=\frac{1}{R}\int_0^R D^2(s)ds, \tag{4}$$

the answer being a number which has its greatest magnitude when $\rho(xy)$ and $\rho'(xy)$ are identical and is smaller as they are dissimilar, regardless of positioning or orientation.

With modern computers, the above procedures should be feasible.

---

[1] A. L. Patterson, Z. Krist. **90**, 517 (1935).

[2] Dan McLachlan, Jr., Information and Control **1**, 240 (1958), discusses on page 263 a similar function which is unfortunately not independent of orientation.

Reflection of Electromagnetic Waves at Electron Density Ramps*

Leonard S. Taylor
General Electric Space Sciences Laboratory, Philadelphia, Pennsylvania

(Received April 26, 1961)

In a recent article,[1] Albini and Jahn have reported the results of a study of the transmission of a TEM wave into a planar electron density profile consisting of a ramp (or combination of ramps) terminating in a constant electron density. In many instances a point of considerable importance is whether the electromagnetic field penetrates to any effective extent beyond the initial ramp. If not, the only factors affecting the reflected wave are the gradient of the electron density in the ramp, the properties of the plasma in that ramp, and the frequency (and angle of incidence) of the incident wave. It is physically obvious that there are at least three ways in which this may occur: First, if the ramp passes through the critical density corresponding to the plasma frequency so that the wave is essentially reflected by the ramp; second, if the collision frequency in the ramp is large enough that the wave is almost completely absorbed in the ramp in the high electron density region; or, third, in the case of non-normal incidence, the wave may be refracted out of the ramp without appreciably entering the region beyond the ramp.

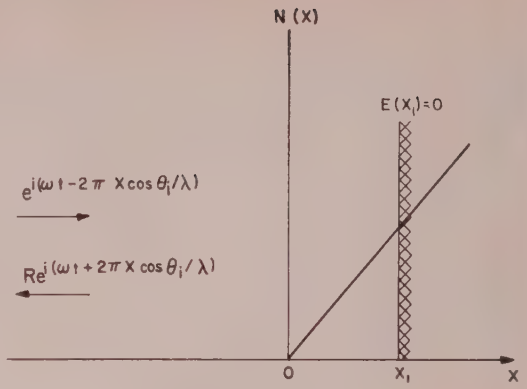
N (X)
E(X$_1$)=0
$e^{i(\omega t-2\pi X\cos\theta_i/\lambda)}$
$Re^{i(\omega t+2\pi X\cos\theta_i/\lambda)}$
0
X$_1$
X

FIG. 1. Boundary condition geometry.

It is interesting that an elementary technique is sufficient to determine the conditions which are necessary to effect the phenomena described above. This method is quite general and has also been applied successfully by the author to another type of electron density profile.[2] In the following we describe this method and the results obtained in the ramp case. We restrict ourselves to the TE wave and employ gaussian units.

We imagine that the ramp is bounded to the right by a perfect reflector (Fig. 1), so that the field is determined by the boundary condition $E(x_1)=0$. This condition determines the voltage reflection coefficient. In the present instance we find[3] in an analysis which does not differ essentially from that of Albini and Jahn that

$$R=(1+iX)^2/(1+X^2),$$

where

$$X=(3\alpha)^{-1}+[J_{1/3}'(\alpha)J_{-1/3}(\alpha_1)-J_{-1/3}'(\alpha)J_{1/3}(\alpha_1)]/[J_{1/3}(\alpha)J_{-1/3}(\alpha_1)-J_{-1/3}(\alpha)J_{1/3}(\alpha_1)].$$

In this expression

$$\alpha=(4\pi/3)(x_1/\lambda)[\omega/\omega_p(x_1)]^2(1-i\nu_c/\omega)\cos^3\theta_i,$$

$$\alpha_1=(4\pi/3)(x_1/\lambda)[\omega/\omega_p(x_1)]^2(1-i\nu_c/\omega)\left[\cos^2\theta_i-\frac{\omega_p^2(x_1)}{\omega^2(1-i\nu_c/\omega)}\right]^{\frac{3}{2}}.$$

Here $\omega_p^2(x_1)=4\pi N(x_1)/me^2$ in the usual notation, ν_c is the collision frequency, θ_i is the angle of incidence, and λ is the free space wavelength.

We now perform a Gedanken experiment: At the left of the plasma profile we place an equipment sensitive to the amplitude and phase of the reflected wave. The plasma density gradient is assumed constant to the right of $x=0$, and the perfect reflector is regarded as a movable plunger inserted from $+\infty$ until a perceptible effect is observed by the instruments when the reflector reaches $x_1=x_c$. For more distant positions of the reflecting wall, the plasma is effectively infinite in extent as far as the incident electromagnetic energy is concerned, and a reasonable explanation of the situation is that the wave does not effectively penetrate beyond x_c. Thus, the density profile beyond x_c is a matter of indifference. The ramp up to x_c determines the field. (Of course, this is not a unique method of defining a critical distance, but it appears to represent the simplest analytical procedure.)

The mathematical equivalent of the experiment described above is to investigate at which values of the parameters $R(x_1)$ is approximately equal to $R(\infty)$. [Poincelot,[4] in a related work, has given an explicit expression for $R(\infty)$, but has not considered the problem in relation to a definition of a critical distance.] Since α is dependent only on the gradient of electron density, which is assumed constant, it is only necessary to investigate the variation of R with respect to α_1. We omit the algebra, only pointing out that a great simplification is achieved by replacing the Bessel functions of argument α_1 by their asymptotic forms. Of course, no unique set of values of the parameters can be chosen because of the possibility of combining in various degrees the three cases mentioned in the first paragraph. The case of greatest interest is for $(\nu_c/\omega)^2 \ll 1$. It is then found that the conditions

$$\omega_p(x_1)/\omega \gg \cos\theta_i, \quad \omega_p(x_1)/\omega \geqslant 2\lambda/x_1$$

are sufficient to insure that the field is limited to the ramp. As expected, large angles and ramp thickness will affect the limitation without exceeding the critical density. We note that even at normal incidence, if the ramp exceeds the critical density, then only a small thickness to wavelength ratio is required. Thus, assuming $\omega_p(x_1)=10\omega$, we only need $x_1 \geqslant \lambda/5$. Since these conditions are equally good for $\nu_c/\omega=0$, we are considering reactive effects only. The behavior described is in accord with the known behavior of a constant density lossless plasma in which the propagation constant is

$$(2\pi/\lambda)[1-(\omega_p/\omega)^2]^{\frac{1}{2}}.$$

* This work was supported by the U. S. Air Force under contract.

[1] F. A. Albini and R. G. Jahn, J. Appl. Phys. **32**, 75 (1961).

[2] L. S. Taylor, IRE Trans. on Antennas and Propagation (to be published).

[3] L. S. Taylor in Proceedings of the 2nd Symposium on Engineering Aspects of Magnetohydrodynamics (Columbia University Press, to be published).

[4] P. Poincelot, Compt. rend. **244**, 2031 (1957).

Voids in Resolidified Drops of Molten Metal

J. C. Kelly
School of Physics, University of New South Wales, Kensington, Australia

(Received April 19, 1961)

IN the course of investigation of the surface tension of liquid metals[1] an unexpectedly wide spread of values was sometimes obtained. The resolidified metal drops were therefore examined and voids discovered.

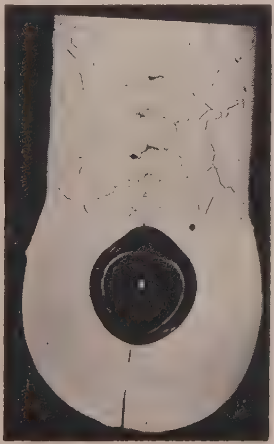

FIG. 1. Central section through a resolidified drop of nickel rod, diameter 5 mm. Minimum void diameter 2.5 mm.

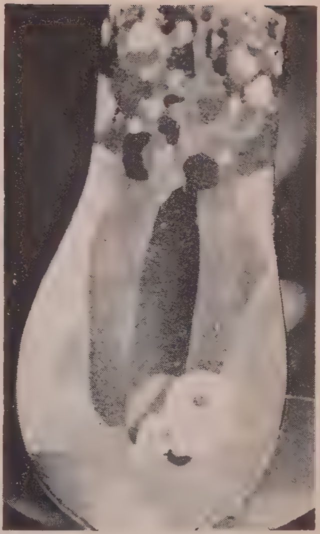

FIG. 2. Central section through a resolidified drop of niobium rod, diameter 5 mm.

The metal rods were suspended vertically in a vacuum system constructed of commercial Pyrex glass piping. End plates of stainless steel were used with Neoprene O-ring seals. The simple electron gun used to melt the end of the rod has been previously described.[2]

The system was pumped by a liquid nitrogen trapped oil diffusion pump capable of maintaining a pressure of 5×10^{-6} torr with the metal drop molten. A central section through a 5-mm diam spectroscopically pure nickel rod, and resolidified drop is shown in Fig. 1. This drop was maintained molten for 9 min and allowed to cool slowly. The size of the central void is considerable, its minimum diameter being 2.5 mm. The surface finish of this void is extremely smooth as may be seen by the reflection of the ring illuminator used to photograph the specimen.

A rapidly cooled drop on the end of a 5-mm-diam rod of spectroscopically pure niobium is shown sectioned in Fig. 2. The milky appearance of the void is due to mounting medium. A large void found in a drop on the end of a 3-mm-diam rod of spectroscopically pure tantalum, is shown in Fig. 3. A number of voids which have not coalesced are shown in Fig. 4. This is a sectioned drop on the end of a 0.6-mm tungsten wire of commercial purity.

It is clear from these observations that voids occur and can maintain themselves for an appreciable time in molten metal drops. Smaller voids of the order of 0.1 mm in diameter have been

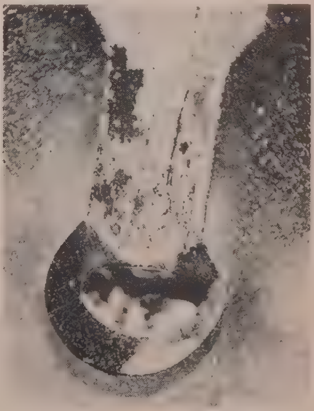

FIG. 3. Central section through a resolidified drop of tantalum rod, diameter 3 mm.

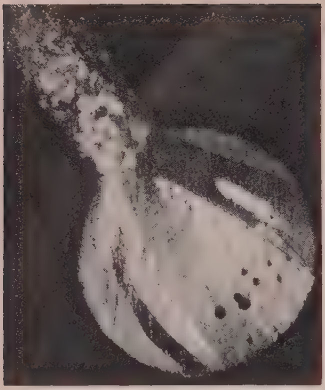

FIG. 4. Central section through a resolidified drop of tungsten wire, diameter 0.6 mm.

found in zirconium rod that has been zone refined by electron bombardment *in vacuo*.

Measurements of liquid metal surface tension based on the contour of the drop[1] or on assumed normal density[3,4] may be in error unless precautions are taken to ensure that the drop is free of voids. The use of rod which has been zone refined under vacuum would seem to be a necessary but not always sufficient condition.

In the drop-weight surface tension method, once a drop has fallen, evidence of its constitution is lost. The drop contour method allows subsequent examination of the drop on which the surface tension measurements have been made.

---

[1] J. C. Kelly, "S.E.R.L. symposium on electron bombardment floating-zone melting and allied electron bombardment techniques" (Baldock, 1959), p. 53.

[2] J. C. Kelly, J. Sci. Instr. **36**, 89 (1959).

[3] A. Calverley, Proc. Phys. Soc. (London) **B70**, 1040 (1957).

[4] A. W. Peterson, H. Kedesdy, P. H. Keck, and E. Schwarz, J. Appl. Phys. **29**, 213 (1958).

Thermal Conductivity in Two-Phase Alloys

J. B. SCHROEDER
Ohio Semiconductors, Division of Tecumseh Products Company, Columbus, Ohio

(Received January 30, 1961)

RECENTLY McHugh, Cosgrove, and Tiller[1,2] proposed a mechanism to account for spuriously high experimental values of the thermal conductivity of a heterogeneous sample. The proposed mechanism involves the creation of circulating electric currents by means of the Seebeck emf between adjacent, chemically differing grains. These currents would transport heat by the Peltier effect which would be added to the heat transferred by normal thermal conductivity. The authors were concerned with the specific case of tellurium segregation during the freezing of bismuth telluride alloys in which the thermal conductivity varied between 1.24 and 2.08×10^{-2} w/cm°C. It is the purpose of this note to evaluate the magnitude of this effect.

Russian workers[3,4] have considered this problem in some detail and found that a very considerable error might be anticipated in the thermal conductivity. The validity of their analysis is open to question for two reasons: First, grain boundary effects were ignored for rather fine-grained material, and second, in a material such as bismuth telluride one would expect lamellar rather than equiaxed grains. The analysis below is confined to a lamellar grain structure which is parallel to the heat current.

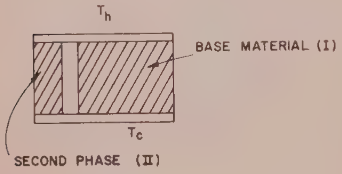

FIG. 1. Idealized two-phase thermal conductivity sample.

For purposes of simplicity let us consider a sample in which the two phases have been isolated into two subsamples with cross sectional areas $A_{\rm I}$ and $A_{\rm II}$ as shown in Fig. 1. The properties of these subsamples will be indicated by subscripts I, for the base material, and II for the second phase. The conventional choice of symbols is made. In the equations below the following definitions are used:

$$\Delta T=T_h-T_c$$
$$\Delta S=S_{\rm I}-S_{\rm II} \tag{1}$$
$$B=A_{\rm I}/A_{\rm II}.$$

The circulating current may be written as

$$I=\frac{\Delta S\Delta T}{(\rho_{\rm I}+\rho_{\rm II}B)\ell/A_{\rm I}}, \tag{2}$$

and the Peltier heat transported by this current will be

$$\dot{Q}_p=\Delta S\Delta TI=\frac{\Delta S^2\Delta T^2}{(\rho_{\rm I}+\rho_{\rm II}B)\ell/A_{\rm I}}. \tag{3}$$

The heat transported by the normal conduction process is

$$\dot{Q}_c=(A_{\rm I}/\ell)(\kappa_{\rm I}+\kappa_{\rm II}/B)\Delta T. \tag{4}$$

The importance of the circulating current to the thermal transport may be estimated from the ratio between Eqs. (3) and (4), this gives

$$R=\frac{\dot{Q}_p}{\dot{Q}_c}=\frac{\Delta S^2\Delta T}{\rho_{\rm I}\kappa_{\rm I}+\rho_{\rm II}\kappa_{\rm II}+\rho_{\rm II}\kappa_{\rm I}B+\rho_{\rm I}\kappa_{\rm II}/B}. \tag{5}$$

Two cases are considered numerically.

Case I:

$$\rho=\rho_{\rm I}=\rho_{\rm II}=1\times10^{-3}\text{ ohm-cm},$$
$$\kappa=\kappa_{\rm I}=\kappa_{\rm II}=1.5\times10^{-2}\text{ w/cm°C},$$
$$S_{\rm I}=-S_{\rm II}=200\ \mu\text{v/°C},$$
$$\Delta T=10\text{°C}.$$

Equation (5) becomes

$$R=\frac{\Delta S^2\Delta T}{\rho\kappa(2+B+B^{-1})}=\frac{0.106}{f_{\rm I}(B)}.$$

Case II:

$$\rho_{\rm II}=200\rho_{\rm I}=2\times10^{-1}\text{ ohm-cm},$$
$$\kappa_{\rm II}=3\kappa_{\rm I}=4.5\times10^{-2},$$
$$S_{\rm II}=-2S_{\rm I}=400\ \mu\text{v/°C}.$$

Equation (5) now becomes

$$R=\frac{0.24}{601+200B+3/B}=\frac{0.24}{f_{\rm II}(B)}.$$

Although the explicit form of $f_{\rm I}(B)$ and $f_{\rm II}(B)$ differ, both increase with decreasing B and must always be greater than unity. When the amount of care exercised in preparing thermoelectric materials is considered, it does not seem reasonable to expect more than a few percent of a second phase, say $B=0.05$. It is now possible to see that the ratio R is quite small for the two cases considered (4.7×10^{-3} and 3.5×10^{-4}, respectively). At room temperature thermal conductivity measurements are accurate to about five percent, so the effect of the Peltier term under these conditions is negligible. The predicted results are generous because it has been assumed that the two phases have opposite conductivity types. Should the conductivity type be the same, ΔS could approach zero.

While the model considered is extremely simple, it seems likely that a more sophisticated treatment would reduce R even further. Some of the possible improvements shall be considered briefly. First, if we consider the current loop as being shorter than the sample, ΔT and therefore R would be reduced. Second, one may include the shorting effect which exists because the samples are in contact along their length; this would undoubtedly decrease the apparent ΔT and increase the apparent ρ's through boundary scattering.

It therefore appears that the proposed mechanism is not valid for two-phase alloys in which the minor phase is present in less than ten volume percent, even though it forms a continuous network. The effect of a second phase may well produce spurious thermal conductivity measurements, but probably through other mechanisms.

[1] J. P. McHugh, G. C. Cosgrove, and W. A. Tiller, Symposium on Thermoelectric Energy Conversion, Dallas, Texas, January 9–12, 1961.
[2] J. P. McHugh, G. C. Cosgrove, and W. A. Tiller, J. Appl. Phys. 32, 621 (1961).
[3] S. V. Airapetiants, Soviet Phys.–Tech. Phys. 2, 429 (1957).
[4] S. V. Airapetiants and M. S. Bresler, Soviet Phys.–Tech. Phys. 3, 1778 (1959).

Charged Dislocations in Ionic Crystals

F. Rueda* and W. Dekeyser
Laboratoium voor Kristallografie en Studie van Vaste Stoffen, Rozier 6, Ghent, Belgium

(Received April 3, 1961)

In a previous paper[1] we described experiments concerning the electrical effects associated with the inhomogeneous deformation (indentation) of rocksalt, as first described by Fishbach and Nowick.[2] Contrary to what was expected, the dislocations were found to behave as if they carried a negative charge. We have extended this work, and this note presents the results obtained.

Pure and doped rocksalt crystals, grown in this laboratory, as well as LiF (Harshaw) and MgO (Péchiney) single crystals were used. Each type of experiment was repeated a considerable number of times and on different specimens. To avoid spurious effects due to surface loops resulting from cleavage, all slabs were chemically polished before the test and manipulated with great care afterwards. The indentations were made with a Leitz microhardness tester and the signals recorded as indicated in Fig. 1. The electrode (except when specifically stated) was evaporated onto the crystal.

The signals recorded when LiF are indented are similar to those obtained with NaCl, i.e., the dislocations behave as if negatively charged. MgO behaves differently, and the dislocations appear to be positively charged. In all cases no change in the magnitude or sign of the charge is observed when the slabs are aged in the atmosphere of the laboratory after polishing; there is no difference between annealed and quenched specimens.

That only dislocation loops coming near the electrode contribute to the signal is shown in rocksalt by the fact that, for a given crystal, no signal is observed unless the load applied to the indentor exceeds a critical value. It is, however, not necessary that loops reach the electrode to have an observable effect. This was seen with an arrangement as shown in Fig. 1 in which a leaf of beaten gold acted as the electrode. It could easily be removed after the indentation and thus permitted the re-etching of a specimen that had been etched before the experiment. This procedure revealed new etchpits in most cases (but not in all) when the indentation was stopped at the time the signal started to develop. These etchpits were distributed in what can be considered as the "projection" on the bottom face of the indentation figure. With the arrangement as illustrated in Fig. 2, a circular metallic ring 6 mm in diameter acted as the electrode, and the crystal was placed on a metallic washer (diameter = 10 mm). The signals observed were positive, negative, or "mixed" (i.e., first positive, then negative). When the signal was positive, slip planes could be detected by etching. They were due to plastic flow on the face of the electrode, i.e., the signal corresponded in these cases to dislocations moving away from the electrode. When the signal was negative, a distribution of etchpits as described previously was observed. The third alternative corresponded to a mixture of both arrangements of etchpits.

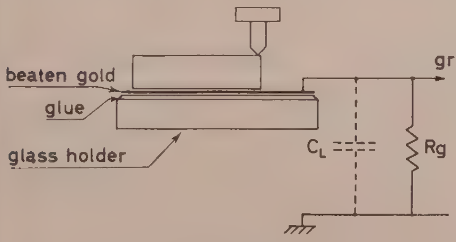

Fig. 1. Experimental arrangement; in general, the electrode is evaporated on the crystal.

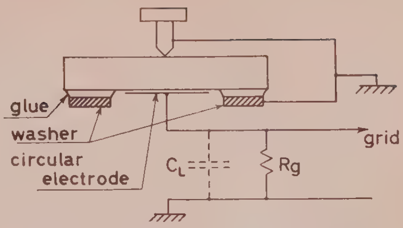

Fig. 2. Crystal glued to a washer in order to introduce dislocations on the bottom face on which the electrode is evaporated.

Doped rocksalt crystals were also examined. When Cd^{++} ions are added (0.2% CdCl$_2$ in the melt) the dislocations behave also as negative and no great change of the induced charge (reduced to equal area of the indentation figure) is seen. When Na$_2$O$_2$ is added (1.0% in the melt) a reversal of sign is observed, i.e., the the dislocations behave as positive in this case, but the induced charge is very small. This means that we must consider the results with MgO crystals with caution as the examined specimens are certainly not of a degree of purity comparable to that of NaCl and LiF.

Although the results with doped crystals indicate an effect of the vacancies present in the crystals on the acquisition of the charge by moving dislocations, this does not necessarily mean that this charge is solely due to the gathering of vacancies by the dislocations during their movement. The lack of a clear correlation between the concentration of the added divalent ions and the intensity of the signal points towards a more complex mechanism. Experiments to find out which factors are dominant are now in progress.

The authors are greatly indebted to the European Research Associates (Brussels) for support of this work. One of us, (R. F.) in particular, expresses his gratitude for a research fellowship.

* On leave from Instituto de Física, Alonso Santa Cruz, Madrid.
[1] F. Rueda and W. Dekeyser, Phil. Mag. (to be published) (1961).
[2] D. B. Fishbach and A. S. Nowick, J. Phys. Chem. Solids 5, 302 (1958).

Low-Temperature Internal Friction Peaks in Single Crystals of NaCl and LiF*

Anthony Taylor
Department of Engineering Physics, Cornell University, Ithaca, New York

(Received April 20, 1961)

A PRELIMINARY study of the internal friction below room temperature, in the kilocycle frequency range, of two types of alkali halide crystals has shown that small amounts of plastic deformation give rise to a well-defined inter nal friction peak.

Hitherto studies of such low-temperature internal friction peaks have been confined to metals: Bordoni[1] first reported the presence of a low-temperature peak in specimens of plastically deformed polycrystalline copper, lead, aluminum, and silver. Later more detailed studies of the behavior of this peak were made on single

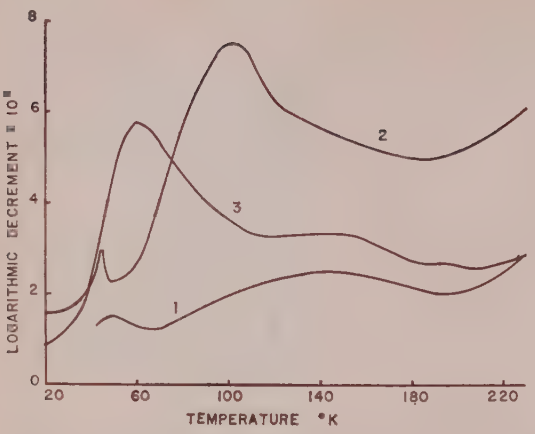

FIG. 1. Logarithmic decrement versus absolute temperature for single crystals of LiF and NaCl. Curve 1, NaCl crystal annealed; curve 2, NaCl crystal slightly deformed; curve 3, LiF crystal slightly deformed.

crystals as well as on polycrystalline samples of copper by Caswell[2] and Paré[3] working in this laboratory and by Niblett and Wilks[4] and others (see review by Niblett and Wilks[5]). This peak has been ascribed by Seeger *et al.*[6] to a relaxation process involving the motion of dislocations over the Peierls potential. To date, low-temperature peaks have also been found in deformed hexagonal metals, Mg and Zn, and in deformed body centered cubic Mo, Ta, Nb, W, but there is some doubt whether all these peaks behave similarly to the Bordoni peak in fcc samples. It therefore seemed worthwhile to examine the low-temperature internal friction of single crystals of sodium chloride and lithium fluoride particularly as it is possible to study simultaneously the distribution of dislocations by etching and by optical birefringence. An early experiment of this type by Currie[7] using a deformed LiF crystal had indicated a peak in the internal friction at about 60°K.

In the present experiments the internal friction was measured at two frequencies, 40 and 6 kc, by observing the decay in the amplitude of oscillation after the driving force had been interrupted. At the higher frequency the determination was carried out with longitudinal vibrations in the apparatus described by Caswell using a two-part composite oscillator formed by joining end to end a $-18.5°$ cut quartz transducer and a bar of the crystal. The joint between the quartz and the specimen was formed with epoxy resin which hardens at room temperature and is known to contribute negligibly to the internal friction of the system. The internal friction was measured in the strain amplitude independent region at about an ϵ of 1×10^{-6}. As there appeared to be no significant annealing or temperature hysteresis effects during the experiments, it was found convenient to make the determinations in cooling from room temperature to 100°K and then in heating from 20° to 120°K.

In Fig. 1 the logarithmic decrement measured at 40 kc is plotted versus temperature for crystal specimens of lithium fluoride and sodium chloride both obtained from the Harshaw Chemical Company. Curve 1 was obtained for NaCl which had been annealed at 650°C and furnace cooled, while curve 2 was obtained after this specimen had been deformed until it was slightly birefringent without removing it from the resonator. It can be seen that the decrement is increased by the deformation and that a distinct peak appears at about 100°K. Curve 3 shows the peak obtained by deforming slightly a crystal of LiF, here the maximum was observed at 60°K.

Parallel experiments to these have been carried out on LiF at 6 kc using the apparatus developed by Paré. Specimens in the form of long rectangular bars, supported horizontally on two fine tungsten wires, were driven electrostatically in their fundamental flexural mode. The curves obtained for slightly deformed crystals were similar in form to those obtained at the high frequency. From the observed variation of the peak temperature with frequency, an activation energy of approximately 0.15 ev was calculated on the basis of a simple relaxation model with a single relaxation time.

Experiments were also carried out on specimens deformed more strongly in compression by amounts up to 5% plastic strain. It was found that the height of the peak over the background increased with deformation in both NaCl and LiF while the peak temperature increased slightly for LiF and hardly at all for NaCl. In the case of heavily deformed LiF there was evidence for the development of a second peak at 140°K.

It is proposed to make a study of the behavior of these peaks in relation to the density of dislocations, annealing treatment, and the impurity concentration.

The writer would like to thank Professor H. S. Sack for his most helpful advice in carrying out this work.

---

* This work was supported by the U. S. Atomic Energy Commission and the Advanced Research Projects Agency.

[1] P. G. Bordoni, Ricerca Sci. **19**, 851 (1949); J. Acoust. Soc. Am. **26**, 495 (1954).

[2] H. L. Caswell, J. Appl. Phys. **29**, 1210 (1958).

[3] V. K. Paré, J. Appl. Phys. **32**, 332 (1961).

[4] D. H. Niblett and J. Wilks, Phil. Mag. **1**, 415 (1956); **2**, 1427 (1957).

[5] D. H. Niblett and J. Wilks, Quart. Suppl. Phil. Mag. **4**, 1 (1960).

[6] A. Seeger, Phil. Mag. **1**, 651 (1956); A. Seeger, H. Donth, and F. Pfaff, Discussions Faraday Soc. **23**, 19 (1957).

[7] D. G. Currie, Engineering Physics Senior Research Project Report, Cornell University (1958).

Angular Dependence of Magnetoresistance in HgSe

THEODORE C. HARMAN
Lincoln Laboratory, Massachusetts Institute of Technology, Lexington 73, Massachusetts*

(Received May 22, 1961)

MERCURY selenide is a II-VI compound which crystallizes in the zinc blende structure. It is a relatively unexplored material which we have prepared in large single-crystal form. Measurements reported here show that the conduction band is spherically symmetric, a fact which should greatly assist the unraveling of other band structure features.

Oriented parallelepiped shaped specimens of HgSe were cut from a homogeneous section of a single-crystal ingot. The samples were homogenized further by annealing. The opposite faces of the specimens were made plane parallel by the usual lapping technique. Measurements carried out before etching yielded a negative longitudinal magnetoresistance which was not reproducible in magnitude. After the sample had been etched,[1] negative effects disappeared and the results were reproducible. The ends of the samples were ultrasonically soldered with indium. Copper current leads were attached to the indium. Platinum wires 4 mils in diameter were resistance welded to one face of the crystal. These wires were used for the resistivity leads and were placed at a distance from the ends greater than the width. The sample length

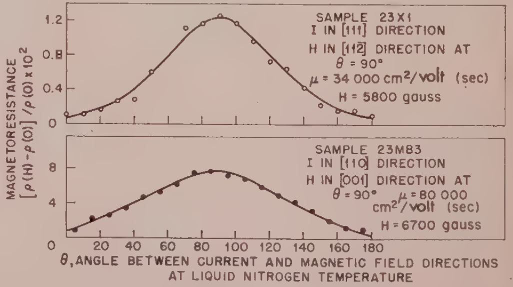

FIG. 1. Variations of $\Delta\rho/\rho(0)$ as H is rotated with respect to I in n-type HgSe at liquid nitrogen temperature and for I directions of [111] and [110].

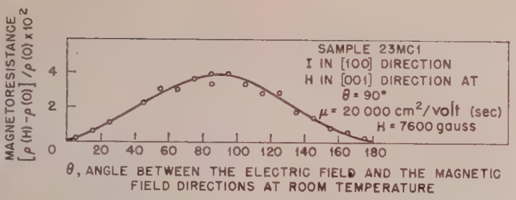

FIG. 2. Variations of $\Delta\rho/\rho(0)$ as H is rotated with respect to I in n-type HgSe at room temperature and for 1 direction of [100].

to width ratio exceeded four. According to Drabble and Wolfe,[2] the short-circuiting effects due to the end contacts is negligible for the probe positions and sample geometry given above, even for an infinite magnetic field. For the transverse magnetoresistance, the magnetic field, the electrical current, and resistivity probe wires were oriented in mutually perpendicular directions. In addition to yielding small area contacts, this arrangement reduces the effect of Hall voltage shorting in the vicinity of the resistivity probe contacts.[3]

The magnetoresistance was measured as a function of angle between the direction of current and the direction of magnetic field at 78°K for HgSe samples 23MB3 and 23X1. These samples had a carrier concentration n_e of $1.8\times10^{17}/\text{cm}^3$ and $1.3\times10^{18}/\text{cm}^3$, respectively, at 78°K. The results of the measurements are shown in Fig. 1. Both samples exhibited a magnetoresistance maximum at 90° and the magnetoresistance approached zero at 0° and 180°. As shown in Fig. 2, a similar behavior is exhibited for sample 23 MCl ($n_e=4.5\times10^{17}/\text{cm}^3$) at room temperature.

These magnetoresistance results are consistent with a model involving a very nearly spherically symmetric conduction band; this is in sharp contrast to similar measurements carried out on n-type silicon[4] and germanium.[5] The presence of a small longitudinal magnetoresistance indicates that there may be a slight anisotropy of the conduction band, but the approximation of a spherically symmetric conduction band should be quite good.

---

* Operated with support from the U. S. Army, Navy, and Air Force.

[1] The author is indebted to Mrs. M. C. Lavine for developing the etch. The first step involves immersion of the sample with agitation for one minute in pure bromine. The second step consists in removal of selenides with a solution of ethyl alcohol and benzene.

[2] J. R. Drabble and R. Wolfe, J. Electronics and Control **3**, 259 (1957).

[3] M. Glicksman, J. Phys. Chem. Solids **8**, 511 (1959).

[4] G. L. Pearson and C. Herring, Physica **20**, 975 (1954).

[5] G. L. Pearson and H. Suhl, Phys. Rev. **83**, 768 (1951).

Thermoelastic Equations and Grueneisen's Relation

A. M. FREUDENTHAL
Columbia University, New York, New York

(Received April 21, 1961)

IN a previous letter[1] it was shown that a basic inconsistency in the conventional formulation of the equations of thermoelastic and thermo inelastic stress-analysis can be removed by the introduction of the Grueneisen relation[2] by which the consequences of the independent specification of the elastic bulk modulus K and of the coefficient of linear thermal expansion are avoided. It has been shown that the introduction of a new physical parameter, the specific thermal pressure $\beta=3\alpha K=\gamma\rho c_v$ kg/cm³/°C, where (ρc_v) denotes the specific heat at constant volume per unit volume and γ is the Grueneisen constant, ensures that the thermal stress problem vanishes whenever the assumption of incompressibility of the medium is made, whereas the conventional formulation provides a physically meaningless solution of the equations. This fact is easily illustrated by comparison of the conventional and the corrected form of the standard equations for the stress function ϕ and the displacement function ψ of the uncoupled plane steady state thermoelastic boundary value problem.[3] Thus

$$\nabla^4\phi=-[\alpha E/(1-\nu)]\nabla^2 T \qquad (1a)$$

is replaced by

$$\nabla^4\phi=-[(1-2\nu)/(1-\nu)]\beta\nabla^2 T \qquad (1b)$$

and

$$\nabla^2\psi=\left[\frac{1+\nu}{1-\nu}\right]\alpha T \qquad (2a)$$

is replaced by

$$\nabla^2\psi=\left[\frac{1-2\nu}{1-\nu}\right]\frac{\beta}{2G}T. \qquad (2b)$$

Both Eqs. (1b) and (2b) vanish for $\nu=\frac{1}{2}$ while Eqs. (1a) and (2a) do not.

The purpose of this letter is to show that the consideration of the Grueneisen relation removes the possibility of (theoretically) uncoupling the thermoelastic equation by the assumption $\alpha\rightarrow 0$[4] without, at the same time, eliminating all equations by the associated condition $K\rightarrow\infty$; it also resolves an apparent inconsistency that arises in the conventional approach to the transient thermoelastic problem when the heat-transfer equations are solved independently of the elastic equations of motion. In this case the temperature satisfies the diffusion equation (infinite velocity) while the associated volume change and resulting thermal stresses should propagate at acoustic velocities.

The well-known coupled equations of thermoelasticity[5] in which α has been replaced by the new parameter β can be written in the form

$$k\nabla^2 T=\rho c_v\frac{\partial T}{\partial t}+\beta T_0\frac{\partial\epsilon}{\partial t} \qquad (3a)$$

$$(K+\tfrac{4}{3}G)\nabla\epsilon^2=\rho\frac{\partial^2\epsilon}{\partial t^2}+\beta\nabla^2 T, \qquad (3b)$$

where ϵ is the volume strain, k the thermal conductivity, and T_0 the (absolute) reference temperature. On eliminating $\nabla^2 T$ and introducing the volume-strain pressure relation in the form

$$p=K\epsilon-\beta T \qquad (4)$$

Eqs. (3) can be combined into the relation

$$K\nabla^2\epsilon=\frac{K}{c^2}\frac{\partial^2\epsilon}{\partial t^2}+\frac{1}{1+4G/3K}\left[\left(1+\gamma\frac{\beta T_0}{K}\right)\frac{\partial\epsilon}{\partial t}-\frac{1}{K}\frac{\partial p}{\partial t}\right], \qquad (5)$$

where the diffusivity $K=k/\rho c_v$ and $c^2=(K+\frac{4}{3}G)/\rho$. Equation (5) is satisfied when the temperature pressure p and the temperature T satisfy, respectively, the equations

$$\nabla^2 p=\frac{1}{c^2}\frac{\partial^2 p}{\partial t^2}+\frac{1}{K'}\frac{\beta T_0}{K}\frac{\partial p}{\partial t} \qquad (6)$$

and

$$\nabla^2 T=\frac{1}{c^2}\frac{\partial^2 T}{\partial t^2}+\frac{1}{K'}\frac{\partial T}{\partial t}=\frac{1}{c^2}\left[\frac{\partial^2 T}{\partial t^2}+\frac{c^2}{K'}\frac{\partial T}{\partial t}\right], \qquad (7)$$

where $K'=K(1+4G/3K)$.

Equations (6) and (7) are of the standard form of the "telegraph equation." Assuming plane harmonic temperature waves of frequency $(\omega/2\pi)$ propagating in the x direction, the component in this direction is proportional to $\exp[i\omega(t-qx)]$; q satisfies the equation

$$q^2=(1/c^2)[1-i(c^2/K'\omega)] \qquad (8)$$

and therefore

$$q=\alpha-i\beta,$$

where

$$\alpha^2=\frac{1}{2c^2}\left[\left(1+\frac{c^4}{K'^2\omega^2}\right)^{\frac{1}{2}}+1\right]$$

and $\qquad (9)$

$$\beta^2=\frac{1}{2c^2}\left[\left(1+\frac{c^4}{K'^2\omega^2}\right)^{\frac{1}{2}}-1\right].$$

Since q is complex, a plane thermal wave propagates with absorption coefficient $\omega\beta$, the magnitude of which depends on the ratio $(c^2/K'\omega)$. When $\omega\ll c^2/K'$ only the conduction term is significant in Eq. (7), which degenerates into the Fourier equation; when $\omega\gg c^2/K'$ only the wave term matters, while in the intermediate region both terms must be retained. In general $(c^4/K'^2\omega^2)\gg1$, so that $\alpha=\beta$ and $\beta\omega\sim(\omega/2K')^{\frac{1}{2}}$. Hence in one wavelength $\lambda=2\pi(\alpha\omega)^{-1}=2\pi(2K'/\omega)^{\frac{1}{2}}$ the amplitude decays by a factor $\exp(-\beta\omega\lambda)=e^{-2\pi}$; the distance travelled before the amplitude is reduced to $(1/e)$ of its initial value is therefore $\lambda/2\pi$.

For the incompressible medium with $K\rightarrow\infty$, $\epsilon\rightarrow 0$, and therefore $c\rightarrow\infty$, Eqs. (5) and (6) vanish; Eq. (7) is again transformed into the Fourier equation for any value of ω, since with $c\rightarrow\infty$ the condition $\omega\ll c^2/K'$ is always satisfied. Thus, uncoupling of the thermoelastic equations (3) is achieved either by the assumption of incompressibility of the medium or by consideration of disturbances of frequency $\omega\ll c^2/K'$. The conventional uncoupling assumption $\alpha=0$ is neither necessary nor physically admissible. The assumption that the thermal pressure in the elastic medium propagates as a damped wave, which underlies the uncoupling of Eqs. (6) and (7), seems to be physically more relevant.

[1] A. M. Freudenthal, J. Appl. Phys. **31**, 434 (1960).

[2] E. Grueneisen, Ann. Physik, **26**, 393 (1908)

[3] S. Timoshenko and J. N. Goodier, *Theory of Elasticity* (McGraw-Hill Book Company, Inc., New York, 1951), pp. 398–433.

[4] P. Chadwick, "Thermoelasticity," in *Progress in Solid Mechanics* edited by I. N. Sneddon-Hill (Intersicence Publishers, Inc., New York, 1960) Vol. 1, p. 280.

[5] A. M. Freudenthal and H. Geiringer, "Mathematical theories of the inelastic continuum," in *Handbuch der Physik* (Springer-Verlag, Berlin, Germany, 1958), Vol. 6, p. 264.

Thermionic Emission from a Tantalum Crystal in Cesium or Rubidium Vapor

H. F. Webster
General Electric Research Laboratory, Schenectady, New York

(Received May 11, 1961)

THERMIONIC emission has been measured from a hemispherical tantalum crystal which has its work function altered by an adsorbed layer of alkali metal. The emission density is strongly dependent upon the crystallographic face of the tantalum and the emission pattern changes are different for cesium and rubidium.

The experimental arrangement is similar to that used by Martin[1] for tungsten but it was modified to permit quantitative measurements of the emission current densities from different crystal faces to be made by a moving pinhole and Faraday cage. The experimental tube is shown in Fig. 1. The tantalum crystal cathode is heated by conduction from the hairpin heater. The anode phosphor screen can be moved from outside the tube by the long lever and flexible diaphragm arrangement. Electrons which are emitted at the ball end of the tantalum cathode at first travel radially away from the ball then turn and strike the phosphor screen where they present an enlarged map of the emission density from the front half of the ball. The electrons from the side of the ball and the shaft strike the anode phosphor screen in an outer ring-shaped region but it is difficult to use this part of the pattern because it is made up of overlapping patterns. The shield serves to prevent electrons from the hairpin heater and back portions of the tantalum cathode from reaching the anode phosphor screen. The extra single-turn tantalum heater around the cathode serves to heat the tantalum crystal to near its melting point by electron bombardment to clean its surface before measurements are started. This heater is not used while measurements are being made. The emission current pattern from the cathode remains fixed with respect to the cathode and thus the pinhole at the center of the screen can be scanned across the pattern and quantitative measurements of the current densities obtained.

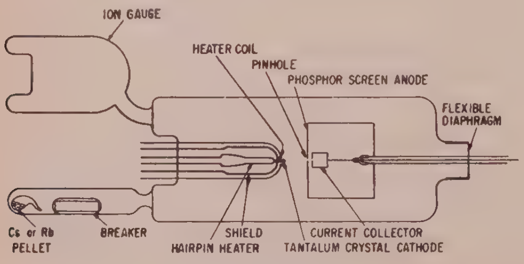

FIG. 1. Experimental tube.

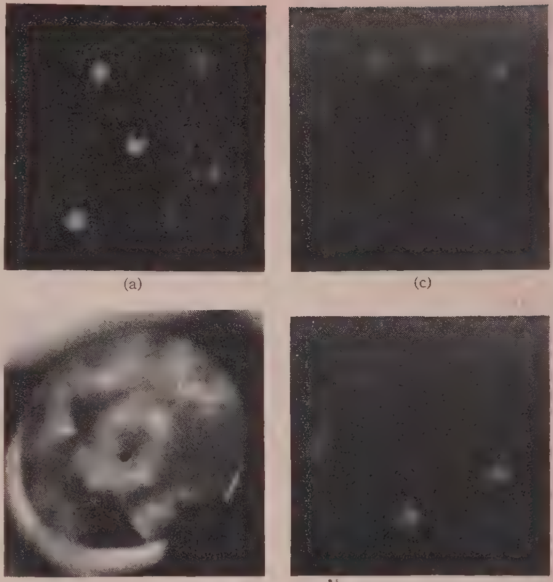

FIG. 2. Thermionic emission patterns from a hemispherical tantalum cathode: (a) and (b) in cesium vapor, 52°C wall temperature and (c) and (d) in rubidium vapor 71°C, wall temperature. The cathode temperatures are: (a) 440°C, (b) 355°C, (c) 535°C, and (d) 390°C. A 110 face projects to the center of the pattern. The position of the grain boundary is clearly visible in (b).

The alkali metal is introduced into the sealed-off tube from the side tube by breaking the glass capsule which has been filled with the alkali metal previously prepared by vacuum distillation. The ion gauge is used to monitor the pressure in the tube before and after the breaking of the capsule but it is not run while thermionic emission measurements are being made.

Tubes containing alkali vapors exhibit low-resistance leakage paths across the glass which make the measurement of small currents difficult. This problem has been dealt with in two ways: first, the low-current lead to the Faraday cage is brought in coaxially and the outer tube is used as a guard ring for the lead; second, the entire tube is operated in an air oven which establishes most of it at a uniform temperature but the flexible diaphragm end of the tube is run hotter to interrupt the conductive path.

The vapor pressure of the alkali metal is established by the coolest temperature of the walls of the tube but it has been found desirable to have as much of the wall area as possible at this coolest temperature in order to ensure equilibrium.

The tantalum cathode was made by hanging a small polycrystalline tantalum rod in a bell jar and heating its lower end by electron bombardment. After heating it above a temperature of 2500°K for about an hour, large grains grow and as a last step it is heated over its melting point. A hanging liquid drop is formed which seeds on the large grains in the shaft and on freezing a ball is formed which usually is made up of a few grains. The tantalum cathode used in this equipment consisted of two grains both of which had the 110 direction on the axis of the rod but which were misoriented by 52°. This hanging drop technique for making cathodes has been used successfully with Ta, W, Mo, Re, and Nb.

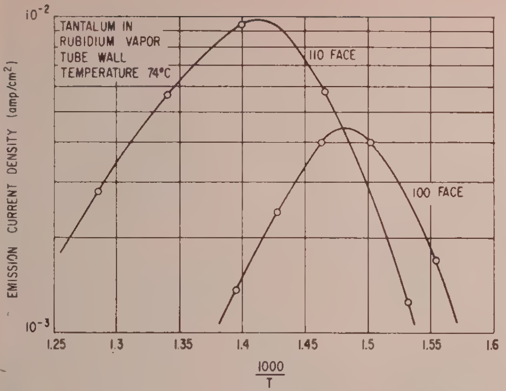

FIG. 3. Log of thermionic emission density from tantalum in rubidium vapor vs reciprocal cathode temperature for the 110 and 100 crystal faces.

The temperature of the emitting end of the tantalum crystal was determined by optical pyrometry for temperatures above 700°C. For temperatures below this, infrared photography was used instead of a thermocouple because the thermocouple could act as a source of electrons which would be confused with the pattern due to the tantalum crystal. A tantalum crystal similar to the one being measured was mounted in a bell jar together with a thermocouple and this was used to establish the photographic density vs tantalum crystal temperature calibration curve for the Kodak infrared film which was used. The photographic method was used down to 400°C.

Figures 2(a) and 2(b) show the emission patterns that are obtained from tantalum in cesium. At high temperatures, only regions very near the 110 face yield strong emission, while at lower temperatures the emission spreads to other parts of the crystal. A different behavior is obtained with tantalum in rubidium as shown in Figs. 2(c) and 2(d). At high temperatures strong emission again is obtained from the 110 regions while at lower temperature this region fades and strong emission is obtained from the 100 regions. Details of this change can be seen in Fig. 3 in which log of emission density is plotted vs reciprocal of cathode temperature. The pinhole was set on the 110 regions and the 100 regions and each region yielded a peak emission but the peaks occurred at different cathode temperatures.

If one wishes to obtain the most emission current density with the least pressure of alkali vapor it is very advantageous to use the proper crystal face for the cathode. Similarly, if one wishes to obtain a surface of minimum work function, again it is advantageous to choose a particular crystal face. Both of these considerations are important in the thermionic energy conversion problem.

The author would like to acknowledge helpful discussions with J. M. Houston and the assistance of T. A. Howlett and F. P. Hession. This work was supported by the Air Force, Cambridge Research Center.

[1] S. T. Martin, Phys. Rev. 56, 947 (1939).

Errata: On Three-Dimensional Space Charge Flow

[J. Appl. Phys. 31, 1371 (1960)]

J. ROSENBLATT*
Physics Department, University of Birmingham, Birmingham, England

AFTER the publication of my paper entitled "Three-dimensional space charge flow" in J. Appl. Phys. 31, 1371 (1960), I became aware of the fact that some of its results had been obtained independently elsewhere. An equation equivalent to Eq. (12) in my paper was derived and its solution under restrictive conditions examined by A. R. Lucas, B. Meltzer, and G. A. Stuart, J. Electronics and Control 4, 160 (1958) and B. Meltzer and R. Lucas, J. Electronics and Control 4, 454 (1958).

The restrictive conditions referred to above correspond to the particular case treated in Eqs. (17), (18), and (19) in my paper. I am indebted to Dr. B. Meltzer for calling my attention to these references.

* On leave of absence with an I.A.E.A. fellowship from Comisión Nacional de Energía Atómica, Buenos Aires, Argentina.

Erratum: Use of $PrCl_3$ in a Solid-State Infrared Quantum Counter

[J. Appl. Phys. 31, 825 (1961)]

JOHN F. PORTER, JR.
Radiation Laboratory, The Johns Hopkins University, Baltimore, Maryland

Last paragraph sentence: "An attenuation of approximately 10^{+10} between pump and detection wavelengths is possible using only two interference filters and crossed polarizers." Should read: An attenuation of approximately 10^{+10} between pump and detection wavelengths is possible using only *three* interference filters and crossed polarizers.

Books Reviewed

Prompt, noncritical reviews appear in this column. Critical reviews of many of the books described here will appear in Physics Today, The Review of Scientific Instruments, *or* American Journal of Physics.

Materials for Nuclear Engineers. A. B. MCINTOSH AND T. J. HEAL, Editors. Pp. 373. Interscience Publishers, Inc., New York, 1960. Price $11.85.

The introductory chapter discusses the use by nuclear engineers of data on the properties of materials; then succeeding chapters concentrate on the behavior and properties of uranium, thorium, plutonium, ceramic fuels, graphite, magnesium, beryllium, and zirconium. The authors of the individual chapters are members of the staff of the United Kingdom Atomic Energy Authority who are or have been primarily engaged in the study and selection of materials and who are in day-to-day contact with the engineering side of that organization.

Relativistic Electron Theory. M. E. ROSE. Pp. 302. John Wiley & Sons, Inc., New York, 1961. Price $9.50.

Relativistic Electron Theory serves as a comprehensive treatment of the single-particle description of relativistic quantum mechanics. Explicitly concerned with spin one-half particles which are not subject to strong couplings, it includes consideration of massless neutrinos.

The book is devoted primarily to a detailed discussion of the Dirac theory, the material basis for almost every application in high-energy physics involving light particles.

NMR and EPR Spectroscopy. J. MARLING, Editor. Pp. 288. Pergamon Press, New York, 1960. Price $12.00.

The basis for this book is the material presented at the Third Annual Varian NMR-EPR Workshop. Its subject matter is designed to appeal to and to instruct scientists who have had extensive training in physics, chemistry, electronics, or biology, who wish to augment their training by learning and/or utilizing NMR-EPR spectroscopy.

The preliminary material defines the background, areas of application, and basic instrumentation of NMR-EPR spectroscopy while the advanced lectures cover the specialized details of instrumentation, theory, research uses, and techniques.

Recent advances are covered in this volume, and the treatment of subjects is new to the extent that much experimental and practical information in the field of NMR-EPR spectroscopy is gathered together for the first time.

Modern Aspects of the Vitreous State, Vol. I. J. D. MacKenzie. Pp. 218. Butterworth, Inc., Washington, D. C., 1961. Price $9.50.

Some general aspects are discussed in Chap. 1. Chapter 2 is concerned with the present status and limitations of x-ray diffraction as a tool towards the solution of glass structure. Two other powerful "tools"—nuclear magnetic resonance and infrared absorption and their findings are treated in Chaps. 5 and 6, respectively. Chapter 3 summarizes the present efforts to answer the important question: "What are the kinetic barriers to crystallization as liquids are supercooled?" The theoretical aspects of the "glass transition" which differentiates a liquid from a glass constitute the subject of Chap. 7. The constitution of phosphate glasses, based primarily on results obtained from a different approach, that of aqueous solution techniques, is discussed in Chap. 4; and finally, the structures of a number of inorganic glass-forming liquids such as the simple oxides and halides are critically reviewed in Chap. 8.

Atomic Energy Waste: Its Nature, Use, and Disposal. E. Glueckauf. Pp. 420. Interscience Publishers, Inc., New York and Butterworths Publications, Ltd., London, 1961. Price $14.00.

The book deals extensively with the great increase in our knowledge of the waste products, and of how they arise, of their chemical processing, and of the effects of their radiations on materials and living organisms. Some contributors concentrate on the large-scale applications of radiation, especially in the fields of food preservation, agricultural applications, and chemical manufacture. Others deal with international legislation on radioactive waste, with aspects of industrial safety, and with the technology and the chemical background of waste disposal.

Thermodynamics. P. T. Landsberg. Pp. 499. Interscience Publishers, Inc., New York, 1961. Price $14.50.

The abstract nature of the subject is always allowed to become fully evident in this book, and it therefore differs materially from existing texts. The scope of the book is strictly limited. Classical nonrelativistic thermodynamics is discussed, and, as the main application, simple systems of weakly interacting particles are treated. On the other hand, more than usual attention is devoted to these, and statistical mechanics is developed and used to reveal alternative interpretations and applications of the thermodynamic treatment. It is hoped that the reader will in this way grasp some of the crucial points in the relationship between thermodynamics and statistical mechanics. Although the available space is divided evenly between these two topics, this is primarily a book on thermodynamics, so that general principles rather than detailed applications or physical mechanisms are emphasized.

Gases at High Densities and Temperatures. Yu N. Ryabinin. Pp. 60. Pergamon Press, New York, 1961. Price $4.50.

This interesting book describes a device in which gases were compressed by the "firing" of a piston in a closed cylindrical volume. The process of compression was isentropic, with a large increase of pressure and temperature. The maximum pressure and temperature obtained during compression reached, respectively, 10 000 kg/cm² and 1500–9000°K (depending on the composition of the gas). Thermodynamic characteristics, radiation spectra, and electrical conductivity of the compressed gases were studied.

Progress in Semiconductors, Vol. V. A. F. Gibson, F. A. Kröger, and R. E. Burgess, Editors. John Wiley & Sons, Inc., New York, 1961. Price $11.00.

Subjects covered in Vol. 5 are: the electrical properties of semiconductor surfaces, the absorption edge spectrum of semiconductors, the chemical bond in semiconductors, indium antimonide, thermal conductivity of semiconductors, magneto-optical phenomena in semiconductors, and the band structure and electronic properties of graphite crystals.

The Hall Effect and Related Phenomena. E. H. Putley. Butterworths Publications, Ltd; London, 1961. Price 50s.

The interpretation of the variation with temperature of the electrical properties of semiconductors to yield information on the energy band structure and effective mass, the intrinsic carrier concentration, electron scattering mechanisms, and the ionization energies and concentration of extrinsic impurities, are described and illustrated by full reference to recent research on semiconductors. The behavior of the principal groups of semiconductors receives a brief review.

Throughout the book the emphasis has been placed upon the evaluation of experimental data. The Hall effect, the electrical conductivity, and the magnetoresistance effect are all considered in detail while the Nernst effect, other galvanomagnetic effects, the thermoelectric effects, and thermal conductivity are also included.

Kinematics of Nuclear Reactions. A. M. Baldin, V. I. Gol'danskii, and I. L. Rozenthal. Pp. 303. Pergamon Press, New York, 1961. Price $6.50.

Kinematics of Nuclear Reactions gives a comprehensive treatment of both classical and quantum kinematics of nuclear reactions. Special features include details of graphical construction methods for kinematics of reactions, and an account of methods used for the analysis of reactions at ultra-high energies, while there are appendixes containing graphs and nomograms of kinematic relations for many important reactions; and also tables of Clebsch-Gordon, Racah, X, Z, and $Z\gamma$ coefficients for important reactions. The book is written specifically with the research worker in experimental nuclear physics in mind.

Techniques of Non-Destructive Testing. C. A. Hogarth and J. Blitz, Editors. Pp. 216. Butterworth, Inc., Washington, D. C., 1961. Price $7.50.

Most of the chapters of this manual are self-contained accounts of the theory and practice of electrical, magnetic, mechanical, and visual testing techniques. Other chapters devoted to ultrasonic, radiological, and thermal comparator methods are supported by thorough introductions to their scientific backgrounds, which help the readers to gain full value from the use of these new and important methods of non-destructive testing. A final contribution outlines the manner in which many of the techniques are in current use within a government establishment.

Partial Differential Equations and Continuum Mechanics. Rudolph E. Langer, Editor. Pp. 397. The University of Wisconsin Press, Madison, Wisconsin, 1961. Price $5.00.

Partial Differential Equations and Continuum Mechanics is composed of the nineteen lectures which were delivered at an international conference conducted by the Mathematics Research Center at the University of Wisconsin from June 7 to 15, 1960. In addition to the lectures, the book contains abstracts of forty-five papers presented at the conference.

Advances in Electronics and Electron Physics, Vol. XIII. L. Marton, Editor. Pp. 454. Academic Press, Inc., New York, 1960. Price $13.50.

Contents of Vol. XIII in this series are as follows: inelastic collisions between atomic systems, field ionization and field ion microscopy, velocity distribution in electron streams, electron probe microanalysis, and television camera tubes; a research review.

Advances in Chemical Physics, Vol. III. I. Prigogine, Editor. Pp. 372. Interscience Publishers, Inc., New York, 1961. Price $11.50.

Contents of Vol. III in this series are as follows: "Mechanisms of organic electrode reactions," by Philip J. Elving and Bernard Pullman; "Nonlinear problems in thermodynamics of irreversible processes," by Thor A. Bak; "Propagation of flames and detonations," by J. O. Hirschfelder and C. F. Curtiss; "Large tunnelling corrections in chemical reaction rates," by Harold S. Johnston; "Aspects recents du diamagnétisme," by A. Pacault, J. Hoarau, and A. Marchand; "Power electrodes and their applications," by Withold Tomassi; "Variational principles in thermodynamics and statistical mechanics of irreversible processes," by Syu Ono; and "Electron diffraction in gases and molecular structure," by Bastiansen and P. N. Skancke.

Decay Schemes of Radioactive Nuclei. B. S. Dzhelepov and L. K. Peker. Pp. 786. Pergamon Press, New York, 1961. Price $20.00.

In this volume, translated from the Russian, full information about decay schemes for radioactive nuclei is newly systematized.

Thermoelectric Materials and Devices. Irving B. Cadoff and Edward Miller. Pp. 344. Reinhold Publishing Corporation, New York, 1960.

Based on a special series of lectures presented at New York University, the book features the contributions of twenty experts and ranges from basic theory to device design.

The first section is devoted to the theory of thermoelectric processes and thermoelectric circuits. This is followed by a general evaluation of materials, both theoretical and experimental, for use as thermoelements. The ensuing chapters discuss materials currently being used and those being considered for future use. The last section of the book concerns the principles of device design and descriptions of some experimental and prototype units which have been built and evaluated.

Power conversion and refrigeration are treated in an integrated manner. A chapter on thermionic conversion has been included for comparison with the "solid-state" conversion processes. Where necessary, the authors include brief reviews of background material.

X-ray Analysis of Organic Structures. S. C. Nyburg. Pp. 434. Academic Press, Inc., New York, 1961. Price $13.00.

This book is primarily an introduction to x-ray analysis for the organic chemist. It takes into account the fact that the average chemist does not have the mathematical and physical background to make use of treatises written by x-ray specialists for x-ray specialists.

The survey of organic materials examined to date has been divided into three main groups: crystalline materials of fairly low molecular weight, crystalline materials of high molecular weight, and fibrous materials.

The Encyclopedia of Microscopy. George L. Clark, Editor. Pp. 693. Reinhold Publishing Corporation, New York, 1961. Price $25.00.

This book is a survey of twenty-six kinds of microscopy. Internationally recognized experts survey the broad field of microscopy in over 140 especially written articles. The biological, medical, pharmaceutical, forensic, chemical, engineering, and industrial applications of microscopy as presented in this encyclopedia are thought to be the most complete and up-to-date ever offered in any kind of text or reference work. Entirely new and unpublished material on the solid image microscopy, the ultrasonic microscope, and on electronic combinations such as flying spot and TV microscopes, is another contribution to this encyclopedia.

The Encyclopedia of Spectroscopy. George L. Clark, Editor. Pp. 787. Reinhold Publishing Corporation, New York, 1961. Price $25.00.

The articles contained in this book are not merely abstracts or highly condensed versions of original manuscripts. Each article was especially written for inclusion in this volume and covers every major aspect of its topic.

In addition to their emphasis on the uses of spectra in chemical analysis, the authors cover the contributions of spectroscopy to all the sciences, including physics, biology and medicine, metallurgy, mineralogy, geology, ceramics, agronomy, astronomy, and astrophysics. Going even beyond these disciplines, the encyclopedia considers the industrial applications of spectroscopy in research routine testing, and on-stream control in plants.

Books Received

Wirbelstrome und Schirmung in der Nachrichtentechnik. Heinrich Kaden. (Volume 10 of Technische Physik in Einzeldarstellungen) Springer-Verlag, Berlin, Germany, 1959. Price DM 66.

Planets, Stars, and Galaxies. Stuart J. Inglis. Pp. 474. John Wiley & Sons, Inc., New York, 1961.

Basic Principles of Fission Reactors. W. R. Harper. Pp. 314. Interscience Publishers, Inc., New York, 1961. Price $7.50.

Essentials of Dielectromagnetic Engineering. H. M. Schlicke. Pp. 242. John Wiley & Sons, Inc., New York, 1961. Price $9.50.

Fundamentals of Modern Physics. Robert Martin Eisberg. Pp. 729. John Wiley & Sons, Inc., New York, 1961. Price $10.50.

The Design of Small Direct-Current Motors. A. F. Puchstein. Pp. 407. John Wiley & Sons, Inc., New York, 1961. Price $12.00.

Fourier Transforms. R. R. Goldberg. Pp. 76. Cambridge University Press, New York, 1961. Price $3.75.

Progress in Ceramic Sciences. J. E. Burke, Editor. Pergamon Press, New York, 1961. Price $10.00.

Transistor Logic Circuits. Richard B. Hurley. Pp. 363. John Wiley & Sons, Inc., New York, 1961. Price $10.50.

Elements of Nuclear Engineering. Glenn Murphy. Pp. 213. John Wiley & Sons, Inc., New York, 1961. Price $7.50.

Shielding Materials for Nuclear Reactors. A. N. Komarovskii. Pp. 145. Pergamon Press, New York, 1961. Price $9.50.

Interscience Monographs and Texts in Physics and Astronomy, Vol. IV, Physics of the Solar Chromosphere. Richard N. Thomas and R. Grant Athay, Editors.

Pp. 422. Interscience Publishers, Inc., New York, 1961. Price $15.50.

Physics and Archaeology. M. J. Aitken. Pp. 181. Interscience Publishers, Inc., New York, 1961. Price $6.00.

Turbulence: Classic Papers on Statistical Theory. S. K. Friedlander and Leonard Topper, Editors. Pp. 187. Interscience Publishers, Inc., New York, 1961. Price $6.00.

General Relativity and Gravitational Waves. J. Weber. Pp. 200. Interscience Tracts on Physics and Astronomy, New York, 1961. Price $4.50, cloth; $2.50, paper.

Extractive Metallurgy of Copper, Nickel, and Cobalt. Paul Queneau, Editor. Pp. 647. Interscience Publishers, Inc., New York, 1961. Price $22.50.

Techniques of High Energy Physics, Vol. V of Interscience Monographs and Texts in Physics and Astronomy. David M. Ritson, Editor. Pp. 540. Interscience Publishers, Inc., New York, 1961. Price $16.75.

Announcements

Internation Symposium on Aero-Space Nuclear Propulsion

An International Symposium on Aero-Space Nuclear Propulsion will be presented by AEC, IRE–PGNS, and NASA at the Riviera Hotel, Las Vegas, Nevada from October 24 to 26, 1961.

The honor speaker will be Dr. Glenn T. Seaborg, Chairman, U. S. Atomic Energy Commission.

Tours will include Jackass Flats Facilities at Nevada Test Site.

Tentative session topics are: Program review, Rover, Pluto, Anp, Snap, advance propulsion systems (Ion, Orion, etc.), engine characteristics and dynamics, recent advances in nucleonic instrumentation, engine simulation and control, nonnuclear instrumentation for areo-space propulsion, effects of nuclear radiation on controls and instruments, and nuclear instrumentation for aero-space propulsion.

Travel Grants

The Inter-University Committee on Travel Grants, representing American colleges and universities, wishes to announce that it is soliciting inquiries and applications from graduate students and scholars who wish to spend all or part of the academic year 1962–1963 engaged in study and research in the Soviet Union as participants in the academic exchange between the United States and the U.S.S.R.

American citizens under forty years of age are eligible if they are *graduate students*, *post-doctoral researchers*, or *faculty members* at the time of application. *Teachers of the Russian language in secondary schools* are also eligible. Persons from all fields of study are encouraged to apply.

A knowledge of Russian adequate to the needs of study and research is required. Other criteria for selection include intellectual ability, maturity, emotional stability, proven scholarly competence or indication of future professional promise, and substantial knowledge of both American and Russian history and culture.

Periods of study and research between one semester and fifteen months can be arranged. Persons wishing to spend a minimum of one academic year in the Soviet Union may be accompanied by their wives. Limitations imposed by the Soviet side prevent exchange participants' taking their families with them.

Funds are available to cover all or part of the exchange participant's expenses, including maintainance of family, depending on the participant's own financial needs and resources.

For further information and applications write to: Stephen Viederman, Deputy Chairman, Inter-University Committee on Travel Grants, 719 Ballantine Hall, Indiana University, Bloomington, Indiana.

Applications must be received no later than December 15, 1961 to be considered for the 1962–1963 exchange.

International Symposium on Photoelasticity

The International Symposium on Photoelasticity will be held on October 29–31, 1961 at Illinois Institute of Technology in Chicago.

The program consists of about 20 papers, 8 from Europe and Asia and the rest from the U. S. A. The topics will include photoelasticity, photoplasticity, photothermalelasticity, dynamic photoelasticity, and special equipment.

Cover Photograph

This month's cover is taken from the article, "Nonbasal Glide in Dislocation-Free Cadmium Crystals. II," by P. B. Price, on p. 1750 of this issue. The sequence of transmission electron micrographs provides direct evidence that immobile dislocation loops can be generated by moving screw dislocations. The photographs were taken while a thin (~2000 A) cadmium crystal was being strained in tension at −100°C inside an electron microscope. The dislocation ABA, originally in the screw orientation and having a 1/3 $[\overline{11}23]$ Burgers vector, became jogged at B while moving in the direction of the arrow. This jog exerted a retarding force which was only relieved when the two segments marked A returned to their original glide plane, thus pinching off an elongated dislocation loop (lying on the basal plane). The other loops in the photographs were formed during the movement of other screw dislocations.

NEW 4″ VACUUM DIFFUSION PUMP

New Design Offers BOTH Greater Speed and Reliability in Service

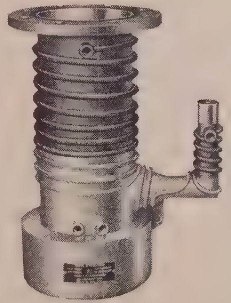

he only fractionating 4″ diffusion ump of its type, the Model HS4-750 tarts pumping at 400 microns – de- ivers 750 liters/sec. from 1 micron own and reaches ultimate pressures n the 10-10 Torr range. Regardless f variations in water temperature nd fluctuations in voltage, perform- nce is assured with only a 6 cfm nechanical backing pump. This out- tanding performance is made pos- ible by a completely new boiler and eater plus the new 4-stage fraction- ting jet design.

he Model HS4-750 combines all the features that add up to an deal diffusion pump: firmly anchored jet . . . silver soldered cooling oils . . . fluid-retaining foreline baffle . . . "cast-in" heater . . . low ackstreaming . . . quick heat-up and cool-down . . . minimum cleaning. mmediately available at $395.00 F.O.B. Newton, Mass.

Vrite for our free catalog containing peed curves . . . see why Model HS4- 50 is the best 4″ pump anywhere.

160 Charlemont Street, Dept. I-20
Newton 61, Massachusetts
DEcatur 2-5800

NRC
EQUIPMENT CORPORATION
A Subsidiary of National Research Corporation

WORLD WIDE HEADQUARTERS FOR . . .

LASER materials
Barium Fluoride, Calcium Fluoride, Magnesium Oxide and other LASER materials in stock and also compounded to your specifications

SINGLE CRYSTALS
Over 75 different single crystals in stock . . or grown to your specifications

THERMOELECTRIC MATERIALS
Including Bismuth Telluride, Calcium Telluride, Lead Telluride, Cuperous Sulphide, etc.

SCINTILLATION CRYSTALS
Including world's largest Plastic scintillators, scintillation blocks, sheets and forms

SEMICONDUCTOR CRYSTALS
Available in wide variety of compounds

NEUTRON DIFFRACTION PLATES
Large diameter metal crystals and plates for neutron spectrometry or diffraction use.

We grow crystals to customer specifications

SINGLE CRYSTAL DIVISION
Semi • Elements, Inc.
SAXONBURG BLVD. • SAXONBURG, PA. • U.S.A.
Phone FLanders 2-1548

THE CENCO LAB JACK

Imitation is the sincerest form of flattery and the Cenco Lab Jack has been overwhelmed with it. While some who have followed offer sound design, or others decent quality, none (as yet) has equalled Cenco's design and quality at the same price.

Developed in collaboration with Dr. Aaron B. Lerner of Yale University, the Cenco Lab Jack's simple, efficient design and precision construction are still its outstanding features. It will hold 100 lbs. easily, with complete stability at all elevations between 3 and 10¼ inches. Its scissors action permits steady, level, and quick raising or lowering—a feature especially noticeable when maneuvering fragile glassware.

With over 25,000 in use throughout the world today, we find only one trouble with the Cenco Lab Jack. It lasts too long.

NO. 19089-001-Cenco — Lerner Lab Jack $34.00

CENTRAL SCIENTIFIC
A Division of Cenco Instruments Corporation
1700 West Irving Park Road,
Chicago 13, Illinois

Mountainside, N. J.
Montreal
Santa Clara
Somerville, Mass.
Toronto
Los Angeles
Birmingham, Ala.
Ottawa

cenco

Vancouver
Houston
Cenco S.A., Breda, The Netherlands

BOSTON AREA SITE OF NEW LABORATORY FOR PHYSICAL SCIENCE

A modern and well-equipped research facility established by P. R. Mallory & Co. Inc. offers the following research staff openings for scientists in solid state physics, thin films, materials, metallurgy and electrochemistry.

THIN FILM SCIENTISTS—To initiate and supervise investigations of fundamental phenomena associated with dielectric, magnetic, resistive and semi-conductor films.

THEORETICAL PHYSICIST—Theoretical studies of basic solid state phenomena.

METALLURGIST—To establish metallurgical laboratory and initiate program of materials research.

ELECTRON MICROSCOPIST—To establish electron microscope facility for investigation of structure of films and other solid surfaces.

ELECTROCHEMISTS—For program on fuel cells and fundamental electrochemical phenomena.

SOLID STATE PHYSICIST—For experimental investigations of bulk properties of thermoelectric, semiconductor, and other interesting materials.

Expressions of interest may be submitted in confidence to Dr. S. P. Wolsky, *Director, Laboratory for Physical Science*. All qualified applicants will receive consideration regardless of race, creed, color or national origin.

P. R. MALLORY & CO. INC.
118 Main Street
Watertown, Massachusetts

10th ANNUAL
PHYSICS SHOW

January 24-27, 1962

Statler Hilton Hotel, N. Y.

An exhibit of scientific instruments, apparatus, components and technical books. Join the more than 60 companies who have reserved space, including:

- Baird-Atomic, Inc.
- Central Scientific Co.
- Consolidated Vacuum Corp.
- E-H Research Labs.
- Ealing Corp.
- Gaertner Scientific Corp.
- General Radio Co.
- Hamner Electronics Co., Inc.
- Harvey-Wells Corp.
- High Voltage Engineering Corp.
- Keithley Instruments, Inc.
- NRC Equipment Corp.
- Pacific Electric Motor Corp.
- Perkin-Elmer Corp.
- Philips Electronics
- Radiation Dynamics, Inc.
- Space Technology Labs.
- Spectromagnetic Industries
- Technical Measurement Corp.
- Varian Associates
- Victoreen Instrument Co.
- Veeco Vacuum-Electronics Corp.
- Welch Scientific Co.

The meeting will bring together five thousand physicist members of the American Physical Society and American Association of Physics Teachers. Over five hundred technical papers will be presented.

A limited number of booths are available.

Please write to:

Mr. T. Vorburger, Exhibit Manager
American Institute of Physics
335 East 45th Street
New York 17, N. Y.

A Superior Detector for Infra-Red Spectroscopy

GOLAY PNEUMATIC DETECTOR*

Among the characteristics that render the Golay Detector superior to other types of detectors for use in infra-red spectroscopy are:

1. **An effective sensitive area $\frac{3}{32}''$ in diameter.**
2. **Sensitivity of 6×10^{-11} watts RMS-ENI when used with "chopped beam" method and with recording time constant of 1.6 second.**
3. **Uniform sensitivity from the ultra-violet through the visible and the entire infra-red, and up to the micro-wave region.**
4. **Improved, drift-free, A. C. operated amplifier with step gain controls and four response periods.**

Write for EPLAB Bulletin No. 10

THE EPPLEY LABORATORY, INC.
SCIENTIFIC INSTRUMENTS
6 Sheffield Ave. • Newport • Rhode Island • U.S.A.

*Fundamental and experimental aspects of this detector are discussed in the following publications: Rev. Sci. Inst. *18*, 347 and 357 ('47); ibid. *20*, 816 ('49); Proc. IRE *40*, 1161 ('52).

278-8

ILFORD plates for electron microscopy

To meet the varied conditions encountered in electron micrography, we offer a complete spectrum of Ilford photographic plates.

If you work with low contrast specimens and need a high contrast, very fine grain emulsion—or if you work with high contrast specimens at relatively high magnifications and need a fast intermediate contrast emulsion—one of the following Ilford plates will meet your requirements:

PLATE	SPEED TO ELECTRONS	CONTRAST	GRAIN	NOTES
Ilford Rapid Process Experimental Plate	Very Fast	Medium to High	Fine	Fastest Plate of this series for all-around use; good contrast.
Ilford N.40 Process Plate	Fast	High	Very Fine	Slightly slower than the Rapid Process Experimental Plate, but with finer grain.
Ilford N.60 Photomechanical Plate	Medium	Very High	Extremely Fine	Excellent for specimens of low contrast which require a fine grain emulsion.

Available from authorized dealers in sizes to fit all makes of instruments. For further details write to:

ILFORD INC. 37 WEST 65th STREET, NEW YORK 23, N. Y.

Just published:

Field Theory Handbook

Including Coordinate Systems, Differential Equations, and their Solutions

By Professor Dr. Parry Moon,
Massachusetts Institute of Technology,
Cambridge, Mass./USA,
and Professor Dr. Domina Eberle Spencer,
University of Connecticut,
Storrs, Conn./USA

With 59 figures. VIII, 236 pages 8 vo. 1961.
Cloth—DM 69,—($17.25)
In English

CONTENTS

Eleven coordinate systems · Transformations in the complex plane · Cylindrical systems · Rotational systems · The vector Helmholtz equation · Differential equations · Functions · Bibliography · Appendix · Symbols · Author Index and Subject Index.

FOR INFORMATION

This book is a compendium of equations for the physicist and the engineer working with electrostatics, magnetostatics, electric currents, electromagnetic fields, heat flow, gravitation, diffusion, optics, or acoustics. It tabulates the properties of 40 coordinate systems, states the Laplace and Helmholtz equations in each coordinate system, and gives the separation equations and their solutions.

Available from every scientific bookseller

SPRINGER-VERLAG • BERLIN
GÖTTINGEN • HEIDELBERG

TRANSLATIONS OF . . . .

SOVIET JOURNALS

Published by the American Institute of Physics with the cooperation of the National Science Foundation.

Soviet Physics—JETP

Monthly. Translation of *Zhurnal Eksperimental'noi I Teoreticheskoi Fiziki* of Academy of Sciences, USSR.

Soviet Physics—SOLID STATE

Monthly. Translation of *Fizika Tverdogo Tela* of Academy of Sciences, USSR.

Soviet Physics—TECHNICAL PHYSICS

Monthly. Translation of *Zhurnal Tekhnicheskoi Fiziki* of Academy of Sciences, USSR.

Soviet Physics—DOKLADY

Bimonthly. Translation of the Physics Section of Proceedings of Academy of Sciences, USSR.

Soviet Physics—ACOUSTICS

Quarterly. Translation of *Akusticheskii Zhurnal* of Academy of Sciences, USSR.

Soviet Physics—CRYSTALLOGRAPHY

Bimonthly. Translation of *Kristallografiya* of Academy of Sciences, USSR.

Soviet Physics—USPEKHI

Bimonthly. Translation of *Uspekhi Fizicheskikh Nauk* of Academy of Sciences, USSR.

Soviet Astronomy—AJ

Bimonthly. Translation of *Astronomicheskii Zhurnal* of Academy of Sciences, USSR.

Send orders and inquiries to:

American Institute of Physics
335 East 45 Street, New York 17, N. Y.

PHYSICISTS

The International Nickel Co., Inc. is seeking Physicists with Doctor's or Master's degrees in Physics or Metallurgy with Physics minor for its Research Laboratory in New Jersey. Previous experience desirable but not essential.

Assignments involve studies of structures and properties of metals and alloys, employing X-ray diffraction, X-ray fluorescence, electron microscopy, electron probe microanalysis, and other advanced laboratory techniques. Publication of papers is encouraged.

Applicants should send complete resume to:

Director of Research, Dept. 20

INCO
TRADE MARK

THE INTERNATIONAL
NICKEL COMPANY, INC.
67 Wall Street
New York 5, New York

All qualified applicants will be considered for employment without regard to race, creed, color or national origin.

High Performance ELECTROMAGNETS and Power Supplies

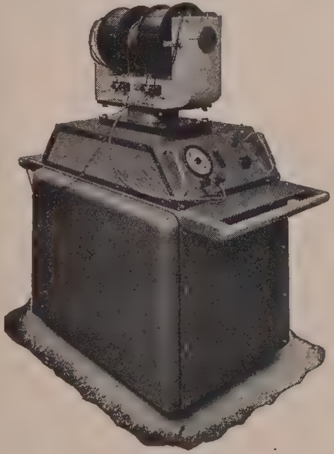

RUGGEDNESS

4″ Electromagnet Type A
(4″ pole diameter)
Fields up to 25,000 gauss.
Homogeneity of at least 1 part in 10^5 in ½ cc.

ROTATION

Rotating Base Type AE
360° scale.
Positive friction lock.

STABILITY

Current-Stabilized Power Supply Unit Type B.

Also available:—
1½″ Electromagnet Type C—for Teaching purposes.
7″ Electromagnet Type E—for Electron Resonance Work.
8″ Electromagnet Type D—for Electron Resonance and Nuclear Magnetic Resonance work.
Direct Reading Magnetometer Type G.
Proton Resonance Magnetometer Type P.

NEWPORT INSTRUMENTS
(Scientific & Mobile) Ltd
10 CRAWLEY ROAD, NEWPORT PAGNELL, BUCKS
Telephone: NEWPORT PAGNELL 401/2

What do you need to know about

PURE FERRIC OXIDES
MAGNETIC IRON OXIDES

Since the final quality of your production of ferrites and magnetic recording media depends on the proper use of specialized iron oxides—you'll find it mighty helpful to have the latest, authoritative technical data describing the physical and chemical characteristics of these materials. This information is available to you just for the asking. Meanwhile, here are the highlights.

PURE FERRIC OXIDES—For the production of ferrites, both hard and soft, we manufacture a complete range of iron oxides having the required chemical and physical properties. They are produced in both the spheroidal and acicular shapes with average particle diameters from 0.2 to 0.8 microns. Impurities such as soluble salts, silica, alumina, and calcium are at a minimum while Fe_2O_3 assay is 99.5+%. A Tech Report tabulating complete chemical analysis, particle shape, particle size distribution, surface area, etc., of several types of ferric oxides, hydrated ferric oxide, and ferroso-ferric oxide is available.

MAGNETIC IRON OXIDES—For magnetic recording—audio, video, computer, and instrumentation tapes; memory drums; cinema film stripping; magnetic inks; carbon transfers; etc.—we produce special magnetic iron oxides with a range of controlled magnetic properties. Both the black ferroso-ferric and brown gamma ferric oxides are described in a Data Sheet listing magnetic properties of six grades.

If you have problems involving any of these materials, please let us go to work for you. We maintain fully equipped laboratories for the development of new and better inorganic materials. Write, stating your problem, to C. K. Williams & Co., Dept. 38, 640 N. 13th St., Easton, Penna.

WILLIAMS
COLORS & PIGMENTS

Pigment Technology at its best

E. ST. LOUIS, ILLINOIS · EASTON, PENNSYLVANIA · EMERYVILLE, CALIFORNIA

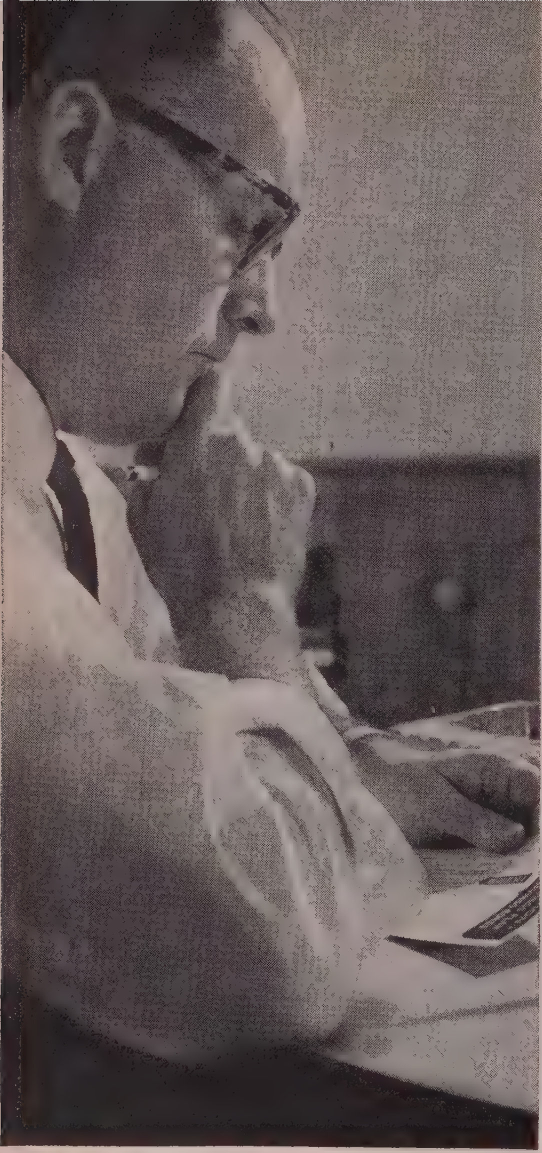

IF YOU DON'T SEE IT, YOU WON'T SPEND IT. Millions of people sign up with the Payroll Savings Plan at work because it helps them save money that otherwise might slip through their fingers.

EVERY Savings Bond you own—old or new—earns ½% more than ever before, when held to maturity.

You save more than money
with U.S. Savings Bonds

The U.S. Government does not pay for this advertising. The Treasury Department thanks The Advertising Council and this magazine for their patriotic donation.

How to Save Money

in spite of yourself

Many Americans have discovered a way to save mone without really changing their spending habits. You simply ask the company where you work to set aside mone every payday for U.S. Savings Bonds. The Payroll Savings Plan makes sure that it goe into savings before you can dribbl it away. And, if you buy a $25.0 Bond a month (cost $18.75) in 4 months you'll have Bonds wort $1,000 at maturity. You reall won't miss it because it adds up t only 63¢ a day.

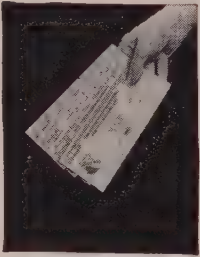

UNCLE SAM PROTECTS THEM. U.S. Savings Bonds are fully backed by the U.S. Government. They can be cashed like money anytime at any bank. Your money is safe, yet readily available in Bonds.

U.S. Savings Bonds are more than a good way to save

• You can save automatically wit the Payroll Savings Plan. • You no earn 3¾% interest to maturity. • Yo invest without risk under a U.S Government guarantee. • You money can't be lost or stolen. • Yo can get your money, with interes anytime you want it. • You sav more than money—you help you Government pay for peace. • Yo can buy Bonds where you work or ban

WILL THEY LIVE IN A PEACEFUL WORLD? Lots of Americans do more than "hope so". They're buying U.S. Savings Bonds to help pay for the strength America needs to help keep the world at peace.

announcing

1" & 2" ULTRA-HIGH VACUUM VALVES

and COMPLETE LINE of MATCHED FITTINGS

- Bakeable to 450° C
- Useful to 10^{-10} mm Hg or lower
- Conductance variable from 60 liter/sec to 10^{-13} liter/sec with 2" valve; from 10 liter/sec to less than 10^{-14} liter/sec with 1" valve
- Constructed entirely of low vapor pressure metals insuring minimum contamination
- Available from stock

WRITE OR PHONE FOR COMPLETE SPECIFICATIONS

GP Granville-Phillips Company

P. O. Box J-198 Pullman, Washington • telephone LOgan 4-1130

MICROWAVE PHYSICISTS and ENGINEERS

We are seeking persons to participate in our *millimeter wave research programs* in the area of semiconductor devices, masers, electron tubes, and special instrumentation. Background in 1 or more of the following fields is required:

- **Microwave Semiconductors & Semiconductor Devices**
- **Microwave Solid State Resonance Phenomena**
- **Microwave Tubes**
- **Microwave Components & Circuits**
- **Millimeter Wave Components & Instrumentation**

Excellent opportunities are offered at the PhD, Masters, and Bachelor level.

Please submit resume to Mr. F. J. Loyer

GENERAL TELEPHONE & ELECTRONICS LABORATORIES

All qualified applicants will receive consideration for employment without regard to race, creed, color or national origin.

Subsidiary of **GENERAL TELEPHONE & ELECTRONICS** GENERAL SYSTEM

208–20 Willets Point Blvd—Bayside, Long Island, New York

WHAT HAPPENS WHEN A NATION SPENDS **MORE** ON GAMBLING THAN IT SPENDS FOR HIGHER EDUCATION?

If you can find any Romans around, ask them. They lived pretty high on the hog in their day. That is, until some serious-minded neighbors from up North moved in. The rest is ancient history.

You'd think their fate would have taught us a lesson.

Yet today we Americans spend twenty billion dollars a year for legalized gambling, while we spend a niggardly four-and-a-half billion for higher education. Think of it! Over four times as much! We also spend six-and-a-half billion dollars a year for tobacco, nine billion dollars for alcoholic beverages, and billions more on other non-essentials.

Can't we read the handwriting on the wall?

Our very survival depends on the ability of our colleges and universities to continue to turn out thinking men and women. Yet today many of these fine institutions are hard put to make ends meet. Faculty salaries, generally, are so low that qualified teachers are leaving the campus in alarming numbers for better-paying jobs elsewhere. In the face of this frightening trend, experts estimat that by 1970 college applications will have doubled.

If we are to keep our place among the leading nations o the world, we must do something about this grim situation before it is too late. The tuition usually paid by college student covers less than half the actual cost o his education. The balance must somehow be made u by the institution. To meet this deficit even the mos heavily endowed colleges and universities have to depend upon the generosity of alumni and public spirite citizens. In other words, they depend upon *you.*

For the sake of our country and our children, won't yo do your part? Support the college of your choice *today* Help it to prepare to meet the challenge of tomorrow. Th rewards will be greater than you think.

It's important for you to know what the impending college cris means to you. Write for a free booklet to HIGHER EDUCATIO Box 36, Times Square Station, New York 36, New York.

ADVERTISING COUNCIL · PUBLIC SERVICE ·

Sponsored as a public service
in co-operation with The Council for Financial Aid to Education

HIGHER EDUCATIO
KEEP IT BRIGHT

PERIODICAL PUBLICATIONS

OF THE

INSTITUTE OF PHYSICS AND

THE PHYSICAL SOCIETY

●

Journal of Scientific Instruments

A monthly publication dealing with the principles, construction and use of scientific instruments.

£6 per annum

British Journal of Applied Physics

A monthly publication dealing with applications of physics, especially in industry.

£6 per annum

Proceedings of the Physical Society

A monthly publication containing papers describing original work in physics.

£12 12*s*. per annum

Reports on Progress in Physics

An annual publication containing comprehensive reviews—issued in April.

£4 4*s*. per annum

Available from:

The Institute of Physics
and The Physical Society
47 Belgrave Square, London S.W.1

PHYSICISTS

Theoretical
Studies in

PLASMA PHYSICS
NUCLEAR PHYSICS
ASTROPHYSICS
MAGNETOHYDRODYNAMICS

Republic's Missile Systems Division has pursued a continuing program of research in these general areas for a number of years. Investigations are now being broadened, and new staff appointments made.

Work is largely at the doctoral level. Prominent university staff members are available for consultation on many projects. Publication of results in appropriate scientific journals is encouraged.

Physicists with advanced degrees are invited to write in confidence to

Mr. Paul Hartman
Technical Employment

All qualified applicants will receive consideration for employment without regard to race, creed, color or national origin.

MISSILE SYSTEMS DIVISION

REPUBLIC
AVIATION CORPORATION

223 Jericho Turnpike, Mineola, Long Island, N.Y.

(A thriving suburban community less than one hour from New York City)

INDEX TO ADVERTISERS

Name — *Page*

AEROSPACE CORPORATION ... viii

ASARCO, AMERICAN SMELTING & REFINING COMPANY xvii

BELL TELEPHONE LABORATORIES vii

CENTRAL RESEARCH LABS., INC. vi

CENTRAL SCIENTIFIC CO. xxi

Manufacturers of Cenco physical apparatus and instruments to meet all requirements of University, College and High School Physics Laboratories. Specializing in high vacuum pumps and development of instruments and apparatus for various sciences.

EASTMAN KODAK COMPANY .. ix

THE EPPLEY LABORATORY, INC. xxiii

FERRANTI ELECTRIC, INC. iii

GENERAL RADIO CO. .... Cover 4

Manufacturers of electronic measuring instruments; vacuum-tube voltmeters, amplifiers, and oscillators; wave analyzers, noise meters and analyzers, stroboscopes, laboratory standards of capacitance; inductance and frequency; impedance bridges, decade resistors and condensers, air condenser and variable inductors; rheostats, variacs, transformers; other laboratory accessories.

Name — *Page*

GENERAL TELEPHONE & ELECTRONICS LABORATORIES xxvii

GRANVILLE-PHILLIPS COMPANY xxvii

HAMNER ELECTRONICS CO., INC. xxxii

THE HARSHAW CHEMICAL CO. .... Cover 2

HARVARD UNIVERSITY PRESS x

HUGHES AIRCRAFT COMPANY xix

ILFORD INC. xxiii

ILIKON CORPORATION ...... Cover 3

THE INTERNATIONAL NICKEL COMPANY, INC. xxv

LINCOLN LABORATORY, M.I.T. . xiv

LOS ALAMOS SCIENTIFIC LAB. . xii

P. R. MALLORY & CO. INC. xxii

NRC EQUIPMENT CORP. xxi

Manufacturers of standard and special high vacuum components, equipment, and systems including mechanical booster, and diffusion pumps; gauges; valves; seals; connectors; melting and heat-treating furnaces; coaters; impregnators; gas in metal analyzers; driers and freeze driers; altitude chambers and leak detectors.

INDEX—*Continued*

Name *Page*

NEWPORT INSTRUMENTS LTD. xxv

RADIO CORP. OF AMERICA xiii

REPUBLIC AVIATION CORP. ... xxix

S. A. M. E. S. xviii

SEMI-ELEMENTS, INC. xxi

STL PRODUCTS, DIV. OF SPACE TECHNOLOGY LABORATORIES iv

SPRINGER—VERLAG xxiv

SYLVANIA ELECTRONIC SYSTEMS, AMHERST LABORATORIES xv

TECHNICAL MEASUREMENT CORP. iii
Nuclear instrumentation—single and multichannel pulse height analyzers, liquid scintillation beta spectrometers, reactor flux plotting systems, sealers, precision high voltage power supplies, ratemeters, linear amplifiers and custom nuclear system design.

VARIAN ASSOCIATES VACUUM DIVISION xi

Name *Page*

WELCH SCIENTIFIC CO., W. M. . xx
Manufacturers of high-vacuum pumps, both mechanical and diffusion; vacuum gauges; electrical measuring instruments; physics equipment; and other items for the physical and chemical laboratories.

C. K. WILLIAMS & CO. xxv

POSITION OPEN

SOLID STATE RESEARCH

Opening for Ph.D. in physical chemistry, physics or metallurgy. We are producers of highest quality silicon and one of our chief research interests in this field is vapor-deposited single-crystal layers. We are interested in having as accurate and comprehensive information as possible on such structures and on their possible application to devices. We are already engaged in electrical and optical studies and are most desirous of deepening and broadening these studies. A sufficiently qualified applicant would have ample opportunity for choosing and exploiting directions as well as specific problems of interest. Other fields of research in semiconductors are gallium arsenide, germanium and thermoelectric materials. Reply in confidence to Box 961-B, Journal of Applied Physics, 335 East 45th St., New York 17, N. Y.

TUBULAR SLIDE CONTACT RHEOSTATS
RESISTORS
Toroidal Winding Machines
REX RHEOSTAT CO.
149-a Babylon Tpke. Roosevelt, L. I., N. Y.

HAMNER

A-8 DESIGN
ULTRA HIGH SPEED, NON-OVERLOAD

LINEAR AMPLIFIERS

Unexcelled A-8 Characteristics . . . PLUS

- NEW LAYOUT WITH FINE GAIN CONTROL
- OPTIONAL PICK-OFF GATE FOR FAST COINCIDENCE WORK
- YOUR CHOICE OF PULSE ANALYZING SECTION

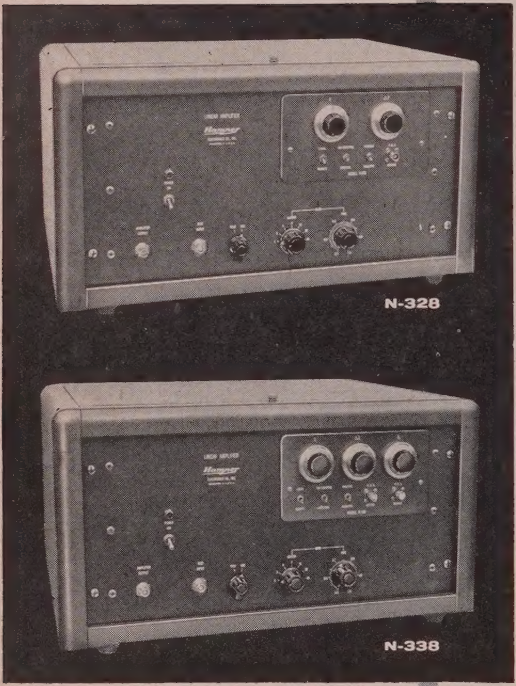

The A-8 Design Amplifier has found wide usage in nuclear physics laboratories where one or more of the following three conditions exist:

1. Very large overload signals will be present.
2. Counting rates up to 250kc will be present.
3. It is required to do medium-fast coincidence work on pulses having slow risetimes.

In these three areas, the A-8 design represents a great improvement over previous units.

These results are achieved through the use of double differentiation with two delay lines, thus providing for fast baseline recovery even under high-duty cycle operation. Overload performance is enhanced by preventing the Amplifier from overloading before differentiation and by not allowing overload to occur inside a feedback loop.

N-308

AMPLIFIER ONLY

Maximum Gain: 7000 in main Amplifier (additional gain of 1, 3 or 10 in Pre-Amp).

Gain Stability: 0.25%/day.

Risetime: About 0.2 μs.

Linearity: 0.1% Integral Linearity, 3-100 volts into 10K or greater load.

Overload Recovery: About 8 μs for 4000 times overload.

Maximum Counting Rate: About 250,000 CPS.

N-318

AMPLIFIER WITH INTEGRAL DISCRIMINATOR

Amplifier Section: See details on N-308.

Discriminator Section: This Discriminator is based on the P. R. Bell Design.

Range: 4-100 volts by 10-turn helipot.

Linearity: Better than 0.5%, 3-100 volts.

Stability: Better than 50 mv/day.

Resolving Time: About 1.2 μs.

Output Pulse: 1 μs wide, +50 volts high into 10K load.

N-328

AMPLIFIER WITH PULSE-HEIGHT ANALYZER

Amplifier Section: See details on N-308.

Output Pulse-Height: (25 volts, positive or negative by switch.)

Baseline:
- Control—By 10-turn helipot.
- Range—3-100 volts by 10-turn helipot.
- Linearity—0.1%, 3-100 volts.
- Stability—Better than 50 mv/day.

Window:
- Control—By 10-turn helipot.
- Width—0-10 volts by 10-turn helipot (0-20, 30, 40 or 50 volts at slight extra cost).

N-338

Amplifier with Integral Discriminator similar to N-318, and independent Pulse-Height Analyzer similar to N-328.

N-670 COINCIDENCE PICK-OFF. In Coincidence Work, the time of the pulse zero crossover is largely independent of pulse-height. For this reason, it is well related in time to the event causing the pulse and is useful for coincidence studies. Coincidence resolving times of from 30-100 mμs can be successfully used. The N-670 is an optional subchassis which detects the zero crossing and presents an output for coincidence work.

Hamner

HAMNER
ELECTRONICS CO., INC.
P. O. Box 531, Princeton, N. J.
PEnnington 7-1320

$^{-3}$ to 10^{-12} mm Hg + AUTOMATIC CURRENT CONTROL . . .

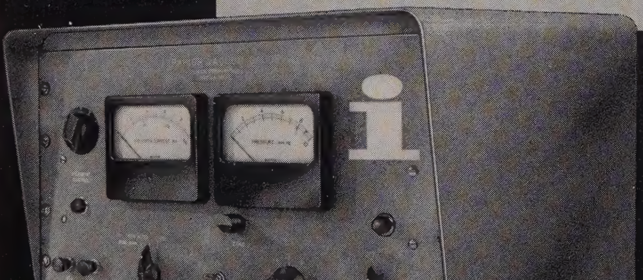

Ilikon's new Model 1020 Ultrahigh Vacuum Gage Control can be used with any Bayard-Alpert or Nottingham type ionization gage to provide stable, linear measurements from 10^{-3} to 10^{-12} mm Hg . . . and the Model 1020 will automatically control a pre-set emission current to less than 1%. These are just two reasons why the Model 1020 is the most versatile gage control available today. $895.00 (includes Model 810 Ionization Gage).

Ilikon also manufactures complete ultrahigh vacuum systems and a full line of system components.

ILIKON

ILIKON CORPORATION · NATICK INDUSTRIAL CENTRE · NATICK, MASSACHUSETTS · CEdar 5-8220

NEW LOCKING CONNECTORS

with Outstanding Characteristics from DC to 8000 Mc

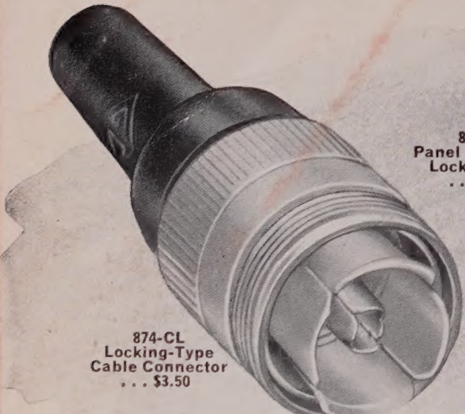

874-CL
Locking-Type
Cable Connector
. . . $3.50

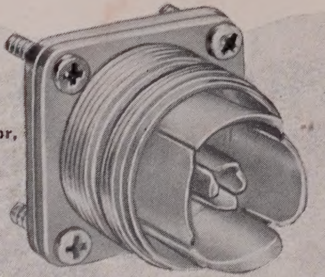

874-PL
Panel Connector,
Locking Type
. . . $3.75

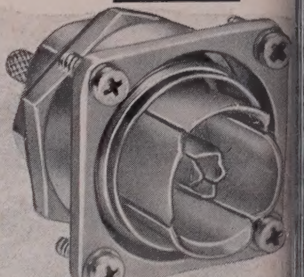

874-PRL Recess
Panel Connect
Locking Type . . . $4

Unlike Most Connectors, the G-R 874...

- ★ has extremely low VSWR . . . typically less than 1.02 to 4 Gc; less than 1.07 to 8 Gc.
- ★ has low leakage; down at least 115 db for locking types at frequencies to 7 Gc.
- ★ is available in locking or non-locking types for semi-permanent or quick connect-disconnect setups.
- ★ forms a rigid, uniform 50-ohm section when connected; provides strong friction-grip contact through multiple-spring fingers.

Quantity and O.E.M. Discounts Available.

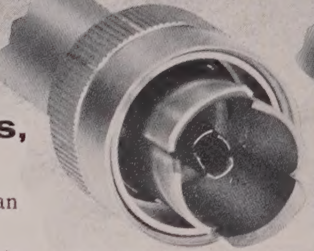

874-BL Basic Locking Connector . . . $2.50
for rigid air lines

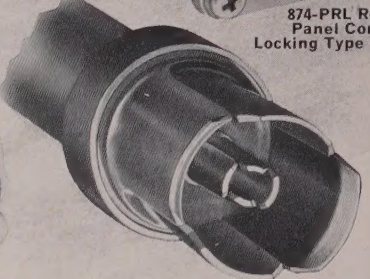

874-B Basic Connector
(Nonlocking) . . . $1.60

Nonlocking Cable and Panel Connectors also available

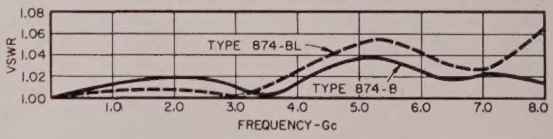

Any 874 Connector Mates with any other . . . Eliminating continual searches for Male or Female Counterparts.

Put One Panel Connector on all your equipment...

yet conveniently give your customer any popular output connection he wants

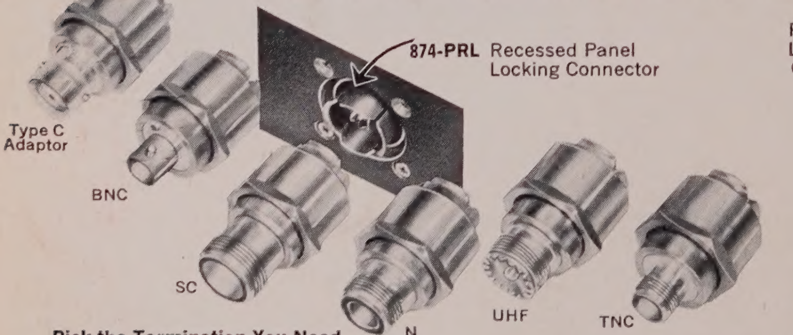

Pick the Termination You Need.
Adaptor Prices, $5 to $10. Other types soon to be available.

Protrudes
Less than
One Inch

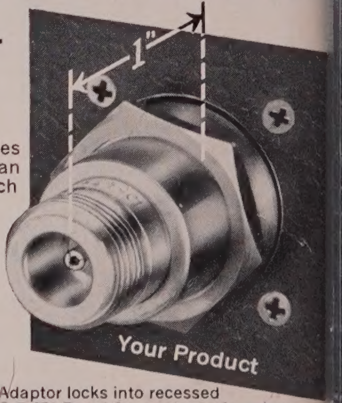

Adaptor locks into recessed G-R 874 Panel Connector to form low-VSWR connection. Panel Connector is co pletely hidden. Resulting fitting can permanent, or readily changed . . . is el trically excellent, trim in appearance.

GENERAL RADIO COMPANY

WEST CONCORD, MASSACHUSETTS

Please Send Me

☐ Complete specifications for the 874 Coaxial Connector.

☐ Engineering Papers: (1) Methods for high precision measurement of VSWR of coaxial connectors (2) Design techniques for improvement of connector VSWR and repeatability of characteristics (3) RF leakage characteristics of popular coaxial cables and connectors, 500 Mc to 7.5 Gc.

NAME________________ TITLE________________

COMPANY________________

DEPT. OR DIVISION________________ Room, Bldg., Code or Mail Station________________

STREET ADDRESS________________

CITY________________ ZONE______ STATE________